Cyclic Deformation, Fracture, and Nondestructive Evaluation of Advanced Materials

SECOND VOLUME

M. R. Mitchell and
Otto Buck, editors

ASTM
STP 1184

STP 1184

Cyclic Deformation, Fracture, and Nondestructive Evaluation of Advanced Materials: Second Volume

M. R. Mitchell and Otto Buck, Editors

ASTM Publication Code Number (PCN):
04-011840-30

ASTM
1916 Race Street
Philadelphia, PA 19103
Printed in the U.S.A.

Library of Congress Cataloging-in-Publication Data

Cyclic deformation, fracture, and nondestructive evaluation of advanced materials. Second volume/M. R. Mitchell and Otto Buck, editors.
p. cm.—(STP: 1184)
Contains papers presented at the Second Symposium on Cyclic Deformation, Fracture, and Nondestructive Evaluation of Advanced Materials held in Miami, Florida, 16–17 Nov. 1992, sponsored by ASTM Committee E-8 on Fatigue and Fracture.
"ASTM publication code number (PCN) 04-011840-30."
Includes bibliographic references and index.
ISBN 0-8031-1989-5
1. Composite materials—Fatigue—Congresses. 2. Non-destructive testing—Congresses. I. Mitchell, M. R. (Michael R.), 1941– . II. Buck, Otto. III. ASTM Committee E-8 on Fatigue and Fracture. IV. Symposium Cyclic Deformation, Fracture, and Nondestructive Evaluation of Advanced Materials (2nd: 1994: Miami, Florida) V. Series: ASTM special technical publication; 1184.
TA418.9.C6C83 1994
620.1'186—dc20 94-32123
CIP

Photocopy Rights

Peer Review Policy

Each paper published in this volume was evaluated by three peer reviewers. The authors addressed all of the reviewers' comments to the satisfaction of both the technical editor(s) and the ASTM Committee on Publications.

The quality of the papers in this publication reflects not only the obvious efforts of the authors and the technical editor(s), but also the work of these peer reviewers. The ASTM Committee on Publications acknowledges with appreciation their dedication and contribution to time and effort on behalf of ASTM.

Printed in Baltimore, MD
October 1994

Foreword

This publication, *Cyclic Deformation, Fracture, and Nondestructive Evaluation of Advanced Materials: Second Volume,* contains papers presented at the Second Symposium on Cyclic Deformation, Fracture, and Nondestructive Evaluation of Advanced Materials, which was held in Miami, Florida, 16–17 Nov. 1992. The symposium was sponsored by ASTM Committee E-8 on Fatigue and Fracture. The symposium co-chairmen were M. R. Mitchell, Rockwell International Science Center, Thousands Oaks, California, and Otto Buck, Ames Laboratory, Iowa State University, Ames, Iowa.

Contents

Overview

About two years have passed since the proceedings of the First Symposium on Cyclic Deformation, Fracture, and Nondestructive Evaluation of Advanced Materials (ASTM STP 1157) were published. As intended, and due to the success of this first symposium, the Second Symposium was held in November 1992 in Miami, Florida, on the same topics, with even greater participation of an international technical community demonstrating an enhanced interest in the implementation and use of engineered advanced metallic, ceramic, and polymeric materials and composites thereof. These materials are now finding their way into structural and engine applications, usually by "insertion programs." However, due to their complex nature, there is still a lot to be learned about their processing, as well as their fatigue and fracture behavior under the service conditions they are exposed to. Inspection methods for the detection of materials damage are, to a large degree, still in their infancy. Their development will clearly be of fundamental importance such that the results can be correlated with the components' remaining life for improved reliability in a fitness-for-service dominated strategy. Academic institutions and aerospace-related research laboratories, as well as industry, have contributed to these proceedings to provide a well-balanced overview of the state-of-the-art of this subject matter.

The first part of the book covers fatigue crack initiation, crack growth, and fracture toughness of advanced structural materials such as silicon nitride, special titanium alloys and steels, particle-reinforced aluminum alloys, cobalt-based alloys, thermoplastics, and graphite-epoxy composites. In some cases, the effects of crack closure as well as crack bridging on fatigue crack growth are discussed. Discussions also include complex multiaxial cyclic deformation and creep behavior. Effects of thermal fatigue on coatings and their optical properties are reported. Other interesting applications include the fatigue and fracture properties of high-strength, high-conductivity alloys, useful to the electric power industry.

The remainder of the book is dedicated to the nondestructive evaluation of advanced materials that may have manufacturing defects and/or have experienced in-service damage. Still very popular for defect and damage detection in these materials is the so-called acoustic-ultrasonic technique, which is a sophisticated form of coin-tapping. In one case, the change of the materials' compliance has been correlated to the overall damage. On the other hand, microfocus X-rays provide information on the location of the defects, as can focused ultrasonic beams in weldments.

The symposium chairmen appreciate, certainly, the cooperation and diligence of the authors of the manuscripts. Each manuscript was thoroughly reviewed by at least three experts in the field. The assistance of the ASTM staff in coordinating the publication efforts is very much appreciated and made our lives so much easier. We, the organizers, hope that we have another opportunity for bringing such a group of experts together at a Third Symposium on Cyclic Deformation, Fracture, and Nondestructive Evaluation of Advanced Materials.

M. R. Mitchell

Rockwell International Science Center, Thousand Oaks CA 91360; symposium chairman and editor

Otto Buck

Iowa State University, Ames Laboratory, Ames, IA 50011; symposium chairman and editor

David C. Salmon[1] *and David W. Hoeppner*[2]

In-Situ SEM Observation of Fatigue Crack Propagation in NT-154 Silicon Nitride

REFERENCE: Salmon, D. C. and Hoeppner, D. W., **"In-Situ SEM Observation of Fatigue Crack Propagation in NT-154 Silicon Nitride,"** *Cyclic Deformation, Fracture, and Nondestructive Evaluation of Advanced Materials: Second Volume, ASTM STP 1184*, M. R. Mitchell and O. Buck, Eds., American Society for Testing and Materials, Philadelphia, 1994, pp. 1–18.

ABSTRACT: A miniature 4-kN servohydraulic three-point bend load frame coupled to a scanning electron microscope (SEM) was developed to allow direct observation of fatigue and fracture processes in ceramic materials at magnifications up to ×20 000. Two series of fatigue crack growth experiments were conducted on Norton/TRW NT-154 silicon nitride, one using the in-situ three-point bend system and the other using compact tension specimens in a conventional test system. The objectives of the work were to ascertain whether crack growth under cyclic loading is a manifestation of a load-level dependent mechanism or a true cyclic effect, and to identify mechanisms of fatigue crack propagation at a microstructural level. Tests were conducted at room temperature and load ratios of 0.1 to 0.4, both in air and vacuum. Results of both series showed a marked load ratio effect and a distinct cyclic loading effect. Crack propagation was highly discontinuous, occurring on individual cycles at a rate approaching that for fracture and arresting between these growth increments for hundreds or thousands of loading cycles. Between growth increments there were no detectable changes at the crack tip; however, crack wake features such as bridges and interlocking grains decayed and lost their ability to transfer load.

KEYWORDS: ceramics, silicon nitride, fatigue (materials), scanning electron microscopy, crack propagation, residual stress, advanced materials

Utilization of monolithic ceramics in structural applications has been limited by two major obstacles: low toughness and poor reliability. Development of reliable life prediction methods is dependent, in part, on an understanding of the growth characteristics of subcritical cracks that may eventually lead to failure. Subcritical crack growth in ceramics can occur as a result of a variety of factors, including sustained loading, cyclic loading, and environment. This work focuses on growth resulting from fatigue loading, a field that has tended to receive less attention than other forms of subcritical growth in ceramics. The word "fatigue" in this work is used in accordance with ASTM Standard Definitions of Terms Relating to Fatigue (E 1150-87) and refers to a cyclic loading process, not a sustained or monotonic loading process as is often the case in ceramics literature.

Early work on fatigue of ceramics and glasses often suggested that these materials were not subject to degradation from cyclic loading, but that observed subcritical crack growth was simply a manifestation of environmentally assisted sustained-load cracking [*1*]. The lack of appreciable crack tip plasticity furthered the notion that fatigue was of little importance,

[1] Senior mechanical engineer, Sarcos Research Corporation, 360 Wakara Way, Salt Lake City, UT 84108.

[2] Professor of Mechanical Engineering, Quality and Integrity Design Engineering Center, The University of Utah, 3209 MEB, Salt Lake City, UT 84112.

although experimental evidence of this phenomenon in ceramics existed as early as 1956 [*2*]. Since about 1985 the pace of research has increased and fatigue has been reported to occur in transforming ceramics [*3–5*], nontransforming materials such as alumina [*6,7*] and silicon nitride [*8–14*], and ceramic composites [*15–18*]. Much of the experimental work has involved generation of stress-life data, which is outside the scope of the present work. Crack growth results from "physically long" cracks—those exceeding several millimetres in length—frequently appear to follow a Paris relationship, but with exponents that are typically 10 to 40 times the values associated with metals [*19–22*]. The presence of crack growth thresholds also has been reported, usually based on the operational definition in ASTM Standard Test Method for Measurements of Fatigue Crack Growth Rates (E 647-88a) of that stress intensity range corresponding to a growth rate of 10^{-10} m/cycle. The extreme sensitivity of growth rate to small changes in stress intensity makes it difficult to distinguish the asymptotic behavior often seen in metals. Work on "small" cracks, including both natural cracks and those induced by indentation, has shown that growth occurs at applied stress intensity ranges significantly below the "long crack" threshold. This behavior has been explained in terms of the restricted crack tip shielding due to the limited crack wake and residual stress fields in the case of indentation-induced cracks. In all cases, however, the understanding of fatigue crack propagation mechanisms is at a very preliminary stage. While various mechanisms have been postulated, experimental confirmation is generally lacking [*1,15,23,24*].

This experimental investigation was conducted to achieve the following objectives:

1. To ascertain whether crack growth under cyclic loading in silicon nitride is a manifestation of an environmentally assisted load-level based mechanism, or whether an intrinsic cyclic-load crack growth mechanism exists.
2. To identify, in a qualitative way, mechanisms of crack propagation at a microstructural level.

Experimental Procedure

Two series of fatigue crack propagation experiments, one using compact tension (C(T)) specimens and the other three-point bend specimens, were conducted on Norton/TRW NT-154 silicon nitride at room temperature (22 to 25°C). The microstructure of NT-154, shown in Fig. 1, consists of silicon nitride grains (dark), some of which are elongated, plus an yttrium-rich intergranular phase (light). The material is hot isostatically pressed and has undergone an intergranular phase crystallization heat treatment.

Compact Tension Crack Growth Tests

The C(T) tests were conducted on specimens of width, W, 25.4 mm and thickness, B, 6.35 mm in air (15 to 30% relative humidity) using a 10-Hz sinusoidal waveform and load ratios of 0.1, 0.2, 0.3, and 0.4. Seven specimens were used, but 25 tests were conducted by stopping each test just prior to specimen fracture. Crack lengths were monitored both optically and by an automated compliance technique [*25*]. Precracks were formed from chevron notches using cyclic tension-tension loading and two to four load-shedding steps. The test procedure followed ASTM E 647-88a as closely as feasible. Several requirements in the standard were difficult to satisfy, however, and the deviations are listed below:

1. Precrack lengths were too short in some tests. The standard requires a minimum precrack length 1.6 mm past the chevron for the specimen size used. In the worst case the precrack was only 0.6 mm past the chevron.

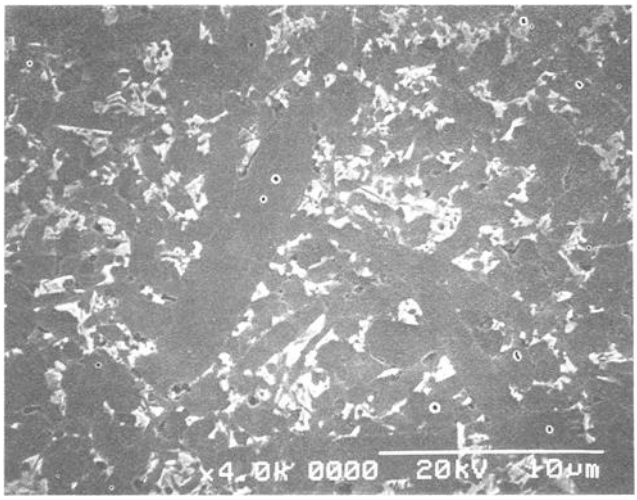

FIG. 1—*Microstructure of NT-154 silicon nitride polished with 0.25-μm diamond paste and plasma etched.*

2. The crack length variation between front and back faces of the specimen was 1 to 1.5 mm in numerous tests. The standard requires that this deviation not exceed 0.65 mm.
3. Precracking load levels were in numerous cases higher than the initial testing load levels, leading to possible transient effects at the start of tests. The small amount of crack extension in each test made this difficult to avoid.
4. The crack growth increment between data points was approximately 0.015 mm, a value much smaller than the recommended 0.25 to 1 mm. The small distance over which growth is stable (1 to 1.5 mm in these tests) makes the recommended values unsuitable. The effect of choosing a value so small is an increase in scatter in the data.

At least one test at each load ratio was conducted without any of these deviations from the standard. Valid and invalid data were compared, and in all cases the scatter bands overlapped. It is suggested that the relaxation of the requirements of the standard had a minimal effect on results while making execution of the tests much simpler. It is important to note that the standard has been developed primarily for metals.

In-Situ Three-Point Bend Crack Growth Tests

Fatigue crack growth tests also were conducted on two Vickers indented three-point bend specimens of dimensions 3 by 6 by 24 mm. These tests were conducted in vacuum (10^{-5} torr) using a miniature 4-kN servohydraulic load frame coupled to the chamber of a scanning electron microscope (SEM). This system allowed direct observation and video recordings of the fatigue process to be made at magnifications up to approximately ×20 000. The details of this system will be discussed separately in another paper. Tests were conducted at load ratios of 0.1 and 0.3 using a 10-Hz sinusoidal waveform except during videotaping, when the frequency was reduced to 0.5 Hz. Specimens were prepared for testing by polishing of the tensile face with 0.25 μm diamond paste, Vickers indentation using a 60-N load, plasma etching in CF_4 plus 4% O_2 for 5 min, and sputter-coating with a gold-palladium alloy to avoid charging in the SEM.

Results and Discussion

Compact Tension Test Results

A plot of crack growth rate, *da/dN*, versus Mode I stress intensity range, ΔK, for the 25 C(T) tests is presented in Fig. 2. A clear load ratio effect is evident, and certain sets of data where low crack growth rates were obtained suggest the presence of a fatigue crack growth threshold. By replotting the data as a function of maximum stress intensity, K_{max}, as done in Fig. 3, the effect of load cycling is more clearly demonstrated. For a given value of K_{max}, the stress intensity at every point in time during a cycle at $R = 0.4$ is greater than or equal to the corresponding

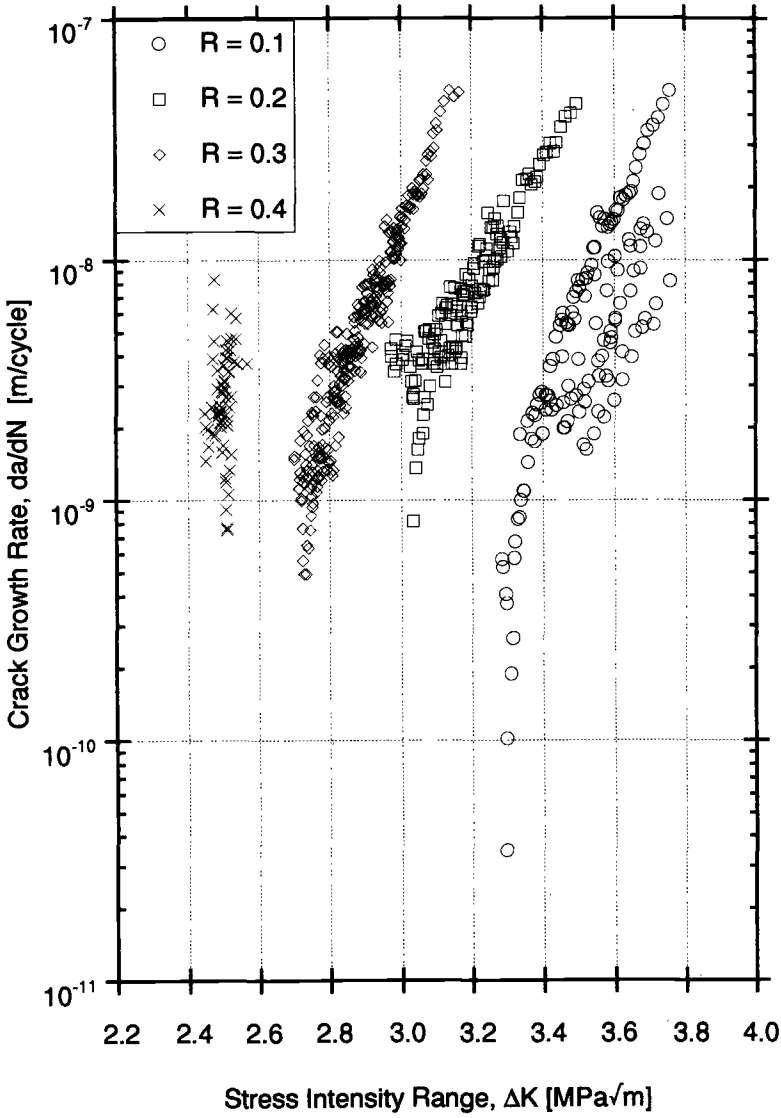

FIG. 2—*Compact tension fatigue crack growth data. Sinusoidal 10-Hz load waveform, in air.*

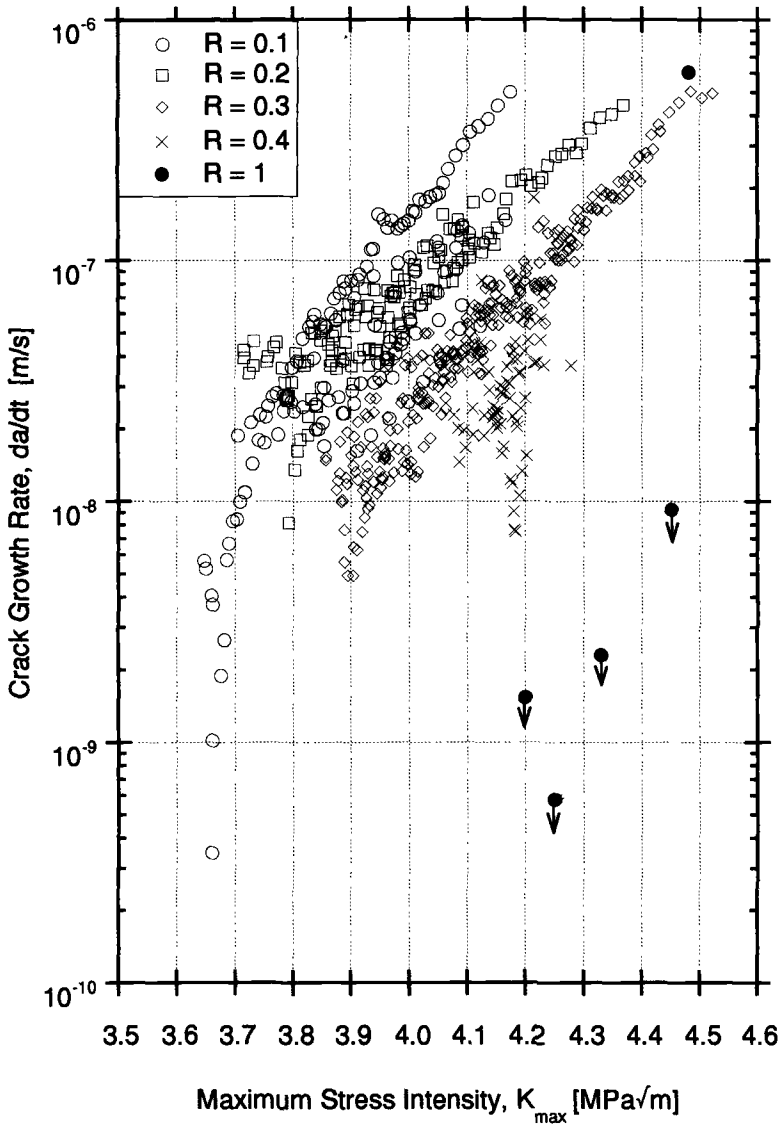

FIG. 3—*C(T) crack growth data for both sustained and cyclic loading. Sustained load data points with arrows indicate upper bounds on crack growth rate.*

value at $R = 0.1$. If crack growth is load level dependent, then the high load ratio data would be expected to fall above those for lower load ratios. In fact, the opposite is seen. This suggests that crack growth is not simply a manifestation of sustained-load cracking or a function of load level alone. In this figure, time-based rather than cycle-based crack growth rate is plotted in order to include sustained load data ($R = 1$). These data were generated using the same servohydraulic test system as the fatigue data and therefore include the noise associated with such a system. In most cases, no crack growth was detected. In this situation an upper bound was placed on the crack growth rate based on the resolution of the optical crack length measurement method.

Three-Point Bend Test Results

A plot of crack growth rate, *da/dN*, as a function of stress intensity range, ΔK, for the three-point bend specimens is shown in Fig. 4. Stress intensity factors were estimated using a solution by Newman and Raju [*26*], assuming that the crack was semicircular in shape, a fact later confirmed by fractography. The value of stress intensity at the specimen surface was used to correlate fatigue data. This is the largest value along the crack front and also corresponds to the location at which the cracks were measured. The fact that the *K*-solution is for a pure

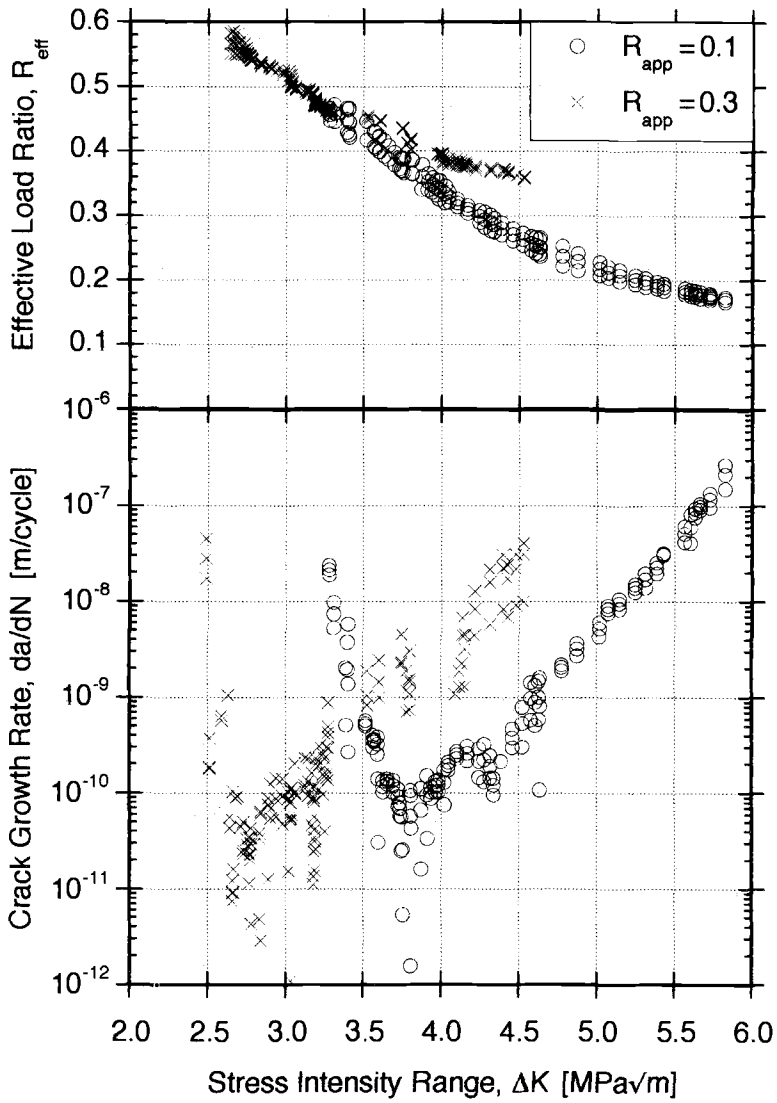

FIG. 4—*Three-point bend specimen fatigue crack growth data. Sinusoidal 10-Hz load waveform, in vacuum. Constant applied load ratios of 0.1 and 0.3 result in decreasing effective load ratios due to the presence of wedging-induced residual stresses.*

bending condition and three-point bending was used in the tests introduces an error, but comparison between bend specimens is still meaningful.

The V-shaped crack growth response seen in Fig. 4 suggests that the crack driving force at the beginning of the test was significantly greater than that accounted for by the applied stress intensity alone. SEM observation of the indentation area revealed that the crack within the indentation did not open at any time during a loading cycle, yet just beyond the indentation the crack opening was typically about 0.5 μm even with no external load applied. It therefore appears that the indentation acts to wedge the crack open and causes a tensile residual stress field to exist at the crack tip. Wedging by the indentation was much more severe than wedging caused by debris, and therefore debris-induced closure effects that may be present in natural cracks are likely to be masked here.

This type of crack growth behavior, in which there is an initial negative dependence of growth rate on stress intensity, has been seen previously by numerous investigators, including Horibe [*27*] on silicon nitride, Hoshide et al. [*28*] on alumina and silicon nitride, Liu and Chen [*29*] on zirconia, and Yoda [*30*] on soda-lime glass under sustained loading. The analysis of Anstis et al. [*31*] is used here to estimate the magnitude of the residual stress field. The residual stress intensity component, K_r, is assumed to be of the form,

$$K_r = \chi_r P a^{-3/2}$$

where P is the indentation load, a is the total surface crack length, and χ_r is given by,

$$\chi_r = \S_V^R \, (E/H)^{1/2}$$

where E and H are elastic modulus and hardness, respectively, and $\S_V^R$ is a dimensionless parameter dependent only on indenter geometry and crack shape. The subscript and superscript indicate a Vickers indenter and radial crack geometry, respectively. For NT-154, E and H values of 340 000 and 14 700 MPa, respectively, were used. A value for $\S_V^R$ of 0.016 determined by Anstis et al. [*31*] was used. It is assumed here that K_r does not vary with applied load. However, as external load is applied and the wedged crack faces tend to separate, the residual stress intensity will decrease. Presumably, if a sufficiently large load could be applied to separate the crack faces completely, the wedging contribution would disappear. For the material and indentation type studied here, fracture occurred before evidence of any opening within the indentation could be seen using the SEM. It is suggested, therefore, that the decrease in the residual stress intensity over the range of loads used in the tests is small enough to justify the assumption that K_r does not vary with applied load. The effective stress intensity, K_{eff}, is defined as the sum of the applied and residual components, K_{app} and K_r.

With K_r constant, the applied and effective stress intensity ranges, ΔK_{app} and ΔK_{eff}, are equal, and therefore the abscissa of Fig. 4 can be considered to represent either quantity. The effective load ratio, $R_{eff} = K_{min\ eff}/K_{max\ eff}$, does not remain constant through each test. When the crack is short and the wedging effects are most pronounced, R_{eff} is substantially higher than R_{app}. As the test progresses, R_{eff} approaches the constant value of the applied load ratio. Thus, the V-shape to the data sets in Fig. 4 is, at least in large part, a manifestation of the same mean stress or load ratio effect seen in Fig. 2. This is confirmed by the fact that the point of intersection of the two crack growth data sets, at $\Delta K \approx 3.4$ MPa$\sqrt{\text{m}}$, corresponds to the stress intensity range at which the effective load ratios for the two data sets are equal (at $R_{eff} \approx 0.44$).

As was the case with the C(T) data, it is useful to plot the bend data as a function of maximum stress intensity to clarify the role of cyclic loading. A plot of both crack growth rate and effective load ratio as functions of $K_{max\ eff}$ is shown in Fig. 5. By the same argument presented for the

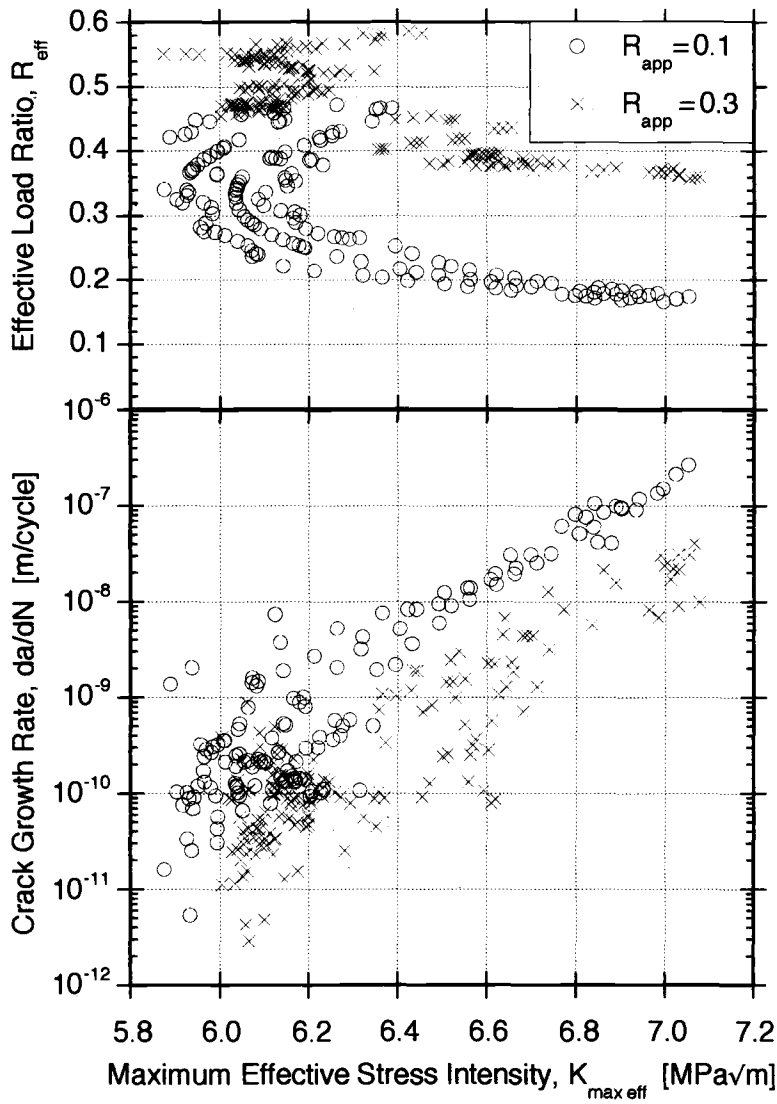

FIG. 5—*Three-point bend specimen fatigue crack growth data plotted as a function of maximum effective stress intensity.*

C(T) results, the following condition must be satisfied to conclude that load cycling is important in determining the crack growth response (for a given value of $K_{max\ eff}$):

$$\left(\frac{da}{dN}\right)_{R_{app}=0.1} > \left(\frac{da}{dN}\right)_{R_{app}=0.3}$$

However, since R_{eff} changes throughout the tests, it is also necessary to ensure that the test conducted at the lower applied load ratio also has a lower effective load ratio, i.e.,

$$(R_{eff})_{R_{app}=0.1} < (R_{eff})_{R_{app}=0.3}$$

If this second condition is satisfied, then the stress intensity at every point during a cycle in the $R_{app} = 0.1$ test is less than or equal to that at the corresponding point in the $R_{app} = 0.3$ test (for a given $K_{max\ eff}$). Since Fig. 5 shows both conditions to be satisfied throughout the tests, it is suggested that in vacuum as well as air crack growth is not simply load-level dependent but that the cyclic nature of the loading plays an important role.

A comparison of the bend and C(T) data shows that the bend data are shifted towards higher stress intensities. This offset is believed to be related to the fact that the constant bending moment K-solution does not precisely reflect the three-point bend configuration and the fact that the bend specimen crack front is curved and the stress intensity varies along it. Clearly, fatigue lives estimated from these two sets of data would differ greatly. The sensitivity of crack growth rates to small changes in stress intensity makes life prediction using the conventional approach of integration of crack growth rate–stress intensity curves extremely difficult since K is very seldom known with sufficient accuracy to make the prediction useful. The apparent presence of a threshold stress intensity range for crack growth in both cases is nevertheless a meaningful result.

As a final observation, the residual stress field associated with an indentation may offer a unique advantage for crack growth testing. Near the indentation, the total stress intensity decreases as the crack length increases. This provides the opportunity to conduct K-decreasing crack growth tests using constant amplitude loading, avoiding the complications of a test system configured to shed load automatically as the test progresses.

SEM Observations

A key feature of the load frame developed for the bend experiments is its ability to permit dynamic observation of the specimen. It is frequently assumed in describing and modeling fatigue crack propagation that the same process repeats every loading cycle. This is not the case in NT-154. Fatigue cracks propagated multiple grain diameters during one cycle and then arrested for hundreds or thousands of cycles before advancing again. During a growth cycle, the crack extension occurred at extremely high rates; all growth appeared to take place between two successive video frames recorded 1/30 s apart in time. Both the amount of crack advance during a growth cycle and the frequency of occurrence of growth cycles increased with increasing applied stress intensity. Only surface observation is possible with the system, and therefore the possibility exists that this is a free-surface effect. Fractography, however, revealed no difference in fracture surfaces between near surface material and bulk material in the bend specimens.

The observed discontinuous nature of crack growth illustrates that the crack growth rate curves presented previously must be considered to be average responses. On a local level crack growth rates vary many orders of magnitude above and below the average. Although the total stress intensity (applied plus residual) decreases with crack length near the indentation, this factor cannot be completely responsible for crack arrest after a growth cycle because the same behavior was seen at crack lengths beyond that where the total stress intensity begins to increase with crack length.

Discontinuous crack growth has been observed previously in both ceramics and metals. Sylva and Suresh [*32*] tested single-edged notched zirconia specimens under monotonic and cyclic

four-point bending. Arrest of cracks less than 1 mm in length occurred after growth of several tens of micrometres. Further growth in the zirconia was obtained only by raising the stress intensity range, whereas continued cycling at the same loads did cause additional growth in NT-154. In the work of Dauskardt et al. [*19*] on a SiC-whisker-reinforced alumina composite, multiple crack growth rate minima were observed on indented specimens, consistent with the pattern of crack arrest seen in the present investigation. Because only crack growth rate plots are presented, it is unclear whether crack arrest occurred, but the reported tendency for crack extension between successive minima to increase with increasing stress is consistent with the results of the present investigation. Lankford and Davidson [*33*] observed discontinuous growth in 7XXX series aluminum alloys using an SEM-coupled load frame, although the mechanisms are certainly quite different from those in silicon nitride and other ceramics. A single striation was found to be created, not in one loading cycle as frequently assumed, but only after numerous cycles during which the crack tip blunts and damage of some form accumulates.

Fatigue cracks in NT-154 showed a mixture of intergranular and transgranular growth. Features visible in the crack wake included bridging, grain interlocking, and friction, all of which serve to transfer load across the crack wake and shield the crack tip. Examples of friction between crack surfaces are illustrated in Figs. 6 and 7. The direction of tensile stress is horizontal in all SEM micrographs. In some cases, as in Fig. 7, friction resulted in development of branch cracks. The secondary crack on the left of Fig. 7*a* was formed by cyclic frictional loading. This crack grew away from the tip of the dominant crack (i.e., downward in the photograph) and joined the main crack near the bottom of the picture to form a 1-μm particle shown in Fig. 7*b*.

Figure 8 illustrates an example of grain interlocking. The interlocking appeared to be severe enough to necessitate the development of a second crack (in the upper right area of the figure). This also resulted in the formation of a bridge, the most commonly seen feature in the crack wake. Bridge structures formed during single cycle advances of the crack and were subsequently destroyed by cycling. Figure 9 shows a series of micrographs of a bridge. In Fig. 9*a*, taken approximately 3000 cycles after the bridge formed, both the left and right cracks are open, indicating that a load is being transferred across the bridge. The main crack tip is 50 μm

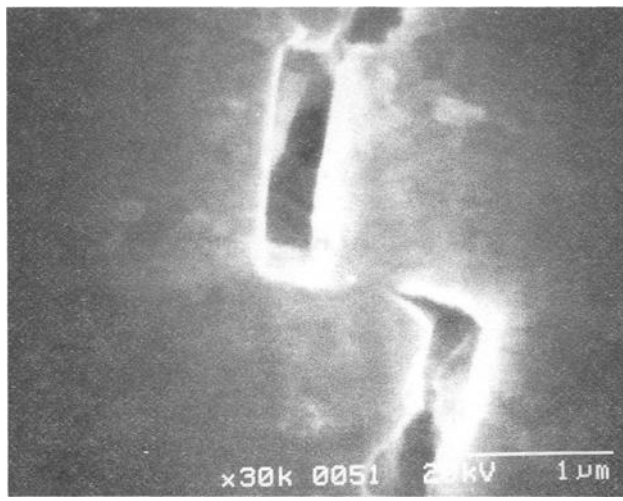

FIG. 6—*Area of friction in crack wake. Tensile stress in all micrographs is oriented horizontally.*

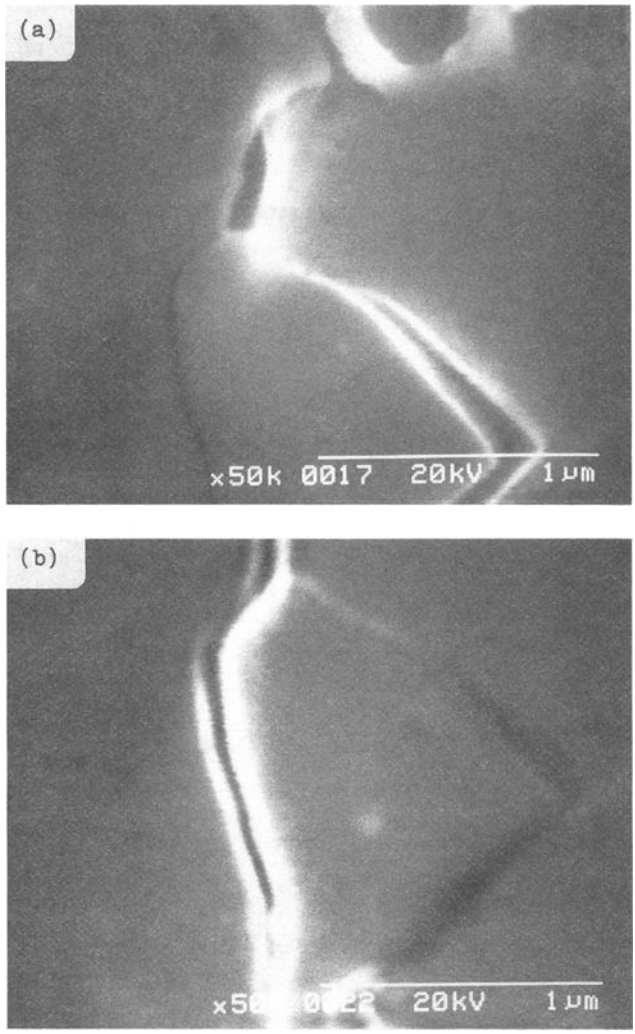

FIG. 7—*Crack wake friction caused formation of secondary crack* (a) *that later resulted in formation of a 1-µm diameter particle* (b).

above the top of the image. One thousand cycles later, and after 16 µm of crack tip extension, Fig. 9*b*, the right crack appears to be dominating. In Fig. 9*c*, the final micrograph of the series, taken after an additional 700 cycles and 20 µm of crack growth, the left crack appears closed and the right branch has joined the main crack, preventing further load transfer across the bridge.

A similar situation is seen in Fig. 10. The micrograph shown in Fig. 10*a* was taken immediately after a one-cycle increment of crack growth during which the crack tip advanced from a position about 7 µm below the photograph to about 6 µm above the top of the picture. After 400 cycles and another 12 µm growth increment, the lower micrograph was taken. During this interval the crack circumvented the grain identified by the letter "B" to connect with the upper

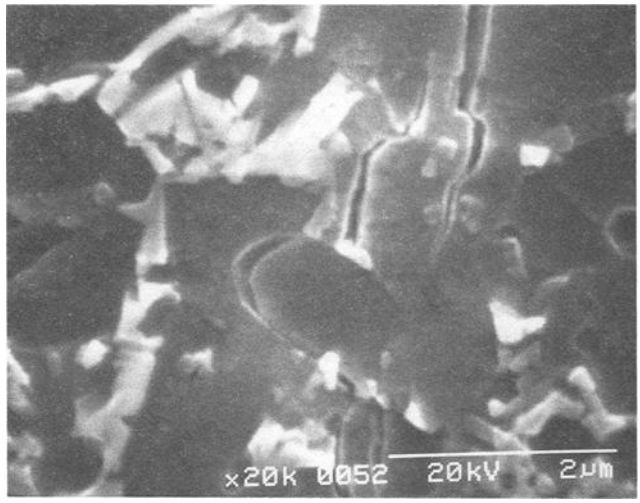

FIG. 8—*Interlocking grain and bridge structure in crack wake.*

crack. Both pictures were taken at maximum load. The crack-opening displacement is significantly larger in the micrograph shown in Fig. 10*b*. Although part of the increase is due to the extension of the crack tip, the degeneration of the bridge has also contributed to the larger displacement. After decay of the bridge, the transgranular crack part way through grain "B" remained almost closed.

The observations presented here deal mainly with effects in the crack wake; information concerning the crack tip was difficult to obtain with the SEM. The fineness of the crack made it doubtful that the tip was visible. Visualization of crack tip processes in this material appears to require higher resolution than the current SEM can provide.

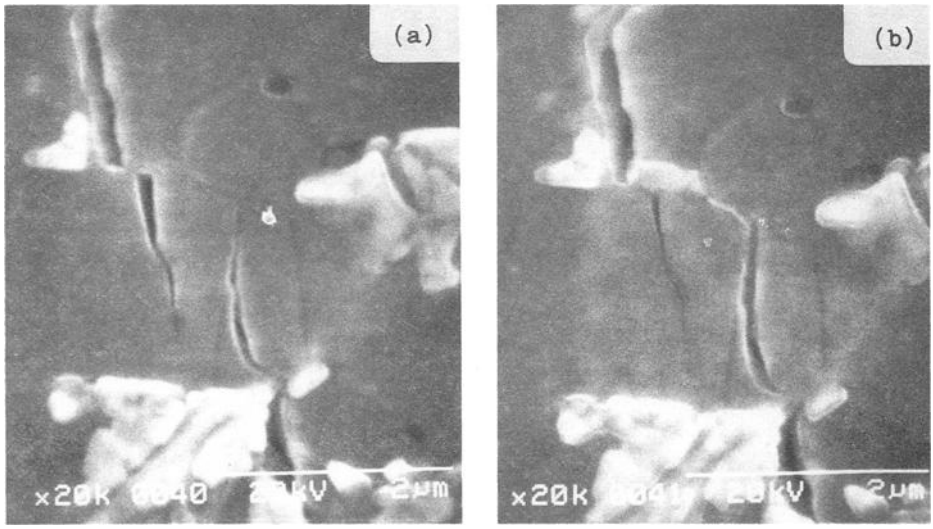

FIG. 9—*Decay of bridge from cyclic loading. Crack tip is 50 μm above top of image in* (a), *66 μm in* (b), *and 86 μm in* (c).

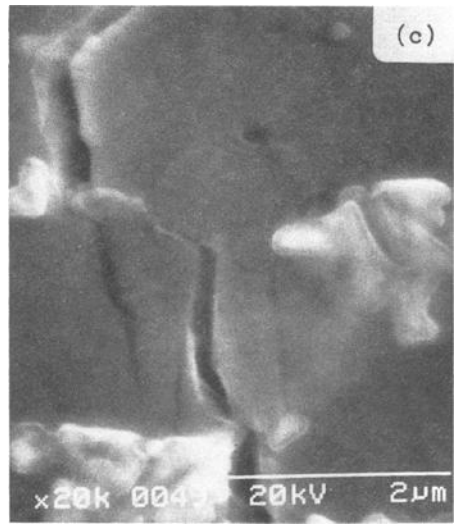

FIG. 9—*Continued.*

Fracture surface examination following testing revealed little difference between fatigue and fast fracture regions of the fracture surfaces. A comparison is shown in Fig. 11. This similarity is consistent with a mechanism involving periodic high growth rate increments.

Mechanisms of Fatigue Crack Propagation

The observations of crack growth made here suggest a mechanism in which "damage" accumulates after an increment of growth. This damage involves degradation of bridges and other similar crack-wake traction-reducing processes and also may include crack tip processes not resolved with the present SEM. When the damage reaches a critical level, perhaps corresponding to sufficient shielding degradation, a fast fracture mechanism becomes active. During extension additional bridges and interlocking features are formed and the crack tip moves away from any "damaged zone" formed at its previous arrest point. The crack tip shielding imparted by the newly developed features may be sufficient to cause the observed crack arrest.

Recent work by Lathabai et al. [*34*] on alumina using an SEM-coupled load frame has indicated similar results concerning the degradation of bridges during cyclic loading. They suggest that the crack tip driving force is more suitably represented by including a shielding term in addition to the applied and residual stress contributions. The shielding term is based on estimates of friction between sliding facets at interlocking sites and is negative and therefore reduces the total stress intensity. This approach appears to hold promise for assessing whether the crack arrest observed in NT-154 is accounted for by the concurrent formation of shielding features.

Summary and Conclusions

A series of fatigue crack growth experiments was conducted at room temperature in vacuum on NT-154 silicon nitride using Vickers indented three-point bend specimens and a miniature servohydraulic load frame coupled to an SEM. A second series of tests was performed on

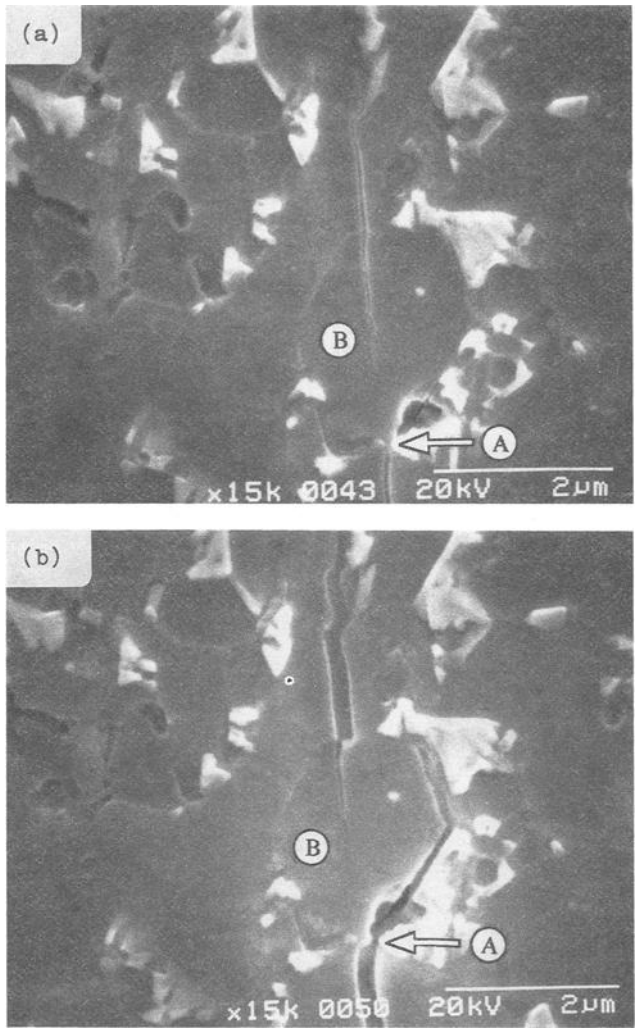

FIG. 10—*Bridge formed when crack was diverted by grain boundary at A. Intergranular cracking continued around grain B, destroying bridge. Bridge is shown immediately after formation in* (a) *and after 12 μm of additional extension in* (b).

compact tension specimens in room temperature air. The following conclusions are drawn from the work:

1. Stable crack propagation occurs in NT-154 under cyclic loading in both laboratory air (15 to 30% relative humidity) and vacuum (10^{-5} torr) conditions. A mechanism for crack growth exists independent of environmentally assisted and sustained-loading crack growth mechanisms.
2. Fatigue crack growth occurs in a discontinuous manner. Growth is incremental, taking place on a single cycle at a high rate perhaps approaching that for fracture. Between these increments there is no detectable crack extension. Local crack growth rates, therefore, are

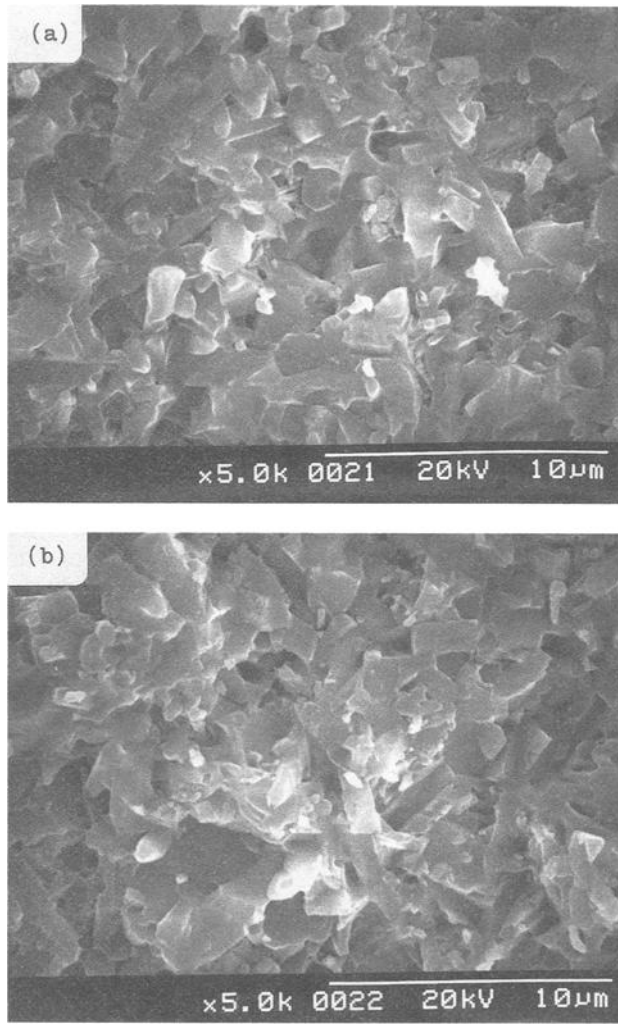

FIG. 11—*Fatigue* (a) *and fast fracture* (b) *surfaces of bend specimen tested at* R = *0.3. Their similarity is consistent with a mechanism involving periodic high growth rate increments.*

orders of magnitude faster or slower than the average response represented by conventional fatigue crack growth data.

3. Crack wake features such as interlocking grains and crack bridges, which initially transfer load across the crack surfaces, degenerate and fracture during cycling between growth increments. In doing so these structures lose their ability to transfer load.
4. The residual stress field associated with a Vickers indentation has a significant effect on fatigue crack growth rates. Crack closure effects related to debris in the crack wake appear to be insignificant compared to the wedging effect of the indentation.
5. Fatigue crack growth data both from bend specimens after compensation for residual stress effects and from compact tension specimens show the presence of a crack growth thresh-

old. Although the crack growth curves are extremely steep compared to those of metals, the data do show a sigmoidal shape not represented by a Paris equation.

6. Fracture surfaces in fatigue and fast fracture regions appear similar and show a mixture of transgranular and intergranular fracture. This similarity is consistent with a fatigue mechanism involving periodic high-rate growth increments.

Acknowledgments

The authors wish to thank Allied Signal Aerospace Co. and Rolls-Royce plc for their support of this work. The technical assistance provided by the NASA Lewis Research Center is also gratefully acknowledged.

References

[*1*] Evans, A. G., "Fatigue in Ceramics," *International Journal of Fracture,* Vol. 16, 1980, pp. 485–498.

[*2*] Williams, L. S., "Stress-Endurance of Sintered Alumina," *Transactions of the British Ceramic Society,* Vol. 55, 1956, pp. 287–312.

[*3*] Dauskardt, R. H., Yu, W., and Ritchie, R. O., "Fatigue Crack Propagation in Transformation-Toughened Zirconia Ceramic," *Journal of the American Ceramic Society,* Vol. 70, 1987, pp. C-248–C-252.

[*4*] Tsai, J.-F., Yu, C.-S., and Shetty, D. K., "Fatigue Crack Propagation in Ceria-Partially-Stabilized Zirconia (Ce-TZP)-Alumina Composites," *Journal of the American Ceramic Society,* Vol. 73, 1990, pp. 2992–3001.

[*5*] Liu, S.-Y. and Chen, I.-W., "Fatigue of Yttria-Stabilized Zirconia: I, Fatigue Damage, Fracture Origins, and Lifetime Prediction," *Journal of the American Ceramic Society,* Vol. 74, 1991, pp. 1197–1205.

[*6*] Lin, C.-K. J., Mayer, T. A., and Socie, D. F., "Cyclic Fatigue of Alumina," *Cyclic Deformation, Fracture, and Nondestructive Evaluation of Advanced Materials, ASTM STP 1157,* M. R. Mitchell and O. Buck, Eds., American Society for Testing and Materials, Philadelphia, 1992, pp. 3–27.

[*7*] Ewart, L. and Suresh, S., "Crack Propagation in Ceramics under Cyclic Loads," *Journal of Materials Science,* Vol. 22, 1987, pp. 1173–1192.

[*8*] Kishimoto, H., Ueno, A., and Kawamoto, H., "Crack Propagation Characteristics of Sintered Si_3N_4 under Static and Cyclic Loads," *Journal of the Society of Materials Science, Japan (Zairyo),* Vol. 36, 1987, pp. 1122–1127.

[*9*] Kishimoto, H., Ueno, A., and Kawamoto, H., "Crack Propagation Behavior of Sintered Silicon Nitride under Cyclic Loads (Influence of Difference in Materials)," *Transactions of the Japan Society of Mechanical Engineers (Nippon Kikai Gakkai Ronbunshu),* Part A, Vol. 56, 1990, pp. 50–55.

[*10*] Ueno, A., Kishimoto, H., Kawamoto, H., and Asakura, M., "Crack Propagation Behavior under Cyclic Loads of High Stress Ratio and High Frequency," *Engineering Fracture Mechanics,* Vol. 40, 1991, pp. 913–920.

[*11*] Beals, J. T. and Bar-On, I., "Fracture Toughness and Fatigue Crack Propagation of Silicon Nitride with Two Different Microstructures," *Ceramic Engineering and Science Proceedings,* Vol. 11, No. 7–8, 1990, pp. 1061–1071.

[*12*] Matsuo, Y., Hattori, Y., Katayama, Y., and Fukuura, I., "Cyclic Fatigue Behavior of Ceramics," *Progress in Nitrogen Ceramics,* F. L. Riley, Ed., Martinus Nijhoff Publishers, Boston, 1983, pp. 515–522.

[*13*] Horibe, S., "Fatigue of Silicon Nitride Ceramics under Cyclic Loading," *Journal of the European Ceramic Society,* Vol. 6, 1990, pp. 89–95.

[*14*] Nishi, M., Ueda, K., and Sugita, T., "Strength Reliability Evaluation of Ceramics (2nd Report)—Fatigue Crack Growth Characteristics and Life Prediction of Si_3N_4," *Journal of the Japan Society of Powder and Powder Metallurgy,* Vol. 36, No. 7, 1989, pp. 865–869.

[*15*] Lewis, D. and Rice, R. W., "Comparison of Static, Cyclic, and Thermal-Shock Fatigue in Ceramic Composites," *Ceramic Engineering and Science Proceedings,* Vol. 3, 1982, pp. 714–721.

[*16*] Suresh, S. and Han, L. X., "Fracture of Si_3N_4-SiC Whisker Composites under Cyclic Loads," *Journal of the American Ceramic Society,* Vol. 71, No. 3, 1988, pp. C-158–C-161.

[*17*] Morrone, A. A., Nutt, S. R., and Suresh, S., "Fracture Toughness and Fatigue Crack Growth Behaviour of an Al_2O_3-SiC Composite," *Journal of Materials Science,* Vol. 23, 1988, pp. 3206–3213.

[18] Suresh, S. and Brockenbrough, J. R., "Theory and Experiments of Fracture in Cyclic Compression: Single Phase Ceramics, Transforming Ceramics and Ceramic Composites," *Acta Metallurgica,* Vol. 36, No. 6, 1988, pp. 1455–1470.

[19] Dauskardt, R. H., James, M. R., Porter, J. R., and Ritchie, R. O., "Cyclic Fatigue-Crack Growth in a SiC-Whisker-Reinforced Alumina Ceramic Composite: Long- and Small-Crack Behavior," *Journal of the American Ceramic Society,* Vol. 75, No. 4, 1992, pp. 759–771.

[20] Steffen, A. A., Dauskardt, R. H., and Ritchie, R. O., "Cyclic Fatigue Life and Crack-Growth Behavior of Microstructurally Small Cracks in Magnesia-Partially-Stabilized Zirconia Ceramics," *Journal of the American Ceramic Society,* Vol. 74, No. 6, 1991, pp. 1259–1268.

[21] Dauskardt, R. H., Marshall, D. B., and Ritchie, R. O., "Cyclic Fatigue Crack Propagation in Magnesia-Partially-Stabilized Zirconia Ceramics," *Journal of the American Ceramic Society,* Vol. 73, No. 4, 1990, pp. 893–903.

[22] Steffen, A. A., Dauskardt, R. H., and Ritchie, R. O., "Small-Crack Behavior and Safety-Critical-Design Criteria for Cyclic Fatigue in Mg-PSZ Ceramics," *Cyclic Deformation, Fracture, and Nondestructive Evaluation of Advanced Materials, ASTM STP 1157,* M. R. Mitchell and O. Buck, Eds., American Society for Testing and Materials, Philadelphia, 1992, pp. 69–81.

[23] Ritchie, R. O. and Dauskardt, R. H., "Cyclic Fatigue of Ceramics: A Fracture Mechanics Approach to Subcritical Crack Growth and Life Prediction," *Journal of the Ceramic Society of Japan (Nippon Seramikkusu Kyokai Gakujutsu Ronbunshi),* Vol. 99, No. 10, 1991, pp. 1047–1062.

[24] Fujii, T., Majidi, A. P., and Chou, T. W., "Are There Fatigue Effects on Ceramics and Ceramic Matrix Composites under Cyclic Loading?" *Advanced Metal and Ceramic Matrix Composites: P/M Processing, Process Modelling and Mechanical Behavior,* R. B. Bhagat et al., Eds., The Minerals, Metals and Materials Society, Warrendale, PA, 1990, pp. 253–262.

[25] Smith, F. M., "Quantitative Representation of Microstructural Contributions to Fatigue Crack Growth," Ph.D. thesis, The University of Utah, Salt Lake City, UT, 1988.

[26] Newman, J. C. and Raju, I. S., "An Empirical Stress-Intensity Factor Equation for the Surface Crack," *Engineering Fracture Mechanics,* Vol. 15, 1981, pp. 185–192.

[27] Horibe, S., "Cyclic Fatigue Crack Growth from Indentation Flaw in Si_3N_4," *Journal of Materials Science Letters,* Vol. 7, 1988, pp. 725–727.

[28] Hoshide, T., Ohara, T., and Yamada, T., "Fatigue Crack Growth from Indentation Flaw in Ceramics," *International Journal of Fracture,* Vol. 37, 1988, pp. 47–59.

[29] Liu, S.-Y. and Chen, I.-W., "Fatigue of Yttria-Stabilized Zirconia: II, Crack Propagation, Fatigue Striations, and Short-Crack Behavior," *Journal of the American Ceramic Society,* Vol. 74, No. 6, 1991, pp. 1206–1216.

[30] Yoda, M., "Subcritical Crack Growth Characteristics on Compact Type Specimens and Indentation Cracks in Glass," *Journal of Engineering Materials and Technology,* Vol. 111, 1989, pp. 399–403.

[31] Anstis, G. R., Chantikul, P., Lawn, B. R., and Marshall, D. B., "A Critical Evaluation of Indentation Techniques for Measuring Fracture Toughness: I, Direct Crack Measurements," *Journal of the American Ceramic Society,* Vol. 64, No. 9, 1981, pp. 533–538.

[32] Sylva, L. A. and Suresh, S., "Crack Growth in Transforming Ceramics under Cyclic Tensile Loads," *Journal of Materials Science Letters,* Vol. 24, 1989, pp. 1729–1738.

[33] Lankford, J. and Davidson, D. L., "Fatigue Crack Micromechanisms in Ingot and Powder Metallurgy 7XXX Aluminum Alloys in Air and Vacuum," *Acta Metallurgica,* Vol. 31, 1983, pp. 1273–1284.

[34] Lathabai, S., Rödel, J., and Lawn, B. R., "Cyclic Fatigue from Frictional Degradation at Bridging Grains in Alumina," *Journal of the American Ceramic Society,* Vol. 74, 1991, pp. 1340–1348.

DISCUSSION

O. Buck[1] *(written discussion)*—I would like to ask two questions:

1. Could you tell us how the compact tension crack growth data compare with those obtained on the bend test specimen?
2. Your SEM chamber seems to be large enough to install an acoustic emission detector.

[1] Ames Laboratory, Iowa State University, Ames, IA 50011.

Couldn't you use such a detector to determine a correlation with the discontinuous growth that you observe with the SEM?

D. C. Salmon and D. W. Hoeppner (authors' closure)—

Question 1

Precise comparisons are difficult to make here because the effective load ratio varied in each bend test but remained constant in each C(T) test. Nevertheless, the bend data tend to be shifted towards higher stress intensities by 2 to 3 MPa$\sqrt{m}$. In terms of a ratio, this amounts to a factor of approximately 2 and illustrates the magnitude of the problems encountered in using such data for life prediction. The difference is thought to be due to the fact that a pure bending K-solution was used for the three-point bend specimens, and the fact that the surface value of K was used to correlate fatigue data. The value of K along the curved crack front varies and is maximum at the surface.

The notion that the K-solution used here is not well-suited to the specimen is also supported by fracture toughness data. Fracture toughness tests on C(T) specimens of NT-154 done in accordance with ASTM E 399 yielded results of 4.85 $\pm$ 0.08 MPa$\sqrt{m}$, which agreed with the values of 4.81 $\pm$ 0.22 MPa$\sqrt{m}$ determined by the indentation fracture method on bend bars (uncertainties represent standard deviations). In contrast, monotonic tests on indented bend bars, where the pure bending K-solution was used, produced toughness values of 6.33 $\pm$ 0.54 MPa$\sqrt{m}$, about 1.5 MPa$\sqrt{m}$ higher than obtained by the other techniques. Subcritical crack growth that preceded fracture in these tests was monitored using the SEM and accounted for in calculation of toughness values.

Question 2

Determining the subsurface behavior is a critical next step in this work, and acoustic emission appears to be a technique that holds promise. There is sufficient room in the SEM chamber for transducers, although the current loading fixture design limits access to some surfaces of the specimen. Straightforward modifications to the load frame should allow for sufficient access.

Yoshiharu Mutoh,[1] *Manabu Takahashi,*[1] *and Akira Kanagawa*[1]

Fatigue Crack Growth Behavior of Surface Cracks in Silicon Nitride

REFERENCE: Mutoh, Y., Takahashi, M., and Kanagawa, A., **"Fatigue Crack Growth Behavior of Surface Cracks in Silicon Nitride,"** *Cyclic Deformation, Fracture, and Nondestructive Evaluation of Advanced Materials: Second Volume, ASTM STP 1184,* M. R. Mitchell and O. Buck, Eds., American Society for Testing and Materials, Philadelphia, 1994, pp. 19–31.

ABSTRACT: Cyclic fatigue crack growth tests of silicon nitride specimens with surface cracks as well as through-the-thickness cracks were carried out. The surface crack length was measured by a surface film gage technique. The fatigue crack growth rate for surface cracks was less than that for through-the-thickness cracks. From SEM observations, more significant bridging was found in the wake of surface cracks compared to through-the-thickness cracks. From evaluations of the stress shielding effect due to bridging based on the measurements of the crack mouth opening displacement, it was found that the crack growth curve determined from the crack tip stress intensity factor K_{tip} for surface cracks almost coincided with that for through-the-thickness cracks.

KEYWORDS: fatigue crack growth, cyclic fatigue, surface cracks, bridging, crack tip stress intensity factor, surface film technique, silicon nitride

Studies of fatigue crack growth behavior in structural ceramics to investigate the basic characteristics and mechanisms of fatigue crack growth have been carried out mainly on long, through-the-thickness cracks. According to these results in zirconia [*1–6*], alumina [*7–10*], and silicon nitride [*11–13*], cyclic loading accelerates the crack growth rate, especially in the low-crack-growth-rate regime compared to static loading. The acceleration of crack growth rate due to cyclic loading is considered to result from the degradation of the stress shielding effect in the crack wake due to cyclic deformation [*14,15*]. Several stress shielding mechanisms have been considered in the literature: phase transformation for partially stabilized zirconia (PSZ), unbroken or grain bridging for alumina and silicon nitride, and fiber bridging for composites. These stress shielding phenomena are expected to result in crack length and crack geometry dependencies of the fatigue crack growth rate. For example, fatigue crack growth rates of silicon nitride were found to decrease with crack extension under constant K_{max} tests [*15*]. Because of low toughness, large cracks will not be allowed to exist in ceramic components at any stage such as sintering, machining, and maintenance. Therefore, fatigue and fracture behavior of small surface cracks induced during sintering or machining is of significance in practice. However, there is no guarantee of predicting the crack growth behavior of a small surface crack based on results from long, through-the-thickness cracks. In fact, fatigue crack growth rates for small corner cracks in LAS/SiC-fiber glass ceramics [*16*] and for small surface cracks in Mg-PSZ [*17*] display a negative dependency on the applied stress intensity.

The objective of the present study is to investigate the cyclic fatigue crack growth behavior of small surface cracks in silicon nitride, which is one of the major candidate materials for

[1] Department of Mechanical Engineering, Nagaoka University of Technology, Nagaoka-shi 940-21, Japan.

potential structural components in high-performance turbine applications. Fatigue crack growth processes are observed in detail to discuss the mechanism of fatigue crack growth. Fatigue crack growth behaviors are examined in terms of the da/dN-K_{tip} (crack tip stress intensity) curve as well as the conventional da/dN-K_a (applied (far field) stress intensity) curve.

Experimental Procedure

The material used is a hot isostatic pressing (HIP) sintered silicon nitride (Si_3N_4) with additives of 2 wt% alumina (Al_2O_3) and 5 wt% yttria (Y_2O_3). Young's modulus, the bending strength, and the fracture toughness of the material are 318 GPa, 1120 MPa, and 6.4 MPa$\sqrt{m}$, respectively.

A surface crack was introduced into bending-type specimens with dimensions of 3 by 4 by 40 mm using a Vickers indentor. Indentation loads were controlled to obtain various crack sizes. To remove residual stresses around the surface crack induced by the indentation, the indented surface was ground up to 4 ~ 5 times the indentation depth and subsequently lapped to remove residual stress induced by grinding. A fracture toughness test of the surface crack specimens was carried out to confirm the removal of residual stress. Figure 1 shows the relationship between ground depth and normalized fracture toughness K_{IC}(surface crack)/K_{IC}(standard through-the-thickness precrack). It was found that fracture toughnesses of the specimens with ground depths over 3 ~ 4 times the indentation depth are essentially constant and equal to that obtained using a specimen with a through-the-thickness precrack. Micrographs of introduced surface cracks are shown in Fig. 2. Fatigue crack growth tests were carried out using a servohydraulic fatigue test machine under four-point bending with a loading span length of 10 mm and a supporting span length of 30 mm in controlled room temperature air (20°C, 55% relative humidity). Square waveform loading with a frequency of 2 Hz and a stress ratio of 0.1, where the maximum applied load was constant for each specimen, was used. The surface

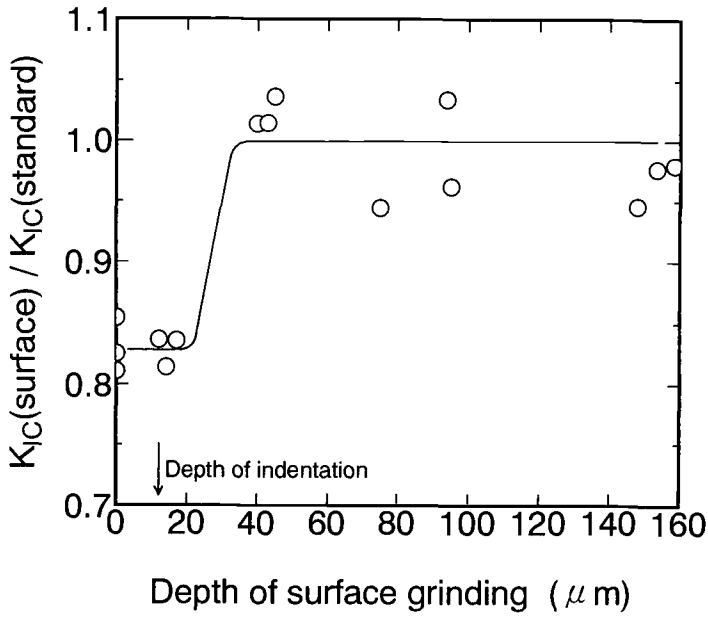

FIG. 1—*Relationship between ground depth and fracture toughness of a surface-cracked specimen.*

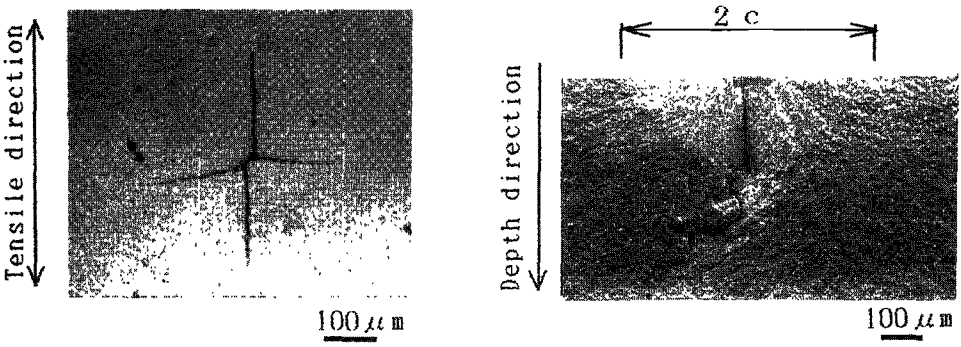

FIG. 2—*Morphology of surface cracks introduced in an Si_3N_4 specimen.*

crack length was measured using a film technique. An optical microscope was also used to measure the crack length. The surface film technique is an extension of the electrical potential method to a nonconductive solid, where a thin film of conductive material is either glued or sputter-deposited to the surface [*1,18*]. In the present study, a Pd-Pt film with a thickness of 0.2 ~ 0.5 μm was deposited by a vacuum evaporation technique onto the window area of the specimen surface, which was made by masking. The Pd-Pt layer is then connected to an electrical circuit by a conductive paste (silver paint), as shown schematically in Fig. 3. The electrical resistance of the Pd-Pt layer is approximately several to some tens kΩ depending on the film dimensions. Figure 4 shows the measuring system used. In the preliminary fatigue crack growth test, the measurement of electrical resistance as well as the crack length measurement by optical microscopy was carried out to investigate the relationship between electrical resistance and crack length. The following calibration equation was obtained

$$\frac{R_j}{R_i} = \frac{(1 - 2c_i/W_g)(1 - 1.19L_g/W_g \cdot 2c_j/W_g)}{(1 - 2c_j/W_g)(1 - 1.19L_g/W_g \cdot 2c_i/W_g)} \tag{1}$$

$$(0.12 < 2c/W_g < 0.6,\ 0.55 < L_g/W_g < 0.75)$$

where

L_g = the film gage length,
W_g = the film gage width, and
R_i = the electrical resistance of film gage at the crack length of $2c_i$.

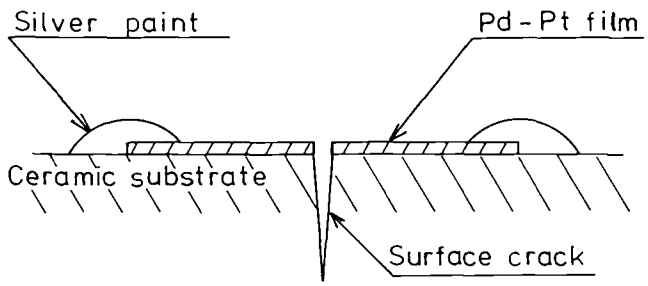

FIG. 3—*Schematic illustration of the surface film gage method.*

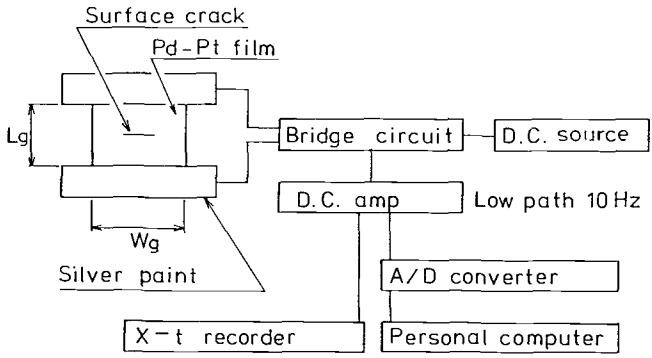

FIG. 4—*The measuring system for the surface film gage method.*

The relationship between the estimated crack length based on the calibrating Eq 1 and the measured crack length is shown in Fig. 5. As can be seen from the figure, the surface crack length can be measured accurately according to the present surface film gage technique, where the discrepancy between the estimated and measured crack lengths is less than 3%. The *K*-values of surface cracks were calculated by using the Newman-Raju equation [*19*], where the ratio of surface crack length, $2c$, and crack depth, a, was determined on the fracture surface after completing the crack growth tests. The morphology of the fatigue crack path and the crack opening profile was observed in detail using a low-vacuum scanning electron microscope with a Robinson-type reflex electron detector, in which ceramic materials can be observed directly without conductive film deposition.

Fatigue crack growth tests of specimens with through-the-thickness cracks were also carried

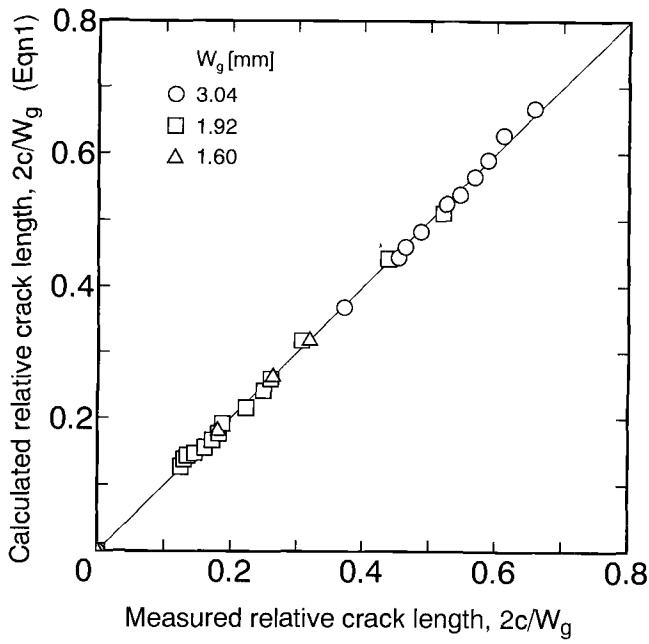

FIG. 5—*Relationship between surface crack lengths measured by an optical microscopy and by the surface film gage method.*

out for comparison of fatigue crack growth behaviors between surface cracks and through-the-thickness cracks. A through-the-thickness precrack was introduced into the bending-type specimen with dimensions of 5 by 10 by 55 mm. The method of precracking was as follows: A series of surface cracks were introduced by the indentation technique in the thickness direction on the center-of-tension–side surface. Then cyclic load was applied to grow into a through-the-thickness precrack with a length of approximately 1 mm. Fatigue crack growth tests were conducted in a servohydraulic fatigue test machine under three-point bending with a span length of 40 mm and a square waveform of loading with a frequency of 2 Hz and a stress ratio of 0.1, where the maximum applied load was constant during the test. The crack mouth opening displacement was measured using a strain gage (gage length of 1 mm) attached to the front surface of the specimen crossing the crack mouth, where deformation induced in the strain gage was assumed to be due to the crack mouth opening displacement. The crack mouth opening displacement measured by using a strain gage coincides well with that observed in situ in a fatigue test machine with a scanning electron microscope.

Results

Figure 6 shows the relationship between the applied maximum stress intensity factor K_a and fatigue crack growth rates *da/dN* and *dc/dN*. The crack growth rate for through-the-thickness cracks was higher than that for surface cracks in the low-crack-growth-rate region, where cyclic-dependent crack growth is dominant. The crack growth curves for surface cracks with

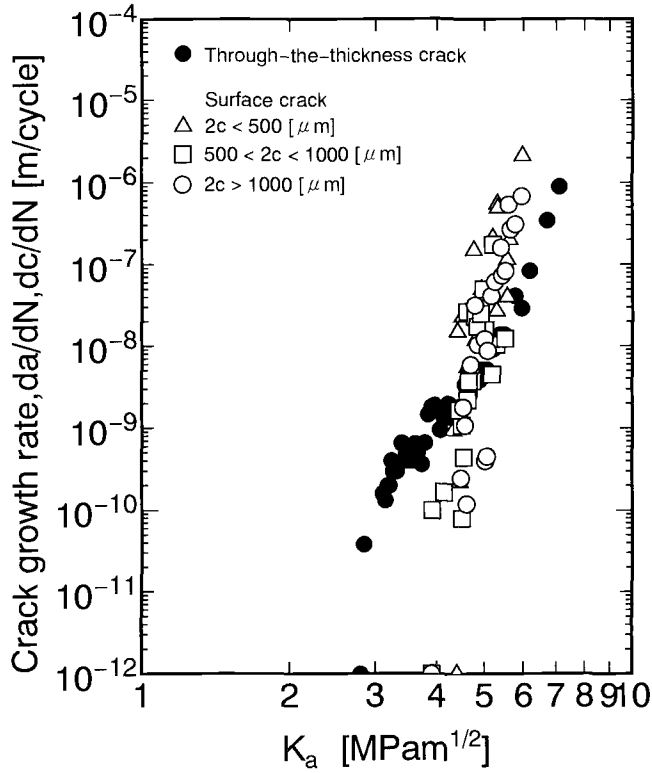

FIG. 6—*Relationship between the applied maximum stress intensity factor* K_a *and fatigue crack growth rates* da/dN.

various crack sizes almost coincided regardless of initial crack length. Figure 7 shows the relationship between the threshold stress intensity factor and the surface crack length $2c$. It was found that the threshold values for crack growth for surface cracks were almost constant regardless of crack length and in the range of 4.1 to 4.5 MPa$\sqrt{m}$, which was higher than that for through-the-thickness cracks (3.5 MPa$\sqrt{m}$).

Figure 8 shows SEM micrographs of the tip region of an initial surface crack and the fatigue crack paths of a surface crack and a through-the-thickness crack in silicon nitride. Grain-bridging elements were observed even in the initial surface crack. Significant development of bridging was found in the wake of the surface crack compared to the through-the-thickness crack.

Discussion

The grain-bridging zone in the wake of the crack exerts compressive traction on the crack surfaces, which shield the crack tip from far field stresses. The crack tip stress intensity factor, K_{tip}, is therefore reduced from the applied stress intensity factor, K_a, by the shielding stress intensity factor due to bridging, K_b. That is,

$$K_{tip} = K_a - K_b \tag{2}$$

The relationship is schematically shown in Fig. 9. Using the crack tip opening displacement instead of the stress intensity factor, a relationship similar to Eq 2 is obtained. The relationship between the crack tip opening displacement and the crack mouth opening displacement depends on the type of loading. Since the bridging stress distribution and the bridging zone length are not known, the relationship when the bridging force is applied on the crack surface is difficult to estimate. In this study, it is assumed that a relationship similar to Eq 2 also holds for the crack mouth opening displacement.

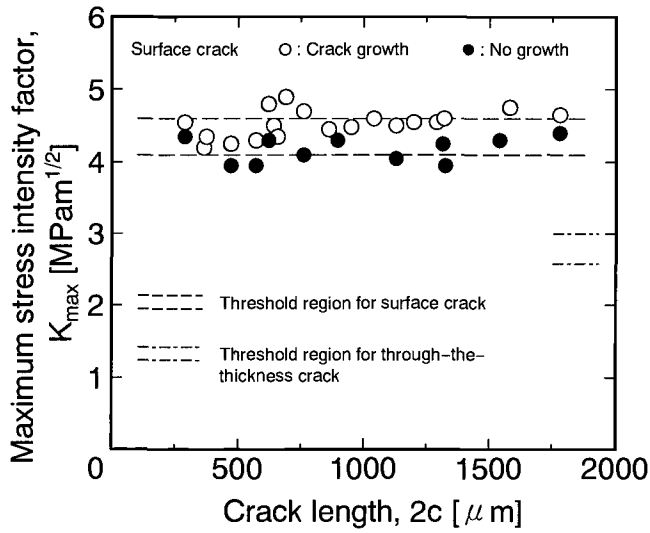

FIG. 7—*Relationship between the threshold stress intensity factor and the surface crack length 2c.*

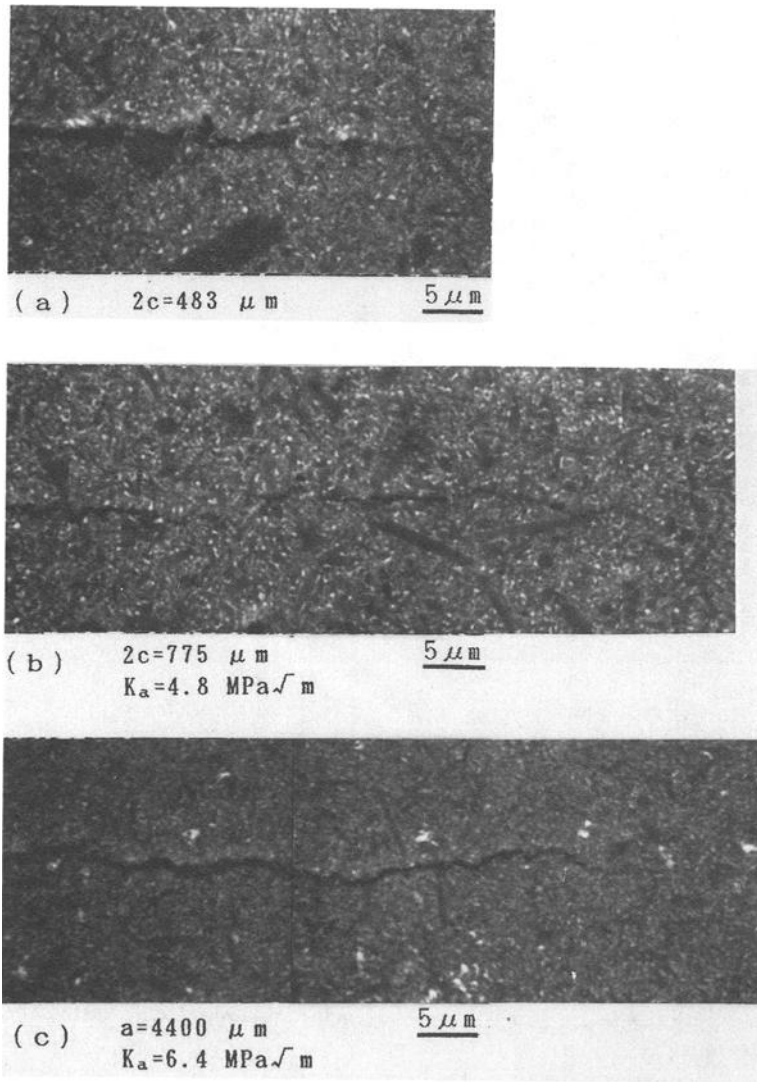

FIG. 8—*SEM micrographs of the tip region of an initial surface crack* (a) *and the fatigue crack paths of a surface crack* (b) *and a through-the-thickness crack* (c).

That is,

$$\delta_e = \delta_t - \delta_b \tag{3}$$

where

δ_e = the crack mouth opening displacement experimentally measured,
δ_t = the crack mouth opening displacement theoretically estimated, and
δ_b = the crack mouth opening displacement due to the bridging force.

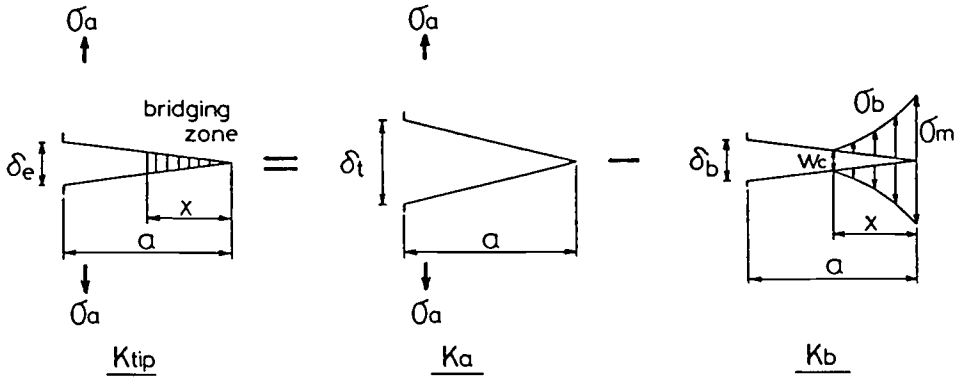

FIG. 9—*Schematic illustration of the relationship among* K_{tip}, K_a, *and* K_b.

In the case of through-the-thickness cracks, the K_{tip} value is obtained from the measured δ_e-value as [*20*]

$$K_{tip} = \frac{\delta_e E'}{4a}\sqrt{\pi a}\,\frac{F(a/W)}{V(a/W)} \tag{4}$$

where

$$F\left(\frac{a}{W}\right) = \frac{1.99 - (a/W)(1 - a/W)[2.15 - 3.93(a/W) + 2.7(a/W)^2]}{(1 + 2a/W)(1 - a/W)^{2/3}}$$

and

$$V\left(\frac{a}{W}\right) = 1.45 - 2.8\left(\frac{a}{W}\right) + 13.71\left(\frac{a}{W}\right)^2 - 2.96\left(\frac{a}{W}\right)^3 - 36.9\left(\frac{a}{W}\right)^4 + 70.7\left(\frac{a}{W}\right)^5$$

Figure 10 shows the relationship between crack length and stress intensity factors K_a, K_{tip}, and K_b for through-the-thickness cracks under a stress ratio of 0.1.

In the case of surface cracks, the K_{tip} value is obtained according to the method proposed by Torii et al [*21*]. In their method, the crack mouth opening displacement curve of the surface crack is approximated with the combined two functions: V_1 for the near center region and V_2 for the far center region, which are given as

$$V_1(x) = Ax^3 + Bx^2 + Cx + D \tag{5}$$

$$V_2(x) = G(c - x)^{1/2} + H(c - x)^{3/2} \tag{6}$$

where

A, B, C, D, G, and H = constants, and
x = the distance from the center of the surface cracks.

The crack opening stress $\sigma_{yy}(t)$ is given as

$$\sigma_{yy}(t) = \frac{1}{4\pi}\int_{-c}^{c}\frac{E'}{x - t}\frac{\partial V}{\partial x}\,dx \tag{7}$$

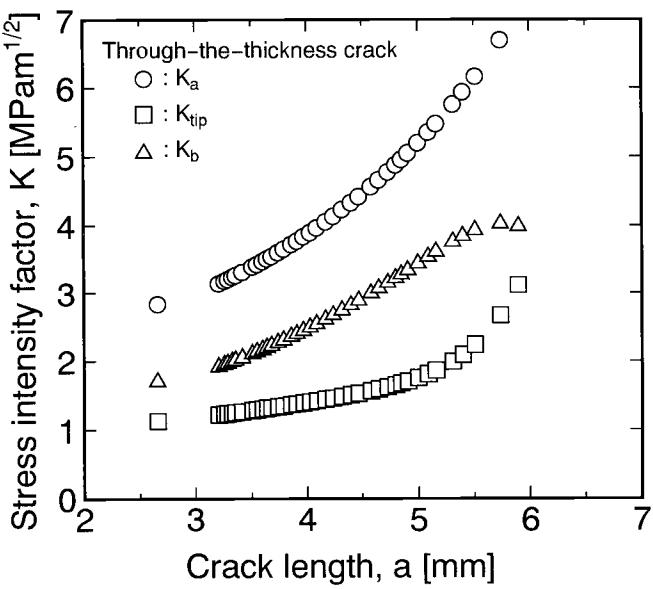

FIG. 10—*Relationship between crack length and stress intensity factors,* K_a, K_{tip}, *and* K_b *for through-the-thickness cracks.*

where

V = the approximated COD curve given by Eqs 5 and 6, and
$E' = E/(1 - V^2)$.

Finally, the stress intensity factor of the surface crack is estimated by the following equation.

$$K_I = \frac{1}{\sqrt{\pi c}} \int_{-c}^{c} \sigma_{yy}(x) \sqrt{\frac{c + x}{c - x}}\, dx \tag{8}$$

Figure 11 shows the measured crack mouth opening displacement at the applied bending stress σ_a = 200 MPa under the fatigue crack growth test. In the figure, the fitted curves combining Eqs 5 and 6 are also indicated. Based on these results, K_{tip} values were determined using Eqs 7 and 8. The results are shown in Fig. 12. The stress intensity factors K_a and K_b are also shown in the figure.

From the foregoing results, the fatigue crack growth curves shown in Fig. 6 were rearranged using the crack tip stress intensity factor K_{tip}. As can be seen from Fig. 13, the crack growth curves for through-the-thickness cracks and surface cracks coincide in the low crack growth rate region. The ratios of K_{tip} and K_a are shown in Fig. 14. The ratio K_{tip}/K_a for surface cracks is lower than that for through-the-thickness cracks, which indicates that the stress shielding effect at the crack tip is significant in surface cracks compared to through-the-thickness cracks. This result does not contradict the SEM observations shown in Fig. 8, where the bridging develops more significantly in the surface crack. The slower crack growth rate of surface cracks compared to through-the-thickness cracks results from the marked bridging and the consequent low value of K_{tip}.

V-shaped crack growth curves were observed for indentation surface cracks in Al_2O_3, Si_3N_4 [*22*], and SiC-reinforced Al_2O_3 [*23*], where the residual stress induced by indentation was not removed. However, when the effective value of stress intensity factor K_{eff} was evaluated to

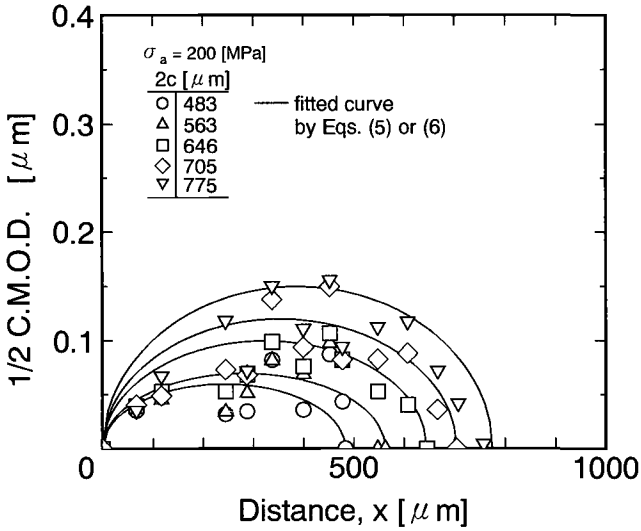

FIG. 11—*The crack mouth opening displacement of a surface crack at the applied stress of 200 MPa measured by a high magnification SEM observation.*

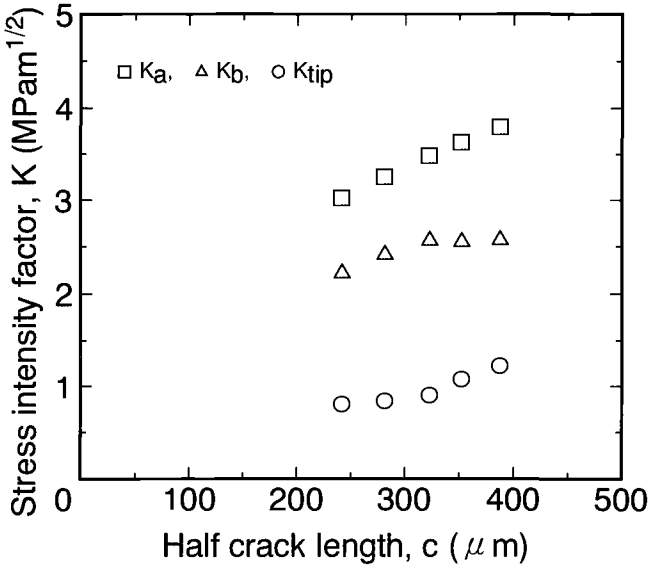

FIG. 12—*Relationship between the surface crack length and stress intensity factors,* K_a, K_{tip}, *and* K_b *for a surface crack.*

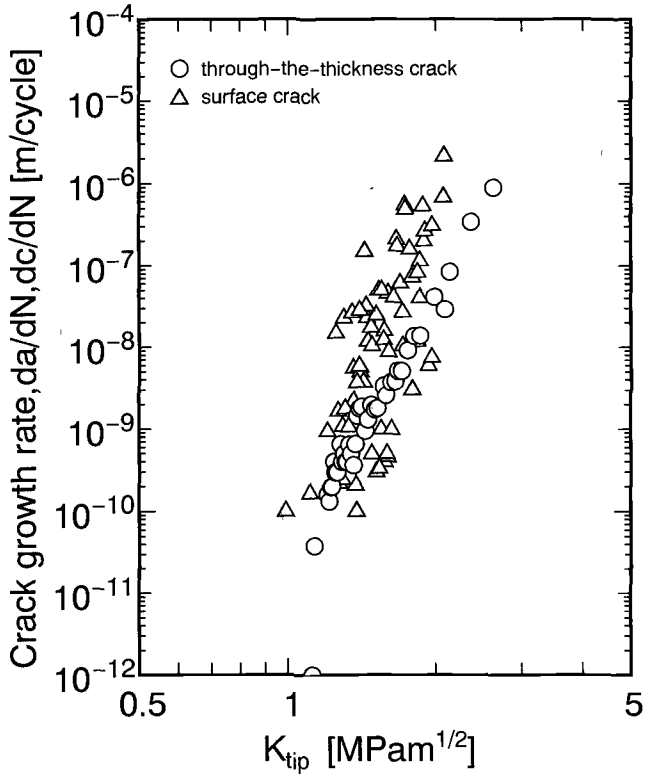

FIG. 13—*Relationship between crack tip stress intensity factor* K_{tip} *and crack growth rate.*

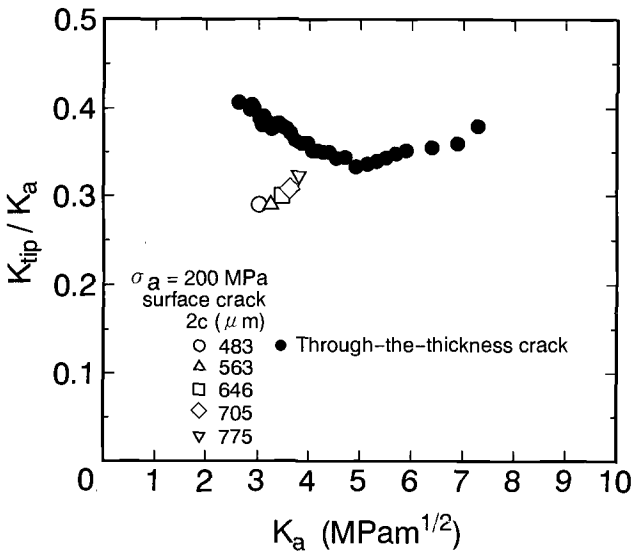

FIG. 14—*The ratios* K_{tip}/K_a *for a surface crack and a through-the-thickness crack.*

take into account the residual component based on the indentation analysis, the crack growth curve da/dN-K_{eff} showed a monotonic positive slope. The crack growth curve da/dN-K_{eff} for Si_3N_4 [*22*] almost coincides with the present crack growth curve for surface cracks shown in Fig. 6, where the residual stress was removed before fatigue crack growth tests. A similar negative dependency of the crack growth rate on K has been reported for surface cracks initiated from the notch corner in Mg-PSZ [*17*] and LAS-SiC_f [*16*]. Accounting for the shielding effect in the calculation of an effective (crack tip) stress intensity K_{tip}, the positive power-law dependency of growth rates on K_{tip} was found [*16*]. The crack growth behavior of naturally initiated surface cracks in porous Ce-PSZ has been reported [*24*]. Since the surface cracks initiated at pores at a lower stress level than the transformation stress, the crack growth rate for surface cracks was faster than that for long cracks with stress shielding due to phase transformation.

From the foregoing discussion, small-crack effects are significant in many advanced ceramic materials. Taking into account the stress shielding effects due to phase transformation, bridging, residual stress, etc. in calculating effective (crack tip) stress intensity K_{tip}, the positive power-law crack growth curve, which coincides with that for the long through-the-thickness crack, is obtained. Since the small surface crack in this study ($2c > 200$ μm) is large enough compared to microstructural length (the grain size is approximately a few microns), the crack growth behavior of microstructurally short cracks in ceramic materials remains, at present, uncertain.

Conclusions

1. The surface crack length was measured successfully with good accuracy using the developed surface film gage technique with Pd-Pt sputter-deposited thin film.

2. When the crack growth curve was arranged by the applied K-value, the crack growth rate for surface cracks was lower than for long through-the-thickness cracks in the low crack growth rate region, where cyclic-dependent crack growth is dominant.

3. From SEM observations, more significant bridging was found in the wake of surface cracks compared to through-the-thickness cracks.

4. Arranging the crack growth curve by the crack tip stress intensity factor K_{tip}, where the stress shielding effect due to bridging is taken into consideration, the crack growth curve for surface cracks coincided closely with that for through-the-thickness cracks.

5. Since the stress shielding effect depends on various factors such as crack geometry, crack length, loading history, etc., the apparent crack growth curve in ceramic materials is variable. Using the effective (crack tip) stress intensity factor, K_{tip}, to take into account the stress shielding effect, a unique crack growth curve is expected for each ceramic.

References

[*1*] Dauskardt, R. H., Yu, W., and Ritchie, R. O., "Fatigue Crack Propagation in Transformation-Toughened Zirconia Ceramic," *Journal of the American Ceramic Society,* Vol. 70, No. 10, 1987, pp. C248–C252.

[*2*] Grossmuller, A., Zelizko, V., and Swain, M. V., "Fatigue Crack Growth in Ceramics Using a Compressive Loading Geometry," *Journal of Materials Science Letters,* Vol. 8, 1989, pp. 29–31.

[*3*] Sylva, L. A. and Suresh, S., "Crack Growth in Transforming Ceramics Under Cyclic Tensile Loads," *Journal of Materials Science,* Vol. 24, 1989, pp. 1729–1738.

[*4*] Dauskardt, R. H., Marshall, D. B., and Ritchie, R. O., "Cyclic Fatigue-Crack Propagation in Magnesia-Partially-Stabilized Zirconia Ceramics," *Journal of the American Ceramic Society,* Vol. 73, No. 4, 1990, pp. 893–903.

[*5*] Tsai, J.-F., Yu, C.-S., and Shetty, D. K., "Fatigue Crack Propagation in Ceria-Partially-Stabilized Zirconia [Ce-TZP]-Alumina Composites, *Journal of the American Ceramic Society,* Vol. 73, 1990, pp. 2992–3001.

[6] Liu, S.-Y. and Chen, I.-W., "Fatigue of Yttria-Stabilized Zirconia: II, Crack Propagation, Fatigue Striations, and Short-Crack Behavior," *Journal of the American Ceramic Society,* Vol. 74, No. 6, 1991, pp. 1206–1216.

[7] Ewart, L. and Suresh, S., "Crack Propagation in Ceramics Under Cyclic Loads," *Journal of Materials Science,* Vol. 22, 1987, pp. 1173–1192.

[8] Reece, M. J., Guiu, F., and Sammur, M. F. R., "Cyclic Fatigue Crack Propagation in Alumina Under Direct Tension-Compression Loading," *Journal of the American Ceramic Society,* Vol. 72, No. 2, 1989, pp. 348–352.

[9] Fett, T., Martin, G., Munz, D., and Thun, G., "Determination of da/dN-ΔK_I Curves for Small Cracks in Alumina in Alternating Bending Tests," *Journal of Materials Science,* Vol. 26, 1991, pp. 3320–3328.

[10] Lathabai, S., Rodel, J., and Lawn, B. R., "Cyclic Fatigue from Frictional Degradation at Bridging Grain in Alumina," *Journal of the American Ceramic Society,* Vol. 74, No. 6, 1991, pp. 1340–1348.

[11] Tanaka, T., Okabe, N., and Ishimaru, Y., "Fatigue Crack Growth and Crack Closure of Silicon Nitride Under Wedge Effect by Fine Fragments," *Transactions of JSMS,* Vol. 38, No. 425, 1987, pp. 137–143.

[12] Ueno, A., Kishimoto, H., Kawamoto, H., and Asakura, M., "Cyclic Propagation Behavior of Sintered Silicon Nitride Under Cyclic Load of High Frequency and High Stress Ratio," *Transactions of JSMS,* Vol. 39, No. 446, 1990, pp. 1570–1575.

[13] Mutoh, Y., Takahashi, M., Oikawa, T., and Okamato, H., "Fatigue Crack Growth of Long and Short Cracks in Silicon Nitride," *Fatigue of Advanced Materials,* R. O. Ritchie, R. H., Dauskardt, and B. N. Cox, Eds., MCEP Ltd., Birmingham, England, 1991, pp. 211–225.

[14] Kishimoto, H., Ueno, A., and Kawamoto, H., "Crack Propagation Behavior of Sintered Silicon Nitride Under Cyclic Loads," *Mechanical Behavior of Materials, VI(ICM-6),* M. Jono and T. Inoue, Eds., Pergamon Press, Vol. 2, 1991, pp. 357–364.

[15] Mutoh, Y. and Takahashi, M., "Mechanisms of Fatigue Crack Growth in Silicon Nitride," *Theoretical Concepts and Numerical Analysis of Fatigue,* C. J. Beevers and A. F. Blom, Eds., MCEP Ltd., Birmingham, England, 1992, pp. 541–558.

[16] Luh, E. H., Dauskardt, R. H., and Ritchie, R. O., "Cycle Fatigue-Crack Growth Behavior of Short Cracks in SiC-Reinforced Lithium Aluminosilicate Glass-Ceramic Composite," *Journal of Materials Science Letters,* Vol. 9, 1990, pp. 719–725.

[17] Steffen, A. A., Dauskardt, R. H., and Ritchie, R. O., "Cyclic Fatigue Life and Crack-Growth Behavior of Microstructurally Small Cracks in Magnesia-Partially-Stabilized Zirconia Ceramics," *Journal of the American Ceramics Society,* Vol. 74, No. 6, 1991, pp. 1259–1268.

[18] Ogawa, T. and Suresh, S., "Surface Film Technique for Crack Length Measurement in Nonconductive Brittle Materials: Calibration and Evaluation," *Engineering Fracture Mechanics,* Vol. 39, No. 4, 1991, pp. 629–640.

[19] Raju, I. S. and Newman, J. C., *Engineering Fracture Mechanics,* Vol. 11, 1979, pp. 817–829.

[20] *Stress Intensity Factor Handbook,* Y. Murakami, Ed., Pergamon Press, Elmsford, NY, 1987.

[21] Torii, T., Honda, K., Fujibayashi, T., and Hamano, T., "An Evaluation Method of Crack Opening Stress Distributions and Stress Intensity Factors Based on Opening Displacements Along a Crack," *Transactions of JSMS,* Vol. 55, No. 515, 1989, pp. 1525–1531.

[22] Hoshide, T., Ohara, T., and Yamada, T., "Fatigue Crack Growth from Indentation Flaw in Ceramics," *International Journal of Fracture,* Vol. 37, 1988, pp. 47–59.

[23] Dauskardt, R. H., James, M. R., Porter, J. R., and Ritchie, R. O., "Cyclic Fatigue-Crack Growth in SiC-Whisker-Reinforced Alumina Ceramic Composite: Long- and Small-Crack Behavior," *Journal of the American Ceramic Society,* Vol. 75, No. 4, 1992, pp. 759–771.

[24] Cardona, D. C. and Beevers, C. J., "Formation and Growth of Short Fatigue Cracks in a Zirconia-Ceria Alloy," *Scripta Metallugica,* Vol. 23, 1989, pp. 945–950.

K. Schulte,[1] *K.-H. Trautmann,*[2] *R. Leucht,*[2] *and K. Minoshima*[3]

Fatigue Response of Metal Matrix Composites

REFERENCE: Schulte, K., Trautmann, K.-H., Leucht, R., and Minoshima, K., **"Fatigue Response of Metal Matrix Composites,"** *Cyclic Deformation, Fracture and Nondestructive Evaluation of Advanced Materials: Second Volume, ASTM STP 1184,* M. R. Mitchell and O. Buck, Eds., American Society for Testing and Materials, Philadelphia, 1994, pp. 32–47.

ABSTRACT: Results are presented on the fatigue behavior of continuous fiber-reinforced aluminum and titanium alloys, both reinforced with SiC fibers. The pure aluminum matrix was reinforced with the "Tyranno" fiber of Ube, Japan, while the Ti6Al4V matrix was reinforced with the SCS-6 fiber of Textron. Also investigated was an Al-2.5Li alloy reinforced with α-Al_2O_3 FP fiber from DuPont.

The fatigue behavior of the MMC composites was observed to be superior when compared to the fatigue behavior of bulk matrix material. This was especially true for the case of tension-compression loading, where the overall superior compressive behavior of MMCs played a dominant role.

Failure in an MMC with unidirectional reinforcement normally initiates at or near imperfections, such as misaligned fibers, voids, foreign inclusions, or surface damage with subsequent fatigue crack propagation. An answer is given as to whether the variation of stiffness due to damage development can be used as a damage analogue. Finally, an explanation of the fracture behavior is given.

KEYWORDS: metal matrix composites, continuous fiber reinforcement, fatigue, damage mechanisms, silicon-carbide fibers, aluminum matrix, titanium matrix, internal stresses

Conventional materials are being tailored close to their ultimate properties. New technological requirements demand even further improvements in materials. Metal matrix composites (MMC) are candidate materials to reach this goal. Present interest in MMCs is focused primarily on light alloys reinforced with fibrous or particulated phases to achieve major increases in selected mechanical properties or thermal stability. This new interest is related mainly to the fact that ceramic-based reinforcements have become available and are now comparatively inexpensive. Al_2O_3- or SiC-based fibers, whiskers, or particles, as well as carbon fibers are used to reinforce aluminum, magnesium, or titanium matrix alloys [*1*]. The present study will focus on continuous fiber-reinforced aluminum and titanium alloys.

With the increasing application of metal matrix composites, it becomes more and more important to understand their mechanical behavior and especially their fatigue properties. Fatigue damage in metal matrix composites can cause significant stiffness reduction [*2*] without failure. This paper will therefore concentrate on the fatigue response of metal matrix composites reinforced with continuous fibers.

Material Details

Results discussed in this paper are from experiments performed on a number of composite systems which contain various high-strength fibers from different manufacturers. The fibers

[1] Technical University Hamburg-Harburg, 21073 Hamburg, Germany.
[2] DLR, Institute of Materials Research, 51140 Köln, Germany.
[3] Kyoto University, Kyoto 606-01, Japan.

TABLE 1—*Mechanical properties of various types of fibers.*

Fiber Type	Trade	Supplier	Density, g/cm^3	Diameter, μm	Tensile Strength, MPa	Elastic Modulus, GPa	Strain to Failure, %	α,[a] 10^{-6} k^{-1}
α-Al_2O_3	FP	Du Pont	3.9	20	1500	380	0.4	6.4
SiC	Tyranno, Si-Ti-C-O	Ube	2.4	10	2800	200	1.5	3.1
SiC	SCS-6	Textron	3.05	140	3400	420	1.0	3.0

[a] Coefficient of thermal extension.

chosen for this investigation were the SCS-6 SiC fiber from Textron, the Si-Ti-C-O fiber (Tyranno) from Ube, and the α-Al_2O_3 FP fiber from DuPont. The physical properties of each fiber are listed in Table 1. The aluminum matrix materials (Al 1070 and Al-2.5Li) were reinforced with the Tyranno fiber and the FP fiber, respectively. The SCS-6 fiber was used to reinforce the Ti6Al4V matrix.

Mechanical properties of the neat matrix alloys are given in Table 2. The Al 1070 matrix material has a comparatively low fracture stress, but a high strain to failure. When using the Al-2.5Li matrix, coherent δ′ particles form [*3*], leading to precipitation hardening. Therefore a relatively high fracture stress (σ_B) can be observed in the matrix. Using lithium as an alloying element also increases the elastic modulus. In comparison, the titanium matrix has a higher elastic modulus and fracture stress with a low strain to failure.

Manufacturing of the aluminum composites was accomplished by various squeeze-casting techniques. The Si-Ti-C-O fiber-reinforced Al 1070 was fabricated by a vertical squeeze-casting process at Ube, Japan, with a fiber volume fraction of about 55%. The FP fiber-reinforced Al-2.5Li composite was produced via a vacuum melt infiltration process at the University of Bordeaux, France, with a fiber volume fraction of about 30%. In the case of the SCS-6/Ti6Al4V, manufacturing occurred by a diffusion bonding process via hot isostatic pressing (HIP) at 1900 bar and 900°C for 0.5 h. The fiber volume fraction amounted to 45%.

Experimental Details

For mechanical characterization, tension, compression, and fatigue tests were performed on cylindrical hour-glass-shaped specimens with a diameter of 3.8 mm. The specimens had a thread on both ends and were gripped in the female screw such that the load was introduced not only via the threads but also by gripping stresses, as the female screw was cut into four sections with a slot in between so a mechanical gripping load could be applied [*4*].

Tension, compression, and fatigue tests were performed at room temperature on unidirectional composites with fibers in the 0° and 90° direction. Fatigue tests were made at a stress ratio of $R = \sigma_{min}/\sigma_{max} = 0.1$ and $R = -1$ at a frequency of 10 Hz. Strain measurements were

TABLE 2—*Properties of neat metal matrices.*

Neat Matrix	Elastic Modulus, GPa	Tensile Strength, MPa	Strain to Failure, %
Al 1070	69	59	40
Al-2.5 Li	80	160	~25
Ti6Al4V	110	1100	8

performed using clip-on gages. In order to perform *S-N* curves, the fatigue tests were made under load control. Fracture surfaces were studied by scanning electron microscopy (SEM).

Material Characterization

Static Loading

Table 3 summarizes the mechanical properties after tension and compression testing of both 0 and 90° fiber orientation. The stress/strain behavior of the Al_2O_3/Al-2.5Li composite is shown in Fig. 1. Tensile strengths achieved in the 0° direction for both composites were slightly lower as predicted by the rule of mixtures.

The strain to failure is controlled by the fiber failure strain. However, under compressive loading the strength is considerably greater than in tension. This is in agreement with a higher strain to failure under compressive loading. The generally good compressive behavior can be related mainly to the fact that:

1. The metal matrix itself has a relatively high elastic modulus, which allows it to better support the fibers and avoids their shortwave kinking.
2. The ceramic fibers, because of their microstructure, can carry a higher compressive than tensile load.

TABLE 3—*Mechanical properties after tension and compression testing.*

a Si-Ti-C-O/Al

Mechanical Properties	[0°] Fiber Orientation		[90°] Fiber Orientation	
	Tension	Compression	Tension	Compression
σ_B,[a] MPa	920	1605	168	204
ε_B,[b] %	0.89	1.77	1.30	7.80
E,[c] GPa	125	118	102	90

b Al_2O_3/Al-2.5Li

Mechanical Properties	[0°] Fiber Orientation		[90°] Fiber Orientation	
	Tension	Compression	Tension	Compression
σ_B,[a] MPa	538	1460	177	225
ε_B,[b] %	0.36	1.09	1.20	7.40
E,[c] GPa	181	166	126	117

c SCS-6/Ti6Al4V

Mechanical Properties	[0°] Fiber Orientation
σ_B,[a] MPa	1800–2400
ε_B,[b] %	1.1–1.3
E,[c] GPa	190–230

[a] Fracture stress.
[b] Total strain to failure.
[c] Elastic modulus.

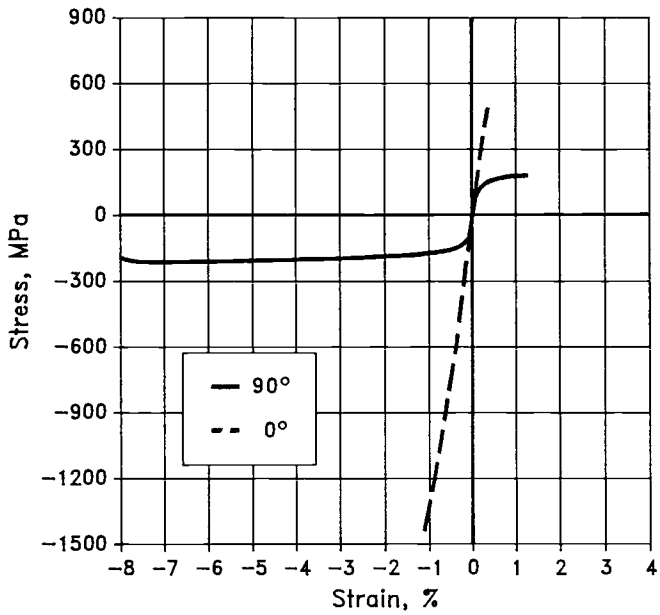

FIG. 1—*Stress-strain behavior of continuous fiber-reinforced Al_2O_3/Al-2.5Li under tension and compression load parallel (0°) and transverse (90°) to fiber direction (four different tests).*

3. The tensile residual stresses stored in the matrix allow high elastic compressive matrix deformations. This is discussed further later in this paper.

In a test transverse to the fiber direction, the fracture stress of the composite exceeds the fracture stress of the aluminum matrix. Due to the fiber reinforcement, an increase of the elastic modulus can also be observed. Despite the fact that the matrix material has a high strain to failure, it cannot be realized in the composite. Only about 1.2% strain to failure can be achieved. Under compressive loading the elastic modulus is not as high as in tension, but the fracture strength is again essentially higher. Therefore the strain to failure is higher by far under compression loading than under tensile loading.

Figure 2 shows a tension test of the SCS-6/Ti6Al4V composite. The knee in this curve is where plastic deformation of the matrix initiates. An exclusively elastic behavior can only be observed at the very beginning of a stress-strain curve. From the SCS-6/Ti6Al4V composite no tests transverse to the fiber direction and no static compression tests were performed; therefore only tension test data are given in Table 3c. Failure mechanisms observed in these various metal matrix composites have been described elsewhere [5].

Fatigue Loading

If fatigue tests are performed at positive R ratios on unidirectional continuous fiber-reinforced composites, superior fatigue properties can be achieved when compared to bulk aluminum alloys. Figure 3 shows the S-N curve for Si-Ti-C-O fiber/Al. When the same material is fatigue loaded ($R = 0.1$) transverse to the fiber direction, its fatigue properties remain comparatively good (Fig. 3*b*). However, at a fatigue load level of $R = -1$, a pronounced influence of the fatigue behavior is observed, and with an increasing number of load cycles the composite reaches the fatigue level of the matrix alloy.

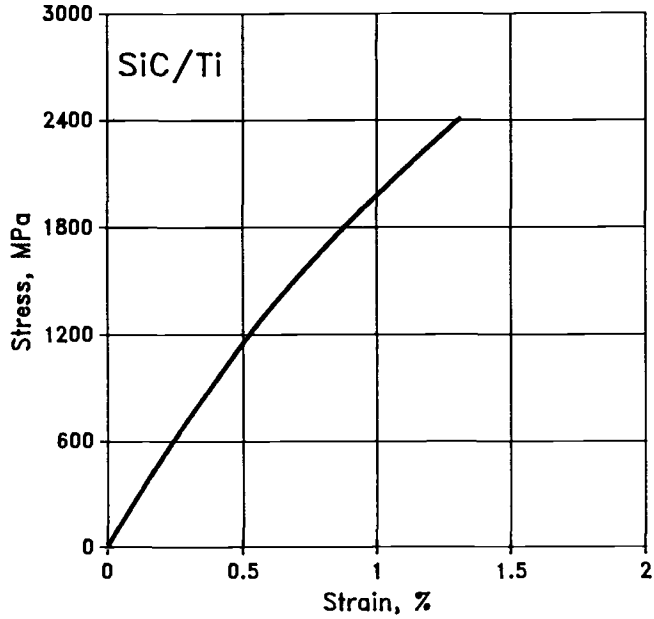

FIG. 2—*Stress-strain behavior of the SCS-6/Ti6Al4V composite during tensile loading.*

Figures 4*a* and 4*b* show the stress-strain response of Al_2O_3/Al-2.5Li after different numbers of load cycles. In the case with σ_{min} = 410 MPa (R = 0.1), which is about 75% of the fracture stress, the specimen exceeds more than 4.7 million load cycles. At $R = -1$ with a total stress variation of 600 MPa, the specimen easily survives more than 3.7 million load cycles. The reduction in the width of the hysteresis loops indicates cyclic hardening. These results again demonstrate the superior fatigue behavior observed for the MMCs. At these high load levels, conventional aluminum alloys would never exceed these high numbers of load cycles.

The fatigue behavior of the SCS-6/Ti6Al4V metal matrix composites is summarized in Fig. 5. The maximum stress in each load cycle is plotted versus the number of cycles achieved until final failure for a tension-compression load ($R = -1$). For comparison, the fatigue behavior of the bulk matrix metal is shown. In the low-cycle fatigue range, the fatigue life of the fiber-reinforced titanium appears to be superior to the fatigue life of the unreinforced metal. In the high-cycle fatigue range both the neat matrix metal and the fiber-reinforced metal reach about the same fatigue life.

Figure 6*a* shows the stress-strain behavior of the SCS-6/Ti6Al4V composite. The maximum stress of various load cycles is plotted versus strain. At the beginning of the first load cycle, indicated in Fig. 6*a* by a dart, the composite first deforms elastically, and at about 0.2% strain the curve kinks and a knee is formed. This formation of a knee in the stress-strain curve can normally be related to plastic matrix deformations. However, plastic matrix deformation in Ti6Al4V can only be observed at strains higher than 0.5%. This gives rise to the assumption that, due to the manufacturing process of the composites, residual tensile stresses are stored in the matrix.

When starting a fatigue test with the first load cycle in the compressive direction, only an elastic and no plastic deformation can be observed down to a compressive stress of −1000 MPa (compare Fig. 6*b*), which is equivalent to −0.44% total strain. However, when loading again in the tensile regime, the same result as observed previously in Fig. 6*a* has to be deter-

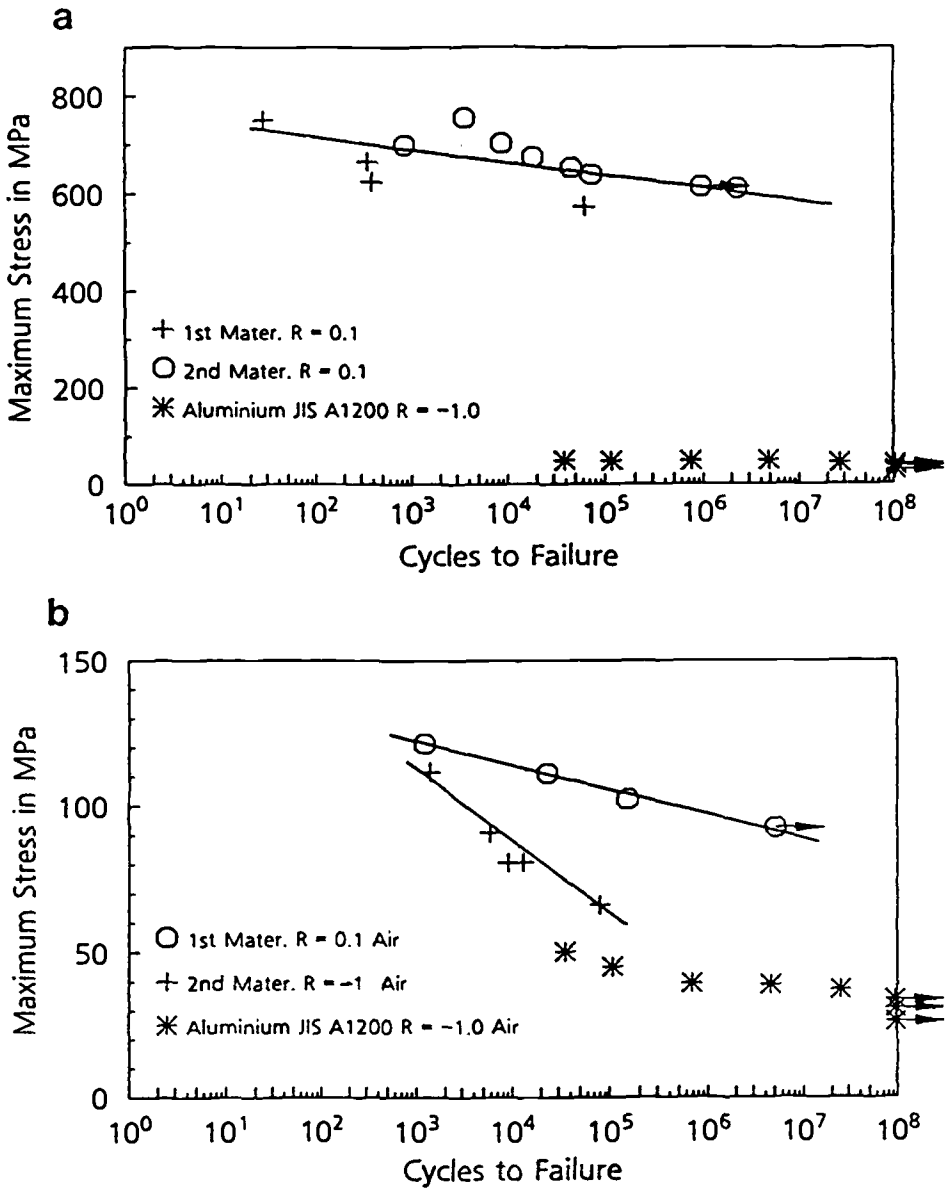

FIG. 3—S-N *curves of Si-Ti-C-O/Al composites:* (a) *fatigue behavior in fiber direction [0°];* (b) *fatigue behavior transverse to fiber direction [90°]. First and second material refer to various manufacturing lots.*

mined, which means the onset of matrix yielding at about 0.2% strain and a knee in the stress-strain curve.

It is now obvious that internal tensile stresses are stored in the matrix due to the manufacturing process. The internal stresses are dependent not only on the fiber and matrix elastic modulus and their thermal expansion coefficients, but also on the plasticity behavior of the matrix, which are all a function of temperature. After cooling from the manufacturing temper-

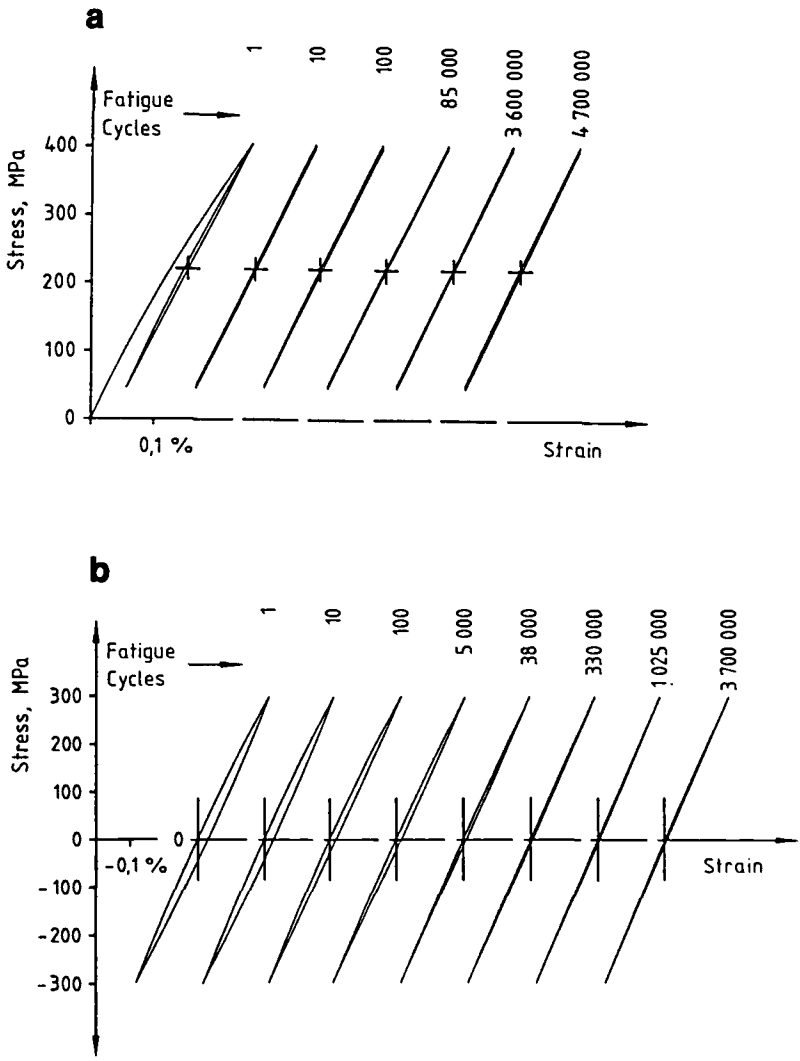

FIG. 4—*Stress/strain behavior with hysteresis loops at various cycle numbers. Al_2O_3/Al-2.5Li [0°]: (a)* R = *0.1,* σ_{max} = *410 MPa,* $N_F > 4.7 \cdot 10^6$ *cycles; (b)* R = *−1,* σ_{max} = *300 MPa,* $N_F > 3.7 \cdot 10^6$ *cycles.*

ature, differential strains are set up due to different thermal expansion coefficients of the fiber and matrix. This tends to set up stresses, but they are at least partly relieved by creep in the matrix. With further cooling, the creep rate drops off and residual stresses build up because the metal is not able to creep as fast as the differential strains are building up. Eventually the yield stress is reached. The stresses may further increase due to the increase in yield stress with decreasing temperature. At room temperature, residual tensile stresses are now in the matrix, and residual compressive stresses are in the fibers.

If one assumes that yielding of the neat matrix alloy begins at about 0.5% strain—in the composite matrix yielding is already observed at about 0.3%—then one can conclude that the internal stress is equivalent to about 0.2% strain. This means a residual tensile stress of about

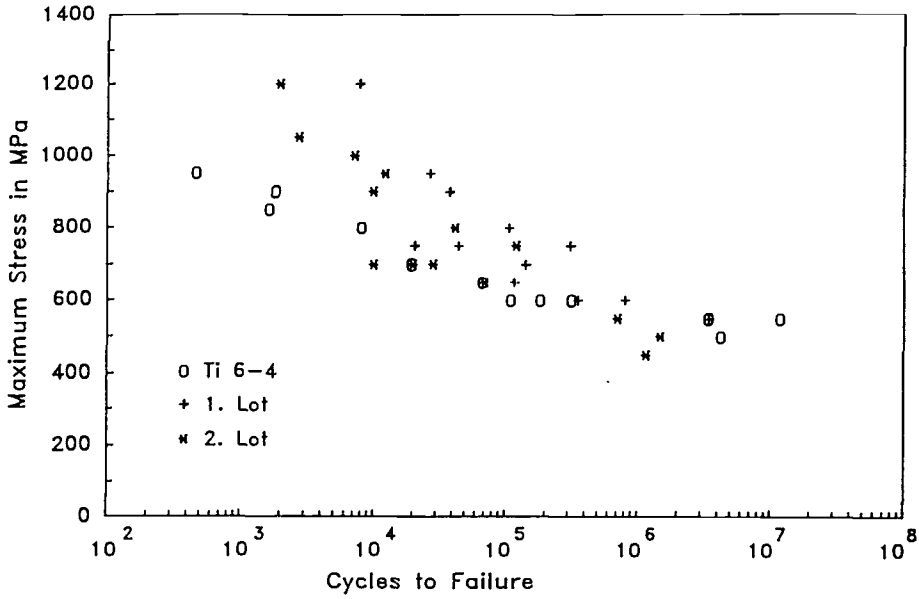

FIG. 5—S-N *curve of the SCS-6/Ti6Al4V composite. Fatigue behavior is in the fiber direction.*

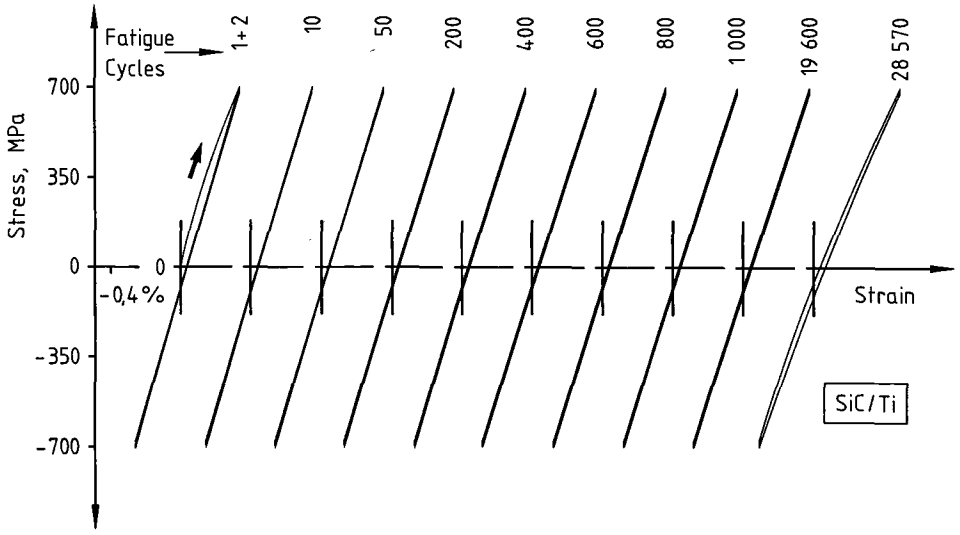

FIG. 6*a*—*Stress/strain behavior with hysteresis loops at various cycle numbers. SCS-6/Ti6Al4V [0°]:* R = *1*, σ_{max} = *700 MPa*, N_F > *28 570 cycles.*

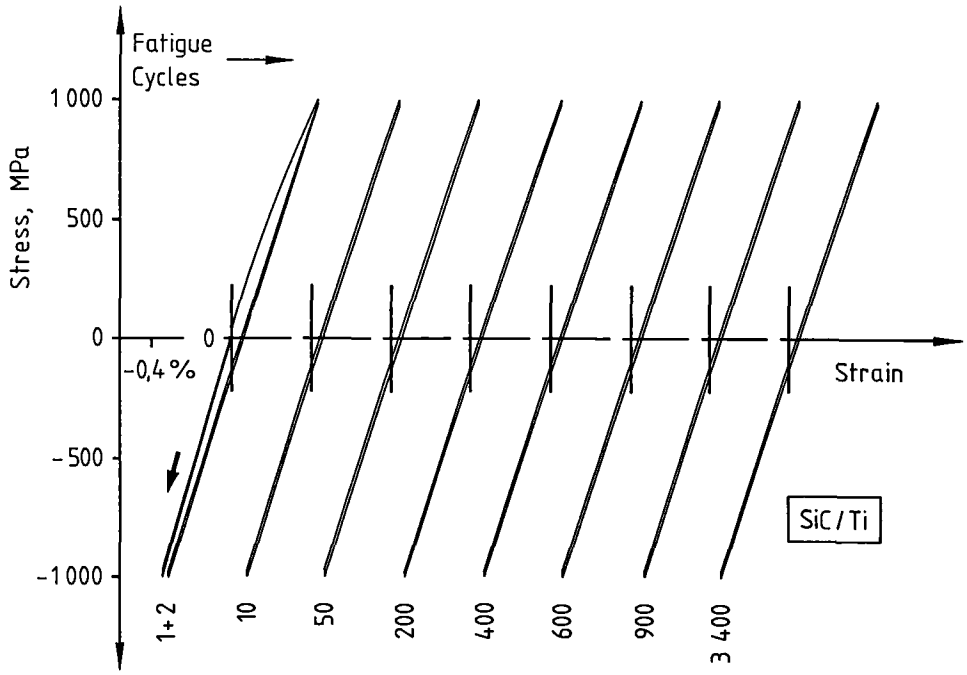

FIG. 6*b*—*Stress/strain behavior with hysteresis loops at various cycle numbers. SCS-6/Ti6Al4V [0°]:* R = −1, σ_{max} = *1000 MPa,* N_F > *3400 cycles.*

450 MPa is stored in the matrix. The high internal stress rate might affect the compressive properties of metal matrix alloys. If the matrix alloy alone is loaded in tension or compression, it deforms symmetrically, as shown schematically in Fig. 7. It deforms first elastically, and the point of yielding under tensile as well as compressive load amounts to about the same value ($\sigma_{yt} \sim -\sigma_{yc}$).

In the composite, due to the residual tensile stresses stored in the matrix, the specimens are, in the unloaded condition, in the status marked by (•). If tensile loading occurs, only a small portion of the metal elastic strength remains, and it begins to deform plastically early, after only a small increase in stress (compare Figs. 2 and 6*a*).

Under compressive load, however, only elastic and no plastic deformation (no knee) is observed in the composite. The composite matrix, being in the status marked by (•) in Fig. 7, has now for its deformation the whole compressive elastic and the additional residual stress part (the tensile part) of the curve available for deformation. It can therefore deform elastically over a wider range. This means that full support of the fibers (only elastic matrix deformation) remains available during a wider range of compressive loading.

During cyclic fatigue loading, stiffness reduction can be used as an analogue to monitor damage development. Its change can be related directly to stress redistributions, which can be expected if internal damage occurs in a fiber-reinforced composite [*6,7*]. Stiffness reduction can also be observed in a metal matrix composite. Figure 6*a* shows that close to final failure the slope of the hysteresis loop is strongly decreased, mainly in the tensile portion of the load cycle. This can be further corroborated by a plot (Fig. 8) where the strain response of each constant amplitude load cycle is plotted versus time. Close to specimen failure the strain amplitude increases. This can be confirmed with the result in Fig. 6*a*.

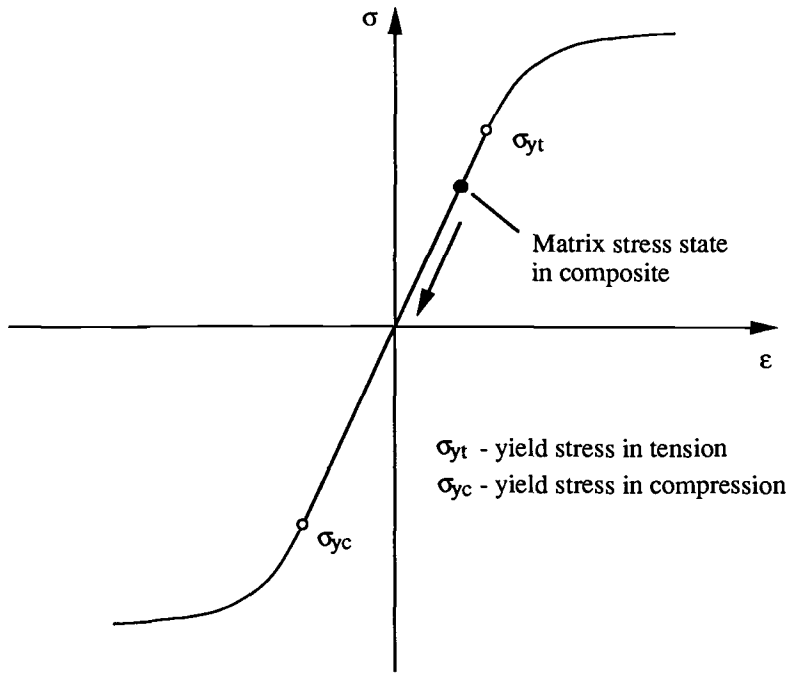

FIG. 7—*Schematic of the matrix stress/strain behavior in tension and compression, illustrating internal stress state:* σ_{YT} = *yield stress under tensile load;* σ_{yc} = *yield stress under compression load.*

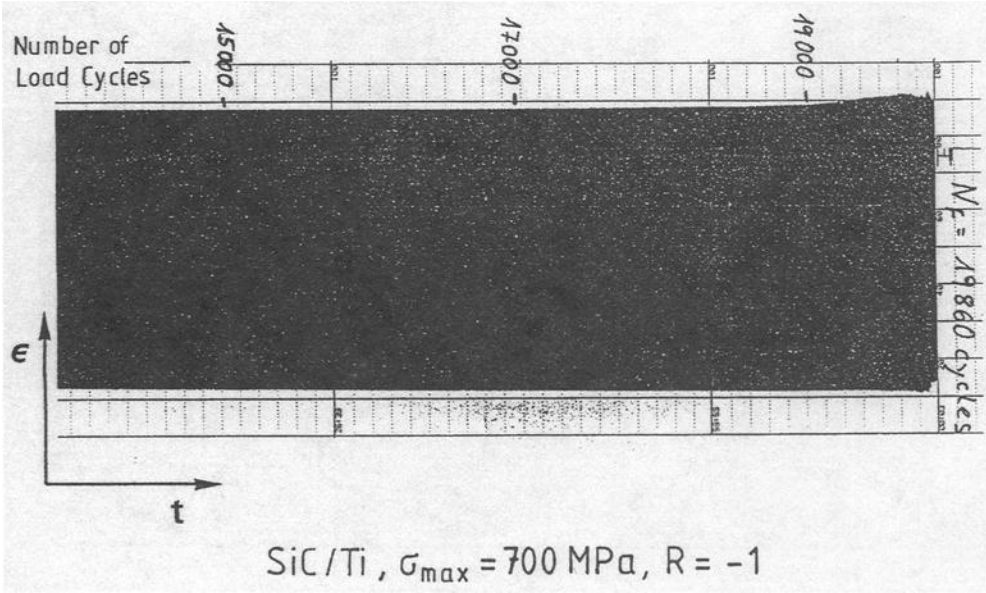

FIG. 8—*Strain amplitude versus time of a constant amplitude fatigue test,* R = −1, σ = 700 *MPa,* N_F = 19 860 *cycles.*

Fatigue Damage Mechanisms

Failure in a metal matrix composite with unidirectional reinforcement normally initiates at or near imperfections or surface damage. Figure 9*a* shows the initiation of a fatigue crack at the specimen surface of a SiC fiber-reinforced aluminum alloy. The specimen was fatigued at 600 MPa ($R = 0.1$) up to $1.02 \cdot 10^6$ load cycles, and it did not fail. At a higher magnification, fiber failure can be distinguished (Fig. 9*b*). The initiation site of the fatigue damage is shown in Fig. 9*c*. The specimen was loaded at $\sigma_{max} = 660$ MPa ($R = 0.1$) for 385 load cycles. Besides an inclusion, much more fiber pullout, which means a more irregular crack front, can be seen close to the crack initiation site. However, a distance away from the initial crack, the fracture surface is relatively smooth and similar to that from the tension test. This is demonstrated in Fig. 9*d*.

An additional test attempted to investigate the fatigue crack propagation behavior on a center-cracked sheet specimen. The test coupon of Si-Ti-C-O/Al had a width of 18 mm and a thickness of 2 mm. The length of the specimen amounted to 60 mm. In the center of the test coupon was a hole with a diameter of 1 mm. Crack starter notches were machined with a length of 0.4 mm. A fatigue test was conducted at $R = 0.1$, with a maximum stress of about 260 MPa. Specimen failure occurred after $3.185 \cdot 10^6$ load cycles. Figure 10 shows the crack propagation. First

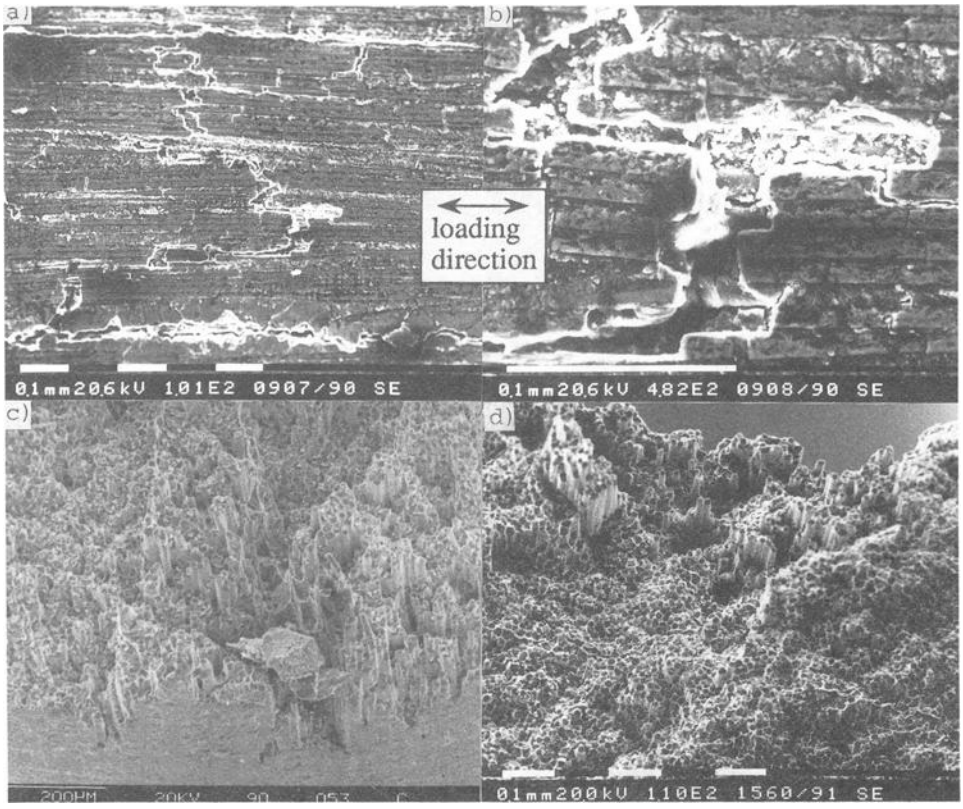

FIG. 9—*Fracture morphology of fatigue-loaded [0°] specimens of Si-Ti-C-O/Al, SEM micrograph:* (a) *Surface of a fatigue-loaded specimen,* $R = 0.1$, $\sigma_{max} = 600$ *MPa,* $N = 1.02 \cdot 10^6$ *cycles. Specimen did not fail;* (b) *High magnification of Fig.* 9a. *Debonding and fiber failure;* (c) *Initiation site of a fatigue-loaded specimen,* $R = 0.1$, $\sigma_{max} = 660$ *MPa,* $N_F = 385$ *cycles. Initiation of the crack at imperfections;* (d) *The crack initiation site is marked by fiber/matrix debonding with fiber pullout.*

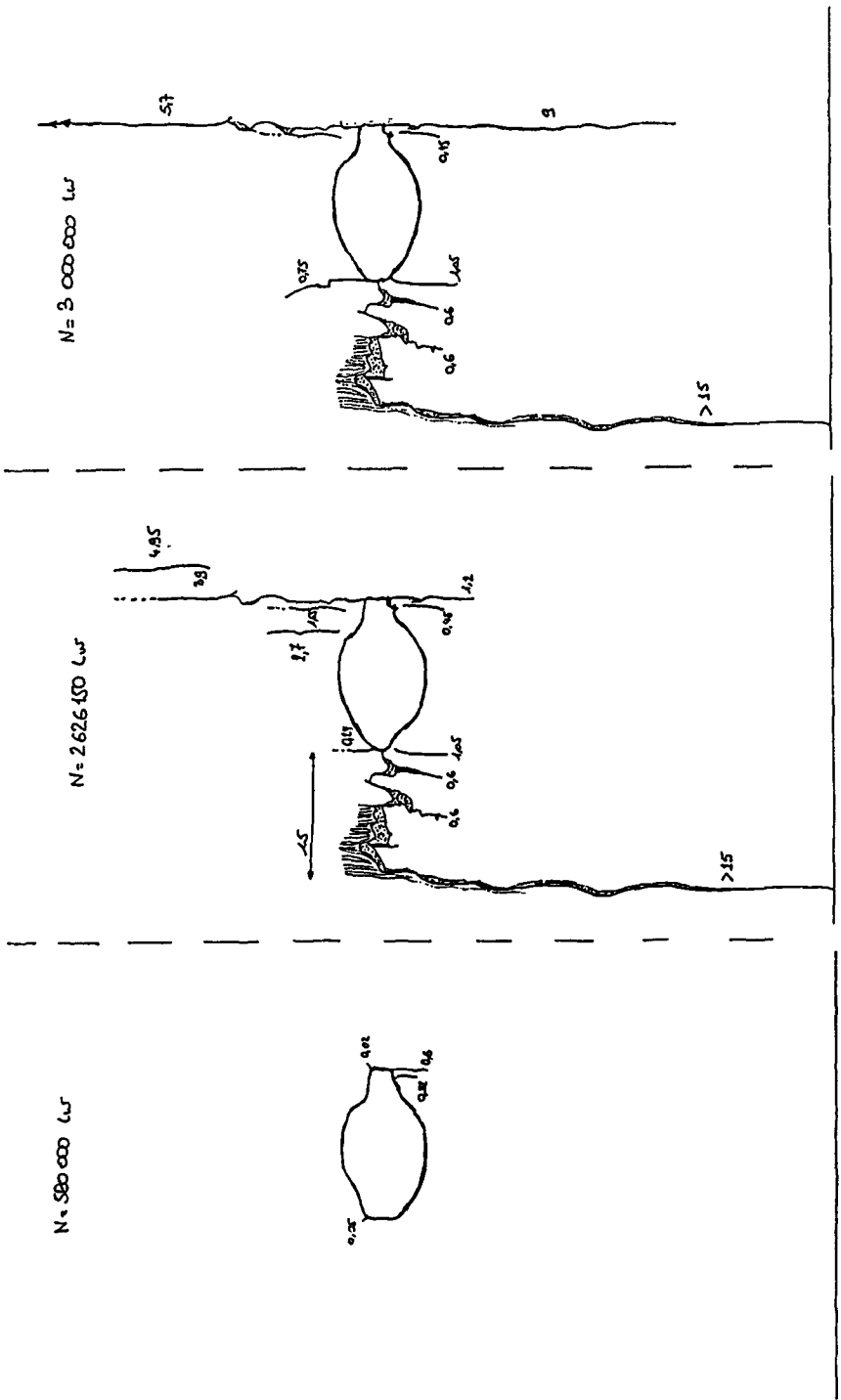

FIG. 10—*Crack configuration at various cycle numbers of a fatigue crack propagation test.* $R = 0.1$, $\sigma_{max} = 260\ MPa$, $N_F = 3.185 \cdot 10^6$ *cycles. Si-Ti-C-O/Al.*

cracks form at the starter notch after $5.8 \cdot 10^5$ load cycles, but they are parallel to the load direction. Their maximum length is 0.6 mm. After $2.6 \cdot 10^6$ load cycles a crack configuration is built up which does not change much until final rupture.

On the left side of the specimen the crack first propagates perpendicular to the fiber and load direction and then turns by 90° and further propagates parallel to the fibers. On the right side of the specimen the direction of crack propagation is, from the beginning, parallel to the fibers. This behavior corroborates the observation made in Fig. 9.

Monolithic, non-fiber-reinforced aluminum alloys after fatigue loading show a typical fracture morphology where fatigue crack propagation during each consecutive load cycle is indicated by striations. However, for composite materials a comparable behavior cannot be expected. Figure 11 shows the fracture surface of a fatigue test performed at $R = 0.1$. An overview of the fracture surface with lower magnification does not show essential differences to a tension test. Only at high magnification in a matrix-rich area can parallel lines be observed that have similarities to fatigue striations. Distinct differences, however, can be observed on the fracture surface of specimens loaded at $R = -1$. Because of tension/compression loading no dimples are formed, but in matrix-rich zones smooth-scaled areas are present showing parallel lines at high magnification, indicating a preferred direction of crack propagation (Fig. 11*b*).

The stress-strain behavior of a Si-Ti-C-O/Al composite with all fibers transverse to the loading direction is shown in Fig. 12*a*. The maximum and minimum stress reached in each consecutive load cycle was 100 MPa with an R ratio of -1. The first six and the last five stress-strain cycles (cycle numbers 1341 to 1345 of the load history) are shown. It becomes evident that a cyclic softening occurs and that a continuous elongation of the specimen with each load cycle takes place.

Looking to the surface of the specimen after 1345 load cycles, shear bands at an angle of 45° to the load axis have developed (Fig. 12*b*). The cyclic load-induced deformation seems concentrated mainly within these shear bands. At the triple point of shear bands, the initiation of a small crack is visible (Fig. 12*c*).

Failure under fatigue loading differs from that under tensile loading. A fatigue crack initiates at the specimen surface and propagates into the interior. The point of crack initiation near the

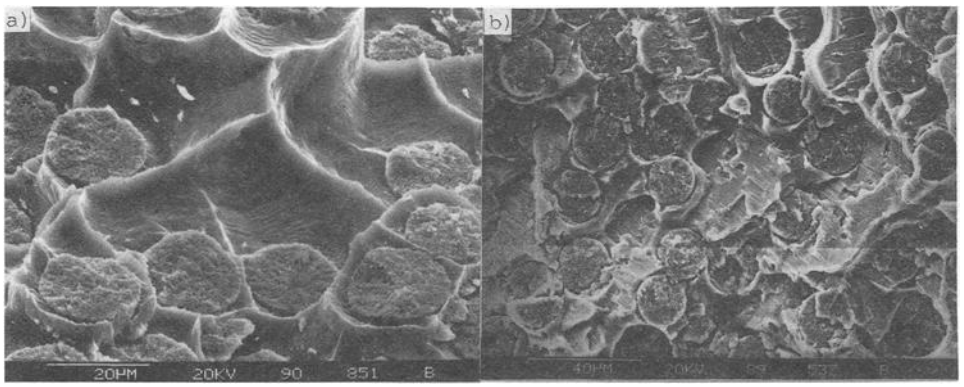

FIG. 11—*SEM micrographs of the fracture surface after a fatigue test. [0°], Al_2O_3/Al-2.5Li:* (a) *Dimples around fibers and formation of striations in matrix-rich areas:* $R = 0.1$, $\sigma_{max} = 410$ *MPa,* $N_F > 4.3 \cdot 10^6$ *cycles;* (b) *No formation of dimples. On matrix-rich flat areas are parallel striation-like lines, which give rise to fatigue crack propagation:* $R = -1$, $\sigma_{max} = 300$ *MPa,* $N_F > 3.7 \cdot 10^6$ *cycles.*

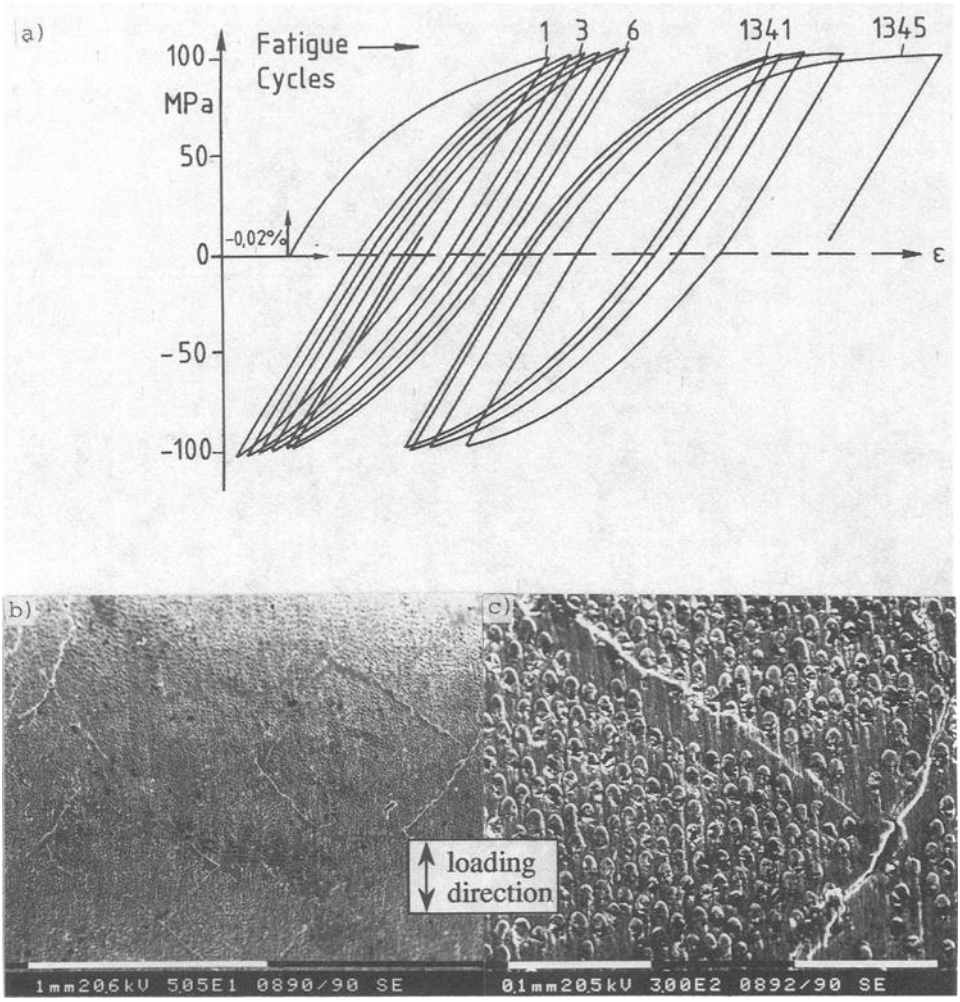

FIG. 12—(a) *Stress/strain behavior with hysteresis loops at various cycle numbers. Si-Ti-C-O/Al, [90°].* R = *−1,* σ_{max} = *100 MPa,* N = *1345 cycles.* (b) *Surface of a fatigue-loaded specimen. Specimen did not fail. Shear band formation in matrix-rich areas.* (c) *High magnification of Fig.* 12b. *Crack initiation at a triple point of shear bands.*

specimen surface often seems associated with fiber splitting (Fig. 13*a*). The crack then turns to the fiber/matrix boundary and further propagates preferentially along the fibers. Figure 13*b* is an example showing the fiber surface. On the fibers small SiC particles can be observed, with which they were coated to hold the fibers away during the manufacturing processes by squeeze casting. Later, when the crack propagates locally transverse to the fibers only in the matrix-rich areas, fatigue striations can be observed (Fig. 13*c*).

Conclusion

The fatigue response of several continuous fiber-reinforced metal matrix composites has been studied. The fiber reinforcement leads, in all cases, to an increase in the elastic modulus.

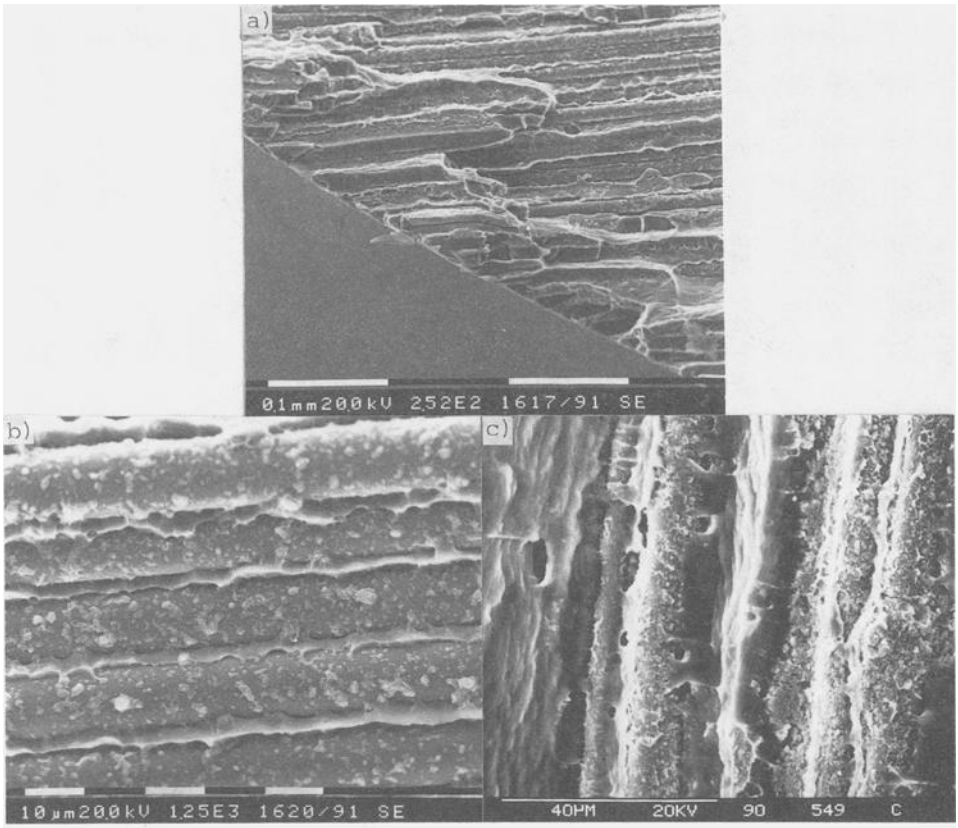

FIG. 13—*SEM micrographs of the fracture surface after a fatigue test, [90°], Si-Ti-C-O/Al,* R = *0.1,* σ_{max} = *120 MPa,* N_F = *1672 cycles. (Loading direction perpendicular to fracture plane.):* (a) *Initiation of the fatigue crack at the specimen edge with fiber splitting;* (b) *Interior of the specimen. Propagation of the crack along the fibers;* (c) *Crack propagation transverse to the fibers (locally) with striation formation.*

Extremely good compressive properties can be achieved. This must be taken as one of the key advantages of metal matrix composites when comparing them with the neat metal matrix, but even more when compared to polymer matrix composites. Internal residual stresses in the composite due to manufacturing significantly influence their properties. The fatigue behavior also increases with fiber reinforcement. During fatigue loading, cyclic softening or cyclic hardening can be observed due to the general matrix response.

The damage mechanisms observed under fatigue loading conditions are significantly different to those under static loading. Cracks initiate at imperfections near the specimen surface. Fatigue crack growth can be identified due to the formation of striations in matrix-rich areas.

References

[*1*] Schulte, K. and Bunk, W., "Metal Matrix Composites—A Promising Alternative to Conventional Alloys?" *Conference Proceedings No. 444, New Light Alloys,* AGARD-Structures and Materials Panel Meeting No. 67, 2–7 Oct. 1988, Mierlo, The Netherlands, 1988, pp. 26.1–26.16.

[2] Johnson, W. S., "Fatigue Testing and Damage Development in Continuous Fiber-Reinforced Metal Matrix Composites," NASA Technical Memorandum 100628, 1988.

[3] Schulte, K., Bockheiser, A., Girot, F., and Kim, G. K., "Characterization of Aluminum Oxide (FP) Fibre Reinforced Al-2.5Li Composites," *Proceedings,* Fourth European Conference on Composite Materials (ECCM-4), J. Füller et al., Eds., 25–28 Sept. 1990, Stuttgart, Germany, pp. 293–300.

[4] Schulte, K. and Trautmann, K. H., "Mechanical Testing of Metal Matrix Composites," *Proceedings,* Composites Testing and Standardization (ECCM-CTS), P. Hoog et al., Eds., 8–10 Sept. 1992, Amsterdam, The Netherlands, 1992, pp. 63–70.

[5] Schulte, K. and Minoshima, K., "Mechanisms of Fracture and Failure in Metal Matrix Composites," *Proceedings,* Twelfth International Riso Symposium on Metal Matrix Composites—Processing, Microstructure, and Properties, Roskilde, Denmark, 1991, pp. 123–147.

[6] Reifsnider, K. L., Schulte, K., and Duke, J. C., "Long-Term Fatigue Behavior of Composite Materials," *Long-Term Behavior of Composites, ASTM STP 813,* T. K. O'Brien, Ed., American Society for Testing and Materials, Philadelphia, 1982, pp. 136–159.

[7] Hahn, H. T. and Kim, R. Y., "Fatigue Behavior of Composite Laminates," *Journal of Composite Materials,* Vol. 10, 1976, pp. 156–180.

Basant K. Parida[1] *and Theodore Nicholas*[1]

Influence of Crack Closure and Stress Ratio on Near-Threshold Fatigue Crack Growth Behavior in Ti-1100

REFERENCE: Parida, B. K. and Nicholas, T., **"Influence of Crack Closure and Stress Ratio on Near-Threshold Fatigue Crack Growth Behavior in Ti-1100,"** *Cyclic Deformation, Fracture, and Nondestructive Evaluation of Advanced Materials: Second Volume, ASTM STP 1184,* M. R. Mitchell and O. Buck, Eds., American Society for Testing and Materials, Philadelphia, 1994, pp. 48–63.

ABSTRACT: In the present study, the fatigue crack growth behavior of a near-α, β-processed titanium alloy, Ti-1100, was investigated with the objective of assessing the influence of crack closure and stress ratio on fatigue threshold. Measurement of the crack-opening load in single-edge tension [SE(T)] specimens was made by near-tip strain gage and DCPD methods. Fatigue threshold stress intensity ranges, ΔK_{th}, determined under constant stress ratio and constant maximum stress intensity, variable stress ratio conditions indicate almost identical values for R above 0.5. It is postulated that while crack closure in the wake of the crack tip is responsible for the no-growth condition in the former case, lack of sufficient damage accumulation at the crack tip as a consequence of the formation of an insignificant reversed plastic zone and large planar slip band formations surrounding the crack tip appears to be responsible for no growth in the latter case. The use of an effective stress intensity based on closure data consolidates most of the threshold data, indicating the independence of the fatigue crack growth data to mean stress or R.

KEYWORDS: crack closure, stress ratio, threshold stress intensity range, effective stress intensity, damage accumulation, near-threshold crack growth behavior

Over the past few decades progressively higher emphasis has been placed on increasing the operating temperatures of gas turbine engines with a view to improve their overall performance. In order to fulfil the objectives of the Integrated High Performance Turbine Enginer Technology (IHPTET) Program of the United States Air Force, several conventional lightweight alloys and intermetallics of titanium are being evaluated for both static and rotating components of advanced gas turbine engines. The historical development of high-temperature titanium alloys has been reviewed extensively [*1,2*], and the advantages of beta field processing, which is characterized by large, transformed beta grains in mixed basketweave and aligned alpha Widmanstatten morphologies, have been reported [*3–5*] for Ti-alloys like IMI-829, Ti-6Al-4V, and Ti-6242-S. In the past these alloys have found very useful applications in compressor stages of gas turbine engines because of their excellent high-temperature strength, creep resistance, and damage tolerance properties. However, their primary limitation arises at temperatures exceeding about 538°C (1000°F), where excessive creep rates and environmental degradation make them unsuitable for practical application. In order to extend the temperature barrier, alloy Ti-1100 was developed [*4*], which is an improvement over Ti-6242-S and offers roughly a 55°C advantage over that alloy, thus enabling the operating temperature to be increased to

[1] Senior research associate, National Research Council, and senior scientist, respectively, Materials Directorate, WL/MLLN, Wright-Patterson Air Force Base, OH 45433-6533.

593°C (1100°F). Before attempting any successful application of this new alloy, a thorough analysis of its fatigue crack growth behavior over the entire temperature range is necessary.

Under the U.S. Air Force Engine Structural Integrity Program (ENSIP) [*6*], it is required to predict accurately fatigue crack growth rate as part of the life prediction methodology for a newly developed material system. It is well known that the major portion of the useful life of any component is spent in fatigue crack initiation and the early phase of crack growth. Therefore, it is important to describe accurately the near-threshold fatigue crack growth behavior and determine the fatigue threshold stress intensity factor. In a recent study, Ghonem et al. [*7*] determined the effects of frequency on the fatigue crack growth behavior of Ti-1100 and observed a dominant asperity-based closure effect for this material at low values of ΔK. Marci et al. [*8,9*] and Doker et al. [*10*] examined some of the issues pertaining to crack-opening load under variable R conditions in a number of materials including Ti-6Al-4V. Doker et al. [*10*] suggested that the crack-opening stress intensity, K_{op}, is always higher than K_{min} even at high stress ratios and that this type of closure might be caused by the cyclic plastic deformation at the crack tip. Therefore, what needs to be examined are the precise effects of the stress ratio on crack closure and the effective threshold stress intensity range under a constant R, decreasing stress intensity condition as well as under a constant K_{max}, linearly increasing R condition. The objective of this work is to critically examine these effects in a damage-tolerant material like Ti-1100 under ambient conditions.

Material and Experimental Procedures

The material used in this investigation was Ti-1100, which was supplied by TIMET, Henderson Plant. Its composition in weight percent is given as: 6.0Al-2.75Sn-4.0Zr-0.4Mo-0.45Si-0.07O-0.02Fe, balance Ti. The material was beta-forged from 1093°C (2000°F), hot rolled above the beta transus to 12.5-mm-thick plates, and stabilized at 593°C (1100°F) for 8 h. The resulting microstructure, shown in Fig. 1, consists essentially of transformed Widmanstatten basketweave formations with aligned colonies of α platelets exhibiting no preferred orientation. Mechanical properties of the material at room and at target temperature (593°C) are given in Table 1.

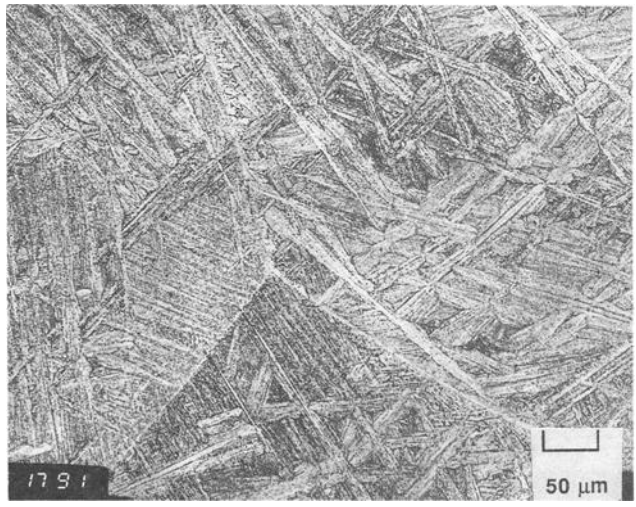

FIG. 1—*Ti-1100: mixed basketweave and aligned α Widmanstatten microstructure.*

TABLE 1—*Ti-1100: Mechanical Properties*[a] *at room and at elevated temperature.*

Temperature, °C	0.2% YS, MPa	UTS, MPa	Young's Modulus, GPa	% Elongation	% Reduction in Area
25	915	980	120	10–12	21–30
593	485	674	82	≈10–12	≈30

[a] From Refs 4, 5, 7.

Flat single-edge-notched tension [SE(T)] specimens of nominal dimensions 124 by 25 by 2.5 mm were machined in the L-T orientation by electrodischarge machining (EDM). Single-edge U-notches with a notch depth of 2.5 mm and a root radius of 0.14 mm were made at the midlength of the specimens. The midsections of all specimens were electropolished on both faces to facilitate optical crack length measurement. Two pairs of electric potential probes were spot-welded to the notched edge of the specimen just above and below the notch with a nominal spacing of 5 mm. Automated measurement of crack length was made by reversing the direct current potential drop (DCPD) method. Another pair of leads with the same nominal spacing attached to the specimen centerline away from the notch plane provided a reference potential for normalization of the electrical potential readings for use in Johnson's equation [*11*] to compute crack length. Figure 2 shows a schematic of the specimen dimensions and transducer locations for crack length and closure measurements.

All tests were conducted using a servocontrolled, electro hydraulic (major-minor) test system, incorporating a large-capacity (9 kN peak-to-peak) electrodynamic shaker and an automated data acquisition system. The mean load on the specimen was applied by the hydraulic actuator, while the oscillatory load amplitude was superimposed by the shaker at any desired frequency, up to a maximum value of 550 Hz. Initially, accurate alignment of the specimen axis with respect to the loading axis and dynamic load calibration at high frequency were ascertained by a strain-gaged specimen. For all tests conducted under this investigation, sinusoidal waveform with a loading frequency of 100 Hz was used unless otherwise indicated. Crack initiation at the root of a relatively sharp U-notch, with a stress concentration factor of around 7, was rather simple. Crack extension was measured with the aid of the DCPD system, which had a resolution of 1 μV, corresponding to a crack length of around 3 μm for a stabilized direct current of 10 A. Crack lengths measured by the electric potential method were periodically verified through optical measurements with the aid of two travelling microscopes mounted on either side of the specimen. In order to perform crack closure measurements, besides the DCPD method, the

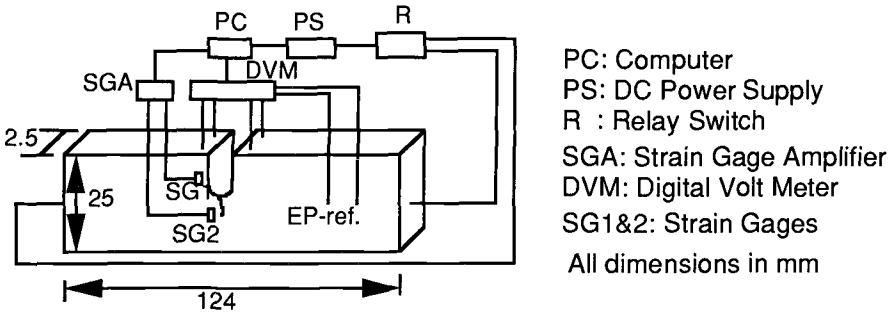

FIG. 2—*Schematic of specimen configuration and transducer locations for crack length and closure measurements.*

"near-tip strain gage technique" was employed. A miniature strain gage with a gage length of 0.381 mm was fixed about 400 μm behind the notch root, with the gage centerline parallel to the notch centerline but offset by 400 μm. This arrangement permitted the determination of closure loads for a short crack as it grew out of the notch root. For closure measurements of long cracks, strain gages were fixed with similar offsets near the tip of long cracks. Acquisition of load and strain data over one loading cycle was carried out at a relatively low frequency of 0.2 Hz. Closure measurements through the DCPD method was carried out in a similar manner. Without reversing the direction of the current, continuous readings of electric potential were made while the load was varied over one cycle.

Decreasing stress intensity threshold tests were conducted according to ASTM standard E 647 [*12*]. For continuous automated load shedding, the coefficient $C = -0.1$ mm^{-1} was used. Decreasing stress intensity threshold tests were followed by constant load, increasing stress intensity tests. The stress ratios considered were 0.1, 0.5, and 0.7. A second series of tests under constant K_{max}, linearly increasing R (as a function of crack length) condition were also conducted. Here, the value of the stress ratio was raised continuously from 0.1 to 0.9 or until no growth condition, whichever occurred first. This high stress ratio, no growth condition test was followed by a constant ΔK, $R = 0.1$ test until the resumption of stable crack growth. This was followed by a constant ΔK, linearly varying R (as a function of number of cycles) test, with $\Delta K = 1.1\ \Delta K_{th\ eff}$ and $K_{max} = K_{min} + \Delta K$, where $\Delta K_{th.eff}$ is the effective threshold stress intensity range obtained from the previous no-growth condition in the constant K_{max}, linearly increasing R test.

Results and Discussion

Crack Closure

Crack closure measurements were made with a near-tip strain gage for fatigue cracks emanating from U-notches under constant amplitude fatigue loading with a stress ratio of $R = 0.1$. Figure 3 shows, on the left, a typical load versus strain curve during a single loading cycle, where ε is the strain in the direction of the crack axis. It may be noted that the shape of this curve is subject to change depending on the relative position of the crack tip with respect to the location of the gage centerline. Determination of the closure load was made with the help of an in-house program, called CPCL, which identifies the load (normally during the unloading portion of the cycle) at which the first data point in the load versus strain curve deviates from the linear portion of the curve. The amount of deviation is based on a specified standard deviation computed from a linear regression of the data within selectable upper and lower windows. The curve on the right of Fig. 3, the differential displacement, depicts the deviation of regressed data from the linear portion of the unloading data during a single loading cycle. It was noted that the magnitude of the closure load or the closure stress intensity was rather insensitive to the strain gage location with respect to the crack tip. Figure 4 shows the variation of K_{cl}/K_{max} with crack length from the notch, where K_{cl} has been derived from the load versus strain data using the standard deviation method described above. Figure 4*A* shows the details for a crack within 0.7 mm of the notch, while Fig. 4*B* shows closure for the longer crack. It is observed that the closure level progressively increases as the crack grows through the short-to-long crack range, where it attains an almost steady value between 0.5 and 0.6. The low closure values at low ΔK for the shorter crack, resulting in a larger ΔK_{eff}, can be used to explain the relatively higher values of *da/dN* observed for short cracks at or below the long crack threshold. As an illustration, Fig. 5 shows fatigue crack growth data for several short and long cracks plotted as *da/dN* versus ΔK. As expected, the short crack data lie above and to the left of the long crack data, but the two types of data merge together as the crack length increases.

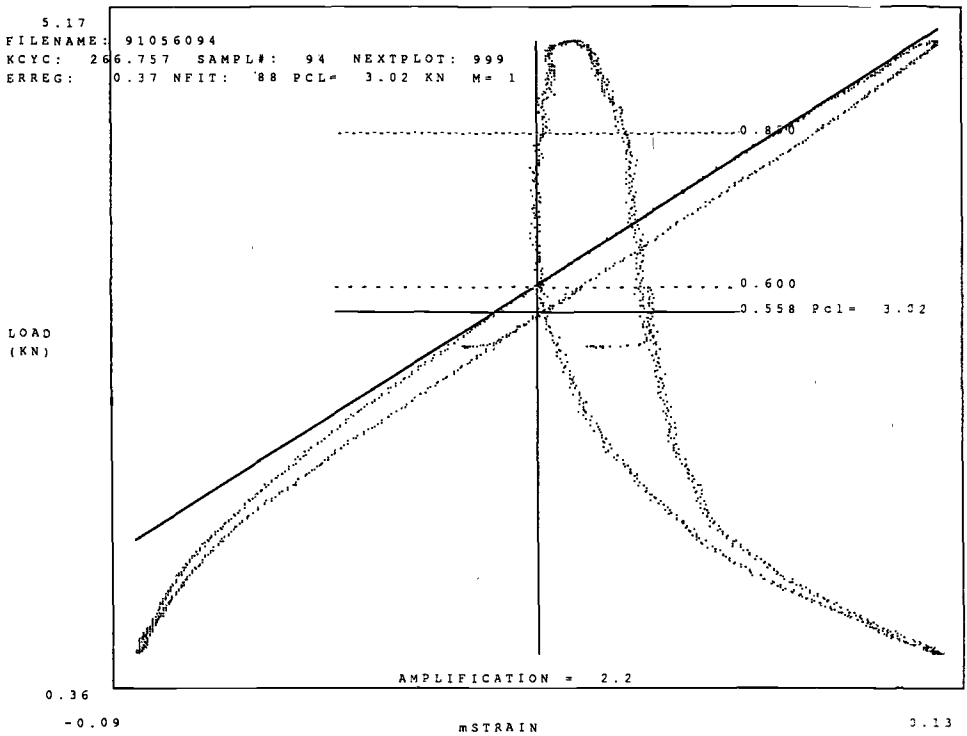

FIG. 3—*Representative traces of load versus near-tip strain data during one loading cycle* (left) *and deviation of regressed data from the linear portion of unloading load-strain data* (right).

Crack closure measurements were also made using the electric potential method. In this method, electric potential readings are taken continuously as the load is varied at a slow rate over one complete cycle. Figure 6 shows typical load versus electric potential curves at different crack lengths from notch for a constant ΔP test (R = 0.1) with P_{max} = 4.5 kN; viz: a = 0 mm, b = 0.3 mm, c = 1.9 mm, d = 4.1 mm, e = 6.0 mm. It is observed that although the magnitude of electric potential progressively increases with crack length, its variation during any cycle of loading and unloading at a given crack length is rather small. For relatively small crack lengths (a to c) up to 1.9 mm, there is no observed nonlinearity, that is, no apparent closure. For larger crack lengths, Curves d and e exhibit a "knee" corresponding to a load of approximately 1.4 kN, which is interpreted as the closure load, corresponding to K_{cl}/K_{max} = 0.31. The observation from Curves b and c indicating no closure at crack lengths varying from 0.3 to 1.9 mm is rather surprising. A closer examination of the tortuous crack path in SEM reveals a number of contact points between the two fracture surfaces under the unloaded condition, as shown in Fig. 7. This could constrain the crack tip to remain open during the entire unloading portion of the cycle, and consequently the potential would not change. Pippan et al. [*13*] examined crack closure of ARMCO iron in air and in an ultra-high vacuum using the potential drop method and reported significant changes in electric potential due to increased contact resistance caused by the formation of oxide layers on fracture surfaces. In comparing the closure load data from the potential drop method with that obtained from the near-tip strain gage results, as shown in Fig. 4, it appears that the DCPD method is unsuitable for accurate determination of closure loads and

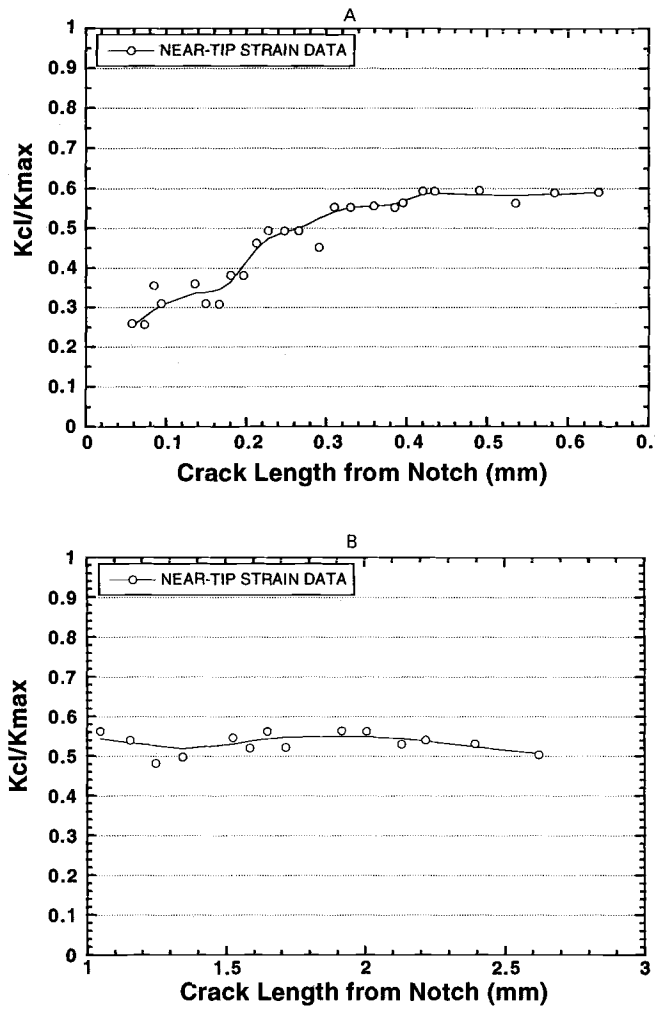

FIG. 4—*Development of closure level with crack length from notch:* (A) *for a short crack emanating from notch;* (B) *for a long crack.*

hence the effective stress intensity factor range, at least for this class of coarse-grained materials. However, the measurement of crack length by the DCPD method is still reliable because the potentials in this case are measured at the mean load.

Effect of Stress Ratio

The results of decreasing stress intensity threshold tests for $R = 0.1$, 0.5, and 0.7 are shown in Fig. 8. The variation of da/dN with ΔK for $R = 0.1$ under the constant load, increasing stress intensity condition is also shown. The increasing and decreasing ΔK data form a single curve for this value of R. It is observed that the near-threshold crack growth rate at a given ΔK increases with increasing stress ratio, while the threshold stress intensity range, ΔK_{th}, decreases.

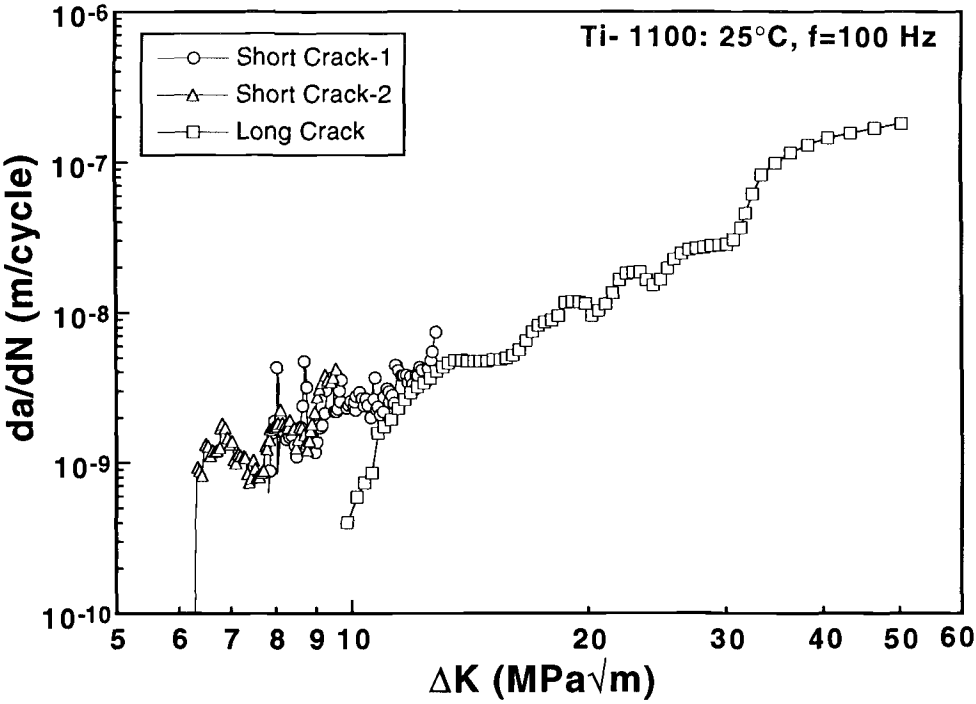

FIG. 5—*Fatigue crack growth rate of short and long cracks in Ti-1100 at room temperature.*

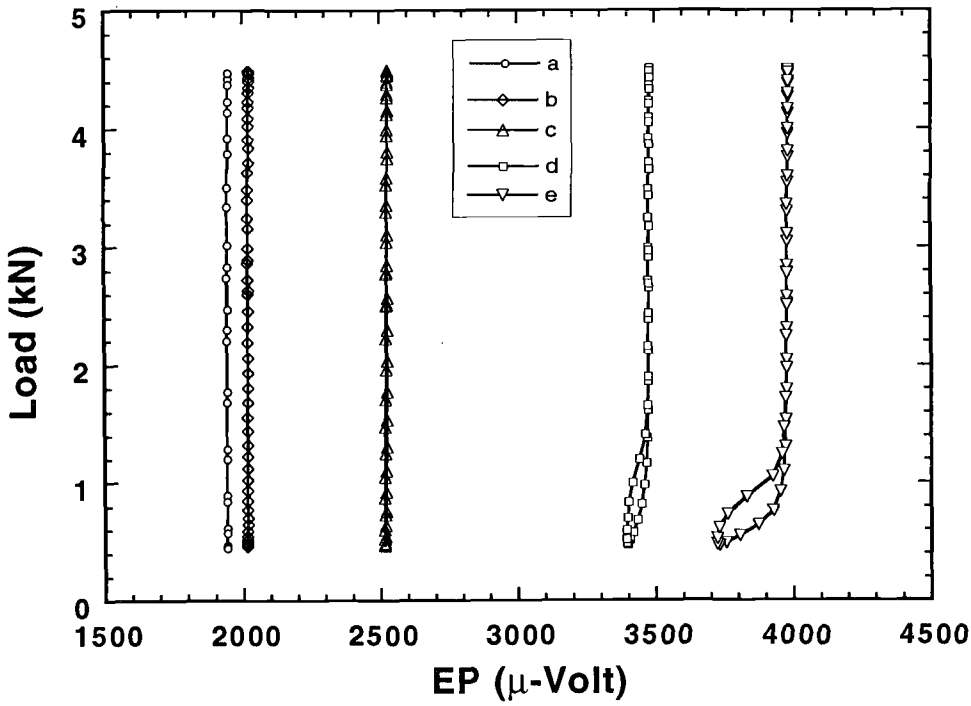

FIG. 6—*Variation of electric potential with load at different crack lengths from notch:* a = *0 mm;* b = *0.3 mm;* c = *1.9 mm;* d = *4.1 mm;* e = *6.0 mm.*

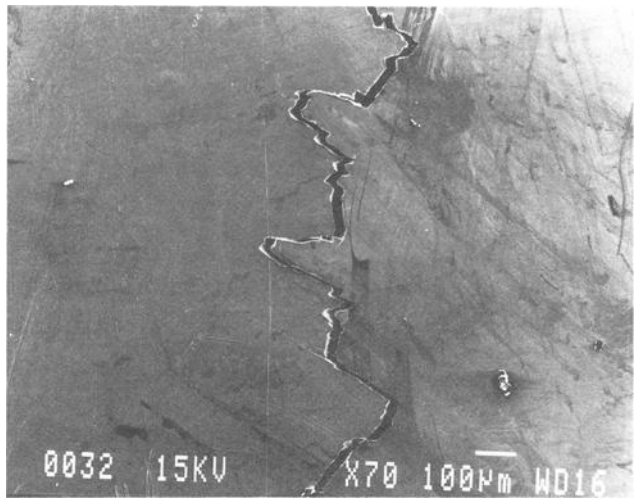

FIG. 7—*SEM micrograph showing crack path tortuosity and early contacts between asperities of fracture surfaces in an unloaded specimen.*

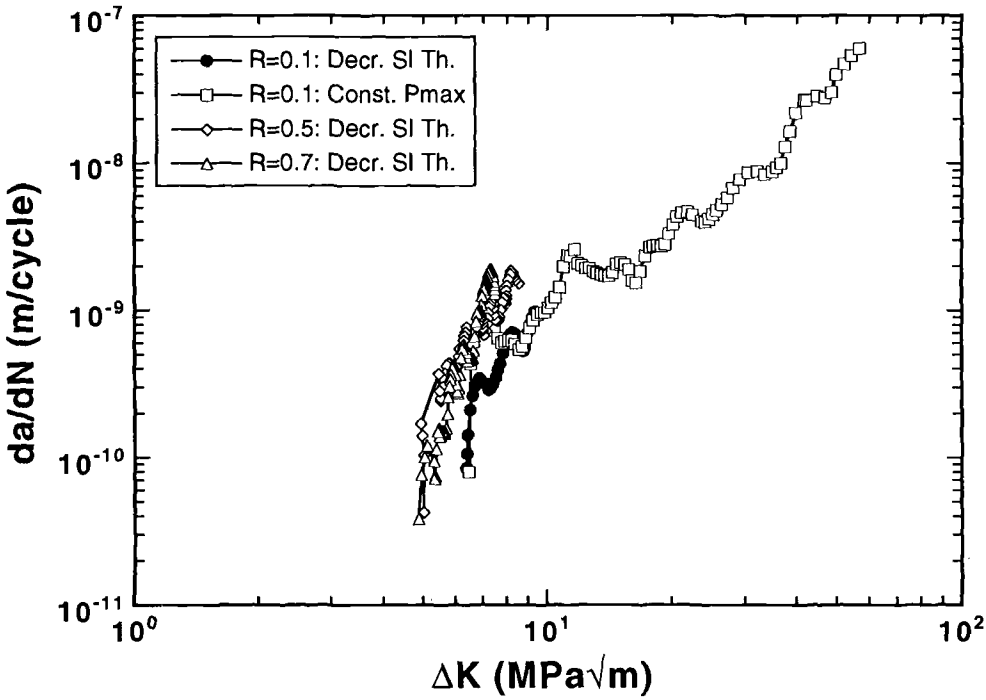

FIG. 8—*Room temperature fatigue crack growth threshold of Ti-1100 under the decreasing stress intensity condition at* R = *0.1, 0.5, 0.7.*

For comparison, the results from a variable R test are presented in Fig. 9, which shows the variation of *da/dN* and R with ΔK for a constant stress intensity (K_{max} = 20 MPa$\sqrt{m}$), linearly increasing stress ratio R (*a*) test. In this decreasing ΔK test, it is seen that a no-growth condition is reached for a value of R of approximately 0.75, corresponding to a stress intensity range of 5.0 MPa$\sqrt{m}$. Since this test commenced with an initial value of R = 0.5 and R was continuously increased with an increase in crack length, the decrease in growth rate and subsequent crack arrest imply that closure is present at values of R up to at least R = 0.7, where the crack arrested. Whereas these closure values are unusually high and, further, are above the values obtained from load-strain plots (see Fig. 4), it is postulated that closure is not the mechanism which affects crack growth rate at these high values of R. Instead, crack growth decreases due to diminishing levels of damage ahead of the crack tip. The no-growth condition is attributed to a lack of sufficient damage accumulation at the crack tip because of the formation of an insignificant reversed plastic zone compatible with a small ΔK. This ΔK_{th}, therefore, represents the closure-free effective threshold stress intensity factor range for the material. Figure 10*a* shows an optical micrograph of the crack-tip region under no-growth condition for over one million cycles. Extensive microcracking and planar slip deformation surrounding the crack-tip region appear to constitute the energy dissipation mechanism. Figure 10*b* shows a high magnification SEM micrograph near the crack-tip region. In this micrograph, it is clearly seen that the planar slip lines on the specimen surface are actually the continuation of a large number of microcracks already present in the fracture surface.

To further illustrate the transition from no growth to crack growth, Fig. 11 shows the variation of *da/dN* and R with crack length under a constant ΔK, linearly varying R (as a function of number of cycles) condition. This test was conducted with ΔK = 1.1 ΔK_{th} and K_{max} = K_{min} + ΔK, where K_{min} is the minimum stress intensity level of the constant K_{max}, R = 0.1 constant amplitude loading applied for stable crack growth following the no-growth condition under constant K_{max}, linearly varying R (*a*) test (see Fig. 12). It can be seen that a no-growth condition

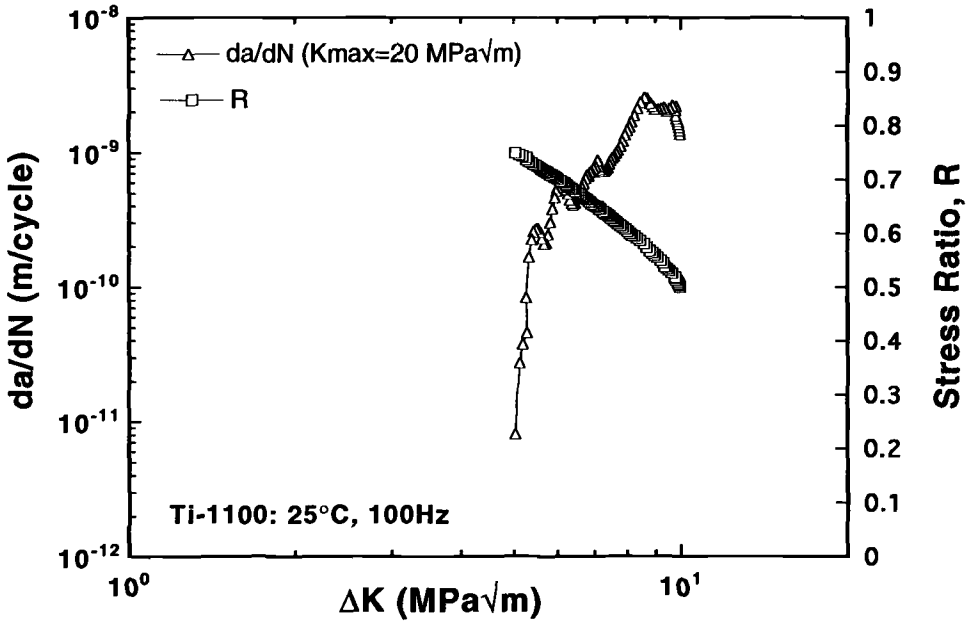

FIG. 9—*Ti-1100: Variation of* da/dN *and* R *under the constant* K_{max}, *linearly varying* R *condition.*

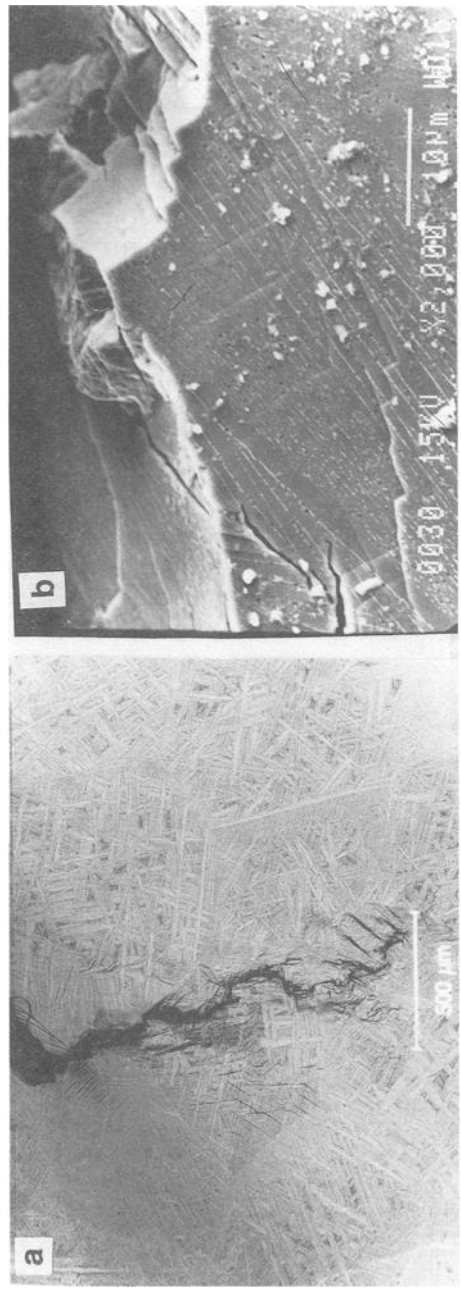

FIG. 10—*Micrographs illustrating extensive microcracking and slip deformations surrounding the crack tip:* (a) *optical micrograph of the tip region of a stationary crack under the constant* K_{max}, *linearly varying* R *condition;* (b) *SEM micrograph of the near-tip region depicting the surface slip lines to be a continuation of microcracks formed in the fracture surfaces.*

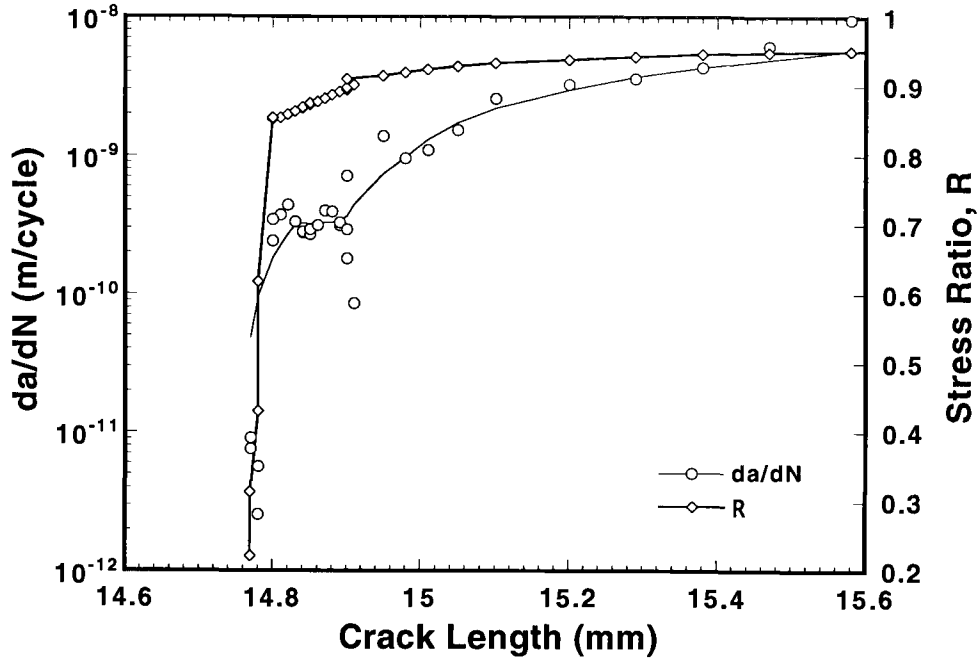

FIG. 11—*Variation of* da/dN *and* R *under constant* ΔK, *linear* R (N) *condition,* ΔK = 5.5 $MPa\sqrt{m}$.

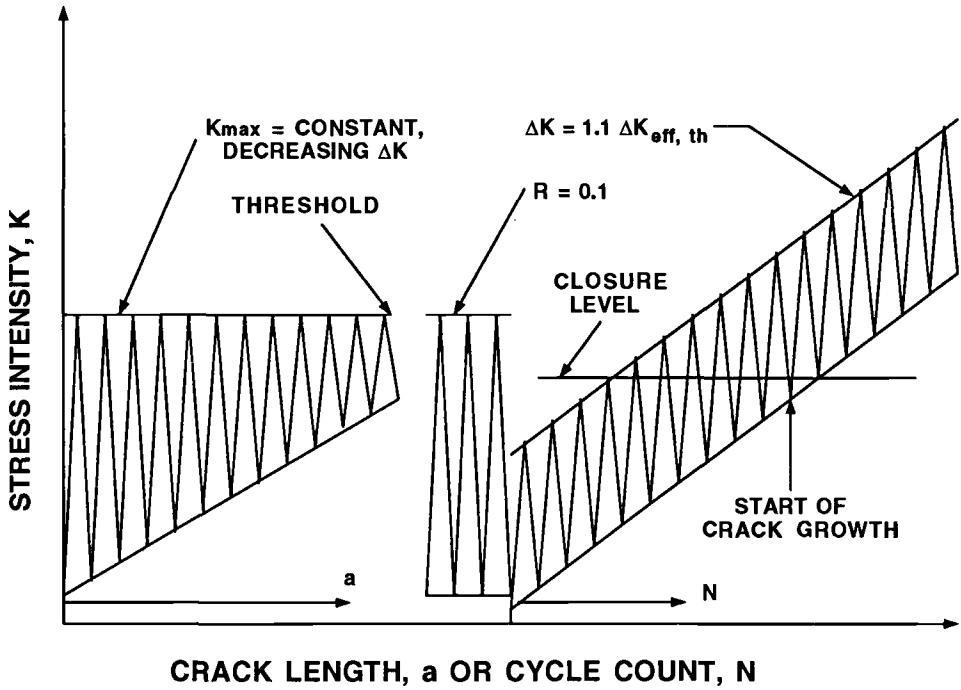

FIG. 12—*Schematic of constant* K_{max}*—linearly varying* R(a) *and constant* ΔK*–linearly varying* R(N) *test.*

persists as the crack tip remains completely or partially closed until R reaches a value of approximately 0.6 to 0.7, when the growth rate progressively increases. As shown schematically in Fig. 12, the crack will start to grow when ΔK_{eff} is above the threshold value. If the crack closure level is above the minimum load, as depicted in Fig. 12, the crack growth rate should increase until K_{min} is greater than K_{cl}. This would imply that the value of K_{cl}/K_{max} is at least as large as the value of R when crack growth begins. As in the previous case, it is postulated here that closure is not a consideration at these high values of R. Rather, the initiation and continuing increase of growth rate at high values of R, observed in Fig. 11, is attributed to attaining a critical level of damage accumulation ahead of the crack tip due to the increase in size of the monotonic plastic zone as K_{max} is increased continuously, and not to any differences in crack closure behavior.

Data from the various tests are compared in Fig. 13 where variation of fatigue crack growth rate, *da/dN*, is shown against the effective stress intensity range, ΔK_{eff}, from the decreasing ΔK threshold tests for stress ratios, R = 0.1, 0.5, and 0.7. Here, $\Delta K_{eff} = K_{max} - K_{cl}$, $K_{cl} \geq K_{min}$, where K_{cl} has been computed from the closure data obtained from the near-tip strain gage traces. Constant K_{max}, variable R test data are also shown in Fig. 13. It is seen that while decreasing stress intensity test data for R = 0.5, 0.7 and constant K_{max}, variable R test data agree very well, decreasing stress intensity data for R = 0.1 appear to be overcorrected for computation of ΔK_{eff}, even with $K_{cl}/K_{max} \approx 0.5$ as determined from conventional load versus near-tip strain data. If the high K_{cl} value of $\approx$0.7 as determined from the constant ΔK, linear R test was used, the R = 0.1 curve would have moved even further to the left instead of consolidating with the other curves. Further, the R = 0.5 data would also move to the left since

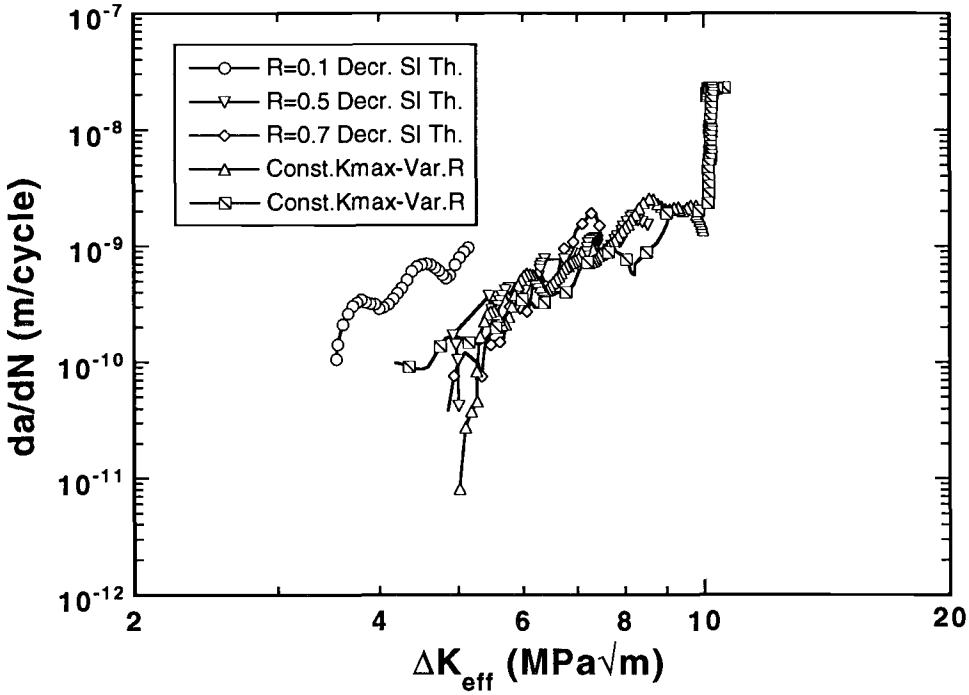

FIG. 13—*Comparison of crack growth rates from decreasing stress intensity (E 647-88a) and constant* K_{max}, *linearly varying* R(a) *test data, corrected for closure, based on near-tip strain data.*

ΔK_{eff} would be approximately 0.6 ΔK. The resulting data would then present a picture showing higher growth rates for lower values of R for the same value of ΔK_{eff}. This would be in the opposite direction of a mean stress effect where higher R would be expected to produce higher growth rates because of higher mean stresses.

The present set of experimental data appear to point towards a lower level of actual closure load than measured. This is based on the general observation that the closure load as determined from load, near-tip strain data possibly constitutes an upper-bound value because the effective closure load that actually affects the crack growth rate may be slightly lower than the load at which deviation from linearity is first observed in a load versus strain plot [*14,15*]. This may be due to superficial contact of the asperities on fractured surfaces or a three-dimensional effect due to nonuniform contact across the width of the specimen. It is probable, therefore, that the closure load level might actually lie around $K_{cl}/K_{max} \approx 0.3$ to 0.4 so as to consolidate all the near-threshold crack growth data at all stress ratios considered. It is thus concluded that there is no mean stress effect to account for in this material, unlike in a less ductile titanium aluminide, Ti-24Al-11Nb [*16*].

As regards the question of possible closure even at high stress ratios due to cyclic plastic deformation at the crack tip as suggested by Doker et al. [*10*], no evidence of this was found during the present experiments. Figure 14 shows the traces of load versus electric potential readings taken: (a) at the end of constant K_{max} linearly varying R (a) test, when $R = 0.808$; (b) at the beginning of constant ΔK linearly varying R (N) test, when $R = 0.292$; and (c) towards the end of constant ΔK linearly varying R (N) test, when $R = 0.841$. It is clearly seen that while crack closure is evident under low stress ratio condition, there is no evidence of closure at higher stress ratios ($R \geq 0.8$).

For comparison purposes, Fig. 15 shows the variation of a fatigue crack growth rate of Ti-1100 and titanium aluminide, Ti-24Al-11Nb, at room temperature, corresponding to $R = 0.1$ and $f = 100$ Hz. It may be observed that besides the crack growth rate being considerably lower at any given stress intensity, Ti-1100 exhibits an appreciably larger crack growth range

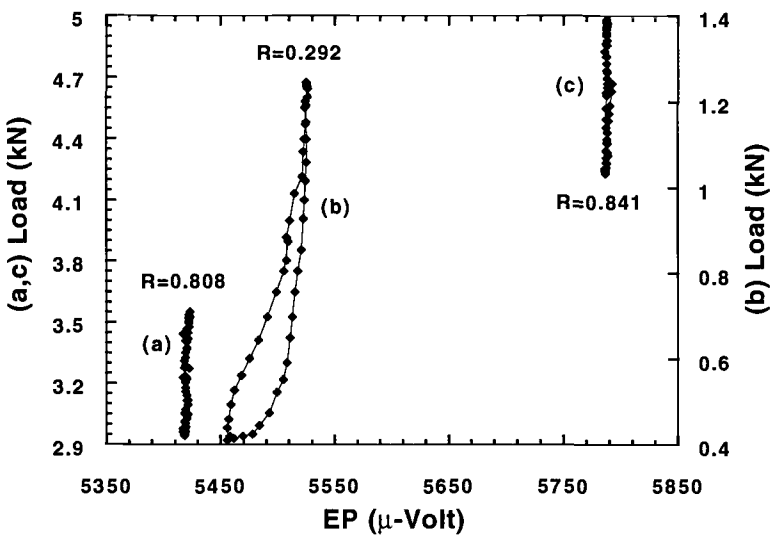

FIG. 14—*Development of closure under different loading conditions:* (a) *at the end of constant* K_{max}, *variable* R *test* (R = *0.808*), (b) *at the beginning of constant* ΔK, *variable* R *test* (R = *0.292*), (c) *at the end of constant* ΔK, *variable* R *test* (R = *0.841*).

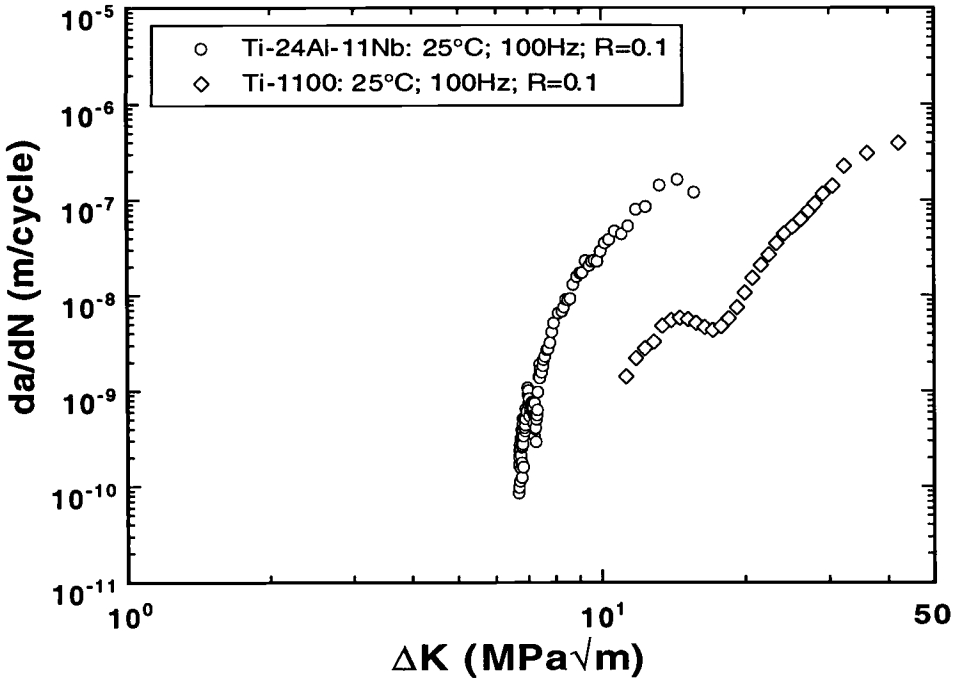

FIG. 15—*Comparison of room temperature fatigue crack growth rate between Ti-1100 and Ti-24Al-11Nb* (f = *100 Hz,* R = *0.1*).

compatible with its larger fracture toughness, which causes this material to be characterized as more damage tolerant.

Conclusions

Based on the crack closure and fatigue crack growth rate analysis of Ti-1100 at room temperature, the following conclusions may be drawn:

1. The near-tip strain measurement method is quite sensitive and appears to provide an upper-bound value for the closure load, especially under the decreasing stress intensity crack growth condition. The electric potential method appears to be unsuitable for accurate quantitative determination of closure loads for short cracks in Ti-1100. This method may, however, be used for qualitative assessment of a closure condition for long cracks.

2. For short cracks, higher crack growth rates are observed at stress intensity ranges below the long crack threshold. Corresponding closure load levels, as determined from near-tip strain data, are found to be relatively lower in the short crack range and develop to the large crack closure level with further crack growth.

3. Fatigue threshold stress intensity range, ΔK_{th}, determined under the decreasing stress intensity, constant R condition and the constant K_{max}, variable R condition are found to have an almost identical value for stress ratios, $R \geq 0.5$. While in the former case the no-growth condition is attributable primarily to crack closure in the wake, lack of sufficient damage accumulation at the crack tip appears to be responsible for no-growth condition in the latter case. Here, damage in the form of extensive microcracking, as well as extensive slip band

formations surrounding the crack tip as a consequence of the formation of a very small reversed plastic zone, leads to a no-growth condition characterized by an effective threshold stress intensity factor range, $\Delta K_{th.eff}$.

Acknowledgment

The support of the U.S. Air Force at the Wright Laboratory Materials Directorate, where this work was performed, is gratefully acknowledged. One of the authors (B. K. Parida) would also like to thank the National Research Council for their support through the Senior Resident Research Associateship Program. The authors wish to acknowledge helpful discussions with J. Jira and the assistance of R. Goodman and N. Schehl in the experimental portion of this work. Thanks are also expressed to Paul Bania of TIMET for providing the material for this investigation.

References

[1] Rosenberg, H. W., "Critical Review: High Temperature Alloys," *Titanium Science and Technology,* Vol. 4, Jaffee and Bunte, Eds., New York, Plenum Press, 1973.

[2] Blenkinsop, P. A., "Critical Review: Developments in High Temperature Alloys," *Titanium Science and Technology,* Vol. 4, G. Lutjering et al., Eds., Deutsche Gesellschaft fur Motallkunde E. V., Oberursel, West Germany, 1985, p. 2323.

[3] Chen, C. C. and Coyne, J. E., "Relationships Between Microstructure and Properties in Ti-6242-Si Alloy Forging," *Titanium '80 Science and Technology,* Vol. 2, H. Kimura and O. Izumi, Eds., TMS-AIME Publications, 1980, p. 1197.

[4] Bania, P. J., "Ti-1100: A New Elevated Temperature Titanium Alloy," Sixth World Conference on Titanium, P. Lacombe et al., Eds., Societe Francaise de Metallurgie, *Proceedings,* Cannes, France, June 1988, pp. 825–830.

[5] Bania, P. J., "An Advanced Alloy for Elevated Temperatures," *Journal of Metals,* Vol. 40, No. 3, 1988, pp. 20–22.

[6] Larsen, J. M. and Nicholas, T., "Cumulative Damage Modelling of Fatigue Crack Growth in Turbine Engine Materials," *Engineering Fracture Mechanics,* Vol. 22, No. 4, 1985, pp. 713–730.

[7] Ghonem, H. and Foerch, R., "Frequency Effects on Fatigue Crack Growth Behavior in a Near-alpha Titanium Alloy," *Elevated Temperature Crack Growth,* MD-Vol. 18, S. Mall and T. Nicholas, Eds., ASME, New York, 1991, pp. 93–105.

[8] Marci, G., "A Fatigue Crack Threshold," *Engineering Fracture Mechanics,* Vol. 41, No. 3, 1992, pp. 367–385.

[9] Marci, G., Castro, D. E., and Bachmann, V., "Fatigue Crack Propagation Threshold," *Journal of Testing and Evaluation,* Vol. 17, No. 1, 1989, pp. 28–39.

[10] Doker, H. and Bachmann, V., "Determination of Crack Opening Load by use of Threshold Behavior," *Mechanics of Fatigue Crack Closure, ASTM STP 982,* J. C. Newman and W. Elber, Eds., American Society for Testing and Materials, Philadelphia, 1988, pp. 247–259.

[11] Johnson, H. H., "Calibrating the Electric Potential Method for Studying Slow Crack Growth," *Materials Research and Standards,* Vol. 5, No. 9, 1965, pp. 442–445.

[12] ASTM Test Method for Measurements of Fatigue Crack Growth Rates (E647-88a), American Society for Testing and Materials, Philadelphia.

[13] Pippan, R., Haas, G., and Stuwe, H. P., "Comparison of Two Methods to Measure Crack Closure in Ultra-High Vacuum," *Engineering Fracture Mechanics,* Vol. 34, No. 5/6, 1989, pp. 1075–1084.

[14] Troha, W. A., Nicholas, T., and Grandt, A. F. Jr., "Three-Dimensional Aspects of Fatigue Crack Closure in Polymethylmethacrylate Material," *Mechanics of Fatigue Crack Closure, ASTM STP 982,* J. C. Newman Jr. and W. Elber, Eds., American Society for Testing and Materials, Philadelphia, 1988, pp. 598–616.

[15] Troha, W. A., Nicholas, T., and Grandt, A. F. Jr., "Observation of 3-D Surface Flaw Geometries During Fatigue Crack Growth in PMMA" *Surface Crack Growth: Models, Experiments, and Structures, ASTM STP 1060,* W. G. Reuter, J. H. Underwood, and J. C. Newman, Jr., Eds., American Society for Testing and Materials, Philadelphia, 1990, pp. 260–286.

[16] Parida, B. K. and Nicholas, T., "Effect of Stress Ratio on Fatigue Crack Growth in a Titanium Aluminide Alloy," *International Journal of Fracture,* Vol. 52, No. 3, 1991, pp. R51–54.

DISCUSSION

O. Buck[1] *(written discussion)*—I would like to comment on the determination of the "effective" stress intensity range (ΔK_{eff}) by using the deviation from linearity in the load-extension curve as an indicator for crack closure. I think this method provides a first approximation for ΔK_{eff} only in that it is an indication of the first contact between the two fracture surfaces. On further unloading, additional contact is being made which eventually produces the total shielding of crack tip (see, e.g., O. Buck, *MRS Bulletin,* Vol. 14, No. 8, 1989, p. 44). This "shielding" stress intensity is somewhat lower than the "closure" stress intensity, which you refer to. Therefore, I believe, it is not surprising that you find an "overcorrection" in your crack growth data.

B. K. Parida and T. Nicholas (authors' closure)—The comments on effective stress intensity through the use of closure loads determined by the offset method are accurate. The authors agree entirely with the discussor's observations and conclusions. The impracticality of using another definition of closure, for example, the intercept method, led the authors to use this simple, yet upper bound method for determining closure levels. This point is discussed briefly in the paper and Refs *14* and *15* address this point in greater detail. Nonetheless, Dr. Buck's comments are appreciated.

[1] Ames Laboratory, Iowa State University, Ames, IA 50011.

Louis J. Ghosn[1], *Pete Kantzos*[2], *and Jack Telesman*[3]

Fatigue Crack Growth and Crack Bridging in SCS-6/Ti-24-11

REFERENCE: Ghosn, L. J., Kantzos, P., and Telesman, J., **"Fatigue Crack Growth and Crack Bridging in SCS-6/Ti-24-11,"** *Cyclic Deformation, Fracture, and Nondestructive Evaluation of Advanced Materials: Second Volume, ASTM STP 1184,* M. R. Mitchell and O. Buck, Eds., American Society for Testing and Materials, Philadelphia, 1994, pp. 64–86.

ABSTRACT: Interfacial damage induced by relative fiber/matrix sliding was found to occur in the bridged zone of unidirectional SCS-6/Ti-24Al-11Nb intermetallic matrix composite specimens subjected to fatigue crack growth conditions. The degree of interfacial damage was not uniform along the bridged crack wake. Higher damage zones were observed near the machined notch in comparison to the crack tip. The interfacial friction shear strength, τ_f, measured in the crack wake using pushout testing revealed lower values than the as-received interface. Interfacial wear also reduced the strength of the bridging fibers. The reduction in fiber strength is thought to be a function of the magnitude of relative fiber/matrix displacements and the degree of interfacial damage. Furthermore, two different fiber bridging models were used to predict the influence of bridging on the fatigue crack driving force. The shear lag model required a variable τ_f in the crack wake (reflecting the degradation of the interface) before its predictions agreed with trends exhibited by the experimental data. The fiber pressure model did an excellent job in predicting both the FCG data and the ΔCOD in the bridged zone even though it does not require a knowledge of τ_f.

KEYWORDS: intermetallic matrix composites, fatigue crack growth, crack bridging, shear-lag model, fiber pressure model, interfacial shear stress, fiber pushout, effective fatigue driving force, fiber strength, interfacial damage

Intermetallic matrix composites (IMC) are candidate materials for high-temperature aerospace applications where high strength and low weight are required. However, before these composites can be implemented, it is necessary to understand the fatigue crack growth process and the evolution of damage in order to accurately predict the lives of composite components.

An important mechanism influencing fatigue crack growth behavior in IMCs is crack bridging. Fatigue cracks become bridged as the crack propagates in the matrix while leaving the fibers intact in the crack wake. The bridging fibers carry part of the applied load and shield the crack tip. Consequently, crack bridging enhances the fatigue crack growth behavior of IMCs in comparison to their unreinforced matrix alloys. Crack bridging has been widely observed in SCS-6/Ti-based composites under fatigue loading conditions [*1–5*].

The effectiveness of fiber bridging in reducing the crack driving force depends on the inter-

[1] Research engineer, Case Western Reserve University, NASA Lewis Resident Research Associate, Mail Stop 49-7, 21000 Brookpark Rd., Cleveland, OH 44135.

[2] Research engineer, Ohio Aerospace Institute, NASA Lewis Mail stop 49-7, 21000 Brookpark Rd., Cleveland, OH 44135.

[3] Material engineer, NASA Lewis Research Center, Mail Stop 49-7, 21000 Brookpark Rd., Cleveland, OH 44135.

facial properties and fiber strength. If the interface strength is too low, the matrix does not transfer enough load to the bridging fibers to effectively shield the crack tip. On the other hand, a strong interface will limit the extent of fiber/matrix sliding, resulting in high fiber stresses and ultimately fiber failures. Therefore, an optimum interface strength is desired to produce effective crack bridging. Likewise, high-strength fibers will also promote better crack bridging.

The interfacial properties of the bridging fibers may also be influenced by the load history. The interfacial wear induced by fiber/matrix sliding can change the interface properties and fiber strength. Unfortunately, very little is known regarding the degradation of these properties as a function of interfacial wear even though these properties are required input into fiber bridging models such as shear lag [*6–8*]. Preliminary measurements of interfacial shear properties did indeed show a decrease in the frictional shear stress with cyclic loading [*9–11*].

In this report, fiber bridging was studied by performing fatigue crack growth testing on a unidirectional SCS-6/Ti-24Al-11Nb (a%) using single edge notch (SEN) and center crack panel (CCP) specimens in a specially designed fatigue loading stage mounted inside a scanning electron microscope. The evolution of interfacial damage in the tested specimens was investigated by performing fiber pushout tests and fiber tensile tests on specimens previously subjected to crack bridging.

Finally, the effect of fiber bridging on the crack opening displacements and effective crack driving forces was studied analytically using the shear lag and fiber pressure models.

Experimental Procedures

Fatigue Crack Growth Testing

Fatigue crack growth testing of a unidirectional 33% fiber volume fraction SCS-6/Ti-24Al-11Nb composite was performed using SEN and CCP specimens. Both specimen geometries are shown in Fig. 1.

Fatigue crack growth testing was performed using a closed loop servo-hydraulic testing machine specially designed for the scanning electron microscope (SEM) [*12*]. This unique loading stage enables real time in situ observations of the fatigue crack growth process at magnifications up to × 10 000. All specimens were tested at room temperature inside the SEM chamber (1×10^{-6} torr). Test frequencies ranged from 1 to 5 Hz. The load ratio R was 0.1 in all cases. Testing was interrupted regularly in order to record the crack opening displacements at maximum and minimum loads and to measure crack extension. When possible, measurements of crack extension and crack opening displacements were made on both surfaces of the specimen. The complete test matrix is shown in Table 1. The material properties assumed in this study are shown in Table 2.

Debond Length Measurements

In order to observe interfacial damage and attempt to determine the extent of fiber/matrix debonding, interrupted fatigue crack growth specimens were examined nondestructively by scanning acoustic microscopy (SAM) [*13*]. This work was performed by General Electric Aircraft Engines [*14*]. The specimens were also chemically etched (using a nitric/hydrofluoric solution) to remove the matrix and expose the fibers. Measurements of the damaged interface lengths were made at high magnifications in the SEM. The total damage zone observed for every fiber was taken as the debond length and used to determine the interfacial frictional shear strength.

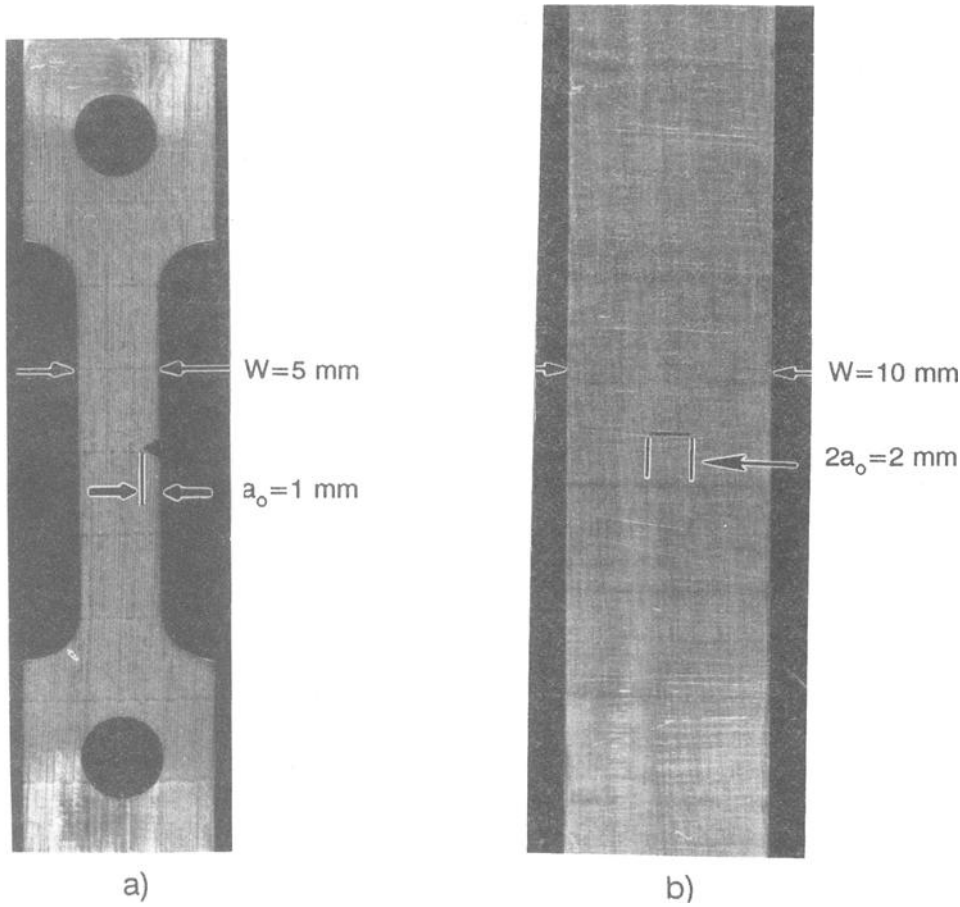

FIG. 1—*Fatigue crack growth specimens:* (a) *single-edge notch (SEN), and* (b) *center crack panel (CCP).*

TABLE 1—*Fatigue crack growth test matrix.*

	Initial Notch, a_0, mm	Width, W, mm	Thickness t, mm	Applied stress $\Delta\sigma = \sigma_{max}$-$\sigma_{min}$, MPa
		SINGLE EDGE NOTCH SPECIMENS		
SEN1[a]	1.054	5.071	1.930	262
SEN2[a]	1.203	5.088	1.860	180, 360
SEN3[a]	1.016	5.085	1.930	180, 248, 276
SEN4[a]	1.031	5.080	1.788	264
SEN5[a]	1.024	5.080	1.753	276
		CENTER CRACK PANEL SPECIMENS		
CCP1	1.015	10.04	0.86	348
CCP2	1.006	9.95	0.89	344
CCP3[a]	1.249	10.14	1.905	228

[a] Heat-treated.

TABLE 2—*SCS-6/Ti-24-11 intermetallic matrix composite properties assumed.*

Composite SCS-6/Ti-24-11			Fiber SCS-6		Matrix Ti-24-11	
Elastic modulus	Transverse, E_{11}, GPa	129	Modulus, E_f, GPa	367	Modulus, E_m, GPa	106
	Axial, E_{22}, GPa	192	Diameter, μm	142		
Poisson's ratio	ν_{12}	0.1905	Volume fraction	0.33		
	ν_{23}	0.2835				
Shear modulus	G_{12}, GPa	69.66				

Fiber Pushout Testing

The frictional properties of the interface were investigated using the fiber pushout test method. Pushout tests were performed on specimens in the as-received condition and specimens previously subjected to fatigue crack growth conditions.

Pushout testing of previously fatigued interfaces was performed in order to determine the actual frictional strength during crack bridging and to study the effect of relative fiber/matrix sliding on the integrity of the interface. Pushout samples with previously fatigued interfaces were obtained near the fracture surface of SEN and CCP specimens that exhibited crack bridging and failed during fatigue loading (Fig. 2).

Pushout specimens were prepared by sectioning with a thin diamond cut-off wheel to obtain slices approximately 1 mm thick. All samples were then polished on both surfaces to a 0.05-μm finish and final thicknesses ranging between 0.25 and 0.40 mm. The 143-μm-diameter fibers were pushed into a support plate with a 0.36-mm-wide groove using flat-bottomed tungsten carbide indenters. A displacement rate of 0.05 mm/min was used. The pushout data were recorded in a form of load versus time in conjunction with acoustic emissions to help identify

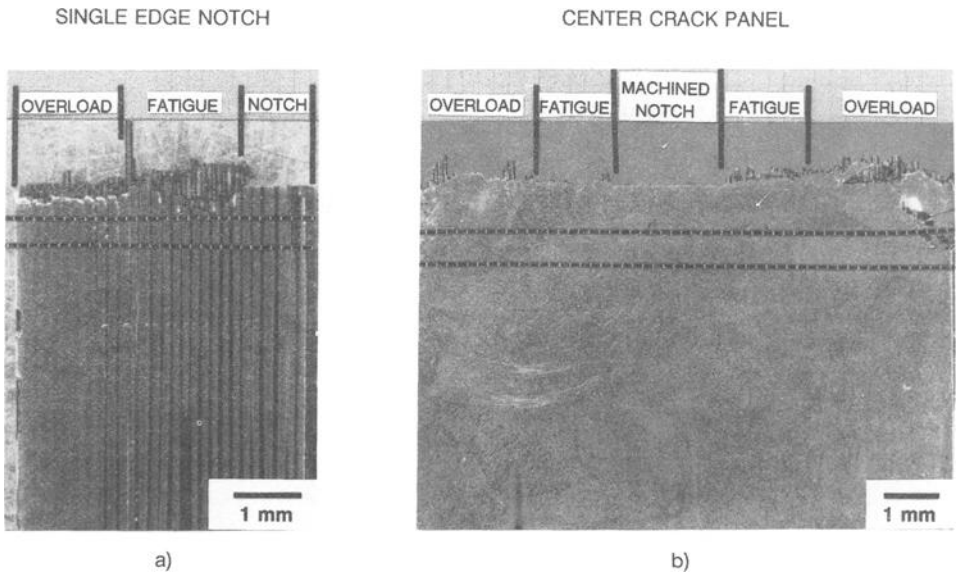

FIG. 2—*Failed fatigue crack growth specimens showing the approximate location of the slices taken for pushout testing:* (a) *SEN3 and* (b) *CCP3.*

the debond load. A more detailed description of the equipment and procedure can be found elsewhere [*15*]. A total of about 250 fibers were tested under the above described procedures.

In order to simulate the effect of relative fiber/matrix sliding that occurs at the interface during crack bridging, multiple reversed pushouts were performed. These pushouts were conducted on specimens in the as-received condition, with the fibers being pushed back and forth (about 10 to 20 μm) three or four times.

Fiber Testing

In order to determine the load carrying ability of bridging fibers and the effect of fiber/matrix sliding on the residual fiber strength, fiber tension testing was performed. Bridging fibers and fibers ahead of the crack tip were chemically removed from interrupted fatigue crack specimens that exhibited bridging. Fibers were extracted from both specimen geometries. The CCP specimen was cycled at $\Delta\sigma = 225$ MPa for approximately one million cycles. The SEN specimen was loaded at $\Delta\sigma = 276$ MPa for three million cycles. Fibers were also extracted from an interrupted SCS-6/Ti-15-3 double edge notch (DEN) specimen which was exposed to about one million cycles at $\Delta\sigma = 276$ MPa. The bridging zone (a-a_0) was approximately 0.31, 0.35, and 0.87 mm for the CCP, SEN, and DEN specimens, respectively. Fibers were tested using a 5.0-mm gage length and a strain rate of 1.27 mm/min.

Analytical Modelling of Fiber Bridging

During crack bridging, the unbroken fibers in the bridged region carry part of the applied load. The effect of bridging fibers was modelled as a closure pressure on the crack wake using two different analytical techniques, the shear-lag model [*8*] and the fiber pressure model [*16*]. The shear-lag model relates the closure pressure, $c(x)$, to the crack opening displacement by assuming a constant interfacial frictional stress (τ_f) along a given debond length [*6*] for monotonic loading. The closure pressure was later modified to account for fatigue loading by relating the closure pressure ranges to the displacement ranges by (from Ref *8*)

$$\Delta c(x) = 2\sqrt{\frac{2\,\Delta u(x)\tau_f V_f^2 E_f E_c^2}{R(1 - V_f)^2 E_m^2}} \tag{1}$$

where

$\Delta c(x)$ = closure pressure ranges (as a function of position along the crack),
E_m = matrix modulus,
E_f = fiber modulus,
V_f = fiber volume fraction,
R = fiber radius,
τ_f = interfacial frictional shear strength, and
$\Delta u(x)$ = Half crack opening displacement ranges (as a function of position along the crack).

In the fiber pressure model, the closure pressure is related to the net tensile and/or bending stresses in the bridged area based on an elementary strength of materials approach. These stresses correspond to the load carried by the debonded fibers irrespective of the interface properties. The resulting closure profiles are given here for both specimen geometries

$$\text{SEN; } \Delta c(x) = \Delta\sigma^{\infty}\left(\frac{W}{W - a_0} + \frac{6Wa_0[0.5(W - a_0) - (x - a_0)]}{(W - a_0)^3}\right) \tag{2}$$

$$\text{CCP; } \Delta c(x) = \Delta\sigma^{\infty}\left(\frac{W}{W - 2a_0}\right) \tag{3}$$

where $\Delta\sigma^{\infty}$ is the applied far-field stress range, a_0 is the initial notch, and W is the specimen width. A review of both analytical models can be found in Ref *17*.

Using both models, a finite element analysis was performed to determine the fatigue crack driving forces and crack opening displacements. For the shear lag model, the closure pressure was applied as a nonlinear foundation pressure. Since the closure pressure in the shear lag models was a function of the unknown crack opening displacements, an iterative scheme was required to solve for these unknown displacements. In the fiber pressure model, the closure pressure was applied simply as a pressure along the bridged area. For simplicity, the FEM analysis utilized an orthotropic homogeneous solution with composite effective properties. The composite stress intensity factor was determined using quarter point singularity elements at the crack tip. The details of the analytical procedure required to measure the closure corrected crack driving force and displacements is found elsewhere [*16*].

Results

Fatigue Crack Growth

The fatigue crack growth process was similar for both SEN and CCP crack geometries. In all cases fatigue cracks initiated readily at the machined notch root where fibers were damaged due to machining. The fibers that were partially cut during machining, if not already broken, usually failed during the first loading cycle. Since many fibers were damaged at the notch, many micro-cracks were initiated through the thickness of the composite. With additional fatigue cycling, these cracks coalesced to form a dominant crack. At times multiple cracks were observed to emanate from the notch. Multiple cracks were observed in both geometries; however, they were more common in the SEN geometry, probably due to the presence of greater bending.

It should be noted that even though fatigue cracks initiated readily, at stress ranges less than 150 MPa, fatigue cracks did not easily propagate into the matrix. At greater stresses, cracks propagated in the matrix, leaving fibers intact behind the crack tip.

Initially all cracks were bridged. Depending on the stress level, cracks that remained bridged were associated with decreasing crack growth rates and eventually crack arrest. When fibers in the crack wake started failing, the crack growth rates accelerated. The remote applied stress for which the specimens eventually exhibited fiber failure was greater than 180 MPa for the SEN geometry and 225 MPa for the CCP geometry.

The fatigue crack growth rates for the tested specimens as a function of the applied stress intensity factor ΔK_{app} are shown in Fig. 3. The crack that remained fully bridged resulted in crack arrest, while the FCG rates of specimens exhibiting some fiber failure were typically higher than those of bridged cracks, but still lower than those of the unreinforced matrix (see Fig. 3). However, as unbridged cracks propagated further in the specimen, fiber failures were observed to occur ahead of the crack tip.

Fractography

The fracture surfaces of both specimens geometries are shown in Fig. 4. As seen on the fracture surface, very little fiber pullout was observed. Fiber failures typically occurred within 1 to 2 fiber diameters from the fracture surface. In the fatigue region, extensive damage was observed in the fiber/matrix interface. In the overload region, however, interfaces were not

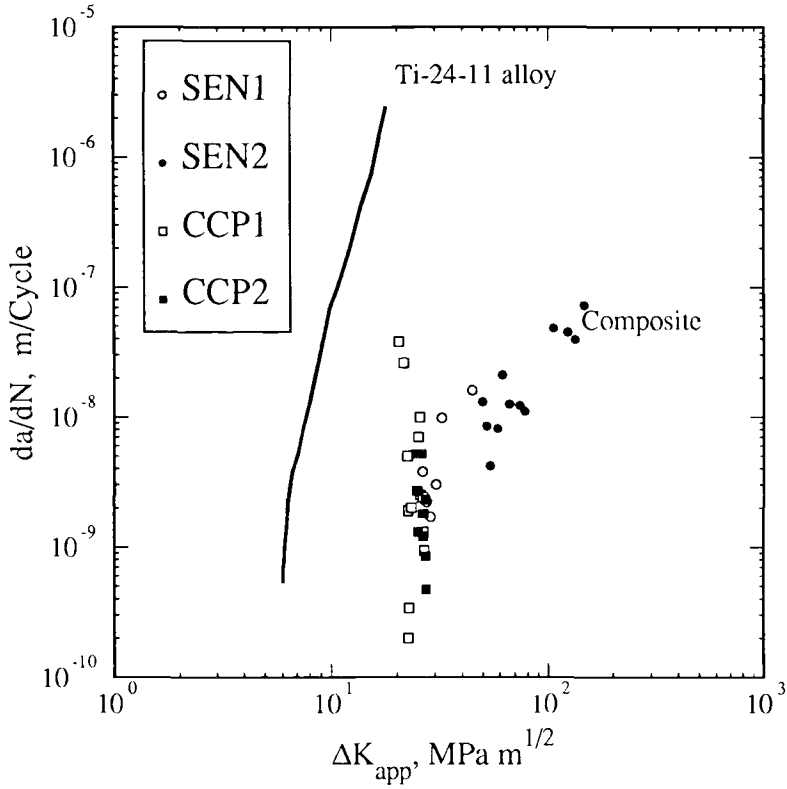

FIG. 3—*Composite fatigue crack growth rates as a function of the applied* ΔK_{app} *in comparison to matrix data.*

damaged. Furthermore, the fracture surface in the fatigue region was littered with debris, presumably from the damaged interfaces and fibers. Again, debris was not observed in the overload region. Interfacial fretting was also observed during fatigue crack growth on the surface of a specimen containing fibers which were partially exposed from polishing (Fig. 5). As seen in Fig. 5, interfacial debris has been ejected from the interface. Interfacial failure in this composite occurred between the carbon coatings on the SCS-6 fiber. These coatings contain weak graphitic phases [*18*] which seem prone to wear during fatigue.

Interface Damage Zone Measurements

In order to determine the extent of interfacial damage, interrupted fatigue crack growth specimens were chemically etched to expose the fibers. Figure 6 shows typical damage observed on the interfaces of fatigued fibers. Interfacial damage was never observed in fibers outside the fatigue crack growth region. Similar debond zones were observed with the scanning acoustic microscope (Fig. 7). The extent of interfacial damage is shown in Fig. 8 for both crack geometries. As shown in Fig. 8, the observed damage zones are greater for fibers near the machined notch in comparison to fibers closer to the crack tip.

By assuming the measured damage zones represent the actual debond length l, the interfacial

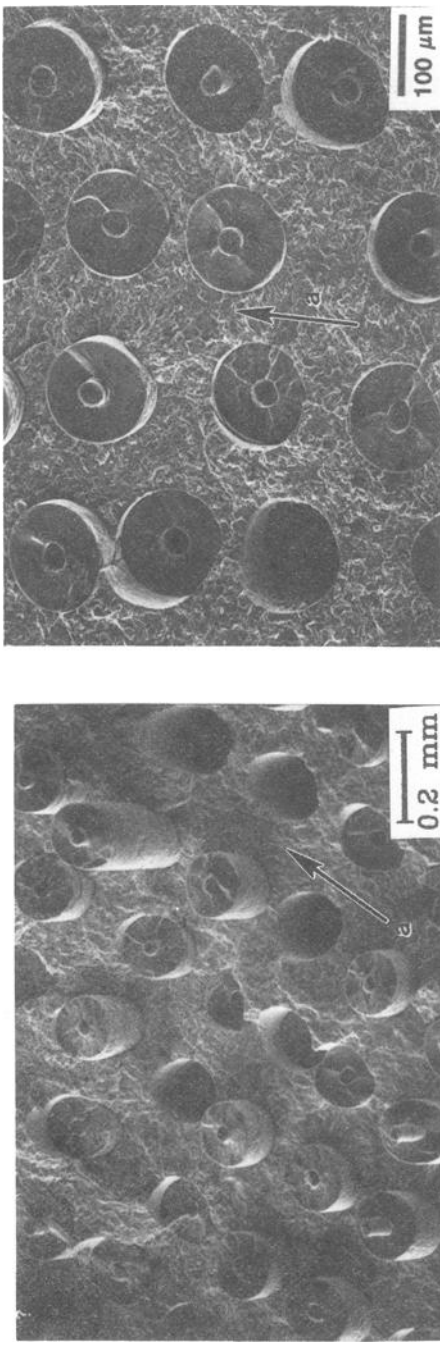

FIG. 4—*Typical micrographs of the fracture surface for:* (a) *SEN and* (b) *CCP.*

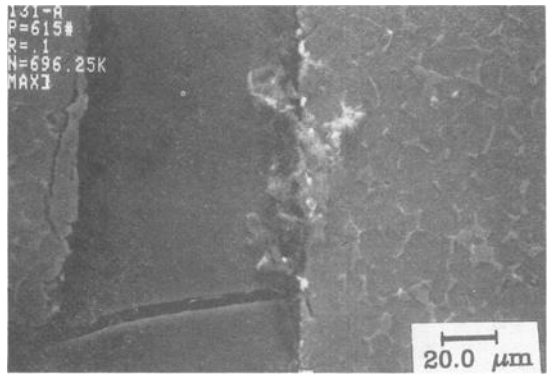

FIG. 5—*Micrograph of a partially exposed fiber showing inter-facial debris (SEN5).*

friction strength can be determined using a shear-lag approach. The relation between l and τ_f, as given by McCartney [7] is

$$l(x) = \sqrt{\frac{u(x)R(1 - V_f)E_fE_m}{\tau_f E_c}} \tag{4}$$

where $l(x)$ is the debond length and $u(x)$ is the crack opening displacement at a given location x. Using the experimentally determined debond lengths and CODs in conjunction with Eq 4, an average friction strength of 23 and 34 MPa were calculated for the CCP and SEN geometries, respectively.

Pushout Testing

As-received condition—A typical pushout response of specimens in the as-received condition is shown in Fig. 9. The debonding event (P_d) coincides with a load drop and pronounced acoustic emissions. Debonding is followed by a gradual decrease in the load as the fiber is displaced. At this point the only resistance to the fiber displacement comes

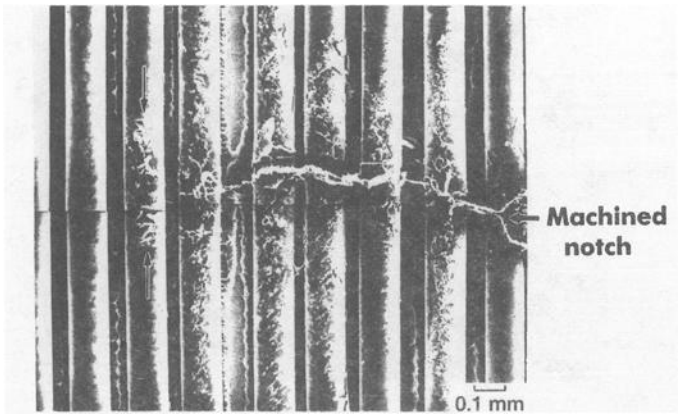

FIG. 6—*Interfacial damage exposed by dissolving the matrix.*

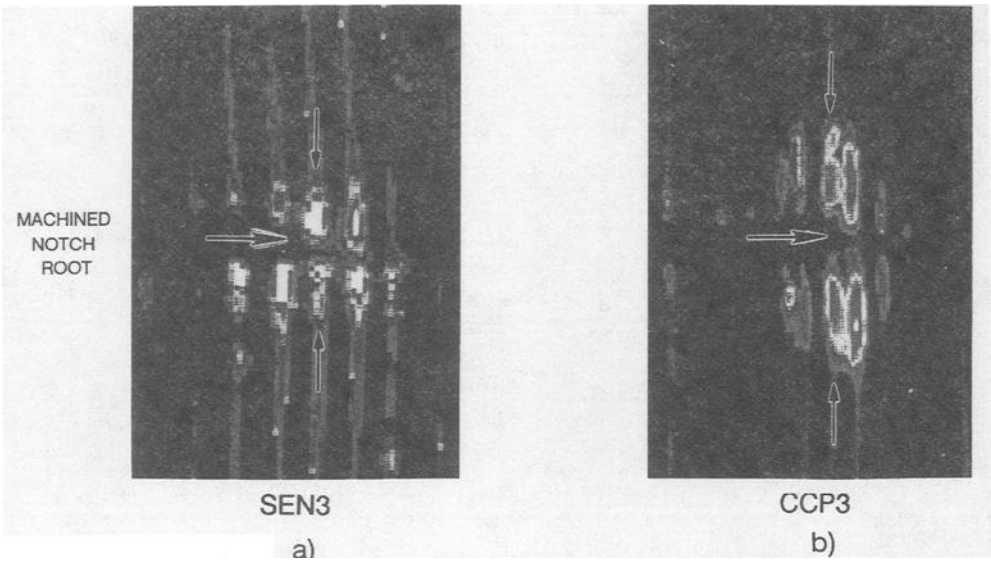

FIG. 7—*Interfacial damage zones as observed by scanning acoustic microscopy for:* (a) *SEN3 and* (b) *CCP3 specimens.*

from the frictional shear stresses at the interface. The load immediately after debonding P_f is considered to be the load needed to overcome friction. The interfacial debond shear stress for the as-received composite was determined to be 122 MPa using a simple force balance (i.e., $\tau_d = P_d/2\pi Rt$). Likewise, the frictional shear stress was calculated to be 75 MPa. The frictional strength derived from the debond zone measurements (τ_f ave. = 28

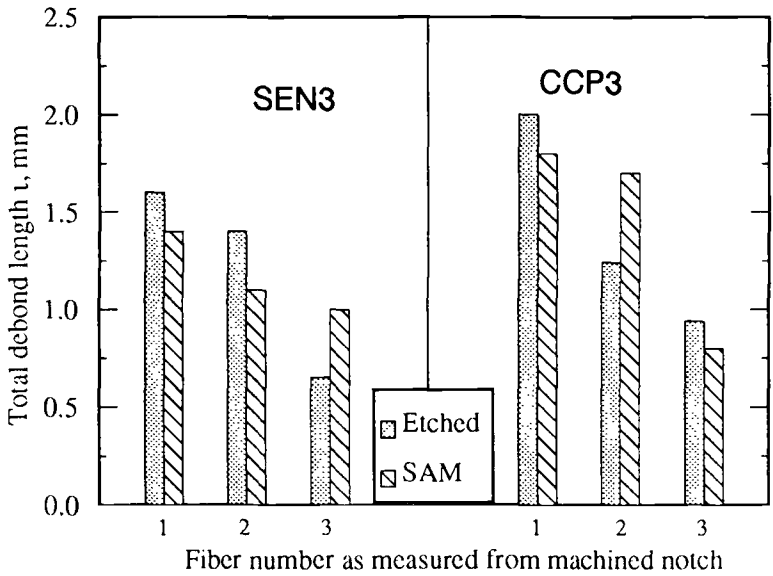

FIG. 8—*Measured interfacial damage zones.*

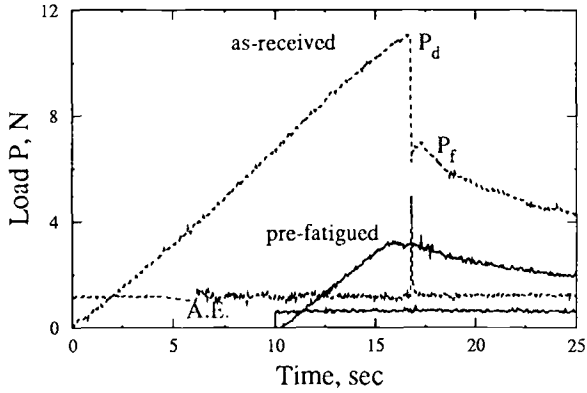

FIG. 9—*Typical pushout response of interfaces in the as-received and pre-fatigued conditions.*

MPa) is significantly lower than the as-received friction strength of τ_f = 75 MPa. This may be attributed to interfacial damage incurred during fatigue sliding.

Previously Fatigued Interfaces—The effect of relative fiber/matrix sliding during crack bridging on the interfacial friction strength, as determined by pushout testing, is shown in Fig. 9 in comparison to the as-received response. The response of the pre-fatigued specimen clearly suggests that these interfaces were already debonded since no load drop or acoustic emission events were observed. The measured average interfacial friction strength of previously fatigued interfaces was calculated to be 32 ± 10 MPa for the SEN specimen and approximately 45 MPa for the CCP specimen. Compared with as-received interfacial frictional strength, this represents about a 57 and 40% decrease in friction strength for the SEN and CCP, respectively. These values are in better agreement with those calculated from the debond zone measurements.

Multiple Reverse Pushout Testing—Multiple reversed pushouts were performed on the as-received specimens in order to simulate the effect of fatigue on the interfacial shear strength. The fibers were typically displaced 10 to 20 μm. The first pushout shows behavior typical of as-received material with a bonded interface (Table 3). Subsequent pushouts show a steady decrease in the frictional resistance of the interface with increasing cycles. After only four pushouts, the frictional shear stress has decreased to 39 ± 7 MPa, which is in the order of the frictional shear strength measured near the fracture surface (see Table 3) of pre-fatigued specimens.

Fiber Tension Testing

Since extensive damage was observed for interfaces that were subjected to cyclic loading, tension testing was performed on bridging fibers to determine the effect of this damage on fiber strength. The results are shown in Fig. 10. The tensile strength of bridging fibers in the CCP specimen was 3530 ± 146 MPa. In comparison, the tensile strength of fibers ahead of the crack tip was 4282 ± 212 MPa. The tensile strength of bridging fibers in the SEN specimen was 3720 ± 480 MPa in comparison to 4150 ± 340 MPa for nonbridging fibers, an insignificant difference for all practical purposes. In the SCS-6/Ti-15-3 DEN specimen, however, bridging fibers near the notch had an average tensile strength of 2664 ± 514 MPa. Fibers near the crack tip, which were subjected to lower fiber/matrix displacements, had an average tensile strength of 3430 ± 286 MPa. Fibers ahead of the crack tip, whose interfaces were not subjected to

TABLE 3—*Interfacial friction strength results from pushout tests and debond length measurements.*

Test Conditions	Type of Technique	Friction Strength, τ_i, MPa
As-received	Pushout	75 ± 6
Fatigue crack growth specimen CCP	Debond lengths	23
	Pushout	45
Fatigue crack growth specimen SEN	Debond lengths	34
	Pushout	32
Multiple reverse pushouts	Initial push	75 ± 6
	Second push	55 ± 6
	Third push	48 ± 8
	Fourth push	39 ± 7

relative fiber/matrix sliding, were significantly stronger with average tensile strength of 4415 ± 684 MPa. The guaranteed minimum strength of the virgin SCS-6 fibers by the manufacturer is 3490 MPa.

Crack Opening Displacement

Measurements of the crack opening displacements (COD) were obtained using the SEM loading stage. Measurements were typically made starting at the root of the machined notch and ending at the crack tip. Typical COD profiles at maximum and minimum loads, shown in Fig. 11, indicate that fatigue cracks remain propped open at minimum load. The displacements at minimum load are usually about half the maximum displacements even though the R ratio was 0.1.

Both the fiber pressure model and shear-lag model were used to predict the ΔCODs during crack bridging. Figure 12 shows the ΔCODs predicted by the fiber pressure model in comparison with experimentally obtained ΔCODs for a variety of crack lengths and applied loads. For the most part, the fiber pressure model predicted the ΔCOD profiles well. Also shown for

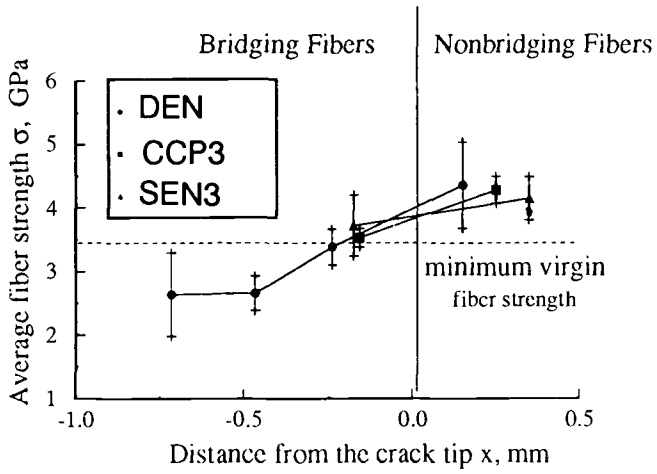

FIG. 10—*Extracted SCS-6 fiber strength values for bridging and nonbridging fibers.*

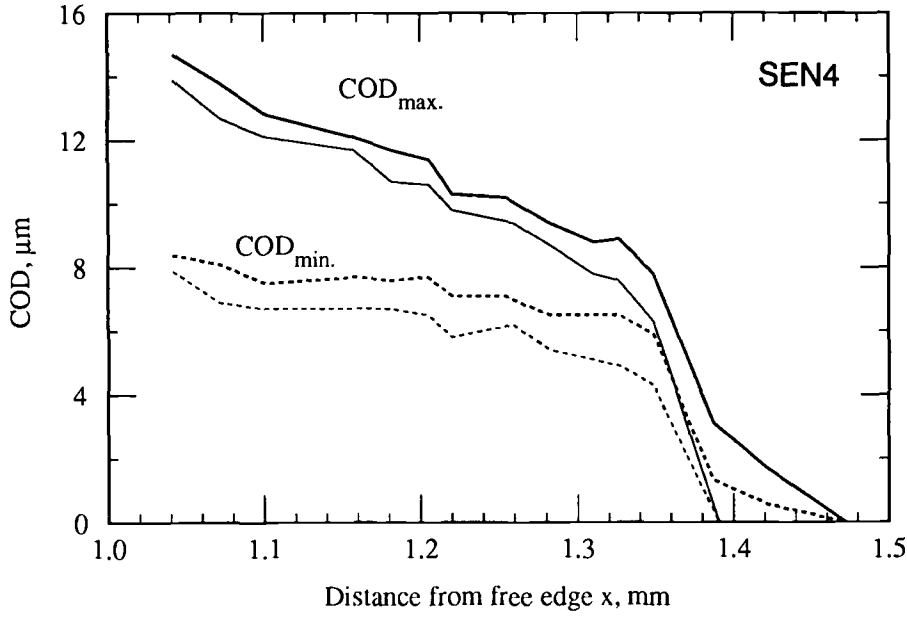

a) SEN

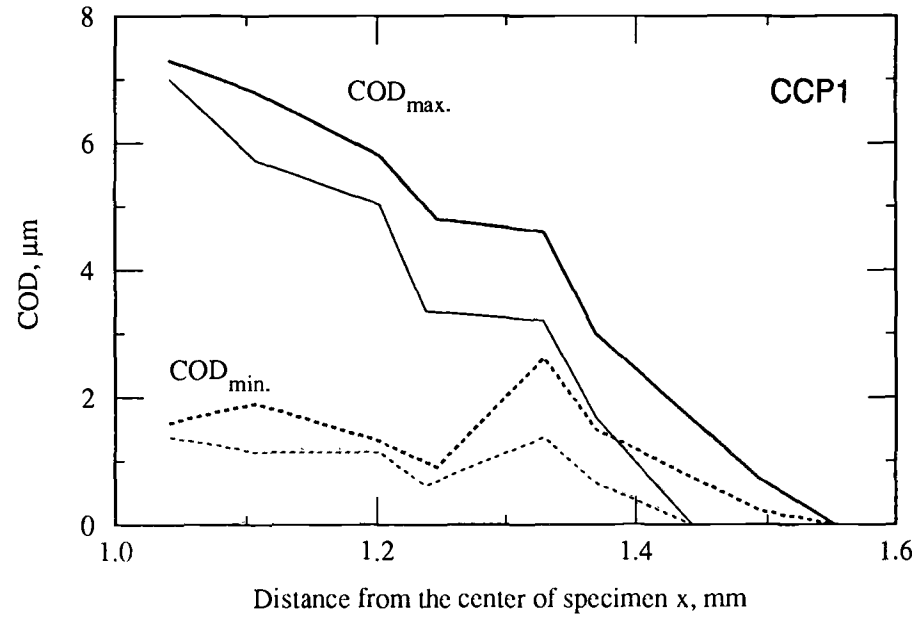

b) CCP

FIG. 11—*Measured crack opening displacements at maximum and minimum loads for:* (a) *SEN4 and* (b) *CCP1.*

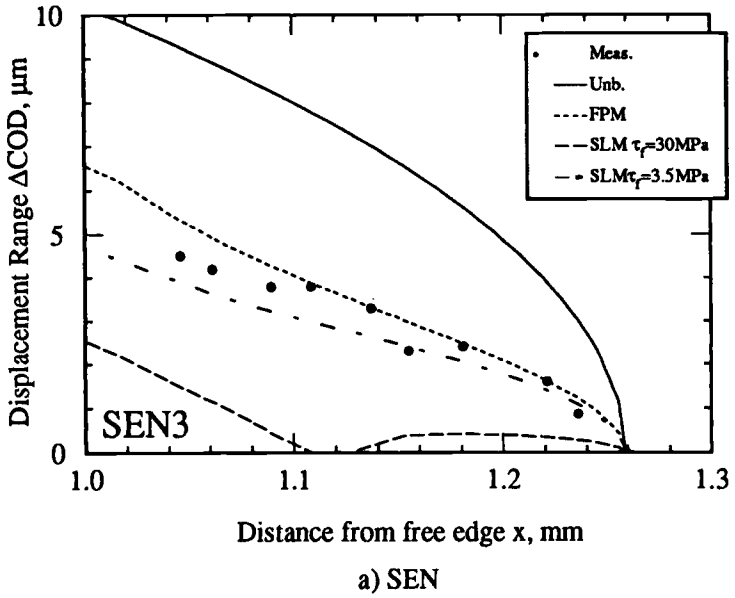

a) SEN

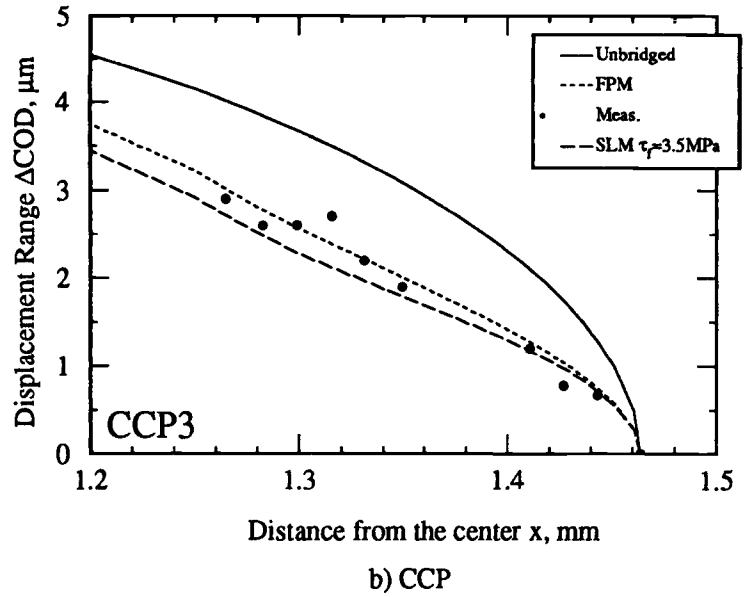

b) CCP

FIG. 12—*Predicted crack opening displacement ranges in comparison to measured values for:* (a) *SEN and* (b) *CCP.*

comparison are the expected ΔCODs for unbridged cracks. As seen in Fig. 12, the measured ΔCODs of bridged cracks are much smaller than the predicted ΔCODs of unbridged cracks.

Predicting the ΔCOD profiles with the shear-lag model requires knowledge of the interfacial friction strength. As a first approximation τ_f = 30 MPa was used based on the pushout results. However, as shown in Fig. 12*a*, the ΔCOD profiles predicted with τ_f = 30 MPa were typically smaller than the measured values. By varying τ_f, it was determined that τ_f = 3.5 MPa generally resulted in good correlation between the observed and predicted ΔCODs for both crack geometries (see Fig. 12).

Even though the predicted ΔCOD profiles using τ_f = 3.5 MPa generally resulted in good correlation with the experimentally measured crack profiles, some inconsistencies were observed. For example, near the crack tip, the shear lag based predictions of the ΔCODs were usually larger than experimental measurements (Fig. 13). This implies that the interfacial friction strength is greater than τ_f = 3.5 MPa near the crack tip. This scenario was modeled by varying τ_f along the crack wake until good agreement with the measured displacements was achieved. As shown in Fig. 13*b*, for the CCP geometry, by varying the interfacial friction strength along the bridged zone, it was determined that a combination of τ_f = 1 MPa near the notch and τ_f = 30 MPa near the crack tip resulted in good agreement for the entire crack profile. For the SEN geometry (Fig. 13*a*), however, a combination of τ_f = 3 MPa near the notch and τ_f = 10 MPa near the crack tip resulted in the best correlation.

Fatigue Crack Driving Force During Crack Bridging

The two models were also used to account for the reduction in the effective crack driving force (ΔK_{eff}), Ref *16*, due to fiber bridging. As shown in Fig. 14, both models predict significantly lower effective fatigue crack driving forces during crack bridging in comparison to an unbridged crack. Furthermore, ΔK_{eff} decreases as the crack length increases. This correlates well with the observed decrease in fatigue crack growth rates before fiber failure.

Since fatigue crack growth during bridging occurs only in the matrix, the composite fatigue crack growth rates were compared to those of the unreinforced Ti-24-11 matrix utilizing the ΔK_{eff} predicted by the models (Fig. 15). As seen in Fig. 15*a*, the effective crack driving force predicted by the fiber pressure model shifts the composite crack growth rates in good agreement with the unreinforced matrix.

The shear lag model with a constant interfacial friction strength of 3.5 MPa substantially overpredicted the composite crack driving force as shown in Fig. 15*b*. However when the τ_f was varied along the crack wake in agreement with the measured ΔCODs, the shear lag calculated ΔK_{eff} brought the composite data in closer agreement with the unreinforced matrix data (see Fig. 15*c*). As also shown, the shear lag model predicts the crack driving force much better for the CCP geometry than the SEN geometry.

Discussion

The results of this study show that relative fiber/matrix sliding during fatigue results in interfacial damage. Interfacial wear degrades the mechanical properties of the interface and fiber which influence the fatigue crack driving force.

Interfacial Properties

Interfacial damage was readily observed on the fracture surface of fatigue specimens and on the interfaces of interrupted specimens. The interfacial damage observed consisted mostly of cracks and spalling in the carbon-rich coatings of the SCS-6 fiber. The damage zones were

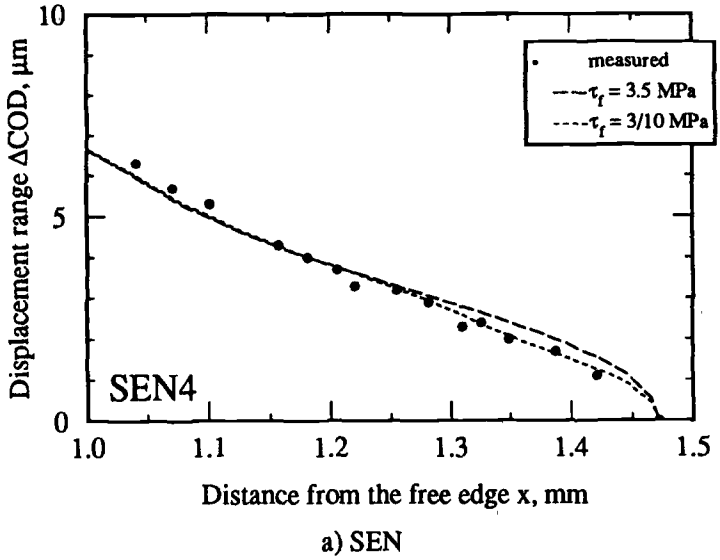

FIG. 13—*Calibration of the SLM with a variable interfacial friction stress for:* (a) *SEN and* (b) *CCP specimens.*

typically in the order of 1 to 2 mm long. Pushout testing of previously fatigued specimens suggest that interfacial damage incurred during fatigue results in drastic deterioration of the frictional properties of the interface. All the factors governing the extent and magnitude of interfacial degradation are not clear at this time; however, multiple reversed fiber pushout testing suggests that interfacial damage can occur very rapidly during fatigue, and maybe as a function of relative fiber/matrix sliding distance (see Table 3).

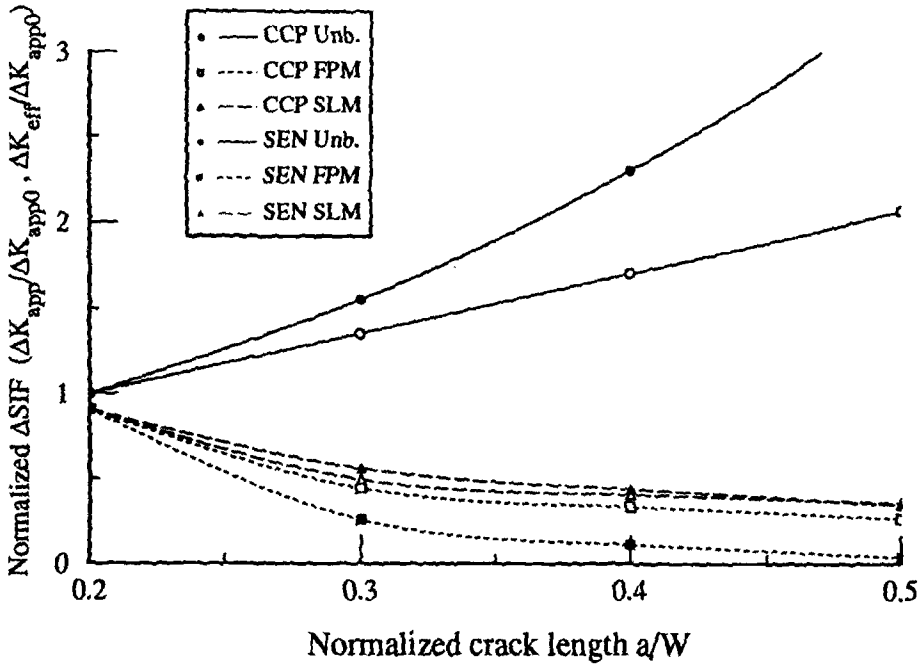

FIG. 14—*Effective normalized stress intensity factors as a function of the crack length, where* K_{app0} *is the applied SIF at the initial crack length* a_0.

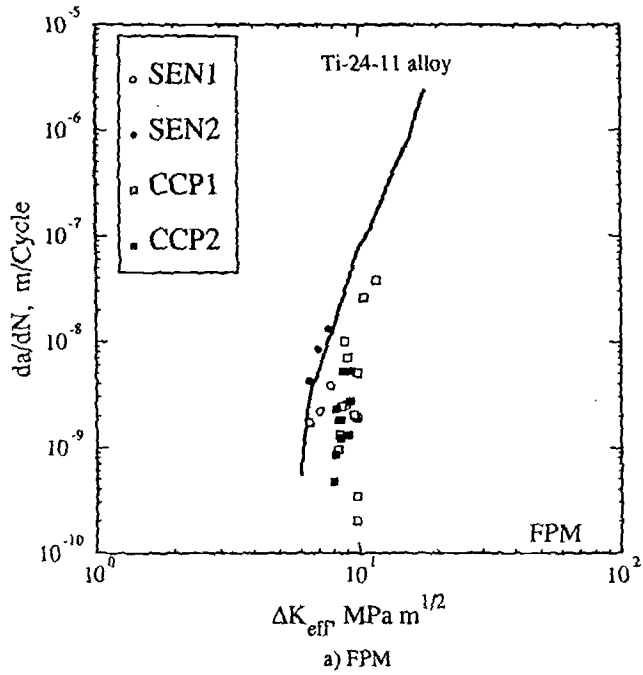

FIG. 15—*Composite crack growth rates plotted as a function of* ΔK_{eff} *in comparison to the matrix data using:* (a) *FPM,* (b) *SLM with constant* $\tau_f = 3.5$ *MPa, and* (c) *SLM with a variable* τ_f.

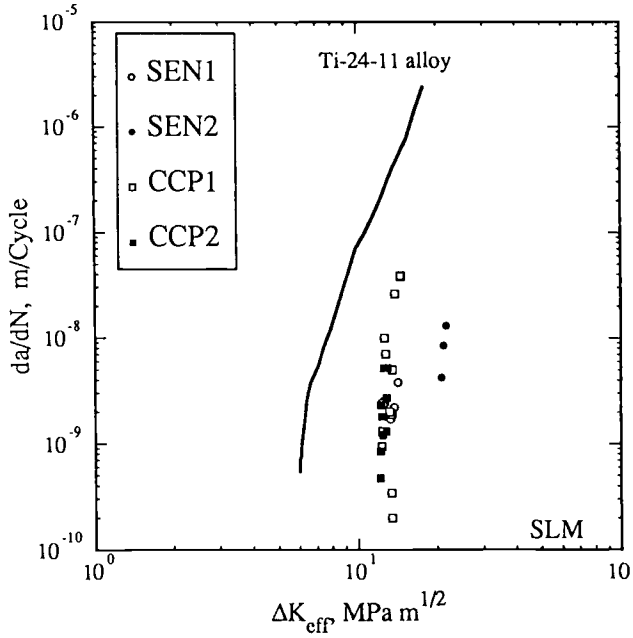

b) SLM τ_f= 3.5 MPa

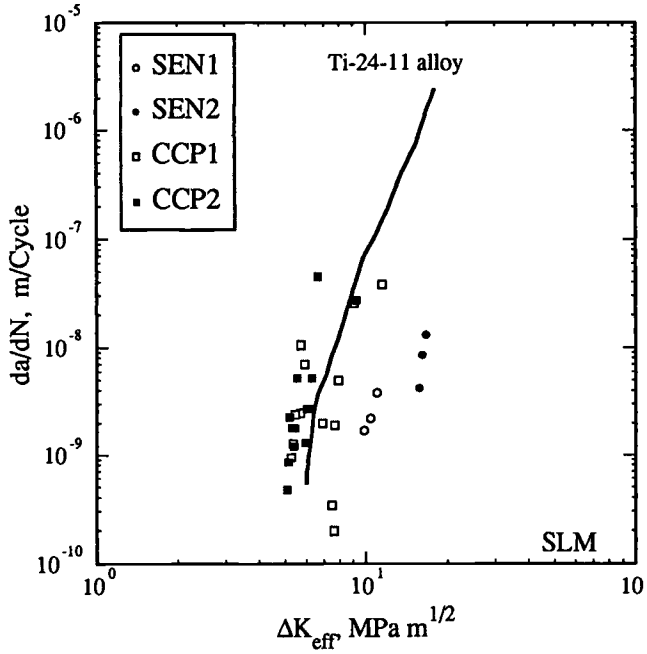

c) SLM variable τ_f

FIG. 15—*Continued.*

Three different methods were used to ascertain the interfacial properties of the bridging fibers. Both pushout testing of the fibers in the bridging zone and debond length measurements resulted in an estimated τ_i of 20 to 30 MPa (as compared to τ_f of 75 MPa for the as-received composite). However, the τ_f which best fit the ΔCOD measurements, from the shear lag model, suggested that the shear strength varies within the crack wake. For the largest portion of the bridged zone, a low τ_f of 1 to 3 MPa fit the measured ΔCODs; however, near the crack tip, a τ_f of 10 to 30 MPa (depending on specimen geometry) was needed to fit the measured displacements.

The discrepancies in the τ_f values calculated through the different methods may be due to several factors. Even though $\tau_f = 1 \sim 3$ MPa obtained from ΔCOD measurements seems considerably lower than the interfacial friction strength observed during pushout testing, it should be noted that the pushout values were obtained at depths approximately 1 mm from the fracture surface. Fractographic examination of the interface revealed that the greatest damage is near the vicinity of the crack plane. The τ_f values obtained from the ΔCOD measurements therefore might reflect the interface conditions near the crack plane.

Fiber Strength

Interfacial wear in the crack wake also resulted in degradation of the tensile strength of the bridging fibers. As seen in Fig. 10, the reduction in the fiber strength was significantly smaller for fibers obtained from the SEN and CCP SCS-6/Ti-24-11 specimens than the fibers obtained from the DEN SCS-6/Ti-15-3 specimen. Furthermore, for the DEN specimen, the strength of bridging fibers increased near the crack tip. Fibers near the crack tip were subjected to lower relative fiber/matrix displacements and displayed smaller damage zones. Fibers ahead of the crack tip, whose interfaces were not subjected to relative fiber/matrix sliding, did not display any interfacial damage and were significantly stronger.

It is not clear why a greater loss in fiber strength was observed in the DEN SCS-6/Ti-15-3 specimen. This phenomenon may be related to a difference in the chemistry of the reaction zones or bonding of the interface between the two matrix alloys. However, comparison of the fiber surfaces revealed that the fibers extracted from the DEN specimen exhibited more damage. As shown earlier by the multiple pushout test method, the relative magnitude of fiber/matrix sliding influences the extent of interfacial damage.

Comparing the ΔCODs of these specimens, certain trends became evident. The ΔCODs for the SEN and CCP specimen were in the order of 4 μm, while the ΔCODs for the DEN specimen were approximately 11 μm at the machine notch. Furthermore, for the DEN geometry, in the case of fibers near the crack tip whose strength did not degrade significantly (3430 ± 286 MPa), the relative ΔCODs were also in the 4-μm range. The strength of these fibers correlates well with the fiber strengths observed in the bridging fibers of the SEN (3720 ± 480 MPa) and CCP (3530 ± 146 MPa) geometries. This suggests that interfacial damage and degradation of the fiber strength during bridging is more likely in the presence of large ΔCODs. Furthermore, damaged fibers extracted from the bridged region typically failed within the damage zone, whereas undamaged fibers ahead of the crack tip typically failed anywhere within the gage section and many times outside the gage. Since the damage is greater near the fracture surface, this explains why little pullout was observed (in the order of 1 to 2 d_f), even though the damage zones were significantly larger ($\simeq 10\ d_f$).

Modelling of the Bridging Process

The shear lag model is predicted on the ability to accurately describe the load transfer from the cracked matrix to the bridging fibers through an interfacial sliding process. As the present

study has shown, the interfacial wear process is very complex, resulting in a nonuniform interfacial damage as a function of the distance from the crack tip and the distance from the crack plane for a given fiber/matrix interface. This nonuniformity of the interfacial damage results in a variable frictional shear strength along the crack wake.

Typical application of the shear lag model assumes a single τ_f value in the analysis. However, due to the factors described above, the use of a single τ_f resulted in the shear lag model overestimating the effective crack driving force, as shown in Fig. 15*b*. When the analysis was performed using a variable τ_f (the same combination of τ_f as previously used in predicting the ΔCODs, Fig. 13), the shear lag model brought the composite FCG data much closer in agreement with the unreinforced matrix data as shown in Fig. 15*c*. Unfortunately, obtaining a single accurate estimate of τ_f is in itself problematic; the need to establish different τ_f values for varied locations within the crack wake further complicates the shear lag modelling process.

While most of the discussion has dealt with the shear lag model, the success of the fiber pressure model in predicting both the measured crack opening displacements and the effective fatigue crack driving forces (Figs. 12 and 15*a*) should be emphasized. This rather straightforward approach in calculating the closure pressure function seems adequate in predicting the effect of bridging.

Interestingly enough, the FPM and the SLM with variable τ_f predict the trends observed during bridging even though the two closure pressures are derived quite differently. Figure 16 shows closure pressure profiles calculated from both models. The closure pressure profile for the fiber pressure model is a function of the crack geometry and applied load. For the CCP geometry the closure pressure profile is constant over the entire bridged region. In the SEN geometry, the presence of bending generally results in greater closure pressure profiles. Bending also results in a slightly decreasing closure pressure profile along the bridging zone (higher near the notch and lower near the crack tip).

In the shear lag model, the closure pressure depends on the interfacial friction strength and crack opening displacements. This is evident by the closure pressure profile, which decreases to zero at the crack tip. In comparison, the fiber pressure model predicts much higher closure pressures near the crack tip. The difference in closure pressure profiles explains why the fiber pressure model typically predicts lower ΔCODs and ΔK_{eff}s in comparison with the shear lag model.

Varying the interfacial friction stress to reflect damaged interfaces also changes the closure pressure profile. As shown in Fig. 16, this results in higher fiber stress near the crack tip. This modification results in a closure pressure profile which is similar to that predicted by the fiber pressure model. Therefore, the FPM fortuitously predicts a closure pressure profile consistent with the observed mechanisms during bridging. Even though the fiber pressure model is not always consistent in predicting the overall ΔCODs, it does seem to predict realistic crack driving forces. This also suggests that the crack driving force during bridging is most sensitive to the closure pressure and ΔCODs near the crack tip rather than the overall crack profile.

Finally, before either of these models can be used to predict fatigue life, it is necessary for these models to accurately predict the onset of fiber failure. This issue will be addressed in future work.

Conclusions

1. The fatigue crack growth process of a unidirectionally reinforced SCS-6/Ti-24Al-11Nb intermetallic matrix composite was studied using a fatigue loading stage mounted inside a scanning electron microscope. The composite exhibited FCG rates orders of magnitude lower than its unreinforced matrix. The decrease in the FCG rates was caused by crack tip shielding resulting from unbroken fibers bridging the crack wake.

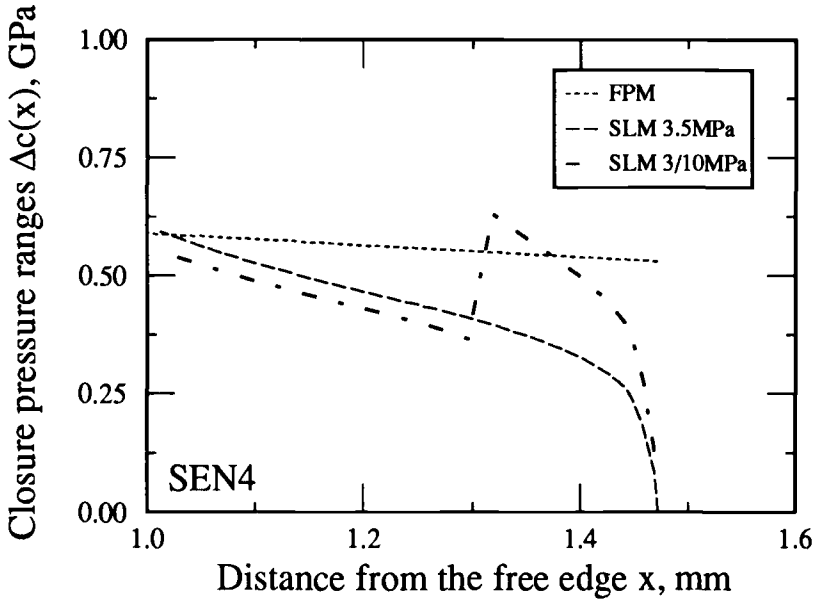

a) SEN

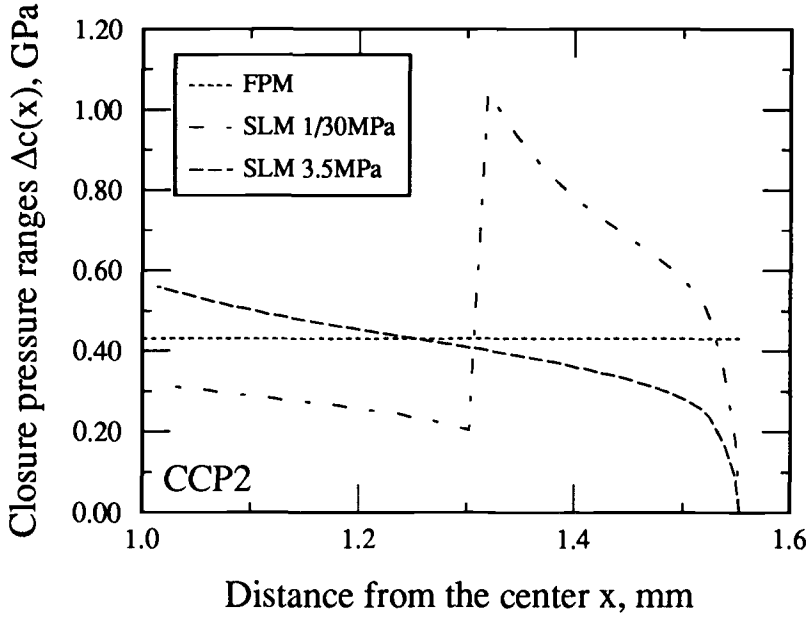

b) CCP

FIG. 16—*Comparison of the closure pressure ranges from the FPM and SLM for:* (a) *SEN and* (b) *CCP.*

2. Interfacial damage in the bridging fibers, induced by relative fiber/matrix sliding, was found to occur in the crack wake of the tested specimens subjected to fatigue crack growth conditions. The interfacial friction shear strength measured in the crack wake using pushout testing revealed lower values than the as-received interface. The degree of interfacial damage was not uniform along the bridged crack wake. Higher damage zones were observed near the machined notch in comparison to the crack tip.

3. The interfacial wear also reduced the fiber strength of the bridging fibers. The reduction in the fiber strength was found to depend on specimen geometry and is thought to increase as a function of the magnitude of relative fiber/matrix displacements.

4. Two different fiber bridging models were used in an attempt to predict the influence of bridging on the fatigue crack driving force in composites. The shear lag model required a variable τ_f in the crack wake before its predictions agreed with the trends exhibited by the experimental data. The fiber pressure model, however, did an excellent job in predicting both the FCG data and the ΔCOD in the bridged zone even though it does not require a knowledge of τ_f.

Acknowledgments

The authors would like to thank Ken Wright and GEAE for providing the material tested. Special thanks is also extended to Rich Klaassen of GE Aircraft Engine-Quality Technology Center for his SAM contribution to this study.

References

[1] Kantzos, P., Telesman, J., and Ghosn, L. J., "Fatigue Crack Growth in a Unidirectional SCS-6/Ti-15-3 Composite," *Composite Materials: Fatigue and Fracture (3rd Vol.), ASTM STP 1110,* T. K. O'Brian, Ed., ASTM, Philadelphia, 1991, pp. 711–731.

[2] Sensmeier, M. D. and Wright P. K., "The Effect of Fiber Bridging on Fatigue Crack Growth in Titanium Matrix Composite," *Proceedings,* Fundamental Relationships Between Microstructures and Mechanical Properties of Metal Matrix Composites, P. K. Liaw et al., Ed., The Minerals, Metals, and Materials Society, Warrendale, PA, 1990, pp. 441–457.

[3] Bakuckas, J. G. and Johnson, W. S., "Application of Fiber Bridging to Fatigue Crack Growth in Unidirectional Titanium Matrix Composites," *Journal of Composites Technology and Research,* Vol. 15, No. 3, Fall 1993, pp. 242–255.

[4] Walls, D., Bao, G., and Zok, F., "Fatigue Crack Growth in a Ti/SiC Composite," *Mechanical Fatigue of Advanced Materials,* R. O. Ritchie, R. H. Dauskart, and B. N. Cox, Eds., MCEP, Birmingham, UK, 1991, pp. 343–356.

[5] Davidson, D. L., "The Micromechanics of Fatigue Crack Growth at 25°C in Ti-6Al-4V Reinforced with SCS-6 Fibers," *Metallurgical Transactions A,* Vol. 23A, 1992, pp. 865–879.

[6] Marshall, D. B., Cox, B. N., and Evans, A. G., "The Mechanics of Matrix Cracking in Brittle-Matrix Fiber Composites," *Acta Metallurgica,* Vol. 33, 1985, pp. 2013–2021.

[7] McCartney, L. N., "Mechanics of Matrix Cracking in Brittle-Matrix Fiber-Reinforced Composites," *Proceedings of the Royal Society of London, Series A,* Vol. 409, 1987, pp. 329–350.

[8] McMeeking, R. M. and Evans, A. G., "Matrix Fatigue Cracking in Fiber Composites," *Mechanics of Materials,* Vol. 9, 1990, pp. 217–227.

[9] Kantzos, P., Eldridge, J. I., Koss, D., and Ghosn, L. J., "The Effect of Fatigue on the Interfacial Friction Properties of SCS-6/Ti-15-3 Composites," in *Advanced High-Temperature Engine Materials Technology Program,* Proceedings of the 4th Annual HITEMP Review, NASA CP 10082, October 1991, pp. 36-1 to 36-11.

[10] Marshall, D. B., Shaw, M. C., and Morris, W. L., "Measurement of Interfacial Debonding and Sliding Resistance in Fiber Reinforced Intermetallics," *Acta Metallurgica et Materialla,* Vol. 40, No. 3, 1992, pp. 443–454.

[11] Warren, P. D., Mackin, T. J., and Evans, A. G., "Design, Analysis and Applications of an Improved Push-Through Test for the Measurement of Interface Properties in Composites," *Acta Metallurgica et Materialla,* Vol. 40, No. 6, 1992, pp. 1243–1249.

[*12*] Telesman, J., Kantzos, P., and Brewer, D., "In Situ Fatigue Loading Stage Inside Scanning Electron Microscope," Lewis Structures Technology—1988, NASA CP3003, Vol. 3, May 1988, pp. 161–172.

[*13*] Gilmore, R. S., Hewes, R. A., Thomas, L. J., III, and Young, J. D., "Broad Band Acoustic Microscopy: Scanned Images with Amplitude and Velocity Information," *Acoustical Imaging,* Vol. 17, 1989, pp. 97–110.

[*14*] Klaassen, R., "Internal Structural Characterization," G.E. Aircraft Interim Report No. 6 for WPAFB Contract No. F33615-88-C-5433, Project No. 2418/02, 15 Jan. 1992.

[*15*] Eldridge, J. I., Bhatt, R. T., and Kiser, J. D., "Investigation Interfacial Shear Strength in SiC/Si_3N_4 Composites," *Ceramic Engineering and Science Proceedings,* Vol. 12, *Proceedings,* 15th Annual Conference on Composites and Advanced Ceramic Materials, 1991, pp. 1152–1171.

[*16*] Ghosn, L. J., Kantzos, P., and Telesman, J., "Modeling of Crack Bridging in a Unidirectional Metal Matrix Composite," *International Journal of Fracture,* Vol. 54, 1992, pp. 345–357.

[*17*] Telesman, J., Ghosn, L. J., and Kantzos, P., "Methodology for Prediction of Fiber Bridging Effects in Composites," *ASTM Journal of Composites Technology and Research,* Vol. 15, No. 3, Fall 1993, pp. 234–241.

[*18*] Ning, X. J., Pirouz, P., Lagerlof, K. P. D., and DiCarlo, J., "The Structure of Carbon in Chemically Vapor Deposited SiC Monofilaments," *Journal of Material Research,* Vol. 5, No. 12, December 1990, pp. 2865–2876.

Hamid Nayeb-Hashemi[1] *and Shahin Pourrahimi*[2]

Synthesis, Strengthening, Fatigue and Fracture Behavior of High-Strength, High-Conductivity P/M Processed Cu-Nb Microcomposite

REFERENCE: Nayeb-Hashemi, H. and Pourrahimi, S., **"Synthesis, Strengthening, Fatigue and Fracture Behavior of High-Strength, High-Conductivity P/M Processed Cu-Nb Microcomposite,"** *Cyclic Deformation, Fracture, and Nondestructive Evaluation of Advanced Materials: Second Volume, ASTM STP 1184,* M. R. Mitchell and O. Buck, Eds., American Society for Testing and Materials, Philadelphia, 1994, pp. 87–108.

ABSTRACT: Materials with both high conductivity and high strength are desired in the design of magnets and rotating electrical machineries. Copper-niobium (Cu-Nb) filamentary microcomposites are such a group of materials. Powder metallurgy techniques (P/M) followed by various deformation processes were used to synthesize these composites. A restacking technique was developed to achieve the high areal reduction necessary to reduce the Nb powder particles to ultra-fine fibers within the Cu matrix. The effects of the Nb volume fraction and size on the evolution of the material microstructure, monotonic tensile properties, and fatigue and fracture behaviors were studied. A strengthening model that combines Cu matrix work hardening, fiber strength, and dispersion-type hardening was developed and shown to predict the yield strength of composites at various stages of deformation processing with reasonable accuracy.

The tensile failure of composites with fully deformed Nb fibers was a shear-type failure (a 45° plane to the specimen axis). However, for composites without fully deformed fibers, the fracture surface had a cup and cone appearance. Fatigue properties of a composite with 18 vol.% Nb and fibers at their fully deformed stage (fiber thickness of 5 to 10 nm) were studied. The mechanisms of crack initiation and propagation were investigated. The final composite failure was due to tensile overload rather than attainment of critical crack length.

KEYWORDS: Cu-Nb microcomposite, powder metallurgy processed, tensile and fatigue behavior, strengthening, damage mechanisms

Nomenclature

a	Crack length
a_c	Critical crack length
A	Filament aspect ratio
α, β	Constants in dislocation hardening models
$\bar{\alpha}$	Crack geometry factor
b	Burger's vector
d	Notched cross-section diameter
D	Overall wire diameter

[1] Professor, Department of Mechanical Engineering, Northeastern University, Boston, MA 02115.
[2] Research associate, Plasma Magnet Laboratory, Massachusetts Institute of Technology, Cambridge, MA 02139.

D_0 Initial overall wire diameter
G Shear modulus
ϵ Total true strain
K^*_{Ic} Notched specimen fracture toughness
r_0 Dislocation core radius
ρ Dislocation density
P_{max} Maximum axial load
τ Shear stress
σ Normal stress
τ_0 Lattice internal frictional shear stress

Introduction

Composites with superior conductivity and high tensile strength are desired in the design of devices such as rotating electrical machineries and high field magnets. High magnetic fields of more than 1 T (about 20 000 times stronger than the earth's magnetic field) are generated by some electromagnets. Such intense fields have important applications in diagnostic medicine, superconductivity, high-energy physics, optics, and fusion engineering [*1–3*].

In order to generate a high magnetic field, an electrical current is passed through loops of wire with high conductivity. The generated magnetic field subsequently interacts with the wires of the coil and exerts a tensile load due to the Lorentz force. The material of the coil should thus be strong enough to support these forces. In the case of pulsating magnets, the fatigue properties of the coils are also important in their design consideration. Combining strength and good conductivity is an engineering and scientific challenge. What usually improves the strength of a given material, i.e., high dislocation densities, second phase particles, precipitates, solid solutions, refined grains, etc., is detrimental to the conductivity of the material.

Composite materials developed by various mechanical workings of two well-dispersed ductile phases have been found to have excellent mechanical properties [*4–6*]. Mechanical working such as rolling, drawing, and swaging of two ductile phase materials results in a structure similar to conventional fiber composites. Cu-Nb microcomposites are among those composites exhibiting high electrical conductivity as well as high strength. These composites normally contain less than 20 vol.% Nb. Due to the very limited mutual solubility of Cu and Nb, the Cu matrix remains essentially pure during the processing of the composite and maintains its high conductivity. The key to achieving high strength for Cu-Nb composites is the attainment of a submicron filamentary structure [*4–10*].

The fabrication technology of filamentary Cu-Nb composites is well established [*4–6*]. In-situ casting, powder metallurgy (P/M), and stacking of elemental components (sometimes referred to as the Levi [*4*] method) are among the various techniques for producing these composites. The initial ingots of a Cu-Nb mixture with Nb particles either in the form of dendrites in the in-situ method or particles in the P/M method are prepared and then deformed to high areal reduction [$R = A_0/A$ (initial cross section area/final cross section area)]. To fabricate high-strength composites with substantial diameter, the stacking and restacking techniques are normally used. The restacked ingot is then further deformed by either cold or hot extrusion to deform initial Nb particles to the final whisker size.

In-situ processing has been the focus of attention and the source of most information regarding the mechanical properties of this material [*7–15*]. However, most the the data are limited to the tensile properties with little or no information about the fatigue and fracture behavior of these composites. Several models have been proposed to describe the strengthening mechanism of the in-situ processed Cu-Nb composites [*10,12*]. However, these models do not explain the behavior of P/M processed composites. The most distinct difference is that for the restacked

P/M composites, strengthening reaches a saturated value in the final stages of areal reduction, but the not-restacked, in-situ Cu-Nb composites exhibit an exponential increase with increased deformation [*8,10,16*].

This paper presents our efforts in developing Cu-Nb microcomposites by powder metallurgy and our understanding of their microstructure, strengthening mechanisms, and fatigue and fracture behaviors. We believe that many properties and observations that developed during this study are significantly different from those exhibited by many cold-worked alloys. These properties and observations are discussed in this paper.

Synthesis of Cu-Nb Composites

In order to understand the effects of the initial Nb particle size and concentration on mechanical properties and electrical conductivity of Cu-Nb composites, four different powder mixtures were processed. Table 1 shows the various starting powder mixtures. The details of the fabrication processes are given in Refs *6, 17,* and *18*. Since some of the terminologies used in subsequent sections are related to the fabrication processes, the fabrication processes are described briefly.

Batches of high-purity Cu-Nb powder mixtures with oxygen content of less than 100 ppm were prepared and placed in Cu cans at tap density. Details of powder selection can be found in Refs *6, 17,* and *18*. Each batch was then pressed, sealed, evacuated, and processed by the conventional method of wire fabrication (swaging, extrusion, and wire drawing). Figure 1 provides the flow diagram of the laboratory-scale processing. Fabrication of each composite involved two steps of restacking, which produced samples with 703 sub-elements. The sub-elements used for restacking included a Cu clad, which was part of the Cu can used for preparation of each extrusion billet. Prior to each restacking, most of the Cu clad was dissolved in nitric acid. However, part of the Cu clad, which amounted to 5% of the overall volume, was left to keep the composite core intact. Wire samples were saved at each stage of processing in order to evaluate the evolution of the material microstructure and the changes in the mechanical properties. All P/M processed composites showed a drawability limit after which the wires started to break. The drawability limit corresponded to an area reduction of about 10^7 from the initial batch cross section. This is related to the final fiber size and fiber morphology and will be explained in the next section.

From processing the laboratory-scale composites it was concluded that both Cu and Nb remain ductile during the fabrication process and that a critical volume fraction of Nb was required to deform Nb particles. Sintering was essential at various stages of processing for bonding between sub-elements. Cold hydrostatic extrusion followed by wire drawing resulted in wires of high strength. For composites with 18 vol.% Nb, most of the Nb particles deformed from the onset of the deformation process. The critical volume fraction of Nb at which the solute particles became interconnected was evaluated from the model proposed by Scher and Zallen [*19*]. The critical concentration was about 15 vol.% for a random distribution of particles

TABLE 1—*Details of the powder mixtures used in the laboratory-scale Cu-Nb composites.*

Designation	Vol.% Nb	Nb Powder (REP), μm	Cu Powder (Chopped Wire), μm
A102	18	250 to 500	250 to 500
A106	18	150 to 250	250 to 500
A104	15	150 to 250	250 to 500
A105	15	250 to 500	250 to 500

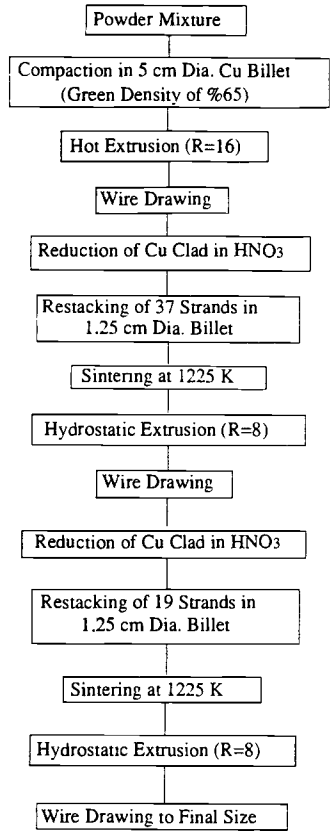

FIG. 1—*Process flow diagram of the laboratory-scale P/M processing of Cu-Nb composites.*

regardless of their shapes. Hence, it appeared that for the 18 vol.% concentrations, interconnectivity of Nb particles was obtained.

Since the laboratory-scale composite resulted in wires with very small diameters at the final stage of processing that were not suitable for fatigue and fracture studies, a larger scale composite with more than 1.5×10^4 sub-elements was manufactured. This resulted in a wire with 3-mm diameter at its drawability limit. Samples of the larger scale composite were also saved at various stages of the processing. Figure 2 shows the process flow diagram of the larger scale composite, called S3 composite. Figure 3 shows the transverse cross section of a laboratory-scale composite with 703 sub-elements.

Analyses of the Cu-Nb Composite Microstructure at Different Stages of Processing

Extensive deformation produced by extrusion and wire drawing causes the grains of a metal to assume a preferred orientation (texturing). Metals with bcc structure such as Nb are known to develop a $\langle 110 \rangle$ texture along the direction of the maximum principal strain [*10,20*]. The model illustrated in Fig. 4 depicts a bcc crystal with a tensile load in the $[\bar{1}10]$ direction. There are four possible slip directions, namely the $\langle 111 \rangle$. Only the $[\bar{1}11]$ and $[\bar{1}1\bar{1}]$ directions accommodate strain parallel to the overall elongation (z axis), and therefore they are favorable slip directions. The [111] and $[11\bar{1}]$ slip directions allow strains along x and y axes. If these two

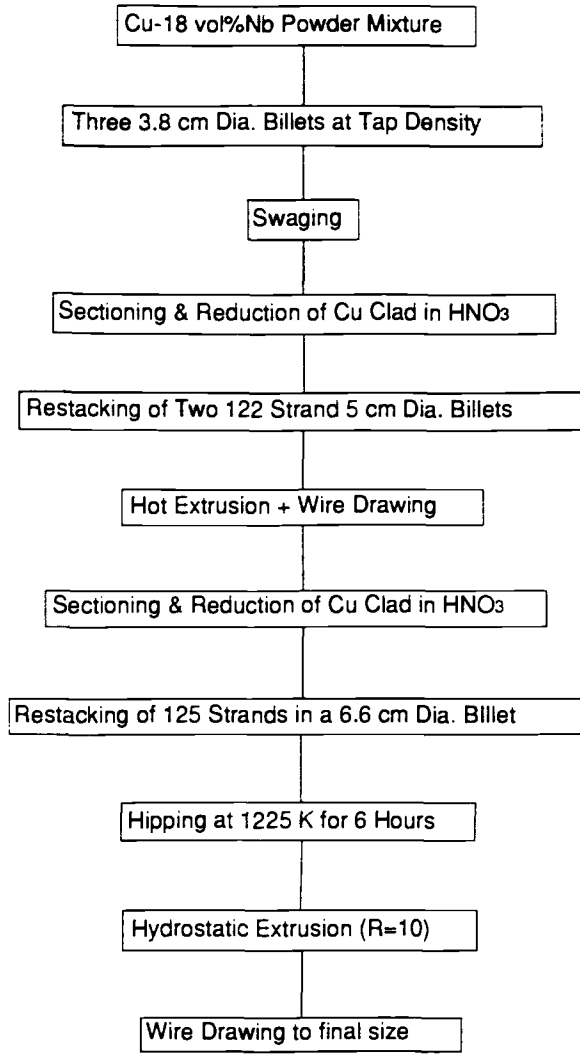

FIG. 2—*Process flow diagram of the S3 composite.*

directions are inactive, a two-dimensional flow proceeds and $\epsilon_y = 0$. However, for axisymmetric deformation they must be in operation. Hosford, in his original work [*20*], provided a comprehensive explanation of the deformation pattern for bcc metals. He showed that the axially symmetric flow requires 50% more slip than that of the plane strain and that deformation in the latter mode is more favorable. Consequently, with strain being suppressed in one of the principal directions, the crystal tends to attain a ribbon-like cross section. However, the thickness-to-width ratio of the Nb filaments does not increase indefinitely; beyond a ratio of 20 to 30, axially symmetric flow prevails. This is due to the work hardening of a slip system in plane-strain deformation which requires more work than an axially symmetric flow.

Study of the microstructure of the P/M processed Cu-Nb composites led to a number of important findings with implications with regard to the fabrication process and the strengthening

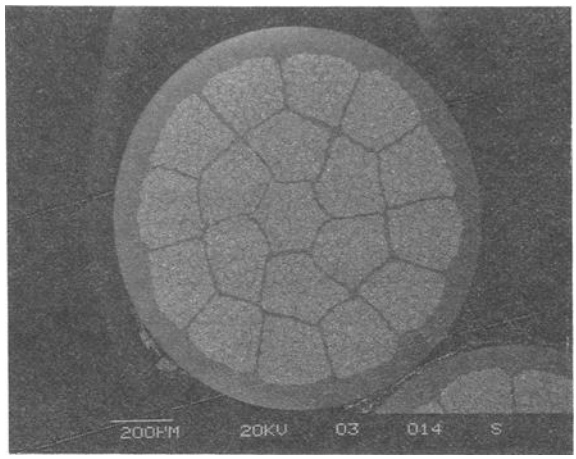

FIG. 3—*Transverse cross section of a laboratory-scale composite with 703 sub-elements.*

mechanism. Nb powder particles are single crystals which, after mixing with Cu and subsequent compaction, assume random orientations with respect to the loading direction of the forming process. Due to the random nature of mixing, the required shear stress to deform individual Nb inclusions varies a great deal, and as a result some do not deform until a later stage of the processing. Therefore, in the early stage of the fabrication process, a significant range of the Nb fiber thicknesses exists across the composite. However, as deformation of Nb particles proceeds from a plane strain to an axisymmetric mode, the fibers become more uniform. This

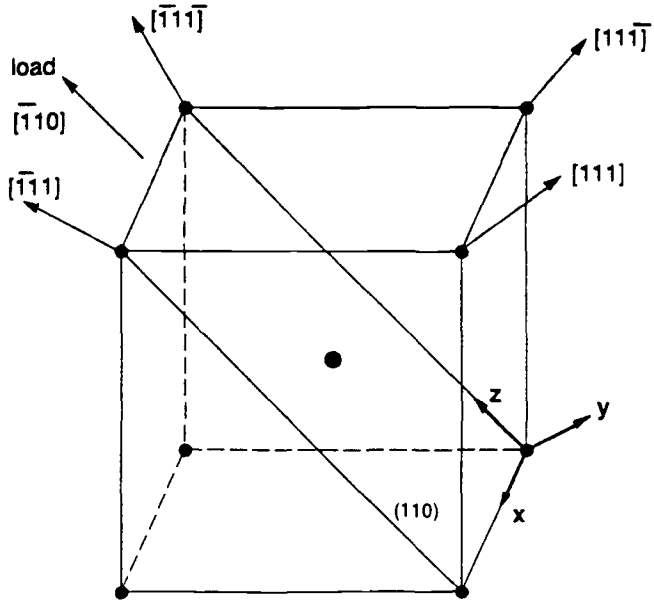

FIG. 4—*Deformation of a bcc crystal structure with a tensile load parallel to the [110] direction.*

is due to the faster reduction of the thickness of fibers in the plane strain deformation mode than in the axisymmetric mode. Onset of the filament formation is influenced by the Nb content in the composite. Examination of the cross sections of samples after hot extrusion, which were fabricated by using the same starting powder but different Nb content, demonstrated that there was a critical Nb content that resulted in deformation of all the Nb particles. For lower concentrations, the Nb particles simply floated in the Cu matrix. This behavior was explained by the percolation effect, which addresses the critical concentration necessary for the inner connectivity of the Nb particles [*6*]. Composites with 18 vol.% Nb exhibited pronounced filament formation from the onset of the process, where samples with 15 vol.% Nb showed many underformed particles at an earlier stage of the deformation. Figure 5 shows the microstructure of an A102 composite (see Table 1) after an areal reduction of $R = 100$.

Two different methods were employed to measure the Nb filament size of various composites in the final stage of processing: (1) Sections of composites at their drawability limit were selected and Cu matrices were dissolved in HNO_3. The exposed fibers were then examined under a scanning electron microscope (SEM). Figure 6 shows samples of Nb fibers extracted from A102 composite after an areal reduction of $R = 1.2 \times 10^7$. Figure 6 shows that the width and thickness of the fibers are in the order of 1 μm and 10 nm, respectively. (2) A more accurate method of measuring fiber sizes was performed by preparing thin sections of the S3 composite before, on, and after the drawability limit for transmission electron microscopy (TEM) studies. (Further deformation beyond drawability limit is possible by flow of the Cu matrix between broken Nb fibers without any change to the Nb fiber size). Details of specimen preparation and results of TEM studies can be found in Ref *6*. TEM studies revealed that once the drawability limit is reached, the overall deformation proceeds without significant change in the fiber dimensions. TEM studies showed that the thickness of the fibers were in the range of 5 to 10 nm with an aspect ratio of 20 to 30.

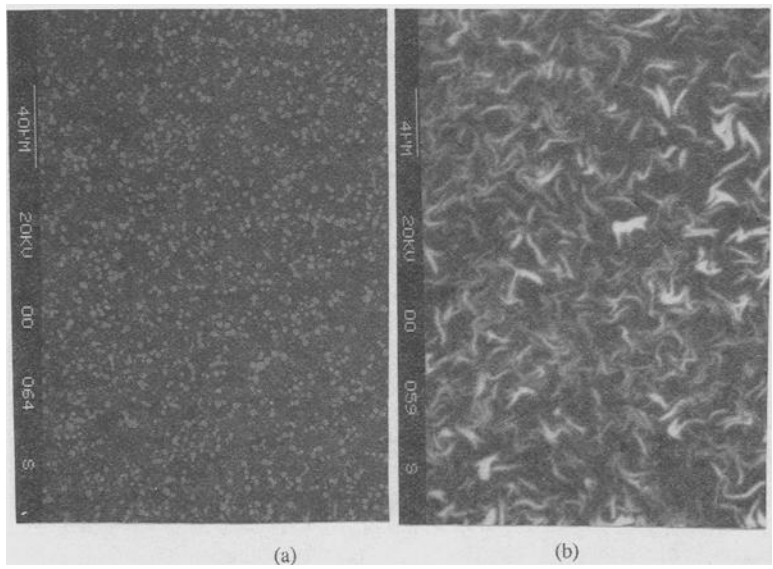

FIG. 5—*Photograph of a transverse cross section of an A102 composite:* (a) *before any deformation,* (b) *after an areal reduction of* R = *100.*

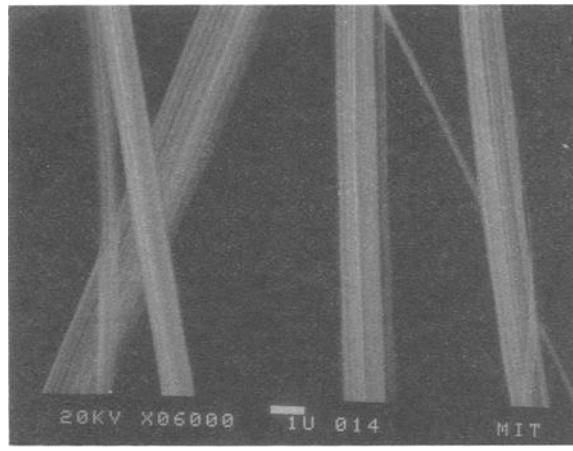

FIG. 6—*Nb fibers extracted from the A102 composite after an areal reduction of* R = 1.2×10^7.

Tensile Behavior of Cu-Nb Composites

ASTM Practice for Constant Amplitude Axial Fatigue Tests of Metallic Materials (E 466-82) was used to measure the tensile properties of the S3 composites [*21*]. However, the laboratory-scale composites were too thin for machining. For these composites, wires with a diameter less than 0.5 mm were mounted on the spool setup, and larger diameter wires were soldered to brass grips [*18*]. None of our specimens failed at the solder junction. Thus, soldering neither softened our composite nor produced any significant stress concentration. Tension tests were performed both under load and displacement control. For most of the laboratory-scale processed composites, only their ultimate tensile strengths (UTSs) and ductilities were evaluated. The yield strengths were also evaluated for a few samples by using an extensometer and an offset plastic strain of 0.2%. Figure 7 shows the ultimate tensile strength of various composites and similarly processed Cu powders versus areal reduction $R = A_0/A$, where A_0 is the composite area after the last sintering process. The results show that the strength of these composites approaches a plateau coincident with the attainment of Nb fiber thickness of 5 to 10 nm. The results show that the initial Nb particle size has little effect on the final ultimate tensile strength of these composites. It is also noted that for the same areal reduction, composites with 20% more Nb (15 versus 18 vol.% Nb in the overall composites) result in composites 50% higher in UTS. This comparison is misleading since fibers in these two composites were not of the same size after final sintering due to the delay in the filament formation at earlier stages. Extensive metallographic studies showed that the fiber size for composites with the same initial Nb powder size but different volume fraction are almost four times smaller for composites with 18 vol.% Nb than those with 15 vol.% Nb at a nominal R. Considering this size difference in comparing the UTS of composites with different volume fraction (i.e., comparison of the UTS of an A104 composite at $R = 2220$ and an A106 composite at $R = 670$) shows a difference of about 15%, which is in fair agreement with the 20% higher Nb concentration. The remaining difference may be explained by various strengthening mechanisms explained later. The same arguments can be extended to the different initial powder sizes.

Tensile properties of the S3 composite at various stages of the process (after the last sintering) were evaluated from specimens tested under both load (45 N/s) and strain (10^{-4} s^{-1}) controlled conditions. Both the yield strength and the ultimate tensile strength of this composite reached a saturation value after a certain amount of areal reduction similar to the laboratory-processed

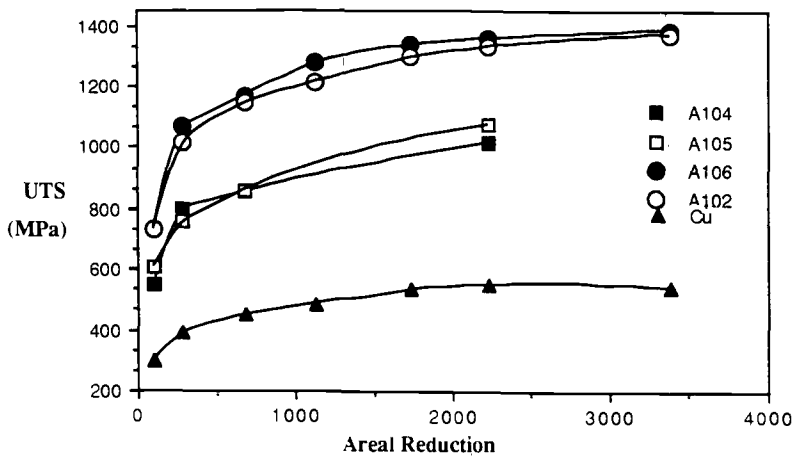

FIG. 7—*UTS versus areal reduction (after the last sintering) for various laboratory-scale P/M processed composites (Table 1).*

composites. The true strain at fracture (ϵ_f) of the S3 composite at its drawability limit was calculated from the measurements of the final gage diameter (D) and initial diameter (D_0) of specimens tested under strain control. Profound necking was observed for this composite. The true strain ϵ_f at fracture was found to be 0.4. This high value of ϵ_f demonstrates the excellent ductility of the S3 composite. Since Nb fibers for this composite were at their drawability limit, necking can be assumed to be a result of fiber fracture and the subsequent flow of the matrix material between broken fibers. This equally plausible mechanism can be due to interaction of dislocations in the Cu matrix with Nb fibers. This may lead to fiber fracture and subsequent flow of the matrix between broken fibers. However, no microcracks were observed on specimens sectioned longitudinally that were polished and studied under the SEM. The UTS, 0.2% offset yield stress (σ_y), and the elastic modules for this composite were obtained from the load-controlled experiments. The average value of these properties from three experiments with a deviation of less than 2% from the mean values were: E = 113 GPa; σ_y = 820 MPa; and UTS = 1035 MPa.

Fracture surfaces of the tension specimens were studied under a scanning electron microscope. For composites with fully deformed Nb fibers, the fracture surface was 45° to the tensile load and was an apparent shear fracture (Fig. 8). A closer examination of the fracture surface revealed that failure was initiated by the fracture of Nb filaments in one of the original subelements. The microcrack then propagated in the matrix material along the deformation bands (45°), resulting to a peak and matching cavity on the fracture surface. The final failure was again along one of the dominant deformation bands leading to an overall slant fracture surface appearance (Fig. 9). Since Nb fibers for these composites can be assumed to be brittle, they provide little resistance to the crack propagation. However, for composites with not fully deformed Nb fibers, these fibers provide bridges between crack surfaces. Fracture surfaces of these composites had a cup-cone appearance, and specimen size did not have any effect on the fracture behavior (Fig. 10).

Various strengthening mechanisms have been proposed to describe the yield strength of the Cu-Nb microcomposite with the processing deformation. Funkenbusch and Courtney [*15*] adhere to a substructual strengthening mechanism, while Spitzig et al. [*7,22*] adhere to an interphase barrier strengthening model. Both models address the sharp increase in the strength of the Cu-Nb composites with increasing deformation. However, the strength of P/M processed

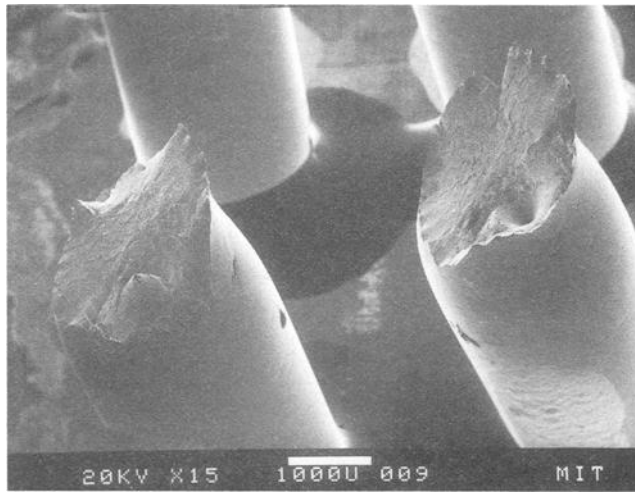

FIG. 8—*Strain-controlled fracture ends of the 3-mm-diameter S3 composites in a tension test.*

restacked composites reaches a saturation value after a certain amount of deformation. The most notable difference between the restacked and not-restacked composites is that, after restacking, the billet should be considered as a continuous filament composite where the filament areal reduction occurs throughout the process. This is not the case for the non-restacked in-situ processed composites. Some of the Nb dendrites may be so small that they may flow in the matrix and may have delayed filament formation.

The saturation of the yield strength of the P/M processed restacked composites with the deformation is related to the work hardening of the Cu matrix due to the increase in the dislocation density, strength of the fibers, and the interaction of the dislocations with the filament/matrix boundaries [*6*]. These contributions are described briefly.

The strength of the cold-worked single crystal metals are related to an increase in dislocation density [*23–25*]. Measurements over a wide range of systems show that the average dislocation density correlates with the flow shear stress τ according to

$$\tau = \tau_0 + \beta G b \rho^{1/2} \tag{1}$$

where τ_0 is the shear stress needed to move a dislocation in the absence of other dislocations, and β is a numerical constant which varies from 0.2 to 0.5 for different fcc metals. G is the shear modulus, b is Burger's vector, and ρ is the dislocation density. The strength of a pure Cu wire is shown (Fig. 7) to saturate with increased deformation. This is as a result of dynamic recovery, i.e., at a certain stage, the dislocation multiplication and annihilation are balanced. Furthermore, in the saturation region of the flow curve, the stresses are high enough so that dislocations can take part in processes that are suppressed at lower stresses. Cross slip is believed to be the main process which reduces the internal strain field.

The upper bound of the dislocation density in the Cu matrix can be estimated by substituting $\tau = \sigma_y/2 = 235$ MPa, $G = 48$ MPa, $\beta = 0.2$, and $b = 0.26 \times 10^{-9}$ m in Eq 1. Since the lattice friction (τ_0) for Cu is small [*26*], its effect on dislocation density calculation is neglected. This analysis yielded a dislocation density of $\rho = 8.8 \times 10^{11}$ cm^{-2}.

Dislocation density in the Cu matrix was also estimated by preparing samples of the S3 composite for the transmission electron microscopy (TEM) studies. Since during wire drawing the fcc Cu grains assume a ⟨100⟩ or ⟨111⟩ texture parallel to the wire axis, the free surfaces of

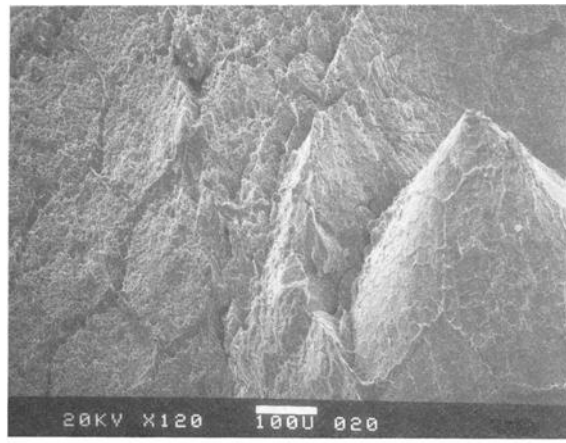

(a)

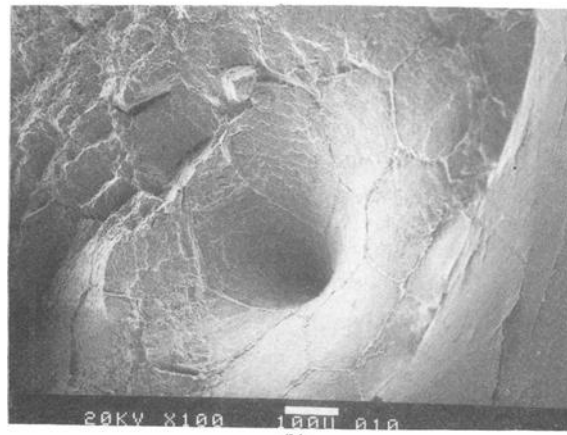

(b)

FIG. 9—*Details of the fracture surface of the 3-mm-diameter S3 composite showing failure initiation by fracture of Nb filaments within one of the original sub-elements, resulting in a peak and cavity.*

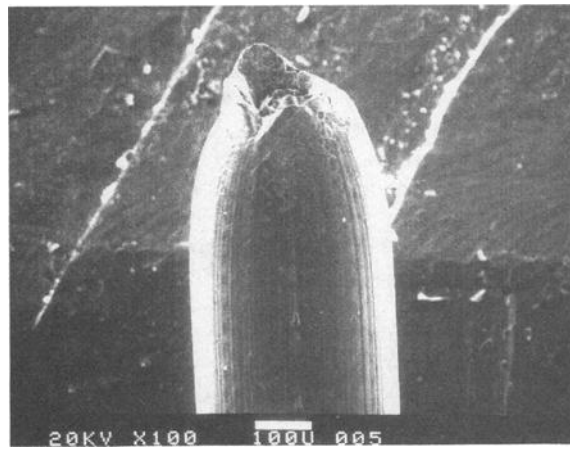

FIG. 10—*Fracture end of a laboratory-scale Cu-Nb composite with fibers not fully deformed.*

the TEM samples intersect the grains on either {011} or {111} planes. With {111} being the closest packed plane, it was expected that some of the grains would be oriented suitably for observation of dislocation lines. At first glance, examination of the TEM micrographs might suggest that the Cu matrix is for the most part dislocation free, as has been concluded by other researchers [27]. Nevertheless, it should be pointed out that samples become electron transparent when their thickness is in the range of a few tens of nanometers. This dimension is about the same as the average spacing of dislocation in a heavily deformed crystal (33 nm for dislocation density of 10^{11}). Hence, for the Cu grains in between the filaments whose transverse dimensions are also smaller than the above value, the observation of dislocations is expected to be infrequent and a matter of statistical probability. Dislocations were, in fact, observed in these regions for all composites regardless of the overall areal reduction. Examples of dislocations are encircled in Fig. 11. Therefore, strain hardening of the Cu matrix is modeled as a polycrystalline medium, and its contribution to the overall strength of the composite entails the superposition of the Cu data on other effects.

Nb fibers produce obstacles in the path of dislocations in the Cu matrix. This results in an increase in the required shear stress to move dislocations. This is similar to the dispersion hardening mechanisms in alloys. Kelly [28] has shown that the plate-like dispersions, whose cross sections are rectangular or elliptical, are more effective than equiaxed particles in the hardening of a matrix. He derived the shear stress required for moving dislocations through plate-like dispersions. His derivations are a modification of Orwan's dispersion hardening mechanism [29] and are suitable for our composite since Nb filaments have rectangular cross sections. The shear stress required to move dislocations through plate-like dispersions are stated as

$$\tau_{(d)} = B \frac{C}{D\left[1 - \frac{\pi}{2A} C\right]} \ln\left[\frac{2D}{\pi r_0}\right] \tag{2}$$

and

$$C = \left[\sqrt{V_f A} + \left(\frac{2}{\pi} - \frac{\pi}{2A}\right) V_f A\right] \tag{3}$$

Here, $B = 0.85\, Gb/2\pi(1 - \upsilon)^2$, $A = D/t$, D and t are filament width and thickness, respectively, r_0 is dislocation core radius assumed to be 1 nm [30], V_f is volume fraction of inclusions, and υ is Poisson's ratio. Equation 2 shows that the shear stress is an inverse function of filament width. Therefore, the strength of the composite increases with areal reduction. Using the typical aspect ratio of $A = 30$ for Nb filaments, the shear stress required to move dislocations in the Cu matrix as a function of the deformation can be calculated.

The contribution of the fiber strength (size) to the strength of the composite at different stages of the deformation can be modeled as a Hall-Petch relation [23]. While the Hall-Petch relation has been derived to reflect the effect of grain size in the strengthening of alloys, its applications to small grains must be made with some caution. Hall-Petch is not valid for very small grains since its derivation was based on large dislocation pileups of more than 50 dislocations. A more general model proposed by Li [31] avoids the description of the stresses at grain boundaries and instead concentrates on the influence of grain size on the dislocation density and, hence, on the flow stress. An equation identical to Eq 1 is suggested for the flow stress. Assuming that the distance between dislocations (L) is equal to the average filament thickness D, the dislocation density is estimated as

$$L = D \approx \rho^{-1/2} \tag{4}$$

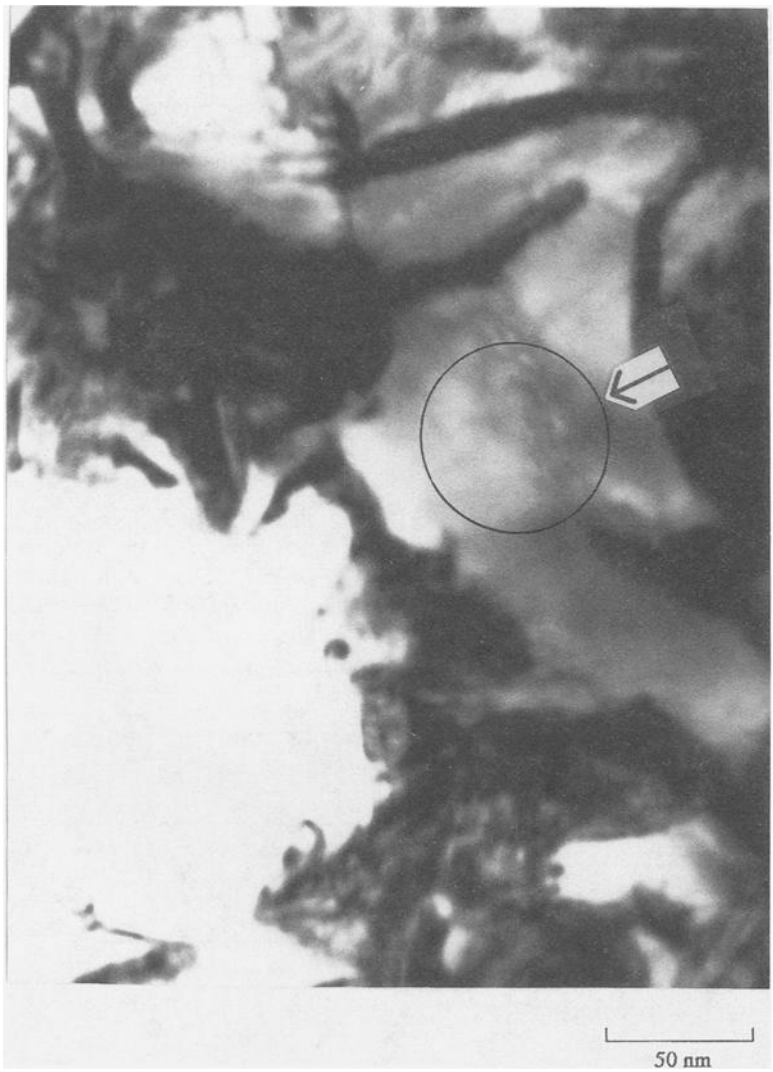

FIG. 11—*TEM micrograph of the transverse cross section of the S3 composite showing dislocations in the Cu matrix.*

substituting in Eq 1, this results in

$$\tau_{Nb} = \tau_0 + \alpha GbD^{-1} \tag{5}$$

where $\alpha = 0.5 \pm 0.1$ for bcc metals. Since τ_0 is small compared to the second term in Eq 5, the Nb flow stress is taken as:

$$\tau_{Nb} = \alpha GbD^{-1} \tag{6}$$

Substituting the Nb thickness of 5 nm observed at drawability limit results in a fiber strength of [$\tau_{Nb} = 0.6 \times (37.5 \times 10^9$ Pa) $(0.285 \times 10^{-9}$ m) $(2 \times 10^8$ m$^{-1})$] 1.28 GPa. This value is close to the theoretical shear strength of Nb [*9*], $\tau_{th} = G/30$.

Various strengthening models outlined above were incorporated in a rule of mixture to predict the yield strength of an A102 composite as a function of the processing deformation. The laboratory-scale A102 composite started with a Cu-18 vol.%. Having defined the strengthening of the Cu matrix as τ_d (dislocation barrier), its contribution to the composite can be expressed by the rule of mixture, which is $0.82\tau_d$. However, due to restacking, the volume fraction of Cu changes and thus is τ_d. This requires a trial and error analyses to update τ_d. A reasonable estimate is suggested as V_{Cu} $(0.82)\tau_d$, where τ_d is evaluated based on the initial Cu volume fraction. After two steps of restacking, the overall concentration of Nb was about 15 vol.% (V_{Nb} = 0.15 and V_{Cu} = 0.85). The yield strength of the composite τ_{com} is expressed as

$$\tau_{com} = V_{Nb}\tau_{Nb} + V_{Cu}(0.82)(\tau_d)_{Cu} + V_{Cu}(\tau_i)_{Cu} \tag{7}$$

At each areal reduction, the value of τ_{Nb} was calculated from Eq 6, τ_d from Eqs 2 and 3, and values for $(\tau_i)_{Cu}$ were obtained from the P/M processed pure cold-worked Cu data [*6*]. Figure 12 shows that the theoretical results agree reasonably well with the experimental data.

Notched Specimen Fracture Toughness

Fracture toughness of the S3 composite wire at its drawability limit was evaluated by preparing three circumferentially notched specimens. The radius at the tip of the notch was less than 18 μm. Details of the specimen preparation can be found in Ref *18*. The specimens were pulled slowly (45 N/s) to failure, and maximum loads at fracture, P_{max}, were measured. The apparent fracture toughness, K^*_{IC}, was evaluated according to the following relation [*23*]

$$K^*_{IC} = \frac{P_{max}}{D^{3/2}}\left[1.72\frac{(D)}{d} - 1.27\right] \tag{8}$$

Here, D is the wire diameter (D = 3 mm), and d is the diameter of the notched cross section (d = 2.7 mm). The results of three measurements were within 0.5% of the average value of K^*_{IC} = 23.4 MPa$\sqrt{m}$.

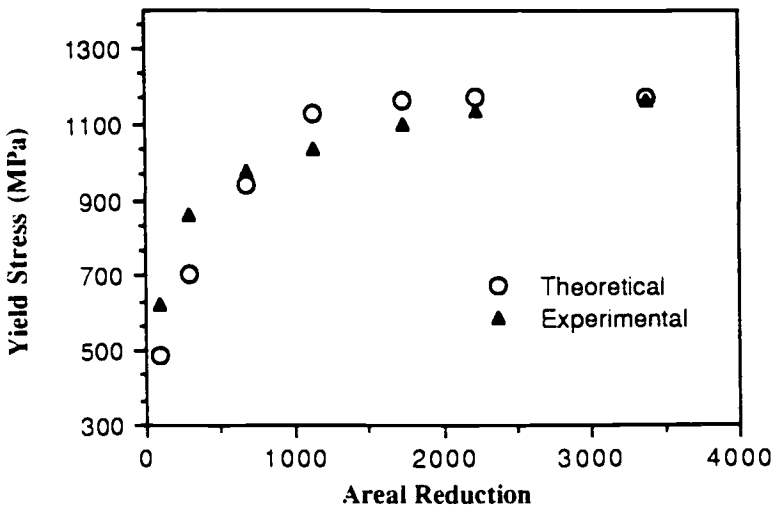

FIG. 12—*Yield stress versus areal reduction (after the last sintering) of an A102 composite compared with results of the theoretical model.*

The ratio of sharp notch strength to the 0.2% offset tensile yield strength, NSR, is of significance as a comparative index of plane-strain fracture toughness. The notch strength is defined as the maximum load at fracture/notch cross section. If NSR is greater than 1.3, the apparent fracture toughness will not be equal to the plane-strain fracture toughness (ASTM Method for Sharp Notch Tension Testing with Cylindrical Specimens (E 602). For our S3 composite, the notch strength and yield strength were 1140 and 820 MPa, respectively, resulting in an NSR value of 1.39. Since NSR is greater than 1.3, larger specimens are needed to measure plane-strain fracture toughness. Since large samples were not available, the value of 23.4 MPa$\sqrt{m}$, which is a little higher than the actual plane strain fracture toughness, can be taken as a first order approximation. This is used in the analysis of the fatigue crack growth described in the next section.

Fatigue of the S3 Composite

Fatigue specimens were machined from the S3 composite wire according to ASTM Practice for Constant Amplitude Axial Fatigue Tests of Metallic Materials (E 466-82) [*21*]. The outer Cu cladding in the reduced diameter area was removed during machining and the composite core exposed. The machined surfaces were polished gradually and finished with 1-μm alumina polishing grit to minimize the possibility of surface defects.

Since, in magnet technology, solenoid wires are subjected to very high pulsating tensile loads, our fatigue experiments were conducted under load control at an R ratio of 0.1 ($R = \sigma_{max}/\sigma_{min}$) and a frequency of 3 to 5 Hz. An extensometer was used to monitor the specimen deformation during cyclic loading. For specimens subjected to the maximum stress exceeding the yield strength of the composite (σ_y = 820 MPa), the first quarter cycle produced plastic deformation. The subsequent unloading and cyclic loading resulted in a very small hysteresis loop. Figure 13 shows a typical stress-strain diagram of an S3 composite specimen during fatigue experiments. The hysteresis loop was stable during the fatigue experiment, and no appreciable specimen elongation (ratcheting) was observed before specimen failure. This behavior is different from those observed for cold-worked copper. Cold-worked copper generally shows softening under cyclic strain-controlled experiments and creeping (ratcheting or cyclic strain-induced creep) under cyclic stress-controlled experiments. However, despite significant cold works during our processing of Cu-Nb microcomposite, the hysteresis loop under cyclic-controlled stress tests was stable, and no cyclic strain-induced creep was observed. This may be justified by considering that the behavior of ultra-thin cold-worked copper is different from copper with significantly higher dimensions. Cyclic softening and hardening occur when dislocations rearrange themselves in a more stable configuration. If cyclic straining causes coarsening of preexisting cell structures, then softening will occur. If the cell structure gets finer, then cyclic straining results in a hardening process [*25*]. Because our Cu matrix is confined between Nb filaments and is considered very thin, rearrangement of dislocations can be extremely difficult. Furthermore, Nb filaments may have contributed to stabilization of cyclic deformation. If we also accept the arguments by Pelton et al. [*27*] that the Cu matrix is for the most part dislocation free (this is not observed, in the current research, as explained earlier), there is no dislocation rearrangement. This may further support that the behavior of ultra thin Cu matrix is different. Deviations from perfect elasticity are caused by a number of different physical phenomena: dependence of the strain on temperature, microplasticity, grain boundary sliding, and other similar effects that caused the strain to be a multivalued function of the stress.

Since the area of the hysteresis loops was very small (the plastic strain range of a typical hysteresis loop was less than 0.01%) and cyclic frequency was low, the energy lost was assumed to be zero, and the entire fatigue experiments were considered to be under the elastic condition. Thus, these experiments may be classified as high-cycle-fatigue experiments.

Under high-cycle-fatigue conditions, the stress amplitude is below the yield strength of the

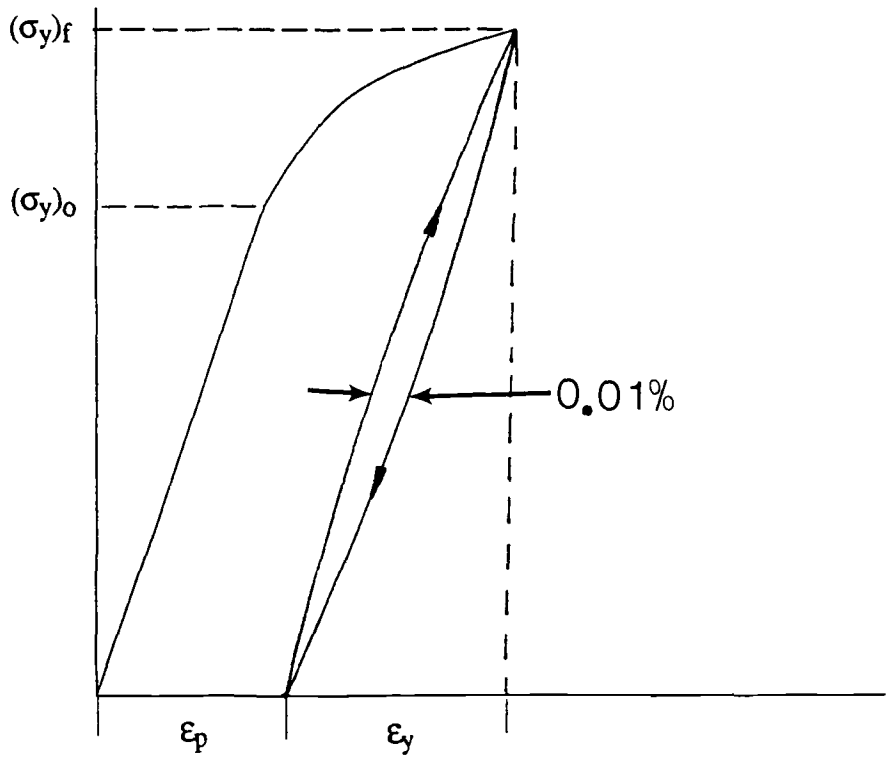

FIG. 13—*Schematic diagram of a typical stress-strain diagram of the S3 composite after initial loading beyond the yield strength and subsequent cyclic loading showing a very small hysteresis loop during cyclic loading.*

material, so that the strain is normally elastic. If the strain were literally purely elastic, fatigue could not result because elastic straining is by definition a reversible process [*32*]. However, this difficulty is associated with the oversimplification introduced by the concept of a yield strength and the assumption of purely elastic deformation below this yield strength. All metals undergo a minor amount of plastic strain even at low stresses. This is called microstrain because at stresses well below the yield strength the magnitude of the plastic strain is small compared to the elastic strains.

Two specimens each were fatigued at various stress levels, and the average fatigue lives were used to construct the S-N curve for this composite (Fig. 14). The deviations from the average life at each stress level was less than 15% so that these data may be used to predict the fatigue life of a magnet constructed from this material.

Fatigue damage mechanisms were studied both by an optical and a scanning electron microscope (SEM). Visible cracks were only observed at some point in the final 10% of fatigue life. For example, in a specimen cycled at 725 MPa (σ_{max} = 725 MPa), no visible crack was observed after 15 000 cycles. However, at 16 000 cycles, many circumferential cracks appeared on the specimen surface. The largest crack at this stage was 4 mm. The specimen failed at about 17 000 cycles. In order to understand the depth of the crack growth at 16 000 cycles, another specimen was fatigued at the same stress levels, and the experiment was halted after 16 000 cycles. The specimen was then sectioned longitudinally and polished. The maximum crack

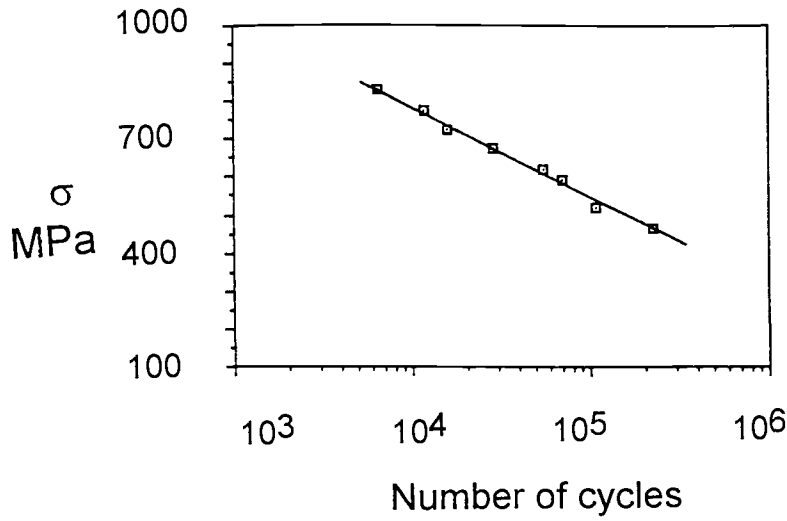

FIG. 14—*Fatigue S-N curve for the P/M processed Cu-18 vol.% Nb composite with a UTS of 1035 MPa.*

depth was found to be 0.1 mm. These results show that the fatigue life of these composites are controlled by crack initiation (Stage 1). Once a circumferential crack is generated, it propagates rapidly into the composite, leading to composite failure.

The mechanism of crack initiation was studied by polishing the surfaces of many specimens before and after failure. The crack was found to be initiated by the PSB mechanism at $\simeq 45°$ to the specimen axis in the Cu boundaries between sub-elements (the Cu boundaries are residual Cu material left from the initial Cu can used to contain the initial powder mixture and the Cu can material left after the second restacking). As one can surmise, the thickness of the latter is greater than the former. Figure 15 shows typical persistent slip band microcracks observed in Cu regions between the Cu-Nb sub-elements. A similar crack initiation mechanism was observed by Polak et al. [*33–34*] in annealed Cu. Microcracks in the Cu boundaries were then apparently linked together rapidly through the Cu-Nb sub-elements and formed long circumferential cracks. Figure 16 shows a typical linkage of the microcracks through Cu-Nb sub-elements.

The radial crack propagation mechanisms were also studied. We believe radial cracks propagate through sub-elements quite readily. However, these cracks get arrested at the Cu boundaries. We believe that the crack arrest mechanism is by crack tip blunting rather than the delamination mechanism generally observed in other composites. The crack then propagates through the Cu boundaries by a mechanism of reversed slip [*35*]. This mechanism develops a typical pattern of ripples, called fatigue striations. Examination of a crack tip in the Cu boundary (Fig. 17) reveals a similar fatigue crack growth mechanism.

The final fracture surfaces of the fatigued specimens were examined under a scanning electron microscope. Figure 18 shows an example of the fatigue/fracture surface of an S3 composite subjected to cyclic loading of $\sigma_{max} = 725$ MPa and $R = 0.1$. The fracture surface shows a radial crack growth region followed by a 45° shear fracture surface. The ratio of the radial crack growth region to the overall composite area is equal to $(1 - \sigma_{max}/\text{UTS})$. This indicates that the final fracture was not controlled by the fracture toughness but rather by the residual strength of the unbroken segment of the composite. This was further confirmed by evaluating

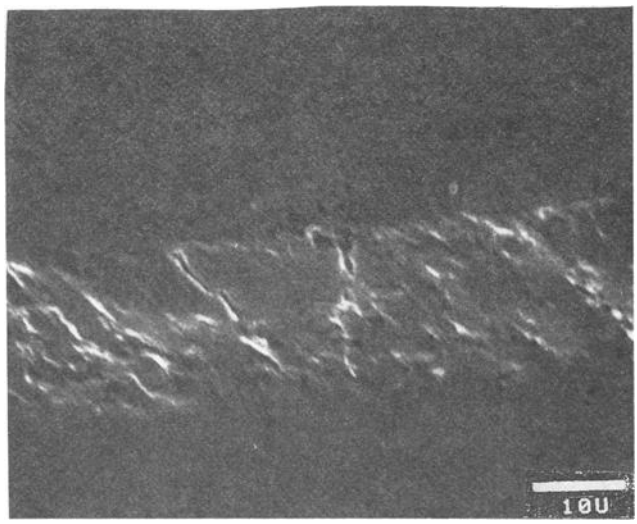

FIG. 15—*Typical persistent slip band microcracks observed in the Cu region between the Cu-Nb sub-elements.*

the critical crack length (a_c) at σ_{max} = 725 MPa, using K^*_{IC} = 23.4 MPa$\sqrt{m}$. The critical crack length was estimated from

$$a_c = \frac{K^{*2}_{IC}}{\pi \bar{\alpha}^2 \sigma_{max}} \tag{9}$$

where $\bar{\alpha}$ is the geometry factor. For an edge crack in a round bar, $\bar{\alpha}$ was taken to be 1.12 [*36*]. The critical crack length was then found to be 0.26 mm, which is three times smaller than the actual crack depth measured before unstable shear fracture. These results may further dem-

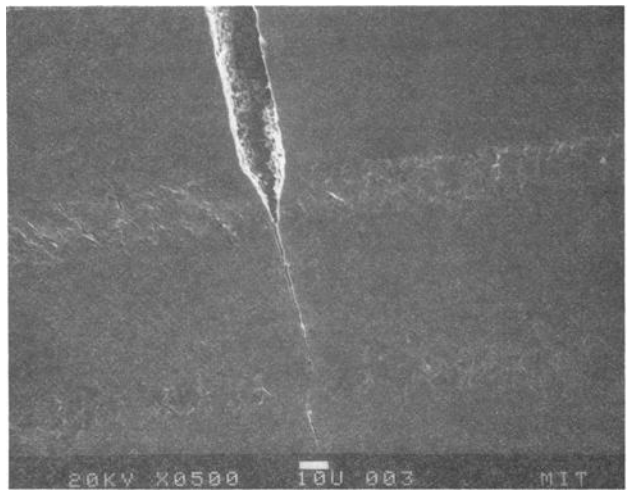

FIG. 16—*Linkage of PSB microcracks across the Cu-Nb sub-elements.*

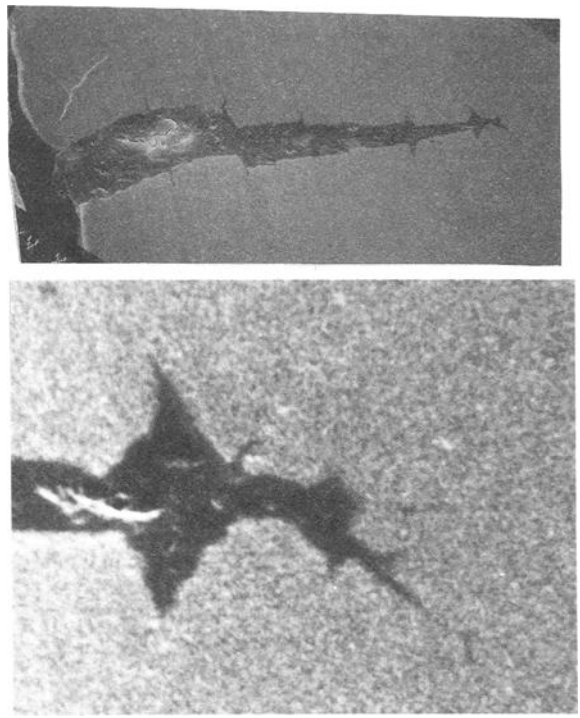

FIG. 17—*Radial crack propagation in the S3 composite:* (a) *radial crack path over several sub-elements;* (b) *crack growth mechanism by the reversed slip mechanism in the Cu boundaries.*

onstrate that unstable crack growth is prevented by the Cu regions between sub-elements. These regions act as crack arresters by blunting the crack tip. The final fracture is due to a tensile overload.

Conclusions

In-situ processing is a well-established technique for fabrication of composites with aligned filaments from two-phase ductile materials. However, in order to obtain a uniform distribution of the second-phase particles (subsequent filaments in the matrix), the initial ingot containing these materials must be cooled uniformly from the liquid state. This can be a difficult process, and segregations of the second-phase material may happen during the cooling process. The P/M process is an alternative technique of producing these composites that overcomes that difficulty.

Cu-Nb microcomposites were successfully prepared by the P/M technique. High-conductivity and high-strength properties of these composites make them suitable in applications where high conductivity and high strength are desired. Effects of the initial Nb particle size and volume fraction on the evolution of the material microstructure and tensile properties were investigated. A critical volume fraction of Nb (between 15 to 18%) was required in order to obtain inner connectivity between particles. This volume fraction was independent of the initial Nb particle size. The Nb particles in the composites with 18 vol.% Nb deformed to the filament's shape from the onset of the processing.

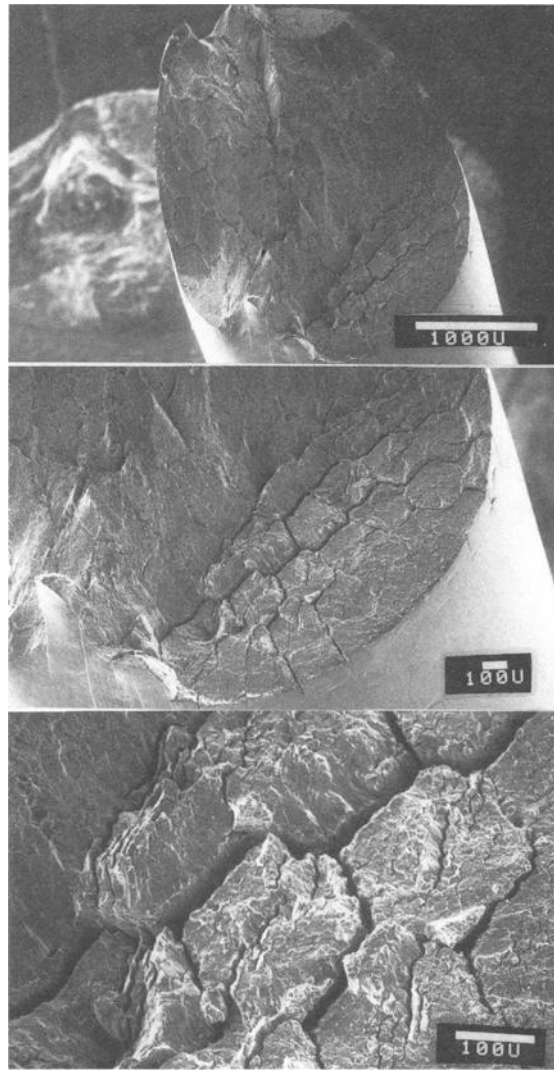

FIG. 18—*Overall fatigue/fracture surface of an S3 composite showing radial fatigue crack growth region and final shear failure due to the tensile overload.*

A model incorporating matrix work hardening, fiber strength, and dispersion-type hardening was developed to predict the yield strength of the composite with the processing deformation. The model predicts the yield strength of the composite during processing deformation reasonably well. The maximum strength for the composites corresponded to the attainment of a minimum Nb fiber thickness of 5 to 10 nm. For composites with fibers in this range, the monotonic tensile failure was of a shear-type failure. However, for composites without fully deformed Nb fibers, the fracture surface had a cup and cone appearance.

Fatigue properties of composites with 18 vol.% Nb and fully deformed fibers (Nb thickness of 5 to 10 nm) were studied. The mechanism of the crack initiation was found to be by formation

of slip bands in the Cu boundaries between sub-elements, which leads to development of long circumferential cracks. Fatigue life in Stage II (crack propagation) constituted only 5 to 10% of the total fatigue life. The radial crack growth rate in the composite sub-elements was quite fast. However, the radial crack growth was periodically halted by the ductile Cu between sub-elements. The radial crack subsequently propagated in this region by the reversed slip mechanism.

The fracture ends of all fatigue samples showed two distinct regions, a surface perpendicular to the loading direction, and a surface showing features of shear fracture. For each experiment, the ratio of the sheared area to the overall area was equal to the ratio of the maximum stress to the UTS. This result indicates that final fracture occurs by tensile overload rather than by attainment of a critical crack length.

References

[1] Isaacs, E. D. and Heiman, D., "Fiber-Optics for Roman Scattering at Low Temperature and High-Magnetic Fields," *Review of Scientific Instruments,* Vol. 58, No. 9, 1987, pp. 1672–1677.

[2] Zientara, G. P. and Neuringer, L. J., "Medical Imaging for the 21st Century," *Perspectives in Computing,* Vol. 8, 1988, pp. 14–24.

[3] Lewis, B. A., Harbison, G. S., Herzfield, J., and Griffen, R. G., "NMR Structural Analysis of a Membrane Protein: Bacteriorhodopsin Peptide Backbone Orientation and Motion," *Biochemistry,* Vol. 24, 1985, pp. 4671–4679.

[4] Levi, P. V., "Permanent Magnets Obtained by Drawing Compacts of Parallel Iron Wires," *Journal of Applied Physics,* Vol. 31, 1960, pp. 1469–1471.

[5] Funkenbusch, P. D., Lee, J. K., and Courtney, T. H., "Ductile Two-Phase Alloys: Prediction of Strength at High-Strains," *Metallurgical Transactions A,* Vol. 18A, 1987, pp. 1249–1256.

[6] Pourrahimi, S., Nayeb-Hashemi, H., and Foner, S., "Strength and Microstructure of Powder Metallurgy Processed Restacked Cu-Nb Microcomposites," *Metallurgical Transactions A,* Vol. 23A, 1992, pp. 573–586.

[7] Spitzig, W. A., Pelton, A. R., and Laabs, F. C., "Characterization of the Strength and Microstructure of Heavily Cold Worked Cu-Nb Composites," *Acta Metallurgica,* Vol. 35, No. 10, 1987, pp. 2427–2442.

[8] Klein, J. D. and Rose, R. M., "Thermal Behavior and Strength of Continuous Filament Cu-Nb Composites," *Journal of Applied Physics,* Vol. 6, No. 6, 1987, pp. 2212–2217.

[9] Karasek, K. R. and Bevk, J., "Dislocation Resistivity in In-Situ Formed Cu-Nb Multifilamentary Composites," *Scripta Metallurgica,* Vol. 14, 1980, pp. 431–435.

[10] Bevk, J., Harbison, J. P., and Bell, J. L., "Anomalous Increase in Strength of In-Situ Formed Cu-Nb Multifilamentary Composites," *Journal of Applied Physics,* Vol. 49, No. 12, December 1978, pp. 6031–6038.

[11] Krotz, P. D., Spitzig, W. A., and Laabs, F. C., "High-Temperature Properties of Heavily Deformed Cu-20% Nb and Cu-20% Ta Composites," *Materials Science and Engineering,* Vol. A110, 1989, pp. 37–47.

[12] Funkenbusch, P. D. and Courtney, T. H., "On the Strength of Heavily Cold Worked In-situ Composites," *Acta Metallurgica,* Vol. 33, No. 5, 1985, pp. 913–922.

[13] Karasek, K. R. and Bevk, J., "Normal-State Resistivity of In-Situ-Formed Ultrafine Filamentary Cu-Nb Composites," *Journal of Applied Physics,* Vol. 52, No. 3, 1981, pp. 1370–1375.

[14] Bevk, J., Sunder, W. A., Dublon, G., and Cohen, D. E., "Mechanical Properties of Cu-Based Composites With In-Situ Formed Ultrafine Filaments," *In-situ Composite IV,* F. D. Lamkey, H. E. Cline, and M. McLean, Eds., Elsevier Science Publishing Co., New York, 1982, pp. 121–133.

[15] Funkenbusch, P. D. and Courtney, T. H., "On the Role of Interphase Barrier and Substructural Strengthening in Deformation Processed Composite Materials," *Scripta Metallurgical,* Vol. 23, 1989, pp. 1719–1724.

[16] Funkenbusch, P. D. and Courtney, T. H., "Reply to Comments on the Role of Interphase Barrier and Substructural Strengthening in Deformation Processed Materials," *Scripta Metallurgical,* Vol. 24, 1990, pp. 1175–1180 and 1183–1184.

[17] Pourrahimi, S., Nayeb-Hashemi, H., and Foner, S., "High-Strength High-Conductivity Cu-Nb Micro-Composite Wire Produced by Powder Metallurgy," *Journal of Materials Science Letters,* Vol. 9, 1990, pp. 1484–1487.

[18] Pourrahimi, S., "Synthesis, Microstructural Analysis, and Mechanical Behavior of Cu-Nb Microcomposites Produced by Powder Metallurgy," Ph.D. thesis, Department of Mechanical Engineering, April 1991, Northeastern University, Boston, MA 02115.
[19] Scher, H. and Zallen, R., "Critical Density in Percolation Process," *Journal of Chemistry and Physics,* Vol. 53, 1970, pp. 3759–3764.
[20] Hosford, W. F., "Microstructural Changes During Deformation of [011] Fiber Textured Metals," *Transactions of the Metallurgical Society of AIME,* Vol. 230, 1964, pp. 12–15.
[21] ASTM Practice for Conducting Constant Amplitude Axial Fatigue Tests of Metallic Materials (E 466-82), *Annual Book of ASTM Standards,* Vol. 3.01, Metal Test Methods, 1992, pp. 564–568.
[22] Spitzig, W. A., Verhoeven, J. D., Trybus, C. L., and Chumbly, L. S., "On the Role of Interphase Barrier and Substructural Strengthening in Deformation Processed Composite Material," *Scripta Metallurgica,* Vol. 24, 1990, pp. 1171–1174 and p. 1181.
[23] Dieter, G. E., *Mechanical Metallurgy,* McGraw-Hill Book Co., New York, 1986, pp. 139–145.
[24] Mott, N. F., "The Work Hardening of Metals," *Transactions of the Metallurgical Society of AIME,* Vol. 218, 1960, pp. 962–967.
[25] Hertzberg, R. W., *Deformation and Fracture Mechanics of Engineering Materials,* John Wiley & Sons, New York, 1976, pp. 121–125.
[26] Frost, H. J. and Ashby, M. F., *Deformation Mechanism Maps,* Pergamon Press, New York, NY, 1982, pp. 20–25.
[27] Pelton, A. R., Laabs, F. C., Spitzig, W. A., and Cheng, C. C., "Microstructural Analysis of In-Situ Cu-Nb Composite Wires," *Ultramicroscopy,* Vol. 22, 1987, pp. 251–266.
[28] Kelly, P. M., "The Effect of Particle Shape on Dispersion Hardening," *Scripta Metallurgica,* Vol. 6, 1972, pp. 647–656.
[29] McClintock, F. A. and Argon, A. S., *Mechanical Behavior of Materials,* Addison-Wesley Publishing Co., 1966, pp. 153–180.
[30] Hall, D., *Introduction to Dislocations,* 2nd ed., Pergamon Press, Elmsford, NY, 1975, p. 90.
[31] Li, J. C. M., "Petch Relation and Grain Boundary Sources," *Transactions of the Metallurgical Society of AIME,* Vol. 227, 1963, pp. 239–247.
[32] Suh, N. P. and Turner, A. P. L., "Elements of the Mechanical Behavior of Solids," McGraw-Hill Book Co., New York, 1975, p. 459.
[33] Polak, J. and Liskutin, P., "Nucleation and Short Crack Growth in Fatigued Polycrystalline Copper," *Fatigue and Fracture of Engineering Materials and Structures,* Vol. 13, No. 2, 1990, pp. 119–133.
[34] Polak, J., Lepisto, T., and Kettunen, P., "Surface Topography and Crack Initiation in Emerging Persistent Slip Bands in Copper Single Crystals," *Materials Science and Engineering,* Vol. 74, 1985, pp. 85–91.
[35] Broek, D., *Elementary Engineering Fracture Mechanics,* Sijthoff & Noordhoff International Publishers B.V., Alphen aan den Rijin, The Netherlands, 1978, p. 50.
[36] Tada, H., Paris, P. C., and Irwin, G. R., "The Stress Analysis of Cracks Handbook," Del Research Corporation, Hellertown, PA, 1973.

Holt A. Murray,[1] *Irving J. Zatz,*[1] *and John O. Ratka*[2]

Fracture Testing and Performance of Beryllium Copper Alloy C17510

REFERENCE: Murray, H. A., Zatz, I. J., and Ratka, J. O., **"Fracture Testing and Performance of Beryllium Copper Alloy C17510,"** *Cyclic Deformation, Fracture, and Nondestructive Evaluation of Advanced Materials: Second Volume, ASTM STP 1184,* M. R. Mitchell and O. Buck, Eds., American Society for Testing and Materials, Philadelphia, 1994, pp. 109–133.

ABSTRACT: When a literature search and discussion with manufacturers revealed that there was virtually no existing data related to the fracture properties and behavior of copper beryllium alloy C17510, a series of test programs was undertaken to ascertain this information for several variations in material processing and chemistry. These variations in C17510 were primarily optimized for combinations of strength and conductivity. While originally intended for use as cyclically loaded high-field, high-strength conductors in fusion energy research, material testing of C17510 has indicated that it is an attractive and economical alternative for a host of other structural, mechanical, and electrical applications.

ASTM tests performed on three variations of C17510 alloys included both *J*-integral and plane strain fracture toughness testing (E 813, E 399) and fatigue crack growth rate tests (E 647), as well as verifying tensile, hardness, Charpy, and other well-defined mechanical properties. Fracture testing was performed at both room and liquid nitrogen temperatures, which bound the thermal environment anticipated for the fusion components being designed. Fatigue crack propagation stress ratios ranged from nominal zero to minus one at each temperature. In order to confirm the test results, duplicate and independent test programs were awarded to separate facilities with appropriate test experience, whenever possible.

The primary goal of the test program, to determine and bound the fracture toughness and Paris constants for C17510, was accomplished. In addition, a wealth of information was accumulated pertaining to crack growth characteristics, effects of directionality, and potential testing pitfalls. The paper discusses the test program and its findings in detail.

KEYWORDS: copper beryllium, fracture toughness, fatigue crack propagation, fractography, conductors, cryogenic testing

The copper-beryllium (CuBe) family of alloys has a 40-year history, having been established in a wide range of high-consequence applications and used extensively for high-production-count components. In general, this family of material is selected for a specific property, whether it is ultimate strength, fatigue resistance, environmental integrity, elevated temperature strength, or thermal conductivity.

In a recent design for a large magnet system, a copper-beryllium alloy was designated as the coil conductor material. The conductor specification combined aggressively engineered structural requirements with the need for high thermal and electrical conductivity. A program was initiated to optimize the mechanical and electrical properties of the candidate alloy while maintaining production process practicality for thick-member, 2.8-cm (1.1-in.), significant-weight (over two metric tons) components. A separate program was initiated which led to the devel-

[1] Engineering and Scientific staff, Princeton University, Plasma Physics Laboratory, PO Box 451, Princeton, NJ 08543.

[2] Research and Development staff metallurgist, Brush Wellman Inc., Cleveland, OH 44110.

opment of a welding technique for large structural members composed of the copper-beryllium alloy.

The following paper describes briefly the requirements for the large magnet design, summarizes the results of the program to simultaneously enhance the mechanical and electrical properties of the selected alloy, and reports in detail on the extensive material characterization program. This paper presents the use of a copper beryllium alloy in the role of a high-performance structural material intended for high-reliability applications.

Magnet Design Requirements

The Burning Plasma Experiment (BPX) at the Princeton (University) Plasma Physics Laboratory (PPPL) is a proposed fusion research device dedicated to the study of a fusion nuclear burn. BPX is dominated by a toroidal field coil (TFC) system composed of 18 coils with 21 turns per coil, producing a 9-T magnetic field at the 2.6-m major radius. The coil current is 308 kA and results in a significant conductor thermal excursion, from an initial 80 K to slightly above room temperature. A key portion of the research device pulse is a 10-s full-parameter flat top when the experimental nuclear burn occurs. The physical design is driven by two requirements: a full load scenario of 3000 machine cycles at 9 T and a half-load operation of 30 000 machine cycles at 6 T.

The complete TFC system is composed of approximately 1.13×10^6 kg (2.5 million lb) of copper-beryllium alloy conductor, arranged in a modified Bitter coil configuration with the turns constructed from a 2.8-cm (1.1-in.)-thick plate. The design is driven by the nose section of the conductor where the copper-based alloy is both the structural and the conductive element of the magnet design. This design configuration, limited by a space envelope, requires the coil conductor in the nose region to resist the induced magnetic loads without any external support structure.

Because of the activation potential of BPX and the mechanical complexity of the magnet systems, replacement of a failed conductor component is a significant task. Therefore, an aggressive quality assurance program and significant engineering margin in the design are planned. A series of ASTM procedures to inspect both the copper beryllium material and the welds have been established. These methods include ultrasonic inspection and X-ray examination.

The electromagnetic loading of the TFC is illustrated in Fig. 1 and summarized below:

1. The vertical separating force, restrained by the conductor and case, is 85×10^6 N (19×10^6 lb).
2. The overturning force of the uncased inner leg, the coil nose, is 16×10^6 N (3.6×10^6 lb).
3. The overturning force of the cased outer leg is 18×10^6 N (4.1×10^6 lb).
4. The centering force of the uncased inner leg is 258×10^6 N (58×10^6 lb).

Candidate Conductor Materials

Once the general system parameters were established, an extensive survey of candidate conductor materials including copper-based materials was performed. No commercially available material was identified which would immediately meet the design criteria for the conductor. Several of the material properties key to this design, including low-temperature characteristics, electrical conductivity, thermal conductivity, fracture toughness, and fatigue response, were unavailable in the literature. The methods of preliminary evaluation of candidate materials included establishing the 15 000 cycle stress range capability for a range of R factors. The

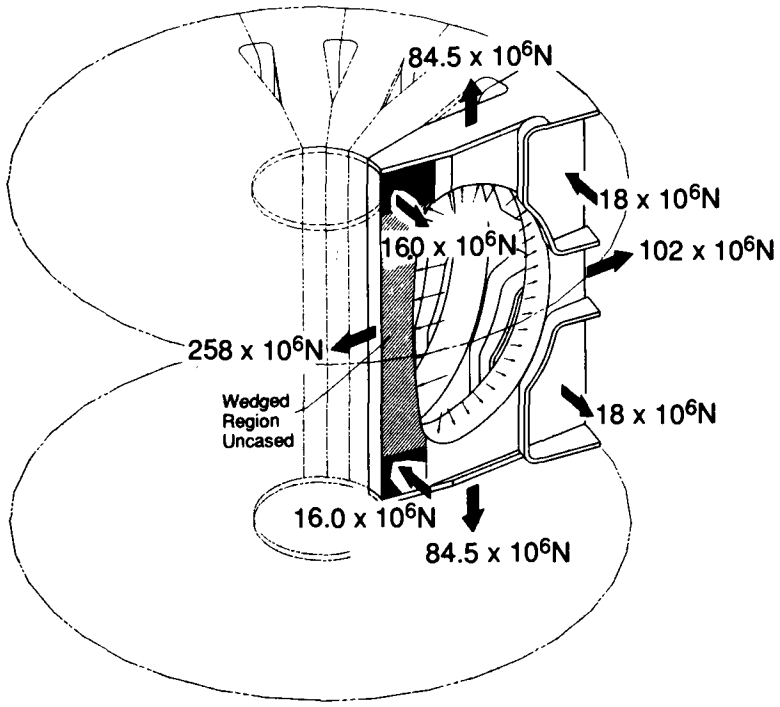

FIG. 1—*The load summary of the BPX TF coil.*

factor R is defined as the ratio of minimum stress divided by the maximum stress. A pure tension fatigue test would be characterized by an R factor of greater than zero. Alternately, a stress range excursion, symmetric around zero, where the compressive range is the same magnitude as the tension would have a R factor of -1. Figure 2 illustrates the relative fatigue performance of several of the candidate coil conductor materials.

Copper-Beryllium Alloy Family

The copper-beryllium alloy family is dominated by copper, typically 98%, and beryllium. In specific compositions, the beryllium is combined with nickel or cobalt to obtain enhanced properties through heat treatment, a sequence of solution annealing and precipitation hardening.

When the beryllium and nickel/cobalt contents are 1.8 to 2.0 and 0.2% by weight, respectively, the commercially available alloy (UNS C17200) exhibits aged properties as detailed in Table 1. When the beryllium and nickel content are 0.2 to 0.6 and 1.4 to 2.2% by weight, respectively, the commercially available alloy (UNS C17510) exhibits age-hardened properties as detailed in Table 2. The abbreviated requirement for one option of conductor material is detailed in Table 3.

The full design specification for the conductor material contains significant detail including demonstrated performance margin in full-size components, biaxial loading capability, fatigue and fracture integrity, low-temperature characteristics to liquid nitrogen, and high thermal and electrical conductivity.

Through a deliberate selection of composition, prescription of processing steps, and selected heat treatment, a range of properties may be achieved within the general specification of the

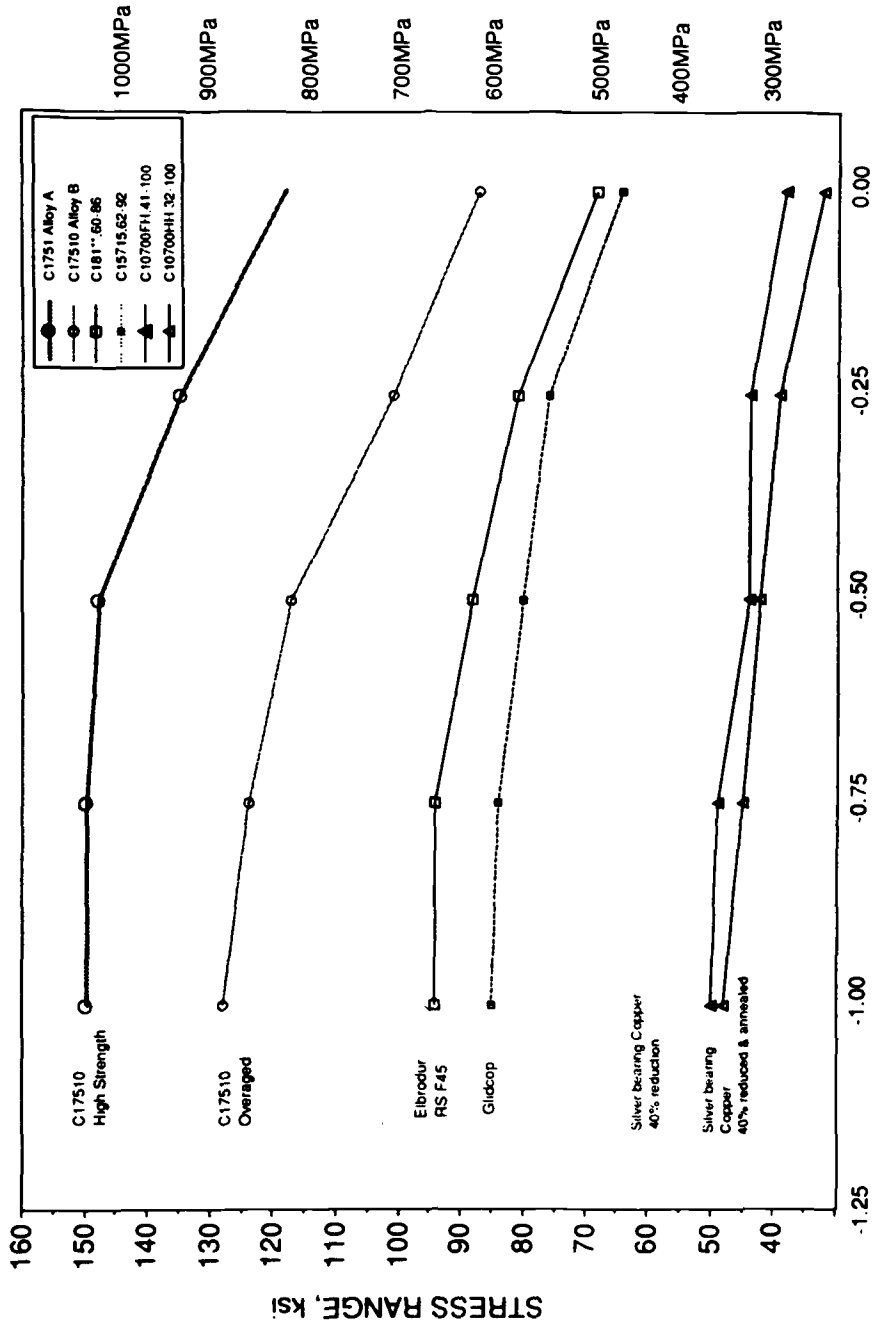

FIG. 2—*The stress range versus* R *for 15 000 cycle life.*

TABLE 1—*Typical characteristics of commercially available UNS C17200 (TH04).*

Material Property	Typical Property Values
Yield strength	1035–1400 MPa (150–200 ksi)
Elongation	5–15%
Fatigue strength, 10^8 cycles	345–414 MPa (50–60 ksi)
Electrical conductivity	15–28% IACS at room temperature

copper-beryllium alloy. Examples of the classic tradeoff between electrical conductivity and yield strength for precipitation-hardenable materials are common. However, there are several processing routes to achieve the same yield/conductivity goal. These alternate processes lead to materials with different fatigue, fracture, and impact properties.

The copper-beryllium alloys can be manufactured to a favorable combination of strength and conductivity by control of composition, thermomechanical processing, and aging treatment. An alloy's properties can be engineered to the requirements of a specific application, for instance where fatigue strength and conductivity levels are targeted by a design. Production of C17510 starts with a direct chill (DC) cast billet followed by a conventional wrought processing and subsequent aging to the required strength or other physical property. The materials examined in this program represent a processing sequence targeted to simultaneously enhance strength and conductivity. During the course of the program over 100 process combinations were investigated to establish the optimum manufacturing sequence and map process parameter sensitivity.

Three large plates have been manufactured for PPPL under the BPX program. Three different specifications were developed, and three distinct alloy variants of C17510 were produced in large plate configurations. The alloy and Brush Wellman's trademark designations for these plates which are used in the following discussions are summarized in Table 4 with the yield strength and electrical conductivity detailed.

Each of the C17510 alloys, designated as A, B, and C, were produced in large plate forms. Alloy A and Alloy B measured 1.9 by 76 by 483 cm (0.75 by 30 by 190 in.), and Alloy C was produced in a plate measuring 2.8 by 127 by 635 cm (1.1 by 50 by 250 in.). Figure 3 illustrates the Alloy C plate next to two TF coils of TFTR, the flagship fusion experimental device for the United States. The process details and specifics of the materials properties are contained in a series of program reports [*1–4*]. The precision electrical conductivity measurements were performed at the National Institute of Standards and Technology and included measurements from 75 to 300 K [*5*].

Further process enhancements have been recently performed to expand the strength and conductivity regime. However, these materials have not yet been characterized beyond the ultimate yield and electrical conductivity at room temperature [*6*]. A sampling of these electrical conductivity and yield strength values are contained in Table 5.

The strength of this copper-beryllium alloy family is derived from the precipitation of meta-

TABLE 2—*Typical characteristics of commercially available UNS C17510 (TF00).*

Material Property	Typical Property Values
Yield strength	552–689 MPa (80–100 ksi)
Elongation	5–20%
Fatigue strength, 10^8 cycles	207–310 MPa (30–45 ksi)
Electrical conductivity	45–60% IACS at room temperature

TABLE 3—*Characteristics of one option of conductor material.*

Material Property	Typical Property Values
Yield strength	724 MPa (105 ksi)
Elongation	15%
Fatigue strength	360 MPa (52 ksi) for 3000 cycles
Fatigue strength	328 MPa (47.5 ksi) for 30 000 cycles
Electrical conductivity	68% IACS at room temperature

stable phases. The precipitation sequence begins from solid solution with the nucleation of Guinier-Preston (GP) zones. As age-hardening progresses, a series of coherent precipitates followed by partially coherent precipitates form from the GP zones. Intermetallic particles known as beryllides, containing Be and Ni, are formed during solidification and also during thermal processing. The combined effect of the precipitates and beryllides is to increase the strength of the alloy. The increase in strength during aging is characteristic of a precipitation-hardenable alloy where the strength reaches a peak value during the aging cycle and decreases as a result of overaging. Electrical conductivity continues to increase during aging as the solute atoms are depleted from solid solution, resulting in a uniform and homogeneous precipitate distribution.

C17510 as a Structural Material

The BPX TF conductor material was required to be a structural member with excellent electrical and thermal conductivity. The physical and conductivity properties of copper-beryllium had to be simultaneously enhanced over commercially available material, and key performance characteristics had to be established. The conductor alloy of choice, a form of C17510, compares favorably with a number of conventional high-performance structural materials as detailed with typical physicals in Table 6.

Each BPX TF conductor turn is essentially a 2.75-cm-thick plate measuring 3.80 by 6.35 m (150 by 250 in.). Due to manufacturing constraints, each turn had to be formed by joining three 1.27 by 6.35 m (50 by 250 in.) plates. Further, each turn had to be joined to the neighboring turn to produce a structurally and electrically continuous element. The design requirements included a weld joint with a 345 MPa (50 ksi) yield strength integrity. A development program was initiated to establish a welding technique to meet the design goal [*7–9*]. The physical aspects of this weld, using C17200 weld filler to join the modified C17510 plate, compare favorably with typical values for more common high-performance structural welds as summarized in Table 7.

TABLE 4—*Designations and properties for three versions of C17510.*

Alloy	Trademark Designation	Electrical Conductivity, %IACS	0.2% Yield Strength, MPa (ksi)
Alloy A	Hycon 3HP™58110	58	758 (110)
Alloy B	Hycon 3HP™70080	70	552 (80)
Alloy C	Hycon 3HP™68105	68	724 (105)

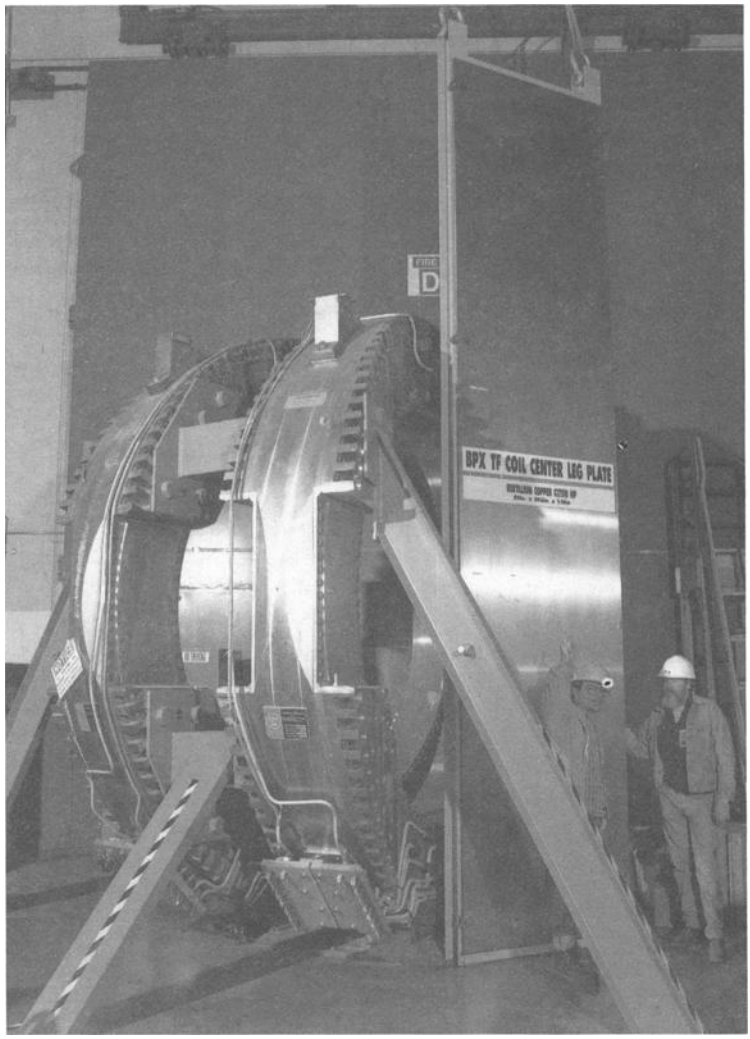

FIG. 3—*The Alloy C plate adjacent to the TFTR TF coils.*

TABLE 5—*Designations and properties for five versions of C17510.*

Heat Designation	Electrical Conductivity, %IACS	0.2% Yield Strength, MPa (ksi)
25030/5259-8	77.0	565 (82.0)
25030/4362-8	74.0	599 (86.9)
25030/4354-8	74.3	590 (85.6)
33881/5047-6	70.5	675 (97.9)
22840/7232-3	63.2	805 (116.9)

TABLE 6—*Typical physicals for a variety of high-performance structural materials.*

Material	0.2% Offset Yield Strength, MPa (ksi)	Ultimate Strength, MPa (ksi)
C17510	723 (105)	792 (115)
Ti Grade 12	413 (60)	517 (75)
Alloy C-4	345 (50)	792 (115)
Alloy 825	310 (45)	689 (100)
316L	172 (25)	482 (70)
304L	172 (25)	482 (70)

Tensile Properties of the Full-Size Plates

Tensile properties of the three full-size plates, designated Alloys A, B, and C, are listed in Table 8. Tension testing was performed at room temperature and 77 K in conformance with the ASTM Standard Test Methods of Tension Testing of Metallic Materials (E 8). In general, the room temperature longitudinal (L) and transverse (T) yield strength, tensile strength, and elongation indicate that the plates are isotropic in tension. The elastic modulus shows similar isotropy for Plates A and C. Plate B shows a lower modulus as a result of unique thermal processing designed to produce the strength and electrical conductivity indicated.

Tensile properties are a function of temperature, demonstrating an increase in yield strength, tensile strength, and ductility at the reduced test temperature. The strength increase occurs independent of modulus, which remains at a value consistent with the room temperature data.

Microstructure

The microstructures of the plates are shown in Fig. 4. The microstructure and the grain size vary between the three plates since similar, but not identical processing procedures were employed. Processing of the plates, including hot and cold rolling, resulted in grain elongation in the rolling direction and compaction in the transverse direction. The average grain size of the plates was measured to be 23.3, 25.1, and 49.8 μm for A, B, and C, respectively. Tensile strength of the plates, detailed in Table 8, is independent of the grain size. Since the material is precipitation hardened, the volume fraction and the distribution of precipitates, not the grain size, establishes the strength and ductility.

TABLE 7—*Typical physicals for a variety of high-performance structural welds.*

Weld Material	0.2% Offset Yield Strength, MPa (ksi)	Ultimate Strength, MPa (ksi)
C17510/C17200	586 (85)	655 (95)
Ti Grade 12	482 (70)	551 (80)
Alloy C-4	551 (80)	723 (105)
825/NiCrMo	482 (70)	758 (110)
316L	448 (65)	586 (85)
304L	413 (60)	551 (80)

TABLE 8—*Mechanical and physical properties of CuBe alloy C17510.*

Plate ID	0.2% Yield Strength, MPa (ksi)			Ultimate Strength, MPa (ksi)			Elongation, (% in 1 in.)			Elastic Modulus, 10^6 MPa (ksi)				Electrical Conductivity, % IACS	
	RT		77 K	RT		77 K	RT		77 K	RT		77 K			
	L	T	L	L	T	L	L	T	L	L	T	L	T	RT	77 K
A[a]	772 (112)	745 (108)	827 (120)	883 (128)	848 (123)	972 (141)	16	16	20	133 (19.3)	132 (19.2)	134 (19.5)	...	58	118
B[b]	565 (82)	579 (84)	634 (92)	676 (98)	662 (96)	124 (118)	20	20	25	119 (17.3)	...	120 (17.4)	...	70	140
C[c]	724 (105)	703 (102)	745 (108)	800 (116)	752 (109)	827 (120)	14	13	15	134 (19.5)	138 (20.0)	131 (19.0)	128 (18.5)	68	165

[a] Brush Wellman Inc. alloy designation Hycon 3HP™58110.
[b] Brush Wellman Inc. alloy designation Hycon 3HP™70080.
[c] Brush Wellman Inc. alloy designation Hycon 3HP™68105.

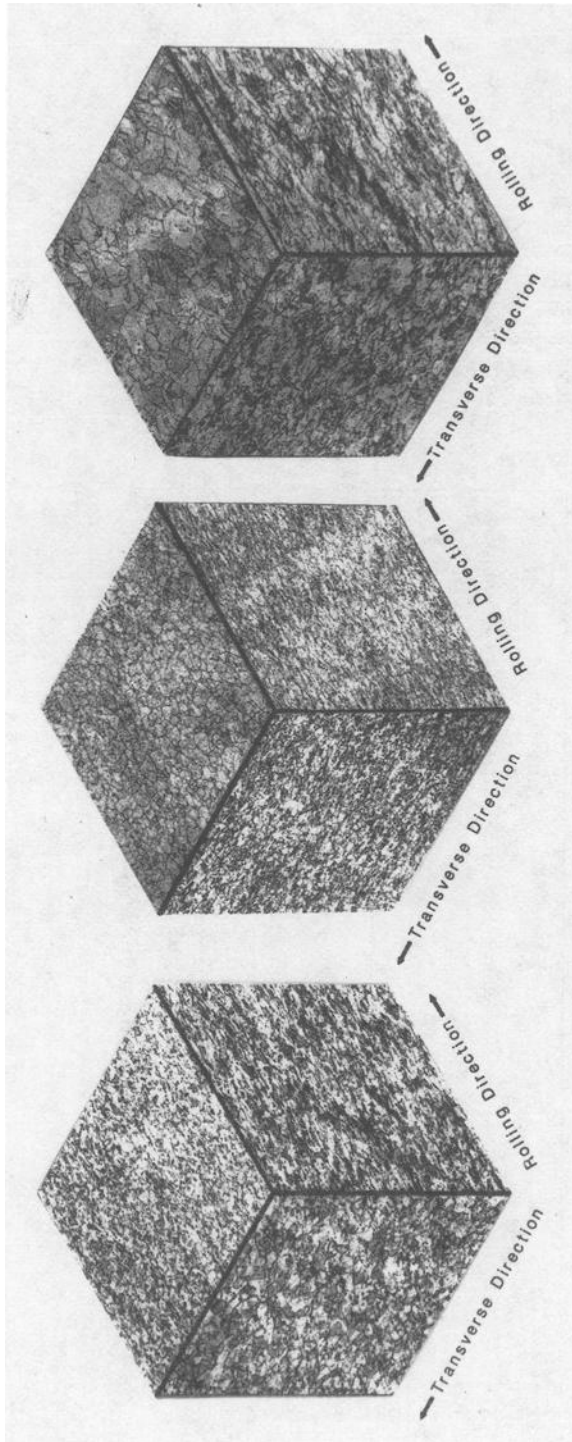

FIG. 4—*Composite microstructure of C17510 plates, left to right, Alloys A, B, and C, at ×60 magnification.*

Charpy V-Notch

Charpy V-notch tests, conducted in accordance with the ASTM Standard Test Methods for Notched Bar Impact Testing of Metallic Materials (E 23), are listed in Table 9. The 77 K liquid nitrogen values show an increase in impact toughness at 77 K as compared with the room temperature data. In addition to these greater toughness values, the macro shear fracture percentage increases slightly. This trend in results was expected since the material has a face center cubic structure.

While the tensile results indicated the material to be isotropic, the impact toughness values for Plate C show otherwise. The room temperature TL and LT values, 16 and 39 J, respectively, show directionality in the impact toughness. The shear fracture percentage substantiates that the LT orientation is inherently tougher than the TL. In reference to the plate processing, the cracks are less blunted in the longitudinal rolling direction than in the transverse direction. The toughness value in the transverse direction increases at 77 K to 24 J without an increase in fibrous fracture.

Fracture Toughness Testing

Over a period of about a year, four independent test programs [*10–14*] were initiated in an attempt to establish the fracture-related material constants of the three candidate CuBe alloys. These tests were to be performed in strict accordance with ASTM standards and included the following in addition to those mentioned previously (ASTM E 8, ASTM E 23):

1. the ASTM Standard Test Method for Plane-Strain Fracture Toughness of Metallic Materials (E 399).
2. the ASTM Standard Test Method for J_{1c}, a Measure of Fracture Toughness (E 813).
3. the ASTM Standard Test Method for Measurements of Fatigue Crack Growth Rates (E 647).

The first test program was awarded for the testing of Alloys A and B [*10–11*]. The second test series examined Alloy A only. The final two programs, initiated after the results of the first two were completed and studied [*12,13*], examined Alloy C, only, which was developed, in part, based on the results of the initial tests on Alloys A and B.

All fracture toughness tests (ASTM E 399 and ASTM E 813) were performed on 19.1-mm (0.75-in.)-thick standard compact tension (C(T)) specimens, conforming with the Alloys A and B plate thicknesses. The fatigue crack growth rate tests were all performed on center cracked panels (M(T)) measuring 290.5 by 101.6 by 9.5 mm (11.4 by 4.0 by 0.375 in.). M(T) specimens are indicated by the ASTM for testing at stress ratios ($R = S_{min}/S_{max}$) that are less than zero.

TABLE 9—*Impact toughness of CuBe alloy C17510, Charpy V-notch.*

Plate ID	Orientation	Room Temperature, J (ft-lb)	% Shear	77 K J (ft-lb)	% Shear
A[a]	LT	50 (37)	30	68 (50)	40
B[b]	LT	81 (60)	50	85 (63)	50
C[c]	LT	39 (29)	55	56 (41)	60
C[c]	TL	16 (12)	5	24 (18)	5

[a] Brush Wellman Inc. alloy designation Hycon 3HP™58110.
[b] Brush Wellman Inc. alloy designation Hycon 3HP™70080.
[c] Brush Wellman Inc. alloy designation Hycon 3HP™68105.

Since the intended application of the alloy as a conductor was for conditions whose value of R would predominantly be less than zero, only M(T) specimens were tested, including those at nominal zero, for consistency. Tests were performed almost entirely at room and liquid nitrogen temperatures. It was anticipated that all varieties of the C17510 alloy would probably be too tough for this specimen thickness to produce consistently valid plane strain ASTM E 399 results, especially at room temperature; therefore, a matrix of ASTM E 399 and ASTM E 813 specimens were prepared with the expectation that the J_{1c} results would be the more valid of the two toughness specimens. Since some materials become more brittle (less tough) while strength increases at lower temperatures, it was anticipated that the ASTM E 399 tests could possibly produce more valid results at liquid nitrogen than at room temperature, with ASTM E 813 tests again to be performed as backup, if necessary.

With so little known about the fracture properties of C17510, certain assumptions had to be made prior to testing. For example, based on the geometry of the proposed toroidal field coil, and the fact that the static properties indicated essentially isotropic behavior, the first two sets of toughness specimens (Alloys A and B) were cut and the tests conducted on only one orientation of the CuBe plate, the LT direction, as indicated in Fig. 5. The intent was to orient the specimens during the tests so that cracks would propagate in the transverse direction, the

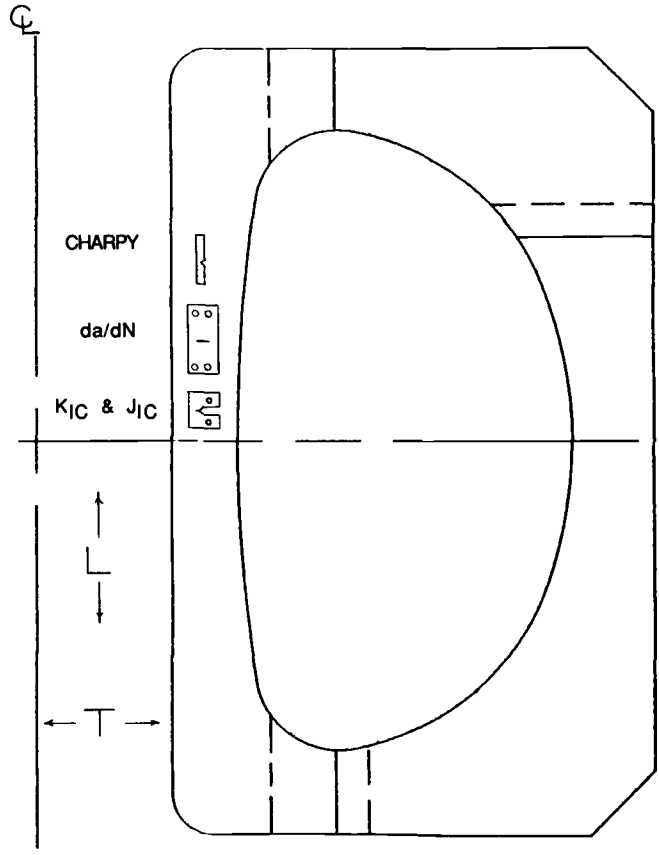

FIG. 5—*Schematic of CuBe plate orientation with respect to the BPX TF coil and test specimens.*

more critical, shorter, radial direction of the magnetic coil. Consistent with this, the principal design loads on the coil are in the longitudinal direction.

While the results of every ASTM E 399 test in the initial programs for Alloys A and B were invalid (the materials, not surprisingly, being too tough and ductile for these specimen thicknesses even at liquid nitrogen temperatures) the failure mechanism for every specimen was similar and unexpected. Rather than the specimen cracking normal to the applied load direction and along the prescribed notch, as is usually the case, the cracks turned near 90° and failed parallel to the load direction. This Mode II-type shearing failure, unusual for metallic materials, was attributed, in part, to the fact that the CuBe plates were primarily rolled in one direction, longitudinally, which may affect the grain structure of the material in such a way as to render that direction a more preferred crack propagation plane than the transverse direction, the direction normal to the rolling and to the applied load. Therefore, regardless of how a C(T) specimen is oriented, it became clear that the preferred crack path and rupture plane will ultimately be in the longitudinal, or rolled, direction. With this knowledge in hand, when the final two test programs for Alloy C were prepared some months later, toughness specimens were cut in both the LT and TL orientations, with valid ASTM E 399 results obtained for the alloy's preferred TL direction. Figure 6 shows typical failed ASTM E 399 specimens for all three alloys in the LT orientation. Figure 7 is a matrix of Alloy C specimens that contrast the effects of temperature and orientation.

The ASTM E 813 fracture toughness tests benefitted from the ASTM E 399 tests that preceded them. Almost all J_{1c} specimens were side-grooved after the precracking portion of each test (per ASTM guidelines). Side-grooving reduces the area of the desired fracture plane normal to the load direction and attempts to force the failure in the preferred transverse direction and within acceptable ASTM standards. In the case of CuBe, side-grooving in the ASTM E 813 tests would help to prevent the crack from making the anticipated near 90° turn experienced in the ASTM E 399 LT tests, where side-grooving is not permitted per the ASTM standard. Figure

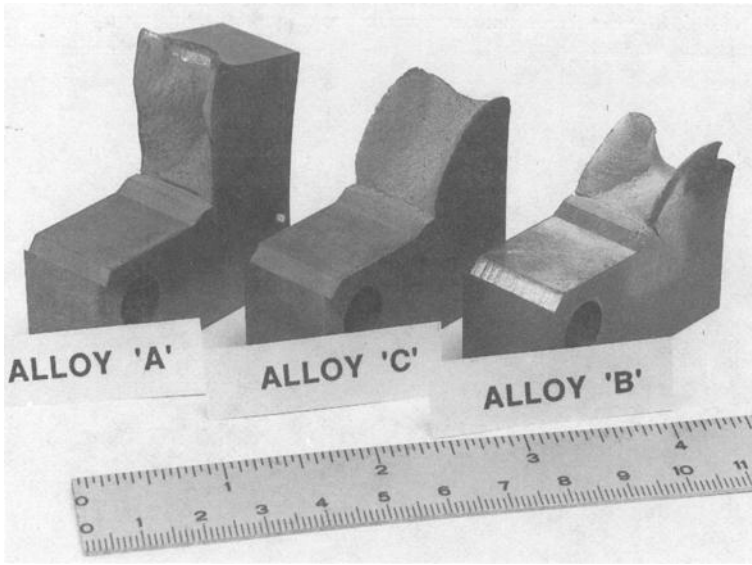

FIG. 6—*Typical plane strain fracture toughness specimens for the three alloys in the LT orientation.*

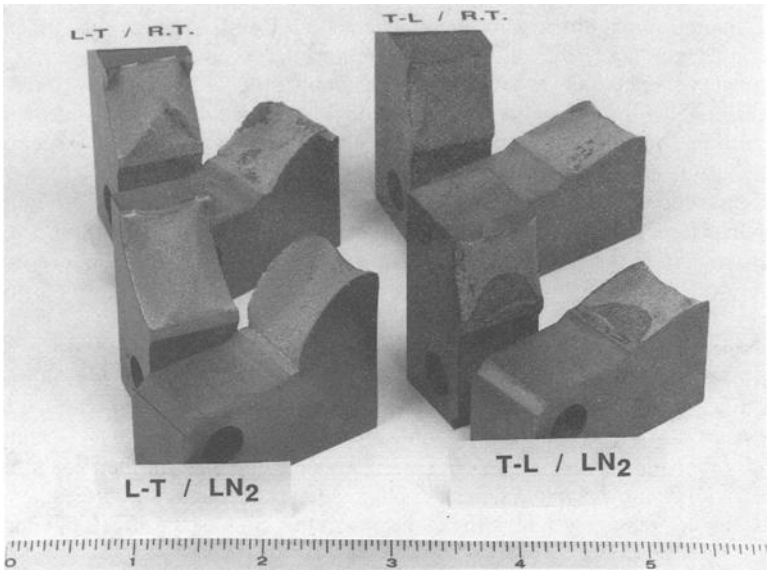

FIG. 7—*Alloy C plane strain fracture toughness specimens indicating orientation and temperature.*

8 shows the effects of side-grooving for the LT orientation of Alloy A. As with the ASTM E 399 tests, the ASTM E 813 tests on Alloys A and B were all of the LT orientation and Alloy C tests examined both LT and TL. Several of the J_{1c} specimens, including side-grooved LTs, produced valid results with others coming extremely close to meeting the ASTM criteria. Figure 9 shows typical failed ASTM E 813 specimens for all three alloys in the LT orientation. Figure 10 is a matrix of Alloy C specimens that contrast the effects of temperature and orientation.

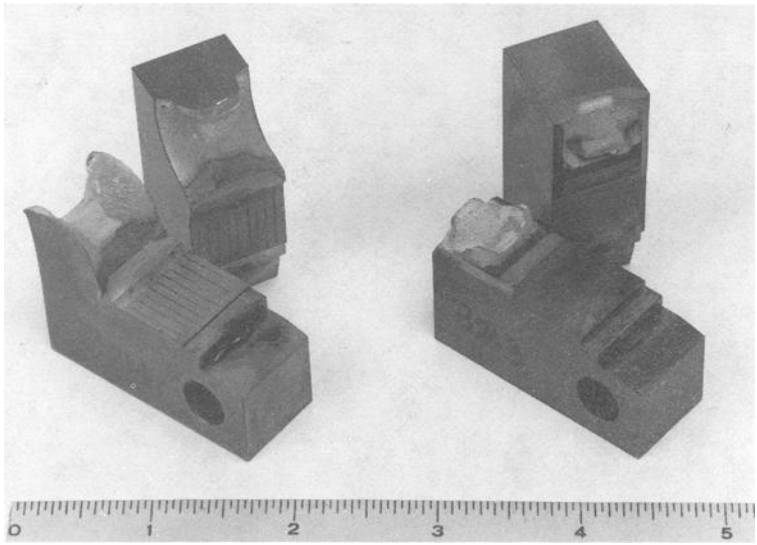

FIG. 8—*The effects of side grooving on* J_{1c} *Alloy A specimens in the LT orientation.*

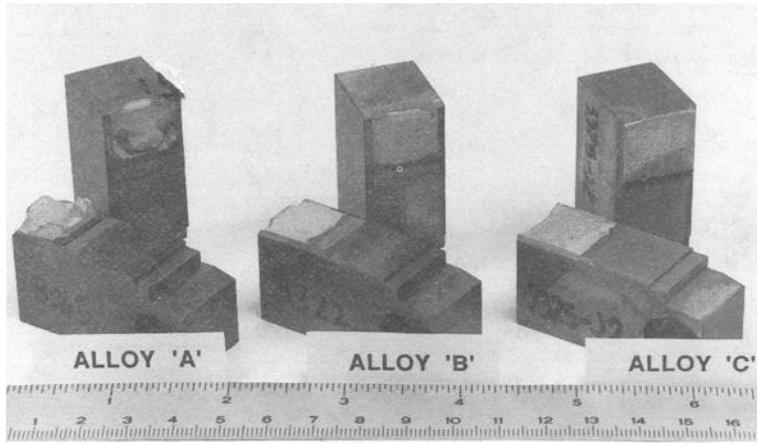

FIG. 9.—*Typical* J_{Ic} *fracture toughness specimens for the three alloys in the LT orientation.*

Based on the limited number of valid J_{Ic} and K_{Ic} tests, the values of fracture toughness for the three C17510 alloys cannot be determined with certainty, but Table 10, which summarizes the toughness testing results, can be used to estimate values of fracture toughness that can be used for comparison with other materials and for life prediction calculations.

Fractography

Representative plane strain fracture toughness (K_{Ic}) compact tension specimens, tested at room temperature and 77 K, were selected for scanning electron microscopy (SEM) examination of the fracture surface. The unusual fractures seen in Fig. 6 were typical of specimens in the LT orientation. In contrast, specimens tested in the TL orientation developed a more conventional planar appearance.

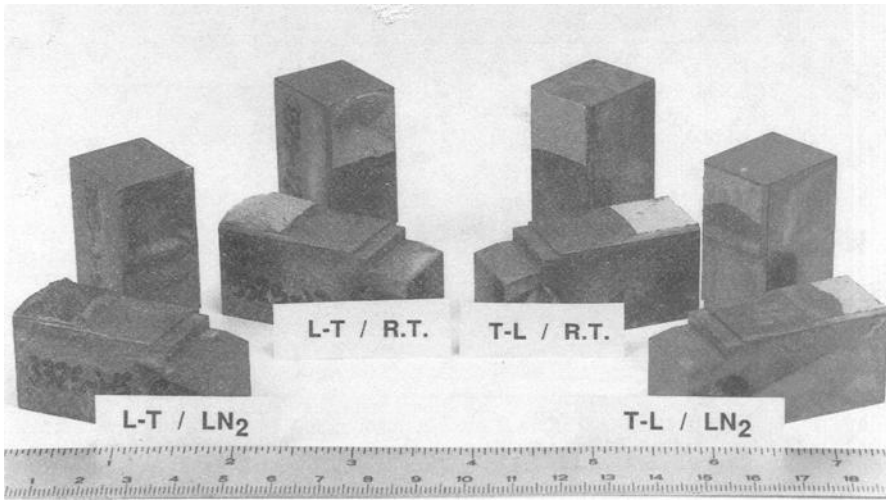

FIG. 10—*Alloy C* J_{Ic} *fracture toughness specimens indicating orientation and temperature.*

TABLE 10*a*—*Summary of fracture toughness testing (ASTM E 399 and E 813),* K_Q.

Alloy	Test Condition[a]	Report Reference	K_Q, MPa $\sqrt{m}$	K_Q, ksi $\sqrt{in.}$
A	LT/RT	[*10*]	102.1, 91.3, 104.3	92.9, 83.1, 94.9
A	LT/RT	[*11*]	81.0, 88.6, 81.3	73.7, 80.6, 74.0
A	LT/INT	[*11*]	91.3, 85.4	83.1, 77.7
A	LT/LN	[*10*]	123.2, 129.3, 128.4	112.1, 117.7, 116.9
A	LT/LN	[*11*]	93.0, 91.5	84.6, 83.3
B	LT/LN	[*10*]	94.6, 101.5, 100.8	86.1, 92.4, 91.7
C	LT/RT	[*12*]	89.3, 83.2	81.3, 75.7
C	LT/LN	[*12*]	100.0, 109.7	91.0, 99.8
C	TL/RT	[*12*]	63.6, 59.2[b]	57.9, 53.9[b]
C	TL/LN	[*12*]	98.6, 95.7	89.7, 87.1

[a] Abbreviations: RT = room temperature, LN = 77 K liquid nitrogen, INT = 150 K.
[b] This specimen was valid according to all ASTM test criteria.

In Fig. 11, the fracture surfaces are shown from Plate C, which was tested oriented in the TL direction at room temperature and 77 K. These specimens exhibit ductile rupture with a mix of conical and shallow dimples. The fracture mode is primarily transgranular with some intergranular character. Small particles, intermetallic beryllides, are seen within several of the dimples. The specimen tested at 77 K displays a greater degree of tearing and a variety of dimple sizes.

Plate C, tested in the LT orientation, displays secondary cracking. These secondary crack paths, shown in Fig. 12, are intergranular and were evidenced both at room temperature and 77 K. The extent of ductile tearing and the development of secondary cracks increases at the low test temperature, as illustrated in Fig. 12. The fracture character and crack propagation is similar for Plates A and B. LT specimens, tested at 77 K are shown in Figs. 13 and 14 for A and B, respectively. Each display transgranular ductile fracture with secondary cracking.

TABLE 10*b*—*Summary of fracture toughness testing (ASTM E 399 and E 813),* J_Q.

Alloy	Test Condition[a]	Report Reference	J_Q, kN/m	J_Q, lb/in.
A	LT/RT	[*10*]	97, 89, 92	554, 508, 526
A	LT/RT	[*11*]	33, 158[b], 37	191, 902,[b] 214
A	LT/LN	[*10*]	218, 262, 162	1243, 1494, 927
A	LT/LN	[*11*]	201, 318[b], 171	1148, 1814,[b] 978
B	LT/RT	[*10*]	85, 75, 80	488, 428, 454
C	LT/RT	[*12*]	23, 20, 27	134, 112, 156
C	LT/RT	[*13*]	135, 143, 135	771, 817, 771
C	LT/LN	[*12*]	54, 94, 73	307, 537, 418
C	LT/LN	[*13*]	257, 251[c], 258	467, 1433,[c] 147
C	TL/RT	[*12*]	26, . . .[d], . . .[d]	151, . . .,[d] . . .[d]
C	TL/RT	[*13*]	56, 57, 55	320, 314, 325
C	TL/LN	[*12*]	72, 71, 63	412, 404, 358
C	TL/LN	[*13*]	130,[c] 128,[c] 134[c]	742,[c] 731,[c] 765[c]

[a] Abbreviations: RT = room temperature, LN = 77 K, liquid nitrogen.
[b] Indication of a J_{IC} specimen that was not side grooved.
[c] This specimen was valid according to all ASTM test criteria.
[d] Indication of not enough valid data points for curve fit.

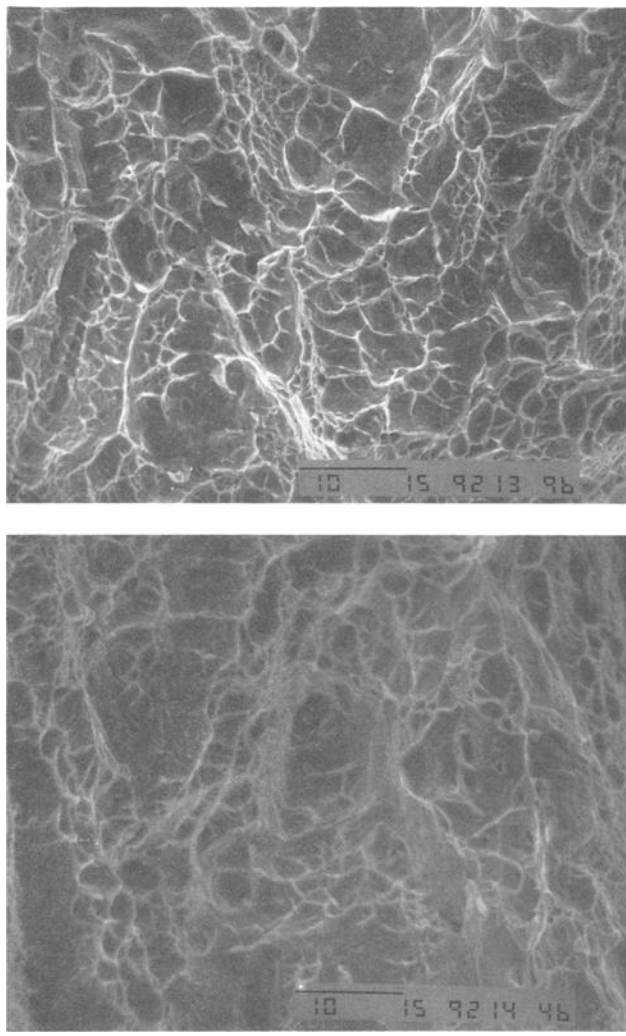

FIG. 11—*SEM micrograph of Alloy C plate, TL orientation, tested at room temperature* (top) *and 77 K* (bottom).

Fatigue Crack Growth Rate Testing

Given the limitations of time and money, the fatigue crack growth rate testing could not be totally comprehensive considering the many variables associated with this type of test, but the tests still produced several significant findings that reflect a greater understanding for the behavior of the C17510 alloy family. As with the toughness tests, the first two test programs performing ASTM E 647 examined the LT orientation of Alloys A and B only. While only a limited amount of crack growth testing was performed on Alloy B at room temperature and $R = -1$, a greater amount of testing was performed on Alloy A, filling a matrix of conditions at R equals nominal zero and minus one at both room and liquid nitrogen temperatures with multiple specimens for each condition duplicated independently at two different test facilities.

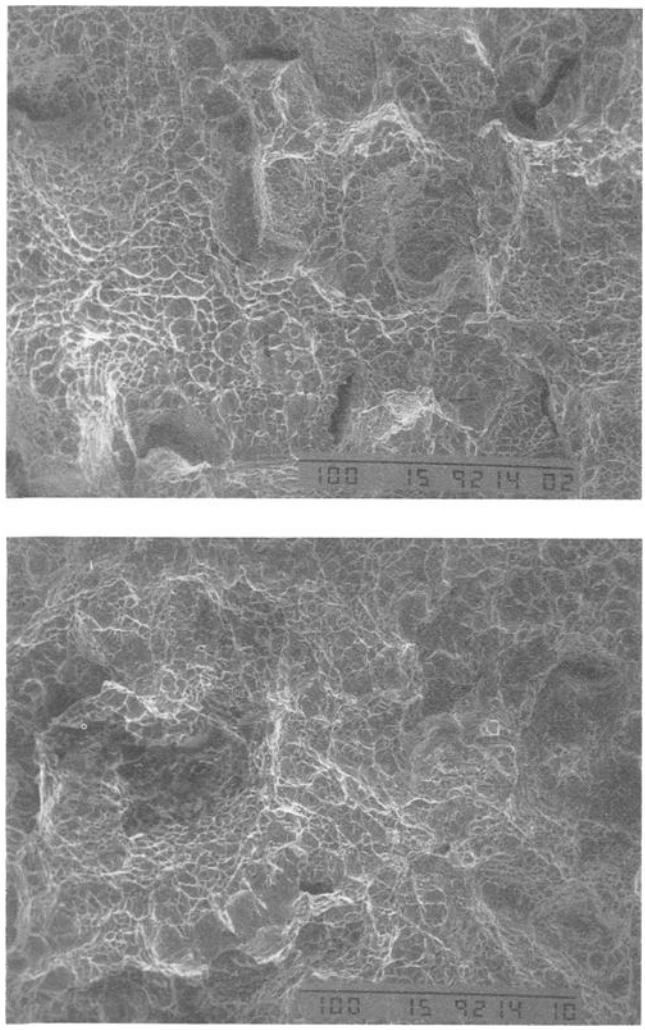

FIG. 12—*SEM micrograph of Alloy C plate, LT orientation, tested at room temperature* (top) *and 77 K* (bottom).

Fortunately, the required M(T) specimen for negative stress ratios was ideally suited to test the LT direction. If the more typical compact-type C(T) specimen had been used, Mode II-type crack propagation paths that turn toward the longitudinal direction would be anticipated. But, by virtue of its symmetry in geometry and load, the M(T) specimen was effectively able to study the more desirable Mode I LT direction crack propagation.

Optical observation of the crack fronts during testing revealed that the crack tip in actuality frequently branched in several directions at once, resulting in multiple crack tips at each front. This resulted in a somewhat irregular cracking plane as the overall crack progressed and continued branching. From a testing standpoint, this is not an overly desirable behavioral pattern; however, from a practical applications standpoint, the multiple crack front is indicative of the materials' ductility and energy absorption capabilities when in service, making it a desirable candidate structural material.

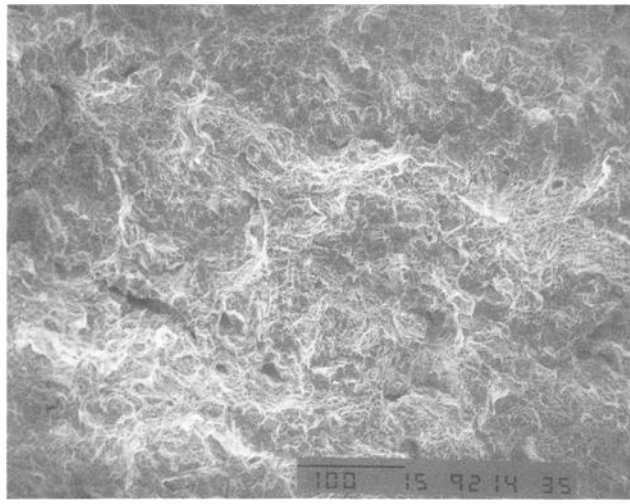

FIG. 13—*SEM micrograph of Alloy A plate, LT orientation, tested at 77 K.*

The latter Alloy C tests, which studied both the LT and TL crack growth orientations, also employed the M(T) specimen exclusively for all tests. In addition to testing multiple specimens in both orientations at both room and liquid nitrogen temperatures for stress ratios of nominal zero and minus one, as with the Alloy A tests, Alloy C tests were also performed at an intermediate value of $R = -0.25$ at room temperature for the LT and TL directions tying it to a performance condition of the BPX conductor.

The principal goal of the ASTM E 647 tests was to study Stage II crack growth and thereby determine the Paris constants from the log-log plots of crack growth rate versus stress intensity range for the three alloys at each set of testing conditions. By coupling the experience of the testing facilities with the evidence that these alloys exhibited classical crack growth behavior, Stage II growth, from which the Paris constants were determined, was chosen for a prescribed

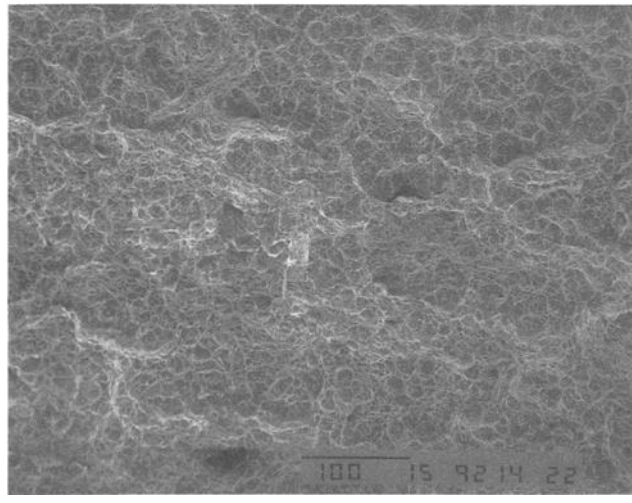

FIG. 14—*SEM micrograph of Alloy B plate, LT orientation, tested at 77 K.*

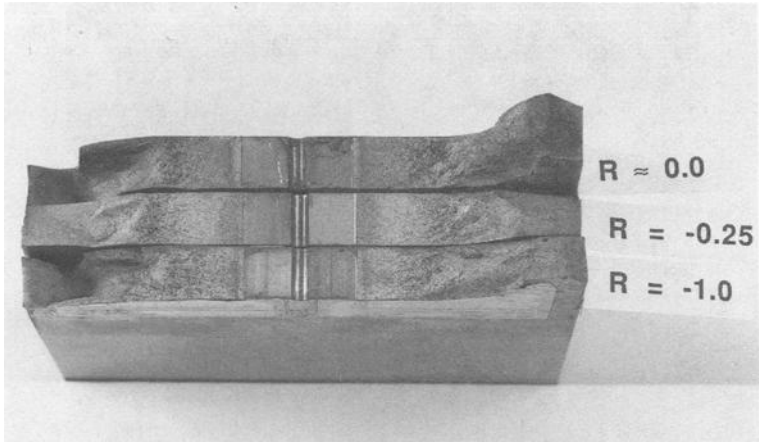

FIG. 15—*Comparison of Alloy C crack growth surfaces for three different stress ratios—room temperature, LT orientation.*

da/dN range that consistently demonstrated the linear behavior typical for this test. Any variation in the Paris constants would help to establish the sensitivity of the alloys to stress ratios and temperature. As a result of this fundamental goal, and the aforementioned testing limitations, no attempt was made to study the more complex crack growth approaches such as closure theory or fitting to the Forman equation. Nevertheless, the crack growth tests provided valuable additional data that supplemented the Paris constants. For example, initial crack growth testing was carefully performed at relatively low applied loads and rates in order to approximate where Stage II growth began. As a result, a rough estimate of Stage I growth and, in turn, an estimate of the threshold stress intensity could be made from the data, which consistently indicated a value of approximately 10 MPa$\sqrt{m}$ (≈10 ksi$\sqrt{in.}$) for the LT direction in all three alloys. TL tests indicated a value of threshold stress intensity that was slightly less than the LT tests (≈8–

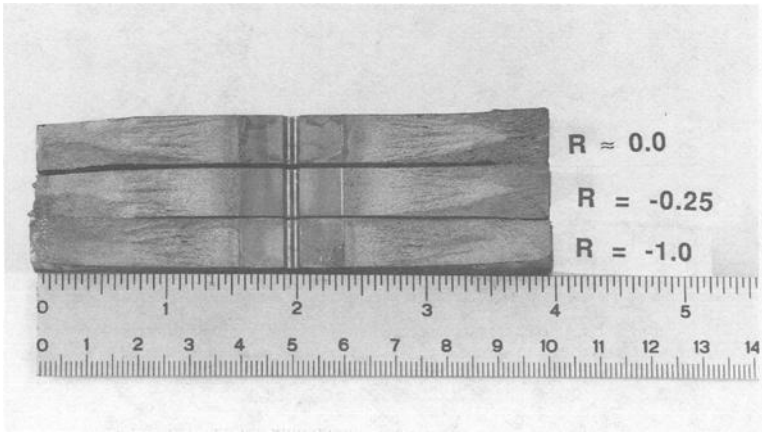

FIG. 16—*Comparison of Alloy C crack growth surfaces for three different stress ratios—room temperature, TL orientation.*

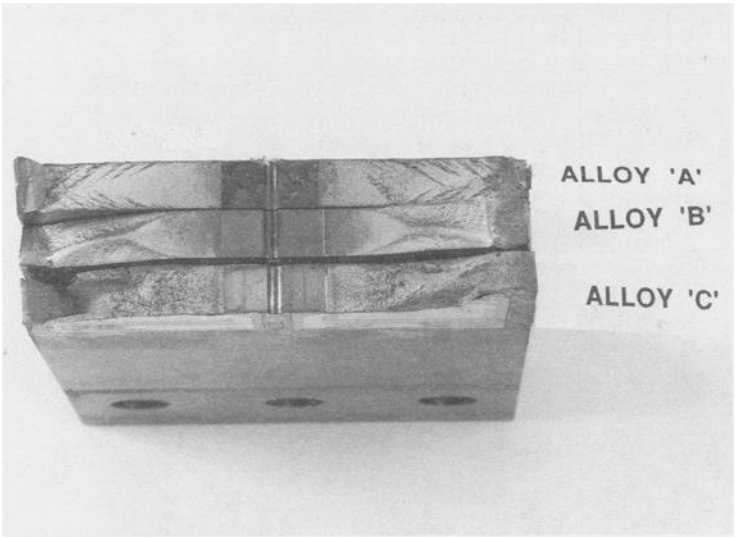

FIG. 17—*Comparison of crack growth surfaces for the three alloys—room temperature, LT orientation,* R = *−1.*

9 MPa$\sqrt{m}$). Similarly, an examination of the final Stage III data points of crack growth just prior to failure yielded approximate values of fracture toughness that could be compared to the values obtained by the toughness tests. Figure 15 compares the surfaces of Alloy C specimens at room temperature in the LT orientation for three different stress ratios. Figure 16 does the same for TL orientation specimens. Figure 17 contrasts the surfaces of the three alloys for room temperature, $R = -1$, LT orientation conditions. Figure 18 compares crack surfaces of Alloy A, LT orientation, for three different temperatures, all at a stress ratio of minus one.

In general, the ASTM E 647 tests in all four test programs went extremely well with frequent tight overlaying of data points and Paris constants nearly duplicated consistently for common testing parameters in the various test programs providing additional validity to the results.

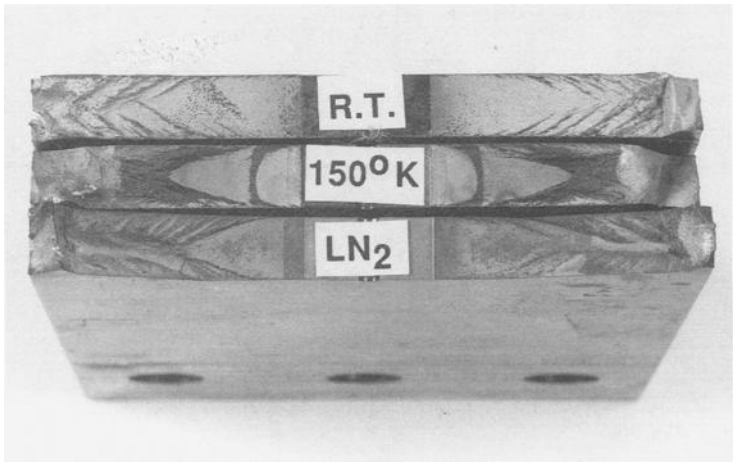

FIG. 18—*Comparison of Alloy A crack growth surfaces at three different temperatures—LT orientation,* R = *−1.*

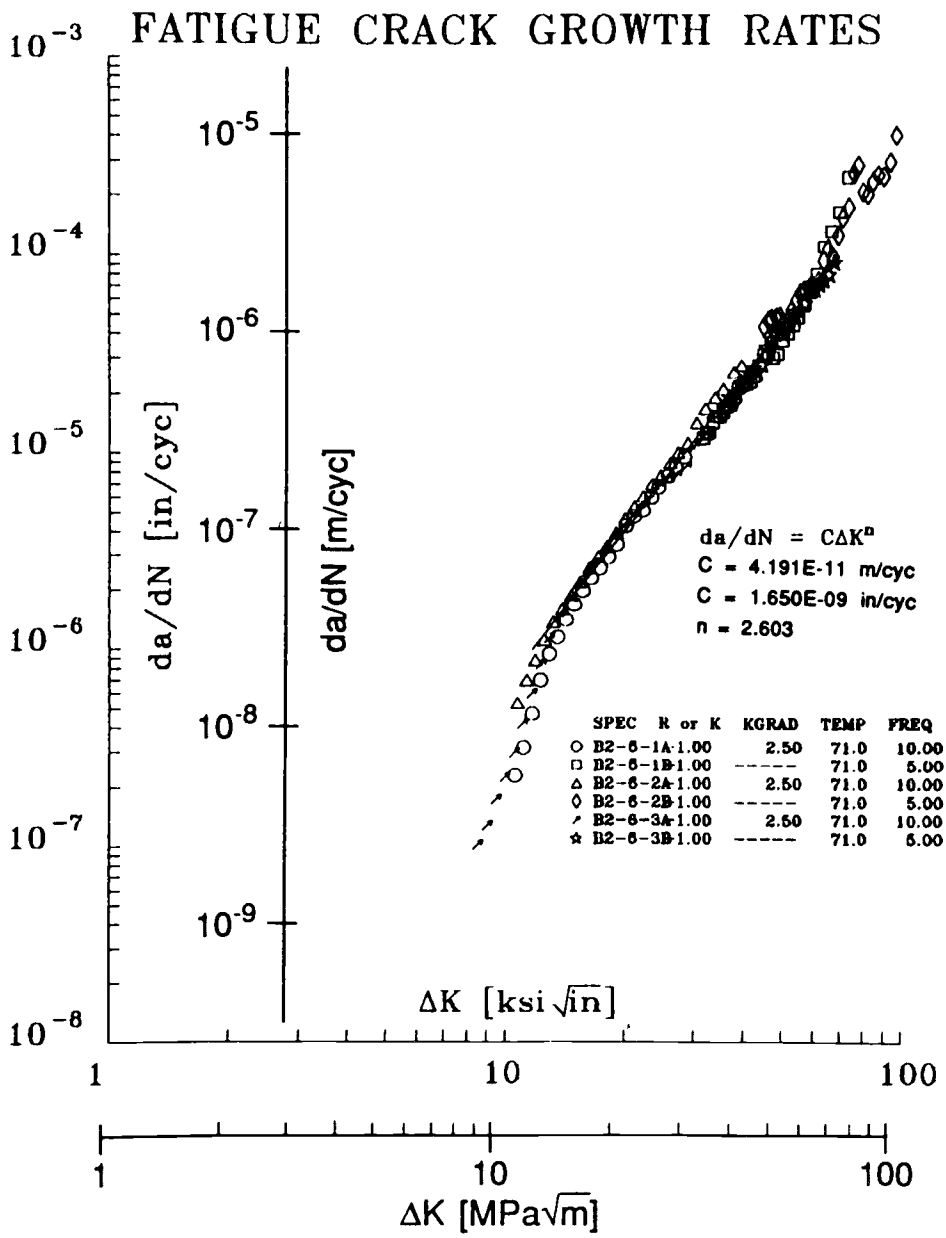

FIG. 19—da/dN *versus* ΔK *plot for three specimens—Alloy A, room temperature, LT orientation,* R = −*1.*

Typical consistency of test results can be seen in Figs. 19 and 20, which depict different conditions for different alloys. Table 11 summarizes the Paris constants from these test programs for all three alloys.

Several fatigue crack growth tests were performed at an intermediate cryogenic temperature of 150 K. This was done to determine the Paris constants at a temperature near to one of the

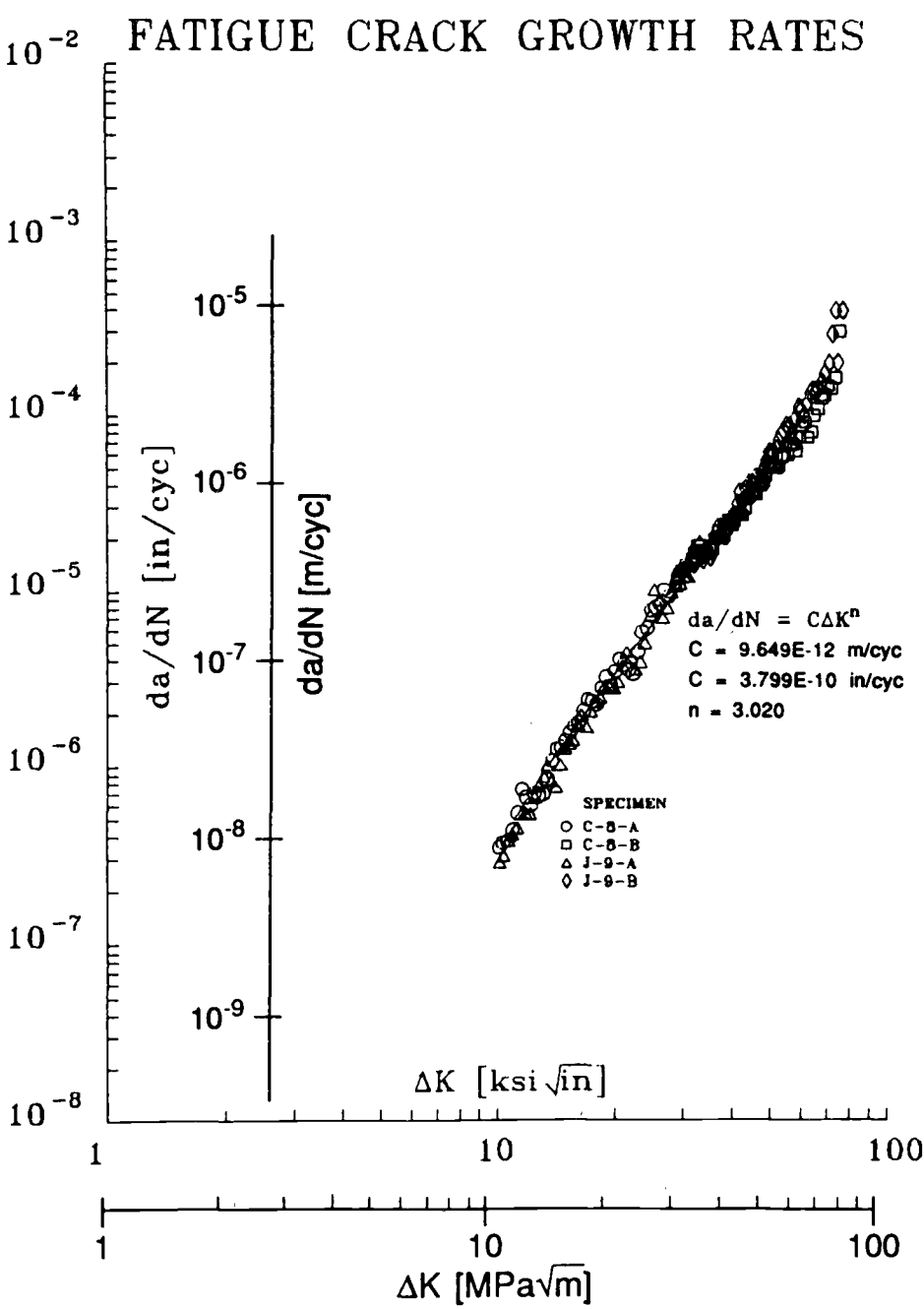

FIG. 20—da/dN *versus* ΔK *plot for two specimens—Alloy C, LT orientation, 77 K,* R = −1.

TABLE 11—*Summary of Paris constants based on fatigue crack growth rate tests (ASTM E 647).*[a,b]

Alloy	Test Condition[c]	Number of Specimens/ Report Reference	C (m/cycle)	C (in./cycle)	n
A	LT/R ≈ 0/RT	2/[*10*]	8.943E-11	3.521E-09	2.330
A	LT/R ≈ 0/RT	2/[*11*]	6.782E-11	2.670E-09	2.460
A	LT/R = −1/RT	3/[*10*]	4.191E-11	1.650E-09	2.603
A	LT/R = −1/RT	2/[*11*]	1.420E-10	5.590E-09	2.270
A	LT/R ≈ 0/LN	2/[*10*]	1.418E-11	5.583E-10	2.812
A	LT/R ≈ 0/LN	2/[*11*]	1.515E-11	5.964E-10	2.878
A	LT/R = −1/LN	3/[*10*]	1.158E-11	4.561E-10	2.895
A	LT/R = −1/LN	2/[*11*]	2.131E-11	8.390E-10	2.834
A	LT/R = −1/INT	3/[*11*]	. . .	. . .	. . .[d]
B	LT/R = −1/RT	2/[*10*]	2.929E-11	1.153E-09	2.866
C	LT/R ≈ 0/RT	2/[*13*]	2.224E-11	8.755E-10	2.728
C	LT/R = −1/RT	2/[*13*]	3.249E-11	1.279E-09	2.777
C	LT/R = −1/RT	2/[*12*]	2.083E-11	8.199E-10	2.879
C	LT/R ≈ 0/LN	2/[*13*]	3.373E-12	1.328E-10	3.055
C	LT/R = −1/LN	2/[*13*]	5.347E-12	2.105E-10	3.100
C	LT/R = −1/LN	2/[*12*]	9.649E-12	3.799E-10	3.020
C	LT/R = −0.25/RT	2/[*12*]	2.045E-11	8.051E-10	2.801
C	TL/R ≈ 0/RT	2/[*13*]	2.601E-12	1.024E-10	3.662
C	TL/R = −1/RT	2/[*13*]	6.515E-12	2.565E-10	3.496
C	TL/R = −1/RT	2/[*12*]	5.017E-12	1.975E-10	3.536
C	TL/R ≈ 0/LN	2/[*13*]	6.365E-13	2.506E-11	3.660
C	TL/R = −1/LN	2/[*13*]	2.446E-12	9.629E-11	3.467
C	TL/R = −1/LN	2/[*12*]	4.592E-12	1.808E-10	3.322
C	TL/R = −0.25/RT	2/[*12*]	4.475E-12	1.762E-10	3.510

[a] Data fit by linear regression analysis.

[b] The Stage II range was generally set between 2.54E-08 to 2.54E-06 m/cycle (1.0E-06 to 1.0E-04 in./cycle) with a few specimens lower bound set at 1.27E-08 m/cycle (5.0E-07 in./cycle).

[c] Abbreviations: RT = room temperature; LN = 77 K, liquid nitrogen; INT = 150 K.

[d] These data were felt to be unreliable due to their scatter.

potential operating levels of the designed magnets as well as to study the linearity of the constants as a function of temperature. Unfortunately, technical difficulties during the tests produced sufficient scatter and uncertainty in the data to render the results invalid. The problem, which resulted from the formation of unanticipated ice crystals at the crack tip, was attributed to the presence of excessive moisture in the cryogenic testing chamber which would not be present in a pure liquid nitrogen bath and not be a concern at room temperature. The importance of obtaining additional crack growth data at additional temperatures remains a high priority.

Summary

Based on the material development program described in this paper, copper-beryllium alloy C17510 shows enormous potential as a structural material that can be utilized in a wide variety of special applications. Originally optimized for use as a low-temperature, high-strength, high-conductivity material in an experimental fusion device, the favorable fracture and fatigue capabilities as well as environmental integrity and excellent welding characteristics of C17510 suggests its use in many other industrial and commercial situations. The alloy has shown potential to be further engineered depending on the specific needs demanded by particular circumstances. While the work presented herein is by no means comprehensive or totally complete,

it represents a first step in what plans to be an ongoing experimental program to further establish C17510 as a viable candidate material, supported by the favorable findings from these material tests. Future work will propose additional specific applications for copper-beryllium in conjunction with additional testing.

Acknowledgments and Note

This work was performed, in part, under U.S. DOE contract DE-AC02-76CH03073.

Note that copper-beryllium, like many industrial materials, poses a health risk only if mishandled. In its usual solid form, as well as for finished parts, and in most manufacturing operations, it is completely safe. However, breathing very fine particles may cause a serious lung condition in a small percentage of individuals. Risk can be minimized with simple, proven, and readily available engineering controls such as ventilation of operations producing fine dust. Information on safe handling procedures is available from Brush Wellman Inc.

References

[*1*] Ellis, R. III and Murray, H., "Optimization of Toroidal Field Coil Conductor Properties for BPX," *Proceedings,* 14th IEEE/NPSS Symposium on Fusion Engineering, San Diego, IEEE catalog number 91CH3035-3, IEEE, New York.

[*2*] Heitzenroeder, P. J., "BPX Toroidal Field Coil Design," *Proceedings,* 14th IEEE/NPSS Symposium on Fusion Engineering, San Diego, IEEE catalog number 91CH3035-3, IEEE, New York.

[*3*] Murray, H.,"Characterization of Copper-Beryllium Alloy C17510," *Proceedings,* 14th IEEE/NPSS Symposium on Fusion Engineering, San Diego, IEEE catalog number 91CH3035-3, IEEE, New York.

[*4*] Spiegelberg, W. D., "Beryllium Copper Plate for the Compact Ignition Tokamak Toroidal Field Coils," Final Report TR-950, Brush Wellman, Inc., Cleveland, OH, March 1989.

[*5*] Thompson, C. A., "Copper Alloy Resistivity Measurements," National Institute of Standards and Technology (NIST) Report Number 814-32-91, National Institute of Standards and Technology, Boulder, CO, September 1991.

[*6*] Spiegelberg, W. D., Ratka, J. O., and Davidge, E. J., "Process Parameter Mapping for Alloy C17510," Final Report TM-1063, Brush Wellman Inc., Cleveland, OH, September 1992.

[*7*] Murray, H., Harris, I. D., and Ratka, J. O., "Development of a Welding Procedure for High Conductivity Copper-Beryllium Alloy C17510," *Proceedings,* 14th IEEE/NPSS Symposium on Fusion Engineering, San Diego, IEEE catalog number 91CH3035-3, IEEE, New York.

[*8*] Harris, I. D. and Ratka, J. O., "Welding Procedure Development for High Conductivity Beryllium Copper," Edison Welding Institute Report Number J5229, Edison Welding Institute, Columbus, OH, 1991.

[*9*] Harris, I. D. and Ratka, J. O., "Gas Metal Arc Welding Procedure Development for Thick Section Beryllium-Copper Plate," Edison Welding Institute Report Number J5491, Edison Welding Institute, Columbus, OH, February 1992.

[*10*] Zatz, I. J. and Murray H., "Final Report of BeCu Material/Crack Propagation Studies Performed by CORRPRO/PSG Engineering, Inc.," PPPL EAD-3989, PPPL-F-910614-14, 14 June 1991, Princeton Plasma Physics Laboratory, Princeton, NJ.

[*11*] Zatz, I. J. and Murray, H., "Final Report of BeCu Material/Crack Propagation Studies Performed by Fatigue Technologies, Inc.," PPPL EAD-4041, 31 July 1991, Princeton Plasma Physics Laboratory, Princeton, NJ.

[*12*] Zatz, I. J. and Murray, H., "Final Report of BeCu Material/Crack Propagation Studies Performed by CORRPRO/PSG Engineering, Inc.," PPPL EAD-4099, 6 November 1991, Princeton Plasma Physics Laboratory, Princeton, NJ.

[*13*] Zatz, I. J. and Murray, H., "Final Report of BeCu Material/Crack Propagation Studies Performed by CORTEST Laboratories," PPPL EAD-4282, 18 Aug. 1992, Princeton Plasma Physics Laboratory, Princeton, NJ.

[*14*] Zatz, I. J. and Murray, H., "Fracture Testing of Copper-Beryllium Alloy C17510," *Proceedings,* 14th IEEE/NPSS Symposium on Fusion Engineering, San Diego, IEEE catalog number 91CH3035-3, IEEE, New York.

V. V. Ogarevic[1] *and R. I. Stephens*[1]

Fatigue of a Particle-Reinforced Cast Aluminum Matrix Composite at Room and Elevated Temperatures

REFERENCE: Ogarevic, V. V. and Stephens, R. I., **"Fatigue of a Particle-Reinforced Cast Aluminum Matrix Composite at Room and Elevated Temperatures,"** *Cyclic Deformation, Fracture, and Nondestructive Evaluation of Advanced Materials: Second Volume, ASTM STP 1184,* M. R. Mitchell and O. Buck, Eds., American Society for Testing and Materials, Philadelphia, 1994, pp. 134–155.

ABSTRACT: Constant amplitude low-cycle fatigue, fatigue crack growth, and variable amplitude fatigue tests were performed on a 20% volume fraction SiC particle-reinforced A356 cast aluminum matrix composite at room temperature at 150°C. Data obtained were analyzed and compared with those of the unreinforced matrix material. Variable amplitude loading fatigue life calculations were performed using commercially available software.

The low-cycle fatigue results revealed that the composite material had somewhat lower fatigue resistance than the unreinforced material at room temperature and that the composite fatigue resistance decreased with increasing temperature. Room temperature fatigue crack growth rates were higher, and ΔK_{th} values were lower in the composite compared to those of the unreinforced material. There was not much difference between the composite fatigue crack growth rates at the two temperatures. Positive R ratio increased fatigue crack growth rates of the composite, but had more effect at room temperature than at 150°C. SEM fractography revealed that pores were preferred fatigue crack initiation sites. For small ΔK, fatigue cracks grew predominantly through the matrix, while with increasing ΔK more and more particles were fractured. Micromechanisms of crack growth were of the ductile type in the matrix, while particles were cleaved. Particle/matrix interface debonding was not observed. Both reasonable and unreasonable fatigue life predictions were obtained with this metal matrix composite using the common low-cycle fatigue and fatigue crack growth approaches.

KEYWORDS: metal matrix composites, aluminum matrix, particulate reinforcement, low-cycle fatigue, fatigue crack growth, variable amplitude loading, fatigue life predictions

Metal matrix composites (MMC) are promising materials for structural applications at room and elevated temperatures. One of the main intentions in MMC development is to replace existing high-temperature materials with a simultaneous increase in service temperature range and specific mechanical properties. Examples of this are potential applications of MMC for turbine and automobile engine components and for aerospace structures.

There are three basic types of MMC: dispersion-strengthened, particle-reinforced, and fiber (whisker)-reinforced [*1*]. Reinforcement is usually an intermetallic compound, an oxide, a carbide, or a nitride. Principal reinforcement materials for MMC today are: silicon carbide (SiC), boron (B), alumina (Al_2O_3), and graphite, while metal matrices are mainly lightweight metals like alloys of aluminum (Al), magnesium (Mg), and titanium (Ti) [*1*].

Experimental evaluation of discontinuously reinforced MMC tensile properties is routinely

[1] Adjunct assistant professor, and professor, respectively, Mechanical Engineering Department, The University of Iowa, Iowa City, IA 52242.

done after each new material is developed. The results show higher strength and stiffness and lower ductility at operating temperatures than corresponding unreinforced matrix material. Fracture toughness and fatigue behavior results, however, are relatively rare in the available literature even from room temperature, not to mention elevated temperatures. It is expected that discontinuously reinforced MMC components will be used at elevated temperatures under variable amplitude loading. Reliable component fatigue life predictions under these conditions are crucial for wide-scale applications of these materials. Available literature data are not comprehensive enough to allow for those predictions even at room temperature. It was the aim of this research to provide such fatigue data and fatigue life prediction schemes for a specific cast aluminum alloy-based SiC particle-reinforced MMC. The results obtained are compared to those of the unreinforced material, which was extensively studied previously [*2–4*].

Material Description

The metal matrix composite used in this research is based on cast aluminum alloy A356 reinforced with 20 vol% SiC particles. The MMC was obtained by adding SiC particles to the melted A356 matrix alloy, which was kept at a certain temperature (proprietary information). The composite was initially cast in ingot form. Ingots were later cast into blocks, from which specimens used in this research were made. To avoid particle clustering, some stirring of the mixture was applied during sand casting until the liquidus temperature was reached. The sand cast blocks were solutionized at 540°C for 12 h, hot water quenched, and artificially aged at 154°C for 5 h (T61 thermal treatment). SiC particles were elongated, with aspect ratios between 2:1 and 5:1. Particle-size distribution had a median of 13 ± 1 μm, with 3% of the particles larger than 25 μm and 94% larger than 5 μm [*5*]. The reinforcement chemical composition was as follows: SiC 98.0% min, free Si 0.3% max, free SiO_2 0.5% max, free C 0.2% max, and free Fe 0.2% max [*5*].

Experiments

The following types of tests were performed on specimens made of the MMC: monotonic tension, smooth specimen constant strain amplitude low-cycle fatigue, constant load amplitude and load-shedding fatigue crack growth and variable amplitude loading with a notched keyhole specimen. All tests were performed at both room temperature and 150°C, which is considered to be a common service temperature for components made of this MMC.

Specimens for testing were obtained by machining sand cast blanks. Sand casting was chosen as an inexpensive, high-quality, reliable way of casting this material. Axial specimen geometry used for monotonic and low-cycle fatigue testing is shown in Fig. 1. The compact tension, C(T), specimen geometry for fatigue crack growth and the keyhole specimen geometry for variable amplitude testing are shown in Figs. 2 and 3, respectively.

All tests were performed using an 89-kN electrohydraulic closed-loop test system with two different controllers, an analog and a digital type. Only variable amplitude loading tests were performed using the digital controller. Elevated temperature testing was performed in an electric-heated environmental chamber attached to the test system frame. The chamber was controlled to within ±1.5°C accuracy. Water-filled cooling coils were attached to the load cell to keep its temperature low. Specimens used in elevated temperature tests were held at 150°C for at least 30 min before testing to allow initial temperature gradients in a specimen to die out.

Monotonic Stress-Strain Behavior

Two axial specimens were used for monotonic testing at room temperature and two at 150°C. Manually operated hydraulic grips were used for holding the specimens in the testing machine

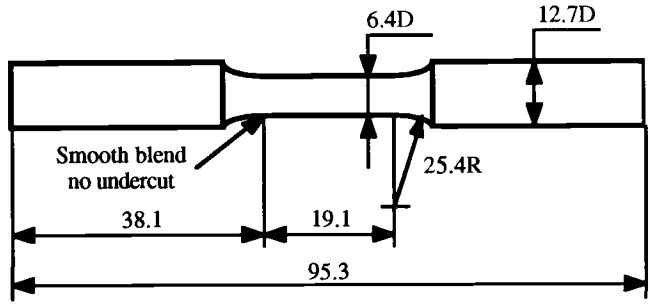

FIG. 1—*Axial specimen for monotonic tension and strain-life tests (all dimensions in millimetres).*

at both temperatures. Strain measurements at both temperatures were performed using a strain-gage-based extensometer with 12.5-mm gage length. All specimens had epoxy dots fixed along the length at approximately 12.5 mm distance, where extensometer knife edges were allowed to dig in to ensure that no slipping occurred during testing and that the specimen surface was not damaged by the knife edges. Load-strain data were recorded using both an X-Y plotter and a digital computer with a data collection device. The computer-collected data were transferred to a portable IBM PC compatible computer for storage and further analysis.

Figure 4 shows plots of computer-collected monotonic (lines) and cyclic (points) stress-strain data of all the specimens tested. Since the plastic and total strain levels were very small (of the order of 1%), it did not make much difference whether true or engineering strains and stresses were used, so only engineering quantities were calculated. The plots in Fig. 4 show that the monotonic stress-strain curves are always increasing, and so the ultimate tensile strength S_{ut} is equal to the fracture strength. Substantial scatter in total fracture strains at room temperature and in the elastic modulus E values at 150°C can be seen from the figure.

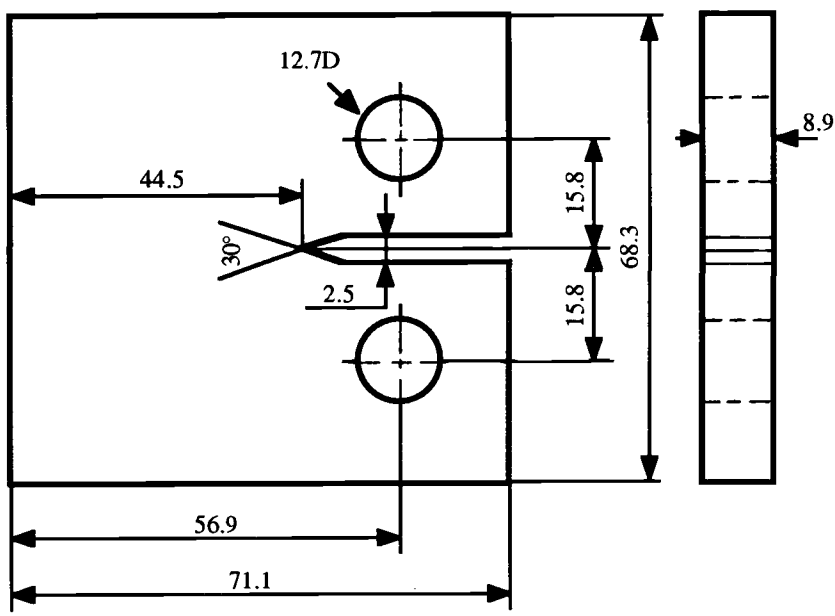

FIG. 2—*C(T) specimen for fatigue crack growth testing (all dimensions in millimetres).*

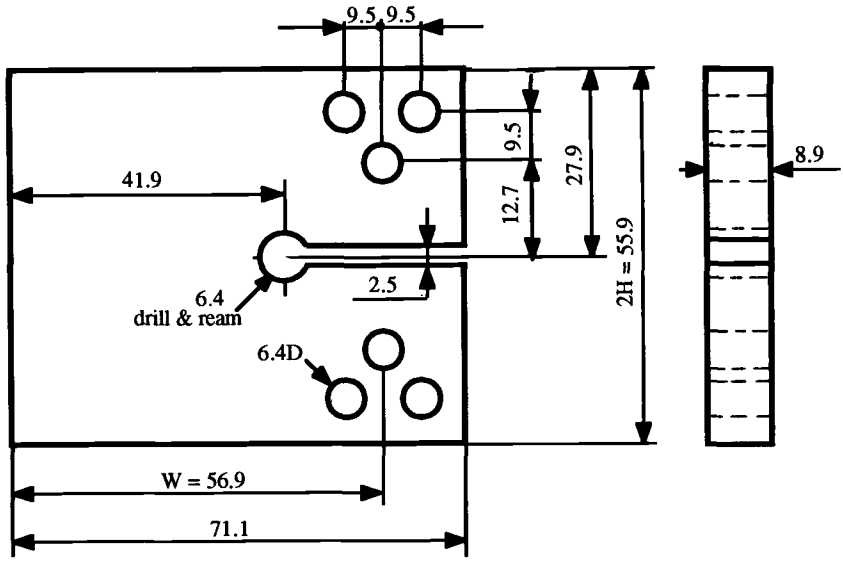

FIG. 3—*Keyhole-type specimen (all dimensions in millimetres).*

Scatter of the order of 30% in E values was observed at 150°C. Scatter of that magnitude for metal matrix composites was not reported in the available literature. Yield strengths at both temperatures were calculated for a plastic strain value of 0.1% ($S_{0.1}$) since 0.2% values ($S_{0.2}$) either could not be obtained from the graphs, owing to very small total strain levels, or the difference between $S_{0.2}$ and S_{ut} was too small. The elongation data were measured directly from

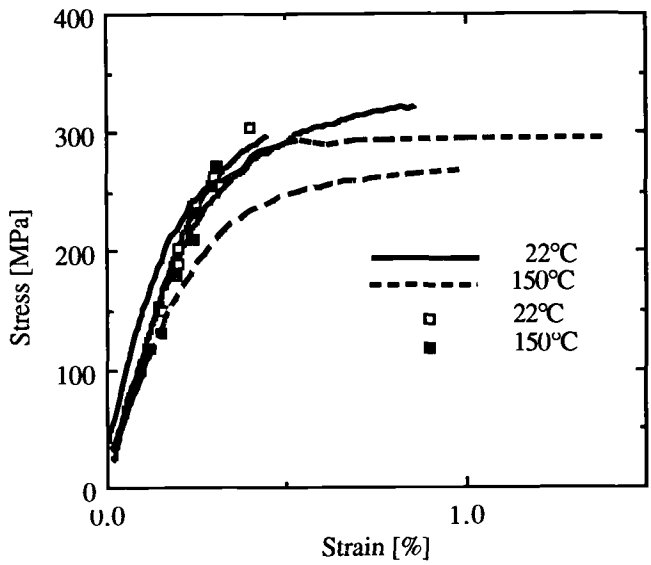

FIG. 4—*Individual monotonic (lines) and cyclic (points) stress-strain data of the metal matrix composite.*

the fractured specimens. Besides small total strain levels, very small values of reduction of area (*RA*) were observed.

The strain-hardening coefficient, K, and the exponent, n, were calculated using a log-log linear regression analysis with the Ramberg-Osgood equation

$$\varepsilon = \varepsilon_{el} + \varepsilon_{pl} = \frac{\sigma}{E} + \left(\frac{\sigma}{K}\right)^{1/n} \tag{1}$$

Average E values at each temperature were used in this equation. Plastic strains were limited to $\varepsilon_{pl} \geq 10^{-4}$ in order to avoid large errors in K and n calculations.

Table 1 summarizes averaged tensile properties of the metal matrix composite and gives representative unreinforced matrix data for comparison [*2,8*]. The average composite elastic modulus value at 150°C decreased by about 5% compared to the respective value at room temperature. A similar decrease can be seen for the unreinforced matrix material. On the other hand, the composite E values were about 45% higher at both temperatures compared to the unreinforced matrix values. The MMC $S_{0.1}$ and S_{ut} values also decreased with increasing temperature, by about 16 and 12%, respectively, while they were 33 and 20% higher, respectively, compared to the unreinforced matrix values. It is important to note that the composite strengths retained their values with increasing temperature much better than the reinforced matrix: for example, $S_{0.1}$ decreased by 16% for the composite and by about 40% for the matrix. This better strength retention by the MMC gives a distinct advantage over the unreinforced material for high-temperature applications. Similar trends occurred for K and n values.

Low-Cycle Fatigue Behavior

Sixteen axial specimens were used for low-cycle fatigue testing at room temperature and fifteen at 150°C. These tests were performed under triangular wave form constant amplitude strain control with three strain ratios, $R = \varepsilon_{min}/\varepsilon_{max} = -1$, 0, and -2. Ten specimens were tested at room temperature and nine at 150°C with $R = -1$, while four and two specimens were tested at each temperature with $R = 0$ and $R = -2$, respectively. The same equipment and procedures were used for specimen gripping, strain measurements, and data recordings as for the monotonic tests at both temperatures. Frequency of the tests was between 1 and 30 Hz, depending on the applied strain level. Hysteresis loops were recorded frequently during each test. All tests were performed until specimens fractured, and this was taken as the failure criterion. The observed load drop just before fracture was in the range of 10% of total load range, which suggests that the fracture criterion of two pieces was correctly chosen. Strain amplitude levels were chosen such that they caused fatigue lives between 10 and 10^6 cycles. Runouts were defined as greater than $3 \cdot 10^6$ reversals, and only two specimens were runouts (those tests were stopped before fracture occurred). Specimens fractured both inside and outside

TABLE 1—*Average tensile properties of the metal matrix composite and the matrix material A356-T6.*

Material	Temperature, °C	*E*, GPa	$S_{0.1}$, MPa	S_{ut}, MPa	Elongation, %	*RA*, %	*n*	*K*, MPa
Composite	22	102	280	318	0.7	3.0	0.107	585
A356-T6[a]	22	70	210	266	1.8	3.0	0.087	397
Composite	150	97	235	279	1.2	3.0	0.085	425
A356-T6[b]	150	67	145	165	...	...	...	...

[a] Data from Ref 2, Material Y.
[b] Data from Ref 8.

the gage length, and only one room temperature specimen fractured in the root radius. This test was classified as invalid, while all 150°C tests were considered valid.

Since an unexpectedly large scatter in the elastic modulus was obtained from 150°C monotonic tension tests, the 150°C E values were estimated from initial portions of the computer-collected hysteresis loops for comparison purposes. Scatter of about 30% was again noticed.

Cyclic stress-strain curves were obtained by connecting the tips of approximately half-life hysteresis loops. The data points for room temperature and 150°C are given in Fig. 4 together with monotonic stress-strain curves for comparison. Very small cyclic plastic strain levels can be seen from the figure, so cyclic yield strengths at both temperatures could not be obtained. Some scatter of the data points was observed at 150°C. Slight cyclic strain hardening was observed at both temperatures, with the maximum stress for the cyclic curve about 30 MPa (i.e., about 10%) larger than the monotonic loading stress at the same strain level. Cyclic elastic moduli E' were assumed to be the same as their respective average monotonic values. The cyclic strain hardening coefficient K' and exponent n' were calculated using log-log linear regression analysis with an equation similar to the Ramberg-Osgood equation

$$\frac{\Delta\varepsilon}{2} = \frac{\Delta\varepsilon_{el}}{2} + \frac{\Delta\varepsilon_{pl}}{2} = \frac{\Delta\sigma}{2E} + \left(\frac{\Delta\sigma}{2K'}\right)^{1/n'} \tag{2}$$

Plastic strain amplitudes were limited to $\frac{\Delta\varepsilon_{pl}}{2} \geq 10^{-4}$ to avoid large errors in K' and n' calculations. The K' and n' values for both temperatures are given in Table 2. The K' and n' values for the unreinforced matrix material at room temperature are given for comparison, and almost a threefold increase in the composite material values can be seen.

Strain amplitude-life $\left(\frac{\Delta\varepsilon}{2} - 2N_f\right)$ data with $R = -1$ for the composite at both temperatures are shown in Fig. 5, together with the unreinforced matrix material room temperature data [2] for comparison. At high strain amplitudes, the composite material exhibited shorter room temperature fatigue lives than the matrix by about an order of magnitude. The difference did not change much with decreasing strain amplitudes, but the number of obtained data points was too small to allow for more precise characterization.

Total, elastic, and plastic strain amplitudes, $\Delta\varepsilon/2$, $\Delta\varepsilon_{el}/2$, and $\Delta\varepsilon_{pl}/2$, respectively, are plotted versus reversals to failure $2N_f$ for $R = -1$ in Figs. 6 and 7 at room temperature and 150°C, respectively. The elastic and plastic parts of the total strain amplitude were obtained for each low-cycle fatigue specimen from computer-collected hysteresis loops by determining the approximate half-life plastic strain amplitude data, $\frac{\Delta\varepsilon_{pl}}{2}$, at the respective mean stress levels (for example at $\sigma_m = 0$ for $R = -1$) and then calculating the elastic strain amplitude as the difference between the total and plastic strain amplitudes.

TABLE 2—*Low-cycle fatigue properties of the metal matrix composite and the matrix material A356-T6 (R = −1).*

Material	Temperature, °C	σ_f', MPa	b	ε_f'	c	K', MPa	n'
Composite	22	520	−0.104	0.0189	−0.717	925	0.155
Composite	150	282	−0.0556	0.0043	−0.447	833	0.162
A356-T6[a]	22	502	−0.119	0.0166	−0.544	383	0.0499

[a] Data from Ref 2, Material Y.

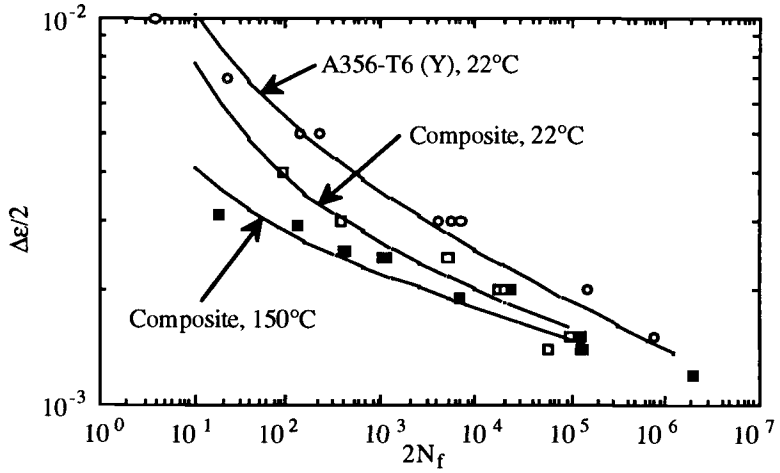

FIG. 5—*Low-cycle fatigue behavior of the metal matrix composite and of the matrix material A356-T6, Material Y [2];* R = −1.

Log-log linear regression lines were fit through the elastic and plastic strain amplitude data for both temperatures in order to obtain the usual low-cycle fatigue properties. The equation for the low-cycle fatigue model is given as [*9,10*]

$$\frac{\Delta\varepsilon}{2} = \frac{\Delta\varepsilon_{el}}{2} + \frac{\Delta\varepsilon_{pl}}{2} = \frac{\sigma_f'}{E}(2N_f)^b + \varepsilon_f'(2N_f)^c \tag{3}$$

Values of $\frac{\Delta\varepsilon_{pl}}{2} \leq 1.5 \cdot 10^{-4}$ were omitted from the regression analysis in order to avoid large errors. The composite low-cycle fatigue properties σ_f', b, ε_f', c are given in Table 2 for both temperatures, together with the matrix room temperature properties [*2*], for comparison. Equa-

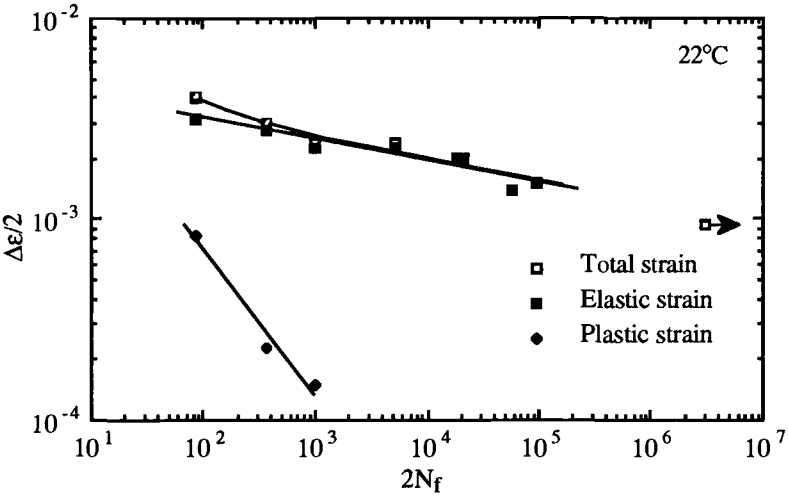

FIG. 6—*Low-cycle fatigue behavior of the metal matrix composite at room temperature;* R = −1.

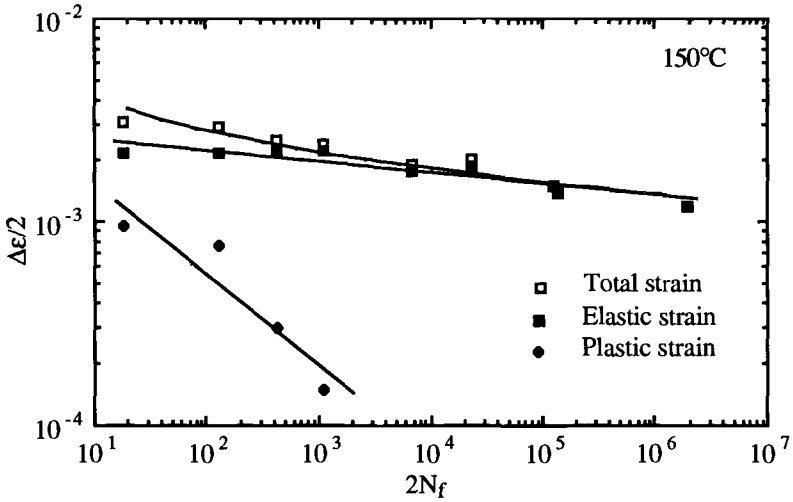

FIG. 7—*Low-cycle fatigue behavior of the metal matrix composite at 150°C;* R = −1.

tion 3 is plotted in Figs. 6 and 7 and previously in Fig. 5. The difference between the composite room temperature low-cycle fatigue properties and the respective matrix data was small except for the value of the exponent c, which exhibited a magnitude about 30% larger for the composite. Approximately a factor of two decrease in the composite low-cycle fatigue properties was obtained at the elevated temperature. The number of data points obtained was considered to be too small to allow for any meaningful statistical analysis.

Very low ductility of the material was the reason that there was no intersection of the elastic and plastic log-log regression lines. Similar results were obtained for the unreinforced matrix material [2] where it was noted that if intersection did occur, it was for $2N_f \leq 30$ reversals.

Diagrams of total strain amplitude versus number of reversals for $R = -1$, 0, and -2 at room temperature and 150°C are presented in Figs. 8 and 9, respectively. Small positive mean stress effects on fatigue lives were found at room temperature and even smaller at 150°C. Significant cyclic mean stress relaxation (of the order of 40%) was noted at 150°C for both tensile and compressive mean stresses, while the relaxation at room temperature was small (of the order of 10%). The ratios of half-life mean stress to stress amplitude for $R = 0$ were between 0.5 and 0.8 at room temperature and between 0.2 and 0.3 at 150°C, while they were less than 0.1 for $R = -2$ at both temperatures. The number of low-cycle fatigue tests was too small to allow for more precise characterization of mean stress influence on constant amplitude fatigue lives.

Fatigue Crack Growth Behavior

Five C(T) specimens were used for fatigue crack growth tests at room temperature and six at 150°C. Specimens were set up in the test system using fork-type grips with pins that allowed for free rotation of the specimens [ASTM Standard Test Method for Measurements of Fatigue Crack Growth Rates (E 647-88a)]. Tests were performed under triangular wave form load control. Load-shedding tests were performed to determine Region I behavior and constant load amplitude tests to determine Region II behavior. Procedures suggested in ASTM E 647-88a were followed in both cases. Two load ratios, $R = 0.05$ and 0.5, were used. The same heating equipment for 150°C testing was used as in the case of low-cycle fatigue testing. Test fre-

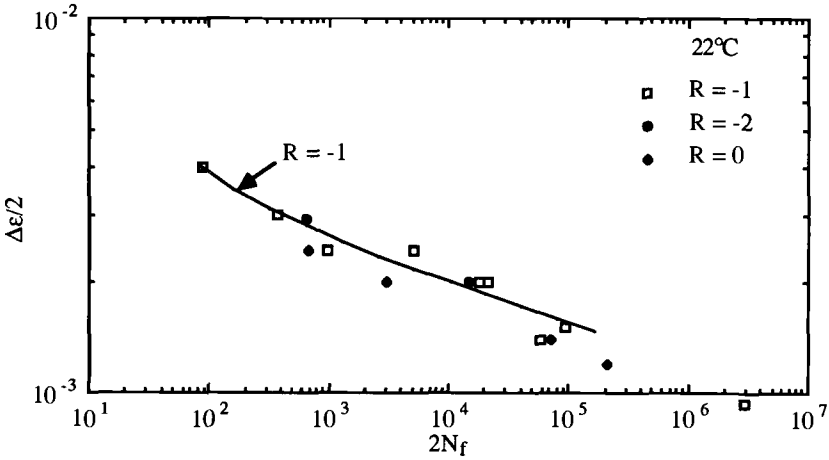

FIG. 8—*Low-cycle fatigue behavior of the metal matrix composite at room temperature;* R = *−1, 0, and −2.*

quencies ranged from 5 to 40 Hz depending on the applied load range. Fatigue crack length was measured visually at both temperatures using a traveling telescope with ×33 magnification and a stroboscope lamp. Acetone cleaning and polishing using 400 and 600 grit was applied to eliminate surface scratches on specimen sides. Fatigue crack fronts were very straight and in a single plane in all specimens tested. Fatigue crack closure effects at room temperature were estimated from fatigue crack opening load values that were determined from load-crack opening displacement (COD) diagrams at room temperature (recorded using both the X-Y plotter and the digital computer) or load-back face strain (BFS) diagrams at 150°C (recorded using the digital computer only).

The sigmoidal shape of the *da/dN-ΔK* curve, commonly observed with other metals, was partially obtained with the metal matrix composite. Region I of the curve, corresponding to a very slow fatigue crack growth rate (between 10^{-10} and 10^{-9} m/cycle) and the log-log linear Region II (between 10^{-9} and 10^{-6} m/cycle) were determined for $R = 0.05$ and 0.50 at both room

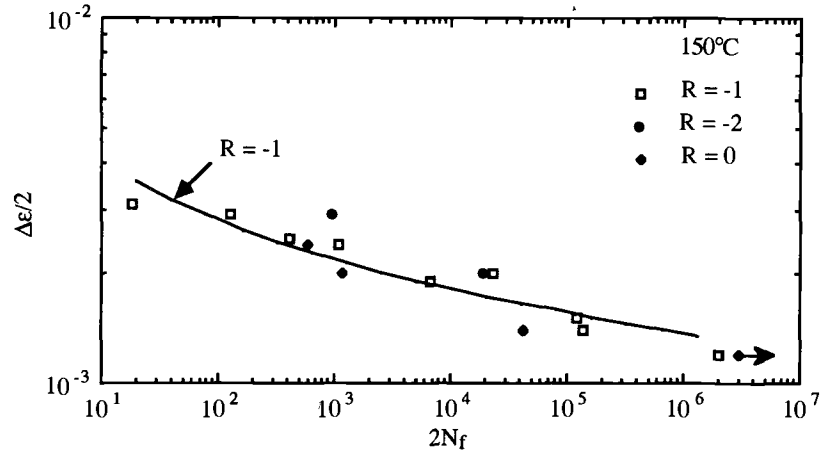

FIG. 9—*Low-cycle fatigue behavior of the metal matrix composite at 150°C;* R = *−1, 0, and −2.*

temperature and 150°C. Region III, corresponding to very fast fatigue crack growth, was much harder to identify due to difficulties in visual crack extension measurements at such high growth rates. In general, the fatigue crack growth rate *da/dN* ranged between 10^{-10} and 10^{-6} m/cycle for all the tests performed.

The expression for the stress intensity factor range ΔK for this C(T) specimen geometry ($H/W = 0.60$) was the same as in ASTM E 647-88a. Figures 10 and 11 represent all specimen *da/dN*-ΔK data for $R = 0.05$ and 0.50 at room temperature and 150°C, respectively. Data were obtained using either the five-point incremental polynomial method in the case of constant load amplitude tests or using the secant method in the case of load-shedding tests (ASTM E 647-88a). Definite load ratio, R, effects can be seen: larger R values caused an increased fatigue crack growth rate. Room temperature fatigue crack growth behavior of the matrix with $R = 0.1$ and 0.5 [*2*] is represented by the lines in Figs. 10 and 11 for comparison. Some scatter in the composite data is present, with the greatest scatter occurring in Region II for $R = 0.05$ at both temperatures. This is probably because more specimens were tested with $R = 0.05$ than with $R = 0.50$. Reasons for the scatter can be attributed to the relatively coarse microstructure of the material, erratic crack growth—especially during the first few millimetres, and difficulties monitoring the crack tip location. The stress intensity factor at fatigue fracture, K_{fc}, was estimated from the data for $R = 0.05$ to be about $K_{fc} = 11$ MPa$\sqrt{\text{m}}$ at both temperatures. In general, K_{fc} is not equal to K_{Ic} [*9,10*], and K_{fc} for this composite material was lower than the room temperature K_{Ic} value of 16.5 MPa$\sqrt{\text{m}}$ [*5*]. For comparison, the room temperature plane-strain fracture toughness K_{Ic} value of the unreinforced matrix A356-T6 was 17.4 MPa$\sqrt{\text{m}}$ [*2*].

One specimen at room temperature and two at 150°C were used for ΔK_{th} determination. The MMC ΔK_{th} values are given in Table 3 along with the matrix values for comparison. The MMC room temperature ΔK_{th} for $R = 0.05$ is higher by 10% than the value at 150°C, while the room

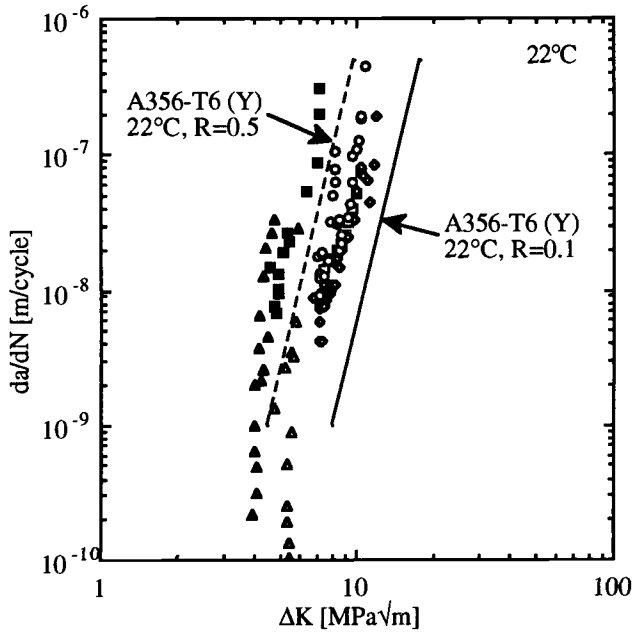

FIG. 10—da/dN-ΔK *data for the metal matrix composite at room temperature; open symbols* R = *0.05, full symbols* R = *0.50.*

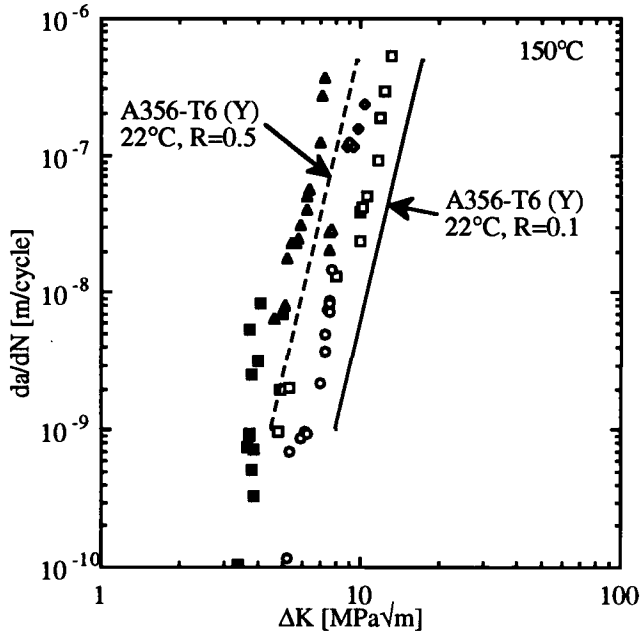

FIG. 11—da/dN-ΔK *data for the metal matrix composite at 150°C; open symbols* R = *0.05, full symbols* R = *0.50.*

temperature ΔK_{th} for 0.5 is higher by 15% than the value at 150°C. The MMC room temperature ΔK_{th} for $R = 0.05$ is lower by 16% than the corresponding matrix ΔK_{th} value and about the same for $R = 0.50$.

The Region II data points were curve-fit using log-log linear regression analysis with the Paris equation

$$\frac{da}{dN} = A(\Delta K)^m \tag{4}$$

The coefficients A and m were calculated for each R ratio and each operating temperature from all specimen *da/dN-ΔK* plots. Correlation coefficients for the linear regression were between

TABLE 3—*Paris equation parameters and threshold values of the metal matrix composite and the matrix material A356-T6 (MPa√m and m/cycle).*

Material	Temperature, °C	R	A	m	ΔK_{th}, MPa√m	$(\Delta K_{th})_{eff}$, MPa√m
Composite	22	0.05	$2.2 \cdot 10^{-13}$	5.4	5.2	3.0
	22	0.50	$4.7 \cdot 10^{-13}$	6.5	3.7	3.7
Composite	150	0.05	$3.8 \cdot 10^{-14}$	6.3	4.7	3.1
	150	0.50	$8.0 \cdot 10^{-13}$	6.1	3.2	3.2
A356-T6[a]	22	0.1	$5.4 \cdot 10^{-17}$	8.0	6.2	3.0
	22	0.50	$7.0 \cdot 10^{-15}$	7.9	3.6	3.6

[a] Data from Ref 2, Material Y.

0.70 and 0.80. The values of the A and m coefficients for the MMC are given in Table 3, together with those for the matrix for comparison. The MMC showed two to four orders of magnitude increase in A values and about 30% decrease in m values at room temperature when compared to the respective matrix values. Increased room temperature crack growth rates of the composite compared to the room temperature matrix values are seen in Fig. 10. About an order of magnitude decrease in A values with a slight increase in m values from room temperature to 150°C were obtained.

Crack opening loads (P_{op}), necessary for crack closure studies, were obtained in both Regions I and II. Crack opening and closing loads were approximately the same. Also, a negligibly small hysteresis was observed. The opening load was determined at the intersection of the linear portions of P-COD or P-BFS curves. No crack closure was observed for $R = 0.50$, based on the P-COD measurements performed. In Region I, the P_{op} values ranged from 45 to 60% of P_{max} at room temperature and from 40 to 50% at 150°C. In Region II, the percentage was estimated to be between 20 and 60% at room temperature, and between 20 and 50% at 150°C. The overall scatter in P_{op}/P_{max}-ΔK data at both temperatures was large and was attributed to difficulties in P_{op} measurements. Slightly smaller closure effects were obtained at 150°C compared to room temperature values. It can be concluded that crack closure is of greater importance in Region I compared to Region II at both temperatures.

The P_{op} value was used to determine the crack opening stress intensify factor, K_{op}, from which an effective stress intensity factor range was defined as

$$\Delta K_{eff} = K_{max} - K_{op} \tag{5}$$

Figures 12 and 13 represent superimposed da/dN-ΔK_{eff} data with $R = 0.05$ and 0.50 for room temperature and 150°C, respectively. The opening load was not measured as frequently as the crack length during testing, which is the reason for the smaller number of data points in Figs. 12 and 13 compared to Figs. 10 and 11. Since no closure was observed for $R = 0.50$, ΔK_{eff} and ΔK are the same for this load ratio. It can be seen from the figures that crack closure can account for the load ratio effects in Region II at both temperatures, while for room temperature in Region I, the ΔK_{eff} data for $R = 0.05$ tend to overshoot the $R = 0.50$ data. This is attributed to inherent difficulties in obtaining accurate P_{op} values and/or insufficient COD gage sensitivity.

Effective ΔK_{th} data with $R = 0.05$ for both temperatures were obtained using the secant method. Only three and two data points between 10^{-9} and 10^{-10} m/cycle were obtained at room temperature and 150°C, respectively, and hence these results are insufficient. Estimated values of ΔK_{eff} are given in Table 3. They are similar to $R = 0.50$ values at 150°C, but lower by about 20% at room temperature. The difference, however, is negligible, keeping in mind the difficulties in P_{op} measurements and the limited data.

Variable Amplitude Loading Fatigue Life Data

Six keyhole specimens were used for variable amplitude loading tests at room temperature and seven at 150°C. The specimens were set up on the testing machine using fork-type three-bolt grips that were secured to precision monoball-type connectors with pins which allowed for free rotation of the specimens. The setup eliminated clamping load problems, allowed for both tension and compression loading, and reduced slack between the grips and the specimens. Fatigue crack lengths were measured visually at both room and elevated temperatures using the same equipment and procedures as for the fatigue crack growth tests. The test frequencies were between 3 and 10 Hz at both temperatures.

Variable amplitude loading tests were performed using the digital controller that was software manipulated from a desktop IBM PC compatible computer. The variable amplitude loading

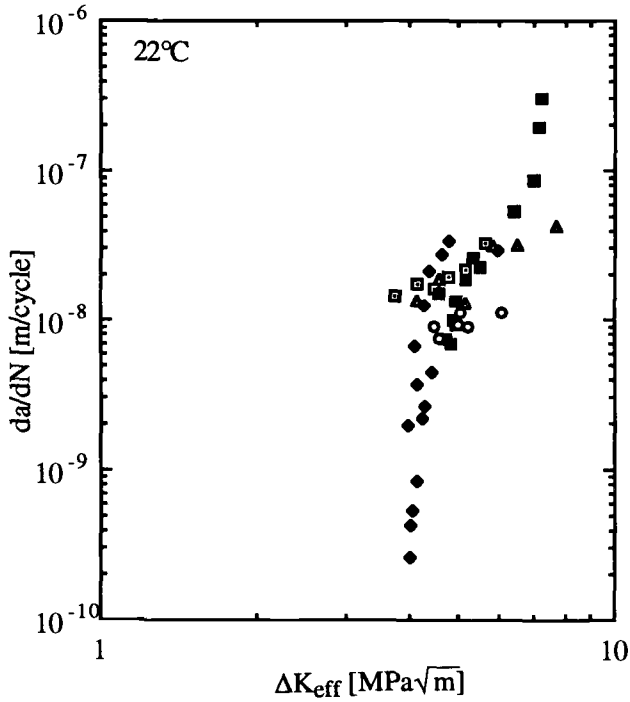

FIG. 12—da/dN *versus* ΔK_{eff} *for the metal matrix composite at room temperature; open symbols* R = *0.05, full symbols* R = *0.50.*

history employed was the altered Skidder history used in Ref *3*. It contained 41 912 reversals and was normalized such that the maximum amplitude was assigned a value of 1000. The loading history was designed to have a substantial number of cycles at intermediate amplitude levels to better distribute fatigue damage. It was rainflow counted using a commercially available software package [*7*]. The rainflow amplitude histogram for the normalized history is given in Fig. 14.

Three different load-scaling factors were used with this normalized load history in an attempt to produce short, intermediate, and long fatigue test lives. These three load-scaling factors corresponded to maximum peak loads of 6.2 (Level 1), 5.3 (Level 2), and 4.4 kN (Level 3), resulting in nominal net stresses at the notch roof of the keyhole specimens of 123, 105, and 87 MPa, respectively.

A two-dimensional, plane stress, elastic finite element (FE) analysis was performed using a general purpose FE software package to obtain the stress concentration factor, K_t, for the keyhole specimen. It resulted in a value of K_t = 3.1. The theoretical elastic stress at the notch root would be K_t = 3.1 times the nominal value or 381, 326, and 270 MPa, respectively. These values were expected to cause local cyclic plastic yielding at the notch root.

Fatigue cracks initiated in the specimen notch root in several places along the specimen thickness. The fronts of fatigue cracks longer than 1.5 mm were essentially straight in all specimens. Specimen fracture surfaces were flat and in a single horizontal plane in all cases.

The total fatigue life in terms of blocks to failure was separated into crack initiation life (defined as the number of loading blocks needed to grow a crack 1.5 mm in length) and crack growth life (from a 1.5-mm crack length to final fracture). The crack growth life for all spec-

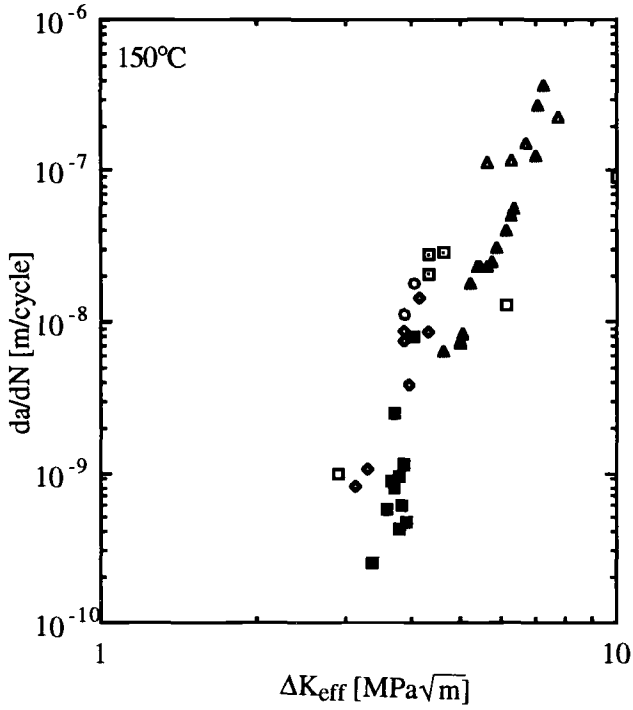

FIG. 13—da/dN *versus* ΔK_{eff} *for the metal matrix composite at 150°C; open symbols* R = *0.05, full symbols* R = *0.50.*

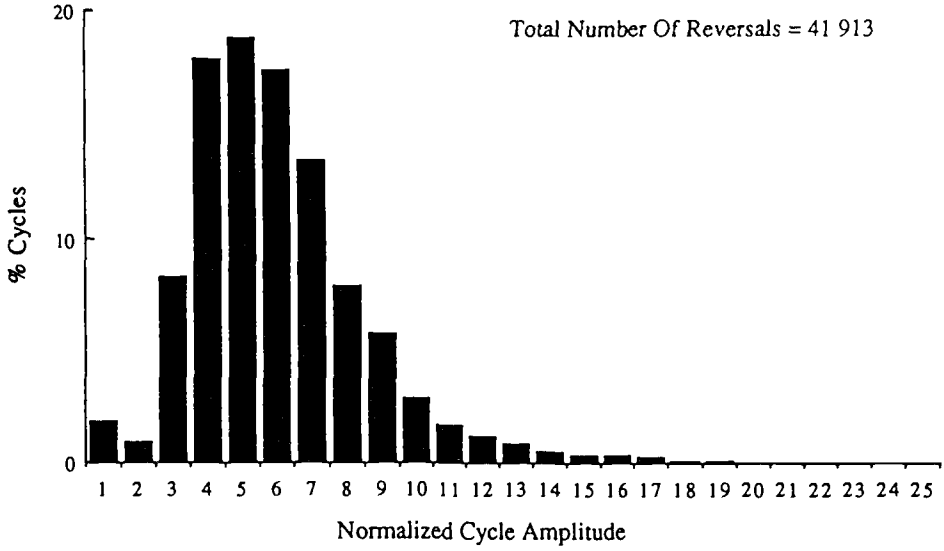

FIG. 14—*Load amplitude histogram for normalized Skidder history [3].*

imens was fairly short, ranging from 13 to 19% of the total life at room temperature and from 6 to 34% at 150°C. Remarkably small scatter (less than 10%) in initiation life and total life results was obtained at room temperature, while it was somewhat larger at 150°C. The small magnitude of scatter is partially attributed to just duplicate or triplicate tests. The initiation and total lives at room temperature were approximately twice those obtained at 150°C.

Table 4 presents averaged variable amplitude loading fatigue life data for the composite and gives the data for the matrix [*3*] for comparison purposes. The comparison, however, cannot be one to one, i.e., the obtained variable amplitude loading fatigue lives for the composite and the matrix cannot be compared directly because of the differences in the specimen geometries and load levels used. Rather, the ratio of fatigue crack initiation life versus total life was used for comparison. This ratio was between 25 and 50% in the room temperature matrix tests, while it was between 80 and 90% in the composite tests at both temperatures. Hence, a substantial portion of the composite variable amplitude loading fatigue life was spent on crack initiation (defined as 1.5-mm crack length), while most of the fatigue life of the unreinforced matrix was spent in crack growth.

Fractographic Analysis

For the low-cycle fatigue specimens, scanning electron microscope (SEM) fractographic analysis revealed that at both temperatures fatigue cracks initiated mostly in shrinkage pores and rarely in particle clusters. No particle debonding was observed, suggesting strong interfaces between the matrix and reinforcement. Persistent slip lines, common fatigue crack initiation sites in many unreinforced metals, were not looked for in the composite since the pores and particle clusters represent ideal crack initiation sites. No significant differences between the fracture morphology and mechanisms at room temperature and 150°C were observed. Figure 15 represents a typical fatigue crack initiation site in the metal matrix composite. Fatigue cracks frequently had several initiation sites, especially in specimens tested at low strain amplitudes. A typical crack initiation site at higher magnification is shown in Fig. 16 at room temperature. Some compressive damage of the surface is visible in the figure. Cracks initially grew predominantly through the matrix, although some broken particles were also visible. Their quantity was estimated to be less than the volume fraction of the reinforcement $V_f = 20\%$, thus allowing the conclusion that cracks tend to avoid particles initially. Particle clustering was rarely

TABLE 4—*Variable amplitude loading average test results for the metal matrix composite and the matrix material A356-T6.*

Material	Temperature, °C	Nominal Stress Level, MPa	Total Life, Blocks	Initiation Life, Blocks	Growth Life, Blocks
Composite	22	123	6.6	5.4	1.2
		105	29.0	23.8	5.2
		87	158.2	140.1	18.1
Composite	150	123	3.2	2.6	0.6
		105	16.7	14.6	2.2
		87	58.3	49.0	9.3
A356-T6[a]	22	97	1.2	0.3	0.9
		81	20.8	9.8	11.0
		65	. . .	140.5	. . .

[a] Data from Ref *3*, Material Y.

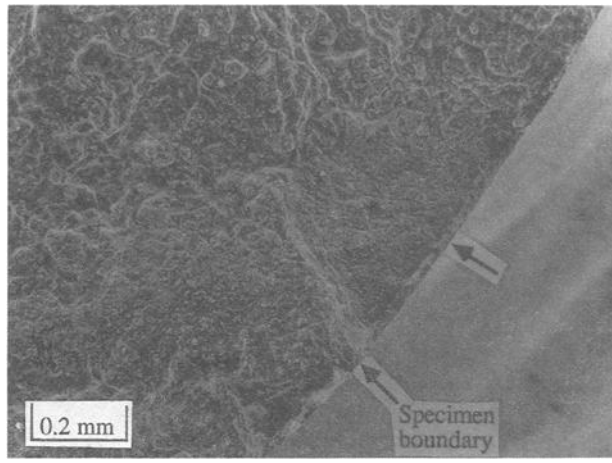

FIG. 15—*Typical fatigue crack initiation site in the metal matrix composite; room temperature test.*

observed, and hence clustering was not considered as a significant contributor to fatigue crack initiation.

For the C(T) specimens, the fatigue crack propagation morphology and mechanisms were similar at both temperatures. At lower ΔK values, fatigue cracks propagated primarily through the matrix, as shown in Fig. 17 for room temperature testing, with a predominantly ductile-type mechanism. Striations in the matrix were rarely visible and only away from particles. Higher ΔK values caused fatigue cracks to propagate through both matrix and reinforcement, cleaving particles ahead of the crack tip. The increasing number of broken particles with increasing ΔK is shown in Figs. 17, 18, and 19 for a room temperature test.

Final fracture surface appearance was similar at both temperatures and is well represented in Fig. 19 for $\Delta K = 10$ MPa$\sqrt{\text{m}}$, which is very close to the final fracture region. Cracks grew through both matrix and reinforcement, leaving a relatively rough fracture surface.

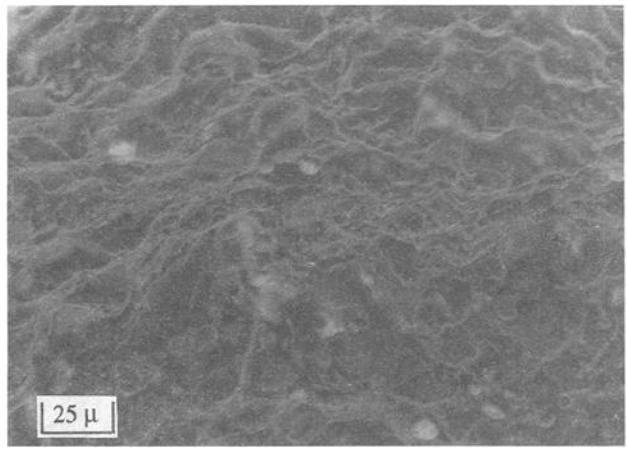

FIG. 16—*Typical fatigue crack initiation site in the metal matrix composite; room temperature test.*

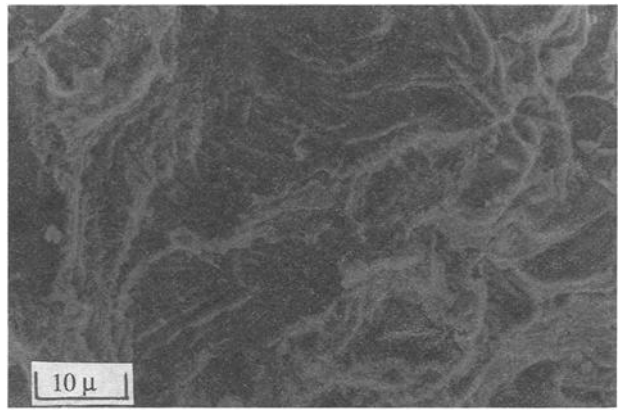

FIG. 17—*Fatigue crack propagation region;* $\Delta K = 5\ MPa\sqrt{m}$*; striations visible; room temperature test.*

Variable Amplitude Loading Fatigue Life Calculations

Fatigue Crack Initiation Life Calculations

The fatigue life of the keyhole specimen was calculated using a two-stage approach, i.e., fatigue crack initiation life and fatigue crack growth life were determined separately and then added to give the total fatigue life. The fatigue initiation life of the keyhole specimen was calculated using the local strain approach [*9,10*]. Over the past two decades of development, this approach has gained widespread use, especially in the ground vehicle industry. It is based on the assumption that the experimental life of smooth, axial, laboratory-tested constant strain amplitude specimens can be related to the fatigue initiation life (i.e., formation of a small macro crack) of a notched component subjected to a variable amplitude loading. The fatigue life associated with the development of a 1.5-mm crack in the keyhole specimen was defined as the fatigue crack initiation life.

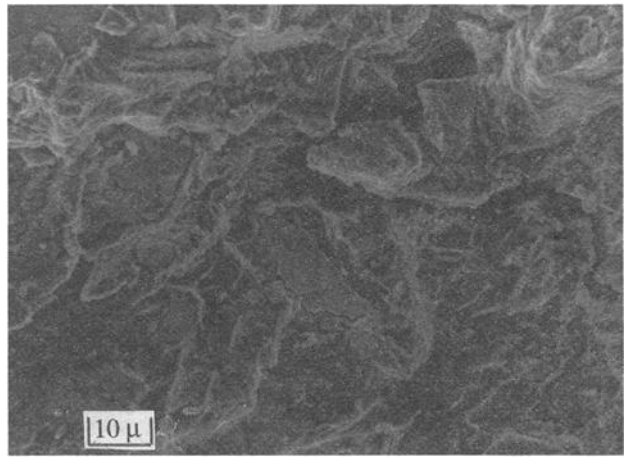

FIG. 18—*Fatigue crack propagation region;* $\Delta K = 8\ MPa\sqrt{m}$*; room temperature test.*

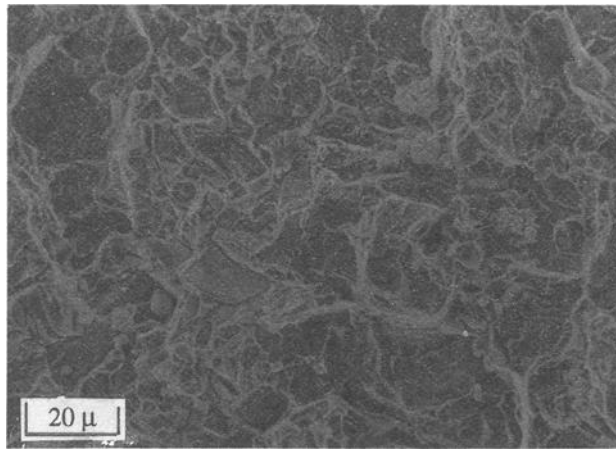

FIG. 19—*Fatigue crack propagation region;* $\Delta K = 10\ MPa\sqrt{m}$*; room temperature test.*

The local strain approach consists of first approximating the notch root stress and strain response using one of the available models, e.g., Neuber [*9,10*] or Glinka rules [*11*]. After that, the number of cycles to failure, N_f, is calculated from the material strain life diagram for the calculated notch root strain amplitude. If the strain amplitude has a nonzero mean value, an appropriate mean stress model needs to be applied to obtain N_f. Two common mean stress models, Morrow and Smith-Watson-Topper (SWT), were used [*9,10*]. Using the linear damage rule [*9,10*], the fatigue damage, D, is obtained as the ratio of the number of applied cycles, N, at the respective strain amplitude, to N_f, or $D = N/N_f$. A variable amplitude loading history is usually cycle counted, e.g., using the rainflow counting procedure [*9,10*], to obtain the total number N of applied cycles at a certain strain level during the loading history. When damages from all strain levels in the history are calculated, the total fatigue damage caused by a single history repetition, D_t, is calculated as the sum of all damages, or $D_t = \Sigma D_i$. Then, if the failure criterion is defined as the sum of damages for all the history repetitions being equal to one [*9,10*], the number of the history repetitions to failure can be calculated as $1/D_t$.

All the above-mentioned calculations necessary to obtain the number of variable history repetitions to initiate a 1.5-mm crack (defined as the fatigue life to crack initiation) were performed using the previously mentioned software package [*7*]. The linear damage rule was used throughout, which completely neglects loading sequence effects. Both the Neuber and the Glinka rules for notch root strain approximations and both the Morrow and the SWT mean stress models for mean stress effect approximations were used, so a total of four possible combinations were calculated at each of the three applied load levels. The difference between the calculated results was negligible for a given test temperature.

The results of the variable amplitude loading fatigue crack initiation life calculations for both temperatures and for the elastic stress concentration factor $K_t = 3.1$ are given in Fig. 20 as open or closed squares. Only the combination of Neuber rule and Morrow mean stress model is presented. About an order of magnitude conservative difference between the calculations and experimental results was obtained for room temperature. Overly conservative calculations, of almost two orders of magnitude, were obtained for 150°C.

A question of the validity of using the K_t value in a fatigue analysis needs to be addressed here. As stated in Refs *9* and *10*, the fatigue strength of a notched component could be predicted as the fatigue strength of a smooth component divided by the elastic stress concentration factor

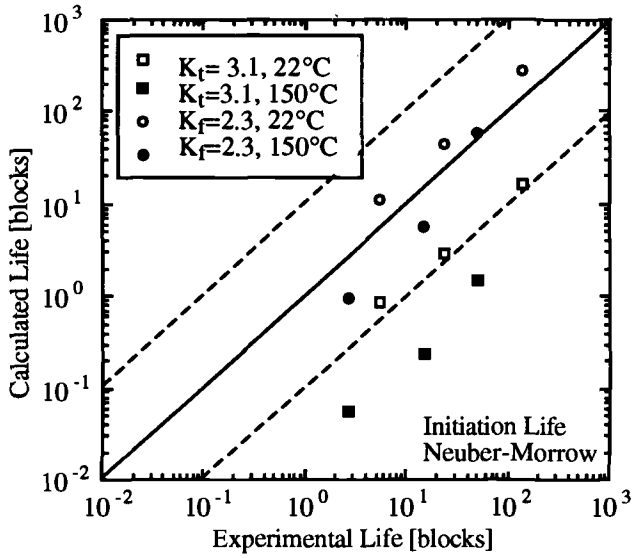

FIG. 20—*Variable amplitude loading fatigue crack initiation life calculations versus experimental results.*

K_t. Experimental results, however, are frequently different [*9,10*], for example when the ratio of smooth and notched component fatigue strengths is not equal to K_t. The ratio is then defined as the fatigue notch factor, K_f. The difference between K_t and K_f can be used to define a fatigue notch sensitivity factor of the material [*10*]

$$q = \frac{K_f - 1}{K_t - 1} \tag{6}$$

In the case of the unreinforced matrix material with $K_t = 3.4$, q was estimated to be 0.625 [*3*], meaning that the matrix is less notch sensitive than predicted by elastic analysis. Assuming for the purposes of comparison that the notch sensitivity factor q of the composite with K_t = 3.1 is equal to the matrix value, the fatigue notch factor of the composite can be calculated as $K_f = 2.3$. The results obtained using this K_f value in the fatigue initiation life predictions are presented in Fig. 20 as open or closed circles. A factor of two to three difference between calculations and experimental results was obtained for both temperatures, but the calculations were slightly nonconservative for room temperature. The above analysis shows the importance of adopting the correct fatigue notch factor in fatigue life prediction analysis. However, proper experimental determination of K_f is hard to perform [*3*]. For some steels K_f is obtained from empirical formulas [*9,10*], but they do not exist for unreinforced aluminum alloys or aluminum composites.

Fatigue Crack Growth Life Calculations

The fatigue crack propagation life was defined as the number of repetitions of the variable amplitude loading history necessary to grow the fatigue crack from the defined 1.5-mm initi-

ation length to final fracture. The calculations were based on a linear elastic fracture mechanics (LEFM) model that relates fatigue crack growth rate, *da/dN*, and stress intensity factor range, $\Delta K = K_{max} - K_{min}$. One commonly used model is the Paris equation [*9,10*], Eq 4. The coefficients A and m were obtained from constant amplitude fatigue crack growth tests and are given in Table 3. The expression for stress intensity factor range, ΔK, for the keyhole specimen geometry ($H/W = 0.49$) is given in Ref *6*. It was derived for a C(T) specimen. The underlying assumption for its use with the keyhole specimen is that after the 1.5-mm crack extension, the crack tip does not "feel" the stress-strain field caused by the presence of the notch [*9,10*]. From the rainflow counted loading history, numerical integration of Eq 4 with the ΔK expression leads to the number of cycles N from initial to final crack length, from which the number of loading history repetitions to fracture can be calculated. No interaction effects were incorporated in the analysis.

Fatigue crack growth life analysis that incorporates crack closure effects can be performed with the software used. It is approximate in the sense that it does not calculate closure on a cycle-by-cycle basis. The program uses an average opening load as a percentage of the maximum load in a load history. Also, the program recalculates the given Paris equation coefficient A for $R = 0.05$, to account for the effective ΔK influence [*10*]. The average opening load at room temperature was estimated as 40% of the maximum load in the history of any of the three load levels used and as 35% at 150°C. Detailed discussion on how the program performs the calculations with and without closure effects is given in Refs *3* and *7*.

Figure 21 presents fatigue crack growth life calculations at room temperature and 150°C. These calculations are for no closure effects and for closure effects with the opening load being 40 and 35% of maximum load in the load history at room temperature and 150°C, respectively. The calculations are unconservative by a factor of three to nine at both temperatures. Closure effects increased the magnitudes of calculated lives by approximately a factor of two at both temperatures.

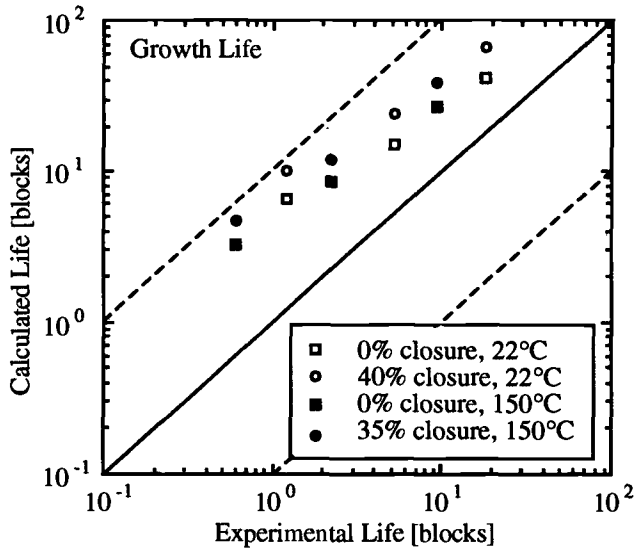

FIG. 21—*Variable amplitude loading fatigue crack propagation life calculations versus experimental results.*

Total Fatigue Life Calculations

Figure 22 presents total fatigue life calculations (obtained by summing the initiation and growth life predictions) with $K_t = 3.1$ and $K_f = 2.3$ and zero crack closure versus experimental results at both temperatures. Crack closure effects were not incorporated in the calculations since they led to more unconservative fatigue crack growth life results than in the case when they were neglected completely. Scatter of about a factor of five can be seen in Fig. 22 at both temperatures, with both conservative and unconservative results. Slightly better calculations were obtained for both temperatures using the elastic stress concentration factor $K_t = 3.1$ instead of the fatigue notch factor $K_f = 2.3$. The difference at 150°C, however, is considered negligible. The calculations for room temperature were conservative if $K_t = 3.1$ was used and unconservative if $K_f = 2.3$ was used. Similar behavior was observed for 150°C, but with less scatter.

Summary and Conclusions

The experimental monotonic stress-strain behavior of the metal matrix composite showed substantial scatter in fracture strains at room temperature and in the elastic modulus values at 150°C. Room temperature yield and ultimate tensile strengths were higher than the respective matrix values. The composite retained strength values with increasing temperature much better than the unreinforced matrix, which gives a distinct advantage to the composite over the unreinforced matrix for high-temperature applications. Also, the composite elastic modulus values were about 45% higher at both temperatures than the room temperature matrix value.

Constant amplitude low-cycle fatigue tests revealed that the room temperature fatigue lives of the composite were shorter than the respective matrix values. The fatigue lives at high strain amplitudes were shorter at 150°C than at room temperature, but the difference decreased with decreasing strain amplitude. Positive mean stresses had small influence on the composite constant strain amplitude fatigue lives at room temperature and even smaller at 150°C.

Room temperature fatigue crack growth rates were higher in the composite than in the matrix by about an order of magnitude. The rates in the composite were about the same at both

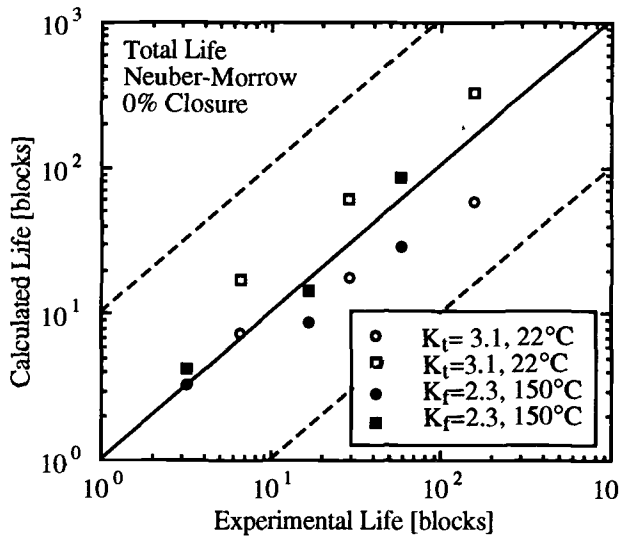

FIG. 22—*Variable amplitude loading total fatigue life calculations versus experimental results.*

temperatures. Increasing the load ratio, R, from 0.05 to 0.50 caused increasing fatigue crack growth rates. Room temperature composite values, ΔK_{th}, were lower by 16% than the matrix values, and they decreased with increasing temperature from room temperature to 150°C by about 10%. Crack closure effects were pronounced for $R = 0.05$, especially in Region I, and were somewhat more pronounced at room temperature than at 150°C.

Variable amplitude loading tests were performed at both temperatures with between 7 and 160 load history repetitions to fracture at room temperature and between 3 and 80 at 150°C. Variable amplitude loading fatigue initiation lives accounted for more that 80% of the total fatigue lives at room temperature and more than 65% at 150°C.

Fractographic analysis revealed that shrinkage porosity was a common crack initiation site. It was observed that cracks initiate and propagate predominantly through the matrix in the low-cycle fatigue specimens. In the C(T) specimens, fatigue cracks propagated preferably through the matrix at low ΔK values, but as ΔK values increased the cracks propagated through both the matrix and the reinforcement with no preferred paths.

Variable amplitude loading fatigue initiation life calculations using a commercially available software package and the elastic stress concentration factor were conservative by almost an order of magnitude at room temperature and by almost two orders of magnitude at 150°C. The calculated results were substantially improved by using the assumed empirical fatigue notch factor, but they tended to be slightly unconservative at room temperature. Fatigue crack growth life predictions were unconservative by almost an order of magnitude at both temperatures. Slightly better results were obtained if no closure effects were incorporated in the calculations. Total fatigue life calculations were closer to experimental results at both temperatures if the elastic stress concentration factor was used. Then they differed from the experimental results by about a factor of three at both temperatures. Thus both reasonable and unreasonable fatigue life predictions should be anticipated with this metal matrix composite using commercially available life prediction software.

References

[1] Taya, M. and Arsenault, R. J., *Metal Matrix Composites. Thermo-Mechanical Behavior,* Pergamon Press, New York, 1989.

[2] Stephens, R. I., Ed., "Fatigue and Fracture Toughness of A356-T6 Case Aluminum Alloy," SAE Special Publication SP-760, Society of Automotive Engineers, Warrendale, PA, August 1988.

[3] Lease, K. B., "Verification of Variable Amplitude Fatigue Life Methodologies for a Cast Aluminum Alloy," SAE Technical Paper 910163, Society of Automotive Engineers, Warrendale, PA, 1991.

[4] Lease, K. B. and Stephens, R. I., "Fatigue of A356-T6 Cast Aluminum Alloy Under Variable Amplitude Loading," *Proceedings,* Fourth International Conference on Fatigue and Fatigue Thresholds, Fatigue 90, 1990, pp. 151–157.

[5] Klimowicz, T., Duralcan Co., manufacturer's documentation and private communication, 1990.

[6] Wessel, E. T., "State of the Art of the WOL Specimen for K_{Ic} Fracture Toughness Testing," *Engineering Fracture Mechanics,* Vol. 1, 1968, pp. 77–103.

[7] LifEst Software User's Manual, SoMat Corporation, 1988.

[8] "Aerospace Structural Metals Handbook," Vol. 3, Air Force Materials Laboratory, Mechanical Property Data Center, Belfour Stulen, Inc., 1991.

[9] Fuchs, H. O. and Stephens, R. I., *Metal Fatigue in Engineering,* Wiley Interscience, New York, 1980.

[10] Bannantine, J. A., Comer, J. J., and Handrock, J. L., *Fundamentals of Metal Fatigue Analysis,* Prentice Hall, Englewood Cliffs, NJ, 1990.

[11] Glinka, G., "Energy Density Approach to Calculation of Inelastic Strain-Stress Near Notches and Cracks," *Engineering Fracture Mechanics,* Vol. 22, No. 3, 1985, pp. 485–508.

R. Craig McClung[1] *and Robert S. Alwitt*[2]

Thermal Fracture and Fatigue of Anodized Aluminum Coatings for Space Applications

REFERENCE: McClung, R. C. and Alwitt, R. S., **"Thermal Fracture and Fatigue of Anodized Aluminum Coatings for Space Applications,"** *Cyclic Deformation, Fracture, and Nondestructive Evaluation of Advanced Materials: Second Volume, ASTM STP 1184,* M. R. Mitchell and O. Buck, Eds., American Society for Testing and Materials, Philadelphia, 1994, pp. 156–177.

ABSTRACT: A concern for the use of anodized aluminum as Space Station thermal control surfaces is the potential degradation of critical optical properties due to oxide coating cracking. This cracking may be induced by differential thermal expansion during hot adhesive bonding of the radiator assembly or during 30 years of exposure to sunlight/darkness cycles in low earth orbit (LEO). This paper summarizes investigations into the effects of temperature and humidity on coating stresses and cracking. Experimentally measured coating residual stresses after anodizing and sealing are shown to be strongly dependent on humidity. Two sets of tests are used to study cracking directly: one determines the temperature (T_c) at which cracks first appear during a single heating cycle, while the other involves rapid thermal cycling (RTC) between maximum and minimum temperatures. The effects of several test parameters on cracking are reviewed, with special attention to temperature, coating thickness, and humidity. Fatigue models are developed to describe the observed cracking and to serve as the basis for predictions of LEO cracking. The physical characteristics of cracks and related substrate plastic deformation in both T_c and RTC tests are discussed briefly.

KEYWORDS: anodized aluminum coatings, low earth orbit, humidity, stress, thermal fatigue, fracture, cracks, life prediction

Thermal control is a key design issue for Space Station. Thermal control surfaces, such as radiator panels, are required to maintain critical solar absorptance and thermal emittance properties for 30 years in a severe space environment characterized by atomic oxygen exposure, ultraviolet (UV) radiation, micrometeoroid impact, and thermal cycling. One of the leading candidates for these surfaces is a 0.5 to 1.0-mil (12.5 to 25-μm)-thick sulfuric acid anodized oxide coating on aluminum alloy sheet. A particular concern for the anodized aluminum is the potential degradation of optical properties due to cracking caused by differential thermal expansion of the substrate and coating. This cracking can occur both during the hot adhesive bonding step in radiator fabrication and during 30 years of exposure to 90-min sunlight/darkness thermal cycles in low earth orbit (LEO).

This paper summarizes the results of a joint experimental-analytical program on the fracture and fatigue behavior of anodized aluminum coatings. Two sets of experiments were used to study coating cracking during thermal excursions. The first set studied cracking during a single thermal cycle, identifying the minimum temperature (T_c) at which cracks first began to appear in the coating. The second set of tests involved so-called "rapid thermal cycling" (RTC)

[1] Group leader, Southwest Research Institute, PO Drawer 28510, San Antonio, TX 78228-0510.
[2] President, Boundary Technologies Inc., 366 Lexington Dr., Buffalo Grove, IL 60089.

between minimum and maximum temperatures at rates which were accelerated relative to LEO conditions. Fatigue models were developed to describe the observed cracking and to serve as the basis for predictions of LEO cracking. The investigations have been documented in greater detail elsewhere [*1*].

Anodizing is an electrochemical process in which the surface of an aluminum alloy is oxidized to form an aluminum oxide coating of uniform thickness [*2*]. A characteristic structural feature is a microporosity introduced by the dissolving power of the acid anodizing bath. The pores are aligned normal to the surface and arranged in a roughly hexagonal cellular pattern. Typical dimensions of this structure for coatings considered here are 15 nm pore diameter and 42 nm cell diameter, corresponding to about 13% pore volume and a pore density of 8×10^{10} cm^{-2}. The protective qualities of the oxide are remarkably improved by a "sealing" step following oxidation, in which (most commonly) the anodized metal is immersed in hot water and the oxide reacts to form a hydrated oxide. Since the reaction product has a lower density than the anodic oxide, sealing causes a substantial reduction in porosity and actually closes off most of the columnar pores.

Substrates used in most of the study were 25-mil (0.635-mm)-thick Al 5657 alloy in the H25 or H242 temper, 10-mil (0.254 mm) Al 5657-H28, 12-mil (0.305 mm) Al 3002-H18, and 25-mil Al 3002-H25. The substrates were first chemically polished in a mixture of concentrated nitric and phosphoric acids at 97°C, which removed about 0.5 mil (12.5 μm) of metal from each surface. Anodizing was typically in 20% sulfuric acid at 22°C and 15.0 V, resulting in an average current density of 15.2 mA/cm^2. Anodizing time was adjusted to get nominal coating thicknesses of 0.5 mil (12.5 μm) and 1.0 mil (25 μm). Sealing was in 95°C water for 5 or 20 min.

Coating Stresses

A key step in the development of fracture and fatigue models is the accurate evaluation of coating stresses under both test and application conditions. The stress in the coating at some elevated temperature is the sum of a residual growth stress at ambient (room) temperature (RT) and a thermal stress induced by differential thermal expansion

$$\sigma_c^{max} = \sigma_c^{RT} + \Delta\sigma_c^{thermal} \tag{1}$$

The residual stresses present in the coating at room temperature after the anodizing, hot water sealing, and drying processes have been evaluated experimentally using classical bent strip analysis. The coating elastic modulus and coefficient of thermal expansion have also been determined experimentally, permitting calculation of stress changes due to differential thermal expansion. Complete details have been published separately [*3*], and only a brief summary is given here.

The coating stress after anodization was always tensile, typically around 15 to 30 MPa (2 to 4 ksi), and was independent of substrate and coating thickness. Immersion in hot water for the seal reaction initially caused a large tensile stress in the coating due to the large difference in thermal expansion coefficients, but as the seal reaction continued this stress was greatly reduced. After drying at ambient temperature and humidity, the sealed stress was always compressive, typically around 20 to 50 MPa (3 to 7 ksi), and this compressive stress increased with increasing seal time. Upon exposure to dry air, the oxide stress first became less compressive and then shifted to tensile. The magnitude of the final residual stress at room temperature depended strongly on humidity, as shown in Fig. 1. Limited measurements (not shown on Fig. 1) in vacuum found that coating stresses were similar to measured values at <0.025 ppm water. Although precise measures of humidity were not available in the driest air atmospheres and

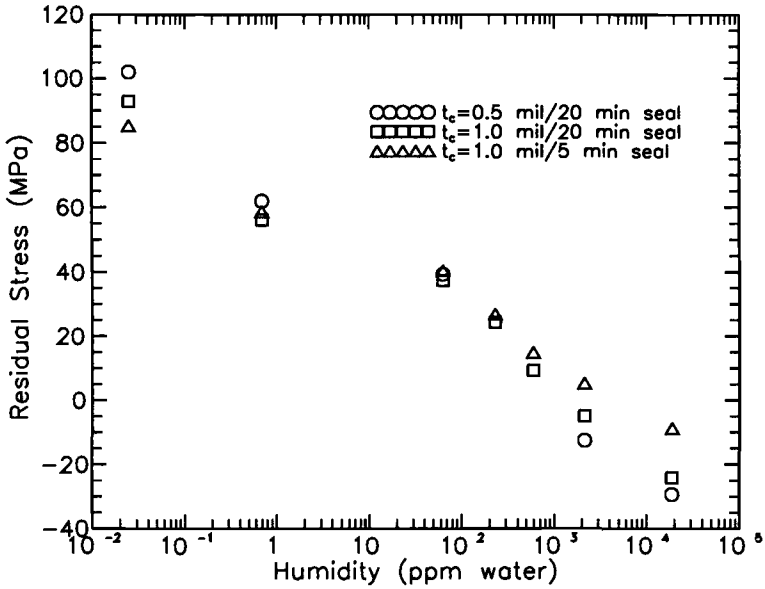

FIG. 1—*Effect of humidity on room temperature residual coating stress.*

corresponding stresses were still increasing very slowly when testing was terminated after several weeks, there appears to be an approximately linear relation between residual coating stress and log humidity over a wide range of moisture content, perhaps reaching limiting values at the extremes. Specimens could be cycled between ambient and dry humidities with reversible changes in stress, although stresses took much longer to stabilize during drying than during reexposure to ambient. Further discussions of the possible reasons for these phenomena are given in Ref *3*.

The thermal stresses induced in the coating by heating of a coupon which is constrained against bending (e.g., anodized on both sides or bonded to a radiator assembly) are given by [*4*]

$$\Delta\sigma_c^{\text{thermal}} = \frac{E_s(\alpha_s - \alpha_c)\Delta T}{(1 - \nu_s)(m + 1/n)} \tag{2}$$

where $m = t_c/t_s$ and $n = [E_c(1 - \nu_s)]/[E_s(1 - \nu_c)]$. Here E is elastic modulus, t is thickness, α is the thermal expansion coefficient, ν is Poisson's ratio, and the subscripts "s" and "c" denote substrate and coating.

Use of this equation requires information about α_c, ν_c, and E_c. These values are not necessarily the same as for the coating material in bulk form, and they were not available in the literature for this particular coating type, so experimental determination was necessary. Measurements of α_c were conducted by dilatometry on 1-mil (25-μm)-thick anodic oxide coupons which had been isolated by chemically dissolving the aluminum substrate [*1*]. The coefficient of thermal expansion was determined to be approximately 4×10^{-6} °C^{-1}, which is close to that for bulk alumina and which is a factor of five less than the thermal expansion coefficient for the aluminum substrate. Poisson's ratio for the coating was chosen to be 0.28, the average of several reported values for polycrystalline bulk alumina, since small variations in ν_c have a negligible impact on calculated stresses. The mechanics relationships between coating stress

and bent strip deflection which were exploited in the bent strip measurements of stresses developed in processing made it possible to calculate the coating modulus from strip deflections at different temperatures [*3,4*]. The biaxial modulus, $E_c/(1 - \nu_c)$, was constant over a range of humidities from 0.01 to 100 ppm water with an average value of 107 GPa (15 500 ksi). For $\nu_c = 0.28$, this implies $E_c = 77$ GPa, which is close to the value for the aluminum substrate. At higher humidities, including ambient atmospheres, the calculated modulus value was significantly higher (E_c around 138 GPa). Careful investigations suggested, however, that measured values of bent strip deflection in ambient atmospheres at high temperatures were also influenced by stress components due to water loss and therefore did not lead to a true modulus measurement. Nevertheless, the "effective" modulus calculated was still found to be a valid and useful tool for calculating total stress changes during heating in ambient atmospheres.

All mechanics equations used here characterize coating stress as the average stress across the thickness of the coating and neglect any possible stress gradients. In order to determine if significant stress gradients were present, isolated oxide coupons were prepared as described above and subjected to different temperatures and humidities. Even a small stress gradient, if present, would cause noticeable curling of the isolated oxide. If we assume a simple linear stress gradient (from $-\sigma_{max}$ to $+\sigma_{max}$) across the oxide thickness, then the magnitude of σ_{max} can be estimated from

$$\sigma_{max} = \frac{4E_c t_c z}{l^2(1 - \nu_c)} \tag{3}$$

where l is the length of the isolated oxide, and z is the measured midsection deflection. Any nonzero average coating stress (as discussed above) occurs due to reactions against the substrate, and hence is lost when the substrate is dissolved.

All sealed and unsealed coatings exhibited zero or negligible curvature at ambient temperature and humidity, indicating negligible stress gradients. Sealed coatings did, in general, exhibit measurable curvature at higher temperatures (T_{max} = 65 to 120°C) under ambient humidity, or at ambient temperatures under low humidity (5 to 20 ppm). Estimated stress gradients at the highest temperatures or lowest humidities were typically on the order of σ_{max} = 1 to 15 MPa (0.2 to 2 ksi) for 0.5-mil coatings and 10 to 40 MPa (1.5 to 6.0 ksi) for 1.0-mil coatings. Estimated stresses in two 2.0-mil (51-μm) coatings heated to around 95°C were as high as σ_{max} = 100 MPa (15 ksi). There does appear, therefore, to be a trend towards larger stress gradients in thicker coatings. This may have implications for coating cracking, as will be noted later.

Unfortunately, the scatter from one experiment to the next was large, and so it was not possible to develop a rigorous quantitative characterization of stress gradients which might be included in life models. Fortunately, however, the estimated stress gradients in most tests, especially for 0.5-mil coatings, were less than 15 MPa (usually less than 3 MPa), and these changes in stress were found to be relatively insignificant in comparison to the maximum nominal stresses characteristic of T_c and RTC tests. Even if the slightly larger stresses at the coating surface were responsible for initiating coating cracking, it should still be possible to characterize tendencies for cracking adequately with a measure of the average coating stress. For these reasons, stress gradients were neglected in subsequent analyses.

Coating Cracking

Single Thermal Cycle

Fabrication of the actual radiator assembly involves hot adhesive bonding of large anodized face sheets to an aluminum honeycomb core and the aluminum heat pipes. The current speci-

fications of the radiator subcontractor are to vacuum bag and cure the assembly at 175°C (350 °F) for 90 min in a 45-psi (310 kPa) autoclave. The T_c tests served as a simple simulation of this hot adhesive bonding process, but they also served as a general indicator of cracking tendencies with a possible link to cracking during long-term thermal cycling.

The T_c specimens were flag-shaped aluminum coupons with a 2 by 2 in. (50 by 50-mm) body and a 0.25 by 1.5 in. (6 by 38-mm) handle which had been anodized and sealed on both sides to avoid the large thermal deflections associated with one-sided anodization (as observed in the bent strip tests). Within two days after anodizing, these coupons were placed in an oven (with environmental control, as appropriate) in sets of three and heated in 10°C temperature steps starting at about 100°C. The coupons were held at each temperature for 10 to 15 min and then removed for a visual inspection to count the number of cracks which formed at each subsequent heating step. The temperature at which cracks first occurred on a given coupon was recorded as the cracking temperature, T_c. The test was continued to temperatures above T_c to obtain further information about the number of cracks which formed at each subsequent heating step and to facilitate confirmation of T_c. Most T_c tests were conducted in ambient (uncontrolled) humidities, but a few tests were conducted at controlled dry humidities as low as 5 ppm.

Once cracking initiated, crack density increased with increasing temperature. Sometimes a single crack developed on one coupon at a relatively low temperature, with no further crack development until a substantially higher temperature. These single cracks were discounted as sports, as were cracks which occasionally initiated at coupon corners or visible surface defects.

The average stress in the coating at T_c, denoted as σ_{cr}, was estimated for each test according to Eqs 1 and 2 using the room temperature residual stress and effective modulus values corresponding to the nominal test humidity. Results for σ_{cr}, graphed as a function of coating thickness, are shown in Fig. 2 for tests at ambient humidity. The lowest σ_{cr} values shown in Fig. 2 correspond to T_c values on the order of 100°C, while the highest σ_{cr} values represent stress estimates at T = 200°C in tests where cracking had not yet initiated at this temperature. These "run-out" tests were suspended at 200°C due to the development of plastic deformation in the substrate. For reference purposes, note that the estimated cracking stress σ_{cr} for 0.5-mil, 20-min seal coatings on 25-mil Al 5657 at a median T_c of 130°C is about 296 MPa (43 ksi). If we assume that the "true" elastic modulus is given by the low humidity value and define a mechanical failure strain as σ_{cr}/E_c, resulting values generally range from 0.003 to 0.007 and greater. These failure strains are similar to those reported [*5–7*] for sulfuric and chromic acid anodic films of comparable thicknesses.

The data show a general decrease in the fracture stress σ_{cr} with increasing coating thickness. Similar trends have been reported in previous work on a variety of anodized coatings [*6–10*], including other studies of thermal cracking in similar sulfuric acid coatings [*11*]. This phenomenon is not clearly understood. Since coating fracture may be defect controlled, the lower strength associated with thicker coatings could be a classical Weibull "size effect": for a general population of distributed defect sizes, there is a greater chance of finding a larger defect in a larger volume of material. The larger defect would lead to a decreased strength. The observed decreases in strength in our work, however, are larger than can be predicted from simple calculations of Weibull size effects alone. Another possible explanation follows from the observed increase in the stress gradient for thicker coatings at elevated temperatures, noted earlier. The additional increase in tensile stress at the surface of the coating at elevated temperatures for thicker coatings, which is not reflected in these calculations of nominal σ_{cr}, may lead to fracture at lower nominal coating stresses.

Within the scatter of the available data, there appears to be no significant effect of substrate thickness or alloy type (5657 versus 3002) on fracture stress. The primary exceptions to this trend are some of the tests on 10-mil 5657 coupons in which cracking did not occur at temperatures up to 200°C, which are not yet fully understood. Effects of alloy composition are discussed further below. Note that the actual value of T_c does change with substrate thickness

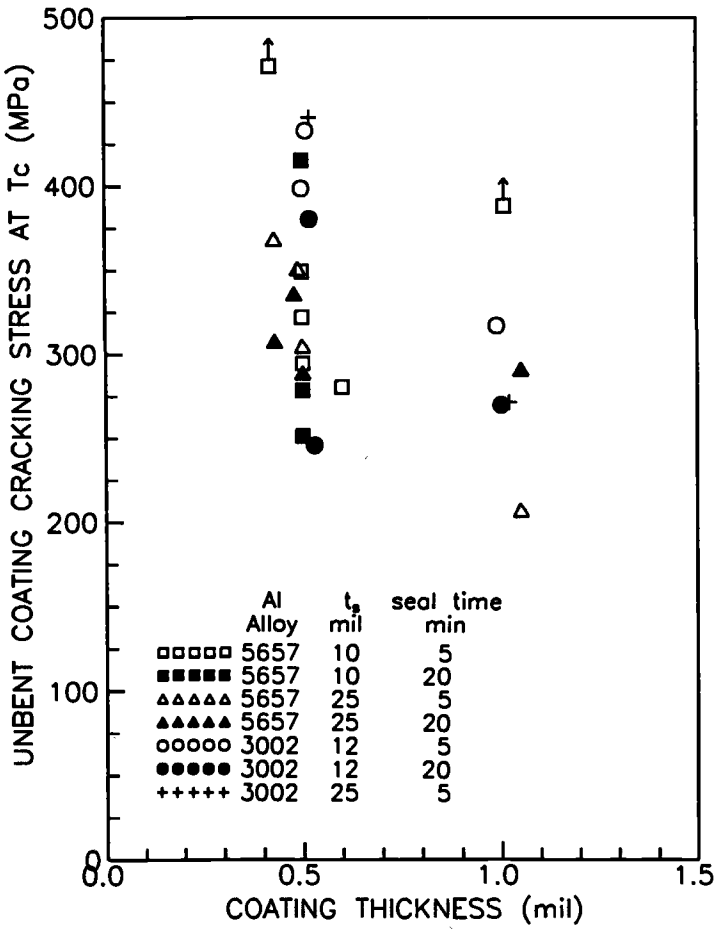

FIG. 2—*Estimated coating stresses at first appearance of cracks in ambient humidity* T_c *tests.*

since thinner substrates allow more stress relaxation in the coating, but the actual cracking stresses in the coatings are roughly the same.

A limited number of T_c tests conducted in humidities as low as 5 ppm water (not shown in Fig. 2) suggested that dry environments had no significant effect on the critical cracking temperature. This seems unlikely at first glance, in view of the large effect of low humidity on residual stresses. Careful studies of weight (water) loss at various temperatures and humidities [*3*] have suggested, however, that at typical T_c temperatures (>100°C) the moisture content of the coating is primarily controlled by the thermal driving force, and the test atmosphere probably has little effect. Then coatings in both atmospheres will have the same water content at each temperature and presumably have the same stress. Estimates of ambient σ_{cr} which employ ambient values of room temperature residual stress and "effective" elastic modulus in fact are similar to σ_{cr} values calculated for dry conditions, possibly because the larger "effective modulus" incorporates the effects of changing water content.

Since anodized sheet will often be stored for long periods prior to adhesive bonding, the effect of T_c on long-term storage in dry and humid environments was evaluated in another series of tests [*12*]. Coupons were stored for about 36 days in either dry, ambient, or humid

(90% relative humidity) environments. After storage, the coupons were removed from the chambers and crack tested in ambient air. Storage in the humid atmosphere had a dramatic effect on cracking tendencies, depressing T_c values and increasing final crack densities significantly. The coupons stored in ambient atmospheres cracked much less heavily than those in wet atmospheres, but both T_c and total cracking performance were significantly degraded from dry coupons. Dry storage coupons performed the same as coupons tested within one day after anodizing.

Another small test series investigated the effects of composition or material condition on cracking [*12*]. One set of tests evaluated the effect of three different tempers on cracking. Instead of determining T_c, the cracking behavior at a typical bonding temperature of 175°C was observed. Crack densities were higher in the softer material, although the crack opening displacement (as described later in the discussion of substrate deformation) decreased significantly in the softer material. A brief set of tests exploring the effects of alloy composition found a lower T_c for 20 mil (0.508 mm) Al 1199-H19 and a higher T_c for one set of Al 6061-T6 coupons (in comparison to 25-mil 5657). One set of Al 1100 coupons did not crack at temperatures up to 200°C. Direct metallographic inspections revealed that the density of second phase intermetallic particles in the coating for all these alloy substrates increased in the same order as increases in T_c, although it is not entirely clear how these two observations might be mechanistically related. Another test series with 4-mil (0.102-mm) Al 1199-O alloy foil also found no cracking up to 200°C, but this can be explained simply by a large decrease in coating stresses due to stress relaxation permitted by the extremely thin substrate (large m in Eq 2).

Cracking in T_c tests is characterized by considerable scatter, as evidenced by Fig. 2. Although crack formation is correlated with an average coating stress, σ_{cr}, coating failure may be associated with local defects at which the local stress is considerably higher. Coatings contain distributions of these defects, and the largest defects in a given population would be expected to control failure. Different defect populations in different specimens, therefore, could lead to large differences in the nominal failure stress. The properties of the coating and the metal seem to affect residual stresses, defect populations, and crack behavior, and the interrelationship of these parameters is not fully understood. Each heating plus inspection step also produces an exchange of water with the ambient atmosphere, which could lead to small changes in material properties. And in some tests conducted on nominally identical coupons under nominally identical conditions, significant differences in T_c were still observed. In short, the "simple" T_c test is not so simple after all. This complexity must be kept in mind when interpreting and applying the results of T_c experiments. Nevertheless, as will be shown later, the T_c test seems to have value as a general indicator of cracking tendencies under both single and multiple thermal cycles.

Individual coating cracks which formed in the T_c tests generally extended all the way across the width of the test coupon without apparent linking, but occasionally they were interrupted by intersections with other cracks. In some T_c experiments, small cracks formed early in the test and later rapidly increased in length and extended across the coupon as the temperature was increased. Crack patterns were random for the most part, but sometimes followed the rolling direction of the aluminum sheet. Total crack densities were relatively low (generally less than 30 cracks per 2 by 2-in. (50 by 50-mm) coupon) even when heating was continued 10 to 30°C above T_c.

Multiple Thermal Cycles (Constant Amplitude)

As noted in the introduction, 30 years of exposure to LEO environment includes roughly 175 000 thermal cycles. Simulating this environment and this duration exactly in an experimental program is not practical. In order to develop a basic understanding of thermal fatigue

behavior in anodized aluminum coatings, a series of simple "rapid thermal cycle" (RTC) tests were conducted at frequencies which were accelerated relative to LEO. Most of these experiments were "constant amplitude" tests in which the minimum and maximum temperatures were fixed throughout the test. In one final test, discussed below, the maximum temperature was systematically alternated between two fixed values.

The RTC apparatus was a sealed enclosure in which coupons (like those used in T_c tests) hanging from a circular chain drive moved between a heated chamber and a cooled chamber, with a small intermediate chamber serving as a thermal buffer. A schematic diagram of the RTC apparatus is shown in Fig. 3. The T_{max} chamber was heated to maintain a target temperature between 30 and 95°C within 0.2°C at an air flow rate of 15 to 20 ft^3/h (0.42 to 0.57 m^3/h). The T_{min} chamber was either held at room temperature or cooled to −40°C by a dry ice bath. The atmosphere was either dry flowing air (nominal 50 to 80 ppm water), dry flowing nitrogen (nominal 10 to 30 ppm), or ambient. The nominal humidity levels for the dry atmospheres were achieved over the first 1000 cycles or so, decreasing rapidly at first and then more slowly as the final moisture content was approached. The cycle period was approximately 10 min (roughly 1000 cycles/week); the longest test ran about 6100 cycles. Test conditions for the five constant amplitude RTC tests are summarized in Table 1.

As many as six sets of three coupons each were included in each test. Each set of three coupons was characterized by a particular combination of coating (thickness, seal time) and substrate (thickness, composition). Most RTC coupons tested were based on nominal 25-mil (0.64-mm)-thick Al 5657 substrates. One wall of the intermediate chamber was a plexiglas viewing window, and all coupons received simple visual inspections at desired intervals to observe and record crack development.

Several key features of typical cracking behavior are illustrated in Fig. 4, based on RTC 4. Cracking is characterized by the total number of cracks which have formed on all three test coupons in a given set. The top graph reveals an incubation period before cracking initiates and a gradual decrease in the rate of formation of new cracks with continued cycling. Within the limitations of our inspection process, cracks did not appear to grow extensively in length following the initiation event, although new cracks sometimes apparently grew instantaneously across the full width of the specimen immediately following their formation (these are henceforth denoted as "long" cracks). Most cracks remained "short" (length on the order of 5 mm). Since some crack growth was observed in the T_c tests with increasing temperature, crack growth with increasing temperature or increasing cycles in the RTC tests cannot be ruled out. Our inspection process was not suitable to make these precise measurements.

The bottom graph in Fig. 4 shows the same data replotted on a semilogarithmic basis. This representation brings out an apparent "steady-state" regime (in this case, beginning around 1000 cycles) characterized by a constant cracking rate with respect to log(cycles). Some cracking initiated at much shorter lives and proceeded at a slower rate before entering the more strongly linear steady-state regime. In some of the other RTC tests, this early cracking did not occur, and initial cracking appeared to belong to the steady-state regime. These observations suggest two ways of characterizing cracking data to develop fatigue models: first, in terms of the "initiation life," the number of cycles to appearance of the first crack; and, second, in terms of the steady-state semilogarithmic rate of formation of new cracks.

Initiation of First Crack—Data for the number of cycles to appearance of the first crack are presented in the framework of a traditional *S-N* (stress-life) diagram in Fig. 5. Included here are relevant data from the first five RTC tests, including different maximum and minimum temperatures and humidities. Also included on the diagram are the ranges of σ_{cr} data from the T_c tests, which may be thought of as one-cycle fatigue tests. All results shown in Fig. 5 are based on anodized 25-mil Al 5657 coupons, so potential variations in life due to substrate composition or thickness have been eliminated. The maximum average coating stresses were

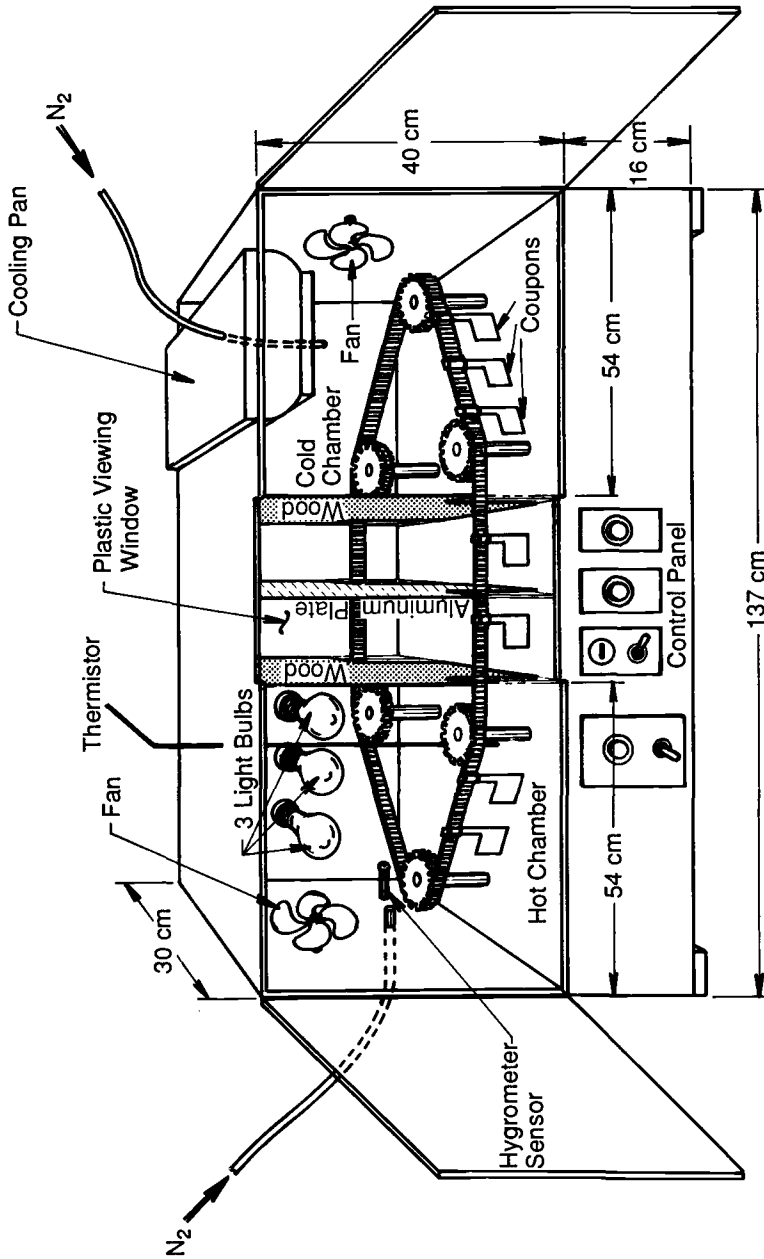

FIG. 3—*Sketch of RTC test apparatus.*

TABLE 1—*RTC test conditions.*

Test Number	T_{max}, °C	T_{min}, °C	Atmosphere	Humidity, ppm
1	70	25	Ambient air	Ambient
2	70	25	Dry air	65
3	70	−40	N_2	15
4	70	25	N_2	25
5	80	25	N_2	15

estimated from Eqs 1 and 2, selecting room temperature residual stresses and elastic moduli which correspond to the nominal test humidity. Note that coating thicknesses are denoted by symbol (filled versus unfilled). Distinctions of seal time have been neglected, since seal time did not appear to have a significant influence on elastic modulus or on room temperature residual stress at humidities experienced in the RTC tests. Arrows to the right indicate run-outs (cracking had not yet initiated when the test was terminated for one reason or another). Arrows to the left indicate that cracking was observed at the first inspection, which means that cracking could have initiated at any time between Cycle 1 and the number of cycles indicated by the symbol.

Several key observations are in order. First, note that as in the T_c tests, the thicker 1.0-mil coatings cracked more quickly than the 0.5-mil coatings. This effect is not explained by trends in the nominal coating stresses. Second, the nominal humidity had a significant effect on cracking tendencies. Compare RTC Tests 1, 2, and 4, which shared identical temperature histories: cracking was never observed in the ambient humidity RTC 1, terminated after 2340 cycles; cracking occurred quickly in the 25 ppm RTC 4; and cracking initiated at slightly larger numbers of cycles in the 65 ppm RTC 2 (this test was abandoned following a damaging temperature spike at 2000 cycles, at which time cracks had not yet initiated in the 0.5 mil/20 min coupons). The effect of humidity on cracking appears to be explained by the effects of humidity on maximum stress.

How do temperatures affect cracking? The successful choice of the estimated *maximum* stress, rather than the stress range, to correlate crack initiation data suggests that T_{max} is the important temperature parameter. What about T_{min}? Compare RTC Tests 3 and 4, which had nominally identical maximum temperatures and humidities but very different minimum temperatures (+25 versus −40°C). Crack initiation lives were quite similar in these two tests. The slightly lower initiation lives in the 1.0-mil coupons from RTC 4 (T_{min} = +25°C) may have been due to a slightly faster approach to the final humidity level, and in any case, a T_{min} effect (if it existed) would have been expected to cause earlier cracking at lower T_{min} (due to the increase in $\Delta\sigma$). Our tentative conclusion is that T_{min} has no significant effect on crack initiation and that σ_{max}, not $\Delta\sigma$, is the proper correlating parameter.

A linear least-squares regression of the 0.5-mil coating crack initiation data, including both RTC and T_c results, yielded a stress-life curve (Fig. 5) of the general form

$$\sigma_{max} = \sigma_{cr}(N_i)^b \tag{4}$$

where N_i is the number of cycles to initiation of the first crack, and b is the fatigue strength exponent (the slope of the *S-N* line in log-log space). In this case, $b = -0.119$, which (by way of comparison to other engineering materials) is a reasonable value. The regression intercept (fatigue strength at one cycle) is 302.7 MPa (43.9 ksi), which is approximately the same as σ_{cr}

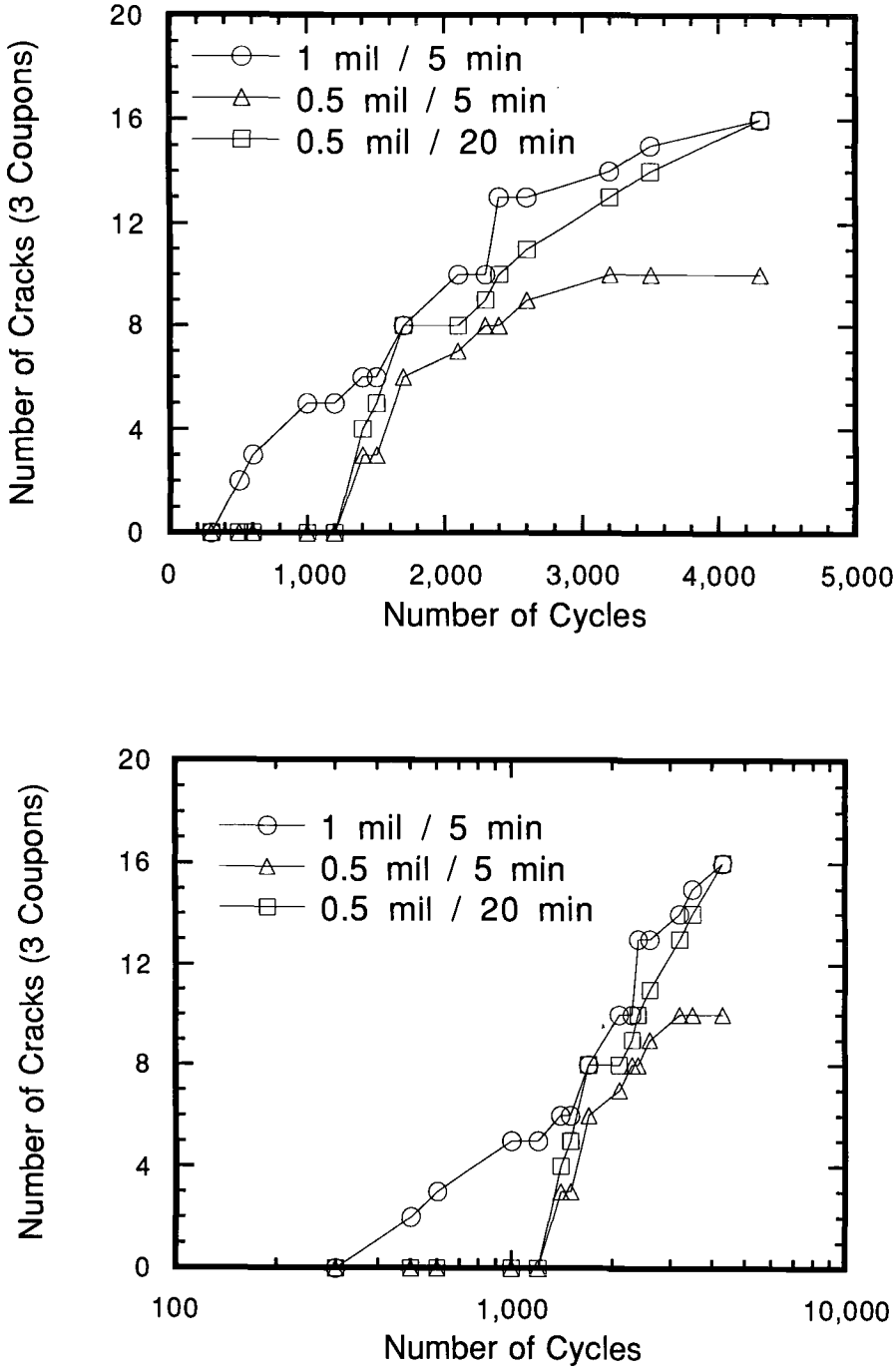

FIG. 4—*Crack development in RTC Test 4:* (top) *linear representation,* (bottom) *semilog representation.*

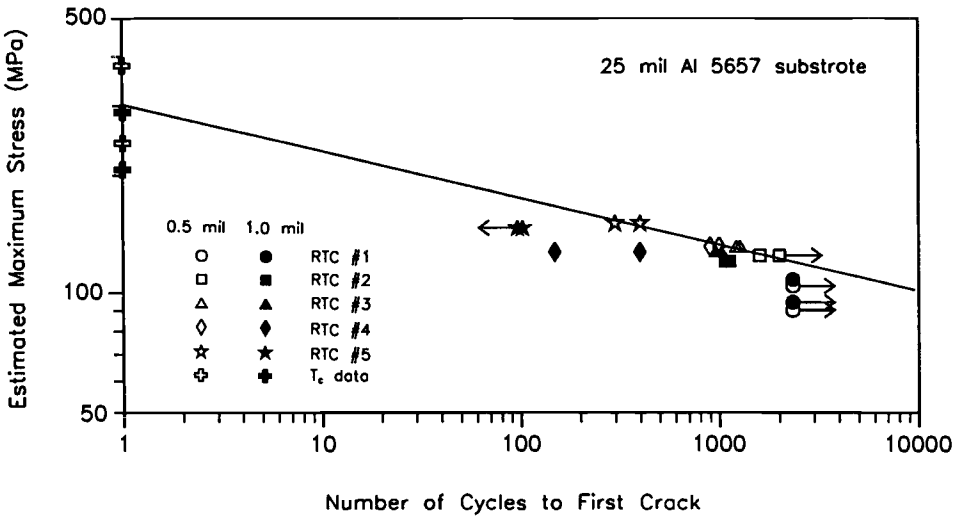

FIG. 5—*Fatigue crack initiation* (S-N) *diagram.*

at the median T_c value of 130°C for 0.5-mil coatings on 5657. A similar fit (not shown) for the 1.0-mil data yielded the similar exponent $b = -0.100$ and a lower intercept.

It is important to note that this best-fit line indicates only the average initiation life at some value of maximum stress. Actual lives demonstrate considerable scatter around this locus of mean values, although the scatter observed (up to $\pm 3x$) is quantitatively typical of high-cycle fatigue in other engineering materials. This scatter appears to be more extensive for the 1.0-mil coatings than for the 0.5-mil coatings. The scatter in fatigue initiation life is probably related to the previously observed scatter in σ_{cr} values, and in fact the joint RTC-T_c construction of Fig. 5 helps to make this point. Variations in strength cause variations in life in proportion to the slope of the fatigue line.

Note how the fatigue life curve helps to explain the absence of observed cracking during RTC 1, conducted at ambient humidity. Cracking was not observed in this test apparently because of humidity-dependent changes in residual stresses and effective elastic modulus, which resulted in a net decrease in the maximum coating stress. If this test had been continued for several thousand additional cycles, it is expected that cracking would have initiated.

Further Crack Development—The appearance of the first crack only marks the beginning of the fatigue damage process. Unacceptable degradation of optical properties, if it occurs at all, will be caused by the formation of multiple cracks rather than the growth of the first crack. It was also noted above that the development of multiple cracks can be characterized by a linear increase in the number of cracks with the logarithm of elapsed cycles, which can be described by the form

$$\rho = C \log\left(\frac{N}{N_i^{\text{eff}}}\right) \tag{5}$$

where ρ is a measure of the crack density, in this case the number of cracks on three test coupons; and N is the total number of fatigue cycles. The term N_i^{eff} is the "effective initiation

life," the intersection of the steady-state crack development line with the $\rho = 0$ axis. This is not the same as the initiation life, N_i, from Fig. 5, although if all cracking is associated with the steady-state regime, the two initiation values may be similar. The coefficient C is the slope of the crack development line (with units of new cracks/decade of cycles) and serves to describe the rate of new crack formation.

Linear least-squares regressions of the crack development data were carried out to obtain best estimates of C from Eq 5. Only data which belonged to the linear "steady-state" regime were included in these regressions. RTC Tests 1 and 2 were not included due to the absence of data for multiple cracking. Regressions were conducted on each individual data set (each combination of seal time and coating thickness) for a given RTC test. Seal time was shown to have no discernible effect on C. The available data indicated no simple systematic effects of various test parameters on N_i^{eff}.

The correlation between C and the estimated maximum stress in the coating is shown in Fig. 6. Here the maximum stress criterion appears to explain not only the effects of different humidities and maximum temperatures on cracking, but also the effects of coating thickness. It is not clear what type of curve should be drawn through the data or if the logarithm of one or both variables should be considered, but the monotonic and relatively smooth nature of the stress versus cracking relationship is apparent. Note that here, as for the S-N diagram, σ_{max} rather than $\Delta\sigma$ appears to be the proper choice (i.e., T_{min} does not influence cracking significantly).

A remaining question is how thermal cycling might influence further crack development in coatings which have already sustained some initial cracking from other sources (e.g., initial damage due to the hot adhesive bonding step). In order to address this question, a set of 0.5-mil coupons which had previously been heavily cracked in a T_c test (average of 61 cracks/3 coupons) were included in RTC Test 5. These coupons did exhibit further cracking, but the initiation time (700 cycles) was longer than for the virgin coupons (300 to 400 cycles), and the total number of new cracks (average of 16 per coupon set) was significantly lower (compare

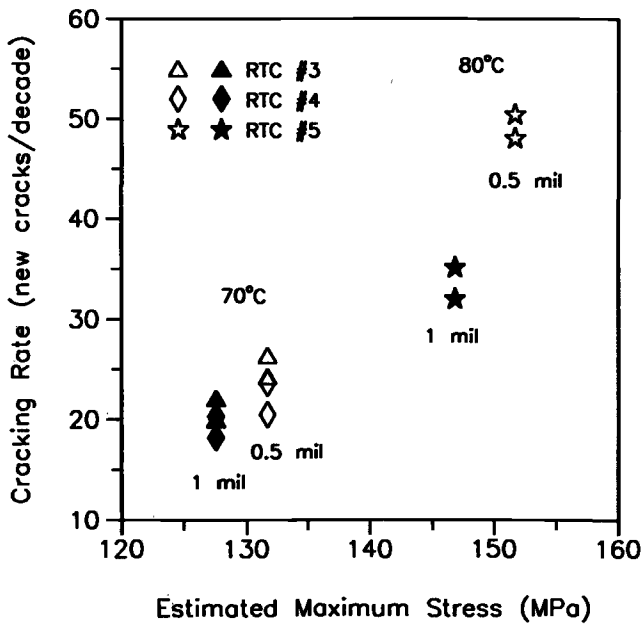

FIG. 6—*Rate of formation of new fatigue cracks.*

43/set average for the virgin coupons). Apparently many of the damage initiation sites had been exhausted by the prior crack formation, so that the two damage processes did not superpose linearly.

Cyclic versus Static Fatigue—The literature is filled with controversy about whether structural ceramics such as alumina actually exhibit a true "cyclic fatigue" effect [*13*]. Several authors have argued from available data that failure due to cracking is actually driven by time-dependent mechanisms and is therefore a function of total time under stress, not total number of cycles [*14*]. This so-called "static fatigue" effect is identified by comparing time-under-stress-to-failure data for specimens which are loaded cyclically or statically. The existence of a true cyclic fatigue effect seems to depend on the particular ceramic under consideration and, in some cases, on the specific experimental conditions.

Do these anodized aluminum coatings exhibit a true cyclic fatigue effect? In order to answer this question, identical test coupons were placed in the elevated temperature chamber of the RTC apparatus for the entire duration of RTC Tests 4 and 5. These coupons, therefore, experienced a total time-at-maximum-stress (time-at-maximum-temperature) which was roughly twice that of the coupons which were cycled between maximum and minimum temperatures. The static coupons could not be inspected until the end of the test, when the chamber was unsealed, so no information on initiation times was available. But the total number of cracks at the end of the test could be compared.

These "static fatigue" coupons did exhibit cracking, but the number of cracks per static coupon at the end of the test was generally only about one third of the number per cycled coupon (which experienced only one half the time-under-maximum-temperature of the static coupons). Figure 7 shows available cracking histories for static and cyclic coupons in RTC 5 compared on the basis of time-at-maximum-temperature. We conclude that there is some static fatigue effect in these anodic coatings, but that there is also a true cyclic fatigue effect which is significantly more damaging.

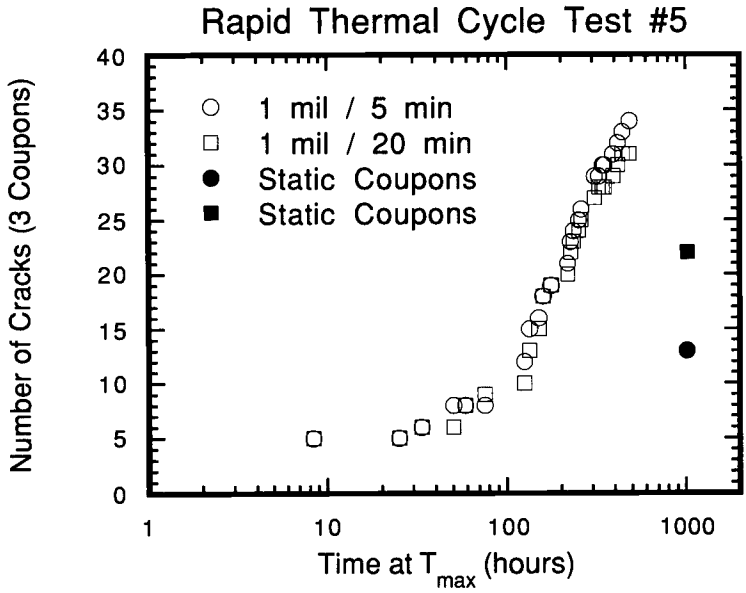

FIG. 7—*Cracking as a function of time at maximum temperature for static and thermally cycled coupons.*

It is interesting to note that nearly all of the cracks on the static coupons were "long," extending across the width of the specimen, similar to cracks observed in the (noncycling) T_c tests and to some of the earliest RTC cracks in the 1.0-mil coatings. In contrast, most of the RTC cracks (and all RTC cracks occurring after about 1000 cycles) were "short." So the physical nature of cracking may be indicative of some distinction between cyclic and static fatigue mechanisms. It is also tempting, based on Fig. 7, to postulate the final number of static fatigue cracks as the log-linear extrapolation of the early (prior to 1000 cycles or 100 h) crack development trends in the cycled coupons, but this may be simply a coincidence. The current database is insufficient to conduct more substantial analysis.

Multiple Thermal Cycles (Variable Amplitude)

Actual LEO thermal histories will not be constant amplitude. The temperature extremes for radiator panels during normal operation are expected to be about −12° to +24°C, but occasional "deep" cycles will also occur between about −93° and +49°C during transitions between operational and nonoperational conditions, with an overall deep cycle frequency around 0.1 to 1%. In order to address the cumulative damage issues associated with more complex thermal histories, a sixth RTC test was conducted. RTC 6 was designed to simulate a realistic thermal history characteristic of LEO, but it was not possible to achieve the complete LEO environment with the RTC apparatus. In particular, the RTC chambers are not capable of achieving negligible humidity. As noted earlier, humidity has a significant effect on the residual coating stresses, and so RTC stresses would be significantly different from LEO stresses at the same temperatures. But by understanding the quantitative relationship between humidity and stress, it was possible to design an RTC test (at *higher* maximum temperatures relative to LEO) in which the maximum stresses would be the *same* as expected in LEO.

The specific history followed in RTC 6 consisted of blocks of approximately 150 automated "operational" cycles with T_{max} = 60°C followed by two manual "deep" cycles with T_{max} = 90°C. Blocks required approximately one day each to complete and were repeated continuously except for weekends, when operational cycles continued without the periodic deep cycles. The T_{min} for both cycle types was kept at 19°C, and the same dry flowing nitrogen atmosphere used in earlier constant amplitude tests was maintained. This thermal history was followed for approximately two months or until 8565 operational and 82 deep cycles had been applied. Similar sets of 25-mil 5657 coupons in triplicate were included in the test, along with sets of 10-mil 5657 coupons which had shown tendencies to higher T_c values and 11-mil 1100 alloy coupons which had been found to have $T_c > 200$°C.

Only the 25-mil 5657 coupons with 1-mil coating and 20-min seal developed clearly observable cracks during this test. These coupons did not crack during the first 154 operational cycles, but did crack extensively after the first deep cycles. No further cracking occurred until about 1100 cycles, at which point the crack density gradually increased at a decreasing rate, as observed during previous RTC tests. The final crack density was 45 cracks per three coupons, and all cracks were more than 1 in. (25.4 mm) long. Linear defects, less than 0.1 in. (2.54 mm) long, were seen on some of the other coupons, but these were not unequivocally identified as cracks until the end of the test. The final crack densities (per three coupons) ranged from one to ten cracks for the other 5657 coupons, and the 1100 coupons remained crack free.

RTC 6 provides information for a particular LEO thermal protocol, but other thermal histories will be encountered in practice. Subsequent predictions of cracking behavior for other histories must rely on interpretation of the more general constant amplitude fatigue models derived from RTC 1 through 5. To have confidence in such predictions, it is important to show that these fatigue models lead to reasonable predictions of RTC 6 results.

The constant amplitude thermal cycling tests do not provide any direct indication of the

proper way to sum damage from a variable amplitude stress history. A reasonable first choice for a cumulative damage initiation criterion is Miner's linear damage rule [*15*], which takes the general form

$$D = \sum \frac{n_i}{N_i} \tag{6}$$

where D is the total damage, n_i is the total number of cycles at stress level i, and N_i is the fatigue life (in this case, the number of cycles to first crack) at stress level i. When cycling occurs in repeated blocks, the total number of blocks to failure can be easily computed as the reciprocal of the total damage per block. A similar prediction for subsequent crack development (multiple crack formation) is not so straightforward due to the nontraditional semilogarithmic damage growth process. An additional complication is the absence of any constant amplitude cracking rate data for stresses as high as the deep cycle maximum stress of 165 to 185 MPa (24 to 27 ksi). We selected a simple linear combination of damage growth due to the different cycle types acting independently.

Based on these fatigue models, the specific equations or data presented earlier for the constant amplitude tests, and the specific thermal histories in RTC 6, the predicted number of cycles to first initiation was approximately 3300 cycles and 2000 cycles for the 0.5-mil and 1.0-mil coatings, respectively. The predicted rate of multiple crack formation was about 10 cracks per decade for the 60°C operational cycles and between 50 and 100 cracks per decade for the 90°C deep cycles (the uncertainty arises because of ambiguities in how to extrapolate from Fig. 6). Based on the assumption that additional crack formation begins at this rate immediately following formation of the first crack (i.e., N_i in Eq 4 is the same as N_i^{eff} in Eq 5), which is a slightly conservative assumption, we obtained *upper bound* estimates for the total number of cracks expected per three coupons after 8600 total cycles: 25 to 50 cracks for the 0.5-mil 5657 coupons and 35 to 65 cracks for the 1.0-mil 5657 coupons.

How do the predictions and actual test results compare? The 1.0-mil coatings first cracked significantly earlier than expected, but this is not inconsistent with previous cracking results. In RTC 5, conducted at a maximum temperature of 80°C, the 1.0-mil coatings had already cracked by the first inspection around 100 cycles (see again Fig. 5; these coupons were not included in the initiation model regression because of the unknown incubation life). The predicted maximum coating stress at 90°C (about 172 MPa or 25 ksi) is not much lower than the lowest σ_{cr} values observed in the 1.0-mil T_c tests. The final number of cracks on the 1.0-mil coupons in RTC 6 was about 45, which compares favorably with our original predictions of 35 to 65 cracks. We do not know exactly when the first cracks appeared on the 0.5-mil coatings, but the presence of multiple cracks at the end of the test (8600 cycles) suggests that our original initiation estimate of 3300 cycles was probably reasonable and perhaps slightly conservative. The upper bound predictions for the total number of cracks at test end (25 to 50) were conservative relative to actual observed cracking (up to ten).

The limited cracking information which can be extracted from RTC 6, then, is generally in agreement with expectations based on the first five RTC tests and the associated fatigue model, including our postulated cumulative damage relationships. The models appear to be accurate or a little conservative in predicting the total amount of cracking which occurs in the early stages of a simulated LEO thermal history.

After 8600 cycles in RTC 6, it was judged that little further information of value would be gained from continuing the same cycling protocol. There remained an interest in differentiating between the fatigue performance of the various alloys included in the test. Therefore, the deep cycles were stopped, and the maximum temperature of the operational cycles was increased from 60 to 65°C for an additional 5016 constant amplitude cycles. Following incubation periods

of differing lengths, additional cracks appeared on all Al 5657 coupons, and some of the small linear defects on the 0.5 coatings lengthened slightly (but remained shorter than 0.25 in.). The Al 1100 coupons remained crack free. Finally, the maximum temperature was increased again to 70°C for an additional 642 cycles. Although all other coatings developed a few more cracks, the Al 1100 coupons still did not exhibit any cracking. In view of the complex thermal histories involved, the relatively few data collected during these late stages of RTC 6 were judged insufficient for further analysis.

Other Physical Characteristics of Damage

Careful scanning electron microscope (SEM) inspection of anodized coatings which cracked at elevated temperatures revealed substantial plastic deformation of the substrate in the vicinity of the oxide crack. This deformation is illustrated in Fig. 8 (top), a cross-sectional view which shows the intersection of the crack with the substrate-coating interface. Copper has been deposited in the crack as an aid to visualization. The substrate deformation is reminiscent of crack tip blunting observed in the ductile fracture of metals. This severe metal "groove" extends along the full length of the crack. Figure 8 (bottom) shows a perspective view of the metal groove in a specimen from which the coating has been removed. These particular photomicrographs were taken from a 12-mil Al 3002 substrate with a 1-mil coating which had been subjected to T_c testing up to $T_{max} = 175$°C. At the opposite surface, a relatively broad, shallow indentation in the metal also follows the crack line. At that surface the oxide deforms to follow this indentation, but does not crack.

At first glance, the driving force for this substrate deformation seems unclear, since at elevated temperatures the stresses in the substrate are nominally compressive. In order to investigate the stress distribution further, a simple two-dimensional finite element (FE) analysis was conducted for a thermally stressed cracked coating system. The model substrate was 8 mil thick with 1-mil coatings on both surfaces. The upper coating contained a crack, while the lower coating was uncracked. Eight-noded isoparametric elements were used throughout the mesh. The small elements near the coating/substrate interface had dimensions of 0.1 mil and 0.05 mil in the x (axial) and y (in-plane transverse) directions, respectively. The system was loaded thermally by a uniform temperature increase of 150°C from a stress-free condition. For simplicity, the deformation response was assumed to be purely elastic (no plastic deformation allowed) and plane strain conditions were also assumed.

The results indicated clearly why severe deformation occurs at the root of the crack. The crack introduces a strong stress singularity which causes severe intensification of the stresses in the substrate under the crack. Although the nominal (uncracked) stress in the substrate under the given loading conditions is 86 MPa (12.5 ksi) compressive in the axial direction (parallel to the interface), the substrate stresses near the crack are tensile in nature and can be very large. See Fig. 9, which shows contours of axial stress σ_{xx} in both substrate and coating near the crack. At the crack tip itself, the FE analysis estimates σ_{xx} to be nearly 700 ksi (4830 MPa) (contours above 80 ksi are too closely spaced together to be shown on the figure). In reality, of course, the substrate stresses near the crack tip will not be nearly this large, due to plastic deformation and the resulting stress relaxation, but the elastic FE analysis properly points out the severe nature of the near-tip stress field. Farther away from the crack, the FE model shows that the substrate stresses return to their nominal levels (σ_{xx} = 12.5 ksi or 86 MPa compressive).

The severity of the local deformation can be judged by comparing the calculated local elastic stresses with the yield strength of the aluminum substrate. At room temperature, σ_{ys} is around 138 to 172 MPa (20 to 25 ksi). At elevated temperatures typical of T_c tests, the yield strength is unknown, but it is estimated to be 34 to 103 MPa (5 to 15 ksi); the decrease is due to thermally enhanced dislocation motion. The inability of the local material to support stresses

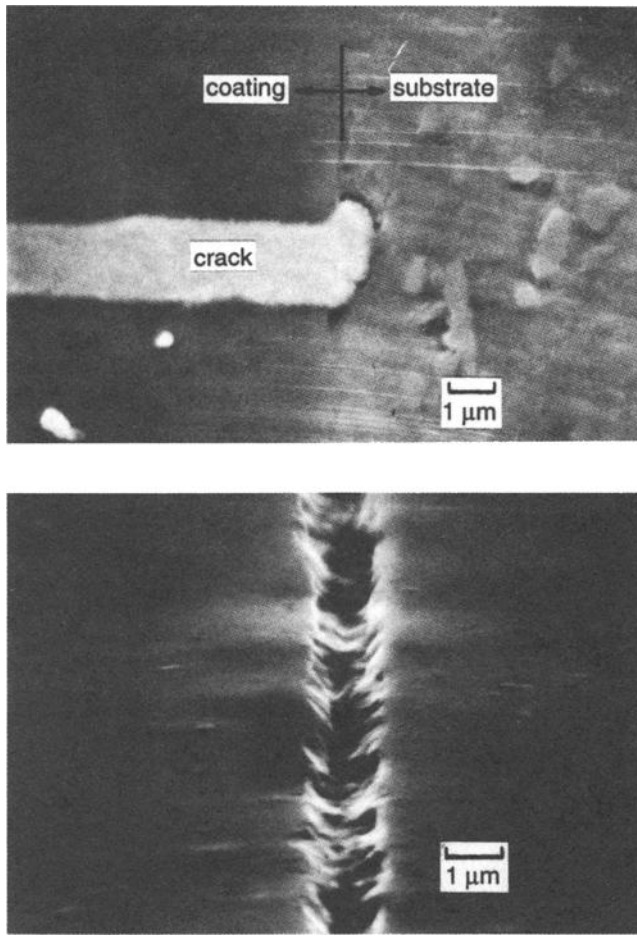

FIG. 8—*SEM micrographs showing severe substrate deformation near coating crack* (top) *cross section showing intersection between crack and coating/substrate interface* (bottom) *aerial view of metal surface after coating has been stripped off.*

which are dramatically higher than the current yield stress causes significant plastic flow. The elastic FE analysis is not able to emulate the physical "groove" formation because this is a plasticity phenomenon, but it clearly demonstrates the reason for the severe deformation.

Deformation of this type was not observed in some T_c coupons which had been heated to lower temperatures. Grosskreutz [*16*] and Edeleanu and Law [*17*] found no evidence of substrate deformation or damage beneath oxide cracks formed by mechanical straining at room temperature. On the other hand, this substrate deformation has been observed to occur in some RTC coupons which experienced a maximum temperature of only 70°C. In particular, this severe substrate deformation is associated with the so-called "long" cracks which form during some RTC tests. Substrate deformation occurs much less severely beneath the so-called "short" cracks (length on the order of 5 mm). Note that the "long" and "short" cracks are also distinguished by their "crack opening displacement" (COD), the separation distance between the two opposite surfaces of the crack. As observed in Fig. 8, the COD for a long crack is often on the order of 1 to 2 μm. In contrast, the COD for a short crack is typically on the order of

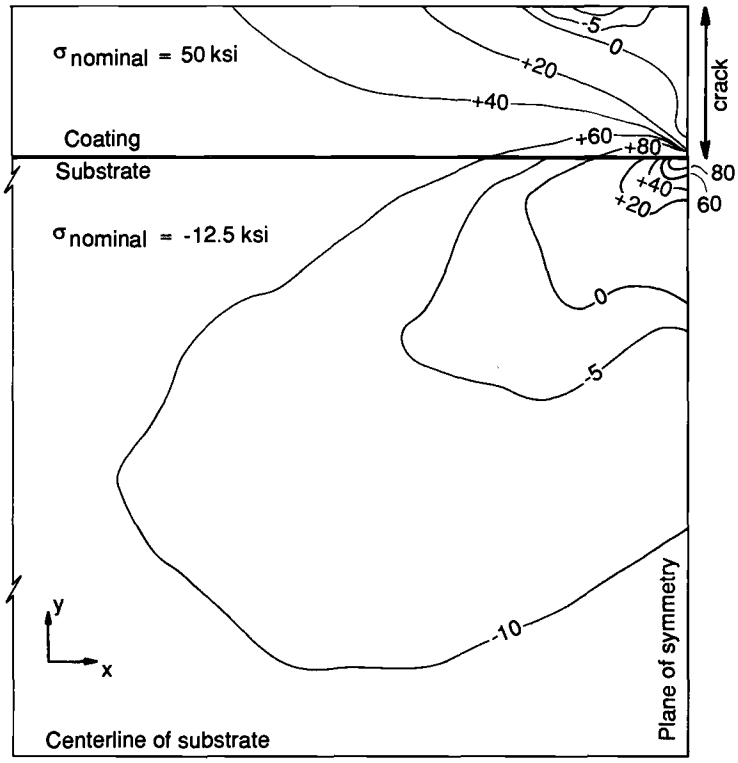

FIG. 9—*Stress distribution in the vicinity of a cracked coating at elevated temperature.*

0.2 μm. The relationship between the crack length, COD, and metal deformation is not entirely clear. It may be that the substrate deformation forces the crack surfaces apart, thereby increasing the COD, and that this increase in the COD encourages the crack to grow in length (which, in turn, initiates more substrate deformation).

The severity of the metal deformation raises the possibility that the groove could serve as an initiation site for fatigue cracks in the substrate. This is not likely in the space application under consideration, since nominal substrate stresses are probably not large enough to nucleate and grow a fatigue crack in the metal. Limited investigations have found no such substrate cracks in T_c or RTC coupons. The phenomenon could be significant in other applications, however, if the substrate carried significant mechanical cyclic loads.

Discussion

The fatigue models proposed provide a rational basis to predict LEO fatigue behavior. While the specific quantitative models derived here apply to this particular materials system (combination of substrate alloy/temper/thickness and coating thickness/seal time), they should provide the proper framework to evaluate other anodized aluminum systems as well. Considerable uncertainties also remain as to the specific thermal histories which will be experienced in LEO, including the maximum temperatures for both operational and deep cycles and the deep cycle frequency, and so it is difficult to make precise statements about expected LEO performance. Based on the Al 5657 studies, however, a few general predictions can be advanced. It appears

that the anodized aluminum panels will experience fatigue cracking in orbit, and that the first cracks will appear relatively early in life—during the first 1000 to 10 000 cycles, which is approximately the first 2 to 20 months. Subsequent crack development, however, is expected to be slow, and those cracks that do form are expected to be extremely small (less than 5 mm). The operational cycles alone will probably contribute fewer than 20 new cracks on a 12 in.^{2} (7750 mm^2) reference area over the panel lifetime. Estimating multiple crack formation due to the deep cycles is more difficult, as discussed earlier, but upper bounds of 100 to 200 small cracks per reference area after 30 years are probably very conservative, especially for thinner coatings.

The important question, however, is not just whether the coatings will crack, but whether expected coating cracking will cause any significant degradation in optical properties such as thermal emittance (α) or solar absorptance (ε). The answer appears to be "no." A set of unusually heavily cracked coatings obtained during T_c testing of coupons which had been stored in humid atmospheres (discussed earlier) were sent to NASA/JSC for optical measurements. The final crack densities on these coupons were as high as 360 cracks per three coupons (12 in.^{2} (7750 mm^2) total reference area), and most cracks were longer than 1 in. (25.4 mm). This level of cracking produced no measurable changes in α or ε when compared to control values from uncracked coupons.

Other anodized coating systems, of course, might experience cracking which is either more or less severe. The apparent link between T_c results and thermal fatigue lives (as expressed in the *S-N* diagram) suggests that T_c testing might provide some initial indication of thermal fatigue resistance and thereby eliminate the need to do comprehensive RTC testing for a new materials system. Similarly, T_c testing might be useful as a part of a quality control system to ensure that the fatigue resistance of a previously qualified materials system has not degraded unacceptably due, for example, to loss of quality in the anodization process. The scatter in T_c results implies that the test could only be interpreted as a gross measure of cracking tendencies, but a large drop in T_c (for example, from 160 to 90°C) might still be a valid indicator that fatigue cracking would significantly increase. The relative performance of 0.5 and 1.0-mil coatings on 5657 and 0.5-mil coatings on 1100 in both T_c and RTC tests would seem to confirm this conclusion.

The possibility of extensive coating cracking occurring during a hot adhesive bonding step cannot be ruled out and is likely at higher bonding temperatures such as 350°F (177°C). A lower bonding temperature such as 250°F (121°C) should cause little or no cracking for a carefully chosen substrate and thinner coating. Unfortunately, a number of complex scale-up and materials handling issues associated with shop fabrication of full-size panels must be addressed before confident predictions of cracking behavior in practice can be forwarded. Nevertheless, it is encouraging that the most extensive cracking observed during this limited study did not cause measurable degradation of optical properties. It is also encouraging that previously cracked coupons exhibited reduced crack development during subsequent thermal cycling.

Conclusions

1. Coating stresses are strongly dependent on humidity.

2. Cracks first initiate during monotonic heating at temperatures ranging from less than 100°C to greater than 200°C and corresponding estimated coating stresses ranging from under 200 MPa (30 ksi) to over 480 MPa (70 ksi). All of the factors which influence T_c (or σ_c) are not fully understood, and scatter is sometimes large.

3. Anodized aluminum coatings exhibit a true cyclic fatigue effect under thermal cycling. Fatigue cracking is characterized by the progressive formation of multiple cracks which do not appear to grow substantially in length following the initiation event, although new cracks sometimes grow instantaneously across the full width of the specimen.

4. Fatigue models have been successfully developed. The first-crack initiation model, which takes the form of a traditional stress-life (*S-N*) diagram, successfully correlates cracking in both T_c and RTC tests at different humidities and temperatures. The crack development model for RTC tests describes a linear increase in crack density with log (cycles) as a function of stress.

5. These fatigue models and simple cumulative damage laws were reasonably successful in predicting cracking during a variable amplitude thermal history representative of LEO environments.

6. Cracking in both T_c and RTC tests occurs more quickly and more severely in thicker coatings.

7. The formation of cracks in the anodic coating at elevated temperature is accompanied by severe local plastic deformation of the substrate at the intersection of the crack and the substrate/coating interface.

8. The fatigue models provide a rational basis to predict the fatigue performance of anodized aluminum coatings in aerospace applications. In particular, the models indicate that fatigue cracking during 30 years of LEO exposure will be insufficient to cause significant changes in thermal emittance and solar absorptance.

Acknowledgments

This research was sponsored by the NASA Lyndon B. Johnson Space Center through the Small Business Innovative Research (SBIR) program under contracts NAS 9-18087 and NAS 9-18350. NASA program monitor Steve Jacobs is thanked for his encouragement and substantial contributions. Frank Maritato, Scott Stillwell, and Jianjiang Xu of BTI conducted most of the experimental investigations, and Chris Kuhlman of SwRI provided significant assistance with the mechanics analyses. Helpful interactions with Joseph Stoyack of LTV Aerospace and Defense (now Loral Vought Systems) are also gratefully acknowledged.

References

[*1*] Alwitt, R. S. and McClung, R. C., "Fabrication and Thermal Cycle Testing of Long-Life Radiator Coatings," final report to NASA Johnson Space Center, Contract NAS 9-18350, July 1992.

[*2*] Wernick, S., Pinner, R., and Sheasby, P. G., *The Surface Treatment and Finishing of Aluminum and Its Alloys,* 5th ed., ASM International, Metals Park, OH, 1987.

[*3*] Alwitt, R. S., Xu, J., and McClung, R. C., "Stresses in Sulfuric Acid Anodized Coatings on Aluminum," *Journal of the Electrochemical Society,* Vol. 140, 1993, pp. 1241–1246.

[*4*] McClung, R. C. and Kuhlman, C. J., "A Critical Assessment of the Analysis of Coating Stresses and their Experimental Measurement," to be submitted.

[*5*] Hill, H. N. and Mason, R. B., "Anodic Coatings on Aluminum—Their Brittleness," *Metals and Alloys,* Vol. 15, 1942, pp. 972–975.

[*6*] Hockenhull, B. S., Gupta, S. S., and Hurst, R. C., "The Mechanical Properties of Anodic Oxides and their Influence on Fatigue Behavior of Aluminium Alloys," *Transactions of the Institute of Metal Finishing,* Vol. 54, 1976, pp. 123–126.

[*7*] Alvey, C. E., Wood, G. C., and Thompson, G. E., "The Mechanical Properties of Porous Anodic Films Formed on Aluminium," *Interfinish '80, Proceedings,* 10th World Congress on Metal Finishing, Kyoto, Japan, 1980, pp. 275–279.

[*8*] Bradhurst, D. H. and Llewelyn Leach, J. S., "The Mechanical Properties of Anodic Films on Aluminium," *Transactions of the British Ceramic Society,* Vol. 62, 1963, pp. 793–806.

[*9*] Michelson, C. E., "How to Prevent Crazing," *SAE Journal,* Vol. 73, 1965, pp. 60–63.

[*10*] Thornton, J. S., Yenawine, D. L., and Thomas, A. D., Jr., "Flexural Properties of Aluminum-Aluminum Oxide Sandwich Composites," *Journal of Composite Materials,* Vol. 3, 1969, pp. 182–185.

[*11*] Jacobs, S. and Duffy, D., "Long-Life/Durable Radiator Coatings for Space Station," *SAE Transactions, Journal of Aerospace,* Section 1, Vol. 97, Paper 881067, 1988, pp. 491–499.

[*12*] Alwitt, R. S. and McClung, R. C., "Cracking of Anodized Coatings on Aluminum," *Plating and Surface Finishing,* Vol. 80, August 1993, pp. 48–51.

[*13*] Lin, C.-K. J., Mayer, T. A., and Socie, D. F., "Cyclic Fatigue of Alumina," *Cyclic Deformation, Fracture, and Nondestructive Evaluation of Advanced Materials, ASTM STP 1157,* American Society for Testing and Materials, Philadelphia, 1992, pp. 3–27.

[*14*] Evans, A. G., "Fatigue in Ceramics," *International Journal of Fracture,* Vol. 16, 1980, pp. 485–498.

[*15*] Miner, M. A., "Cumulative Damage in Fatigue," *ASME Journal of Applied Mechanics,* Vol. 12, 1945, pp. A159–A165.

[*16*] Grosskreutz, J. C., "Mechanical Properties of Metal Oxide Films," *Journal of the Electrochemical Society,* Vol. 116, 1969, pp. 1232–1237.

[*17*] Edeleanu, C. and Law, T. J., "Fracture of Oxide Films on Strained Aluminium," *Philosophical Magazine,* Vol. 7, 1962, pp. 573–581.

Hong Lin[1] *and Hamid Nayeb-Hashemi*[1]

Yield, Plastic Flow, and Fatigue of an Orthotropic Material Under Biaxial Loadings

REFERENCE: Lin, H. and Nayeb-Hashemi, H., **"Yield, Plastic Flow, and Fatigue of an Orthotropic Material Under Biaxial Loadings,"** *Cyclic Deformation, Fracture, and Nondestructive Evaluation of Advanced Materials: Second Volume, ASTM STP 1184,* M. R. Mitchell and O. Buck, Eds., American Society for Testing and Materials, Philadelphia, 1994, pp. 178–203.

ABSTRACT: Yield, plastic flow, and low-cycle fatigue damage behavior of an orthotropic Al-6061-T6 plate were investigated. Anisotropic constitutive relations and multiaxial fatigue damage models of the material were obtained to predict its yield, plastic deformation, and low-cycle fatigue life under multiaxial loading conditions. Low-cycle fatigue tests were conducted along three orientations of the plate at room temperature under three loading conditions, uniaxial tension/compression, torsion, and combined tension/torsion in-phase, to verify the theoretical predictions. The theoretical yield functions and flow relations under combined tension/torsion loading condition agreed with experimental data reasonably well. Four multiaxial fatigue damage models were evaluated and used to predict the low-cycle fatigue life along the three orientations of the plate. A damage model based on the strain vector and an anisotropic shear cracking model gave better predictions than the effective strain and the plastic work models.

KEYWORDS: cyclic stress-strain responses, anisotropic constitutive relations, multiaxial fatigue damage models, orthotropic Al-6061-T6 plate

Nomenclature

M_{ij}	Anisotropic coefficients in the yield function by Shih and Lee (S-L)
α_i, α_j	Constants in the S-L yield function describing the Bauschinger's effect
k	Parameter in the S-L yield function describing the size of the yield surface
F, G, H, L, M, N	Anisotropic coefficients in Hill's yield function
τ_{max}, γ_{max}	Maximum shear stress and maximum shear strain amplitudes
ϵ_n, σ_n	Tensile strain and stress amplitudes normal to the plane of maximum shear
σ_{no}	Mean normal stress amplitude on the plane of maximum shear
n	Material constant
σ_n^{max}	Maximum normal stress amplitude on the plane of maximum shear
σ_y	Yield stress of a material under monotonic tension
σ_1	Maximum principal stress amplitude
ϵ_1	Maximum principal strain amplitude
α	Transformation angle
Q_{ij}	Anisotropic coefficients in the yield function in $x'y'z'$ system
θ, φ	Arbitrary angles in the cross sections of specimens under torsion
σ, τ	Measured normal and shear stress amplitudes

[1] Graduate student and professor, respectively, Mechanical Engineering Department, Northeastern University, Boston, MA 02115.

D Multiaxial fatigue damage model based on the strain vector
A_{ii} Material constants in the D model
B_{ij} Material constants in the D model in the $x'y'z'$ coordinate system
E Young's modulus of a material
λ Ratio of applied strain amplitudes: $\lambda = \gamma/\epsilon$
$\bar{\sigma}$, $\bar{\epsilon}$ Effective stress and effective strain
γ^p, ϵ^p Shear and axial strains, plastic parts
$N_{10\%}$ Number of cycles to failure using the 10% load or torque drop criterion
A_i, B_i Anisotropic material coefficients in the anisotropic shear cracking model: $A_i(\gamma_{max} + B_i\epsilon_n)$

Advanced engineering materials usually exhibit anisotropy in their mechanical behavior. Anisotropic materials such as fiber-reinforced composites and cold-worked metals are used widely in industry for making aerospace, air, ground and sea structures, pressure vessels, power generators, engines, etc. Understanding and modeling of mechanical behavior of anisotropic materials are important for design, manufacture, and quality assurance of these engineering structures. Extensive research has been conducted to model the anisotropic elastic deformation and fatigue failure of fiber-reinforced composites [*1–10*]. But the anisotropic low-cycle fatigue damage behavior of cold-worked metals under multiaxial loading conditions are rarely investigated. In this context, the research reported here deals with the anisotropic plastic deformation and low-cycle fatigue damage behavior of cold-worked 6061-T6 aluminum alloy under biaxial loadings. High temperature and strain rate effects are not considered in this study.

There are at least two types of plastic anisotropy in metals at room temperature and they may not be independent of each other. One is due largely to preferred orientation of grains (texture) and nonrandom distribution of second phase particles or inclusions. These sources result in initial material anisotropy or texture anisotropy, which gives rise to the dependence of yield strength and strain-hardening property on material orientation. Another mechanism of plastic anisotropy is related to the development of back stress or internal residual stress caused by prior plastic deformation, i.e., the Bauschinger effect. The latter is known as plastic deformation anisotropy or strain-induced anisotropy, which is observed upon load reversal and depends on loading history. To model plastic deformation behavior of an anisotropic metal under multiaxial loading conditions, anisotropic constitutive relations are needed which include: (1) a yield function specifying the stress state at which plastic deformation begins; (2) flow relations which relate plastic strain increments to stress deviators; and (3) a hardening rule which describes the variation of the yield surface with plastic deformation. In addition, to predict fatigue life of an anisotropic metal under multiaxial loading conditions, a multiaxial fatigue damage model is needed. In this paper, some background information about anisotropic constitutive relations and multiaxial fatigue damage models are given first. This is followed by both theoretical and experimental investigations of anisotropic yield, plastic flow, and low-cycle fatigue damage behavior of an orthotropic Al-6061-T6 plate. More specifically, these investigations include:

1. The anisotropic constitutive relations of the subject material with respect to its principal anisotropic axes.
2. Transformation of the constitutive relations to a new coordinate system.
3. The development of a strain vector-based multiaxial fatigue damage model.
4. Low-cycle fatigue experiments along three orientations of the plate under axial-torsional biaxial loadings.

Through these investigations, we intend to illustrate our proposed methodology for investigating multiaxial fatigue damage of an anisotropic material. The methodology consists of the modeling of constitutive relations of the subject material, detailed investigation on damage mechanism of the material, and proposing damage controlling parameters to predict fatigue life. This methodology is applied to model the multiaxial fatigue damage of Al-6061-T6 in this work, and it will be further applied to model advanced composite materials.

Background

Anisotropic Constitutive Relations

The yield function which describes the limit of the elastic regime plays an important role in the classical theory of plasticity. It is well established by experimental evidence and theoretical considerations that yielding of metals does not depend on hydrostatic pressure and that plastic deformation occurs with no volume change. Moreover, it has been shown that, based on the stability analysis, the yield surface must be convex, which ensures the uniqueness of the plastic strain increment for a given stress state. These results have led to some restrictions on the expressions of yield functions. Since the plastic deformation behavior of a material is nonlinear, the flow relations are usually defined as relationships between plastic strain increments and stress deviators. The yield function is usually used as the plastic potential to derive the stress deviators (associated flow rule), thus the plastic strain increment vector is normal to the yield surface (normality rule). As a consequence, the exact locations and shapes of initial yield surface and subsequent yield surfaces are very critical in the prediction of plastic deformation.

Two different approaches have been applied to obtain yield functions for anisotropic metals. According to the crystallographic approach [*11,12*], the deformation of a polycrystalline aggregate is accommodated by the activation of slip systems. The crystallographic dependence of the plastic deformation is directly accounted for by the slip systems of the subject metal. Then, the necessary transition from a single crystal to polycrystal is carried out on the basis of statistical distribution of grains and a grain interaction model. In the macroscopic continuum approach [*13–21*], no reference is made to the orientations of individual grains. The yield surface of the polycrystal under consideration is described by an assumed analytical yield function, the parameters of which are determined experimentally. The anisotropic behavior of the polycrystal is thus accounted for only through the characteristics of the assumed yield function, not by means of the crystallographic texture of the material. Although the macroscopic continuum approach sometimes might not accurately predict some detailed behavior of particular metals because of its phenomenonlogical nature, it has been successful in describing the normality of the plastic strain increment vector and the convexity of the initial and all the subsequent yield surfaces. In addition, they are relatively easy to implement in FEM codes.

Two anisotropic yield functions of macroscopic continuum approach are cited here as examples. In 1948, Hill proposed a generalization of the von Mises yield function for the state of anisotropy possessing three orthogonal planes of symmetry. His yield function is expressed as [*13*]

$$2f = F(\sigma_y - \sigma_z)^2 + G(\sigma_z - \sigma_x)^2 + H(\sigma_x - \sigma_y)^2 + 2L\tau_{yz}^2 + 2M\tau_{zx}^2 + 2N\tau_{xy}^2 = 1 \quad (1)$$

where F, G, H, L, M, N are material properties depending on the yield stresses in the three principal material anisotropic directions. Although for an orthotropic material $F \neq G \neq H \neq L \neq M \neq N$, the condition of independence of yielding on hydrostatic stress is assumed in this yielding function. Hill's yield function and an associated flow rule are the most widely used formulations for the modeling of constitutive relations of anisotropic materials [*14–21*].

Shih and Lee [*15*] proposed another anisotropic plasticity theory which extended Hill's original theory by introducing some back stress terms. Their yield function was expressed as

$$3f = M_{ij}(\sigma_i - \alpha_i)(\sigma_j - \alpha_j) - k^2 = 0 \tag{2}$$

where M_{ij} describes the variation of the yield stresses with material orientations, and α_i and α_j describe the strength difference between the tensile and compressive yield stresses. The size of the yield surface is given by the parameter, k. Moreover, the independence of yielding on hydrostatic stress and no volume change during plastic deformation are also assumed in this theory by imposing constraints on the values of M_{ij}.

Multiaxial Fatigue Damage Models

Multiaxial fatigue has been an engineering concern and a research field for a long time [*22–34*]. Many multiaxial fatigue damage models have been proposed following the stress-life and strain-life approach. Three general concepts are also recognized: effective stress/strain, plastic work/energy, and critical plane. The effective stress/strain concept was proposed at the early stage of multiaxial fatigue research and is still being applied continuously [*33–35*]. According to this concept, the two- or three-dimensional stress/strain state is reduced to an effective scalar parameter, usually by using either Tresca or von Mises criterion. An effective parameter-fatigue life relationship can then be obtained similar to the *S-N* correlation. The plastic work/energy concept was proposed in the 1960s [*36,37*], and the hysteresis energy was used to correlate fatigue life. Recently, Garud [*38*] and Ellyin et al. [*39–41*] continued to use this approach to predict low-cycle fatigue life.

The critical plane concept is relatively new compared to the other two approaches. It requires understanding of fatigue cracking behavior of the subject material so that the failure planes can be identified and the load spectra with respect to those planes can be analyzed. In his early research on high-cycle fatigue, Findley used maximum shear stress modified with the normal stress acting on the plane of maximum shear to correlate fatigue life data [*42,43*]. McDiarmid also proposed a critical plane model for high-cycle multiaxial fatigue in the early 1970s [*44,45*] based on the maximum shear stress and maximum normal stress on the plane of maximum shear.

In low-cycle fatigue research, strain parameters instead of stress parameters are usually used in fatigue life prediction models. Brown and Miller proposed a general function $\Gamma(\gamma_{max}, \epsilon_n)$ to model both Case A and Case B cracking systems [*46*]. Recently, stress terms are also introduced in conjunction with strain terms in multiaxial fatigue damage models to account for the mean stress effect and the nonproportional hardening effect. Socie et al. [*47*] proposed a shear cracking model, $\gamma_{max} + \epsilon_n + \sigma_{no}/E$, which simplified the Γ function by Brown and Miller. In this model, a mean stress parameter, σ_{no}, was incorporated to account for the mean stress effect. Fatemi and Socie [*48*] proposed another shear cracking model: $\gamma_{max}(1 + n\sigma_n^{max}/\sigma_y)$ to correlate the shear cracking fatigue data for both in-phase and out-of-phase loadings. In this model, the additional hardening caused by out-of-phase loading was taken into account by σ_n^{max} where n is a material constant, and σ_y is yield strength of the subject material. Moreover, a tensile cracking parameter, $\sigma_1\epsilon_1$[2], was proposed by Smith et al. during uniaxial fatigue [*49*] and has been successfully used by Socie [*50*] for the correlation of multiaxial fatigue data of tensile cracking behavior. However, it should be emphasized that all the above models were obtained

[2] The original notation was $\sigma_1^{max}\frac{\Delta\epsilon_1}{2}$.

by treating the subject materials as isotropic. The effect of anisotropy has not been included in any multiaxial fatigue damage model.

The authors are currently conducting investigations on the cyclic deformation and biaxial fatigue damage behavior of anisotropic Al-6061-T6 [*51,52*]. We have found that the initial material anisotropy played an important role in the modeling of multiaxial fatigue damage. In this work, we will develop general anisotropic constitutive relations and a general multiaxial fatigue damage model to predict the anisotropic plastic deformation behavior and low-cycle fatigue life along any material orientation of the Al-6061-T6 plate. Experimental data of three orientations of the plate under axial-torsional biaxial loadings are compared with theoretical predictions.

Theory

Yield Function in the Principal Orthotropic Directions

The anisotropic constitutive relations in this study are formulated for orthotropic materials possessing three mutually orthogonal planes of symmetry. Typical examples of such materials are fiber-reinforced laminas and cold-rolled metal plates. As shown in Fig. 1, a Cartesian coordinate system, *xyz*, is chosen to coincide with the principal orthotropic axes of an orthotropic plate cold-rolled unidirectionally. The x axis is along the transverse direction (TD), the y axis is along the rolling direction (RD), and the z axis is along the normal direction of the plate. Following the macroscopic continuum anisotropic plasticity theory proposed by Shih and Lee [*15*], the yield function of the plate with respect to the *xyz* coordinate system can be expressed as

$$3f = M_{ij}\sigma_i\sigma_j - k^2 = 0 \tag{3}$$

It can also be expressed in a matrix form

$$3f = [\sigma]^T[M][\sigma] - k^2 = 0 \tag{4}$$

where

$$[\sigma] = \begin{bmatrix} \sigma_x \\ \sigma_y \\ \sigma_z \\ \tau_{xy} \\ \tau_{yz} \\ \tau_{zx} \end{bmatrix} = \begin{bmatrix} \sigma_1 \\ \sigma_2 \\ \sigma_3 \\ \sigma_4 \\ \sigma_5 \\ \sigma_6 \end{bmatrix} \tag{5}$$

$$[M] = \begin{bmatrix} M_{11} & M_{12} & M_{12} & 0 & 0 & 0 \\ M_{12} & M_{22} & M_{23} & 0 & 0 & 0 \\ M_{13} & M_{23} & M_{33} & 0 & 0 & 0 \\ 0 & 0 & 0 & M_{44} & 0 & 0 \\ 0 & 0 & 0 & 0 & M_{55} & 0 \\ 0 & 0 & 0 & 0 & 0 & M_{66} \end{bmatrix} \tag{6}$$

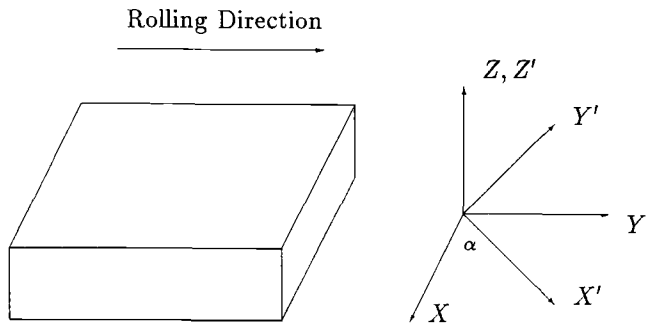

FIG. 1—*An orthotropic plate with two Cartesian coordinate systems* xyz *and* x'y'z'.

where σ_i and σ_j are stress vectors, M_{ij} are anisotropic material coefficients representing the distortion of yield surface, and k is the effective size of the yield surface. In the $[M]$ matrix, the six diagonal terms, i.e., $M_{11}, M_{22}, \ldots, M_{66}$ reflect the anisotropy of yielding stress; three off-diagonal terms M_{12}, M_{23}, and M_{13} represent the plastic Poisson's ratio. There are only six independent anisotropic material coefficients in this formulation because three constraints are imposed

$$M_{11} + M_{12} + M_{13} = 0, \qquad M_{12} + M_{22} + M_{23} = 0, \qquad M_{13} + M_{23} + M_{33} = 0$$

These constraints ensure the independence of yielding from hydrostatic pressure and that plastic deformation occurs with no volume change. For isotropic materials, M_{ij} have the following fixed values, and the yield function reduces to the isotropic von Mises yield condition.

$$M_{11} = M_{22} = M_{33} = 1, \qquad M_{44} = M_{55} = M_{66} = 3, \qquad M_{12} = M_{23} = M_{13} = -0.5$$

But for an anisotropic material, M_{ij} and k must be determined from experiments. In the original yielding function by Shih and Lee, Eq 2, the terms α_i, α_j were introduced to locate the center of initial and subsequent yielding surfaces. In the present study, α_i and α_j are neglected as we intend to model the initial material anisotropy or the distortion of yield surface, a subject receiving relatively rare attention compared to the extensive modeling work about the plastic deformation anisotropy. In addition, isotropic hardening rule is used in this work; thus, the initial yield surface centered at origin can only expand isotropically. The shape of the initial yield surface, however, can be distorted significantly as specified by the anisotropic coefficients M_{ij}. Following the Levy-Mises assumption $d\epsilon_i^p/S_i$ = constant, one can obtain flow relations as

$$d\epsilon_i^p = \frac{3}{2}\frac{d\bar{\epsilon}^p}{\bar{\sigma}} S_i \tag{7}$$

where $\bar{\sigma}$ is the effective stress, and S_i is the generalized stress deviator. They are defined as

$$\bar{\sigma}^2 = M_{ij}\sigma_i\sigma_j \tag{8}$$

$$S_i = \frac{2}{3} M_{ij}\sigma_j \tag{9}$$

Transformation of the Yield Function to a New Coordinate System

The above constitutive relations in the xyz coordinate system can be transformed to other coordinate systems to model anisotropic plastic deformation along any material orientation. In this section, we present a simple transformation as an example which can be used to model the plastic deformation of any material orientation in the xy plane. Define a new Cartesian coordinate system, $x'y'z'$, as follows: the x' and y' axes are still in the xy plane but orientated with an angle α to the x and y axes, respectively, and the z' axis coincides with the z axis. The $x'y'z'$ coordinate system is also shown in Fig. 1.

The stress transformation is given by

$$[\sigma] = [T][\sigma'] \tag{10}$$

where $[T]$ is the transformation matrix expressed as

$$[T] = \begin{bmatrix} m^2 & n^2 & 0 & -2mn & 0 & 0 \\ n^2 & m^2 & 0 & 2mn & 0 & 0 \\ 0 & 0 & 1 & 0 & 0 & 0 \\ mn & -mn & 0 & m^2 - n^2 & 0 & 0 \\ 0 & 0 & 0 & 0 & m & n \\ 0 & 0 & 0 & 0 & -n & m \end{bmatrix} \tag{11}$$

where $m = \cos\alpha$ and $n = \sin\alpha$. The stress vector in the new coordinate system $[\sigma']$ is

$$[\sigma'] = \begin{bmatrix} \sigma_{x'} \\ \sigma_{y'} \\ \sigma_{z'} \\ \tau_{x'y'} \\ \tau_{y'z'} \\ \tau_{z'x'} \end{bmatrix} \tag{12}$$

The yield function expressed with respect to the new coordinate system, $x'y'z'$, is then obtained as

$$3f = [\sigma]^T[M][\sigma] - k^2 = [\sigma']^T[T]^T[M][T][\sigma'] - k^2 = 0 \tag{13}$$

or

$$3f = [\sigma']^T[Q][\sigma'] - k^2 = 0 \tag{14}$$

$$[Q] = [T]^T[M][T] \tag{15}$$

$$[Q] = \begin{bmatrix} Q_{11} & Q_{12} & Q_{13} & Q_{14} & 0 & 0 \\ Q_{12} & Q_{22} & Q_{23} & Q_{24} & 0 & 0 \\ Q_{13} & Q_{23} & Q_{33} & Q_{34} & 0 & 0 \\ Q_{14} & Q_{24} & Q_{34} & Q_{44} & 0 & 0 \\ 0 & 0 & 0 & 0 & Q_{55} & Q_{56} \\ 0 & 0 & 0 & 0 & Q_{56} & Q_{66} \end{bmatrix} \tag{16}$$

where Q_{ij} are the anisotropic material coefficients in the new coordinate system. The six diagonal terms describe the yield strength dependence on material orientation. Three off-diagonal terms, Q_{12}, Q_{23}, and Q_{13}, are the plastic Poisson's ratios, and the other four off-diagonal terms, Q_{14}, Q_{24}, Q_{34}, and Q_{56}, are the coupling terms because the new coordinate system, $x'y'z'$, does not coincide with the principal anisotropic axes of the material. Once M_{ij} and transformation matrix $[T]$ are determined, Q_{ij} can be evaluated from Eq 15 without conducting further tests. The flow relations in the new coordinate system are

$$d\epsilon_{i'}^{p} = \frac{3}{2}\frac{d\bar{\epsilon}^{p}}{\bar{\sigma}} S_{i'} \tag{17}$$

Effective stress is defined as

$$\bar{\sigma}^2 = Q_{ij}\sigma_{i'}\sigma_{j'} \tag{18}$$

The stress deviator are defined as

$$S_{i'} = \frac{2}{3} Q_{ij}\sigma_{j'} \tag{19}$$

Yield and Plastic Flow along the 45° Direction

In this section, we focus on the yield and plastic flow of a specific material orientation, i.e., 45° to the rolling direction in the plate plane (Diagonal Direction DD), to discuss two issues: (1) the assumptions involved in shear stresses: $\tau_{x\theta} = \tau_{xz}$ and $\tau_{y\varphi} = \tau_{yz}$; (2) the coupling terms Q_{14}, Q_{24}, Q_{34}, and Q_{56} in the $[Q]$ matrix.

In our experimental program, shear stresses are measured from solid cylindrical specimens under torsional loading. A cross section of a solid cylindrical specimen subjected to torsion is shown in Fig. 2 where the specimen is along the x axis and the measured shear stress is $\tau_{x\theta}$. θ is an arbitrary angle. The relationship between the measured shear stress, $\tau_{x\theta}$, and the shear stresses, τ_{xy} and τ_{xz}, which are expressed with respect to the xyz coordinate system, is

$$\tau_{x\theta} = \tau_{xz} \cos\theta + \tau_{xy} \sin\theta \tag{20}$$

Similarly, if the specimen is along the y axis, another relationship between the measured shear stress, $\tau_{y\varphi}$, and the shear stresses in the xyz system can be found

$$\tau_{y\varphi} = \tau_{yx} \cos\varphi + \tau_{yz} \sin\varphi \tag{21}$$

where φ is an arbitrary angle similar to θ. As the plate is of orthogonal orthotropy, the shear stresses expressed in orthogonal xyz or $x'y'z'$ coordinate systems are needed in the formulation of constitutive relations rather than the measured shear stresses, $\tau_{x\theta}$ and $\tau_{y\varphi}$. In order to evaluate the shear yielding stress and obtain the anisotropic coefficients M_{55} and M_{66}, we assumed that $\tau_{x\theta} = \tau_{xz}$ and $\tau_{y\varphi} = \tau_{yz}$ in Ref *51*. An obvious question remains unanswered concerning these assumptions: why assume $\tau_{y\varphi} = \tau_{yz}$ rather than $\tau_{y\varphi} = \tau_{xy}$ in Eq 21? Or why assume $\tau_{x\theta} = \tau_{xz}$ rather than $\tau_{x\theta} = \tau_{xy}$ = Eq 20?

This question may be answered by considering the yield and plastic flow along the 45° DD

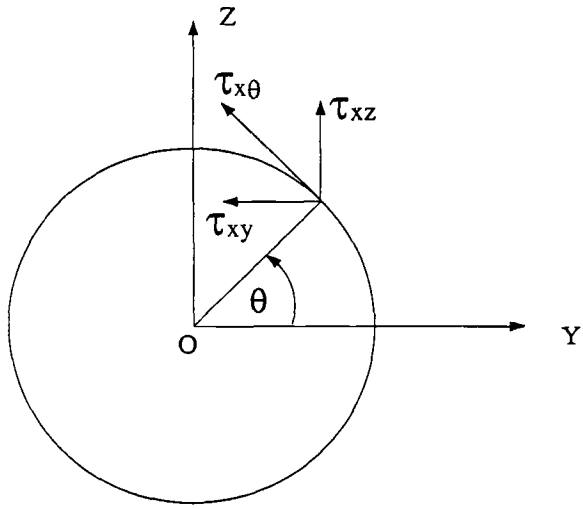

FIG. 2—*Schematic diagram of a cross section of a solid cylindrical specimen under torsion.*

direction. Set the $x'y'z'$ coordinate system with $\alpha = \pi/4$. Then both x' and y' axes are along the 45° direction and a DD specimen can be along either the x' axis or the y' axis, which should result in the same yield function and flow relations.

First, suppose the specimen is along the x' axis under combined proportional axial-torsional loading in strain control. Based on the equilibrium equations and the stress boundary conditions, the stress state on the specimen surface is

$$\sigma = \sigma_{x'} \neq 0, \qquad \tau = \tau_{x'z'} \neq 0$$

$$\sigma_{y'} = \sigma_{z'} = \tau_{x'y'} = \tau_{y'z'} = 0$$

where $\epsilon_{x'}$ and $\gamma_{x'z'}$ are the applied strains. σ and τ are the measured normal and shear stresses, respectively. Note that the applied shear strain has been assumed to be $\gamma_{x'z'}$, and the measured shear stress, $\tau = \tau_{x'\theta}$, has been assumed to be $\tau_{x'z'}$.

The yield function will then be

$$3f = Q_{11}\sigma^2 + Q_{66}\tau^2 - k^2 = 0 \tag{22}$$

The plastic strain increments are

$$\begin{aligned}
d\epsilon^p_{x'} &= (d\bar{\epsilon}^p/\bar{\sigma})Q_{11}\sigma_{x'} \\
d\epsilon^p_{y'} &= (d\bar{\epsilon}^p/\bar{\sigma})Q_{12}\sigma_{x'} \\
d\epsilon^p_{z'} &= (d\bar{\epsilon}^p/\bar{\sigma})Q_{13}\sigma_{x'} \\
d\gamma^p_{x'y'} &= (d\bar{\epsilon}^p/\bar{\sigma})Q_{14}\sigma_{x'} \\
d\gamma^p_{x'z'} &= (d\bar{\epsilon}^p/\bar{\sigma})Q_{66}\tau_{x'z'} \\
d\gamma^p_{y'z'} &= (d\bar{\epsilon}^p/\bar{\sigma})Q_{56}\tau_{x'z'}
\end{aligned} \tag{23}$$

Since the DD direction is not a principal orthotropic direction, coupling existed in plastic range due to the plastic orthotropy of the plate. The above equations show clearly that shear plastic strain, $\gamma^p_{x'y'}$ exists due to the normal stress, $\sigma_{x'}$, which is an axial-torsional coupling. Moreover, the shear plastic strain, $\gamma^p_{y'z'}$, also exists due to the shear stress, $\tau_{x'z'}$, which is the coupling between torsional terms.

The flow relation expressed in terms of the ratio of applied plastic strains against the ratio of measured stresses can be obtained from Eq 23

$$\frac{d\gamma^p}{d\epsilon^p} = \frac{d\gamma^p_{x'z'}}{d\epsilon^p_{x'}} = \frac{Q_{66}}{Q_{11}}\frac{\tau}{\sigma} \tag{24}$$

Now let the specimen be along the y' axis under the same combined proportional axial-torsional loading condition in strain control. Similarly, if the measured shear stress $\tau_{y'\varphi}$ is assumed to be $\tau_{y'z'}$, the following yield function and the flow relation will be obtained

$$3f = Q_{22}\sigma^2 + Q_{55}\tau^2 - k^2 = 0 \tag{25}$$

and

$$\frac{d\gamma^p_{y'z'}}{d\epsilon^p_{y'}} = \frac{d\gamma^p}{d\epsilon^p} = \frac{Q_{55}}{Q_{22}}\frac{\tau}{\sigma} \tag{26}$$

It can be shown from Eq 15 that if $\alpha = 45°$,

$$Q_{11} = Q_{22}, \qquad Q_{55} = Q_{66}$$

Thus the same yield functions, Eqs 22 and 25, as well as the same flow relations, Eqs 24 and 26, are obtained by assuming $\tau_{x'\theta} = \tau_{x'z'}$ when the specimen is along x' and assuming $\tau_{y'\varphi} = \tau_{y'z'}$ when the specimen is along y' axis. This is physically correct because x' and y' are actually along identical 45° directions.

However, if one assumes $\tau = \tau_{y'\varphi} = \tau_{x'y'}$, the following yield function and flow relation will be obtained

$$3f = Q_{22}\sigma^2 + Q_{44}\tau^2 - k^2 = 0 \tag{27}$$

$$\frac{d\gamma^p_{x'y'}}{d\epsilon^p_{y'}} = \frac{d\gamma^p}{d\epsilon^p} = \frac{Q_{24}\sigma + Q_{44}\tau}{Q_{22}\sigma + Q_{24}\tau} \tag{28}$$

Comparing these results with Eqs 22 and 24, one finds that Eq 27 is different from Eq 22 because $Q_{44} \neq Q_{66}$ and that Eq 28 is totally different from Eq 24.

A Multiaxial Fatigue Damage Model based on the Strain Vector

In order to predict the fatigue life of the orthotropic plate under multiaxial loading conditions, we proposed a multiaxial fatigue damage D model based on the strain vector [*53*]

$$D^2 = [\epsilon]^T[A][\epsilon] \tag{29}$$

where the strain vector, $[\epsilon]$, is defined as

$$[\epsilon] = \begin{bmatrix} \epsilon_x \\ \epsilon_y \\ \epsilon_z \\ \epsilon_{xy} \\ \epsilon_{yz} \\ \epsilon_{zx} \end{bmatrix} = \begin{bmatrix} \epsilon_1 \\ \epsilon_2 \\ \epsilon_3 \\ \epsilon_4 \\ \epsilon_5 \\ \epsilon_6 \end{bmatrix} \tag{30}$$

where $[\epsilon]^T$ is the transpose matrix of $[\epsilon]$ and $[A]$ is a matrix of material coefficients which describe the variation of low-cycle fatigue resistance of the material with material orientation. In the xyz coordinate system, the simplest diagonal matrix $[A]$ is chosen for an orthotropic material

$$[A] = \begin{bmatrix} A_{11} & 0 & 0 & 0 & 0 & 0 \\ 0 & A_{22} & 0 & 0 & 0 & 0 \\ 0 & 0 & A_{33} & 0 & 0 & 0 \\ 0 & 0 & 0 & A_{44} & 0 & 0 \\ 0 & 0 & 0 & 0 & A_{55} & 0 \\ 0 & 0 & 0 & 0 & 0 & A_{66} \end{bmatrix} \tag{31}$$

A total of six nonzero material constants exist in this diagonal matrix. For an isotropic material, $A_{11} = A_{22} = A_{33}$ and $A_{44} = A_{55} = A_{66}$ are expected. The above diagonal $[A]$ matrix can be determined from uniaxial fatigue test results along the principal orthotropic axes of an orthotropic material in conjunction with its constitutive relations [*53*].

The major advantage of this D model is that it can be transformed to any new coordinate system to predict low-cycle fatigue life along any new material orientation without conducting further tests. For example, to obtain the general form of the D model in the $x'y'z'$ system, the following strain transformation is carried out

$$[\epsilon] = [T][\epsilon'] \tag{32}$$

where $[T]$ is the transformation matrix given by Eq 11, and $[\epsilon']$ is the strain vector in the $x'y'z'$ coordinate system. Therefore, in the new $x'y'z'$ coordinate system, the fatigue damage model becomes

$$D^2 = [\epsilon']^T[T]^T[A][T][\epsilon'] = [\epsilon']^T[B][\epsilon'] \tag{33}$$

where $[B]$ is the anisotropic material fatigue property matrix in the new coordinate system.

$$B_{ij} = [B] = [T]^T[A][T] \tag{34}$$

Similar to Q_{ij}, B_{ij} can be calculated through Eq 34 if $[A]$ and $[T]$ are determined.

Experimental Verification

Experimental Procedure

The subject material of this investigation is an Al-6061-T6 plate cold-rolled in one direction. The 6061 aluminum alloy is a light-weight, medium-strength, corrosion-resistant structural

TABLE 1—*Chemical composition of Al-6061-T6.*

Mg	Si	Cu	Cr	Fe	Mn	Zn	Ti	Al
1.0	0.6	0.25	0.25	0.7	0.15	0.25	0.15	Balance

material. After the T6 temper treatment, the material retains its texture anisotropy, but the plastic deformation anisotropy due to the prior plastic work is eliminated [*21,51*]. In addition, the material was found to be rate insensitive at room temperature [*54*]. The nominal chemical composition of the material is given in Table 1. The nominal monotonic mechanical properties are given in Table 2.

The orthotropy of the plate was caused by the elongation of grains and the alignment of precipitates along the rolling direction [*51*]. Solid cylindrical specimens 9.5 mm in diameter in the gage length were prepared from the plate along three directions: rolling direction (RD), transverse direction (TD), and 45° diagonal direction (DD). The specimen configuration can be found in Ref *51*. The surface of the specimens was polished successively with finer grits to a mirror-like finish.

Fully reversed controlled-strain low-cycle fatigue tests were performed with the three direction-oriented specimens at room temperature under three loading conditions: pure axial ($\lambda = \gamma/\epsilon = 0$), pure torsional ($\lambda = \infty$), and combined axial-torsional in-phase ($\lambda = 0.8, 2$). Tests were performed using a servohydraulic close-looped Instron 1322 biaxial machine with applied strain rates between 10^{-3} and $10^{-4}s^{-1}$. Normal and shear strains were controlled with an Instron biaxial extensometer of gage length 10 mm. Load-elongation and torque-twist data were recorded by X-Y recorders.

Cyclic Stress Strain Responses

Cyclic stress-strain responses of the three orientations were obtained by using both the constant strain amplitude method and the multiple step test method [*55*]. Same cyclic stress-strain responses were obtained from the two different experimental methods for each orientation. The cyclic stress-strain curves of the three orientations are shown in Figs. 3*A* and 3*B*. In the elastic regime, the three orientations show the same stress responses, which implies that the material is isotropic in the elastic regime. In the plastic regime, however, the cyclic stress responses are different and thus the material is anisotropic. Under axial loading higher stress responses are obtained along the TD orientation, but under torsional loading higher stress responses are obtained from RD orientations. The stress responses of the DD specimens are within those of RD and TD specimens for both axial and torsional loadings. The cyclic stress-strain curves of the three orientations are obtained from multiple companion specimens, and the results shown in Fig. 3 are the average of the multispecimen test results.

TABLE 2—*The nominal mechanical properties of Al-6061-T6.*

E, (MPa)	σ_y, (MPa)	σ_u, (MPa)	φ, (%)
69 000	276	310	12

NOTE: E = Young's modulus.
σ_y = Yield strength.
σ_u = Ultimate tensile strength.
φ = Elongation in 50 mm.

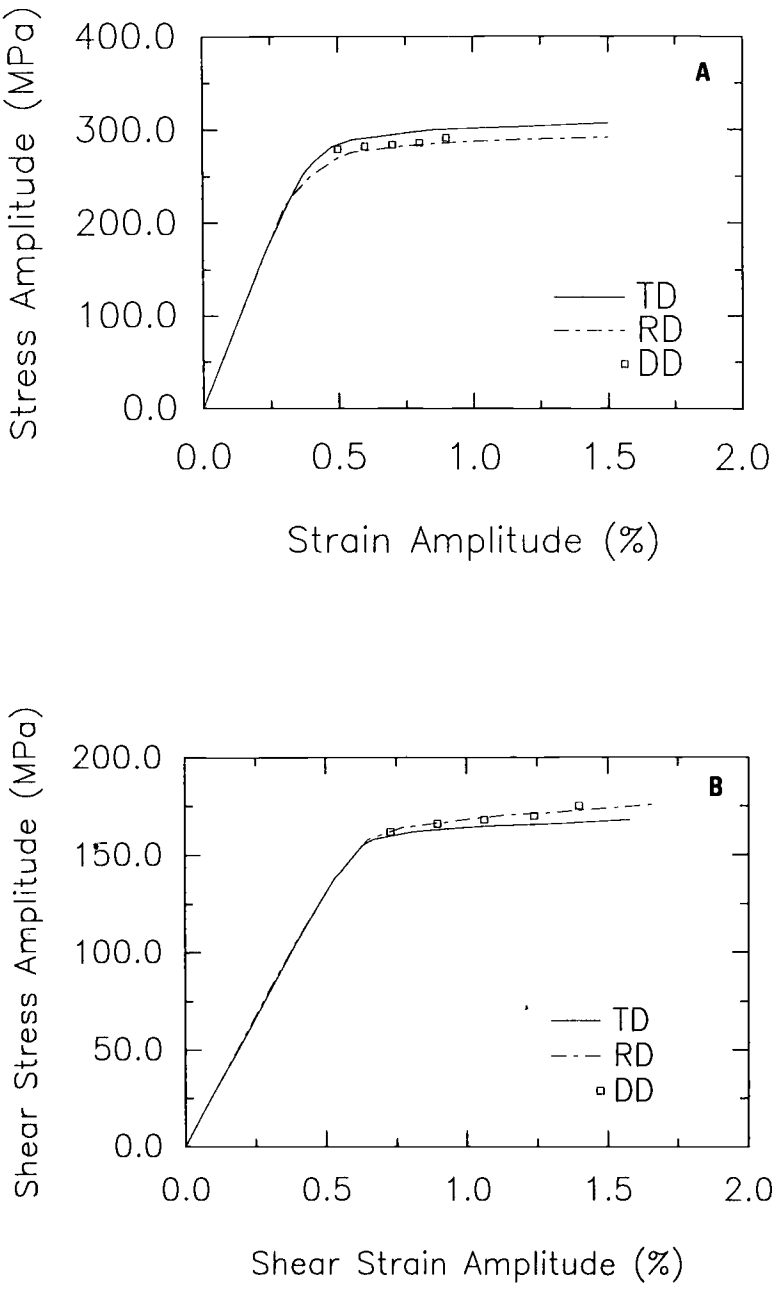

FIG. 3—*Cyclic stress-strain curves of the three orientations—TD, RD, DD:* (a) *under axial loading,* (b) *under torsional loading.*

The anisotropic coefficients, M_{ij}, and the effective size of the yield surface, k, were evaluated from the cyclic stress-strain responses of the three orientations under pure axial and pure torsional loadings with a yielding definition of 0.2% off-set strain, and the results are given below.

$$M_{ij} = [M] = \begin{bmatrix} 1.0 & -0.376 & -0.624 & 0 & 0 & 0 \\ -0.376 & 1.127 & -0.751 & 0 & 0 & 0 \\ -0.624 & -0.751 & 1.375 & 0 & 0 & 0 \\ 0 & 0 & 0 & 2.88 & 0 & 0 \\ 0 & 0 & 0 & 0 & 3.02 & 0 \\ 0 & 0 & 0 & 0 & 0 & 3.13 \end{bmatrix} \tag{35}$$

The effective size of the yield surface is determined as $k = 292$ MPa. The values of M_{11}, M_{22}, and k are obtained directly from the cyclic stress-strain responses of TD and RD specimens under pure axial loadings. The values of M_{33} are found by using the method proposed by Backofen in which two plastic strain ratios, R and P, are measured and the third yield stress along the normal direction can then be determined [*56*]. M_{55} and M_{66} are determined from the cyclic stress-strain responses of RD and TD orientations under pure torsional loading. M_{44} is determined through the results of DD specimens because it is impossible to conduct torsional tests along the normal direction of the plate of 31.25 mm (1.25 in.) thickness. The values of M_{11}, M_{22}, and M_{33} clearly show the orthotropy of the plate. However, the values of M_{44}, M_{55}, and M_{66} are quite close to the isotropic value, which may be due to the shear stress assumptions involved when determining them.

The Q_{ij} matrix in the new coordinate system $x'y'z'$ (x' and y' are 45° to x and y, respectively, z' coincides with z) is also found through Eq 15, and the results are given below.

$$Q_{ij} = [Q] = \begin{bmatrix} 1.065 & -0.376 & -0.688 & 0.0635 & 0 & 0 \\ -0.376 & 1.065 & -0.688 & 0.0635 & 0 & 0 \\ -0.688 & -0.688 & 1.375 & -0.127 & 0 & 0 \\ 0.0635 & 0.0635 & -0.127 & 2.88 & 0 & 0 \\ 0 & 0 & 0 & 0 & 3.075 & -0.055 \\ 0 & 0 & 0 & 0 & -0.055 & 3.075 \end{bmatrix} \tag{36}$$

From the above results of Q_{ij}, it is clear that the coupling terms Q_{14}, Q_{24}, Q_{34}, and Q_{56} are not significant. In addition, the values associated with x' axis are equal to the corresponding values associated with y' axis, namely $Q_{11} = Q_{22}$, $Q_{13} = Q_{23}$, $Q_{14} = Q_{24}$, . . . , etc. This is expected because the x' and y' axes are physically identical when the transformation angle $\alpha = 45°$

Yielding and Plastic Flow Behavior

Based on the results of M_{ij} and Q_{ij}, theoretical yield functions and flow relations for the three orientations under combined axial-torsional loadings can be obtained as follows.

Yield functions

$$\text{Along TD: } M_{11} = 1,\ M_{66} = 3.13,\ k = 292 \text{ MPa},\ \sigma^2 + 3.13\tau^2 = 292^2 \tag{37}$$

$$\text{Along RD: } M_{22} = 1.127,\ M_{55} = 3.02,\ k = 292 \text{ MPa},\ \sigma^2 + 2.68\tau^2 = 275^2 \tag{38}$$

$$\text{Along DD: } Q_{11} = 1.065,\ Q_{66} = 3.075,\ k = 292 \text{ MPa},\ \sigma^2 + 2.89\tau^2 = 283^2 \tag{39}$$

Flow relations

$$\text{TD: } \frac{d\gamma^p}{d\epsilon^p} = 3.13\,\frac{\tau}{\sigma} \tag{40}$$

$$\text{RD: } \frac{d\gamma^p}{d\epsilon^p} = 2.68\,\frac{\tau}{\sigma} \tag{41}$$

$$\text{DD: } \frac{d\gamma^p}{d\epsilon^p} = 2.89\,\frac{\tau}{\sigma} \tag{42}$$

The material constants, M_{ij} and Q_{ij}, in the constitutive relations are obtained based on the experimental data of pure uniaxial loadings. The predictive capability of the constitutive relations must be evaluated with the data of more complicated multiaxial loadings. In this work, tests of combined proportional axial-torsional loadings are carried out to evaluate the predictive capability of the constitutive relations. Figure 4 shows the comparison between the experimental yielding points and theoretical yield functions. The experimental data of flow relations is plotted with the predictions of the theoretical flow relations in Fig. 5. Only the results of DD orientation are shown in Figs. 4 and 5. Similar figures showing the results of TD and RD orientations can be found in Ref *51*. These figures indicate that the predictions of the constitutive relations agree with the experimental data reasonably well. More experiments with other loading paths such as biaxial tension/compression, combined axial-torsional-internal pressure, and nonproportional loadings are needed to further evaluate the predictive capability of the constitutive relations.

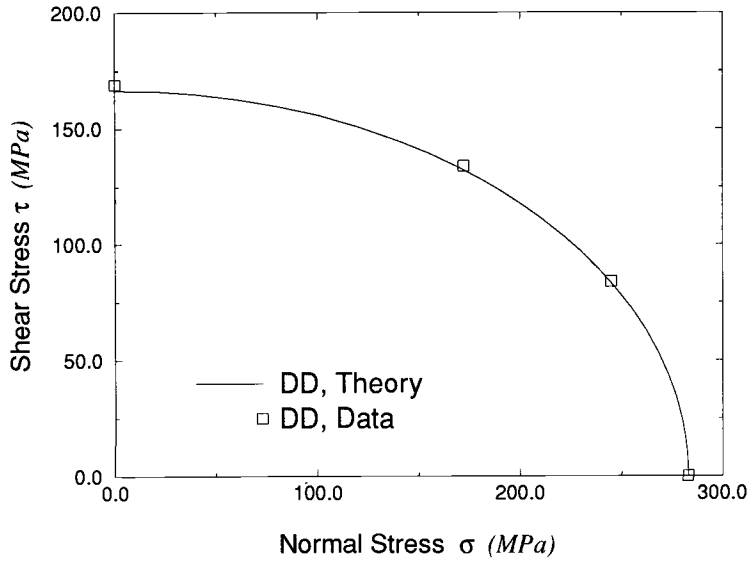

FIG. 4—*Comparison of the experimental yielding points with the predictions of the constitutive relations along DD orientation.*

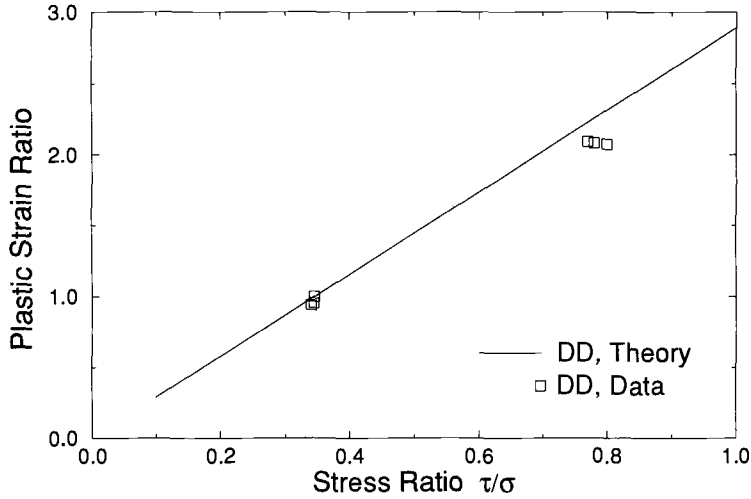

FIG. 5—*Comparison of the experimental flow behavior with the predictions of the constitutive relations along DD orientation.*

Effective Stress-Effective Strain Criteria

Two anisotropic effective stress-effective strain criteria can be evaluated from the constitutive relations obtained in previous sections. One is the von Mises criterion $\bar{\sigma} - \bar{\epsilon}$, and the other is the Tresca criterion $\tau_{max} - \gamma_{max}$. Figure 6 shows the correlation of the two criteria with the experimental cyclic stress-strain responses of the three orientations under the three loading conditions. Obviously the von Mises criterion gives a better correlation for this material.

Fatigue Life Prediction

Fatigue cracking behavior was observed during the low-cycle fatigue tests of the three direction-oriented specimens. After the fatigue tests, the tested specimens were inspected using the liquid penetrant nondestructive testing (NDT) method to reveal cracks and their orientations on specimen surface. Under torsional loading, cracks initiated and grew along the direction of specimen axis, i.e., on the planes of maximum shear. However, no cracks were developed along the circumferencial direction, which is another orientation of the planes of maximum shear. This type of axis-orientated shear cracks was also observed with other materials by other researchers [*26,27,57*]. All the three direction-oriented specimens displayed the same shear cracking behavior. Cracks initiated early and propagated fast along the specimen axis. A few cracks linked and became major cracks. The final length of the major cracks were about several centimetres.

Under axial fatigue loading, all of the three direction-oriented specimens also showed similar shear cracking behavior. Cracks initiated and grew on the planes 45° to the specimen axis, i.e., planes of maximum shear, for the majority of fatigue life. Cracks initiated late and only one or two cracks were visible on specimen surface at the failure point. Under combined axial-torsional loading condition, cracks also initiated early and remained on the planes of maximum shear in all the three directions of specimens. The number of the visible cracks at the failure point under the combined biaxial loading appeared to be more than those under axial fatigue

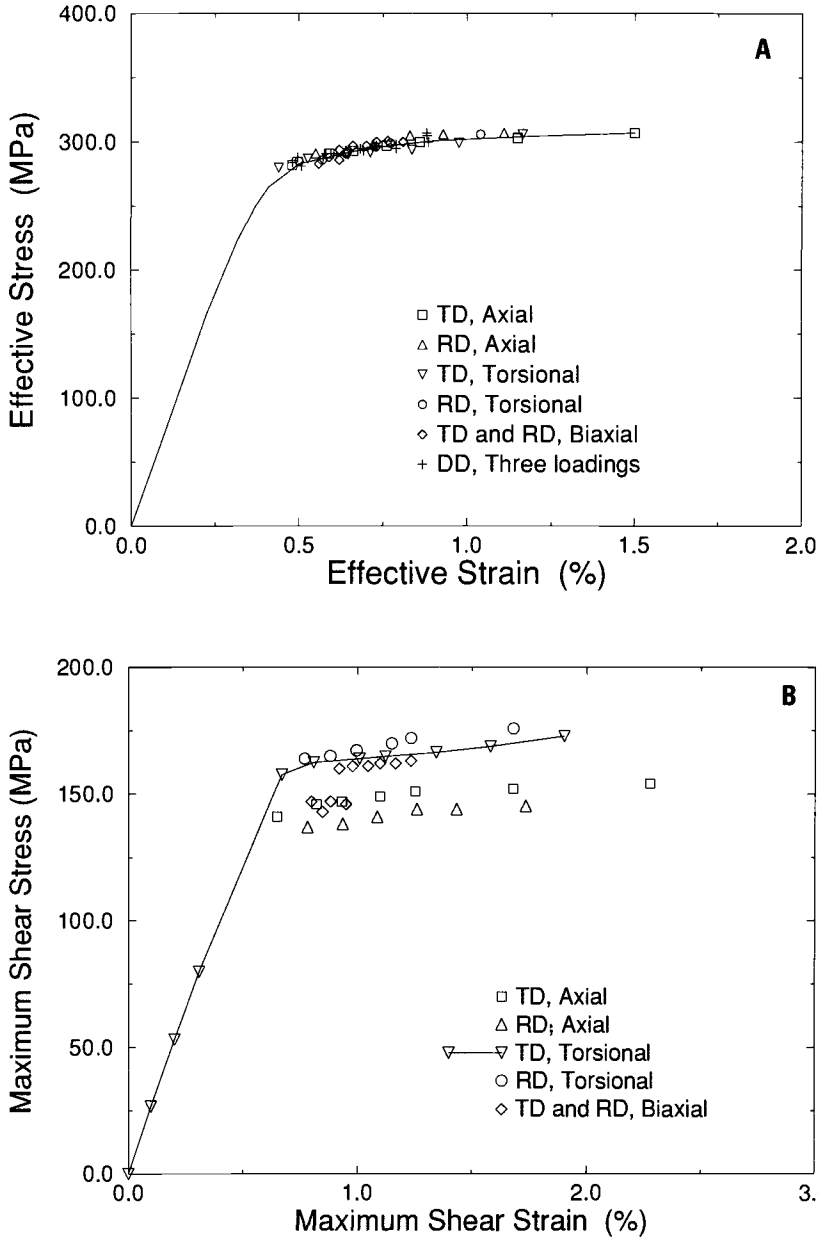

FIG. 6—*The correlations of the two effective stress-effective strain criteria with the experimental cyclic stress-strain responses of the three orientations under three loading conditions:* (A) *von Mises criterion* $\bar{\sigma} - \bar{\epsilon}$, (B) *Tresca criterion* $\tau_{max} - \gamma_{max}$.

loading but less than those under torsional fatigue loading. Apparently, the fatigue cracking behavior of the orthotropic plate is shear damage dominated. The material anisotropy seemed to have negligible effect on the fatigue cracking behavior even though it did affect fatigue life data, which will be shown in the following. Photographs of the shear cracks and their orientations on specimen surface under the three loading conditions can be found in Refs *51* and *53*.

Low-cycle fatigue tests were conducted on the three direction-orientated specimens under three loading conditions: axial, torsional, and combined axial-torsional in-phase. Fatigue failure was defined as 10% load/torque drop. The fatigue test data under pure axial loading and pure torsional loading of the three directions—RD, TD, and DD—are plotted in Fig. 7. The solid lines in Fig. 7 are obtained from linear regressions of the RD and TD data. Under axial fatigue loading, shorter fatigue lives are obtained from TD specimens. But under torsional fatigue loading, RD specimens yield shorter fatigue lives. This observed anisotropy in low-cycle fatigue life is in good agreement with the observed anisotropy in cyclic stress response: TD specimens give higher stress responses and also shorter fatigue lives under strain-controlled axial fatigue; RD specimens give higher stress responses and shorter fatigue lives under strain-controlled torsional fatigue condition.

From the fatigue life data of the three direction-orientated specimens under pure axial and pure torsional loading conditions, the material constants, A_{ii}, in the D model are obtained [*53*]

$$D^2 = [\epsilon_x \epsilon_y \epsilon_z \epsilon_{xy} \epsilon_{yz} \epsilon_{xz}] \begin{bmatrix} 0.527 & 0 & 0 & 0 & 0 & 0 \\ 0 & 0.423 & 0 & 0 & 0 & 0 \\ 0 & 0 & 0.254 & 0 & 0 & 0 \\ 0 & 0 & 0 & 0.919 & 0 & 0 \\ 0 & 0 & 0 & 0 & 1.0 & 0 \\ 0 & 0 & 0 & 0 & 0 & 0.632 \end{bmatrix} \begin{bmatrix} \epsilon_x \\ \epsilon_y \\ \epsilon_z \\ \epsilon_{xy} \\ \epsilon_{yz} \\ \epsilon_{xz} \end{bmatrix} \tag{43}$$

In the new coordinate system $x'y'z'$, the D model is defined by the $[B]$ matrix, which is also determined using Eq 34. The D model is thus obtained for both xyz and $x'y'z'$ systems and can be used to predict the fatigue lives of the three direction-orientated specimens under combined multiaxial loadings. We also evaluated three other multiaxial fatigue damage models. They are: the plastic work model $\bar{\epsilon}^p\bar{\sigma}$ [*39*], the effective strain model $\bar{\epsilon}$, and the anisotropic shear cracking model $A_i(\gamma_{max} + B_i\epsilon_n)$ [*51*]. Each of these three models represents a different concept. The fatigue damage controlling parameters in these models such as $\bar{\epsilon}$, γ_{max}, ϵ_n, etc. are evaluated by using the anisotropic constitutive relations of the plate. Material properties, A_i and B_i, in the anisotropic shear cracking model are evaluated based on the data of pure uniaxial fatigue loadings. The results are: along TD $A_1 = 0.8$, $B_1 = 2.0$; along RD $A_2 = 1.0$, $B_2 = 0.2$; and along DD $A_3 = 0.9$ and $B_3 = 1.1$.

Moreover, four equations relating the four damage models to fatigue lives are obtained from the baseline data of RD specimens under torsional fatigue loading.

$$D = 0.441 - 0.3949(\log N - 3.2368) \tag{44}$$

$$A_i(\gamma_{max} + B_i\epsilon_n) = 0.882 - 0.77(\log N - 3.2368) \tag{45}$$

$$\bar{\epsilon} = 0.93 - 0.4652(\log N - 2.5315) \tag{46}$$

$$\bar{\epsilon}^p\bar{\sigma} = 1.469 - 1.296(\log N - 2.5315) \tag{47}$$

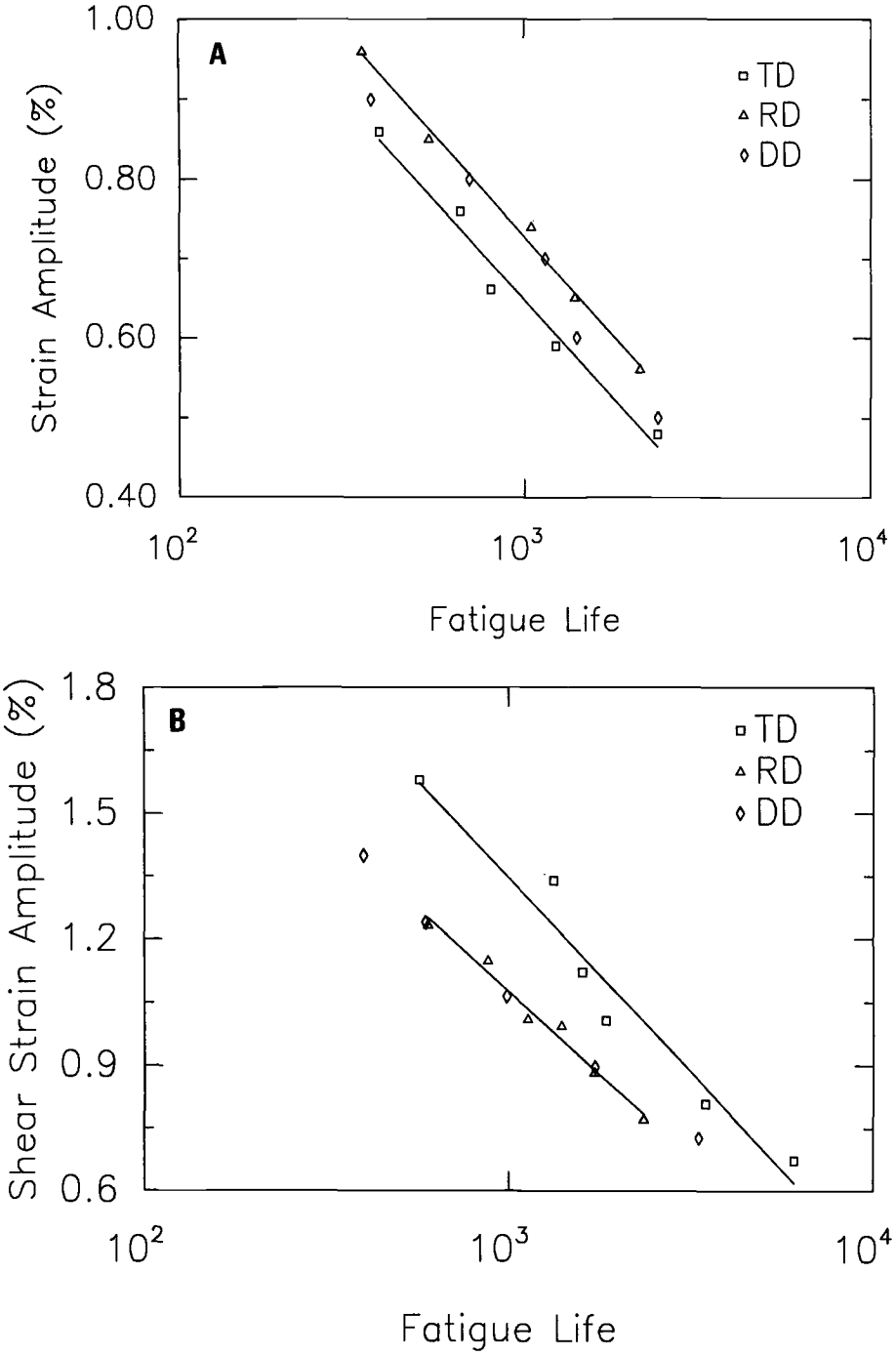

FIG. 7—*Plots of the applied strains against fatigue life of the three direction-oriented of specimens:* (A) *axial loading;* (B) *torsional loading. The two solid lines in* (a) *and* (b) *are obtained from linear regression of the TD and RD data.*

In these equations, the D parameter, the effective strain parameter $\bar{\epsilon}$, and the anisotropic shear parameter $A_i(\gamma_{max} + B_i\epsilon_n)$ are expressed in percentage, and the plastic work parameter, $\bar{\epsilon}^p\bar{\sigma}$, is expressed in MPa. The predicted fatigue lives are calculated with these four equations, and then they are plotted against the actual fatigue lives in Figs. 8 through 11. As shown in Fig. 8, the predictions of the D model are in good agreement with the experimental data, with a scatter factor of 1.5. The plastic work model $\bar{\epsilon}^p\bar{\sigma}$ and the effective strain model $\bar{\epsilon}$ average the biaxial stress-strain responses of multiple material orientations and planes, and neither can reflect the shear damage of the material. Both of them give predictions with scatter factors larger than two, as shown in Figs. 9 and 10. However, both of them can be obtained directly from the constitutive relations of the plate, which allows us to use them to estimate the fatigue life of a new material orientation without conducting further fatigue tests along that orientation. The anisotropic shear cracking model, $A_i(\gamma_{max} + B_i\epsilon_n)$, corresponds with the cracking behavior of the plate and it correlates with the data better than the effective strain and the plastic work models. The predicted lives are within the lines of scatter factor 1.5. The advantage of this model is that it reflects the actual fatigue cracking behavior and thus provides good life predictions. However, the material properties, A_i and B_i, have to be found from the actual fatigue tests along each material orientation under consideration because the controlling parameters, γ_{max} and ϵ_n, are scalars. Although the D model does not reflect the actual fatigue cracking behavior, it offers good fatigue life prediction and it has the convenience of easy transformation. As a result, we think that the D model is superior to the other three models.

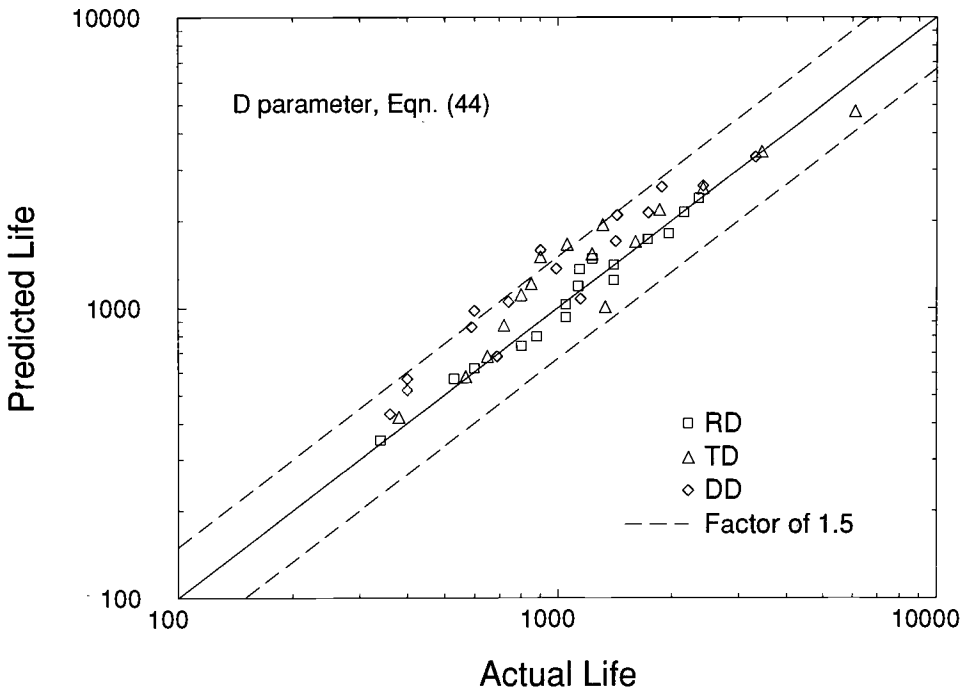

FIG. 8—*Predicted fatigue life against actual fatigue life using the* D *model.*

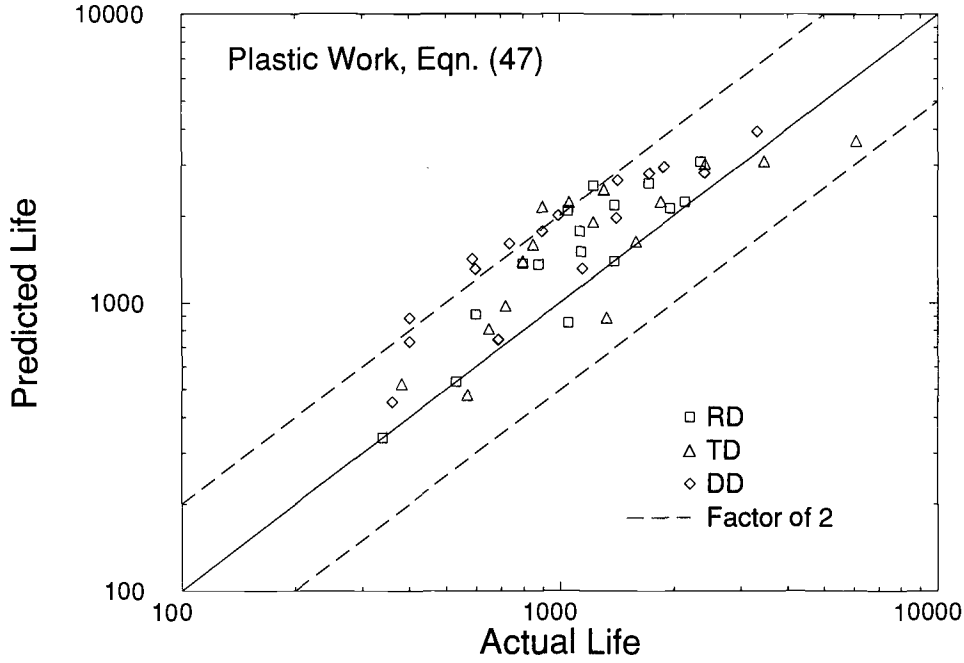

FIG. 9—*Predicted fatigue life against actual fatigue life using the plastic work model.*

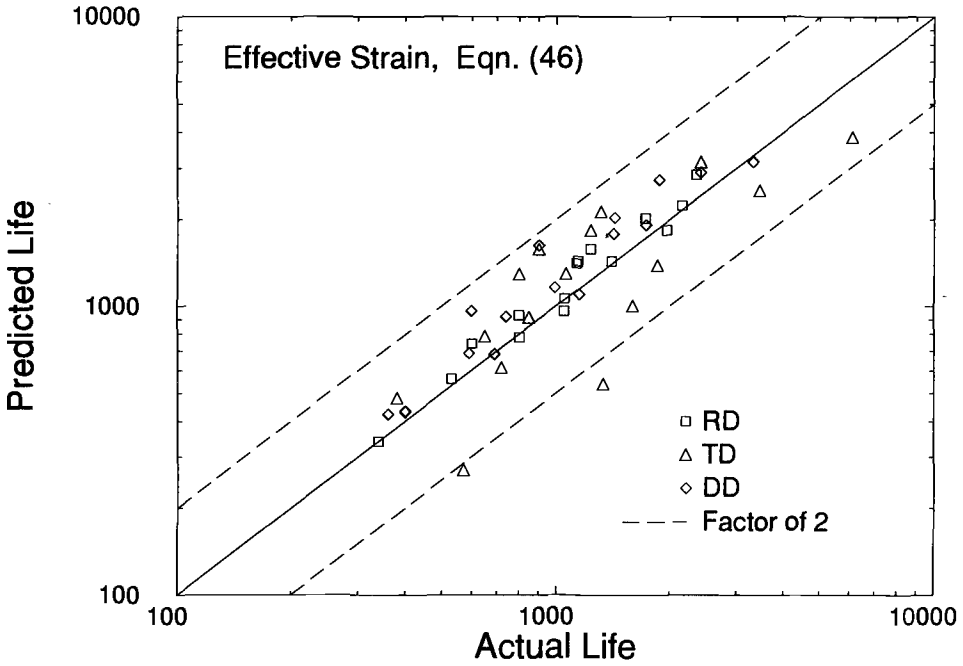

FIG. 10—*Predicted fatigue life against actual fatigue life using the effective strain model.*

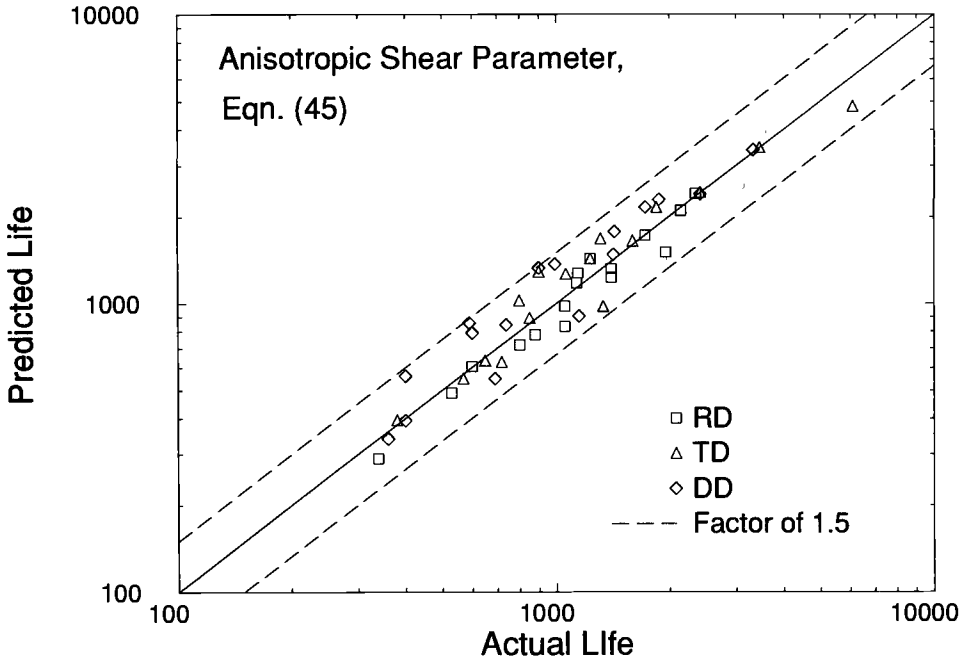

FIG. 11—*Predicted fatigue life against actual fatigue life using the anisotropic shear cracking model* $A_i(\gamma_{max} + B_i\epsilon_n)$.

Discussion

Solid cylindrical specimens were used in this investigation. Under pure torsional or combined axial-torsional loading conditions, there exists a shear stress gradient across the cross section of the solid cylindrical specimen, while in a thin-wall tube specimen, the most commonly used specimen configuration in multiaxial fatigue tests, the shear stress is nearly uniform across the thickness. This specimen geometry difference may not have significant effects on fatigue cracking behavior since crack initiation usually occurs on specimen surface on which the stress response for the same applied strain is the same for both specimen geometries. However, the specimen geometry difference affects torsional fatigue life. In a solid specimen, the rate of Mode III crack growth from the specimen surface into the elastic core must be slower than that in a thin-wall tube with the same applied strain because of the stress gradient that exists in the solid specimen. Consequently, a longer torsional fatigue life can be obtained from solid specimens. However, this specimen geometry effect on torsional fatigue life strongly depends on the definition of fatigue failure. If fatigue failure is defined as the final rupture of the specimen, this effect can be significant. For the 10% torque drop fatigue failure definition used in this work, this effect is relatively insignificant because cracks are still relatively shallow at the 10% torque drop point.

Anisotropic material coefficients M_{ij} and A_{ii} appear in the constitutive relations and in the multiaxial fatigue damage D model of the orthotropic material. These material coefficients are the basic information needed to model the multiaxial plastic deformation and low-cycle fatigue behavior of an orthotropic material. Theoretically, they can be obtained by conducting strain-controlled uniaxial fatigue tests along the three principal orthotropic directions of the material. Then the resulting models can be transformed and used to predict plastic deformation and low-

cycle fatigue life of any material orientation under complicated multiaxial loading conditions without performing further tests. In this work, only combined proportional axial-torsional loadings are performed to test the predictive capability of the constitutive relations and the proposed D model. More experiments with more complicated loading conditions are needed to further verify the accuracy of the theoretical results obtained in this study. Especially, for materials showing obvious mean stress effect and nonproportional hardening effect under controlled strain test conditions, some stress terms may be needed in the D model to take these effects into account [*47,48*].

The anisotropic metal tested in this work was found to be isotropic in the elastic range. As a result, elastic stress-strain relations are used in the calculations without detailed explanation. For fiber-reinforced composite materials, elastic anisotropy is usually significant, and thus it is necessary and important to consider the effects of elastic anisotropy and use anisotropic elastic stress-strain relations to model them.

The plastic deformation of ductile metals that do not contain any voids takes place by dislocation motion, which produces shear deformation on crystallographically determined slip planes, and thus the plastic deformation in ductile metals are generally nondilational, whether they are isotropic or anisotropic. This observation also implies that yielding of ductile metals is independent from the hydrostatic stress. As a result, the conditions of no volume change during plastic deformation, and independence of yielding from the hydrostatic stress are assumed in our yielding function Eq 3 as well as in most anisotropic yielding functions for anisotropic metals [*13–21*]. These conditions are valid for our material, which is void free in its original state and is only subjected to moderate plastic strain, i.e., on the order of 10^{-3}. In fact, the predictions of the theoretical constitutive relations agree with experimental data very well, as discussed in this paper. However, these assumptions should not be applied to some special materials such as: porous materials, polymers which are subjected to structural transformation during plastic straining, or some composite materials in which distributed damage and microvoids may develop during plastic deformation. In these cases, plastic dilation effects must be considered in both constitutive relations and fatigue damage models.

Conclusion

1. Anisotropic constitutive relations of an orthotropic Al-6061-T6 plate are obtained by using the macroscopic continuum approach. In terms of yielding and plastic flow behavior, the predictions of the theoretical constitutive relations agree with the experimental data along three orientations of the plate under combined tension/torsion in-phase reasonably well. This indicates that the formulations of the constitutive relations are quite successful. More tests with more complicated loading conditions are needed to further evaluate the theoretical formulations.

2. The effective strain model and plastic work model offer similar fatigue life predictions with a scatter factor of two. Both of them can be obtained directly from constitutive relations of the subject material and thus can be applied to estimate the fatigue life of any material orientation without conducting further tests. In this respect, the effective strain and plastic work concepts are still useful even though neither considers the actual fatigue cracking behavior.

3. The anisotropic shear cracking model reflects the actual observed fatigue cracking behavior and gives better fatigue life predictions than the effective strain model and the plastic work model. However, the values of the anisotropic coefficients in this model depend on material orientations and they have to be determined by testing each orientation under consideration. This makes the model rather difficult to apply.

4. The D model, which is based on the strain vector, also gives better fatigue life predictions than the plastic work model and the effective strain model. It has the advantage of easy transformation as well. Once the material constants in $[A]$ matrix are determined, this model can be

applied to predict fatigue life of any material orientation without conducting further tests. Considering both the capability of prediction and the possibility of transformation, the D model seems to be the best among the models evaluated.

5. In this work, we have developed and illustrated a methodology to investigate multiaxial fatigue damage behavior of an anisotropic solid. It can be summarized as follows: first, the anisotropic constitutive relations of the material should be obtained, which is the basis for the evaluation of fatigue damage-controlling parameters; secondly, the fatigue cracking behavior should be investigated which will help to identify the fatigue damage-controlling parameters; and finally, a multiaxial fatigue damage model is sought considering both the transformation issue and the actual fatigue cracking behavior. This methodology is successfully applied to the orthotropic Al-6061-T6. We believe that it can also be applied to advanced composite materials, even though the fatigue cracking behavior may be much more complicated.

References

[1] Wang, S. S., Chim, E. S. M., and Socie, D. F., "Biaxial Fatigue of Fiber-Reinforced Composites at Cryogenic Temperature. Part I: Fatigue Fracture Life and Mechanisms," *Journal of Engineering Materials and Technology, Transactions,* American Society of Mechanical Engineers, New York, Vol. 104, 1982, pp. 128–136.

[2] Soemardi, T. P., Lai, D., and Bathias, C., "Static and Fatigue Biaxial Testing of Fiber Composites using Thin Walled Tubular Specimens," *Inelastic Deformation of Composite Materials,* G. J. Dvorak, Ed., Springer-Verlag, New York, 1991, pp. 581–603.

[3] Ikegami, K. and Yoshida, M., "Constitutive Relations of Hybrid Fiber Reinforced Plastics of GFRP/CFRP and GFRP/AFRP under Combined Stress State," *Inelastic Deformation of Composite Materials,* G. J. Dvorak, Ed., Springer-Verlag, New York, 1991, pp. 623–638.

[4] Guess, T. R., "Biaxial Testing of Composite Cylinders Experimental-Theoretical Comparison," *Composites,* 1980, pp. 139–148.

[5] Nahas, M. N., "Survey of Failure and Post Failure Theories of Laminated Fiber-Reinforced Composites," *Journal of Composites Technology & Research,* Vol. 8, 1986, pp. 138–153.

[6] Owen, M. J. and Griffiths, J. R., "Evaluation of Biaxial Stress Fatigue Surface for a Glass Fabric Reinforced Polyester Resin under Static and Fatigue Loading," *Journal of Material Science,* Vol. 13, 1978, pp. 1521–1537.

[7] Krempl, E. and Niu, T. M., "Graphite/Epoxy $[\pm 45°]_s$ Tubes. Their Static Axial and Shear Properties and Their Fatigue Behavior under Completely Reversed Load Controlled Loading," *Journal of Composite Materials,* Vol. 16, 1982, pp. 172–178.

[8] Hashin, Z. and Rotem, Z., "A Fatigue Failure Criterion for Fiber Reinforced Materials," *Journal of Composite Materials,* Vol. 7, 1973, pp. 448–464.

[9] Tsai, S. W. and Wu, E. M., "A General Theory of Strength of Anisotropic Materials," *Journal of Composite Materials,* Vol. 5, 1971, pp. 58–80.

[10] Swanson, S. R., Messick, M., and Tian, Z., "Failure of Carbon/Epoxy Laminate under Combined Stress," *Journal of Composite Materials,* Vol. 21, 1987, pp. 619–630.

[11] Hutchinson, J. W., "Elastic-Plastic Behavior of Polycrystalline Metals and Composites," *Proceedings,* Royal Society (London), Vol. A319, 1970, pp. 247–272.

[12] Lin, T. H., "A Physical Theory of Plasticity and Creep," *Journal of Engineering Materials and Technology, Transactions,* American Society of Mechanical Engineers, New York, Vol. 106, 1984, pp. 290–294.

[13] Hill, R., "A Theory of the Yield and Plastic Flow of Anisotropic Metals," *Proceedings, Royal Society (London),* Vol. A193, 1948, pp. 281–297.

[14] Edelman, R. and Drucker, D. C., "Some Extensions of Elementary Plasticity," *Journal of the Franklin Institute,* Vol. 251, 1951, p. 581.

[15] Shih, C. F. and Lee, D., "Further Developments in Anisotropic Plasticity," *Journal of Engineering Materials and Technology, Transactions,* American Society of Mechanical Engineers, New York, Vol. 100, 1978, pp. 294–302.

[16] Frederking, R. M. W. and Sidebottom, D. M., "An Experimental Evaluation of Plasticity Theories for Anisotropic Metals," *Journal of Applied Mechanics, Transactions,* American Society of Mechanical Engineers, New York, Vol. 38, 1971, pp. 15–22.

[17] Harvey, S. J., "The Use of Anisotropic Yield Surfaces in Cyclic Plasticity," *Multiaxial Fatigue, ASTM STP 853,* American Society for Testing and Materials, Philadelphia, 1985, pp. 49–53.

[18] Budianski, B., "Anisotropic Plasticity of Plane Isotropic Sheets," *Mechanics of Material Behavior*, G. J. Dvorak and R. T. Shield, Eds., Elsevier, Amsterdam, 1984, pp. 15–29.
[19] Voyiadjis, G. Z. and Foroozesh, M., "Anisotropic Distorsional Yield Model," *Journal of Applied Mechanics*, Vol. 57, 1990, pp. 537–547.
[20] Barlat, F., Lege, D. L., and Brem, J. C., "A Six-Component Yield Function for Anisotropic Materials," *International Journal of Plasticity*, Vol. 7, 1991, pp. 693–712.
[21] Stout, M. G., Hecker, S. S., and Bourcier, R., "An Evaluation of Anisotropic Effective Stress-Strain Criteria for the Yield and Flow of 2024 Aluminum Tubes," *Journal of Engineering Materials and Technology, Transactions*, American Society of Mechanical Engineers, New York, Vol. 105, 1983, pp. 242–249.
[22] Forsyth, P. J. E., *The Physical Basis of Metal Fatigue*, American Elsevier Publishing Co., New York, 1969.
[23] Frost, N. E., Marsh, K. I., and Pook, L. P., *Metal Fatigue*, Oxford University Press, London, 1974.
[24] Suresh, S., *Fatigue of Materials*, Cambridge Press, London, 1991.
[25] Gough, H. J., *The Fatigue of Metals*, Van Nostrand and Co., New York, 1926.
[26] Miller, K. J. and Chandler, D. C., "High Strain Torsion Fatigue of Solid and Tubular Specimens," *Proceedings of the Institution of Mechanical Engineers*, Vol. 184, 1969–70, pp. 433–448.
[27] Hurd, N. J. and Irving, P. E., "Factors Influencing Propagation of Mode III Fatigue Cracks under Torsional Loading," *Design of Fatigue and Fracture Resistant Structures, ASTM STP 761*, American Society for Testing and Materials, Philadelphia, 1982, pp. 212–233.
[28] Nayeb-Hashemi, H., McClintock, F. A., and Ritchie, R. O., "Micromechanical Modeling of Mode III Fatigue Crack Growth in Rotor Steels," *International Journal of Fracture*, Vol. 23, 1983, pp. 163–185.
[29] Nayeb-Hashemi, H., McClintock, F. A., and Ritchie R. O., "Effect of Friction and High Torque on Fatigue Crack Propagation in Mode III," *Metallurgical Transactions*, Vol. 13A, 1982, pp. 2197–2205.
[30] Hurd, N. J. and Irving, P. E., "Smooth Specimen Fatigue Live and Microcrack Growth Mode in Torsion," *Multiaxial Fatigue, ASTM STP 853*, American Society for Testing and Materials, Philadelphia, 1985, pp. 267–284.
[31] Bannantine, J. A. and Socie, D. F., "Observation of Cracking Behavior in Tension and Torsion," *Low Cycle Fatigue, ASTM STP 942*, American Society for Testing and Materials, Philadelphia, 1988, pp. 899–921.
[32] Lanza, G., "Strength of Shaft Subjected to Both Twisting and Bending," *Transactions*, American Society of Mechanical Engineers, New York, 1886, pp. 130–144.
[33] Gough, H. J. and Pollard, H. V., "The Strength of Metals under Combined Alternating Stresses," *Proceedings of the Institution of Mechanical Engineers*, Vol. 131, 1935, pp. 3–54.
[34] Sines, G., "Fatigue Criterion under Combined Stresses or Strains," *Journal of Engineering Materials and Technology, Transactions*, American Society of Mechanical Engineers, New York, Vol. 103, 1981, pp. 82–90.
[35] Dowling, N. E., "Torsional Fatigue Life of Power Plant Equipment Rotating Shafts," DOE/RA/29353-1, Westinghouse R&D Center, 1982.
[36] Feltner, C. E. and Morrow, J., "Microplastic Strain Hysteresis Energy as a Criterion for Fatigue Fracture," *Journal of Basic Engineering, Transactions*, American Society of Mechanical Engineers, New York, Vol. 83, 1961, pp. 15–22.
[37] Halford, G. R., "The Energy Required for Fatigue," *Journal of Materials*, Vol. 1, 1966, pp. 3–18.
[38] Garud, Y. S., "A New Approach to the Evaluation of Fatigue under Multiaxial Loadings," *Journal of Engineering Materials and Technology, Transactions*, American Society of Mechanical Engineers, New York, Vol. 103, 1981, pp. 118–125.
[39] Lefebre, D., Neale, K. W., and Ellyin, F. A., "A Criterion for Low Cycle Fatigue Failure under Biaxial State of Stress," *Journal of Engineering Materials and Technology, Transactions*, American Society of Mechanical Engineers, New York, Vol. 103, 1981, pp. 1–6.
[40] Ellyin, F. and Golos, K., "Multiaxial Fatigue Damage Criterion," *Journal of Engineering Materials and Technology, Transactions*, American Society of Mechanical Engineers, New York, Vol. 110, 1988, pp. 63–68.
[41] Ellyin, F., Golos, K., and Xia, Z., "In-Phase and Out-of-Phase Multiaxial Fatigue," *Journal of Engineering Materials and Technology, Transactions*, American Society of Mechanical Engineers, New York, Vol. 113, 1991, pp. 112–118.
[42] Findley, W. N., "Combined Stress Fatigue Strength of 765-T61 Aluminum Alloy with Superimposed Mean Stresses and Correction for Yielding," Technical Note 2924, NACA, 1953.
[43] Findley, W. N., *Journal of Engineering Materials and Technology, Transactions*, American Society of Mechanical Engineers, New York, Vol. 79, 1957, pp. 337–347.

[44] McDiarmid, D. L., "Failure Criteria and Cumulative Damage in Fatigue under Multiaxial Stress Conditions," Ph.D. thesis, City University, London, 1972.
[45] McDiarmid, D. L., "A General Criterion of Fatigue Failure under Multiaxial Stress," *Proceedings,* International Conference on Pressure Vessel Technology, American Society of Mechanical Engineers, New York, 1973, pp. 851–862.
[46] Brown, M. W. and Miller, K. J., "A Theory for Fatigue Failure under Multiaxial Stress-Strain Condition," *Proceedings of the Institution of Mechanical Engineers,* Vol. 187, 1973, pp. 745–755.
[47] Socie, D. F., Wail, L. E., and Dittmer, D. F., "Biaxial Fatigue of Inconel 718 Including Mean Stress Effect," *Multiaxial Fatigue, ASTM STP 853,* American Society for Testing and Materials, Philadelphia, 1985, pp. 463–478.
[48] Fatemi, A. and Socie, D. F., "A Critical Plane Approach to Multiaxial Fatigue Damage Including Out-of-Phase Loading," *Fatigue and Fracture of Engineering Materials and Structures,* Vol. 11, 1988, pp. 145–165.
[49] Smith, R. N., Waston, P., and Topper, T. H., "A Stress-Strain Function for the Fatigue of Metals," *Journal of Materials,* Vol. 5, 1970, pp. 767–778.
[50] Socie, D. F., "Multiaxial Fatigue Damage Models," *Journal of Engineering Materials and Technology, Transactions,* American Society of Mechanical Engineers, New York, Vol. 109, 1987, pp. 293–298.
[51] Lin, H. and Nayeb-Hashemi, H., "Effects of Material Anisotropy on Cyclic Deformation and Biaxial Fatigue Behavior of Al-6061-T6," *Advances in Multiaxial Fatigue, ASTM STP 1191,* ASTM, Philadelphia, pp. 151–182.
[52] Lin, H., Nayeb-Hashemi, H., and Pelloux, R. M., "Constitutive Relations and Fatigue Life Prediction for Anisotropic Al-6061-T6 Rods under Biaxial Proportional Loadings," *International Journal of Fatigue,* Vol. 14, No. 4, 1992, pp. 249–259.
[53] Lin, H., Nayeb-Hashemi, H., and Pelloux, R. M., "A Multiaxial Fatigue Damage Model for Orthotropic Materials," *Fatigue and Fracture of Engineering Material Structures,* Vol. 16, No. 7, 1993, pp. 723–742.
[54] Krempl, E. and Lu, H., "Comparison of the Stress Responses of an Aluminum Alloy Tube to Proportional and Alternate Axial and Shear Strain Paths at Room Temperature," *Mechanics of Materials,* Vol. 2, 1984, pp. 183–192.
[55] Pickard, A. C. and Knott, J. F., "Effects of Testing Method on Cyclic Hardening Behavior in Face-Centered Cubic Alloys," *Low Cycle Fatigue, ASTM STP 942,* American Society for Testing and Materials, Philadelphia, 1988, pp. 58–76.
[56] Backofen, W. A., *Deformation Processing,* Addison-Wesley, 1972, p. 47.
[57] Nayeb-Hashemi, H., "Failure Modes of Specimens Containing Surface Flaws under Cyclic Torsion," *Experimental Mechanics,* Vol. 27, 1987, pp. 51–56.

Peter J. Bonacuse[1] *and Sreeramesh Kalluri*[2]

Cyclic Axial-Torsional Deformation Behavior of a Cobalt-Base Superalloy

REFERENCE: Bonacuse, P. J. and Kalluri, S., **"Cyclic Axial-Torsional Deformation Behavior of a Cobalt-Base Superalloy,"** *Cyclic Deformation, Fracture, and Nondestructive Evaluation of Advanced Materials: Second Volume, ASTM STP 1184,* M. R. Mitchell and O. Buck, Eds., American Society for Testing and Materials, Philadelphia, 1994, pp. 204–229.

ABSTRACT: The cyclic, high-temperature deformation behavior of a wrought cobalt-base superalloy, Haynes 188, is investigated under combined axial and torsional loads. This is accomplished through the examination of hysteresis loops generated from a biaxial fatigue test program. A high-temperature axial, torsional, and combined axial-torsional fatigue database has been generated on Haynes 188 at 760°C. Cyclic loading tests have been conducted on uniform gage section tubular specimens in a servohydraulic axial-torsional test rig. Test control and data acquisition were accomplished with a minicomputer. The fatigue behavior of Haynes 188 at 760°C under axial, torsional, and combined axial-torsional loads and the monotonic and cyclic deformation behaviors under axial and torsional loads have been previously reported. In this paper, the cyclic hardening characteristics and typical hysteresis loops in the axial stress versus axial strain, shear stress versus engineering shear strain, axial strain versus engineering shear strain, and axial stress versus shear stress spaces are presented for cyclic in-phase and out-of-phase axial-torsional tests. For in-phase tests, three different values of the proportionality constant, λ (the ratio of engineering shear strain amplitude to axial strain amplitude, γ_a/ε_a), are examined, viz., 0.86, 1.73, and 3.46. In the out-of-phase tests, three different values of the phase angle, ϕ (between the axial and engineering shear strain waveforms), are studied, viz., 30, 60, and 90° with $\lambda = 1.73$. The cyclic hardening behaviors of all the tests conducted on Haynes 188 at 760°C are evaluated using the von Mises equivalent stress-strain and the maximum shear stress-maximum engineering shear strain (Tresca) curves. Comparisons are also made between the hardening behaviors of cyclic axial, torsional, and combined in-phase ($\lambda = 1.73$ and $\phi = 0°$) and out-of-phase ($\lambda = 1.73$ and $\phi = 90°$) axial-torsional fatigue tests. These comparisons are accomplished through simple Ramberg-Osgood type stress-strain functions for cyclic, axial stress-strain and shear stress-engineering shear strain curves.

KEYWORDS: axial-torsional loading, multiaxiality, in-phase loading, out-of-phase loading, cyclic deformation, equivalent stress-strain curve, cobalt-base superalloy, elevated temperature

Nomenclature

N	Cycle number
N_f	Cyclic life
n'	Cyclic axial strain-hardening exponent
n_t'	Cyclic torsional strain-hardening exponent
E, G	Young's and shear moduli
K'	Cyclic axial strength coefficient
K_t'	Cyclic torsional strength coefficient
Δ	Denotes range of the variable

[1] Research engineer, U.S. Army Research Laboratory, Vehicle Propulsion Directorate, NASA Lewis Research Center, Cleveland, OH.

[2] Senior research engineer, NYMA, Inc., NASA Lewis Research Center, Cleveland, OH.

γ, ε Engineering shear and axial strains
γ_a, ε_a Engineering shear and axial strain amplitudes
γ_{max} Maximum engineering shear strain (Tresca)
ε_e, ε_p Axial elastic and plastic strains
ε_{eq} von Mises equivalent strain
λ Proportionality constant, γ_a/ε_a
ν_e, ν_p Elastic and plastic Poisson's ratios
ν_{eff} Effective Poisson's ratio
σ, τ Axial and shear stresses
σ_a, τ_a Axial and shear stress amplitudes
σ_{eq} Von Mises equivalent stress
τ_{max} Maximum shear stress (Tresca)
ϕ Phase angle between axial and engineering shear strain waveforms

Introduction

The imperatives of higher efficiency and improved performance in gas turbines require that the rotating speeds, power extraction per turbine stage, and operating temperatures all be increased beyond the current levels. This may mean that the materials used in the hot section are being pushed up to and beyond their recommended usage limits. It is important that the deformation behavior of these materials be understood at temperatures and loading conditions that approximate the service conditions of the component. Design decisions for these materials are currently being made with material properties and databases that have been extrapolated from lower-temperature, uniaxial, fatigue and deformation data. These extrapolated data may imply a behavior that is significantly different from the material's actual response under service conditions.

The cyclic deformation behavior of polycrystalline metallic materials under combined axial-torsional loading conditions has been the subject of several investigations [*1–9*]. These studies were conducted on tubular specimens of low-alloy steels [*1,3,7*], stainless steels [*1,2,4–8*], and a superalloy [*9*] at both room [*1–7,9*] and elevated [*1,8*] temperatures. Different types of waveforms, including sinusoidal [*2–9*], triangular [*1,4,6*], and trapezoidal [*4–7*], were employed as command inputs for the axial and engineering shear strains. In this study, the cyclic deformation behavior of a wrought cobalt-base superalloy, Haynes 188, has been investigated under axial-torsional loading conditions at 760°C. Haynes 188 is currently used in many aerospace gas turbine and rocket engine applications, e.g., the combustor liner for the T800 turboshaft engine for the RAH-66 Comanche helicopter and the liquid oxygen posts in the main injector of the space shuttle main engine.

The objective of this paper is to disseminate the cyclic deformation data collected in the course of performing high-temperature, axial-torsional fatigue tests on Haynes 188 and to relay some observations about the collected data. Various independent as well as simultaneous combinations of axial and torsional loads were imposed on 36 specimens in the test program. The following axial-torsional deformation results are discussed: (1) the effect of the ratio of the engineering shear strain amplitude to the axial strain amplitude (proportionality constant, λ) on the in-phase (proportional) deformation behavior, and (2) the effect of phase angle (ϕ) between the axial and engineering shear strains (out-of-phase or non-proportional) on the cyclic and stabilized stress response. The cyclic hardening under different axial-torsional loading conditions is presented through plots of hysteresis loops at several cyclic increments and plots of stress range versus number of cycles. In addition, the presentation format consists of normalized plots of stable (near half-life) axial and torsional hysteresis loops as well as normalized plots of the axial strain versus engineering shear strain and the axial stress versus shear stress for

the near half-life conditions. Also, results of regressed fits to the Ramberg-Osgood equation with the stabilized cyclic deformation data under various axial-torsional loading conditions are reported. The stabilized deformation behaviors of the in- and out-of-phase axial-torsional experiments are compared.

All tests described in this paper were conducted in air at 760°C. This temperature was chosen because Haynes 188 displays a marked drop in ductility at this temperature [*10*]. This ductility minimum is most likely due to complex interactions between mobile solute atoms and dislocations. Understanding the deformation behavior at this temperature will advance our ability to assess this material's usefulness in advanced gas turbine applications.

Experimental Program

The cobalt-base superalloy, Haynes 188, was supplied by a commercial vendor in the form of hot-rolled, solution-annealed round bars with a nominal diameter of 50.8 mm (manufactured to Aerospace Material Specification 5772A). The chemical composition of the superalloy in weight percent is as follows: <0.002 S; 0.002 B; 0.012 P; 0.1 C; 0.4 Si; 0.034 La; 0.75 Mn; 1.24 Fe; 13.95 W; 21.84 Cr; 22.43 Ni, with cobalt making up the balance. The grains in the supplied material were equiaxed and ranged in size from 45 to 65 μm. The specifications for machining the specimens were explicitly designed to minimize surface work hardening. No post machining heat treatment was performed on the tubular specimens.

Thin-walled tubular specimens with a nominal outer diameter of 26 mm, a nominal inner diameter of 22 mm, and a nominal gage length of 25 mm (Fig. 1) were used in all experiments. The tubular specimens in the axial-torsional test program were heated to the test temperature of 760°C using a 10-kHz, 10-kW induction heating system with a three-coil (each of the coils is independently moveable) fixture. In all tests, the temperature in the gage section was maintained to within ±7°C of the control temperature. A servohydraulic axial-torsional load frame capable of ±223 kN of axial load and ±2.26 kN-m of torque was used in all experiments. A commercial, water-cooled, axial-torsional extensometer was employed for strain measurement. Further detail on the testing equipment can be found in Refs *11* to *13*.

Data acquisition and test control were accomplished with a minicomputer and associated electronic hardware. Detailed information on the data acquisition and control hardware and software for the cyclic axial-torsional experiments can be found in Ref *13*. Data were acquired at 500 points per loading cycle to ensure that significant, high-rate deformation phenomenon and the peak stresses and strains were accurately acquired.

Constant strain-rate (triangular) axial and/or engineering shear strain waveforms were imposed on all specimens. The frequency of both of the command waveforms was 0.1 Hz for all tests; therefore, the strain rate from test to test varied depending on the amplitudes of the strain waveforms. The difference in the strain rates between the smallest and the largest amplitude tests was, at most, a factor of 7. Because the differences in strain rates were relatively small, little or no strain rate effect on the deformation behavior is expected in the tests performed. The engineering shear strain at the mean radius of the tubular specimen was controlled in all the experiments that had an imposed engineering shear strain. In calculating the shear stress at the mean radius of the specimen, the shear stress was assumed to be uniformly distributed through the thickness of the tubular specimen. In all experiments, the test control software incorporated a graduated five-cycle load up. This allowed for better test control at the onset of the serrated yielding behavior that is often displayed by Haynes 188 when large plastic strains are present. In almost every case this five-cycle load up resulted in some initial plastic deformation in the specimens; therefore, some initial hardening was introduced before the first cycle data were collected.

The test matrix of the axial-torsional test program is shown in Table 1. Five different values

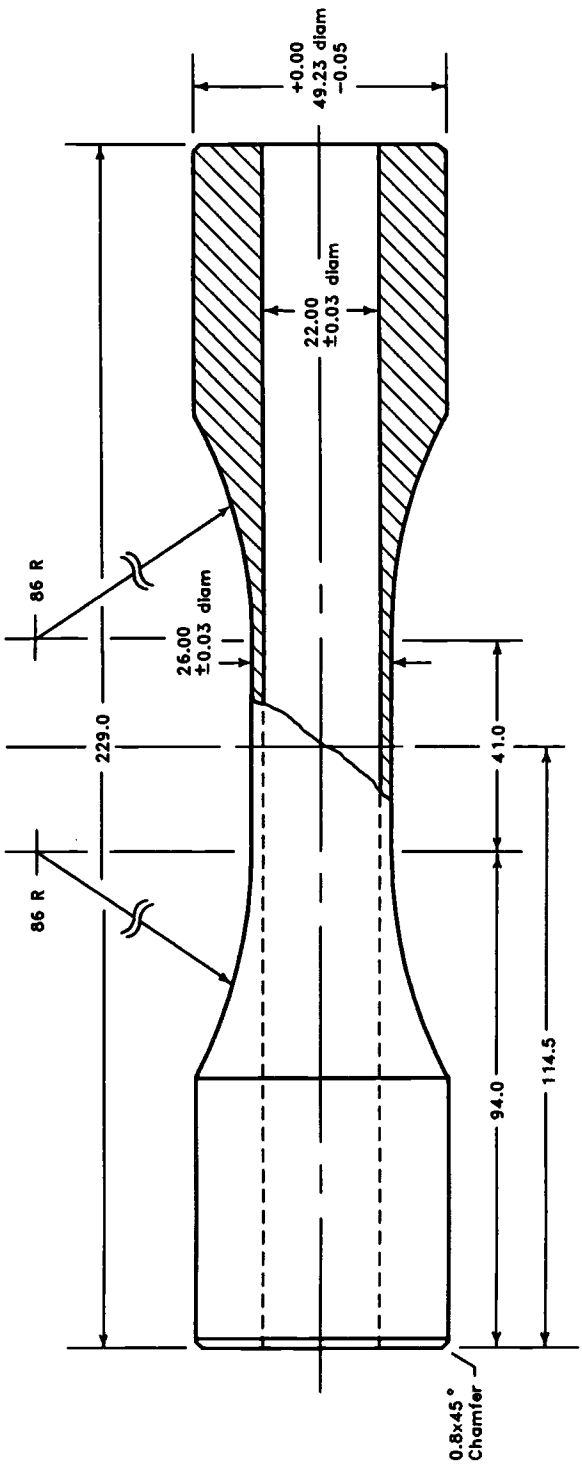

All dimensions are in millimeters.

FIG. 1—*Geometry of thin-walled tubular specimen.*

TABLE 1—*Axial-torsional test matrix for Haynes 188 at 760°C.*

	λ				
ϕ	0	0.86	1.73	3.46	∞
0°	7	2	6	2	7
30°	...	...	1	...	...
60°	...	...	2	...	...
90°	...	...	9[a]	...	...

[a] Two tests were performed with sinusoidal strain command waveforms.

of the proportionality constant, λ, and four phase angles, ϕ, have been investigated in the axial-torsional experiments. The number of tests conducted for each test condition, which is given by a set of λ and ϕ values, is shown in Table 1. In Fig. 2, a simple schematic is presented of the imposed strains during an in-phase and an out-of-phase axial-torsional fatigue test.

Results

The effect of strain cycling on the shapes of the hysteresis loops is illustrated in Figs. 3 to 6. Axial and torsional loops at 1, 10, 100, and 1000 cycles are plotted for cyclic axial-torsional experiments performed with phase angles, ϕ, of 0, 30, 60, and 90°. In all cases, Haynes 188 exhibited cyclic strain hardening, which is characterized by an increase in the stress range and an associated reduction in the width of the hysteresis loop.

To facilitate direct comparison of the axial and shear cyclic hardening rates of specimens that were subjected to in-phase (proportional) strain paths with different ratios of engineering shear to axial strain amplitudes, the stress ranges were normalized by the first cycle's (after the five-cycle load up) stress range. Plots of the normalized axial component of the in-phase cyclic stresses versus the number of cycles and the normalized shear component of the in-phase cyclic stresses versus the number of cycles are shown in Figs. 7 and 8. For the axial component of stress, all the in-phase axial-torsional tests exhibited a similar cyclic hardening rate, which was

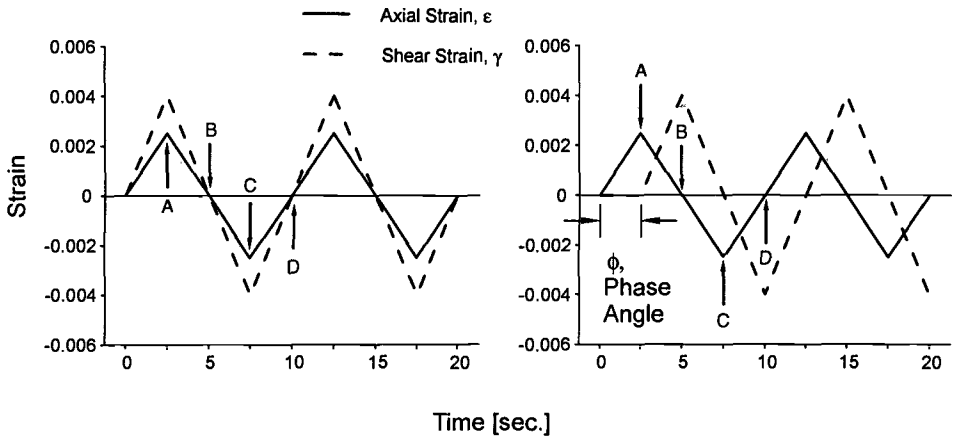

FIG. 2—*Schematic of loading waveforms for axial-torsional in-phase and out-of-phase tests.*

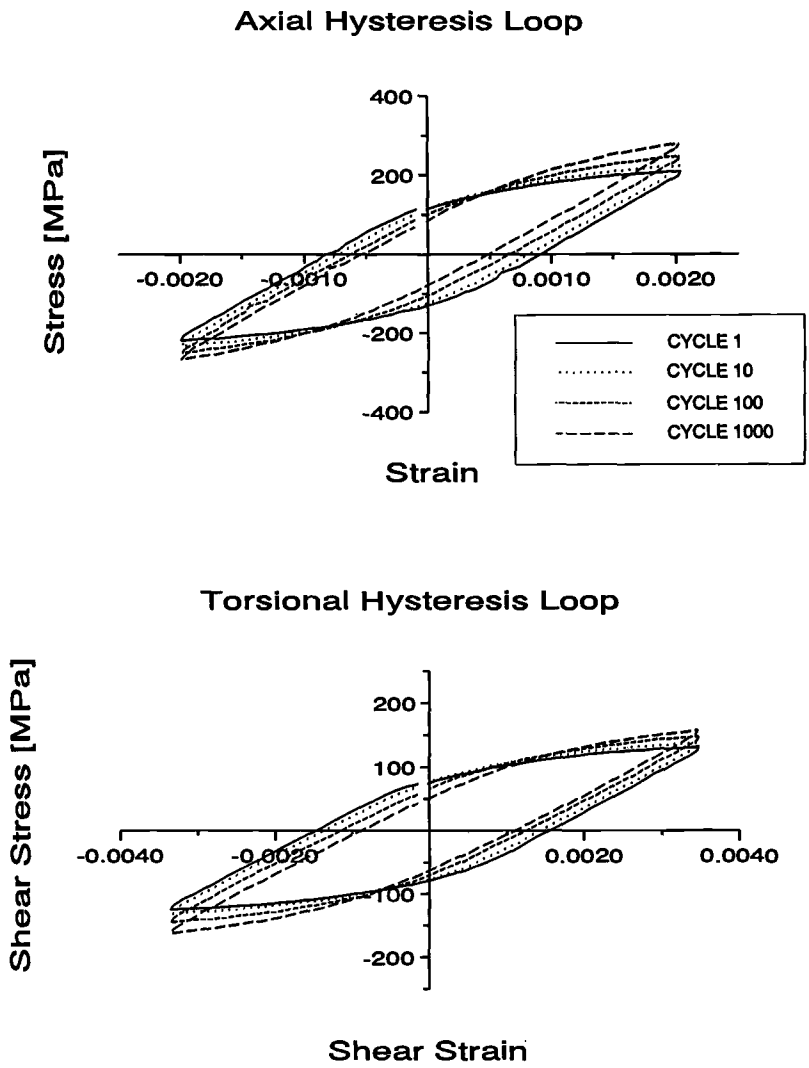

FIG. 3—*Evolution of axial and torsional hysteresis loops, $\lambda = 1.73$, $\phi = 0°$.*

lower than that observed in the axial test. For the shear component of stress, all the in-phase tests exhibited a cyclic hardening rate that was similar to the torsional test.

The cyclic hardening rates of specimens subjected to the same nominal axial and engineering shear strain amplitudes, with phase angles between the axial and torsional command waveforms of 0, 30, 60, and 90°, are compared in Figs. 9 and 10. In these figures the axial and shear stress ranges are plotted against the number of cycles. Both the axial and shear stress components clearly indicate higher first cycle hardening as the phase angle, ϕ, increases from 0 to 90°. This pattern of increased hardening with phase angle is maintained throughout the life of the out-of-phase tests. In plotting the near half-life hysteresis loops from the out-of-phase tests, the stress and strain components were normalized with half the range (amplitude) of the corre-

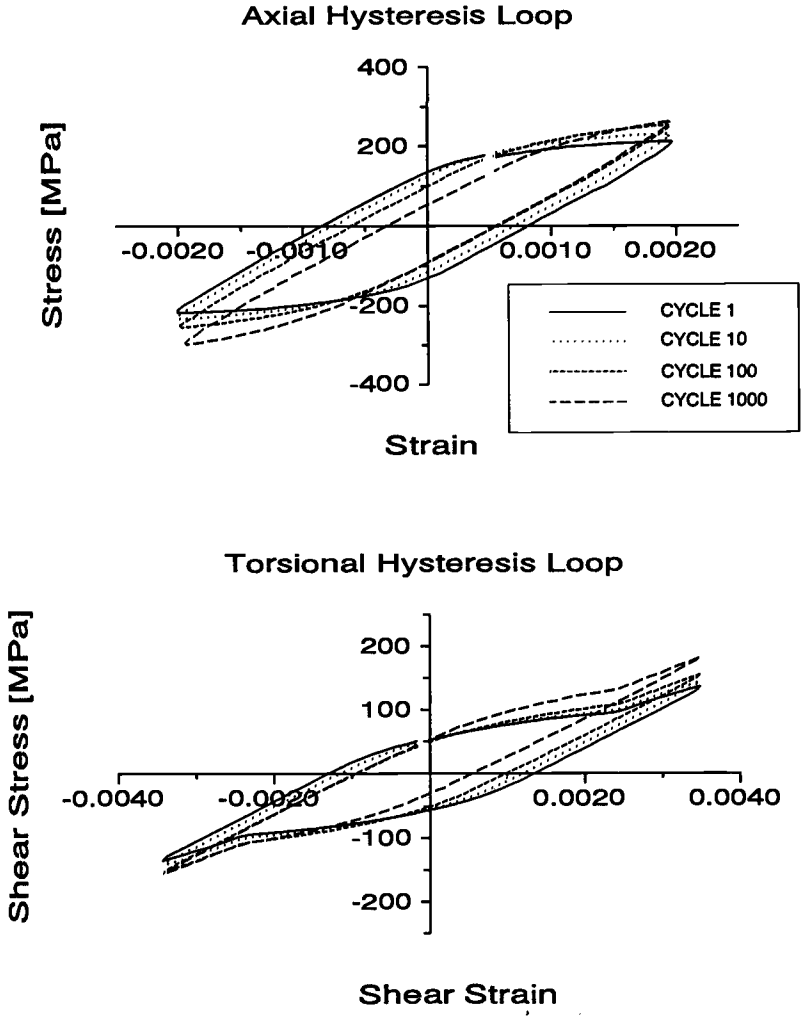

FIG. 4—*Evolution of axial and torsional hysteresis loops, $\lambda = 1.73$, $\phi = 30°$.*

sponding variable so that the shapes of the hysteresis loops for different ϕ values could be compared. By normalizing the variables, the isotropic hardening effects are concealed so that the kinematic effects can be compared directly. The maximum and minimum values of the strains and stresses in the near half-life axial and torsional loops are listed in Table 2. Figures 11 through 14 are the near half-life, normalized, axial (σ/σ_a versus $\varepsilon/\varepsilon_a$), and torsional ($\tau/\tau_a$ versus γ/γ_a) hysteresis loops from four specimens, which were subjected to the same nominal axial and engineering shear strain amplitudes but with four different phase angles (ϕ) between the strain waveforms. Also displayed in each figure are the normalized plots of the axial strain ($\varepsilon/\varepsilon_a$) versus the engineering shear strain (γ/γ_a) and the axial stress (σ/σ_a) versus the shear stress (τ/τ_a). The normalized axial strain-engineering shear strain plots display the strain path imposed on the specimen. The labels A, B, C, and D in Fig. 2 illustrate where each of the strain

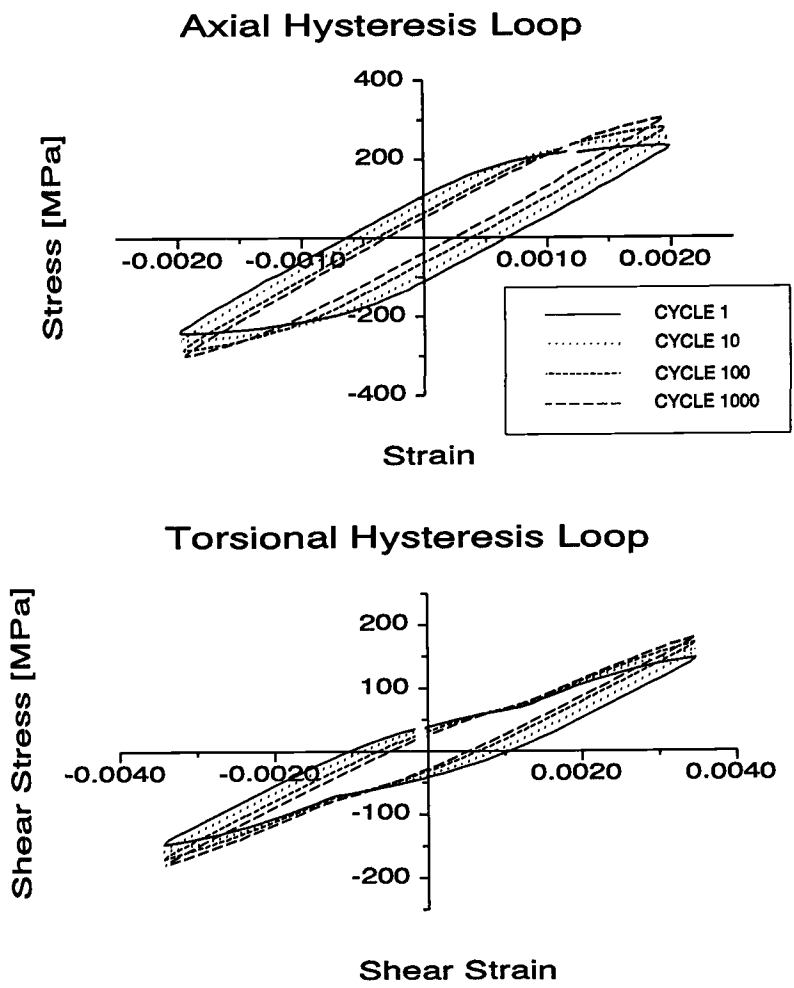

FIG. 5—*Evolution of axial and torsional hysteresis loops, $\lambda = 1.73$, $\phi = 60°$.*

reversals and zero crossings occur for the axial strain. The labels are repeated at the corresponding points in the normalized figures (Figs. 11–14). The small discontinuities seen in the normalized axial strain versus engineering shear strain and the normalized axial stress versus shear stress plots are due to a seal friction problem in the axial actuator of the test rig, which resisted all attempts of compensation.

For each axial-torsional test conducted, the von Mises equivalent stress, von Mises equivalent strain, the maximum shear stress, and the maximum engineering shear strain (Tresca stress and strain) were computed from the near half-life hysteresis loop data. For each of these quantities, the calculation was performed at each of the 500 collected data points around the cycle to determine the maximum and minimum values. Performing the equivalent and maximum shear calculations in this way was not specifically necessary for the case of the in-phase tests, but it was required for the out-of-phase experiments because the maximum values of the equivalent

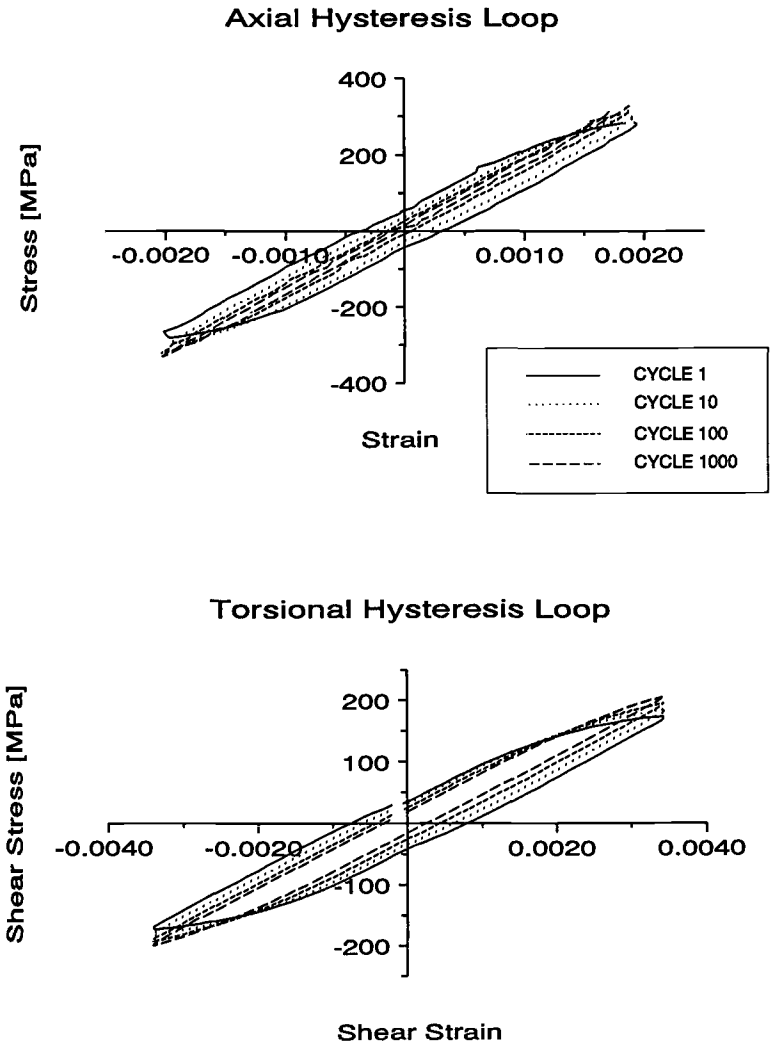

FIG. 6—*Evolution of axial and torsional hysteresis loops, $\lambda = 1.73$, $\phi = 90°$.*

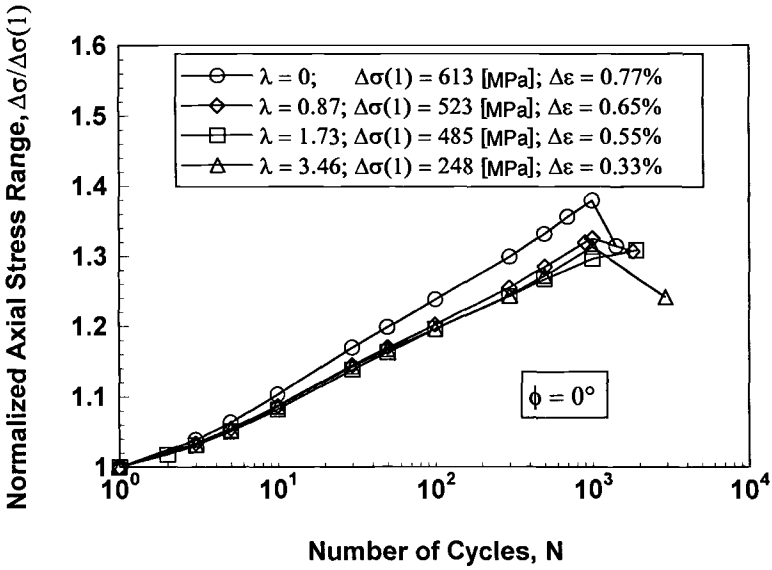

FIG. 7—*Cyclic variation of the normalized (to first cycle axial stress range) axial stress range for in-phase experiments.*

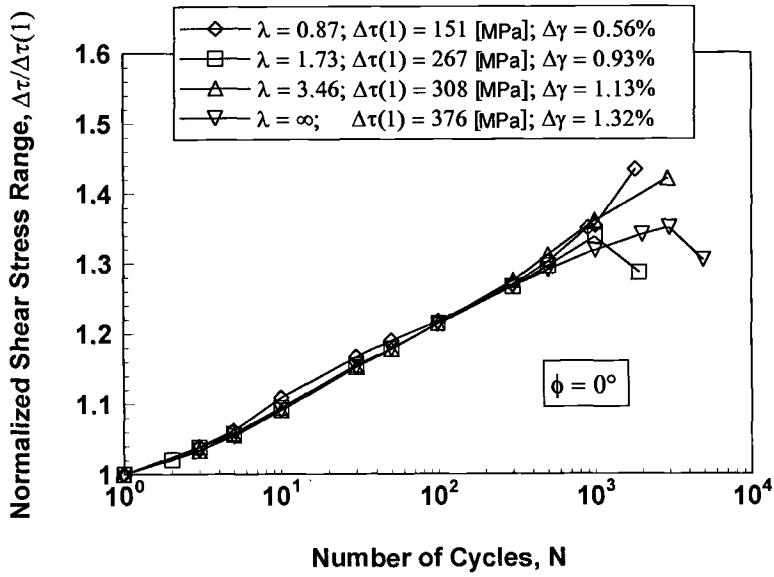

FIG. 8—*Cyclic variation of the normalized (to first cycle shear stress range) shear stress range for in-phase experiments.*

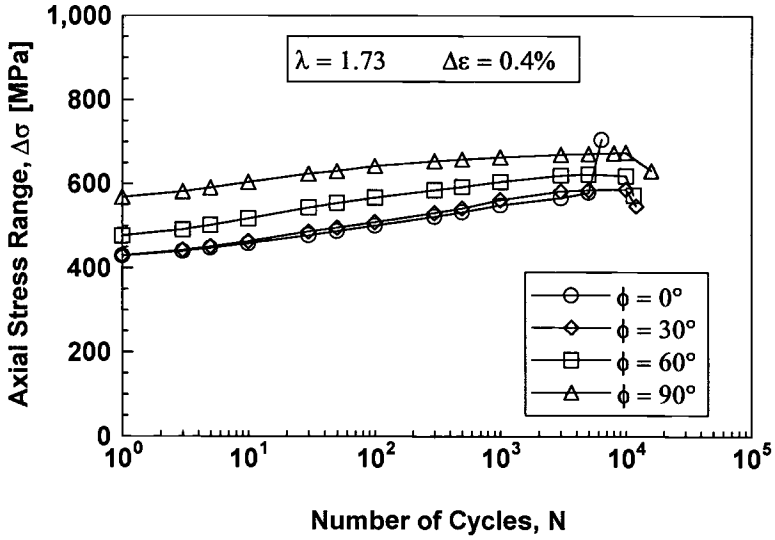

FIG. 9—*Cyclic variation of axial stress range for out-of-phase experiments.*

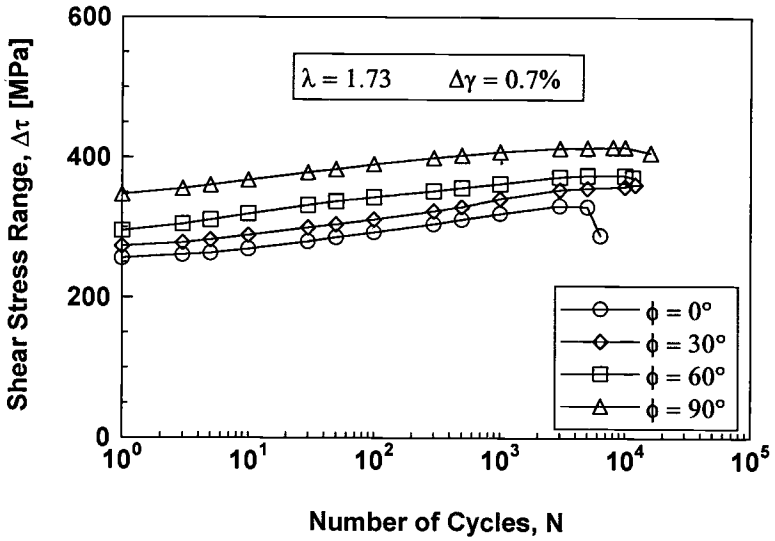

FIG. 10—*Cyclic variation of shear stress range for out-of-phase experiments.*

TABLE 2—*Maximum and minimum strains and stresses in the near half-life axial and torsional hysteresis loops, $\lambda = 1.73$.*

			Axial Strain, ε, %		Axial Stress, σ, MPa		Engineering Shear Strain, γ, %		Shear Stress, τ, MPa	
ϕ	N	N_f	Max	Min	Max	Min	Max	Min	Max	Min
0°	3000	6 261	0.21	−0.20	287	−279	0.35	−0.34	163	−168
30°	6000	12 136	0.19	−0.20	277	−309	0.35	−0.35	186	−171
60°	6000	11 564	0.19	−0.19	313	−310	0.35	−0.35	188	−187
90°	8000	16 003	0.19	−0.20	345	−329	0.34	−0.34	211	−204

or maximum shear stress and strain may not coincide with peak axial or torsional stresses and strains in the out-of-phase experiments.

An effective Poisson's ratio (ν_{eff}) was computed based on the measured axial stresses and strains. At each point around the hysteresis loop, ν_{eff} was computed with the following equation

$$\nu_{eff} = \left[\frac{\varepsilon_e \nu_e + \varepsilon_p \nu_p}{\varepsilon}\right]$$

where

$$\varepsilon_e = \sigma/E \tag{1}$$

and

$$\varepsilon_p = \varepsilon - \varepsilon_e$$

Values of $E = 170.2$ GPa, $G = 64.4$ GPa, and $\nu_e = 0.321$, determined from the averages of all measured values of Young's and shear moduli, were used in computing ν_{eff}. A value of 0.5 was assumed for ν_p. For the seven tests performed with $\lambda = \infty$ (torsional loading only), a value of 0.5 was assumed for ν_{eff}. For axial-torsional loading, the von Mises equivalent stresses and strains were determined by

$$\varepsilon_{eq} = \sqrt{\varepsilon^2 + \frac{3}{4}\frac{\gamma^2}{(1 + \nu_{eff})^2}} \tag{2}$$

$$\sigma_{eq} = \sqrt{\sigma^2 + 3\tau^2} \tag{3}$$

The maximum shear stress and maximum engineering shear strain (Tresca stresses and strains) within a given cycle of loading for the axial-torsional tests were determined according to

$$\gamma_{max} = \sqrt{(1 + \nu_{eff})^2\varepsilon^2 + \gamma^2} \tag{4}$$

$$\tau_{max} = \frac{1}{2}\sqrt{\sigma^2 + 4\tau^2} \tag{5}$$

The maximum and minimum of these calculated values were stored and used to calculate the range and amplitude of each variable (this was done to prevent any bias due to mean stresses

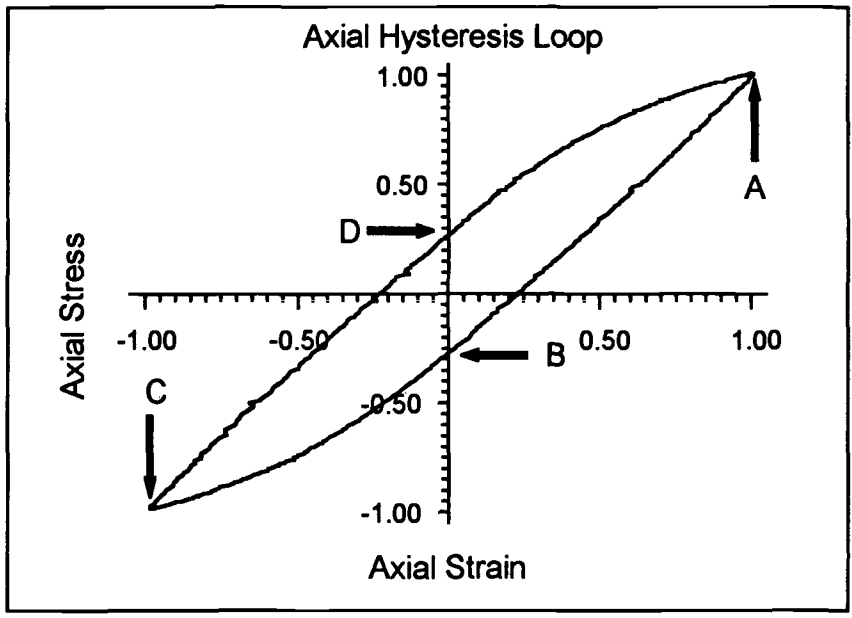

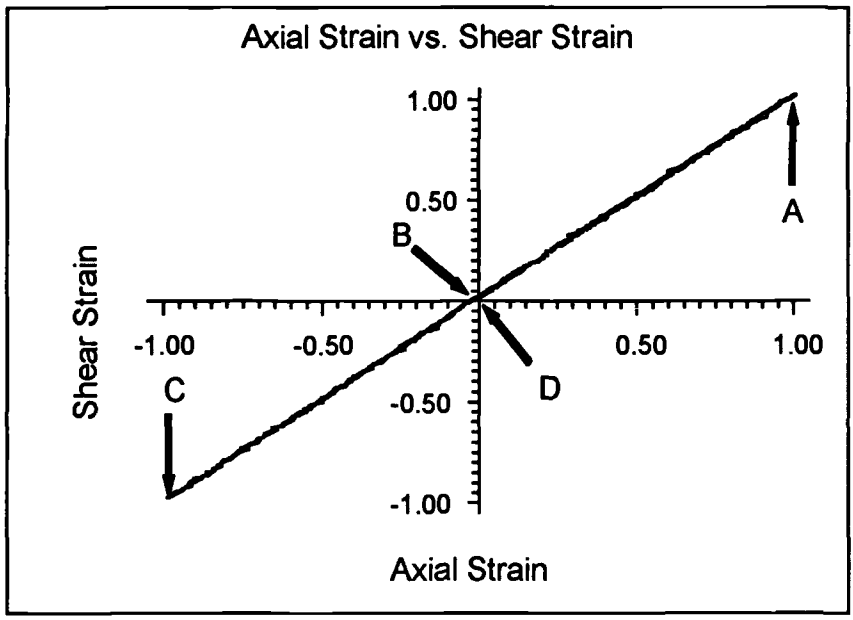

FIG. 11—*Normalized loops, $\lambda = 1.73$, $\phi = 0°$: axial hysteresis loop, torsional hysteresis loop, axial strain versus engineering shear strain, and axial stress versus shear stress.*

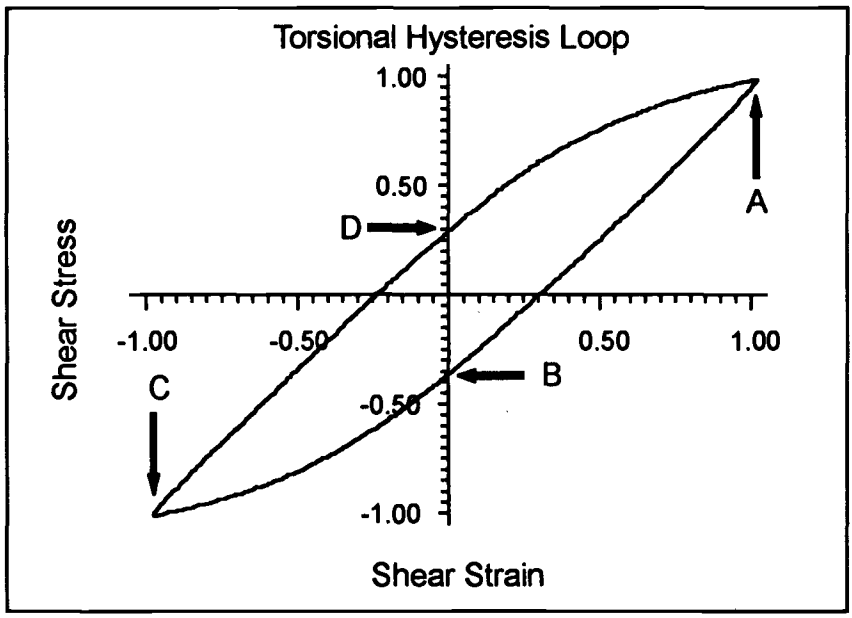

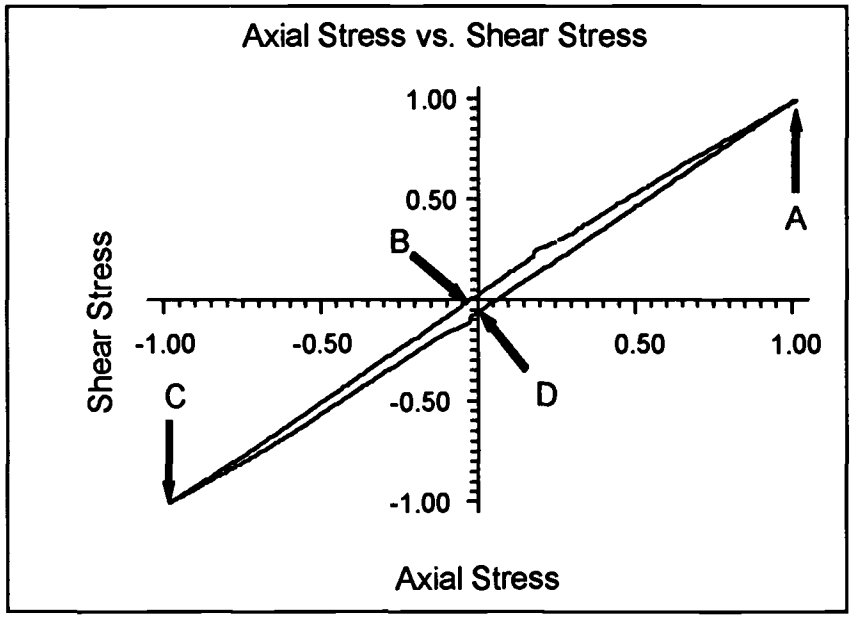

FIG. 11—*Continued.*

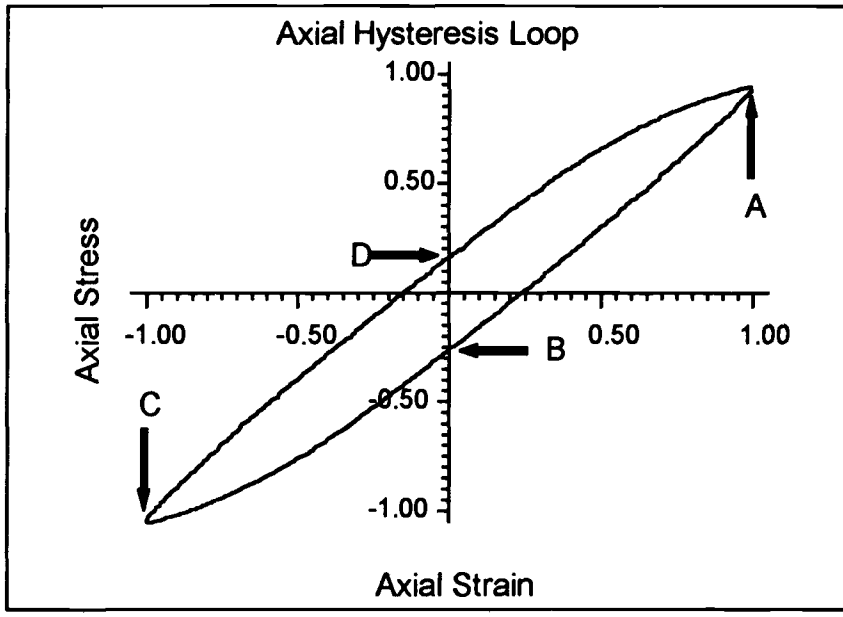

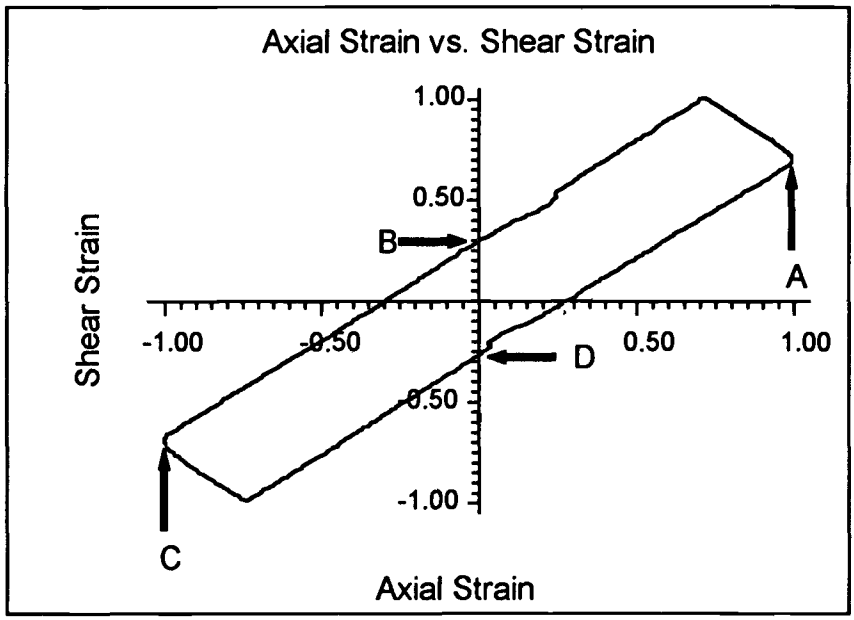

FIG. 12—*Normalized loops, $\lambda = 1.73$, $\phi = 30°$: axial hysteresis loop, torsional hysteresis loop, axial strain versus engineering shear strain, and axial stress versus shear stress.*

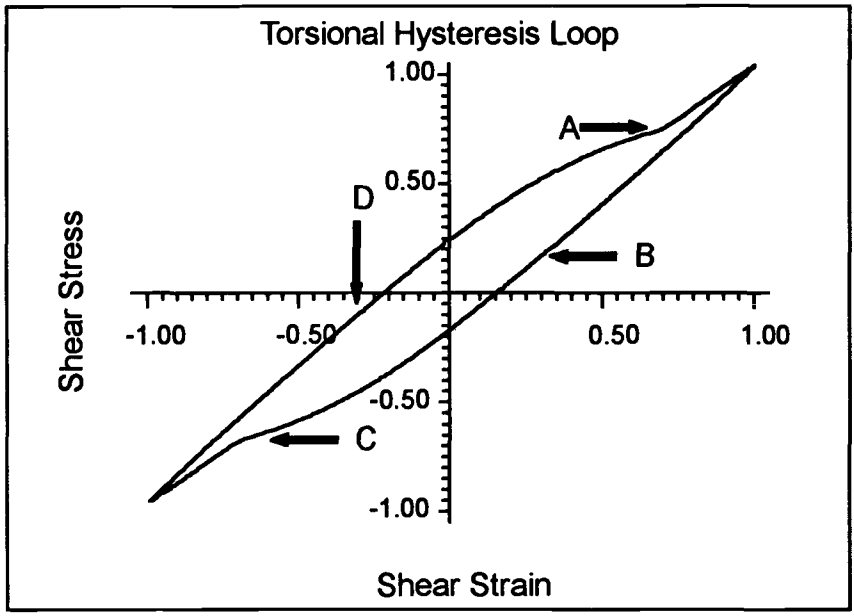

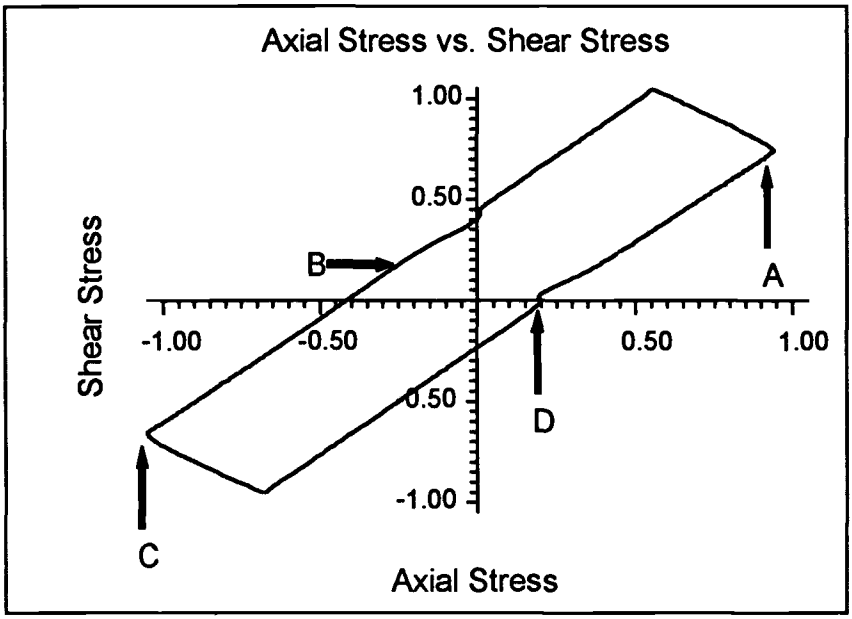

FIG. 12—*Continued.*

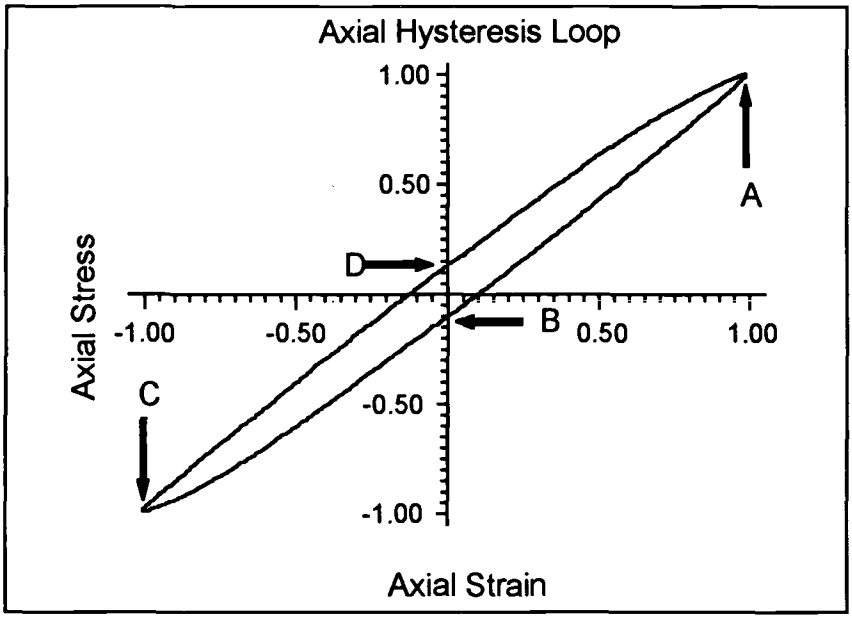

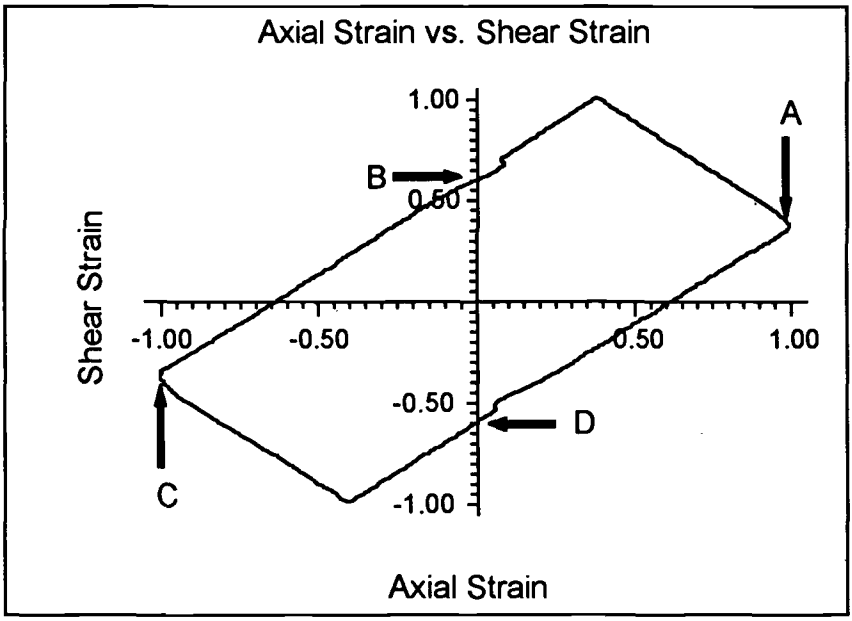

FIG. 13—*Normalized loops, $\lambda = 1.73$, $\phi = 60°$: axial hysteresis loop, torsional hysteresis loop, axial strain versus engineering shear strain, and axial stress versus shear stress.*

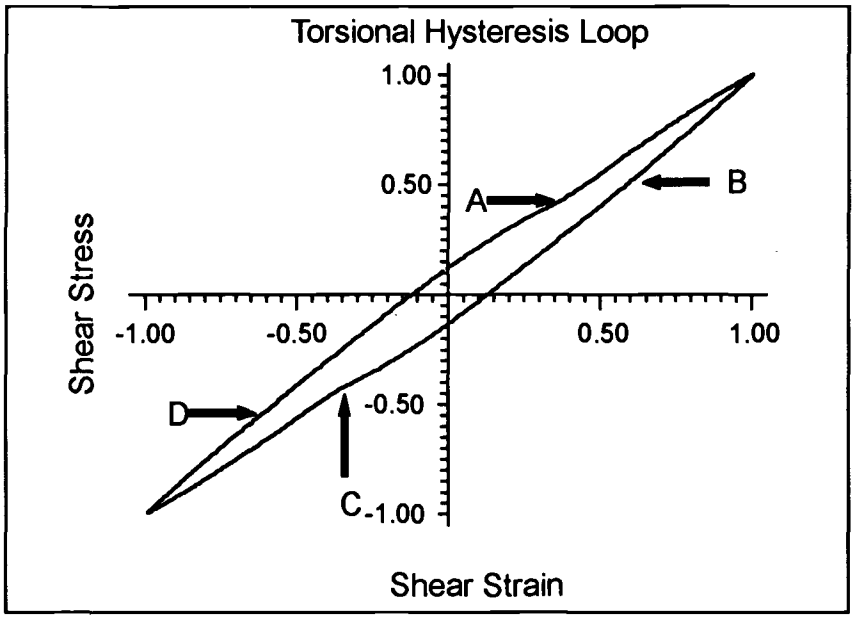

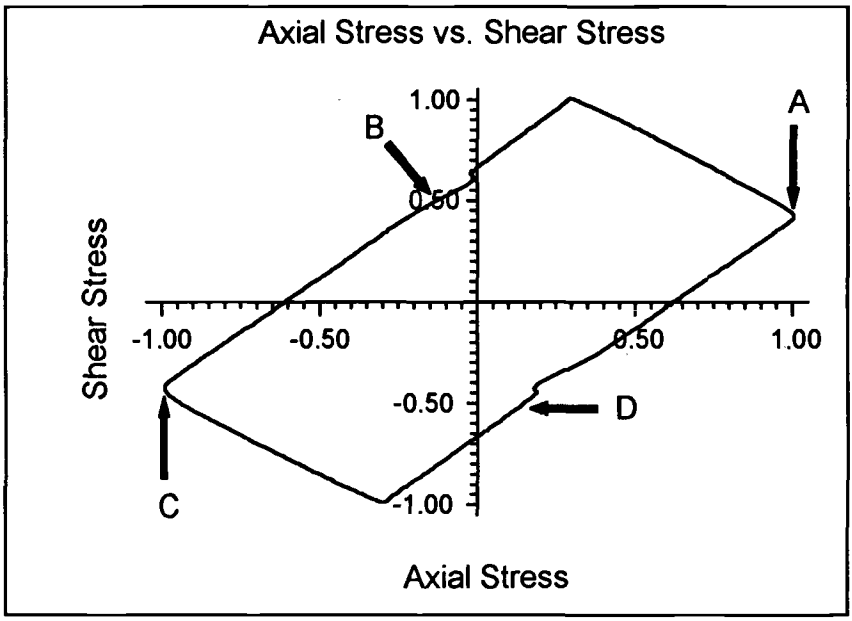

FIG. 13—*Continued.*

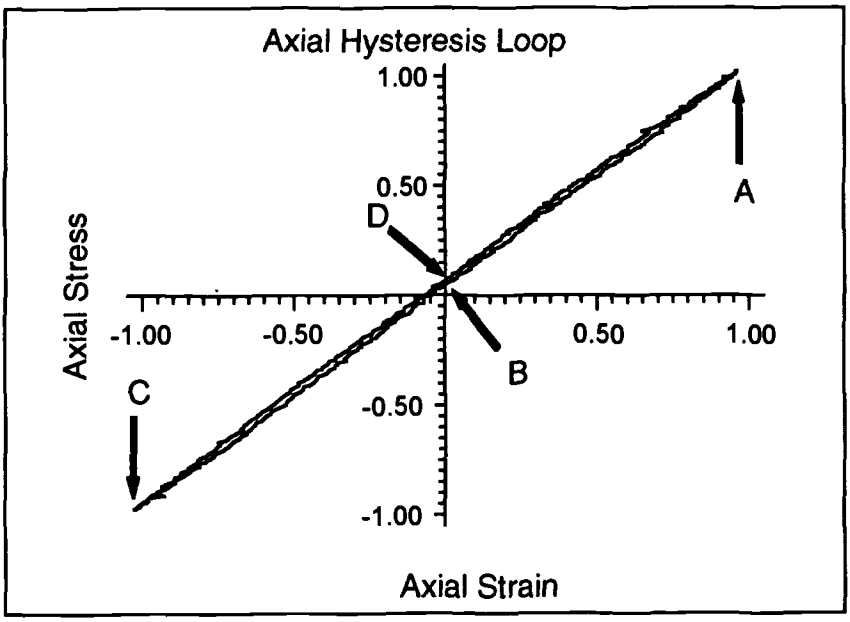

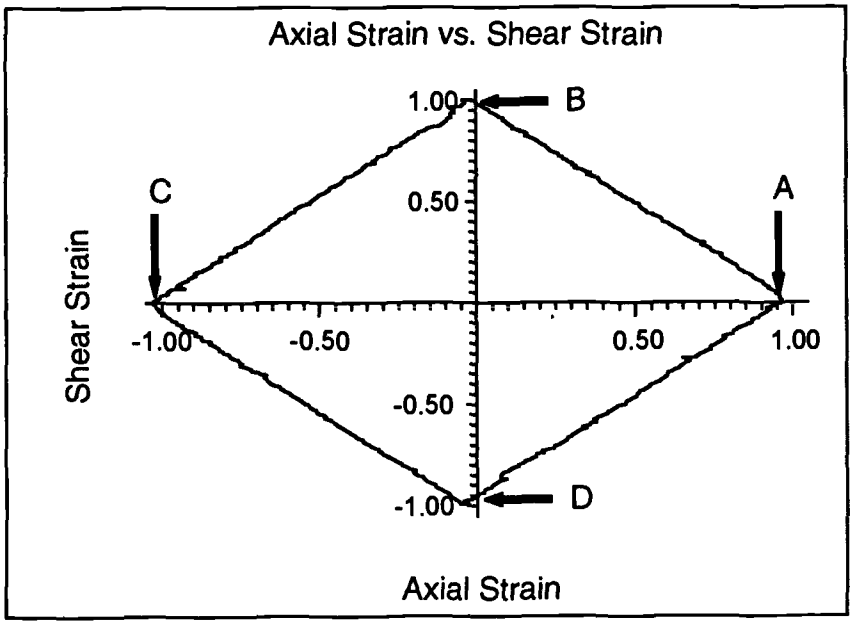

FIG. 14—*Normalized loops, $\lambda = 1.73$, $\phi = 90°$: axial hysteresis loop, torsional hysteresis loop, axial strain versus engineering shear strain, and axial stress versus shear stress.*

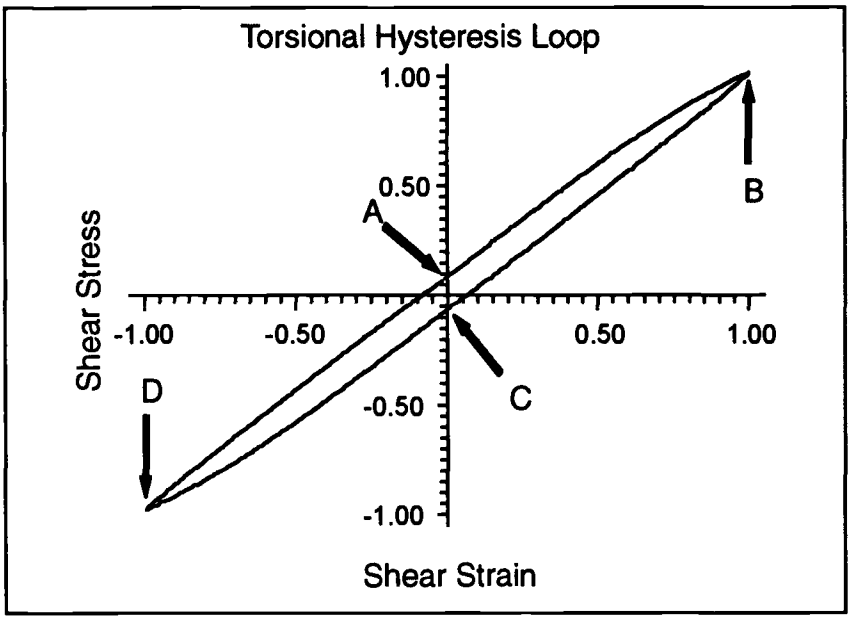

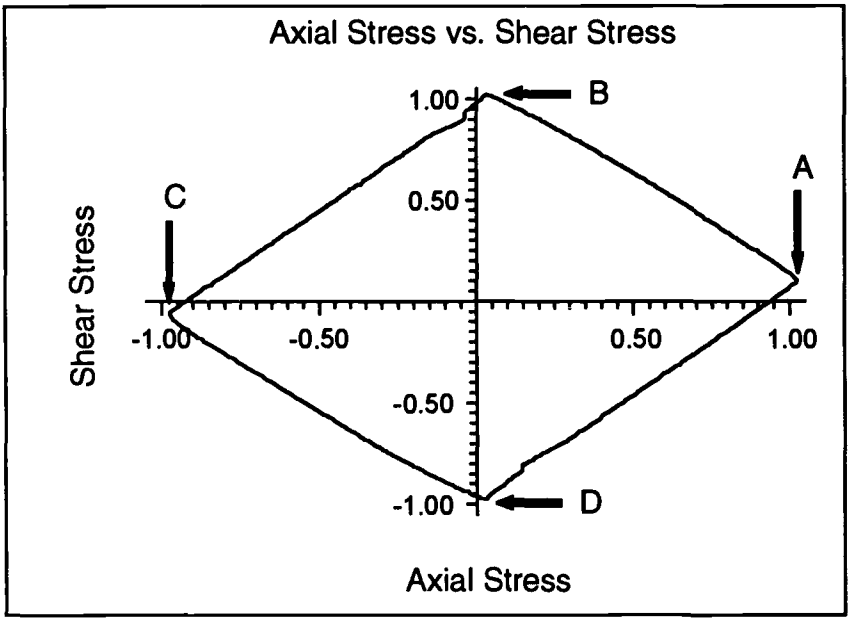

FIG. 14—*Continued.*

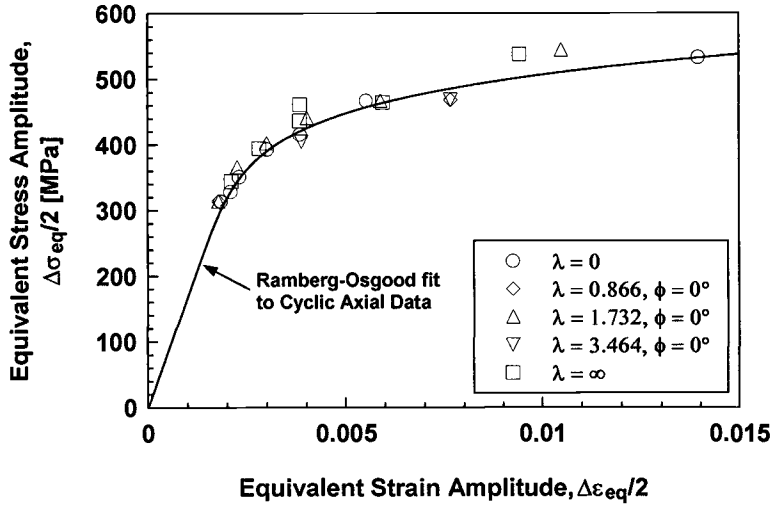

FIG. 15—*Equivalent stress-strain (von Mises) data: in-phase experiments.*

or strains). The sign (positive or negative) of each of the calculated values was determined by the sign of quantity that had the larger absolute magnitude. The results of these computations for the in-phase experiments are shown in Figs. 15 (von Mises) and 16 (Tresca). Out-of-phase test results are shown in Figs. 17 (von Mises) and 18 (Tresca). In the von Mises equivalent stress-strain figures, a curve representing the Ramberg-Osgood equation fit to the cyclic axial data ($\lambda = 0$) is also plotted. In the maximum shear stress versus maximum engineering shear strain figures, a curve representing the Ramberg-Osgood equation fit to the cyclic torsional data ($\lambda = \infty$) is shown. In all four plots both the cyclic axial ($\lambda = 0$) and cyclic torsional ($\lambda = \infty$) data are also displayed. Some axial strain ratchetting[3] was observed in the torsional experiments ($\lambda = \infty$), but it was not used to compute the von Mises or Tresca strains.

The Ramberg-Osgood stress-strain curve obtained from the cyclic axial data seems to represent the in-phase axial-torsional data better than the maximum shear stress-maximum engineering shear strain curve obtained from the cyclic torsional data. Both the von Mises equivalent stress-strain curve and the maximum shear stress-maximum engineering shear strain curve underestimate the cyclic hardening in the out-of-phase axial-torsional tests where $\phi = 90°$. Two out-of-phase axial-torsional tests with $\phi = 90°$ were conducted with sinusoidal waveforms also at a frequency of 0.1 Hz. The cyclic hardening in these tests was similar to the cyclic hardening in tests conducted with triangular waveforms (Figs. 17 and 18), indicating that the effect of waveform (or small differences in strain rate) is not significant for Haynes 188 at 760°C.

[3] Similar axial strain ratchetting has been observed under torsional loading by several researchers [*14–17*]. In the majority of the torsional tests ($\lambda = \infty$) on Haynes 188 at 760°C, the mean axial ratchetting strain was positive and increased in magnitude with the number of cycles. However, for all the torsional experiments, the magnitude of the mean axial ratchetting strain near half-life was relatively small compared to the amplitude of the imposed engineering shear strain. Therefore, the axial ratchetting strain was not used in computing the von Mises and Tresca strains for the torsional experiments.

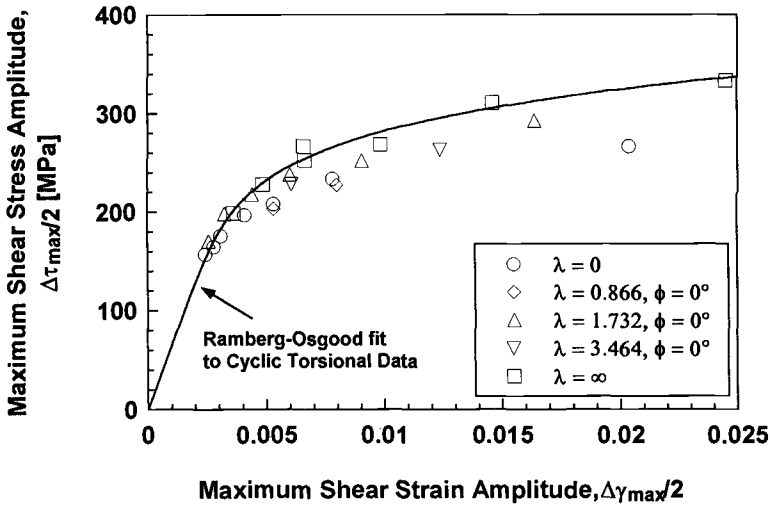

FIG. 16—*Maximum shear stress-engineering shear strain (Tresca) data: in-phase experiments.*

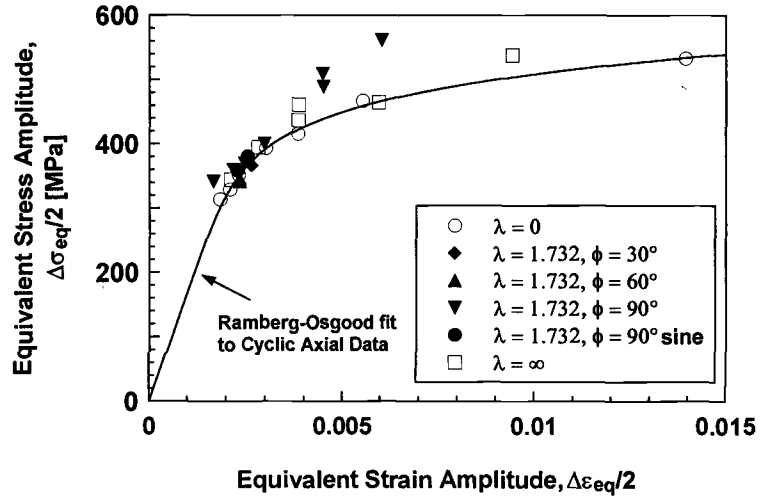

FIG. 17—*Equivalent stress-strain (von Mises) data: out-of-phase experiments.*

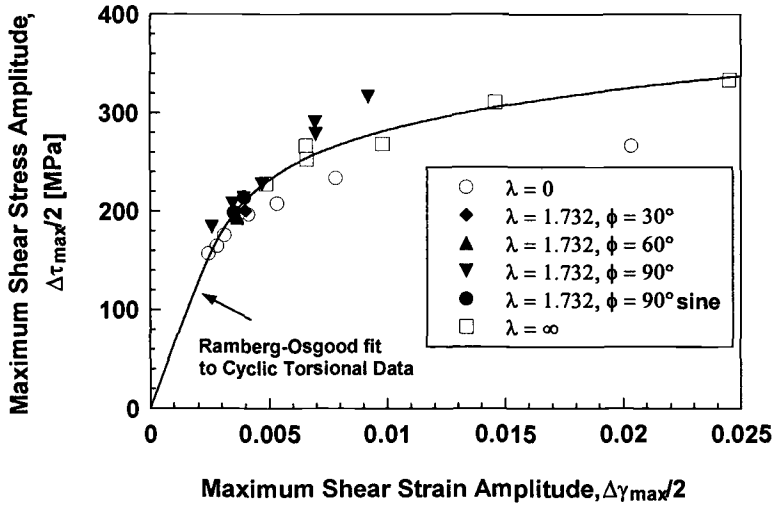

FIG. 18—*Maximum shear stress-engineering shear strain (Tresca) data: out-of-phase experiments.*

Table 3 contains constants for a Ramberg-Osgood type of cyclic stress-strain relation for the various loading conditions. The forms of these relations are

$$\varepsilon = \frac{\sigma}{E} + \left[\frac{\sigma}{K'}\right]^{1/n'} \quad \text{for the axial stress-strain relation}$$

or (6)

$$\gamma = \frac{\tau}{G} + \left[\frac{\tau}{K'_t}\right]^{1/n'_t} \quad \text{for the shear stress-strain relation}$$

These constants were determined in a previous study [*18*] by performing linear least squares fits to the logarithms of the near half-life stress amplitudes versus the logarithms of the near half-life inelastic strain amplitudes for each of the loading conditions listed in Table 3. The axial and shear stresses corresponding to the axial and engineering shear strains of 0.5% are

TABLE 3—*Ramberg-Osgood constants for axial and shear cyclic stress-strain curves under various loading conditions; Material: Haynes 188 at 760°C.*

Loading Parameters		Ramberg-Osgood Constants[a]				Stress at 0.5% Strain	
ϕ	λ	K', MPa	n'	K'_t, MPa	n'_t	σ, MPa	τ, MPa
0°	0	891	0.113	...	...	450	...
0°	∞	...	...	589	0.142	...	232
0°	1.73	1272	0.259	604	0.262	290	131
90°	1.73	2571	0.238	1247	0.230	563	256

[a] From Ref *18*.

also listed in Table 3. In both the axial and shear cases, cyclic stresses are lower under in-phase loading ($\lambda = 1.73$, $\phi = 0°$) and higher under out-of-phase loading ($\lambda = 1.73$, $\phi = 90°$) than the stresses corresponding to the individual axial ($\lambda = 0$) or torsional ($\lambda = \infty$) loading cases.

Discussion

The cycle-dependent hardening rate, as indicated by the normalized stress values for the in-phase tests (Figs. 7 and 8), seems to be independent of any non-zero proportionality constant, λ. However, the normalized stress range in the axial ($\lambda = 0$) test exhibited a slightly higher cycle-dependent hardening rate than the three in-phase tests. Similar behavior was not observed in the normalized shear stress ranges. The reason for this difference in the axial and torsional hardening rates of the in-phase tests is not apparent at present. In the out-of-phase tests, both the axial and shear stress ranges exhibited similar cycle-dependent hardening patterns.

It can be seen in Figs. 11 through 14 that the phase angle, ϕ, between the axial and engineering shear strain command waveforms has a substantial effect on the near half-life kinematic hardening behavior. The widths of both the axial and torsional hysteresis loops decrease markedly with each 30° increment of phase angle. This can also be observed in Figs. 3 to 6 and 9 and 10, which show the decrease in the widths of the hysteresis loops and the corresponding increase in the axial and shear stress ranges as the phase angle increases from 0 to 90°. Other researchers have reported similar behavior under out-of-phase axial-torsional loading [*2,4,7,9*]. The additional hardening that occurs in the out-of-phase axial-torsional loading is attributable to crystallographic slip in multiple directions, which is caused by the rotation of the principal axes that occurs in out-of-phase loading [*2,9,19*].

The von Mises criterion is a good estimator of the cyclic in-phase deformation behavior of Haynes 188 at 760°C. As can be seen in Fig. 15, all of the in-phase data fall on or just above the Ramberg-Osgood fit to the cyclic axial data ($\lambda = 0$). The torsional ($\lambda = \infty$) von Mises equivalent data show the largest deviation from the Ramberg-Osgood fit with as much as a 10% higher stress amplitude at the same equivalent strain amplitude. The maximum shear stress-strain, or Tresca approach, however, almost always overestimates the amount of cyclic hardening in the in-phase and axial experiments (Fig. 16). In the worst instance, the axial maximum shear stress amplitude is overestimated by 18%.

Both the von Mises and the Tresca approaches fail to adequately account for the extra hardening observed in the out-of-phase, axial-torsional experiments, especially those with a phase angle of 90° (Figs. 17 and 18). The 90° out-of-phase experiments exhibit as much as 20% more hardening than the Ramberg-Osgood fit to the cyclic axial data and as much as 15% more hardening than that estimated by the maximum shear stress-strain or Tresca approach. Kanazawa et al. [*2*] accounted for the additional hardening in the sinusoidal waveform, out-of-phase axial-torsional experiments on 1% Cr-Mo-V steel by using a rotation factor, which is a ratio of the shear strain range at 45° from the maximum shear plane to the maximum shear strain range. This factor was an attempt to account for the movement of dislocations within and across multiple crystallographic slip systems in the material. They were able to correlate both the in- and out-of-phase cyclic deformation data to within the same scatter band by using the rotation factor in conjunction with the maximum shear stress-strain (Tresca) approach. For Haynes 188 at 760°C, the von Mises equivalent stress-strain curve, at least for the in-phase data, appears to represent the cyclic deformation data better than the maximum shear stress-strain method. Therefore, a method based on the von Mises approach, with appropriate flow and hardening rules to account for the phase angle-dependent hardening, might be able to estimate the additional hardening observed in the out-of-phase tests.

Conclusions

The cyclic deformation behavior of a wrought cobalt-base superalloy, Haynes 188, has been investigated at 760°C under various axial-torsional loading conditions. The following conclusions were drawn from the study of hysteresis loops and cyclic hardening behaviors under different loading conditions.

1. Under in-phase (proportional) loading, the ratio of the imposed engineering shear to axial strain amplitudes had little or no effect on the relative amounts of cycle-dependent hardening in either the axial or shear directions.
2. In out-of-phase (non-proportional) loading, for a given ratio of engineering shear to axial strain amplitudes and phase angles ranging from 0 to 90°, similar cycle-dependent hardening trends were observed for the axial and shear stress ranges. However, on an absolute basis, the largest stresses were observed when the phase angle was 90°, and the smallest stresses were observed when the phase angle was 0°.
3. The amount of hardening exhibited by Haynes 188 at 760°C and the shapes of the axial and torsional hysteresis loops under out-of-phase axial-torsional loading were directly dependent on the phase angle between the axial and engineering shear strain waveforms.
4. The equivalent stress-strain curve (von Mises) adequately estimated the cyclic deformation behavior of Haynes 188 at 760°C under in-phase (proportional) axial-torsional loading. However, the von Mises equivalent stress-strain criterion was not able to accurately estimate the extra hardening in the out-of-phase (non-proportional) experiments.
5. The maximum shear stress-strain (Tresca) criteria did not adequately estimate either the in-phase or the out-of-phase axial-torsional cyclic deformation behavior of Haynes 188 at 760°C.
6. When multiaxial loading conditions exist in a structure, the use of either the Von Mises or the Tresca Criterion to estimate the cyclic deformation behavior does not always yield the actual cyclic deformation behavior of the material, especially under out-of-phase loading.

References

[1] Brown, M. W. and Miller, K. J., "Biaxial Cyclic Deformation Behavior of Steels," *Fatigue of Engineering Materials and Structures,* Vol. 1, 1979, pp. 93–106.

[2] Kanazawa, K., Miller, K. J., and Brown, M. W., "Cyclic Deformation of 1% Cr-Mo-V Steel under Out-of-phase Loads," *Fatigue of Engineering Materials and Structures,* Vol. 2, 1979, pp. 217–228.

[3] Garud, Y. S., "Prediction of Stress-Strain Response under General Multiaxial Loading," *Mechanical Testing for Deformation and Model Development, ASTM STP 765,* R. W. Rohde and J. C. Swearengen, Eds., American Society for Testing and Materials, Philadelphia, 1982, pp. 223–238.

[4] Cailletaud, G., Kaczmarek, H., and Policella, H., "Some Elements on Multiaxial Behavior of 316L Stainless Steel at Room Temperature," *Mechanics of Materials,* Vol. 3, 1984, pp. 333–347.

[5] McDowell, D. L. and Socie, D. F., "Transient and Stable Deformation Behavior Under Cyclic Nonproportional Loading," *Multiaxial Fatigue, ASTM STP 853,* K. J. Miller and M. W. Brown, Eds., American Society of Testing and Materials, Philadelphia, 1985, pp. 64–87.

[6] McDowell, D. L., "An Experimental Study of the Structure of Constitutive Equations for Nonproportional Cyclic Plasticity," *Journal of Engineering Materials and Technology,* Vol. 107, 1985, pp. 307–315.

[7] Fatemi, A. and Stephens, R. I., "Cyclic Deformation of 1045 Steel Under In-Phase and 90 Degree Out-of-Phase Axial-Torsional Loading Conditions," *Multiaxial Fatigue: Analysis and Experiments,* SAE Publication AE-14, G. E. Lease and D. Socie, Eds., Society of Automotive Engineers, Inc., Warrendale, PA, 1989, pp. 139–147.

[8] Takashi, Y. and Ogata, T., "Description of Nonproportional Cyclic Plasticity of Stainless Steel by a Two-Surface Model," *Journal of Applied Mechanics,* Vol. 58, 1991, pp. 623–630.

[9] Jayaraman, N. and Ditmars, M. M., "Torsional and Biaxial (Tension-Torsion) Fatigue Damage Mechanisms in Waspaloy at Room Temperature," *International Journal of Fatigue,* Vol. 11, No. 5, 1989, pp. 309–318.

[10] Nickel Base Alloys, International Nickel Company, Inc., New York, 1977.

[11] Bonacuse, P. J. and Kalluri, S., "Elevated Temperature Axial and Torsional Fatigue Behavior of Haynes 188," NASA TM 105396, AVSCOM TR-91-C-045, June 1992.

[12] Kalluri, S. and Bonacuse, P. J., "In-Phase and Out-of-Phase Axial-Torsional Fatigue Behavior of Haynes 188 at 760°C," *Advances in Multiaxial Fatigue, ASTM STP 1191,* D. L. McDowell and R. Ellis, Eds., American Society for Testing and Materials, Philadelphia, 1993, pp. 133–150.

[13] Kalluri, S. and Bonacuse, P. J., "A Data Acquisition and Control Program for Axial-Torsional Fatigue Testing," *Application of Automation Technology to Fatigue and Fracture Testing, ASTM STP 1092,* A. A. Braun, N. E. Ashbaugh, and F. M. Smith, Eds., American Society for Testing and Materials, Philadelphia, 1990, pp. 269–287.

[14] Poynting, J. H., "On Pressure Perpendicular to the Shear Planes in Finite Pure Shears, and on the Lengthening of Loaded Wires when Twisted," *Proceedings of the Royal Society, London, Series A,* Vol. 82, 1909, pp. 546–559.

[15] Poynting, J. H., "Changes in Dimensions of Steel Wire when Twisted and Pressure of Distortional Waves in Steel," *Proceedings of the Royal Society, London, Series A,* Vol. 86, 1912, pp. 543–561.

[16] Swift, H. W., "Length Changes in Metals under Torsional Overstrain," *Engineering,* Vol. 163, 1947, pp. 253–257.

[17] Wack, B., "The Torsion of a Tube (or a Rod): General Cylindrical Kinematics and Some Axial Deformation and Ratchetting Measurements," *Acta Mechanica,* Vol. 80, 1989, pp. 39–59.

[18] Kalluri, S. and Bonacuse, P. J., "High Temperature Axial-Torsional Fatigue Testing: Tubular Specimen Design Issues," presented at the Symposium on Experimental Methods for High Temperature Material Behavior Characterization during the 1992 ASME Applied Mechanics, Materials, and Aerospace Summer Meeting, Scottsdale, Arizona, 28 April–1 May 1992, American Society of Mechanical Engineers, New York.

[19] Bonacuse, P. J. and Kalluri, S., "Axial-Torsional Fatigue: A Study of Tubular Specimen Thickness Effects," *Journal of Testing and Evaluation,* JTEVA, Vol. 21, No. 3, May 1993, pp. 160–167.

A. A. Moftakhar,[1] *G. Glinka,*[1] *D. Scarth,*[2] *and D. Kawa*[3]

Multiaxial Stress-Strain Creep Analysis for Notches

REFERENCE: Moftakhar, A. A., Glinka, G., Scarth, D., and Kawa, D., **"Multiaxial Stress-Strain Creep Analysis for Notches,"** *Cyclic Deformation, Fracture, and Nondestructive Evaluation of Advanced Materials: Second Volume, ASTM STP 1184,* M. R. Mitchell and O. Buck, Eds., American Society for Testing and Materials, Philadelphia, 1994, pp. 230–243.

ABSTRACT: A method for predicting time-dependent stresses and strains in the case of localized creep has been developed. This method is based on strain energy density considerations and is an extension of the method previously developed by the authors for localized time-independent plasticity problems. The solution method has been derived in a general form so that it may be applied to multiaxial notch tip stress states. This technique has been used to predict creep effects and the associated stress redistribution at the root of a notched zirconium alloy pipe and in a thin notched plate made of aluminum, both subjected to thermal creep. The predictions have been compared with the finite element data and good agreement obtained. The computational time for calculating the notch tip stresses and strains was much shorter than that required for the finite element analysis. The method can be particularly useful for the analysis of creep effects in the case of cyclic loading with hold times where the FEM calculations are very time consuming.

KEYWORDS: creep, stress-strain, fracture, multiaxial

Nomenclature

E	Modulus of elasticity
$f(\sigma)$	Function representing stress dependency of creep law
$f(\sigma^{n-1})$	Value of $f(\sigma)$ calculated at the time-increment $(n-1)$
$g(\alpha)$	Internal state variable
P	Applied load
t	Time
T_k	Temperature in Kelvin
Δt_n	The nth time increment
$y(\beta)$	Internal state variable
ε_{ij}^n	Notch tip strain components determined at the nth time increment
ε_{ij}^e	Notch tip strain components calculated from a linear elastic analysis
ε_{ij}^{aU}	Upper bound estimation of notch tip strain components
ε_{ij}^0	Notch tip strain components calculated from a linear elastic analysis for load level P_0
ε_{ij}^t	Notch tip strain components at time t
ε_{ij}	Strain component

[1] Research assistant and professor, respectively, Department of Mechanical Engineering, University of Waterloo, Waterloo, Ontario, Canada N2L 3G1.

[2] Senior research engineer, Ontario Hydro, Research Division, 800 Kipling Ave., Toronto, Ontario, Canada M8Z 5S4.

[3] Consultant, Wardrop Engineering Inc., 77 Main St., Winnipeg, Manitoba, Canada, R3C 3H1.

ε_{ij}^{et} Elastic strain components at time t
ε_{ij}^{p} Time-independent plastic strain components due to the applied load P_0
ε_{ij}^{pt} Time-dependent plastic strain components at time t
$\dot{\varepsilon}_{ij}^{pt}$ Rate of time-dependent plastic strain components at the nth time increment
$\dot{\varepsilon}_{ij}^{et}$ Rate of the elastic strain components at time t
ν Poisson's ratio
σ_{ij} Stress components
$\dot{\sigma}_{ij}$ Rate of stress components
σ_{kk} Hydrostatic stress
$\dot{\sigma}_{kk}$ Rate of hydrostatic stress
σ_{eq} Equivalent stress
σ_{ij}^{aU} Upper bound estimation of notch tip stress components
σ_{ij}^{t} Notch tip stress components at time t
σ_{ij}^{0} Notch tip strain components calculated from a linear elastic analysis for load level P_0
σ_{ij}^{qU} Upper bound estimate of notch tip stress components
σ_{ij}^{e} Notch tip stress components calculated from a linear elastic analysis
σ_{ij}^{n} Notch tip stress components determined at the nth time increment
Ω Total strain energy density

Introduction

Advanced technology with its resulting liabilities and economic considerations requires implementation of finite life design methods to ensure safe and reliable operation of engineering structures and components. Most engineering structures are designed with elasto-plastic material containing geometrical or material discontinuities. When such components are loaded, local nonuniform triaxial stress fields occur with the highest stress concentration near the discontinuities. In order to minimize cost and weight, localized plastic deformation of the material near the discontinuities is often allowed. However, under repeated loads, cyclic deformation within the localized plastic zone usually controls the life of such components.

Stresses and strains within the local plastic zone are dependent on the applied load level and response of the material to the load over time (i.e., creep). Most engineering materials do not display significant time-dependent deformation at room temperature. In such situations, localized plastic deformation is virtually time-dependent. However, in an elevated temperature environment, after instantaneous deformation due to loading has occurred, materials may continue to deform in a time-dependent manner. The former is referred to as localized time-independent plasticity and the latter as localized time-dependent plasticity.

The understanding and description of the localized time-independent and the localized time-dependent deformation in terms of all stress and strain components are key factors in life prediction methodology of notched components subjected to cyclic loading. The visco-plastic finite element programs are expensive and time consuming, particularly when simulating cyclic loading with more than a few reversals.

To date, no simplified method capable of predicting the localized time-dependent multiaxial stresses and strains has been developed. Only a few authors have tried to extend the approximate solutions developed for localized time-independent plasticity problems to predict time-dependent stresses and strains in simple two-dimensional notched components. Two of the methods extended include Neuber's rule [*1*] and the equivalent strain energy method [*2*].

Sakane and Ohnami [*3*] studied the hold-time effect on the fatigue life of cylindrical notched specimens made of SUS 316 (S31600) stainless steel at 600°C in air. They employed a modified form of Neuber's rule presented in the *ASME Boiler and Pressure Vessel Code Case* N-47 to

simulate the notch root time-dependent behavior. They have demonstrated that the modified Neuber's rule yielded nonconservative fatigue life predictions for the notched specimens subjected to cyclic loading with a hold time in comparison with the experimental results.

Kurath [*4*] investigated the possibility of extending the fatigue life prediction method based on the local strain approach to include time-dependent deformation. He also employed a modified form of Neuber's rule to simulate the notch root stress-strain time-dependent behavior in members made of titanium alloy, Ti-6Al-4V, at room temperature, and acceptable fatigue life predictions were obtained in comparison with the experimental values.

Both studies estimated the notch root time-dependent stress and strain using the modified forms of Neuber's rule, but none of the predicted results were compared directly to the measured notch tip strains. All comparisons were made only in terms of fatigue life. Since errors in damage models influence the predicted fatigue life, it is difficult to assess the accuracy of these methods in terms of the predicted time-dependent notch tip stresses and strains.

Kubo and Ohji [*5*] have developed a simple solution for predicting notch tip time-dependent stresses and strains in plane stress and plane strain notched specimens. Their work is essentially an extension of the equivalent strain energy method proposed by Molski and Glinka [*2*]. It is known, however, that the equivalent strain energy method underestimates notch tip inelastic stresses and strains [*6*] depending on notch geometry, stress level, and state of stress. Therefore Kubo and Ohji have proposed an experimental correction factor of about 1.20 and obtained acceptable results for a few specific cases. Unfortunately, the degree of underestimation resulting from the application of the equivalent strain energy method differs from one case to another. Thus the constant correction factor of 1.20 limits the applicability of the method to the few specific cases analyzed by Kubo and Ohji [*5*], and therefore it cannot be generalized.

All the simplified solutions discussed above are applicable only to cases in which the state of stress at the notch tip is uniaxial. This limitation is due to the fact that all of them have been derived from simplified formulae applicable to plane stress and plane strain cases.

Because of the similarities between time-independent and time-dependent localized plasticity phenomena, extension of the methods developed for multiaxial time-independent plasticity seems to be justified for localized creep applications. However, a major deficiency is the absence of a generalized approach to localized time-independent plasticity problems.

Moftakhar and Glinka [*7*] have recently developed a lower bound and an upper bound solution for estimating local notch tip stresses and strains in the case of time-independent multiaxial localized plasticity. In contrast to Neuber's rule and the equivalent strain energy density equation, the solution method has been derived in a generalized form which is applicable to uniaxial and multiaxial stress states. Extension of the upper bound solution method [*7*] to the localized creep problems is the subject of this study.

The Notch Tip Stress-Strain Upper Bound Relationship

The relationship for predicting the upper bound values of the notch tip stress and strain components in the case of localized time-independent plasticity has been given in Ref *7*. The relationship has been derived in terms of a scalar parameter known as total strain energy density

$$\Omega = \varepsilon_{ij}\sigma_{ij} = \int_0^{\varepsilon_{ij}} d\varepsilon_{ij}\sigma_{ij} + \int_0^{\sigma_{ij}} \varepsilon_{ij} d\sigma_{ij} \tag{1}$$

It has been shown [*7*] that, after initiation of plasticity at the notch tip, the total strain energy density calculated at the notch tip of an elasto-plastic body, Ω^a, becomes smaller than the analogous value, Ω^e, calculated from a linear elastic stress field. It has also been proven that the total strain energy density in the notch tip, Ω^a, remains smaller than the hypothetical elastic

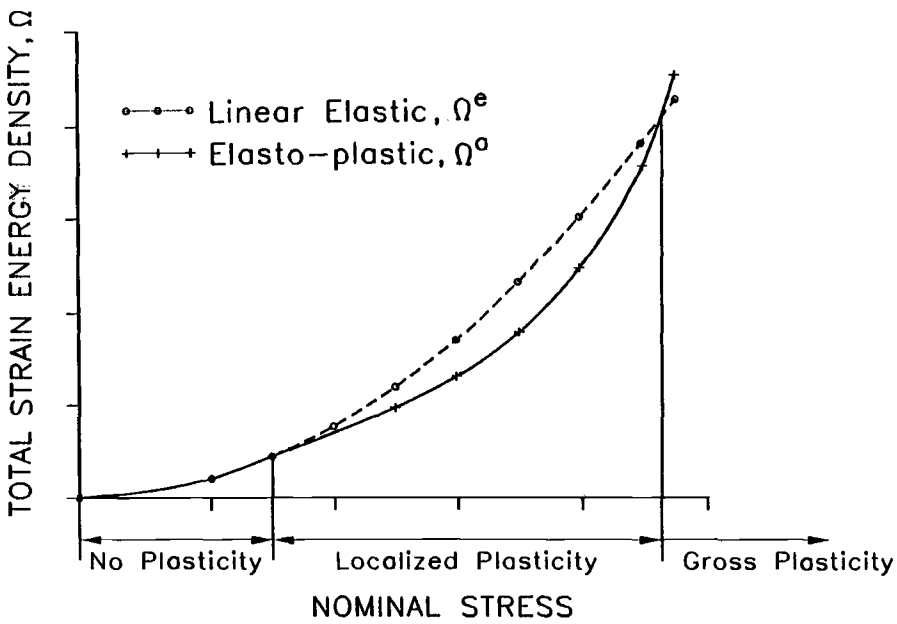

FIG. 1—*Variation of the total strain energy density at the notch tip as a function of the applied load.*

one, Ω^e, as long as the plastic deformation is a local event restricted to a zone near the notch tip. A typical variation of the two parameters, Ω^a and Ω^e, is schematically shown in Fig. 1. After some mathematical manipulations, the following relationship for the upper bound notch tip stress and strain components has been derived.

$$\varepsilon_{ij}^{aU}\sigma_{ij}^{aU} = \varepsilon_{ij}^{e}\sigma_{ij}^{e} \tag{2}$$

Localized plasticity was the essential assumption made for the derivation of Eq 2. An extension of Eq 2 for the analysis of localized creep problems is discussed below.

Extension of the Upper Bound Relationship for the Localized Creep Problems

Consider a notched body loaded to a certain load level, P_0, and then held under this load for a prolonged period of time. In the case of creeping materials, the notched body will continue to deform in a time-dependent manner after the instantaneous deformation due to the fact that the applied load, P_0, has occurred. However, due to the high local stress at the notch tip and also the power-law dependency of the creep strain rate on the stress, the creep of the material may be restricted to a zone near the notch tip. In such a case, the stresses and strains within the notch tip zone change with time due to the creep without any significant change of the far-field stress and strain. Since the stresses and strains on the right-hand side of Eq 2 are calculated on the basis of the theory of linear elasticity, they are linearly dependent on the applied load, P_0. In other words they change only when the far-field stress and strain change. Therefore, during the hold time period in which the applied load is held constant, the right-hand side stresses and strains in Eq 2 do not change and remain constant as long as creep deformation is localized. The constant value is equal to that evaluated at time $t = 0$. However, the stress and

strain components on the left-hand side of Eq 2 change with time. It follows that in the case of localized creep during the hold time period, Eq 2 takes the form of Eq 3.

$$\varepsilon_{ij}^{t}\sigma_{ij}^{t} = \varepsilon_{ij}^{0}\sigma_{ij}^{0} \tag{3}$$

The equality in the form of Eq 3 states that the notch tip total strain energy density remains constant during the hold time period as long as the creep deformation is restricted only to a zone near the notch tip.

The strain components on the left-hand side of Eq 3 can be decomposed into three parts,

$$\varepsilon_{ij}^{t} = \varepsilon_{ij}^{et} + \varepsilon_{ij}^{p} + \varepsilon_{ij}^{pt} \tag{4}$$

Substitution of Eq 4 into Eq 3 results in

$$\varepsilon_{ij}^{0}\sigma_{ij}^{0} = \varepsilon_{ij}^{et}\sigma_{ij}^{t} + \varepsilon_{ij}^{p}\sigma_{ij}^{t} + \varepsilon_{ij}^{pt}\sigma_{ij}^{t} \tag{5}$$

The mechanically induced plastic strains, ε_{ij}^{p}, are nonrecoverable when small unloading occurs. In other words, during the hold time period, only a tradeoff between elastic unloading and time-dependent deformation takes place.

According to most contemporary creep laws, the creep strain rate, $\dot{\sigma}_{ij}^{pt}$, is related to the current stress, σ_{ij}^{t}, and a set of internal variables. Therefore, the rate form of Eq 5 may be adopted. Differentiating Eq 5 with respect to time, t, yields

$$0.0 = \dot{\varepsilon}_{ij}^{et}\sigma_{ij}^{t} + \varepsilon_{ij}^{et}\dot{\sigma}_{ij}^{t} + \dot{\varepsilon}_{ij}^{p}\dot{\sigma}_{ij}^{t} + \dot{\varepsilon}_{ij}^{pt}\sigma_{ij}^{t} + \varepsilon_{ij}^{pt}\dot{\sigma}_{ij}^{t} \tag{6}$$

The elastic strain rate, $\dot{\varepsilon}_{ij}^{et}$, can be expressed in terms of time-dependent stress rate such that

$$\dot{\varepsilon}_{ij}^{et} = \frac{1 + \nu}{E}\dot{\sigma}_{ij}^{t} - \frac{\nu}{E}\dot{\sigma}_{kk}^{t}\delta_{ij} \tag{7}$$

Subsequent substitution of Eq 7 into Eq 6 results in

$$0.0 = \left(\frac{1 + \nu}{E}\dot{\sigma}_{ij}^{t} - \frac{\nu}{E}\dot{\sigma}_{kk}^{t}\delta_{ij}\right)\sigma_{ij}^{t} + \left(\frac{1 + \nu}{E}\sigma_{ij}^{t} - \frac{\nu}{E}\sigma_{kk}^{t}\delta_{ij}\right)\dot{\sigma}_{ij}^{t} + \dot{\varepsilon}_{ij}^{p}\dot{\sigma}_{ij}^{t} + \dot{\varepsilon}_{ij}^{pt}\sigma_{ij}^{t} + \varepsilon_{ij}^{pt}\dot{\sigma}_{ij}^{t} \tag{8}$$

Using the time-integration method, Eq 8 can be written in a form suitable for the numerical solution. The time axis is divided into a succession of time steps, Δt_i, $i = 1, 2, \ldots$, beginning at time, t_0. Then instead of seeking for a solution to stresses, σ_{ij}^{t}, over the entire hold time period, t, an approximate solution consisting of discrete values of σ_{ij}^{t} at the end of each time step can be found, i.e., σ_{ij}^{1} at time t_1, σ_{ij}^{2} at time t_2, etc., starting from the known initial value of σ_{ij}^{0} at time $t = 0$. The time derivatives can be approximated by a backward difference over the time step, Δt_n

$$\left(\frac{d\sigma_{ij}}{dt}\right)^{n} \simeq \frac{\sigma_{ij}^{n} - \sigma_{ij}^{n-1}}{\Delta t_n} \tag{9}$$

where $\Delta t_n = t_n - t_{n-1}$.

Further substitution of Eq 9 into Eq 8 yields

$$0.0 = \left(\frac{1+\nu}{E}(\sigma_{ij}^{n} - \sigma_{ij}^{n-1}) - \frac{\nu}{E}\delta_{ij}(\sigma_{kk}^{n} - \sigma_{kk}^{n-1})\right)\sigma_{ij}^{n} + \left(\frac{1+\nu}{E}\sigma_{ij}^{n} - \frac{\nu}{E}\sigma_{kk}^{n}\delta_{ij}\right)(\sigma_{ij}^{n} - \sigma_{ij}^{n-1}) + \varepsilon_{ij}^{p}(\sigma_{ij}^{n} - \sigma_{ij}^{n-1}) + \Delta t_n(\dot{\varepsilon}_{ij}^{pt})^n\sigma_{ij}^{n} + (\sigma_{ij}^{n} - \sigma_{ij}^{n-1})\sum_{i=1}^{n}\Delta t_n(\dot{\varepsilon}_{ij}^{pt})^n \quad (10)$$

The mechanically induced plastic strain components, ε_{ij}^{p}, are known from the time-independent elasto-plastic analysis. The plastic time-dependent strain rate components, $\dot{\varepsilon}_{ij}^{pt}$, are given by creep law of material in terms of state of stress and a set of internal state variables such that

$$\dot{\varepsilon}_{ij}^{pt} = f(\sigma)g(\alpha)y(\beta) \quad (11)$$

Using Eq 11, the plastic time-dependent strain rate, $\dot{\varepsilon}^{pt}$, over the nth time-step, Δt_n, can be approximated as

$$(\dot{\varepsilon}_{ij}^{pt})^n = f(\sigma^{n-1})g(\alpha)y(\beta) \quad (12)$$

Therefore, in the view of Eq 12, unknown parameters in Eq 10 are reduced only to the components of notch tip stress tensor, σ_{ij}^{n}, at the nth time interval.

Calculation of Time-Dependent Stresses and Strains at the Notch Tip

For a notch with a traction free surface (Fig. 2), the stress tensor at the notch tip has in general only three independent nonzero components, i.e.

$$\sigma_{ij} = \begin{vmatrix} 0 & 0 & 0 \\ 0 & \sigma_{22} & \sigma_{23} \\ 0 & \sigma_{23} & \sigma_{33} \end{vmatrix} \quad (13)$$

Having known the material constitutive law, the creep law of the material and the mechanically induced plastic strain components, ε_{ij}^{p}, a general solution to the stress field problem at the notch tip requires definition of three unknowns. The unknown parameters in Eq 10 are the three nonzero stress components given in Eq 13. It follows that two more relationships are needed for a complete solution. However, there are several specific cases in which the number of nonzero components of the notch tip stress tensor is reduced to only one element, and as a consequence, Eq 10 alone is sufficient for predicting the time-dependent notch tip stress and strain components.

In notched bodies under a plane stress state, the number of independent nonzero components of the notch tip stress tensor is reduced to only one component, σ_{22}.

$$\sigma_{ij} = \begin{vmatrix} 0 & 0 & 0 \\ 0 & \sigma_{22} & 0 \\ 0 & 0 & 0 \end{vmatrix} \quad (14)$$

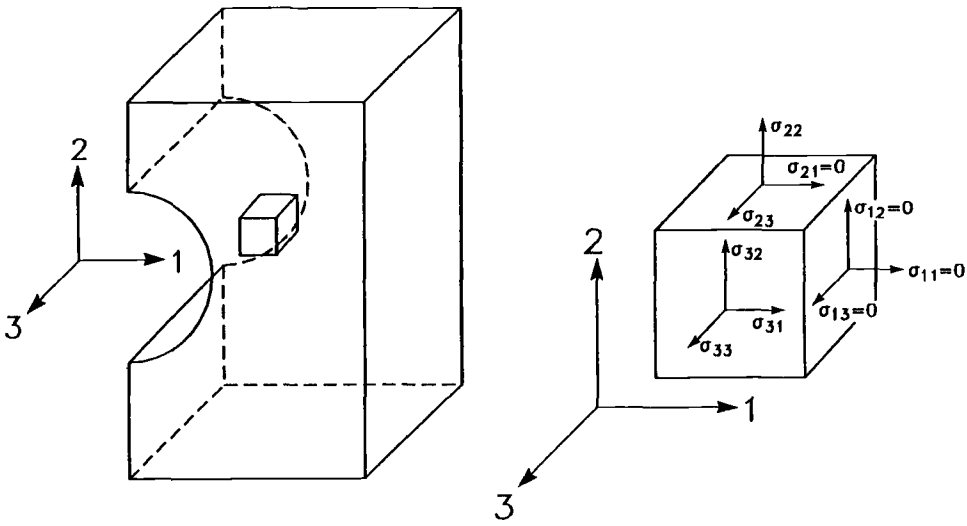

FIG. 2—*State of stress on the traction-free surface at the notch tip.*

Consequently, Eq 10 is reduced to the following form

$$0.0 = \left(\frac{1+\nu}{E}(\sigma_{22}^{n} - \sigma_{22}^{n-1}) - \frac{\nu}{E}\delta_{22}(\sigma_{22}^{n} - \sigma_{22}^{n-1})\right)\sigma_{22}^{n} + \left(\frac{1}{E}\sigma_{22}^{n}\right)(\sigma_{22}^{n} - \sigma_{22}^{n-1}) + \varepsilon_{22}^{p}(\sigma_{22}^{n} - \sigma_{22}^{n-1}) + \Delta t_n(\dot{\varepsilon}_{22}^{pl})^n\sigma_{22}^{n} + (\sigma_{22}^{n} - \sigma_{22}^{n-1})\sum_{i=1}^{n}\Delta t_n(\dot{\varepsilon}_{22}^{pl})^n \quad (15)$$

The creep law, Eq 11, and Eq 15 can be used to solve for the unknown stress component, σ_{22}^{n}, at the nth time interval.

In the case of plane strain, the notch tip stress tensor has only two nonzero components.

$$\sigma_{ij} = \begin{vmatrix} 0 & 0 & 0 \\ 0 & \sigma_{22} & 0 \\ 0 & 0 & \sigma_{33} \end{vmatrix} \quad (16)$$

Having known the creep law of the material and the mechanically induced plastic strain components, ε_{ij}^{p}, a solution to the stress field problem at the notch tip requires definition of two unknowns. The unknown parameters in Eq 10 are the two nonzero stress components shown in Eq 16. It follows that one more relationship is needed. The additional relationship can be formulated using the plane strain definition, i.e.

$$0.0 = \varepsilon_{33}^{t} = \varepsilon_{33}^{et} + \varepsilon_{33}^{p} + \varepsilon_{33}^{pl} \quad (17)$$

Using the elastic constitutive law of the material, Eq 17 at time increment "n" can also be written as

$$0.0 = \left(\frac{1+\nu}{E}\sigma_{ij}^{n} - \frac{\nu}{E}\delta_{ij}\sigma_{kk}^{n}\right) + \varepsilon_{ij}^{p} + \sum_{i=1}^{n}\Delta t_n(\dot{\varepsilon}_{ij}^{pl})^n \quad (18)$$

The creep law, Eq 11, Eq 18, and Eq 10 can be used to solve for the unknown stress components, σ_{22}^n and σ_{33}^n, at the nth time interval. The time integration continues until the following condition is satisfied

$$\sum_{i=1}^{n} \Delta t_n = t_{\text{hold}} \tag{19}$$

A similar set of equations can also be formulated for any multiaxial stress state. In a general multiaxial stress state, the number of unknown stress components at the traction free notch tip is less than or equal to three (Eq 13). It follows that, in addition to Eq 10, two more relationships are needed in such a case. Fortunately it has been found that, as long as the creep deformation of the notched body is localized, the following parameters remain approximately constant during the loading and the hold time period.

$$\frac{\varepsilon_{22}^t \sigma_{22}^t}{\varepsilon_{ij}^t \sigma_{ij}^t} \simeq \frac{\varepsilon_{22}^0 \sigma_{22}^0}{\varepsilon_{ij}^0 \sigma_{ij}^0} = \omega \tag{20}$$

$$\frac{\varepsilon_{33}^t \sigma_{33}^t}{\varepsilon_{ij}^t \sigma_{ij}^t} \simeq \frac{\varepsilon_{33}^0 \sigma_{33}^0}{\varepsilon_{ij}^0 \sigma_{ij}^0} = \beta \tag{21}$$

$$\frac{\varepsilon_{23}^t \sigma_{23}^t}{\varepsilon_{ij}^t \sigma_{ij}^t} \simeq \frac{\varepsilon_{23}^0 \sigma_{23}^0}{\varepsilon_{ij}^0 \sigma_{ij}^0} = \gamma \tag{22}$$

The constancy of parameters, ω, β, and γ, is thought to be attributed to the far-field constraint imposed on the notch tip deformation.

Any two of Eqs 20 through 22 provides the two additional independent relationships required for a complete formulation of the notch tip stress and strain problem in a general multiaxial stress state. Subsequently, Eq 10 together with the material creep law, Eq 11, and Eq 20 and Eq 21 form a set of three independent equations necessary for a general solution to the notch tip stress field at time t. The complete set of equations is also given in the Appendix.

Assessment of the Proposed Method

Semi-Ellipsoidal Notch in a Pressure Pipe

Numerical calculations using finite element method were carried out to assess the prediction capability of the proposed solution method. Finite element results were generated by both the ANSYS [*8*] and ABAQUS [*9*] programs to establish confidence in the FEM solutions. The geometry of the Zr-2.5%Nb alloy pressure tube with an internal semi-ellipsoidal axial notch is shown in Figs. 3 and 4. The tube was subjected to a multiaxial load composed of an internal pressure of 10 MPa and a longitudinal stress of 125 MPa at temperature 250°C. The mechanical properties for Zr-2.5%Nb material used in this study were

$$E = 94\,400.0 \text{ MPa} \qquad \nu = 0.4$$

Creep strains were predicted using the isotropic thermal creep law [*10*] given in the following form

$$\dot{\varepsilon}^{pt} = (1.3834 \times 10^{-7}\, \sigma_{eq}^{3.3} t^{-0.88} + 6.3388 \times 10^{-4} \exp(0.015\, \sigma_{eq})) \times \exp\left(-\frac{7000}{T_K}\right) \tag{23}$$

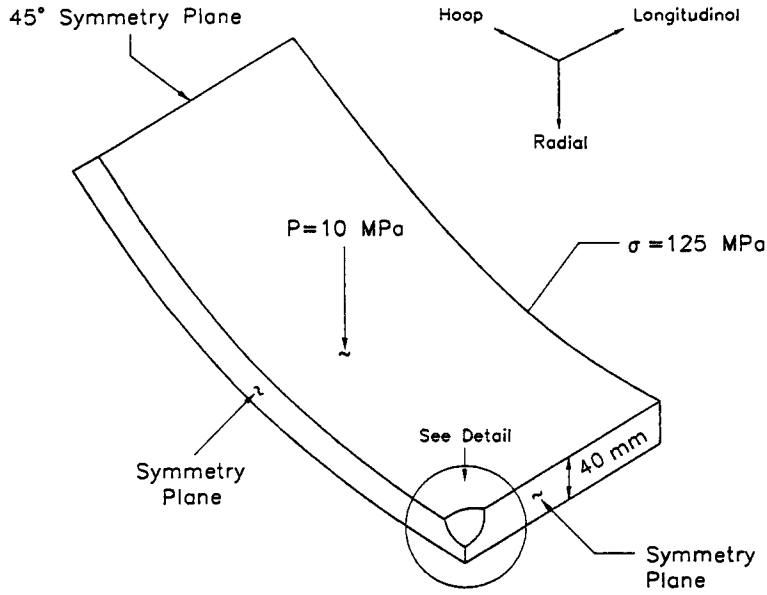

FIG. 3—*Schematic representation of the notched pressure tube used in the analysis, all dimensions in millimetres.*

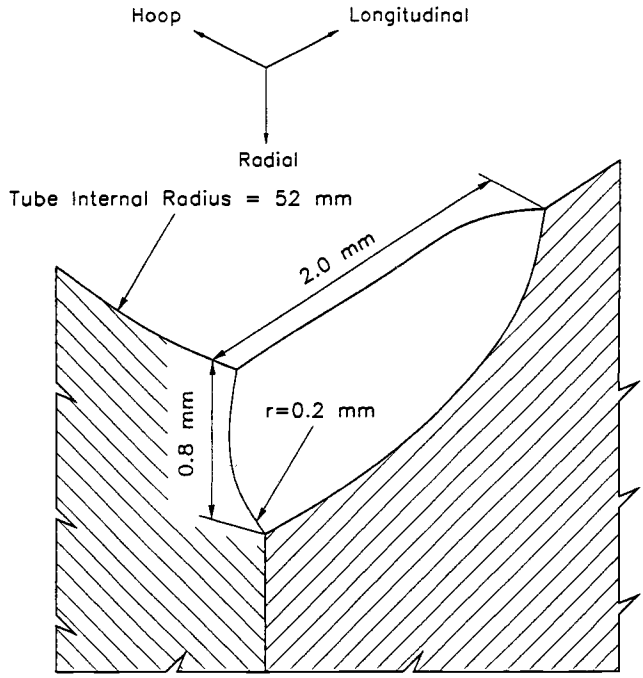

FIG. 4—*Detailed geometry of the semi-ecliptic notch in the pressure tube, all dimensions in millimetres.*

The notch tip stress components at time, $t = 0$, obtained from the linear elastic FEM analysis were

$$\text{Hoop stress} = \sigma^0_{22}\ 670.0\ \text{MPa}; \qquad \text{Axial stress} = \sigma^0_{33} = 347.0\ \text{MPa};$$

$$\text{Radial stress} = \sigma^0_{11} = 0.0; \qquad \sigma^0_{23} = \sigma^0_{32} = 0.0$$

The comparison between the time variation of the notch tip stress and strain components obtained by the present method and the FEM results is given in Figs. 5 and 6. It is apparent that the predicted stresses and strains agree well with the FEM results. It is also interesting to note that after 100 000 h of creep the predicted stresses and strains were slightly underestimated in comparison with the FEM data. This is attributed to the fact that, after 100 000 h, the creep deformation was not localized, and the far-field stresses and strains started to change with time as well.

Semi-Circular Double Edge Notches in a Thin Plate

A set of data for time-dependent notch tip stress and strain, calculated for a double edge notch specimen (Fig. 7) with the theoretical stress concentration of $K_t = 2$, was borrowed from Ref *11*. The specimen was made of pure aluminum with the stress-strain relationship given in

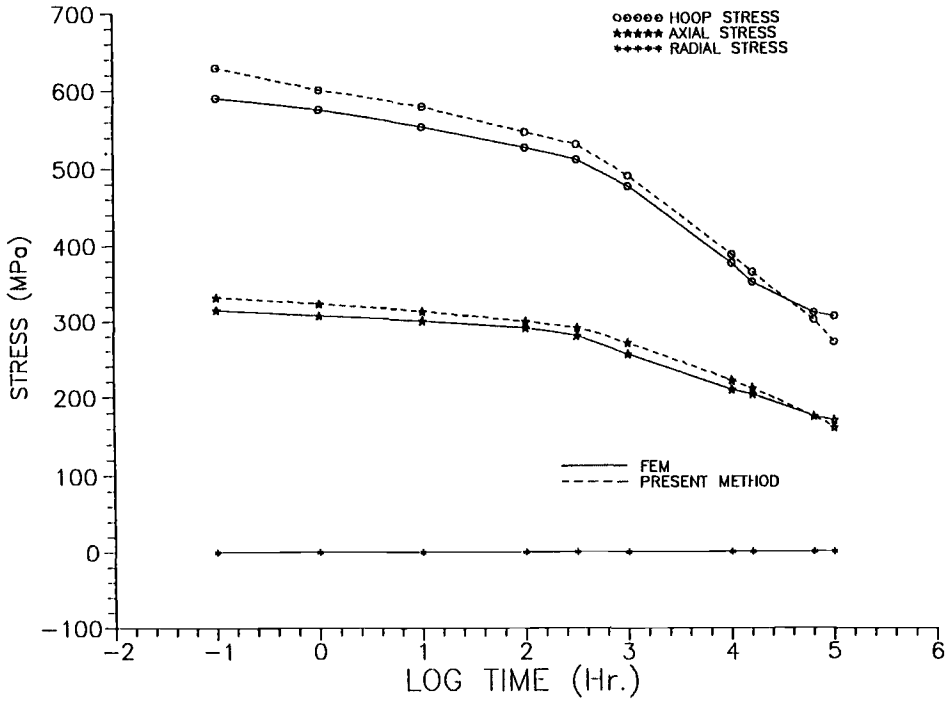

FIG. 5—*Time variations of the notch tip stress components at the notch tip of the pressure tube.*

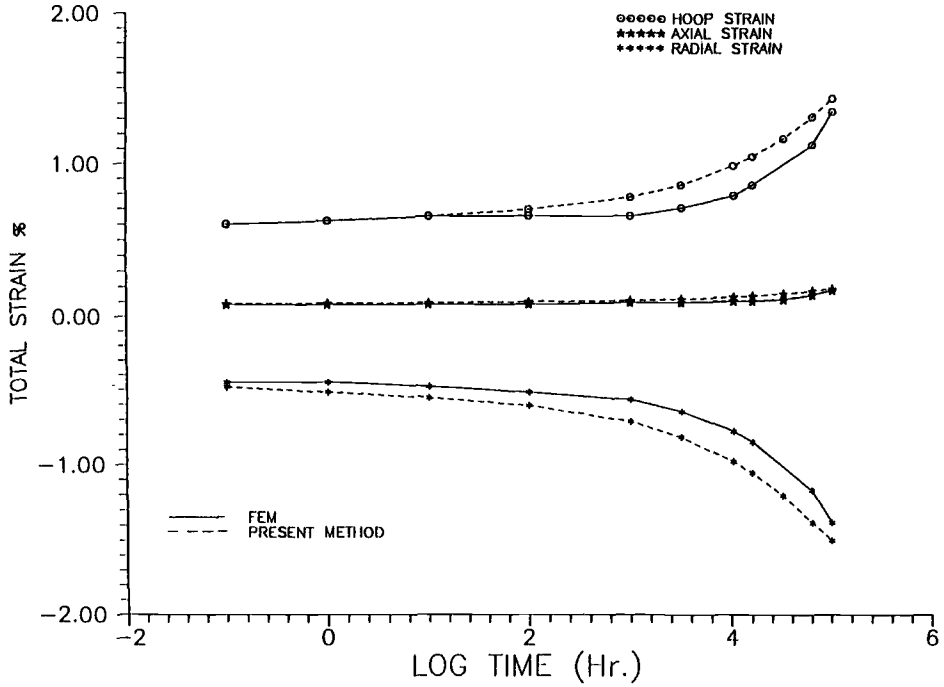

FIG. 6—*Time variation of the notch tip strain components in the pressure tube.*

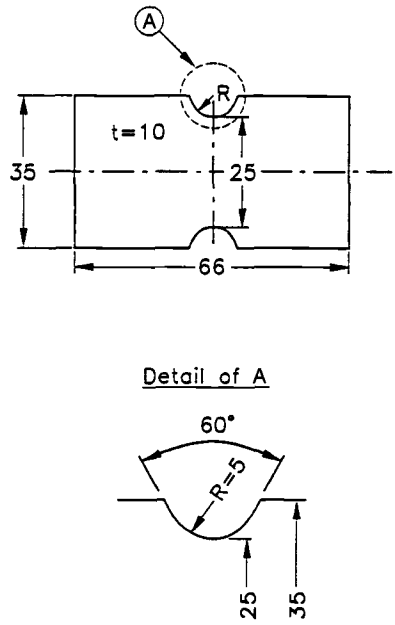

FIG. 7—*Geometry and dimensions of the double edge notch specimen, all dimensions in millimetres.*

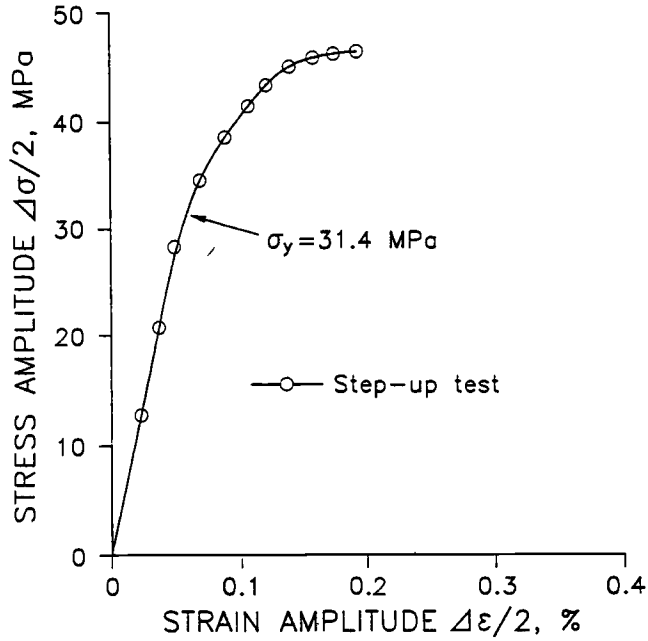

FIG. 8—*The stabilized stress/strain curve of the pure aluminum material.*

Fig. 8. The model was subjected to a nominal tensile stress of 29.7 MPa at temperature of 437 K. The creep law was approximated by the relationship given [*11*] below.

$$\varepsilon^{pt} = F\{1 - \exp[-Rt]\} + Gt \tag{24}$$

where

$$F = \exp[0.136\,\sigma^t - 12.9]; \qquad R = 7.5\left(\frac{\sigma^t}{29.3}\right)^{3.0}; \qquad G = \exp[0.306\,\sigma^t - 19.6]$$

The notch tip stresses and strains were computed by the finite element method and compared with the strain measured by high-temperature resistance strain gages to establish the reliability of the FEM solutions. In contrast to the notched pressure tube, the applied load was high enough to induce time-independent plasticity at the notch tip prior to the creep-induced deformation. The time-dependent inelastic notch tip stress and strain were calculated first using the method described in Ref *12*. Then the notch tip stress and strain variations during the hold time period were determined by the present method. It is worth noting that due to the high nominal stress the far-field region started creeping after approximately 30 min, and as a consequence the localization of creep was not strictly preserved and therefore the effects of the far-field creep [*13*] were also included into the analysis. The calculated stresses and strains were compared with those obtained by Umeda et al. [*11*], and good agreement was achieved as shown in Fig. 9.

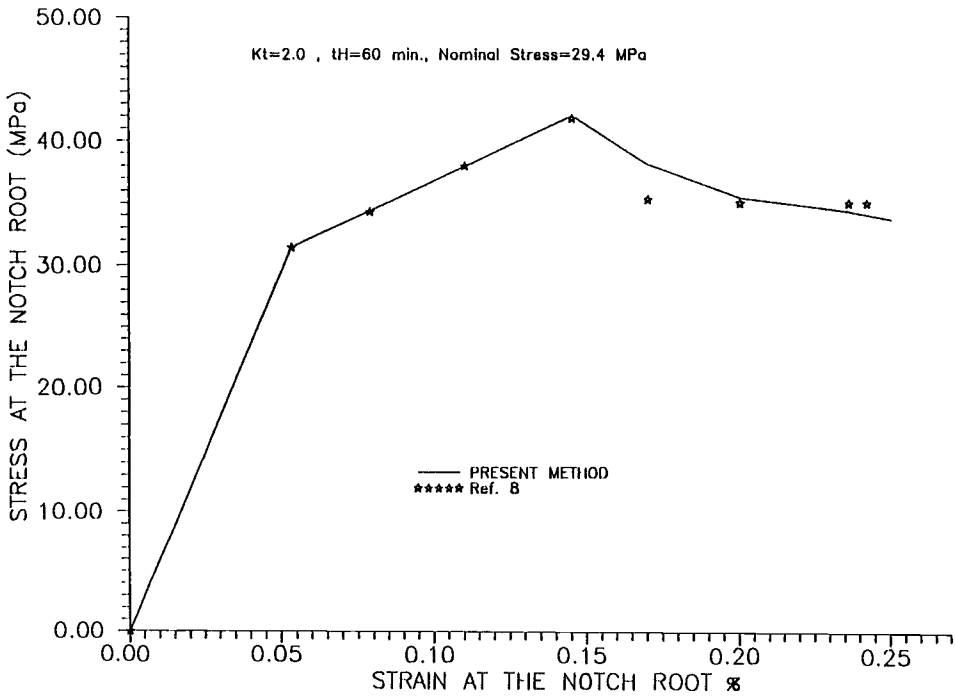

FIG. 9—*Comparison of calculated notch tip stress and strain.*

Conclusions

A simple method for predicting time-dependent stress and strain components in notches has been developed. The method is based on strain energy considerations. Localized creep deformation is the essential assumption made for derivation of the solution method. It has been shown that, in the case of localized creep, the rate of change of total strain energy density at the notch tip is zero. The solution method has been derived in a general form and may be applied to uniaxial as well as multiaxial stress states. The predictions of the method agreed well with the results of FEM analysis as long as the creep deformation was localized. The computational time for calculating the time-dependent notch tip stresses and strains, in each time interval, is limited to that needed for the solution of a set of three nonlinear equations. The method is much less time-consuming and expensive than the available visco-plastic FEM programs. The method can be particularly useful for the analysis of creep effects in the case of cyclic loading with hold times where the FEM calculations are very time-consuming.

APPENDIX

Equations Required for a Complete Solution of Time-Dependent Notch Tip Stress and Strain Components

Rate of change of the total strain energy density at the notch tip

$$0.0 = \dot{\varepsilon}^{el}_{ij}\sigma'_{ij} + \varepsilon^{el}_{ij}\dot{\sigma}'_{ij} + \varepsilon^{p}_{ij}\dot{\sigma}'_{ij} + \dot{\varepsilon}^{pl}_{ij}\sigma'_{ij} + \varepsilon^{pl}_{ij}\dot{\sigma}'_{ij} \tag{1}$$

Creep law

$$\dot{\varepsilon}_{ij}^{pt} = f(\sigma)g(\alpha)y(\beta) \tag{2}$$

Elastic constitutive law

$$\varepsilon_{ij}^{et} = \frac{1+\nu}{E}\sigma_{ij}^{t} - \frac{\nu}{E}\sigma_{kk}^{t}\delta_{ij} \tag{3}$$

Decomposition of the total strain components

$$\varepsilon_{ij}^{t} = \varepsilon_{ij}^{et} + \varepsilon_{ij}^{p} + \varepsilon_{ij}^{pt} \tag{4}$$

Contribution of each pair of coaxial stresses and strains to the total strain energy density

$$\frac{\varepsilon_{22}^{t}\sigma_{22}^{t}}{\varepsilon_{ij}^{t}\sigma_{ij}^{t}} \simeq \frac{\varepsilon_{22}^{0}\sigma_{22}^{0}}{\varepsilon_{ij}^{0}\sigma_{ij}^{0}} = \omega \tag{5}$$

$$\frac{\varepsilon_{33}^{t}\sigma_{33}^{t}}{\varepsilon_{ij}^{t}\sigma_{ij}^{t}} \simeq \frac{\varepsilon_{33}^{0}\sigma_{33}^{0}}{\varepsilon_{ij}^{0}\sigma_{ij}^{0}} = \beta \tag{6}$$

References

[1] Neuber, H., "Theory of Stress Concentration of Shear-Strained Prismatical Bodies With Arbitrary Non-Linear Stress-Strain Law," *Journal of Applied Mechanics,* American Society of Mechanical Engineers, Vol. 28, 1961, pp. 544–550.

[2] Molski, K. and Glinka, G., "A Method of Elastic-Plastic Stress and Strain Calculation at a Notch Root," *Material Science and Engineering,* Vol. 50, 1981, pp. 93–100.

[3] Sakane, M. and Ohnami, M., "A Study of the Notch Effect on the Low Cycle Fatigue of Metals in Creep-Fatigue Interacting Conditions at Elevated Temperature," *Journal of Engineering Materials and Technology,* American Society of Mechanical Engineers, Vol. 105, 1983, pp. 75–80.

[4] Kurath, P., "Extension of the Local Strain Fatigue Analysis Concepts to Incorporate Time Dependent Deformation in Ti-6Al-4V at Room Temperature," T.&A.M. Report No. 464, The University of Illinois, Urbana, IL, 1984.

[5] Kubo, S. and Ohji, K., "Development of Simple Method for Predicting Plane-Strain and Axi-symmetric Stress Relaxation at Notches in Elastic-Creep Bodies," *JSME International Journal,* Vol. 45, 1989, pp. 417–422.

[6] Glinka, G., "Calculation of Inelastic Notch-Tip Strain-Stress Histories under Cyclic Loading," *Engineering Fracture Mechanics,* Vol. 22, 1985, pp. 839–854.

[7] Moftakhar, A., "Localized Time Independent and Time-Dependent Plasticity at Notches," Ph.D. dissertation, Mechanical Engineering Department, University of Waterloo, Waterloo, Canada (under preparation).

[8] DeSalvo, G. J. and Gorman, R. W., "ANSYS, Engineering Analysis System User's Manual," Vol. I and II, 1989.

[9] Hibbit, H. D., Karlsson, B. I., and Sorensen, P. E., "ABAQUS Theory Manual, Version 4.8," 1989.

[10] Bell, L. G., "Creep Tests on Zr-2.5Nb Pressure Tubing at 300°C," Hawker Siddeley Engineering, Report No. HSER-FCP-66-002, Ontario Hydro Research Division, Canada.

[11] Umeda, H., Sakane, M., and Ohnami, M., "Comparison of Local Strain at the Notch Root Between FEM Analysis and Experimental Strain Measurement Under Creep-Fatigue Conditions," *JSME International Journal,* Vol. 30, No. 268, 1987, pp. 1543–1550.

[12] Moftakhar, A. and Glinka, G., "Elastic-Plastic Stress-Strain Analysis Methods for Notched Bodies," *Proceedings,* International Conference on Theoretical Concepts and Numerical Analysis of Fatigue, Birmingham, UK, 15–18 May, 1992.

[13] Moftakhar, A., Glinka, G., Scarth, D., and Kawa, D., "A Solution Method for the Problem of Irradiation and Thermal Creep in Notched Zirconium Components," *Creep and Fracture of Engineering Materials and Structures,* B. Willshire and R. W. Evans, Eds., 1993, pp. 459–468.

Apostolos Fafitis[1] *and Sebastian A. Jayamaha*[1]

Effect of Axial Force and Bending Moment Interaction on the Response of Elastoplastic Concrete Frames to Cyclic Loading

REFERENCE: Fafitis, A. and Jayamaha, S. A., **"Effect of Axial Force and Bending Moment Interaction on the Response of Elastoplastic Concrete Frames to Cyclic Loading,"** *Cyclic Deformation, Fracture, and Nondestructive Evaluation of Advanced Materials: Second Volume, ASTM STP 1184,* M. R. Mitchell and O. Buck, Eds., American Society for Testing and Materials, Philadelphia, 1994, pp. 244–254.

ABSTRACT: The objective of this paper is to illustrate the application of a recently developed inelastic failure analysis method to frames under proportional cyclic loading. The method takes into account the effect of bending moment and axial force interaction in the formation of plastic hinges during the loading-unloading cycles. For structures where the axial forces are predominant, this interaction is important. The frame is loaded with a system of concentrated loads that are increased incrementally close to collapse and then unloaded. If, during the loading process, sections of the structure develop moments M_i and axial force P_i such that the points (M_i, P_i) are outside the yield curve, a redistribution takes place that brings these points onto the curve. After several load cycles, if the loading is not excessive, the structure adjusts to the loading and the response becomes stable (shakedown). In the process of redistribution, if other sections produce points outside the yield curve, the redistribution is repeated until no points (M, P) lie outside. As a first approximation, the moment-axial interaction (yield) curve was assumed to be a straight line. To improve the accuracy of the analysis, a nonlinear yield curve was derived that depends on the material properties of the section. Comparison of analytical results with those of other researchers indicate that the developed method can handle the issue of moment-axial interaction with accuracy.

KEYWORDS: elasto-plastic, axial-bending interaction, frame, cyclic loading, yielding, arch

Nomenclature

M_i	Bending moment during an iteration of section i
P_i	Axial force during an iteration of section i
M_{pi}	Plastic bending moment capacity of section i
P_{pi}	Plastic axial force capacity of section i
M_{bi}	Balanced bending moment of section i
P_{bi}	Balanced axial force of section i
a_{ij}	Axial force at i due to the given unit moment at j
ΔM_i	Amount of moment needed to bring the point back on to the yield curve
ΔP_i	Amount of axial force needed to bring the point back on to the yield curve
N	Number of sections outside the interaction diagram during an iteration

[1] Associate professor and research associate, respectively, Arizona State University, Civil Engineering Department, Tempe, AZ 85287.

Introduction

For many years, engineers have based the analysis and design of structures on linear elastic theory. The results have been satisfactory; the buildings and bridges have withstood the test of time. However, the design methods that are based on linear elasticity neglect the ability of some materials and structures to carry stress beyond the linear elastic limits. More importantly, ductility in redundant structures permits a redistribution of stress beyond the elastic limit and these redistributed stresses can often carry considerable additional loads.

The concept of taking into account bending moment and axial force has been studied in the past. Onat and Prager [*1*] described the mechanical behavior of beams made of an elastic-plastic material in terms of bending moment and the angle of flexure per unit length. An extensive study of the analysis of elasto-plastic arches under loads increasing up to collapse was conducted by Cohn and Abdel-Rohman [*2*] in which both linearized and nonlinear yield curves are assumed in the analysis. Numerical results of this study illustrate the effect of bending moments, axial forces, and deformation on the inelastic behavior of arches.

The connection between mathematical programming and structural plasticity was first identified by Charnes and Greenberg in 1951 [*3*]. Their study was carried further using linear programming with plastic limit analysis by Dorn and Greenberg [*4*]. Recently, Loi and Wong [*5,6*] have proposed mathematical programming formulations, based on the plastic hinge concept, similar to the formulations pioneered by Maier et al. [*7,8*], then by Ueda and Yao [*9*], Orbison et al. [*10*], and Franchi and Cohn [*11*]. Typically, nonlinear yield surfaces are used, thereby making it necessary to resort to, for example, multistep iterative techniques [*10*] or enclosed yield surfaces approximation by Bozzo and Gambarotta [*12*], deformation analysis at plastic collapse by Maier et al. [*8*], and combined elastoplastic and limit analysis by Maier et al. [*7*] in order to satisfy both the yield condition and the equilibrium requirement.

An incremental analysis method was proposed by Oliveto and Cuomo [*13*] in which material nonlinearities are accounted for by inserting infinitesimal rigid-plastic elements between elastic members. Only elastic-perfectly plastic and linearly hardening models were considered.

Elasto-Plastic Analysis

When a structure is loaded outside the linear elastic limits, some sections enter the "plastic state," thus allowing the structure to "adapt" to the loading. A section under bending moment (M) and axial force (P) is said to be in a "plastic state" if the point (M, P) lies on the yield curve $M = f(P)$. If it lies inside the area defined by the yielding curves, it is in an elastic state. Points outside this area are not allowed. A yield curve (or interaction diagram) on the M-P space of the form $M = f(P)$ that depends on the material properties of the section and can simulate with acceptable accuracy the behavior of reinforced concrete columns has been recently developed [*15*]. If the loading does not exceed the capacity of the structure, a redistribution of bending moment and axial force takes place and the sections with (M, P) outside the yield curve are brought back onto the yield curve. The developed algorithm carries out this redistribution and brings all outside points back onto the yield curve for each loading increment. This feature makes the method numerically efficient. In the process of redistribution, if other sections produce points outside the yield curve, the redistribution is repeated until no points (M_i, P_i) lie outside the yield curve. The redistribution process converges rapidly, usually within two to three iterations. If the loading exceeds the capacity of the structure, then the iteration process diverges rapidly.

The frame is first analyzed for the given system of loads by the linear elastic method. Load is increased incrementally, and each section is checked after each increment to determine which joints develop a bending moment and axial force outside the yield curve. A hinge is inserted

in all such sections, a unit moment couple is applied (one hinge at a time), and the axial forces and bending moments, due to each couple, are calculated. The axial force at each of these hinges is called the axial force coefficient, a_{ij}. If the equation of the yield curve for section i is assumed linear for both compressive and tensile members, then the M-P relationship is written as

$$M = \left(1 - \frac{P}{P_{pi}}\right) M_{pi} \tag{1}$$

where M_{pi} and P_{pi} are plastic moment and axial capacities of section i, respectively. If, during an iteration, the bending moment M_i and axial force P_i of section i produce a point outside the yield curve, a moment ΔM_i and an axial force ΔP_i is employed to bring the point back onto the curve. The stress in section i is thus adjusted from M_i, P_i) to ($M_i + \Delta M_i$, $P_i + \Delta P_i$) so that Eq 1 is then satisfied

$$M_i + \Delta M_i = \left(1 - \frac{P_i + \Delta P_i}{P_{pi}}\right) M_{pi} \tag{2}$$

If the structure is not loaded beyond its capacity, a redistribution will take place, and the adjustment in M_i and P_i will be automatic. This adjustment can be seen as change in P at Section i due to change in M at all sections j that have entered the plastic state. Therefore, the axial force adjustment ΔP_i can be written in terms of the axial force coefficients and moment increments ΔM_j

$$\Delta P_i = \sum a_{ij} \Delta M_j \tag{3}$$

Substituting Eq 3 into Eq 2, one obtains the set of N linear simultaneous equations

$$\sum_{j=1}^{N} a_{ij} \Delta M_j + \frac{P_{pi}}{M_{pi}} \Delta M_i = P_{pi} - \frac{P_{pi}}{M_{pi}} M_i - P_i \qquad (i = 1 \ldots N) \tag{4}$$

If the equation of the yield curve for section i is assumed parabolic, then the M-P relationship can be written as

$$M = \left(1 - \frac{P}{P_{pi}}\right) M_{pi} + aP^2 + bP \tag{5a}$$

where

$$a = \frac{M_{bi} - \left(1 - \dfrac{P_{bi}}{P_{pi}}\right) M_{pi}}{[P_{bi}(P_{bi} - P_{pi})]} \tag{5b}$$

$$b = -aP_{pi} \tag{5c}$$

By proper choice of the parameters, this curve can be made to simulate with acceptable accuracy the *M-P* relationship of relatively brittle sections like reinforced concrete or ductile sections like steel subjected to axial compressive force and bending moment.

As mentioned previously, if the stress (M_i, P_i) of a section lies outside the curve, an adjustment ΔM_i and ΔP_i is needed to bring it back on the curve. Therefore ($M_i + \Delta M_i$) and ($P_i + \Delta P_i$) must satisfy Eq 5a

$$M_i + \Delta M_i = \left(1 - \frac{(P_i + \Delta P_i)}{P}\right) M_{pi} + a(P_i + \Delta P_i)^2 + b(P_i + \Delta P_i) \tag{6}$$

Substituting Eq 3 into Eq 6, one then obtains the set of N nonlinear simultaneous equations

$$a\left(\sum_{j=1}^{N} a_{ij}\Delta M_j\right)^2 + \left(\sum_{j=1}^{N} a_{ij}\Delta M_j\right)\left(2aP + b - \frac{M_{pi}}{P_{pi}}\right) - \Delta M_i + A_i = 0 \tag{7a}$$

where

$$A_i = aP_i^2 + \left(b - \frac{M_{pi}}{P_{pi}}\right) P_i + M_{pi} - M_i \tag{7b}$$

By solving this set of simultaneous equations, the moment adjustments ΔM_i ($i = 1, 2, \ldots N$) are calculated. Then, using Eq 3 ΔP_i are calculated. All members are checked again to see if, as a result of the redistribution that took place, any sections developed stress (M, P) outside the plastic state. If so, the same procedure will be repeated until all points lie on the yield surface.

Numerical Example

The method described previously will be used to analyze the fixed circular arch shown in Fig. 1 with the data required for the analysis. The circular arch is discretized into 20 members with equal capacities. Only half of the structure is considered due to symmetry. It is apparent that all members are subjected to a large axial force, and bending moments and the interaction effects cannot be neglected.

Using linear yield curves, the elastic limit of the structure was found to be $W_e = 8996$ kN. Beyond this load the structure behaves nonlinearly. It achieves a load $W > W_e$ by plastic hinges and redistribution of axial force and bending moments. Initially, the load was increased by 1000 kN increments. If the load could not be sustained by the structure at a particular increment, then the load increment was reduced to half, and so on. Only near the ultimate load were 1-kN increments used. This method has given an ultimate load of $W_u = 11\,920$ kN. At this load the method converges, whereas at the next load increment it does not converge. For $W_u = 11\,920$ kN, the bending moments and axial forces of all sections before redistribution are given in Table 1. These are the bending moments and axial forces produced by a linear elastic analysis. At ultimate load, bending moment and axial force of Joint 11 (Member 10) give a point outside the yield curve, whereas all other sections remain inside the interaction diagram. Note that in this example all sections have the same linear yield curve. To bring Joint 11 back on to the

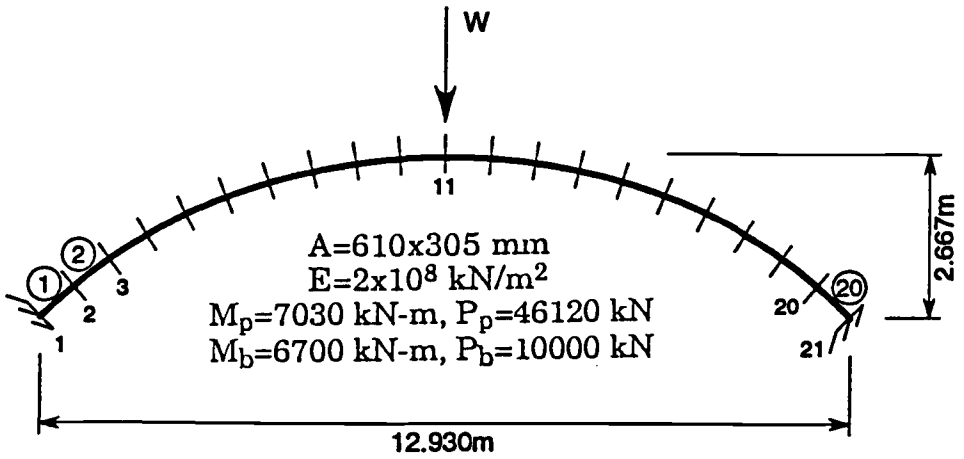

FIG. 1—*Discretized fixed circular arch.*

yielding curve, a hinge is introduced and unit moment is applied. The bending moments and axial forces of each section due to the unit moment are shown in Table 2, which will be used in the redistribution process of bending moments and axial forces. After the redistribution according to the developed method, the new bending moments and axial forces for all sections are calculated and given in Table 3. At this point, no section produces a point outside the interaction diagram and no further redistribution is necessary. Selected sections are shown in Fig. 2, which gives a pictoral view of the redistribution process.

The same arch was subjected to cyclic loading. The analysis for cyclic loading process will be explained using Fig. 3. For a loading $(-W)$, Joint 11 develops a bending moment M_{11} and an axial force P_{11} such that the point (M_{11}, P_{11}) is outside the yield curve (Fig. 3*a*, Point 1). The change in M_{11} and P_{11} (ΔM_{11} and ΔP_{11}) is calculated as described previously. These changes have an effect on the bending moments and axial forces of all members as is seen in Figs. 3*b*, 3*c*, and 3*d* for Members 5, 1, and 3, respectively. This is the effect due to permanent plastic deformation of Section 11, and it is permanently built into the structure.

Upon unloading (by applying a load $+W$), the bending moment and axial force of Section 11 do not become zero, as would be the case in elastic behavior (Fig. 3*a*, Point 3). Similarly, Sections 6, 1, and 3 of Figs. 3*b*, 3*c*, and 3*d* develop nonzero bending moment and axial forces

TABLE 1—*Moments and axial due to* W = *11 920 kN (elastic analysis).*

Joint	P^a	M^b	I/O^c	Joint	P	M	I/O
1	−13 878.3	−2739.9	*I*	2	−13 854.1	−991.2	*I*
3	−13 979.9	884.8	*I*	4	−14 033.4	1996.9	*I*
5	−14 033.4	2599.8	*I*	6	−13 895.3	3202.7	*I*
7	−13 924.0	1768.5	*I*	8	−13 749.0	461.7	*I*
9	−13 492.8	−1481.6	*I*	10	−13 130.0	−4061.5	*I*
11	−13 130.0	−7316.2	*O*	...	...	...	...

NOTE—All units are in kilonewtons and meters.
[a] P = axial.
[b] M = moment.
[c] I = inside interaction diagram and O = outside interaction curve.

TABLE 2—*Moment and axial distribution coefficients (couple at Joint 11).*

Joint	P^a	M^b	Joint	P	M	Joint	P	M
1	0.490	0.581	2	0.487	0.321	3	0.508	0.054
4	0.521	−0.178	5	0.535	−0.385	6	0.559	−0.569
7	0.566	−0.705	8	0.578	−0.824	9	0.586	−0.913
10	0.591	−0.972	11	0.591	−1.000	...	...	...

NOTE—All units are in kilonewtons and meters.
[a] P = axial.
[b] M = moment.

TABLE 3—*Moments and axial due to* W_u *= 11 920 kN (after first iteration).*

Joint	P^a	M^b	I/O^c	Joint	P	M	I/O
1	−15 111.3	−4201.0	*I*	2	−15 078.2	−1796.1	*I*
3	−15 257.0	751.0	*I*	4	−15 344.9	2444.7	*I*
5	−15 322.3	3569.6	*I*	6	−15 326.2	4694.5	*I*
7	−15 348.8	3543.7	*I*	8	−15 201.8	2535.1	*I*
9	−14 966.6	815.5	*I*	10	−14 617.5	−1615.3	*I*
11	−14 617.5	−4799.9	*I*	...	...	...	...

NOTE—All units are in kilonewtons and meters.
[a] P = axial.
[b] M = moment.
[c] I = inside interaction diagram and O = outside interaction curve.

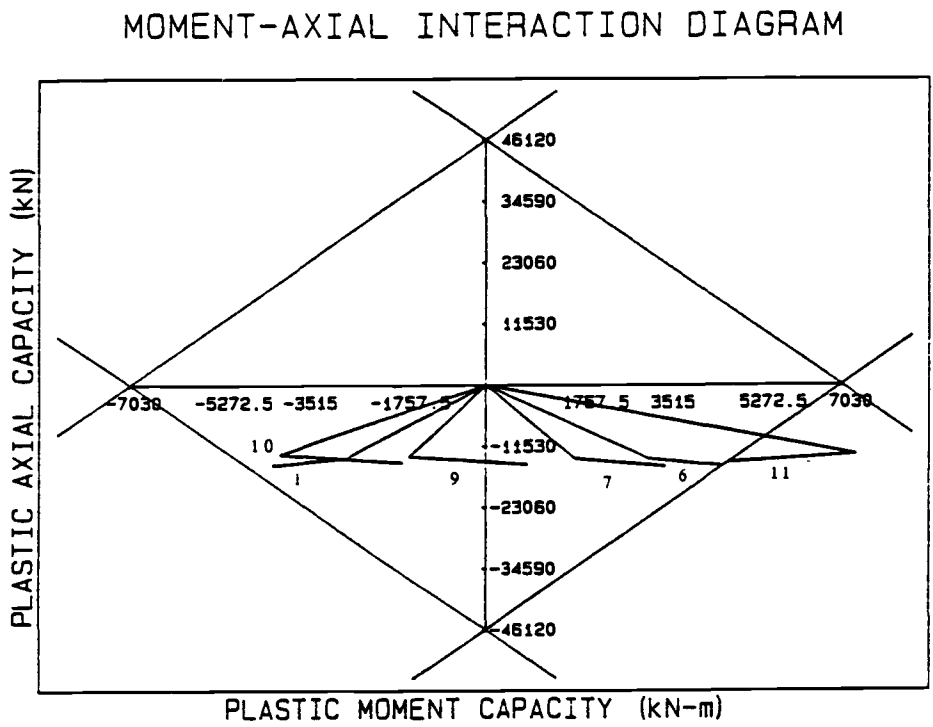

FIG. 2—M-P *interaction diagram after final redistribution* (W_u *= 11 920 kN).*

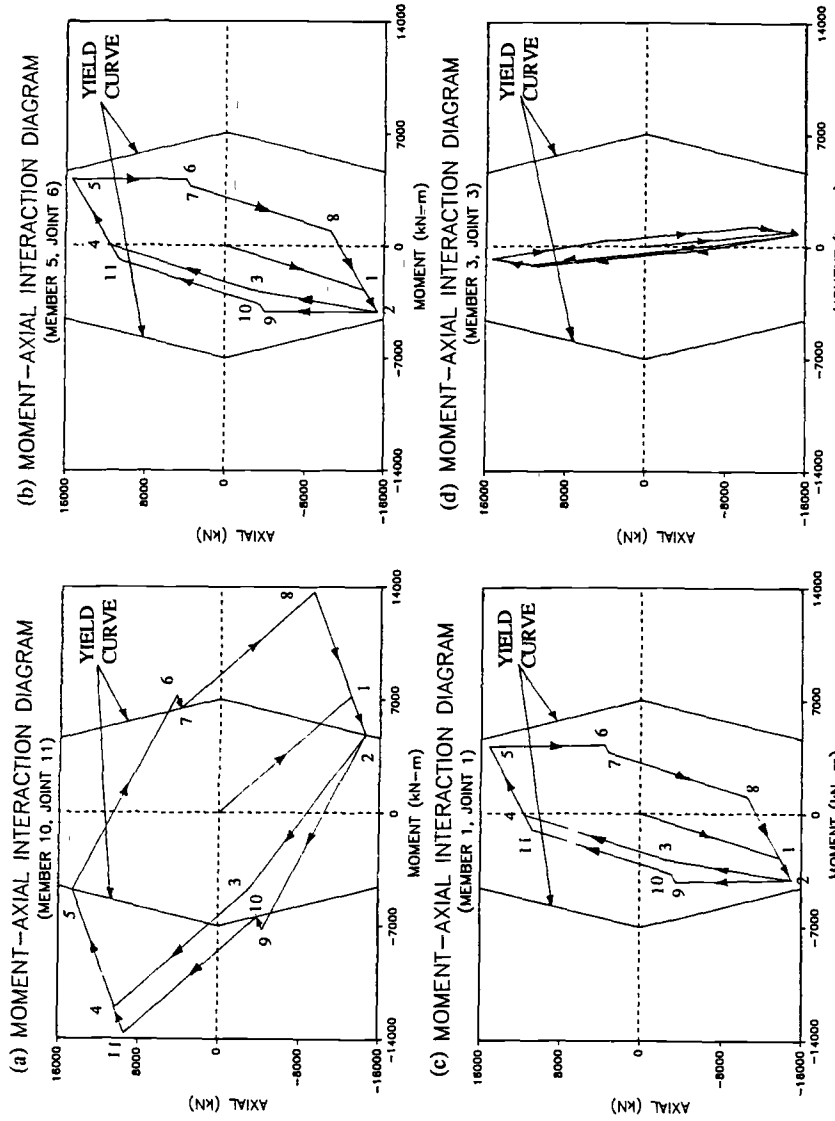

FIG. 3—*Moment-axial interaction diagram under cyclic loading.*

TABLE 4—*Moments and axial due to* W_u = *15 553 kN (elastic analysis).*

Joint	P^a	M^b	I/O^c	Joint	P	M	I/O
1	−18 144.8	−3579.5	*I*	2	−18 112.9	−1278.2	*I*
3	−18 278.7	1189.6	*I*	4	−18 349.5	2658.0	*I*
5	−18 380.9	3460.3	*I*	6	−18 299.0	3596.2	*I*
7	−18 210.2	2399.7	*I*	8	−17 982.6	703.6	*I*
9	−17 649.0	1825.4	*I*	10	−17 176.1	−5187.2	*I*
11	−17 176.1	−9431.8	*O*	...	...	...	...

NOTE—All units are in kilonewtons and meters.
[a] P = axial.
[b] M = moment.
[c] I = inside interaction diagram and O = outside interaction curve.

due to the permanent deformations of the first loading $-W$ (Point 3 in Figs. 3*b*, 3*c*, and 3*d*). Note that these sections have always remained within the elastic range.

The response stabilizes after one cycle and repeats itself at all subsequent cycles. Section 11 is subjected to reversals of plastic deformations of equal magnitude, whereas Sections 6, 1, and 3 remain elastic, moving on the same loop (11-5-8-2-11) of Fig. 3.

The fixed circular arch shown in Fig. 1 was analyzed again using nonlinear yield curves to get a better approximation. The elastic limit of the structure was found equal to W_e = 10 815 kN. Using nonlinear yield curves, this method has given an ultimate load of 15 553 kN. At ultimate load, the bending moments and axial forces at each section of the ten elements of the half-arch are shown in Table 4. The bending moment and axial force of Section 11 (Member 10) give a point outside the yield curve. To bring Section 11 back onto the yielding curve, a hinge is introduced and unit moment is applied. The bending moments and axial forces of each section due to this couple are shown in Table 2. After the redistribution, the new bending moments and axial forces for all sections are calculated and given in Table 5. At the ultimate load, the behavior of some selected sections before and after redistribution is shown in Figs. 4*a* and 4*b*. At this ultimate load the method converges, whereas at the next load increment it does not converge. For load $W > W_u$, in the process of redistribution of axial forces and bending moments, the structure collapses by forming a hinge at Joint 6. At ultimate load, Eqs 3 and 7 gave $\Delta M_1 = -3635.51$ kN-m and $\Delta P_1 = -2150.10$ kN, respectively. This is the amount of bending moment and axial force needed to bring Joint 11 back on to the yield curve.

TABLE 5—*Moments and axial due to* W_u = *15 553 kN (after redistribution).*

Joint	P^a	M^b	I/O^c	Joint	P	M	I/O
1	−19 927.0	−5693.3	*I*	2	−19 882.3	−2443.6	*I*
3	−20 124.6	994.3	*I*	4	−20 245.2	3303.5	*I*
5	−20 324.8	4860.2	*I*	6	−20 330.1	5664.5	*I*
7	−20 269.7	4963.8	*I*	8	−20 082.6	3698.8	*I*
9	−19 779.4	1493.2	*I*	10	−19 326.2	−1652.9	*I*
11	−19 326.2	−5796.3	*I*	...	...	...	...

NOTE—All units are in kilonewtons and meters.
[a] P = axial.
[b] M = moment.
[c] I = inside interaction diagram and O = outside interaction curve.

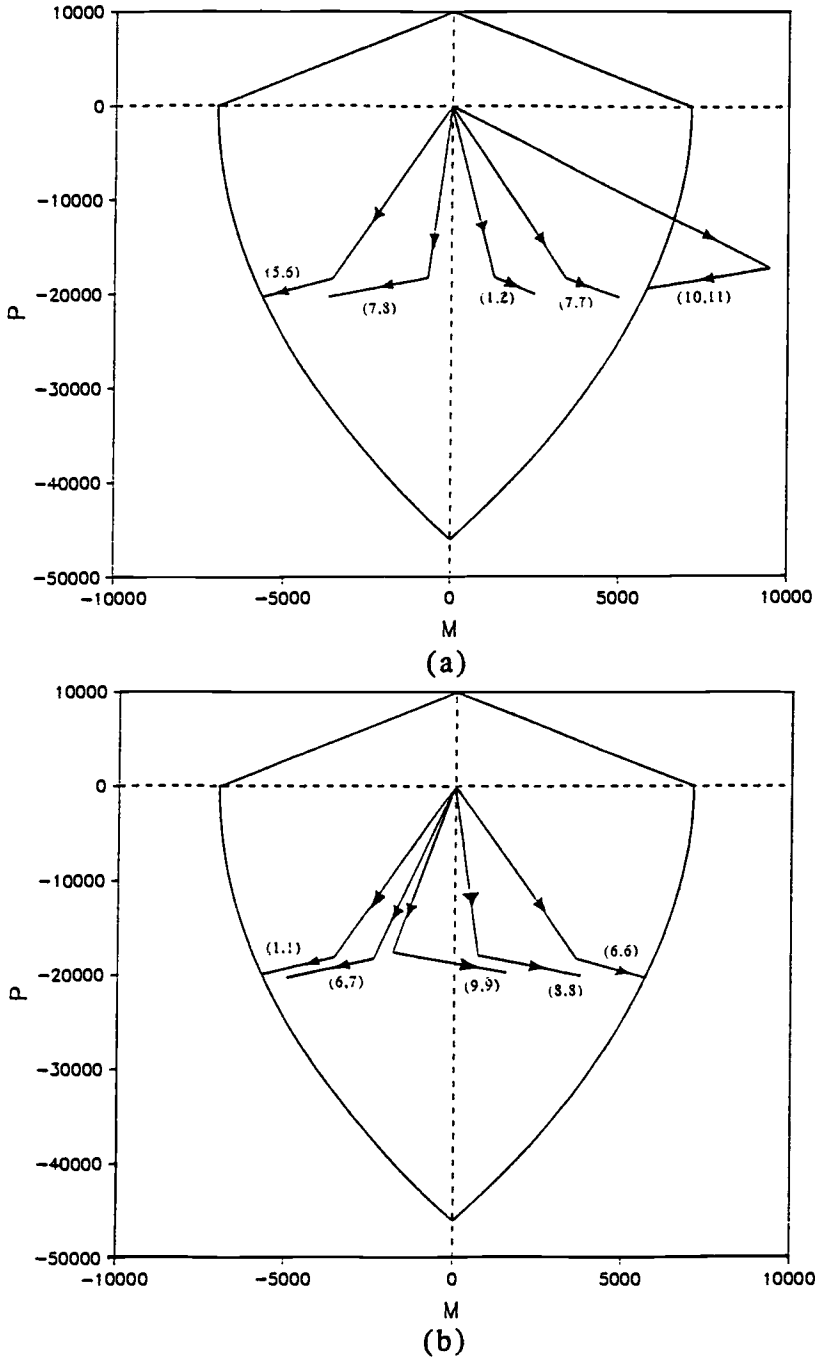

FIG. 4—M-P *interaction diagram* (W_u = *15 553 kN*).

TABLE 6—*Comparison of arch example results.*

Authors	Assumption	Ultimate Load, kN
Fafitis/Jayamaha [*14*]	Nonlinear yield curve, Eq 5	15 533
Loi/Wang [*6*]	5 Hyperplanes/quadrant	13 360
Cohn/Rohman [2]	2 Hyperplanes/quadrant	12 760
Fafitis/Jayamaha [*15*]	1 Hyperplane/quadrant, Eq 1	11 920
Cohn/Rohman [2]	1 Hyperplane/quadrant	10 870

Conclusion

An iterative method developed for elasto-plastic analysis of plane frames taking into account the interaction of axial force and bending moment in yielding has been successfully used for analysis of arches. The fixed circular arch of the example has been previously studied by other investigators [*2–5*]. The results obtained by those authors using different methods of analysis are presented in Table 6. Wang and Loi [*6*] have assumed an elliptic yield curve $(N/N_p) + (M/M_p)^2 = 1$ with five hyperplanes per quadrant. Hyperplanes are linear segments that are approximations of the yield curve. It is noted that Eq 5 gives a very good approximation to the yield curve assumed in Ref *6*. For one hyperplane, Cohn and Rohman [*2*] have reported an ultimate load that is about 9% less than what was obtained in Ref *15*. Numerical results obtained for the fixed circular arch example in this paper demonstrate the significant role of the yield curve assumed and the major influence of axial force on the ultimate load. Also, it is noted that ultimate load is sensitive to the size of the elements of the discritized arch. Originally, yield curves were assumed to be linear. Finally, nonlinear yield curves were used for the compression members. This has considerably improved the results. The results compare favorably with results obtained by other investigators. Under proportional cyclic loading, the structure adjusts to the loading and the response becomes stable after a few cycles, as shown in Fig. 3.

References

[*1*] Onat, E. I. and Prager, W., "Limit Analysis of Arches," *Journal of the Mechanics and Physics of Solids*, Vol. 1, 1953, pp. 77–89.

[*2*] Cohn, M. Z. and Abdel-Rohman, M., "Analysis up to Collapse of Elasto-Plastic Arches," *Computers & Structures*, Vol. 6, 1976, pp. 511–517.

[*3*] Charnes, A. and Greenberg, H. J., "Plastic Collapse and Linear Programming," *Bulletin of the American Mathematical Society*, Vol. 57, 1951, p. 480.

[*4*] Dorn, W. S. and Greenberg, H. L., "Linear Programming and Plastic Limit Analysis of Structures," *Quarterly Journal of Applied Mathematics*, Vol. 15, 1957, pp. 155–174.

[*5*] Wong, M. B. and Loi, F. T., *Elasto-Plastic Analysis Using Piecewise Linearized Yield Surface*, 10th Australasian Conference on the Mechanics of Structures and Materials, University of Adelaide, Australia, 1986, pp. 591–597.

[*6*] Tin-Loi, F. and Wong, M. B., "Nonholonomic Computer Analysis of Elastoplastic Frames," *Computational Methods in Applied Mechanics and Engineering*, Vol. 72, 1989, pp. 351–364.

[*7*] Maier, G., Giacomini, S., and Peterlini, F., "Combined Elastoplastic and Limit Analysis via Restricted Basis Linear Programming," *Computational Methods in Applied Mechanics and Engineering*, Vol. 19, 1979, pp. 21–48.

[*8*] Maier, G., Grierson, D. E., and Best, M. J., "Mathematical Programming Methods for Deformation Analysis at Plastic Collapse," *Journal of Computers and Structures*, Vol. 7, 1977, pp. 599–612.

[*9*] Ueda, Y. and Yao, T., "The Plastic Node Method: A New Method of Plastic Analysis," *Computational Methods in Applied Mechanics and Engineering*, Vol. 34, 1982, pp. 1089–1104.

[*10*] Orbison, J. G., McGuire, W., and Abel, J. F., "Yield Surface Applications in Nonlinear Steel Frame Analysis," *Computer Methods in Applied Mechanics and Engineering*, Vol. 33, 1982, pp. 557–573.

[*11*] Franchi, A. and Cohn, M. Z., "Computer Analysis of Elasto-Plastic Structures," *Computational Methods in Applied Mechanics and Engineering*, Vol. 21, 1980, pp. 271–294.

[*12*] Bozzo, E. and Gambarotta, L., "Inelastic Analysis of Steel Frames for Multistory Buildings," *Computers and Structures,* Vol. 20, No. 4, 1985, pp. 707–713.

[*13*] Oliveto, G. and Cuomo, M., "Incremental Analysis of Plane Frames with Geometric and Material Nonlinearities," *Engineering Structures,* Vol. 10, January 1988, pp. 2–11.

[*14*] Fafitis, A. and Jayamaha, S. A., "Elasto-Plastic Analysis of a Fixed Circular Arch with Bending Moment and Axial Force Interaction," *Proceedings,* International Conference Computational Structures Technology, Heriot-Watt University, Edinburgh, UK, 20–22 Aug. 1991, pp. 367–375.

[*15*] Fafitis, A. and Jayamaha, S. A., "Elasto-Plastic Analysis of a Fixed Circular Arch with Bending Moment and Axial Force Interaction," *Structural Engineering Review,* No. 3, 1991, pp. 205–210.

M. Elahi,[1] *K. L. Reifsnider,*[1] *and R. E. Swain*[2]

Influence of Fiber-Matrix Interface on Dynamic Response of CFRP

REFERENCE: Elahi, M., Reifsnider, K. L., and Swain, R. E., **"Influence of Fiber-Matrix Interface on Dynamic Response of CFRP,"** *Cyclic Deformation, Fracture, and Nondestructive Evaluation of Advanced Materials: Second Volume, ASTM STP 1184,* M. R. Mitchell and O. Buck, Eds., American Society for Testing and Materials, Philadelphia, 1994, pp. 255–264.

ABSTRACT: The static and dynamic response of fiber-reinforced composite coupons with various levels of fiber surface treatments was investigated using the classical approach of strain measurement (stiffness degradation using an extensometer), as well as a dynamic phase and dynamic gain (dynamic compliance) response measurement method proposed by Elahi et al. [*1*]. From the experimental results, the property data are shown to correlate with the classical method of damage monitoring and demonstrate the advantages of the phase and gain response analysis. The proposed approach makes it possible to monitor continuously the fatigue damage evolution in any material system in real time without the use of an extensometer or strain gages, making it an ideal candidate for studying damage under high temperature or extremely corrosive environments where the usage of extensometers is either not practical or not possible.

KEYWORDS: fatigue, composite, frequency response, phase lag, stiffness, interface

Fatigue failure can occur if the residual strength of a material degrades to the level of applied load [*2–4*]. This degradation can be caused by matrix cracking [*5*], delamination [*6*], fiber fracture [*7*], and interfacial debonding [*8*]. Any combination of these may be responsible for fatigue damage, which may result in reduced fatigue strength and stiffness [*2–8*]. Material properties, specimen geometry, stacking sequence, waveform type, loading, waveform frequency, loading mode, loading rate, time, and temperature are also critical variables in any fatigue study or service environment [*9–13*]. Variation in any of these variables could result in different damage evolution mechanisms and processes.

The interfacial region formed between fibers and matrix plays an important role in engineering and mechanical properties of composites. Fiber surface treatment [*14*] and fiber sizing [*15*] are often used to produce different interphase regions. Madhukar and Drzal [*16–18*] have studied, in great detail, the influence of fiber-matrix adhesion on the longitudinal compressive properties, in-plane and interlaminar shear behavior, tensile, and flexural behavior of graphite/epoxy composites. Curtis and Morton [*19*] discussed the effect of fiber surface treatment on the compressive strength of CFRP laminates. Most of the work presented in the literature is concerned with the influence of fiber-matrix bonding strength on the static properties of laminates. To the authors' knowledge, studies of the influence of the interface on the fatigue response of fibrous composites are very limited and are mainly concerned with flexural fatigue behavior. Vincent et al. [*20*] studied the role of interfaces on the flexural fatigue behavior of

[1] Graduate research assistant and Alexander Giacco professor, respectively, Materials Response Group, Engineering Science and Mechanics Department, Virginia Polytechnic Institute and State University, Blacksburg, VA 24061-0219.

[2] Engineer, Smith & Nephew Richards, Inc., Memphis, TN 38116.

unidirectional glass/epoxy composites. Shih and Ebert [*21*] presented results on the influence of adhesion strength (resulting from the presence of Silane coupling treatment) on performance of unidirectional fiber glass composites under four-point flexural fatigue.

An attempt is made to investigate the role of the fiber-matrix interface on the dynamic mechanical properties of carbon fiber-reinforced composites. Several investigators have utilized dynamic stress-strain signals in order to characterize the fatigue damage development by monitoring phase and stiffness. This procedure requires use of an extensometer or an attached strain gage to measure strain. In high-temperature or high-frequency fatigue tests, there is always the possibility of extensometer slippage, and it is difficult to attach any strain measurement device to a specimen inside a furnace. Another shortcoming of an extensometer procedure is associated with the fatigue testing of unidirectional materials. Such tests may cause a great deal of matrix splitting on the specimen surface which, in turn, limits the use of an extensometer by disrupting the position of the extensometer contact points.

The technique developed by the authors [*1*] uses the load and stroke signals from a servohydraulic test frame to measure parameters such as phase lag and gain to obtain the damping and dynamic modulus quantities, respectively. Specimens representing different levels of fiber surface treatment were subjected to longitudinal fatigue loading. By continuous real time monitoring of dynamical mechanical properties of these specimens, the influence of fiber-matrix interface was investigated. The results indicate a good correlation between the dynamic modulus obtained using load-strain signals and the dynamic modulus using the load-stroke signals.

In its most basic form, the present dynamic mechanical signal analysis scheme resembles a macroscopic dynamic mechanical analyzer (DMA) instrument, enabling the operator to monitor dynamic phase lag and dynamic compliance.

Several researchers [*22–24*] have reported success in being able to infer interface bonding by performing small-scale dynamic mechanical analysis (DMA) test. Others [*25*] have used the DMA to detect changes in the thermomechanical properties of laminates that have been damaged by fatigue loading. The present test technique combines the analyses of the DMA without the need to "scale down" the specimen size or loading conditions. Thus, typical fatigue testing benefits from the ability to analyze the specimen as a dynamic component in a forced vibration problem. The present method is also unique in that load and stroke signals from the control circuit of the test machine are used, eliminating the need for strain gages, extensometers, or other contact with the specimen. This is especially important for high-temperature testing in a furnace where the use of such devices is very difficult.

Experimental Procedure

Three material systems representing three different levels of fiber surface treatments—20%, 50%, and 100% surface treatment (fiber manufacturer proprietary information)—were fatigue cycled (tension-compression, $R = -1$) under load-control using a 100-kN servohydraulic testing machine at a frequency of 10 Hz under a sinusoidal waveform. Center notch specimens made of intermediate modulus carbon fibers (Courtauld's 32-550, where fibers possess a 220-GPa tensile modulus and a 3.8-GPa tensile strength with a nominal diameter of 7 μm) and toughened epoxy matrix (Hysol's HC 9106-3) [*26*], with a stacking sequence of $[0/90]_{8s}$ were used. These specimens had an average length of 152.4 mm, width of 25.4 mm, and a thickness of 4.2 mm. Using a diamond core drill, a 6.35-mm-diameter center hole was placed in the geometric center of the coupons.

Based on the tensile and compressive strength of these materials, the specimens were fatigue cycled at 75% of their ultimate compressive strength with $R = -1$. A grip pressure of 8.27 MPa was used. A 25.4-mm gage length extensometer was used to measure the strain across

the hole, and the notch temperature was measured using a thermocouple placed at the surface close to the longitudinal tangent to the hole.

The dynamic data acquisition was performed using the new experimental technique developed by the authors. This method utilizes the frequency response measurement of load/stroke signals to characterize the fatigue damage in terms of parameters such as phase lag and gain (compliance). The frequency response, $H(f)$, is calculated as the ratio of the cross spectrum, G_{xy}, to the load signal power spectrum, G_{xx}, where

$$G_{xy} = F_x F_y^*$$

where

F_y^* = stroke signal liner spectrum's complex conjugate,
F_x = load signal linear spectrum, and
$G_{xx} = F_x F_y^*$.

The experimental setup for this technique is shown in Fig. 1. This technique employs a software routine for real time data acquisition. The details of the approach are explained elsewhere [*1*].

Results and Discussion

Swain [*26*] conducted numerous experiments to investigate the role of the interface in the static strength of the same materials used in this research. From the transverse flexure testing of 20, 50, and 100% fiber surface-treated specimens, average strength values of 120.7, 120.0, and 136.0 MPa, average failure strain values of 1.93, 2.08, and 2.05%, and average bending stiffness values of 6.83, 6.48, and 7.10 GPa were reported, respectively.

Tensile and compressive strengths of these material systems were used to determine the

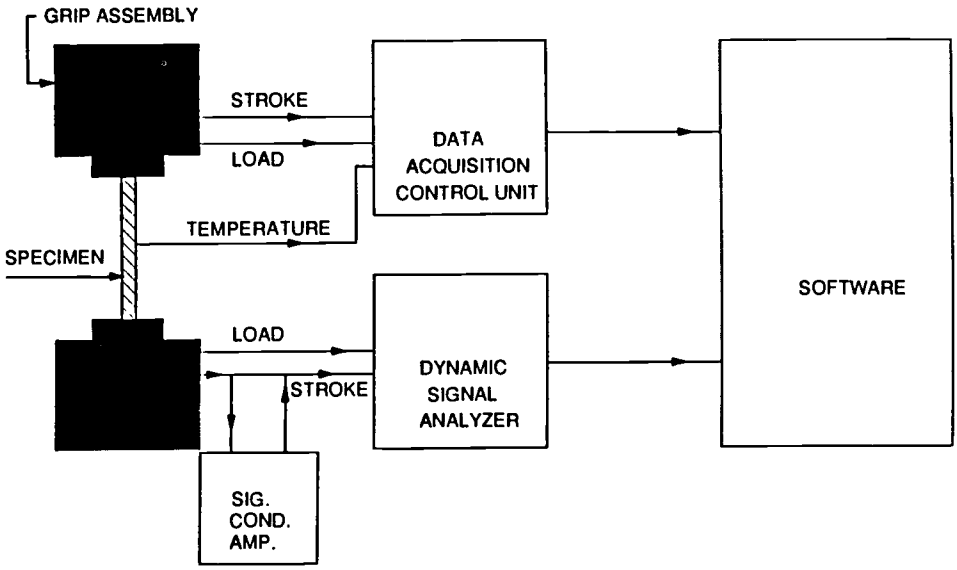

FIG. 1—*Schematic of the experimental setup.*

applied fatigue load levels. The average notched tensile strength values (5.39, 5.40, and 5.36 GPa) as well as compressive strength values (3.93, 3.92, and 3.65 GPa) are basically unchanged by the degree of surface treatment. The same holds true for the average tensile modulus values (46.88, 51.02, and 48.95 GPa) and compressive modulus values (44.82, 45.51, 46.19 GPa). The preceding values are based on averages of five data points where the coefficient of variation never exceeded 6%. Lack of any significant variation in the static mechanical properties of these materials as a function of various levels of surface treatments indicates that the fiber surface treatment does not necessarily influence the quasi-static response of materials, at least for this particular material system.

Using the dynamical mechanical analysis proposed by the authors [*1*], the following results were obtained utilizing mainly load and stroke signals. Operating at applied stress levels of 291.66, 291.66, and 270.97 MPa, average fatigue lives of 100, 135, and 200 k cycles were obtained for the 20, 50, and 100% fiber surface-treated material systems, respectively. Operating in load control, the maximum actuator displacement (i.e., the stroke signal) was recorded for each specimen, continuously, and plotted as a function of normalized life (Fig. 2). The notch temperature (at the highest stressed area corresponding to the area near the longitudinal tangent to the hole) was recorded for each specimen (Fig. 3). An average equilibrium temperature of 81, 85, and 77°C was recorded, respectively. Application of the dynamic signal analyzer frequency response measurement, where the frequency response is calculated as the ratio of the stroke signal (output) cross spectrum to load signal (input) power spectrum [*27*], resulted in measurements of phase lag and gain (a measure of dynamic compliance, volt/volt) corresponding to load and stroke signals at the excitation frequency.

The phase lag response relating to load and stroke signals was used to plot Fig. 4, corresponding to the tangent of the phase lag for 20, 50, and 100% fiber surface-treated specimens. This may be a good indicator of damage rate; the large values at the beginning and end are

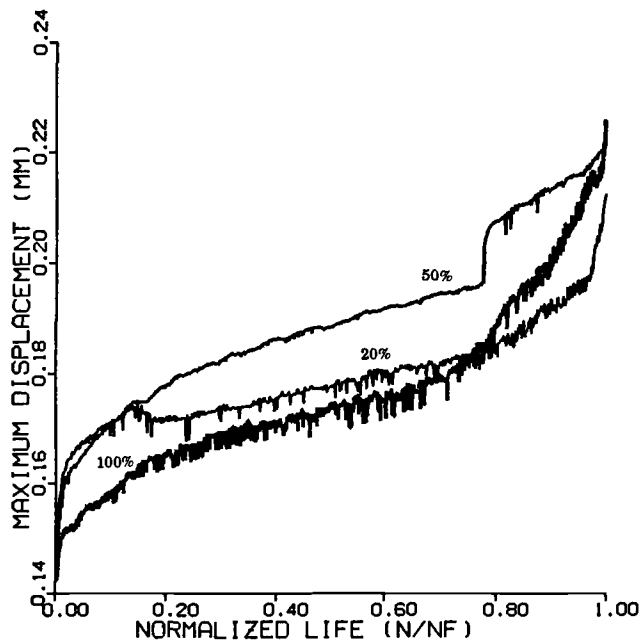

FIG. 2—*Maximum displacement versus life for 20, 50, and 100% treatments.*

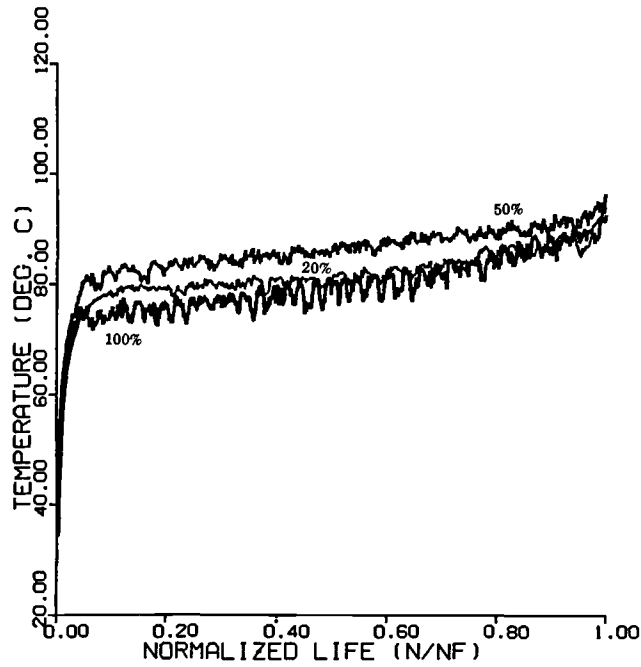

FIG. 3—*Temperature as a function of life.*

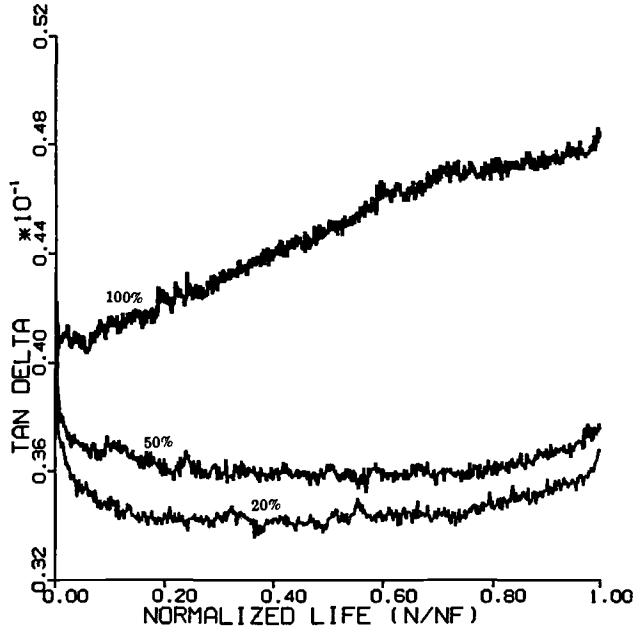

FIG. 4—*Tan delta as a function of life, using load/stroke.*

also shown by stiffness degradation curves, ΔE. Figure 4 indicates that the phase response corresponding to 100% surface treatment stands apart from the responses of the other two treatments. Using the gain values and the appropriate conversion factors, the dynamic modulus (magnitude of the complex modulus, $E = (E'^2 + E''^2)^{1/2}$) [*28*] as a function of life was also plotted (Fig. 5). An unsupported gage length of 50.8 mm was used in these measurements. Again the 100% surface-treatment material system behaved differently from the other systems. After obtaining the dynamic modulus and phase lag (using *load-stroke* signals), the storage modulus (energy storing part, in-phase component) and the loss modulus (energy dissipating part, out-phase component) could easily be calculated. Considering the whole axial cyclic fatigue as a problem of forced longitudinal vibration (with one end fixed and other end free to move upon application of load), the unsupported length is found to have a significant influence on the dynamic response of these materials (as expected). By reducing the unsupported length from 50.8 to 25.4 mm, the specimen response was altered, as shown in Fig. 6.

For comparison purposes, dynamic modulus based on load-strain measurement was also recorded during the life of each specimen (Figs. 7 and 8). Dynamic modulus values obtained from the load-stroke signals having an unsupported length of 50.8 mm were found to be twice the dynamic modulus values obtained from the load-strain measurement using an extensometer (Figs. 5 and 7). This is suspected to be due to the effective gage length and its role in the formulation of the dynamic modulus. Changing the effective gage length to 25.4 mm from the original 50.8 mm resulted in a closer correlation between the two measurements. The remaining discrepancy is believed to be due to uncertainties in the exact effective unsupported length and the nonuniformity of the strain field. The extensometer is attached directly over the center hole and measures strains along a strip near the center of the width of the specimen, while the

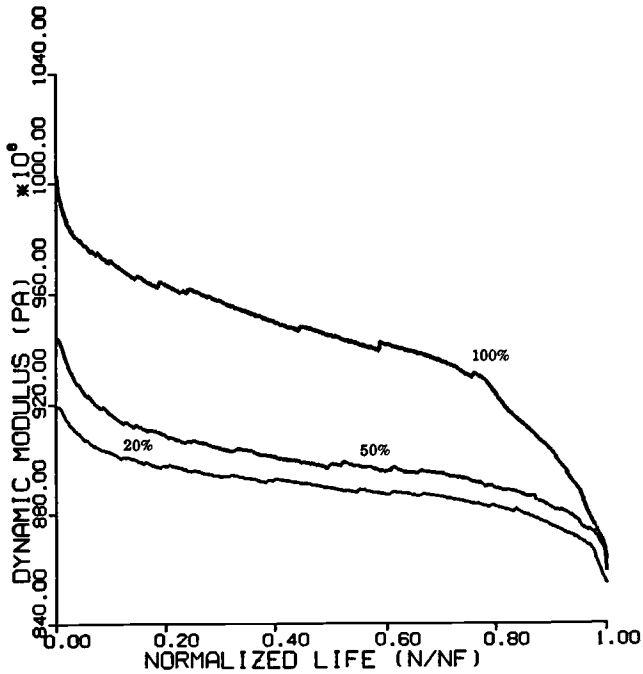

FIG. 5—*Dynamic modulus as a function of life, using load/stroke.*

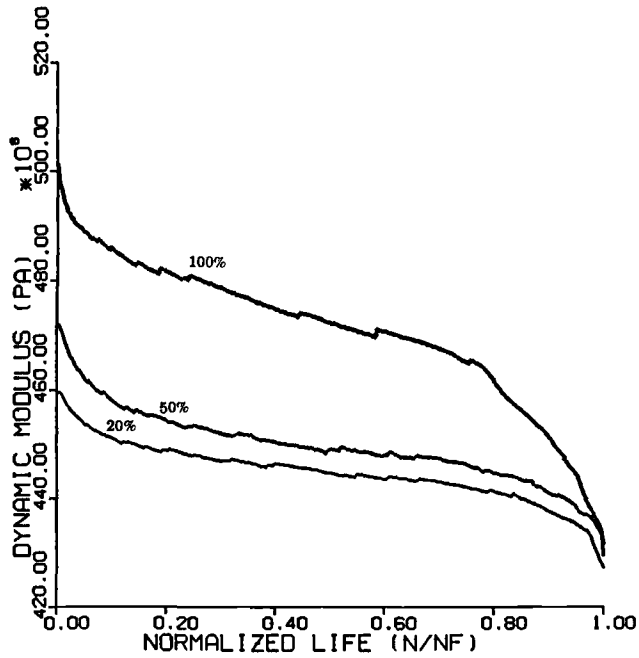

FIG. 6—*Dynamic modulus versus life, using load/stroke, U.S.L. = 25.4 mm.*

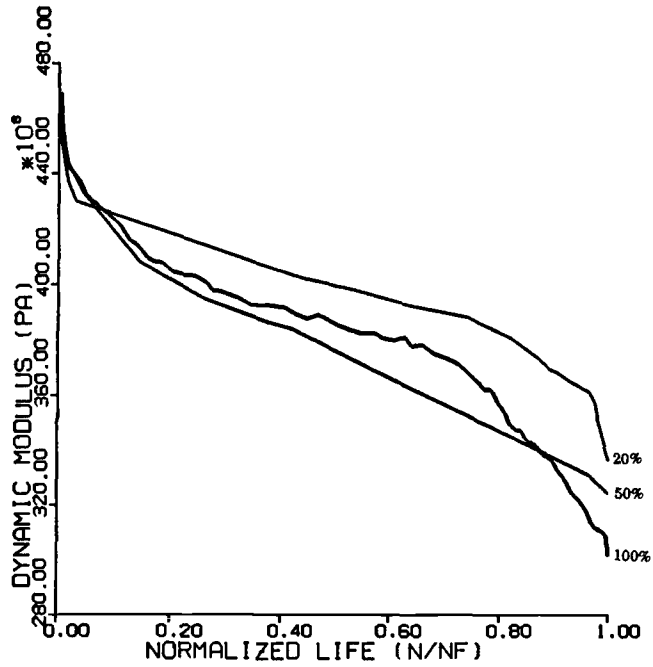

FIG. 7—*Dynamic modulus versus life, load/strain, gage length = 25.4 mm.*

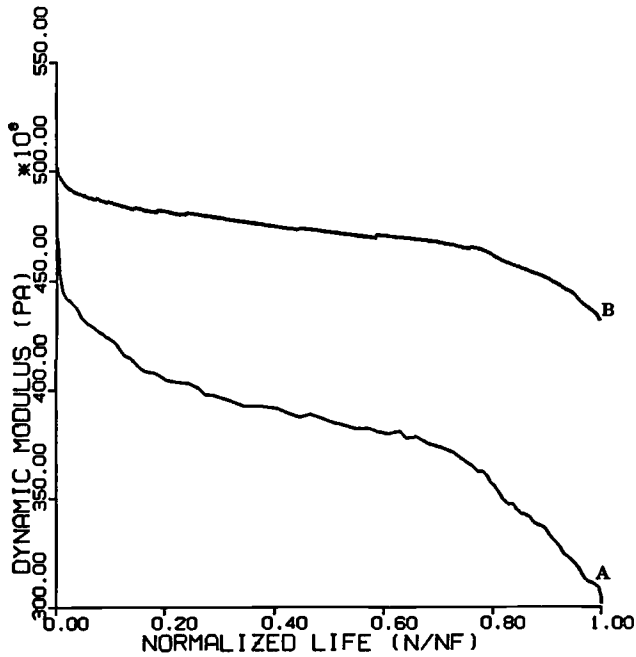

FIG. 8—*Modulus versus life obtained using (A) stroke (B) strain.*

displacement measured for the dynamic measurements are average values for the entire width and length of the specimens.

Conclusion

The present results indicate that the dynamic load and stroke signals from the controllers of standard servo-hydraulic test frames can be interpreted with a waveform analysis device during the cyclic loading of composite materials in a manner that provides information about dynamic modulus and phase lag directly related to the damage development processes in those materials. It is further shown that the measured parameters can provide quantitative information about the level of damage and the rate of damage development during such tests (see Figs. 4 and 5), a particularly valuable result since the quantitative measurement of damage *rate* during testing is otherwise very difficult.

Although static mechanical properties are found to be insensitive to any composite property differences caused by the three different fiber surface treatments studied, differences were clearly shown by the present dynamic mechanical approach. Large behavior differences between the materials with different surface treatments could be identified from the phase lag and gain response of the specimens monitored in real time throughout the life of each specimen. The dynamic mechanical response of these materials under cyclic loading indicates damage and damage rate for 20 and 50% fiber surface-treated specimens are almost the same, whereas for 100% fiber surface-treated specimens damage is much more extensive and occurs at a faster rate than the other two.

If this dynamic mechanical approach, as shown repeatedly, is found to be characteristic for certain conditions, then such things as health monitoring of structures using such a methodology may be possible.

Acknowledgments

The authors gratefully acknowledge the support of the Virginia Institute for Material Systems at Virginia Polytechnic Institute & State University, Blacksburg, VA.

References

[1] Elahi, M., Razvan, A., and Reifsnider, K. L., "Characterization of Composite Materials Dynamic Response Using Load/Stroke Frequency Response Measurement," *Composite Materials: Fatigue and Fracture, ASTM STP 1156,* Vol. 4, W. W. Stinchcomb and N. E. Ashbaugh, Eds., American Society for Testing and Materials, 1993.

[2] Lorenzo, L. and Hahn, H. T., "Fatigue Failure Mechanisms in Unidirectional Composites," *Composite Materials: Fatigue and Fracture, ASTM STP 907,* American Society for Testing and Materials, Philadelphia, 1986, pp. 210–232.

[3] Rotem, A., "Fatigue and Residual Strength of Composite Laminates," *Engineering Fracture Mechanics,* Vol. 25, No. 516, 1986, pp. 819–827.

[4] Tsai, S. W. and Hahn, H. T., *Introduction to Composite Materials,* Technomic, Westport, CN, 1980.

[5] Talrefa, R., *Fatigue of Composite Materials,* Technomic Publishing Co. Inc., Westport, CN, 1987, Chapter 5.

[6] Herakovich, C. T., "On the Relationship Between Engineering Properties and Delamination of Composite Materials," *Journal of Composite Materials,* Vol. 15, July 1981, pp. 338–348.

[7] Razvan, A. and Reifsnider, K. L., "Fiber Fracture and Strength Relationship in Unidirectional Graphite/Epoxy Composite Materials," *Theoretical and Applied Fracture Mechanics,* Vol. 16, No. 1, 1991, pp. 81–89.

[8] Piggot, M. R., "The Interface—An Overview," *Proceedings,* 36th International SAMPE Symposium, 15–18 April 1991, pp. 1773–1786.

[9] Herakovich, C. T., "Influence of Layer Thickness on the Strength of Angle-ply Laminates," *Journal of Composite Materials,* Vol. 16, May 1982, pp. 216–227.

[10] Pagano, N. J. and Pipes, R. B., "The Influence of Stacking Sequence on Laminate Strength," *Journal of Composite Materials,* Vol. 5, January 1971, pp. 55–57.

[11] Razvan, A., Bakis, C. E., Wagnecz, L., and Reifsnider, K. L., "Influence of Cyclic Load Amplitude on Damage Accumulation and Fracture of Composite Laminates," *Journal of Composite Technology and Research,* Vol. 10, No. 1, Spring 1988, pp. 3–10.

[12] Dan-Jumbo, E., Zhou, S. G., and Sun, C. T., "Load-Frequency Effect on Fatigue Life of IMP6/APC-2 Thermoplastic Composite Laminates," *Advances in Thermoplastic Matrix Composite Materials, ASTM STP 1044,* G. M. Newaz, Ed., American Society for Testing and Materials, Philadelphia, 1989, pp. 113–132.

[13] Curtis, D. C., Moore, D. R., Slater, B., and Zahlan, N., "Fatigue Testing of Multi-Angle Laminates of CF/PEEK," *Composites,* Vol. 19, No. 6, November 1988.

[14] Drzal, L. T., Rich, M. J., and Lloyd, P. F., "Adhesion of Graphite Fibers to Epoxy Matrices: I. The Role of Fiber Surface Treatment," *Journal of Adhesion,* Vol. 16, No. 1, 1983, pp.1–30.

[15] Drzal, L. T., Rich, M. J., and Koenig, M. F., "Adhesion of Graphite Fibers to Epoxy Matrices: II. The Effect of Fiber Finish," *Journal of Adhesion,* Vol. 16, No. 2, 1983, pp. 133–152.

[16] Madhukar, M. S. and Drzal, L. T., "Effect of Fiber-Matrix Adhesion on the Longitudinal Compressive Properties of Graphite/Epoxy Composites," *Proceedings,* Fifth Technical Conference of the American Society for Composites, 1990, pp. 849–858.

[17] Madhukar, M. S. and Drzal, L. T., "Fiber-Matrix Adhesion and its Effects on Composite Mechanical Properties, I. In-Plane and Interlaminar Shear Behavior of Graphite/Epoxy Composites," *Journal of Composite Materials,* Vol. 25, August 1991, pp. 932–957.

[18] Madhukar, M. S. and Drzal, L. T., "Fiber-Matrix Adhesion and its Effects on Composite Mechanical Properties, II. Tensile and Flexural Behavior of Graphite/Epoxy Composites," *Journal of Composite Materials,* Vol. 25, August 1991, pp. 958–991.

[19] Curtis, P. T. and Morton, J., "The Effect of Fiber Surface Treatment on the Compressive Strength of CFRP Laminates," *Progress in Science and Engineering of Composites,* T. Hayashi, K. Kawata, and S. Umekawa, Eds., ICCM-IV, 1982, pp. 219–226.

[20] Vincent, L., Fiore, L., and Fournier, P., "Fatigue Behavior of GFRP: Some Considerations about Interfaces," *Developments in the Science and Technology of Composite Materials: ECCM3,* A. R. Bunsell, P. Lamicq, and A. Massiah, Eds., 1988, pp. 609–614.

[21] Shih, G. C. and Ebert, L. J., "The Effect of the Fiber/Matrix Interface on the Flexural Fatigue

Performance of Unidirectional Fiberglass Composites," *Composites Science and Technology,* Vol. 28, 1987, pp. 137–161.

[22] Chua, P. S., "Dynamic Mechanical Analysis Studies of the Interphase," *Polymer Composites,* Vol. 8, No. 5, 1987, pp. 308–313.

[23] Banerjee, A., Ogale, A. A., and Edie, D. D., "Interfacial Characterization of Composites by Dynamic Mechanical Analysis," *Tomorrow's Materials Today,* Proceedings of the 34th International SAMPE symposium, 1989, pp. 1395–1399.

[24] Ke, Y., Wang, S., Meng, X., Su, B., Tian, X., Qi, Z., and Wu, R., "Effects of Cyclic Loading on the Dynamic Viscoelastic Properties of Epoxy Composites," *Proceedings,* the International Symposium on Composite Materials and Structures, T. T. Loo, and C. T. Sun, Eds., 1986, pp. 676–681.

[25] Osiroff, R. and Stinchcomb, W. W., "Damage Mechanical Analysis as a Complementary Damage Characterization Technique for Composite Materials," *Damage Detection and Quality Assurance in Composites, ASTM STP 1128,* American Society for Testing and Materials, Philadelphia, 1991.

[26] Swain, R. E., "The Role of the Fiber/Matrix Interphase in the Static and Fatigue Behavior of Polymeric Matrix Composite Laminates," Doctor of Philosophy dissertation, Virginia Polytechnic Institute and State University, Blacksburg, VA, February 1992.

[27] "The Fundamentals of Signal Analysis," Application Note 243, Hewlett Packard Co., 1989.

[28] Aklonis, J. J. and Macknight, W. J., *Introduction to Polymer Viscoelasticity,* 2nd ed., Wiley-Interscience, New York.

Mark P. Connolly[1]

A Substructuring Approach to the Fatigue Modeling of Polymeric Matrix Composite Materials

REFERENCE: Connolly, M. P., **"A Substructuring Approach to the Fatigue Modeling of Polymeric Matrix Composite Materials,"** *Cyclic Deformation, Fracture, and Nondestructive Evaluation of Advanced Materials: Second Volume, ASTM STP 1184,* M. R. Mitchell and O. Buck, Eds., American Society for Testing and Materials, Philadelphia, 1994, pp. 265–277.

ABSTRACT: A fatigue model for fiber-reinforced polymeric matrix composites is proposed. This model uses a substructuring approach to predict the behavior of composite laminates based on an integration of simpler composite elements. These simpler composite elements are known as "elemental blocks" and are two-layer laminates such as [0/90] or [0/45]. These laminates are chosen in order to capture the influence of the constraint between laminae on the fatigue performance. Tension-tension fatigue tests were conducted on a number of elemental block geometries, and the modulus degradation for each of the geometries was measured and described using simple functions. The results showed that the damage accumulation and concomitant reduction in stiffness varied systematically from geometry to geometry. Using these results, a simple fatigue model is proposed to predict the behavior of more complex composites by combining the degradation functions for the individual elemental blocks. This model is based on classical lamination theory and uses the measured stiffness reduction for each elemental block, as a function of the number of cycles, to predict the overall composite stiffness matrix. In order to test the model predictions, fatigue tests were conducted on more complex composites consisting of a number of elemental blocks, and the accumulation of damage was measured again using compliance and strain gages attached to the specimen surface. These results were compared with model predictions and reasonable agreement was obtained between the measured and predicted stiffness degradation.

KEYWORDS: composite materials, fatigue, graphite epoxy, life prediction, modulus degradation

Although composite materials have demonstrated long life in service, there is at present no generic fatigue life prediction methodology available similar to the approaches used for metals. For example, fatigue in metals can be modeled by assuming self-similar crack growth, where a single crack can be monitored, detected, and described by linear elastic fracture mechanics. The fatigue behavior of composites cannot be described in this way since damage develops as a result of a collection of competing or interacting failure modes, and the engineering properties, at any instant, cannot be inferred from a micromechanics-type analysis. For composite materials, damage is often distributed and micromechanical models require large computational effort in order to achieve meaningful descriptions of the stress fields associated with a given damage state.

One approach to obtaining the fatigue life of composites structures is to ignore the micromechanical details of fatigue failure and to use an empirical relationship such as the stress/B-

[1] Senior research engineer, Southwest Research Institute, P.O. Drawer 28510, San Antonio, TX 78228-0510.

basis life approach [*1*], where the applied stress is related to the number of cycles to failure through a curve established from fatigue test data. For metals, this approach works well because of the isotropic material properties and the ability in many cases to scale the results. For composites, use of the stress-life curve approach requires conducting tests on large numbers of specimens in order to account for additional variables such as fiber orientation and methods of construction and fabrication.

Other approaches have defined the fatigue life of composites by assuming that the fatigue failure of a structural laminate is governed by the failure of a critical element [*2–4*]. For example, for fiber-dominated laminates under tension-tension fatigue loading, the critical element is the 0° layer, but alternative representation of the critical element, such as fibers, plies, or portions of laminates, may be needed to model failure under different loading and geometric conditions. This critical element concept can be used in concert with the so-called residual strength degradation [*5–7*] or stiffness degradation models [*8*]. For the residual strength approach, the instantaneous strength degradation is related to the cyclic loading by a deterministic equation that is normally determined from fatigue tests. Stiffness degradation models relate the reduction in the modulus to the cyclic loading. These strength and moduli distributions can then be used to define the loading on the critical element. Examples of these strength degradation models are given in Ref *9*, where the static strength is multiplied by fatigue functions in order to extend the static failure criterion to the fatigue domain. The fatigue functions are determined experimentally for single lamina and are a function of the mean stress level, the temperature, and the frequency of loading. These functions are then used to predict the behavior of more complex composites.

A similar approach is used in this paper to describe the fatigue failure of composite plates. Stiffness degradation is used to define damage accumulation. A substructuring approach is used to predict the fatigue behavior of composite laminates based on the integration of simpler composite elements. These simpler composites are known here as "elemental blocks" and are simple laminates such as [0/90] or [0/45]. A key difference between this approach and the stiffness degradation methods described above is the use of two layers to define the elemental blocks. The choice of two-layer laminates as the basic building block recognizes the influence of the constraint imposed between lamina on the fatigue failure since experimental observations have shown that the development of matrix cracking, interfacial debonding, delamination, and ultimate failure is strongly dependent on the details of the layer to layer interactions [*10*].

This approach is also compatible with the continuum damage theories for composite structures where the relationships governing the behavior of the composite are assumed to depend on internal state variables, which act to modify the stiffness matrix for an undamaged material [*11–15*]. For example, in Refs *14* and *15*, damage is modeled using a representative volume element (RVE) of material chosen in order to reflect the size and distribution of subcritical damage. For matrix cracking, the analysis is based on a very small element incorporating a single crack, whereas, for delamination, the analysis is based on a sublaminate composed of the ply directly above and below the delaminated interface. All of these damage modes are then incorporated into a damage-dependent lamination equation. In the approach used here, a damage-dependent lamination equation is also derived; but in this case, the damage function is obtained empirically from fatigue tests conducted on each of the elemental blocks. Consequently, this approach does not consider the development of matrix cracking and delamination separately in the analysis, but models these through the measured stiffness changes in an elemental block as a function of the number of cycles. This modeling philosophy dictates the selection of two-layer laminates as the basic building block since delaminations normally occur at the interface between two layers. A further consideration in the choice of the two-layer elements is the need to ensure that the properties of the building block are measurable on an engineering scale. For example, use of this approach could spur the development of a fail-safe

philosophy for composites where damage accumulation, expressed in terms of modulus reduction, would be prevented from becoming catastrophic by nondestructive evaluation (NDE) and preventive maintenance.

For each elemental block, fatigue tests were performed, and the modulus reduction was measured using compliance and strain gages attached to the specimen. These data are used to describe a functional relationship between the modulus reduction and the number of cycles to failure. These functional relationships for each elemental block are incorporated into a model based on classical lamination theory to describe the behavior of more complex composites. Finally, fatigue tests were performed in order to test the validity of the proposed approach.

Experimental Tests on Elemental Blocks

An extensive experimental program was conducted in order to obtain the stiffness data for each elemental block and also to test the proposed approach. Static tension and tension-tension fatigue tests were conducted on specimens consisting of the basic elemental blocks and the more complex composites. In all, a total of six specimen types were fabricated, with the specimen geometries given in Table 1. The first four specimen types in Table 1 consist of multiples of the four basic elemental block geometries, [0/45], [45/−45], [45/90], and [0/90]. The elemental block geometries were not tested directly since they are not balanced or symmetric. The two last specimen types in Table 1 (B5 and B6) consist of a combination of the basic elemental blocks and are termed here multielement laminates. These specimens were tested in order to correlate the behavior with predictions based on the analysis presented here. The specimens were fabricated from AS-4-3501 graphite epoxy prepreg. As shown in Table 1, the number of layers for each of the specimens varied between 8 and 16. The overall average fiber volume fraction was 65%, and the void content for all specimens was less than 1%. The specimens were 18 mm wide and 205 mm long and were prepared in accordance with ASTM Test Method for Tensile Properties of Fiber-Resin Composites (D 3039-76).

Each of the specimens given in Table 1 was subjected to tension tests to determine the tensile strength, elastic modulus, and fracture strain, and the results are given in Table 2. The values of the static tensile strengths were used to select the maximum stresses imposed during cyclic loading.

For the fatigue tests, an automated closed-loop servo-hydraulic system was used to control and monitor the tests. This system is shown in Fig. 1 and uses a PC-compatible computer for automatic signal generation and data analysis. A clip gage and a strain gage was attached to the specimen surface, the output of which was input to an analog to digital card on the computer. The clip and strain gage data were converted on a real time, cycle-by-cycle basis to the elastic modulus using software on the PC. This software compared the cyclic strain to the load output data for the up and down portions of the cyclic curve in order to obtain the secant modulus.

TABLE 1—*Geometry of specimens tested.*

Specimen	Specimen Geometry	Elemental Block Geometry
B1	$[0/45_2/0_2/-45_2/0]_s$	[0/45]
B2	$[45/-45_2/45_2/-45_2/45]_s$	[45/−45]
B3	$[90/-45_2/90_2/45_2/90]_s$	[90/45]
B4	$[0/90_2/0_2/90_2/0]_s$	[0/40]
B5	$[0/90/45/-45]_s$	...
B6	$[0/45_2/-45_2/90]_s$	...

TABLE 2—*Mean tensile properties of specimens tested.*

Specimen	Tensile Strength, MPa	E_{xx} Elastic Modulus, GPa	Fracture Strain, %
$[0/45_2/0_2/-45_2/0]_s$	1021	84	1.18
$[45/-45_2/45_2/-45_2/45]_s$	145	19	1.73
$[90/-45_2/90_2/45_2/90]_s$	138	23	0.93
$[0/90_2/0_2/90_2/0]_s$	966	77	1.25
$[0/90/45/-45]_s$	580	54	1.08
$[0/45_2/-45_2/90]_s$	366	43	1.25

The offset strain was not recorded. The clip gage was used to measure the modulus parallel to the loading direction, termed here E_{xx}, and the strain gage was used to measure the modulus perpendicular to the loading direction, termed here E_{yy}. All of the specimens given in Table 1 were tested under tension-tension loading at an R ratio of 0.1. The tests were conducted under load control at a frequency between 1 and 5 Hz.

For the elemental block geometries (Specimens B1 to B4 in Table 1), the E_{xx} and E_{yy} moduli were obtained as a function of the number of cycles. Figure 2 shows a plot of the normalized E_{xx} moduli as a function of the number of cycles for all four of the elemental blocks tested. The E_{yy} moduli exhibited little or no change during the fatigue tests for each of the elemental blocks tested. Although it is expected that E_{yy} should exhibit small changes as damage accumulates, the strains and stresses in the y direction are much smaller than those in the x direction and, consequently, have only a very small influence on the overall response of the elemental blocks tested.

The E_{xx} moduli curves shown in Fig. 2 are characteristic of the elemental block tested. As an example for the [0/90] case (Specimen B4 in Fig. 2), the E_{xx} modulus increased in the early

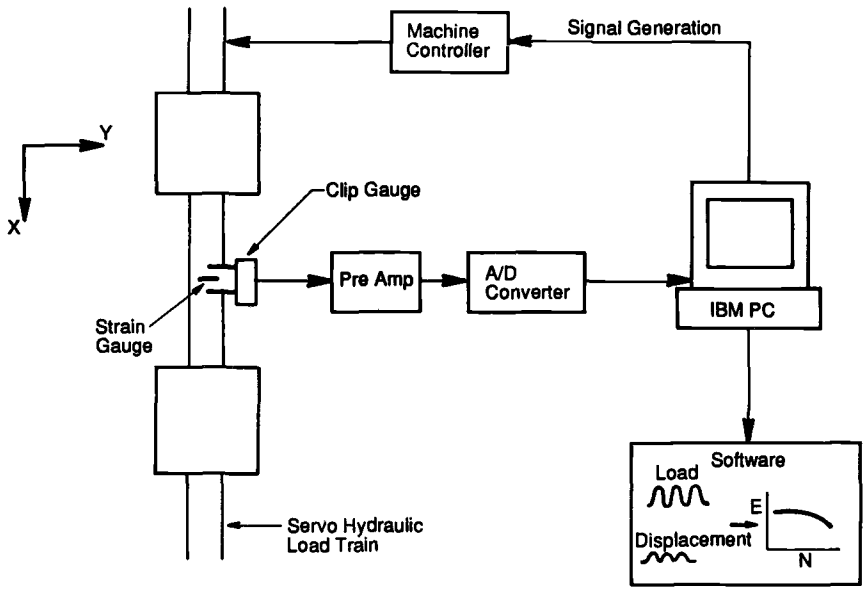

FIG. 1—*Schematic diagram of experimental setup used to conduct the fatigue tests on the composite specimens.*

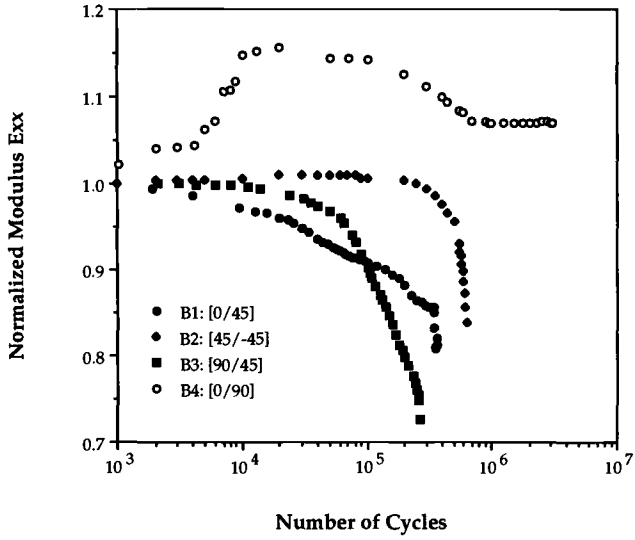

FIG. 2—*Normalized modulus as a function of the number of cycles for the four elemental block geometries tested.*

portion of the fatigue life. This result, although unexpected, was characteristic of all the [0/90] specimens tested. This increase in the modulus is probably a result of a slight misalignment in the 0° layers, which are free to align themselves in the direction of the load as the 90° layers fail. For the [90/45] case (Specimen B3 in Fig. 2), failure is primarily matrix dominated with a steady decrease in the modulus with increasing cycles.

The results given in Fig. 2 are characteristic of the individual elemental blocks, but are given for only one load level. Tests were also conducted at different load levels, and the results showed that the form of the curves varied systematically with load level. Figure 3 shows a plot of the moduli variations at three load levels for the [0/90] case (Specimen B4 in Table 1). Figure 3 shows that the form of the moduli curves is similar for the three load levels tested, with an initial increase in the moduli with the number of cycles. This increase in the moduli occurs as the 90° layers fail, which was consistent with observations of the specimens during testing, where damage to the 90° layers was evident early in the life, whereas the 0° layers remained intact. The results shown in Fig. 3 indicate that the moduli curves can be conveniently divided into two regimes, the first characterized by failure of the 90° layers, termed here *before-transition*, and the second by failure of the 0° layers, termed here *after-transition*. Furthermore, it is evident from Fig. 3 that the total fatigue life expended in each of these two regimes is dependent on the applied load level. For example, for the 80% ultimate tensile strength (UTS) case, the 90° layers begin to fail in the first few cycles, and the remaining life is dominated by the 0° layers. At lower stress levels, given by the 60% UTS case in Fig. 3, the number of cycles before transition increases. The limiting case is reached for the 40% UTS case, which was a runout. For this situation, failure of the 90° layers occurred early in the life, and although the remaining load was carried by the 0° layers, it was not sufficient to cause failure after 3×10^6 cycles. Figure 3 also shows that there is some variation in the final values of the moduli and in particular the lower moduli values for the 40% UTS case. This is due to the fact that at these low load levels, failure occurs as a result of delaminations that grow from the specimen edges, resulting in lower measured moduli than for the other two cases.

It is clear from the above discussion that for an elemental block consisting of a weaker and

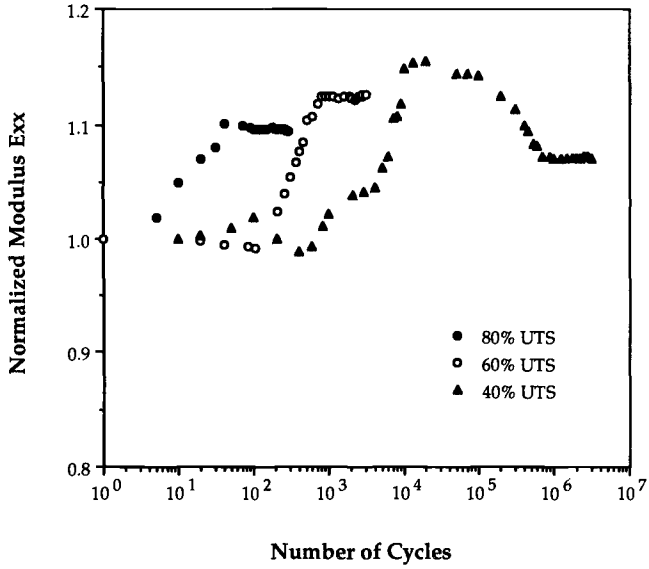

FIG. 3—*Influence of load level on the modulus reduction behavior of a [0/90] elemental block.*

a stronger phase, such as the [0/90] case cited above, there is a transition in the modulus reduction curve, from failure of the weaker phase to failure of the stronger phase. This trend was also evident from the tests conducted on the [0/45] specimens and is consistent with Reifsnider's [*1*] use of the critical and subcritical element approach. For the [45/90] and [90/45] cases, this type of transition was again evident, but the demarcation between the regimes was not as well defined. This is due to the fact that, for these two cases, failure is primarily matrix dominated.

This transition from failure of the weaker phase to failure of the stronger phase enables the modulus degradation results to be normalized. This normalization is performed for each of the two regimes. For example, the data given in Fig. 3 were divided into the moduli before and after transition. For each of these regimes the data were normalized with respect to the number of cycles to transition and the number of cycles from transition to failure, respectively. Figure 4 shows the modulus data for the [0/90] case before transition, normalized with respect to the number of cycles to transition, for the three different loading cases given in Fig. 3. Figure 4 shows that this normalization reduces the modulus-reduction curves obtained at different load levels to one curve that is independent of the load level tested. This same normalization was applied to the other elemental block geometries that exhibited a transition-type behavior. Using this approach, simple linear functions are used to describe the normalized modulus (E_{xxN}) at any number of cycles, N, and these are given as

$$E_{xxN} = 1.0 + A(N/N_T) \tag{1}$$

for the period before transition (N_T). After transition the modulus degradation is given by

$$E_{xxN} = (1.0 + A)[1.0 + B(N - N_T)/N_F] \tag{2}$$

The constants A and B for each of the four elemental block geometries tested in Table 1 are given in Table 3. It can be seen from Table 3 that, for the [90/45] elemental block, there was no clear demarcation between the two regimes, and for this situation the transition life N_T was

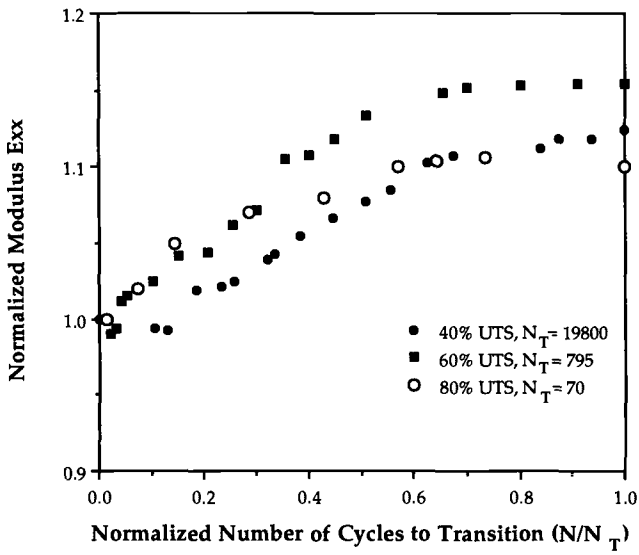

FIG. 4—*Normalized modulus before transition versus normalized number of cycles to transition for [0/90] elemental block.*

set equal to the total life N_F and the constant B was set equal to zero. The modulus in the y direction, E_{yyN}, was set to the E_{yy} modulus at zero cycles. The shear modulus, E_{xy}, was not measured but was also assumed to be independent of N, giving

$$E_{yyN} = E_{yy},\ E_{xyN} = E_{xy} \tag{3}$$

In order to use the functions given by Eqs 1 and 2 and Table 3, it is necessary to define the number of cycles to transition, N_T, and the number of cycles to failure, N_F, as a function of the applied stress range. Figure 5 shows these data expressed in the form of *S-N* curves for the number of cycles to failure, N_F. For the [90/45] elemental block geometry, the transition life is taken as the total life. The constants in the *S-N* curve for the number of cycles to transition and the number of cycles to failure are given in Table 4. Equations 1, 2, and 3, together with the *S-N* data given in Table 4, are now incorporated into the fatigue model described below in order to predict the fatigue behavior of more complex multielement laminates.

Fatigue Model for the Elemental Block Approach

The model proposed here is based on classical lamination theory. The relationship between stress and strain can be formulated in terms of the well-known stiffness matrix for orthotropic materials, which requires four elastic constants, namely the longitudinal elastic modulus, E_L,

TABLE 3—*Constants used in modulus functions.*

Elemental Block Geometry	*A*	*B*
[0/45]	−0.075	−0.100
[45/−45]	−0.021	−0.147
[90/45]	−0.180	0.0
[0/90]	0.18	−0.034

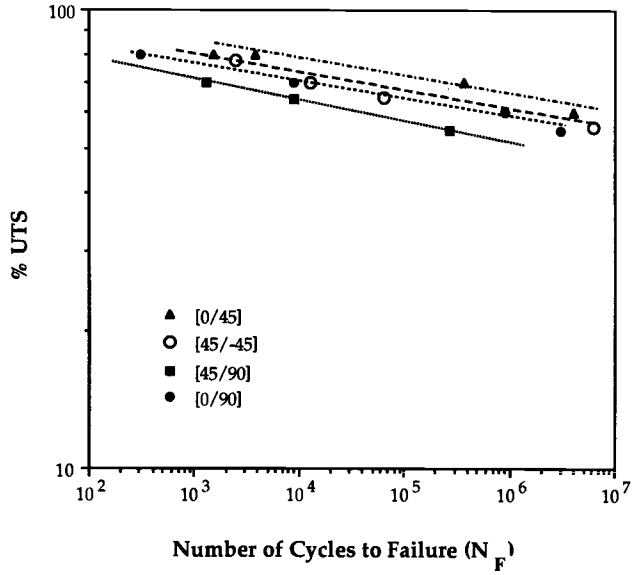

FIG. 5—*Stress life* (S-N) *curves for elemental blocks tested.*

the transverse elastic modulus, E_T, the Poisson's ratio, ν_{LT}, and the in-plane shear modulus, G_{LT}. For complete modeling of the stiffness degradation in composite materials, it is necessary to consider all four material properties. Talreja [*16*] showed that, for testing of a unidirectional glass fiber composite, E_L exhibited little or no change up to final failure, whereas the shear modulus and the Poisson's ratio exhibited large variations. These changes were attributed to the matrix cracking and are consistent with the results shown in Fig. 3 for the regime where the 0° layers dominate, which shows little change in E_{xxN} up to final failure. These results suggest that for unidirectional composites tested in tension, all four material property terms are needed in the modulus reduction. However, from the results obtained here, it is evident that measurements of changes in E_{xx} and E_{yy} correlate well with damage observed during the fatigue tests. Furthermore, the measurement of the other material properties is time consuming and difficult, requiring shear tests, which would seriously hamper the practicality of the approach proposed here.

The basis of the proposed approach is that the modulus functions obtained for each elemental block geometry can be used to predict the behavior of more complex composites. Consider the case of the $[0/45_2/-45_2/90]_s$ composite given in Table 1, which is analogous to following six elemental blocks: [0/45], [45/−45], [−45/90], [−45/90], [−45/45], and [0/45]. The [0/90/45/

TABLE 4—*Constants used in* S-N *curve approach where* N = C $(S/S_{UTS})^m$ *to define transition life* N_T, *and total life* N_F.

	Transition N_T		Total N_F	
Geometry	*C*	*m*	*C*	*m*
[0/45]	1.7	−28.5	4.1	−28.8
[45/−45]	29.8	−17.5	2.12	−25.3
[90/45]	0.8	−21.0	0.8	−21.0
[0/90]	0.9	−10.9	1.3	−24.5

$-45]_s$ elemental block in Table 1 can be divided as follows: [0/90], [90/45], and [45/−45] (together with the other three symmetric blocks); but in this case, the shared 90 and 45° layers in each of the elemental blocks have half the thickness of the layers in the original composite.

The model used here to analyze the composites is based on classical lamination theory, where a global stiffness matrix is constructed from the stiffness matrices of the each of the layers. The approach adopted here is similar, except in this case the elemental blocks rather than the layers are used to construct the global extensional stiffness matrix. The model, as presently formulated, only applies to symmetric laminates under tension or compression; therefore, the coupling and bending stiffness matrices are ignored. The global extensional matrix, A_{ij}, is obtained from

$$A_{ij} = \sum_{k=1}^{n} (E_{ij})_k \tag{4}$$

where n is the total number of elemental blocks, and $(E_{ij})_k$ is the stiffness matrix for each elemental block k. The stiffness matrix, $(E_{ij})_k$, is obtained from the addition of the two stiffness matrices, Q_{ij}, for each of the individual layers, l, as follows

$$E_{ij} = \sum_{l=1}^{2} (Q_{ij})_l h_l \tag{5}$$

where h_l is the thickness of each layer, l. In order to model the influence of the modulus degradation, the elemental block stiffness values are modified by the modulus degradation functions given by Eqs 1 and 2. However, these functions are given in terms of the moduli in the x and y directions, that is, E_{xx} and E_{yy} for each of the elemental block specimens given in Table 1, whereas we require the individual moduli terms E_{ij} in the elemental block stiffness matrix. This is a form of inverse problem, where the terms of the stiffness matrix, E_{ij}, must be obtained such that the net result satisfies the conditions on E_{xxN}, E_{yyN}, and E_{xyN}, given by Eqs 1 to 3. For each of the elemental block specimens the following operations are performed on each of the entries in the elemental block matrix

$$(E_{ij})_N = [(A_{ij})^*]^{-1} \cdot E_{ij}/(A_{ij})_0 \tag{6}$$

where $(E_{ij})_N$ is the elemental block stiffness matrix as a function of the number of cycles, N. E_{ij} is the elemental block stiffness matrix at $N = 0$ cycles. $(A_{ij})_0$ is the global stiffness matrix at $N = 0$ cycles obtained from Eq 4. $(A_{ij})^*$ is the modified global stiffness matrix given by

$$(A_{ij})^* = [(A_{ij})_0]^{-1} \tag{7}$$

where

$$A^*_{11} = A_{11}/E_{xxN} \tag{8}$$

is substituted into $(A_{ij})^*$ after the matrix has been inverted. The A_{11} term is used in Eq 8 since this term in the matrix corresponds to E_{xx}. E_{xxN} in Eq 8 is given by Eqs 1 and 2. Equations 6, 7, and 8 are needed to relate the function E_{xxN}, E_{yyN}, and E_{xyN} described by Eqs 1 to 3 to the changes in the each of the entries, E_{ij}, in the elemental block stiffness matrices.

For the elemental blocks tested in Table 1, the thickness of the two layers was identical. It is proposed to use the elemental block approach when the thickness of the two layers is not identical, such as the case for B5 given in Table 1. In this case, the $[0/90/45/-45]_s$ laminate is

divided into the following elemental blocks: [0/90], [90/45], [45/−45], [45/−45], [90/45], and [0/90], where the shared 90 and 45° layers in each of the elemental blocks have half the thickness of the layers in the original composite. Clearly, as the ratio of the layer's thickness diverges from 1, the functions given by Eqs 1 and 2 no longer apply and the situation becomes analogous to that of a single lamina. For these cases, it is necessary to ensure that the stresses are applied correctly to each elemental block. This is accomplished by ensuring that the integration of the total stresses in the x direction on all the elemental blocks is equal to the forces applied to the multielement laminates. This requires that the stress S_x on any elemental block consisting of two layers of thickness h_1 and h_2 with layer stresses of S_{1x} and S_{2x}, respectively, be averaged as follows

$$S_E = (S_{1x}h_1 + S_{2x}h_2)/(h_1 + h_2) \tag{9}$$

A similar approach is used to normalize the stress with respect to the UTS values given in Table 2 when the thickness of the two layers is not identical. This is required since the *S-N* data in Fig. 4 are given in terms of the stresses normalized with respect to the UTS. The UTS in this case has to be adjusted upwards or downwards to reflect the relative dimensional increase or decrease in the stronger or weaker layer. This adjustment is performed by using the ratios of the thicknesses such as is used in Eq 9. Clearly this approach is not valid when the ratio of stronger to weaker layers is very different from unity.

As the elemental blocks accumulate damage, the modulus changes, resulting in a shifting of stress to other elemental blocks in the laminate. Consequently, each elemental block experiences a stress history that varies from cycle to cycle, and in order to account for this, a miner's rule approach is used to represent the total fatigue life, N_F, for each elemental block according to

$$\sum_{i=1}^{N_F} 1/N_{FS} = 1 \tag{10}$$

where N_{FS} is the fatigue life for an elemental block at stress range, S, obtained from the *S-N* curve given in Fig. 5. A similar approach is used in order to obtain the number of cycles to transition N_T. By using Eqs 1 to 10, it is possible to construct a model for the fatigue failure of a composite laminate consisting of a number of elemental blocks, and these predictions are compared with experimental results in the following section.

Results and Discussion

In order to test the elemental block approach, two composites designated B5 and B6 in Table 1 were fatigue tested. These composites were chosen since they consist of a combination of the elemental block geometries tested above. The material constants used to model these composites were obtained from Mil-HDBK-17 and are given as: E_L = 138 GPa, E_T = 9.7 GPa, G_{LT} = 8.6 GPa, and υ_{LT} = 0.3. When using these constants, good agreement was obtained between the measured and predicted moduli at zero cycles for all the specimens tested in Table 1.

A key consideration in the modeling of these composites is the exact definition of failure of an elemental block. Two approaches were taken in the model. The first assumes that when an elemental block reaches its fatigue life, N_F, given by Eq 10, then it is no longer capable of supporting load and is discounted from the stiffness matrix. The second approach assumes that the composite is still capable of supporting load, and its modulus is given by the extrapolation of the modulus degradation curves beyond N_F. Clearly, these two approaches represent approx-

imations to the true nature of failure of an elemental block, which is constrained by other layers in the laminate.

Figures 6 and 7 show a comparison between the measured and predicted E_{xx} moduli versus the number of cycles for the $[0/90/45/-45]_s$ and the $[0/45_2/-45_2/90]_s$ cases, respectively. Figures 6 and 7 show that the block discount approach, where an elemental block, which has failed according to Eq 10 and is deemed to have a zero stiffness, results in an underprediction of the measured moduli. For example, Fig. 6 shows that the modulus exhibits a very sharp decrease after the first few cycles, which is as a result of failure of the [45/−45] block, followed a few cycles later by failure of the [90/45] block. This results in the remaining life being dominated by the [0/90] block, which produces the increase in the modulus similar to that exhibited in the [0/90] elemental block tests. By using the extrapolated stiffness approach, the agreement between the model and prediction is somewhat closer but is still less than optimum. This poor agreement between model and measurement could be a result of the differing layer thicknesses, where the elemental block approach is no longer strictly valid.

For the $[0/45_2/-45_2/90]_s$ laminate, Fig. 7 shows that the agreement between the model and prediction is improved where the extrapolated modulus approach produces relatively good agreement with the measured modulus. In contrast, the block discount approach produces a large underprediction of the measured modulus, which is a consequence of failure with a concomitant reduction in stiffness of the [45/−45] and the [45/90] blocks early in the fatigue life.

The above results illustrate that the abrupt loss in stiffness predicted when using the block discount methods does not accurately reflect the gradual degradation of the modulus that occurs within the laminate, as evidenced by Figs. 6 and 7. Although the nature of this damage accumulation has been established from the individual elemental block tests through the modulus degradation functions, the behavior of the laminate when the elemental blocks fail or are close to failure is unclear. For example, for the two cases considered here, failure of the weaker elemental blocks is predicted to occur very early in the fatigue life. However, the measured

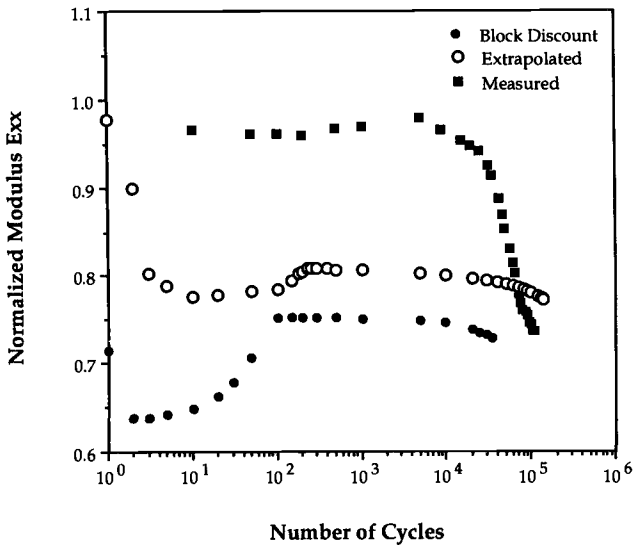

FIG. 6—*Comparison between measured and predicted modulus,* E_{xx}, *as a function of number of cycles for [0/90/45/−45] composite.*

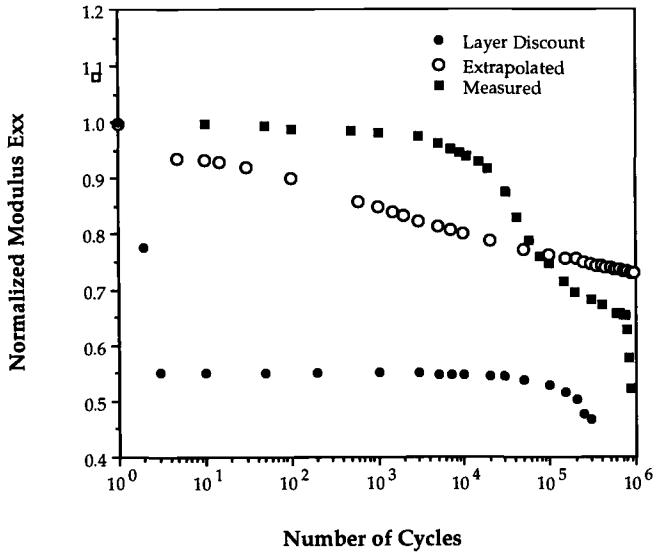

FIG. 7—*Comparison between measured and predicted modulus, E_{xx}, as a function of number of cycles for $[0/45_2/-45_2/90]_s$ composite.*

modulus degradation does not reflect this failure of the weaker blocks. To study these anomalous effects, detailed micromechanical-type observations are currently underway to experimentally map out the distributions of stresses and strains in a laminate as it accumulates damage and fails.

Conclusions

The fatigue behavior of graphite-epoxy-laminated composites was analyzed. The approach used was to substructure the analysis based on simple elemental blocks, which are two layer laminates such as [0/90] or [45/−45]. By conducting fatigue tests on these elemental blocks it was possible to fit functions to describe the elemental block moduli at any number of cycles. These functions were incorporated into a lamination code to predict the fatigue behavior of multielement composites. The results show that the prediction is very sensitive to the exact mechanism of load redistribution within a multielement composite, particularly when an elemental block is close to failure. For example, the assumption that an elemental block carries no load when failure is deemed to have occurred results in substantial underprediction of the measured modulus. Clearly, more work is needed to define exactly the nature of stress redistribution within complex composites.

References

[1] Sendeckyj, G. P., "Fitting Models to Composite Materials Fatigue Data," *Test Methods and Design Allowables for Fibrous Composites, ASTM STP 734,* 1981, pp. 245–260.

[2] Reifsnider, K. L., "The Critical Element Model: A Modeling Philosophy," *Journal of Engineering Fracture Mechanics,* Vol. 25, 1986, pp. 739–749.

[3] Reifsnider, K. L. and Stinchcomb, W. W., "A Critical-Element Model of the Residual Strength and Life of Fatigue-Loaded Composite Coupons," *Composite Materials: Fatigue and Fracture, ASTM STP 907,* H. T. Hahn, Ed., American Society for Testing and Materials, Philadelphia, 1986, pp. 298–313.

[4] Reifsnider, K. L., "Damage and Damage Mechanics," *Fatigue of Composite Materials,* K. L. Reifsnider, Ed., Elsevier Science Publishers, Amsterdam, 1990.
[5] Yang, J. N. and Liu, M. D., "Residual Strength Degradation Model and Theory of Periodic Proof Tests for Graphite/Epoxy Laminates," *Journal of Composite Materials,* Vol. 11, No. 3, April 1977, pp. 176–203.
[6] Yang, J. N., "Fatigue and Residual Strength Degradation for Graphite/Epoxy Composites Under Tension-Compression Cyclic Loading," *Journal of Composite Materials,* Vol. 12, No. 1, January 1978, pp. 19–39.
[7] Whitney, J. M., "Residual Strength Degradation Model for Competing Failure Modes," *Long Term Behavior of Composites, ASTM STP 813,* T. K. O'Brien, Ed., American Society for Testing and Materials, Philadelphia, 1983, pp. 225–245.
[8] Rotem, A.,"Stiffness Change in a Graphite Epoxy Laminate Under Reverse Fatigue Loading," *Journal of Composites Technology and Research,* Vol. 11, No. 2, pp. 59–64.
[9] Rotem, A. and Nelson, H. G., "Fatigue Behavior of Graphite-Epoxy Laminates at Elevated Temperatures," *Fatigue of Fibrous Composite Materials, ASTM STP 723,* K. N. Lauritis, Ed., American Society for Testing and Materials, 1981, pp. 152–173.
[10] Stinchcomb, W. W., Reifsnider, K. L., Yeung, P., and Masters, J., "Effect of Ply Constraint on Fatigue Damage Development in Composite Material Laminates," *Fatigue of Fibrous Composite Materials, ASTM STP 723,* K. N. Lauritis, Ed., American Society for Testing and Materials, 1981, pp. 64–84.
[11] Talreja, R., "Fatigue of Composite Materials," Ph.D. dissertation. Technical University of Denmark.
[12] Harris, C. E., Allen, D. H., and Nottorf, E. W., "Modelling Stiffness Loss in Quasi-Isotropic Laminates due to Microstructural Damage," *Journal of Engineering Materials and Technology,* Vol. 110, 1988, pp. 128–133.
[13] Harris, C. E., Allen, D. H., and Nottorf, E. W., "Prediction of Poisson's Ratio in Cross-Ply Laminates Containing Matrix Crack and Delaminations," *Journal of Composite Technology and Research,* Vol. 11, No. 2, 1989, pp. 53–58.
[14] Allen, D. H., Harris, C. E., and Groves, S. E., "A Thermomechanical Constitutive Theory for Elastic Composites with Distributed Damage Part—I: Theoretical Development," *International Journal of Solids and Structures,* Vol. 23, No. 9, 1987, pp. 1301–1318.
[15] Allen, D. H., Harris, C. E., and Groves, S. E., "A Thermomechanical Constitutive Theory for Elastic Composites with Distributed Damage Part—II: Application to Matrix Cracking in Laminated Composites," *International Journal of Solids and Structures,* Vol. 23, No. 9, 1987, pp. 1319–1338.
[16] Talreja, R., *Fatigue of Composite Materials,* Technomic Publishing Company, Inc., Lancaster, PA, 1987.

DISCUSSION

O. Buck[1] *(written discussion)*—You mentioned that fibers in certain plies fail at the start of fatigue testing. Why then are those plies put into the composite in the first place?

M. P. Connolly (author's response)—The tests were performed on composites with many plies that were off-axis to the direction of load. The results shown here demonstrate that, at high load levels relative to the material strength, many of these off-axes plies fail very early in the fatigue life, and the remaining life is expended in the failure of the plies that are parallel to the direction of loading.

For the specific loading applied here, the optimum design would be unidirectional with the plies parallel to the direction of load. However, in practice, composites are subject to more complex loads than those considered here; for example, biaxial or shear loads, and for these situations, off-axes plies are required. Consequently, these plies must be included in any fatigue methodology even for the simple tension loading considered here. These off-axes plies will fail at lower load levels than the unidirectional fibers. For high load levels this failure can occur very early in the fatigue life. However, at lower loads, which are more typical of service conditions, these off-axes plies would not be expected to fail so early in the fatigue life.

[1] Ames Laboratory, Iowa State University, Ames, IA 50011.

Christopher P. R. Hoppel[1] *and Robert N. Pangborn*[2]

The Evaluation of Fatigue Damage in Short Fiber-Reinforced Styrene-Maleic Anhydride

REFERENCE: Hoppel, C. P. R. and Pangborn, R. N., **"The Evaluation of Fatigue Damage in Short Fiber-Reinforced Styrene-Maleic Anhydride,"** *Cyclic Deformation, Fracture, and Nondestructive Evaluation of Advanced Materials: Second Volume, ASTM STP 1184,* M. R. Mitchell and O. Buck, Eds., American Society for Testing and Materials, Philadelphia, 1994, pp. 278–300.

ABSTRACT: The fatigue behavior of short glass fiber-reinforced styrene-maleic anhydride (S/MA) is investigated in this study. Six material configurations were manufactured into tensile bars by injection molding and tested in tension-tension ($R = 0.1$) fatigue to evaluate the ways the interface controls the change in the mechanical properties of the composite. These materials included unreinforced S/MA as a reference material and composites incorporating fiber reinforcement with different average diameters, two volume fractions, the presence or absence of an interfacial silane coupling agent, and fibers prepared with an acrylonitrile/butadiene latex coating. These materials have been tested under both "wet" (immersed in water at 25°C) and "dry" (50% relative humidity at 25°C) conditions. Three indicators were monitored during fatigue to evaluate the damage in the experimental materials: the degradation of the secant and fatigue moduli, the hysteresis energy per cycle, and the concurrent acoustic emissions produced during fatigue. This information is presented with *S-N* curves to show the relationship between these indicators and the fatigue lives of the materials.

The fatigue performance (life curves and cyclic stress-strain curves) was directly related to the fiber-matrix interface. Since water weakens the interface, especially in the composites without a silane coupling agent, composites tested in the aqueous environment exhibited shorter fatigue lives than the specimens tested in the dry environment. Interfacial coatings that included a silane couplant were found to reduce the effects of water on the fatigue lives of the composites. This damage in the composites was reflected in the decrease in the elastic modulus and the increases in the hysteresis energy and acoustic emissions. These evaluation techniques show that fatigue damage accumulates in a three-stage process in the material.

KEYWORDS: fatigue, short fiber-reinforced composite, hysteresis energy, secant modulus, fatigue modulus, acoustic emission

Short glass fiber-reinforced thermoplastic materials offer higher stiffnesses, strengths, and dimensional stability than unreinforced thermoplastics and can be molded into large and complex shapes using injection molding. These properties make the materials useful for the fabrication of parts such as automobile dashboards, bumpers, and body panels. Despite the increased popularity of these materials, many aspects of their response to applied loads and aggressive environments are not clearly understood. Fatigue behavior and exposure to water are particularly important because many of the current and projected applications of short glass fiber-

[1] Graduate student, Pennsylvania State University, Department of Engineering Science and Mechanics, University Park, PA 16802; present address: U.S. Army Research Laboratory, Attn. AMSRL-WT-PD, Aberdeen Proving Grounds, MD 21005-5066.

[2] Professor of Engineering Mechanics, The Pennsylvania State University, Department of Engineering Science and Mechanics, 227 Hammond Building, University Park, PA 16802.

reinforced materials involve exposure to repetitive loading in various levels of humidity. By characterizing and monitoring the fatigue response of these materials, the fiber treatment and composite processing may be adjusted to afford greater fatigue resistance.

Fatigue failures in composites are generally due to an accumulation of damage due to a number of mechanisms [*1*]. These mechanisms include fiber breakage, fiber debonding and pullout, shear crack formation in matrix along fibers, void formation and coalescence, and matrix crazing and fracture [*2,3*]. The role or relative contribution of each of these mechanisms in the final failure is not completely understood, but the properties and characteristics of the matrix, the reinforcement, and the interface will influence how the damage is manifested in the material. For this study, the interfacial properties of the composite have been varied to determine the effects of the interface on the fatigue life and the degradation of mechanical properties.

Fatigue of Composites

Martin et al. [*4*] have studied the effects of a silane coupling agent on reaction injection molded glass fiber-reinforced Nylon 6. They found that for fatigue tests in a dry environment, the silane couplant, which forms strong bonds between the fiber and the matrix, had very little effect on the fatigue behavior of the composites. However, Peterson et al. [*5*] have shown that for tension tests on glass fiber-reinforced S/MA, the composites were stronger and stiffer when the fibers were coated with a silane couplant than when the fibers were coated with either a ductile latex coating or a coating that did not contain a couplant. They also found that moisture caused the interfacial bond to degrade. When the specimens were soaked in water prior to testing, all of the fiber-reinforced materials suffered some loss in strength and stiffness. The strength losses were much lower in the materials with a protective silane coating on the fibers. Other studies [*6,7*] have shown that exposure to water reduces the fatigue life of glass fiber-reinforced composites. However, these studies did not evaluate how different interfacial coatings might affect the fatigue life.

Effects of Fatigue Damage on Material Properties

During fatigue, damage is incurred that affects both the elastic and inelastic properties. It is important to understand how these mechanical properties are altered by fatigue in order to predict how the response of the materials will change with use. The modification of these properties can also be used to evaluate the damage [*8*]. In the fatigue of composite laminates, Reifsnider et al. [*9,10*] have shown that degradation of the elastic modulus was directly related to the amount of cracking in the laminates. They showed that the development of this damage is a three-stage process. In the first stage, constituting about the first 10% of the fatigue life, most of the damage is manifested as matrix cracks. Also during this first stage, the elastic modulus tends to decrease rapidly as the generation of cracks weakens the composite. As the characteristic damage state is reached at the beginning of the second stage, the rate of damage growth decreases and the elastic modulus and the amount of cracking remain nearly invariant. The third stage of the fatigue process begins at about 80 to 90% of the fatigue life. In this stage, the amount of damage in the composite increases rapidly. This damage is often localized around the site of impending failure and can consist of delamination, fiber fracture, and matrix cracking. The elastic modulus tends to decrease rapidly in this final stage [*9,10*]. Models for fatigue failure prediction [*11,12*], based on the reduction of elastic properties, have been developed for different types of composite materials. These models require that the reduction of elastic properties can be used to establish a suitable failure criterion for the material.

Secant and Fatigue Moduli

Several studies [*13,14*] have also shown that after damage has occurred in a composite material, a knee can form in the tensile hysteresis loop. The elastic modulus, which represents the behavior of the material below the knee point, cannot fully describe this nonlinear response. To evaluate the properties of the material at stresses less than and greater than the knee point, Hahn and Tsai [*14*] introduced the secant modulus, which is defined as the slope between two points on a material's stress-strain curve. Since the secant modulus can include both the elastic and inelastic deformation of the material, it is generally lower than the elastic modulus, which is often denoted as the tangent modulus. Hahn and Kim [*15*] studied the degradation of the secant modulus during the fatigue of glass/epoxy laminates. They found that the secant modulus could be used as a measure of the extent of damage, and that just prior to failure the secant modulus in fatigue decreases to within the scatter of the secant modulus at static failure. The secant modulus at static failure is the slope of a line drawn from the origin to the fracture stress and strain for a tension proof test.

Hwang and Han [*16*] introduced the fatigue modulus for the evaluation of composite materials. The fatigue modulus is the slope of a line drawn from the point of zero stress and strain to the point of maximum stress and strain on each fatigue cycle. Figure 1 shows the secant modulus and the fatigue modulus for a hysteresis curve from a sample of glass fiber-reinforced S/MA. The secant modulus is defined as the slope of a line between the point of highest stress and strain and the point of lowest stress and strain during each fatigue cycle. The fatigue modulus is the slope of the line from the point of highest stress and strain on each cycle to the origin (see Fig. 1). The secant modulus represents the material's compliance. The fatigue modulus represents the compliance as well as the inelastic deformation in the material. Therefore, the fatigue modulus should equal the secant modulus on the first cycle of loading; however, once inelastic deformation occurs, the fatigue modulus will always be lower. The authors proposed that failure occurred when the fatigue modulus equaled the applied stress divided by the failure strain of the composite during a proof test [*16*].

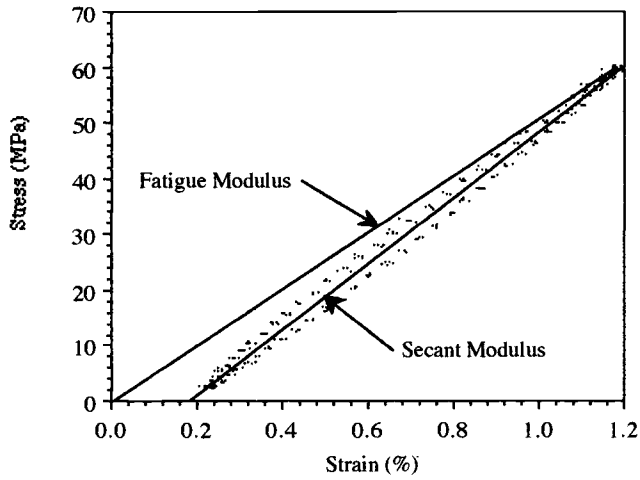

FIG. 1—*Hysteresis curve from the fatigue of C1 material under load control shows the secant and fatigue moduli. The secant modulus is the slope of a line from the point of minimum stress and strain to the point of maximum stress and strain, and the fatigue modulus is the slope of a line from the point of maximum stress and strain to the origin.*

Hysteresis Energy

Another method for evaluating damage during the fatigue process is measuring the hysteresis energy. Part of this energy represents the work stored in the material as damage. However, a much larger portion (99% in some metals [*17*]) of the hysteresis energy per cycle is dissipated through mechanisms such as heat, vibration, and acoustic emission.

Acoustic Emission

Acoustic emissions (AE) are stress waves that emanate from the material due to the formation and growth of defects. On the specimen surface, the acoustic waves can be detected by a piezoelectric transducer, then electronically processed and recorded [*18,19*]. There are several methods of analyzing acoustic emission data. In this study, the data will be analyzed in terms of the number of hits produced by the testing and the corresponding energy of the signals. The number of AE hits generated during testing is proportional to the number of discrete damage or failure-related events that occur. The energy of each acoustic signal is proportional to the energy released by the individual failure event and thus an indication of the severity of the event. For instance, fiber fracture will emit a larger amount of elastically stored energy, accompanied by an AE signal of larger energy, than will mechanisms such as fiber/matrix debonding and matrix cracking [*18,20*].

In a previous study on acoustic emission produced during the fatigue of these materials [*21*], it was shown that the life curves for the composites are comprised of three stages. The first stage is characterized by a large amount of new damage, with acoustic emissions occurring throughout the hysteresis loop. In the second stage, the acoustic emissions are very low in energy, and they tend to occur at the peak load in the fatigue cycle. In the third and final stage, the acoustic emissions start to occur at the lower strains associated with each cycle, and there are more high-energy signals than in the previous stages.

Experimental

Testing Materials

The matrix material for the specimens is styrene-maleic anhydride (S/MA), which is a rubber-modified block terpolymer made by Monsanto Corporation under the brand name Cadon. The properties of S/MA are similar to those of acrylonitrile-butadiene-styrene (ABS). The glass transition for this material is about 110°C [*22*]. Short glass fibers were added to the polymer to increase the strength, stiffness, and dimensional stability. For this study, five variations of the fiber-reinforced material and the unreinforced matrix were tested. These materials are described in Table 1.

TABLE 1—*Material composition.*

Designation	Material Composition	Fiber Volume, %	Fiber Diameter, μm	Fiber Surface Treatment
S/MA	Unreinforced S/MA	0	...	...
C0	S/MA and glass fibers	10	10	Polyurethane and a silane coupler
C1	S/MA and glass fibers	10	13	Polyurethane and a silane coupler
C2	S/MA and glass fibers	5	13	Polyurethane and a silane coupler
C3	S/MA and glass fibers	10	13	Polyurethane and acrylonitrile/ butadiene latex
C4	S/MA and glass fibers	10	13	Polyurethane and no coupler

The short fibers were mixed and extruded with the matrix material, which was then chopped into ~5-mm pellets. To minimize the potential for material variability as a result of processing conditions, all of the tension specimens conforming to ASTM Standard Test Method for Tensile Properties of Plastics (D 638-87b) were injection molded from the compounded and unreinforced S/MA pellets under constant fabrication temperatures, times, and pressures [5]. The gage sections of the tensile bars were 100 mm in length, 12.65 mm in width, and 3.1 mm in thickness.

Testing Equipment

Fatigue testing of the composite materials was conducted on a Model 1350 servohydraulic Instron testing machine. A Hewlett Packard computer with a high-speed data acquisition board was used to periodically sample the stress-strain hysteresis loop at a rate of 30 samples per second. The strain in the specimen was monitored with an extensometer that had a 25.4-mm gage length. The tests were carried out in tension-tension ($R = 0.1$) fatigue under load control at frequencies between 1 and 2 Hz. "Dry" tests were conducted at standard atmospheric conditions (temperature of 25°C and 50% relative humidity). For the "wet" tests, the specimens were submerged in a bath of distilled water at 50°C for 48 h, then cooled to room temperature in distilled water for 30 min prior to testing. The specimens in the "wet" tests were submerged in room temperature water throughout the fatigue cycling.

Acoustic Emission Testing

A Physical Acoustics Corporation (PAC) model Locan AT acoustic emission testing system was employed to monitor the fatigue-induced emissions. This system is capable of monitoring hits, counts, amplitudes, energies, rise times, and durations of acoustic emissions. A PAC Pico wide band (100 to 1.2 MHz) transducer was used to monitor the AE signals generated by the specimen. The signal received by the transducer was amplified by 40 dB using a PAC model 1220A preamplifier and by 20 dB at the Locan AT. At the Locan AT, the AE threshold was set at 45 dB.

Results

Tensile Properties

All of the materials were proof tested to failure in tension at a strain rate of 0.01 mm/mm/s under both wet and dry conditions. Two specimens of each material were tested under wet and dry conditions, and the average strengths, strains to failure, elastic moduli, and absorbed energies are presented in Table 2. The tensile properties of these materials at various strain rates were evaluated extensively in a previous study [5]. The results presented in Table 2 are in agreement with those results.

S-N *Curves*

S-N curves were generated for each of the materials under both wet and dry conditions, as shown in Figs. 2*a* through 2*f*. Each set of data was fit with a power law curve fit

$$SN^B = A \tag{1}$$

where S is the maximum applied stress, N is the number of cycles to failure, and A and B are constants. The power law curves are shown as straight lines on each of the log stress versus

TABLE 2—*Tensile and fatigue properties.*

Material	Tensile Properties at 0.01 mm/mm/s				Constants for *S-N* curves, $SN^B = A$		
	Strength, MPa	Strain-to-Failure, %	Elastic Modulus, GPa	Absorbed Energy, MJ/m^3	*A*, MPa	*B*	Correlation Coefficient, R^2
S/MA dry	47.5	2.00	2.966	65.87	67.13	0.1181	0.779
S/MA wet	45.2	2.01	2.978	67.97	72.90	0.1274	0.799
C0 dry	95.5	2.09	6.857	124.08	152.90	0.1173	0.961
C0 wet	90.3	2.08	6.629	107.85	131.46	0.1127	0.956
C1 dry	93.8	2.03	6.707	117.25	125.98	0.0986	0.941
C1 wet	88.8	2.00	6.652	110.87	112.20	0.0991	0.902
C2 dry	63.5	2.21	4.664	95.03	98.58	0.1099	0.990
C2 wet	62.1	2.30	4.540	100.25	96.89	0.1201	0.998
C3 dry	76.0	1.64	5.377	74.02	118.22	0.1101	0.987
C3 wet	59.9	1.81	5.213	169.00	74.56	0.0913	0.959
C4 dry	85.9	1.90	6.498	119.43	139.48	0.1185	0.924
C4 wet	68.0	1.88	5.763	93.34	90.70	0.0996	0.933

log cycles to failure curves in Fig. 2. The constants *A* and *B* for each of these curves are given in Table 2 along with the correlation coefficient (R^2) for each curve.

The *S-N* curves reveal several important trends in the data. First, the aqueous environment has very little effect on the fatigue life of the unreinforced S/MA. For the fiber-reinforced materials, the fatigue lives are always much lower for the specimens tested in the wet environment. This is most apparent for the materials without the silane coupling agent (the C3 and C4 materials). The effect of moisture on the fatigue lives of the fiber reinforced materials indicates that the water has a deleterious effect on the interface and/or the fibers in the composites. Although the silane coating does not completely prevent these effects, it does reduce the impact of the water compared to the other coatings used in this study.

In general, the materials with the greater tensile strengths had longer fatigue lives. This is known as the "strength-life equal rank assumption" and has been shown to hold true for a wide variety of composite materials in other studies [*23,24*].

Fractography

The fracture surfaces of the specimens were examined after testing in the scanning electron microscope (SEM). Figure 3 shows a photograph of the fracture surface from the unreinforced S/MA. This shows some crack branching occurring in the plane of the fracture surface, but, overall, the fracture surface tended to be very flat, typical of a Mode I fracture. The fracture surfaces of the matrix material did not appear any different when tested in the wet versus dry conditions.

A fracture surface from a composite specimen (shown in Fig. 4) reveals a more tortuous pattern of crack growth. The surface is very uneven, as the reinforcing fibers have caused the crack to deviate from its original path. In the failures of the composite specimens, the fibers generally pulled out of the matrix cleanly, with little or no matrix adhering to them. The holes created by the fiber pullout were usually round and about the same diameter as the fibers, and there was no evidence of fiber fracture on the surfaces. The combination of matrix cracking and fiber pullout was observed on the fracture surfaces of all of the composite materials under both wet and dry conditions.

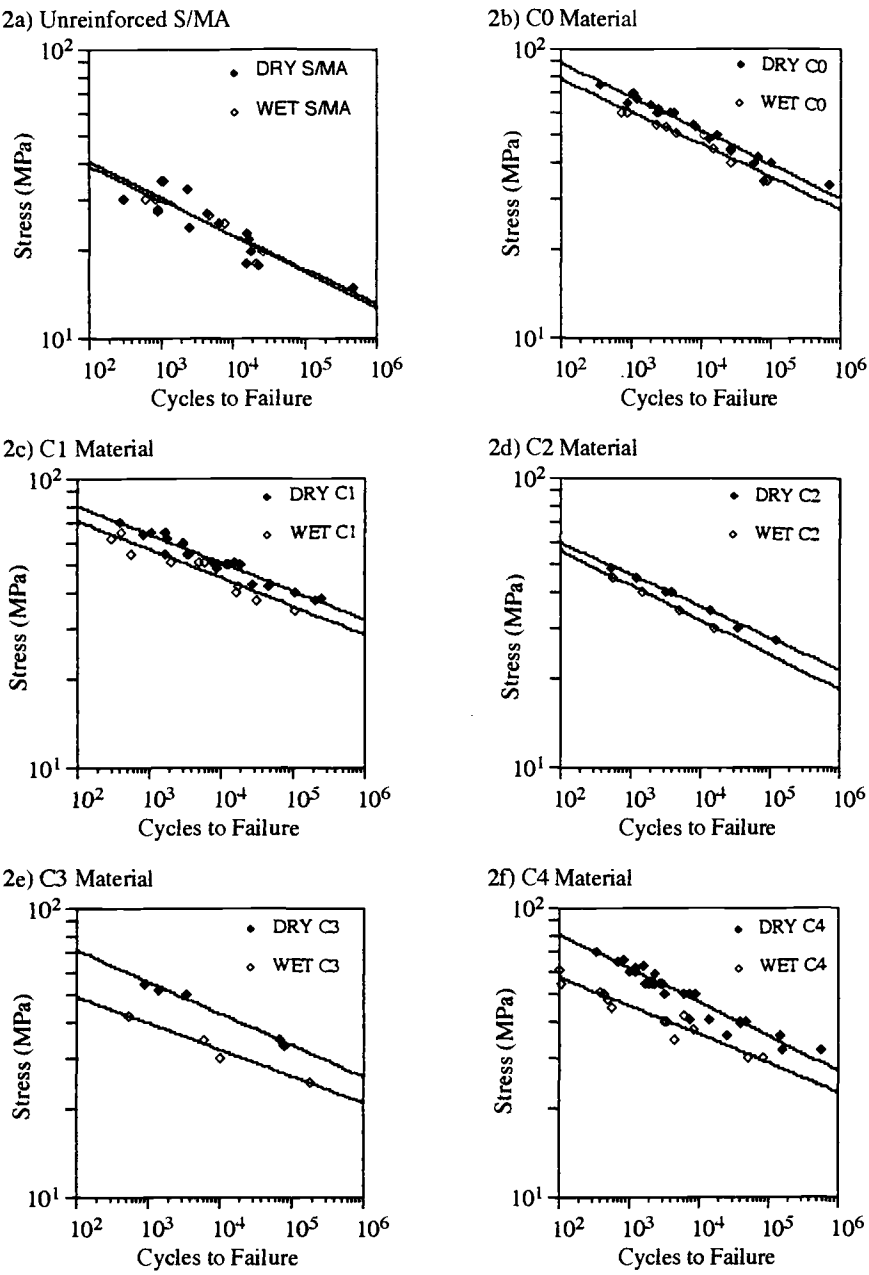

FIG. 2—S-N *curves for the experimental materials. On all graphs, the closed diamonds indicate dry tests and the open diamonds indicate wet tests.*

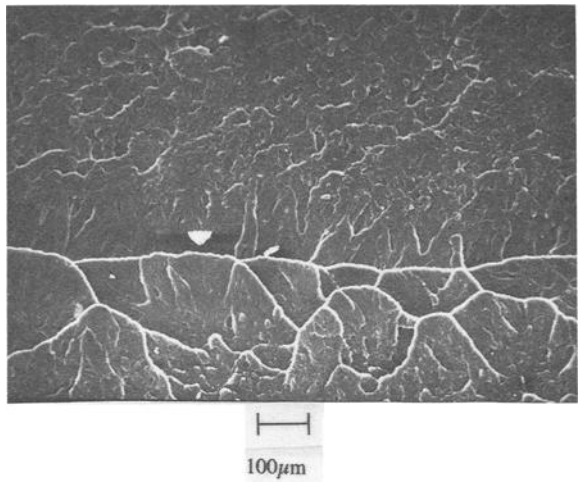

FIG. 3—*Fracture surface of a specimen of unreinforced S/MA.*

Degradation of Fatigue and Secant Moduli

Figures 5*a* through 5*f* shows how the secant and fatigue moduli change with cumulative cycles for the various materials at different stress levels and under both wet and dry conditions. The graphs in Fig. 5 show that, in the fiber-reinforced materials (Figs. 5*a* through 5*e*), the secant and fatigue moduli decay in similar ways. During the first 10 to 20% of the fatigue life, both moduli decrease rapidly. The fatigue moduli tend to decrease faster than the secant, indicating that the material undergoes significant inelastic deformation up to this point. After this initial stage, the material tends to reach a "steady-state" condition and the two moduli decrease at fairly constant rates. After 95% of the fatigue life has been expended, the moduli in some of the tests begin to decrease at a higher rate prior to failure. This final drop in moduli may be due to localized damage associated with impending failure. It was disclosed in only some of the life curves because the localized damage may have not been revealed by the extensometer,

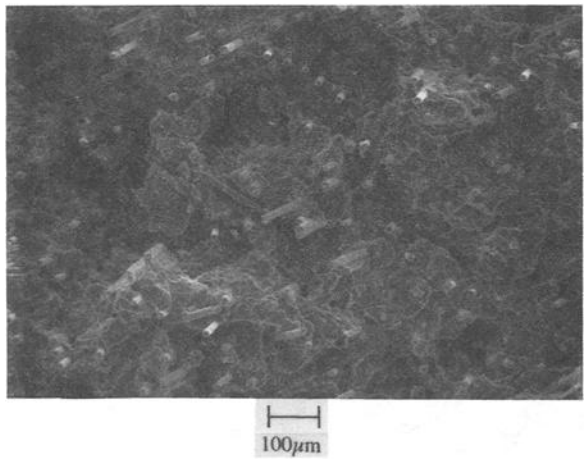

FIG. 4—*Fracture surface of a specimen of C4 material.*

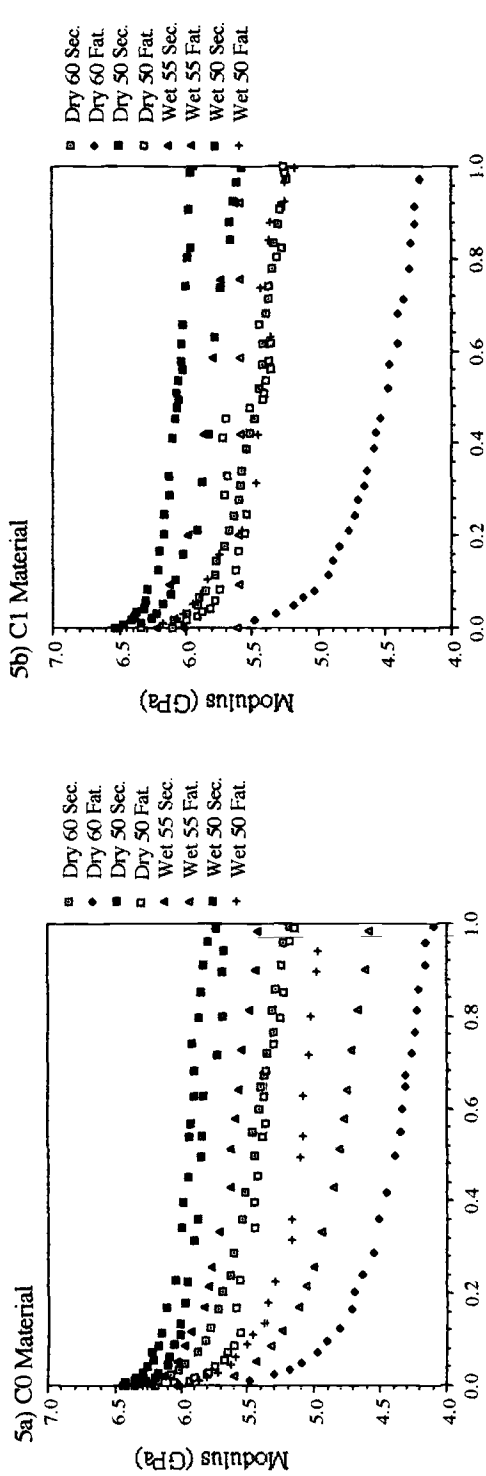

FIG. 5—*Secant and fatigue moduli versus cycles for the six materials used in this study. On each graph, the horizontal axis gives the normalized number of cycles; the vertical axis gives the modulus in GPa. The legends show the test condition (dry or wet), the maximum stress in MPa, and the type of modulus (secant or fatigue).*

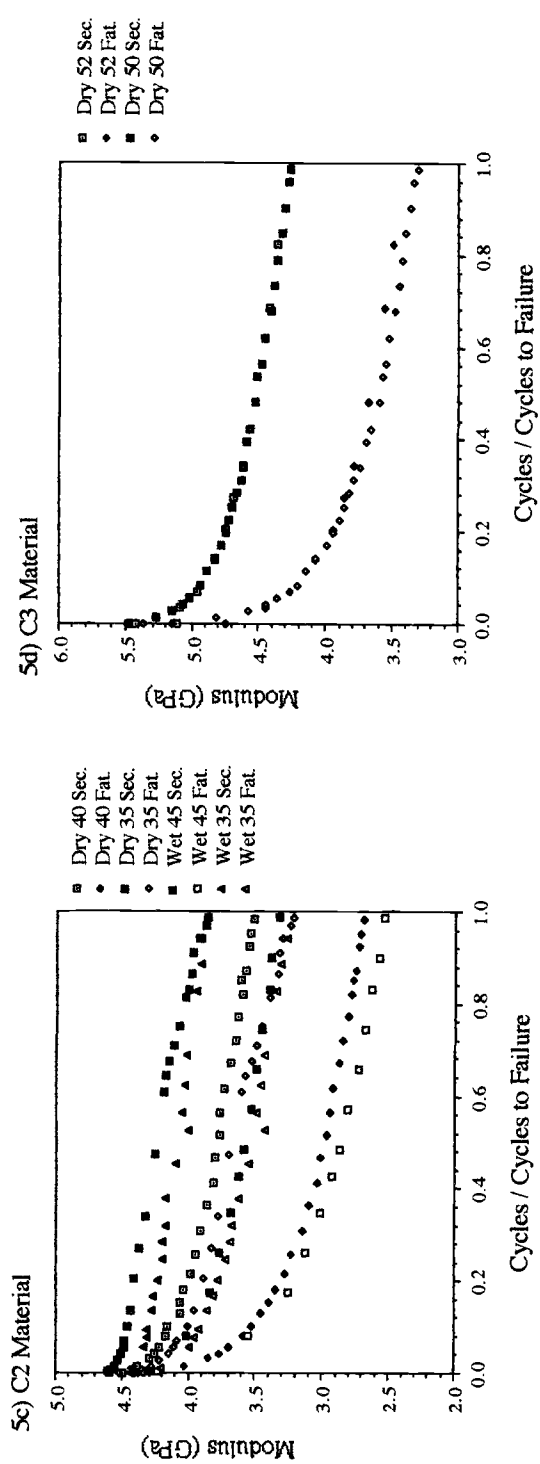

FIG. 5—*Continued.*

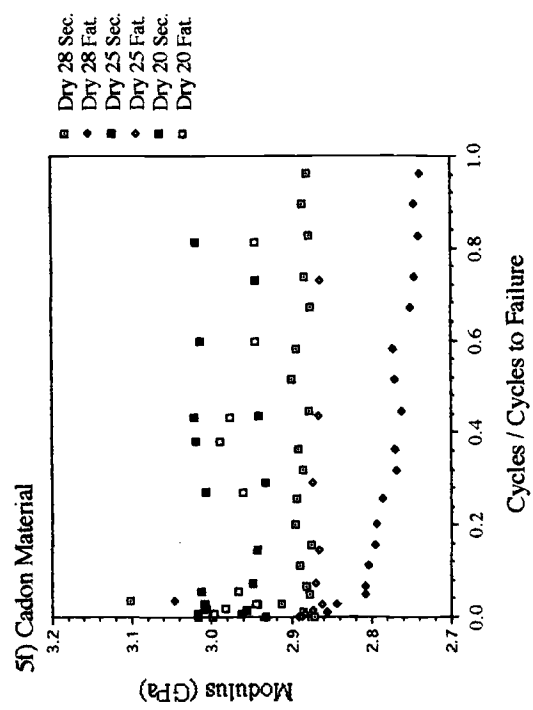

FIG. 5—*Continued.*

which measured the stain over a large range (25.4 mm). The three stages of damage growth shown in these life curves are very similar to the stages of damage growth reported by Reifsnider et al. [*9,10*].

The rate of degradation of the moduli also varied with the applied stress amplitude and the test condition (wet or dry). In general, the moduli decayed at a higher rate and decreased to lower levels when the material was cycled at higher stress and when the material was tested in a wet as opposed to a dry environment.

The life curves for the unreinforced material (shown in Fig. 5*f*) reveal that the moduli have more scatter and do not decrease nearly as much over the life as do those for the composites (Figs. 5*a* through 5*e*). Thus, the loss in stiffness of the composites during the life is clearly a result of reduced reinforcement efficiency, probably due to interfacial damage.

Moduli at Failure

For the fiber-reinforced materials, the values of the moduli at failure varied a great deal among the materials depending on the fatigue stress and the test conditions. This contradicts earlier work that suggests that the secant modulus [*15*] and the fatigue modulus [*16*] reach values at failure that are independent of the applied stress. Figures 6*a* and 6*b* show the secant and fatigue moduli at failure plotted against the normalized stress amplitude for each of the materials.

Figures 6*a* and 6*b* show that for a given material and test condition, the secant and fatigue moduli at failure tend to be lower for higher normalized stress amplitudes. The moduli at failure also tend to be lower for materials with low values of tensile secant moduli (see Table 2). Notice that the results from the materials with 10% fibers (all data except for the S/MA and C2 specimens) all fall within the same bounds. These plots imply that for a given cyclic stress, the moduli at failure could be estimated.

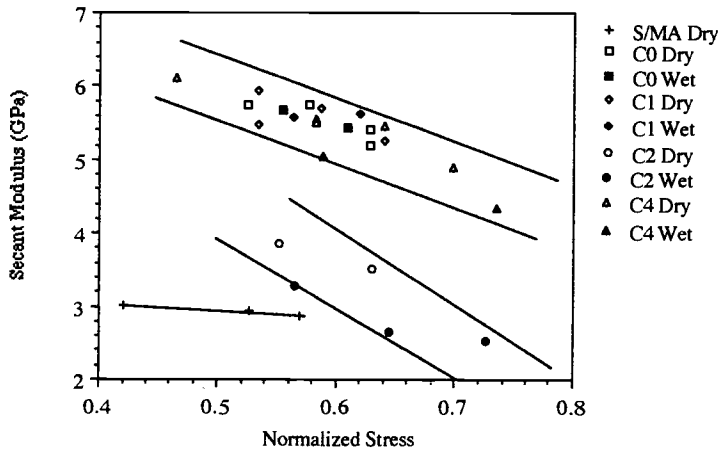

FIG. 6*a*—*The secant moduli at failure for the materials versus the normalized stress amplitude (maximum stress/static tensile strength). The lines outlining the data from the composites with 10 and 5% fibers were added by the authors.*

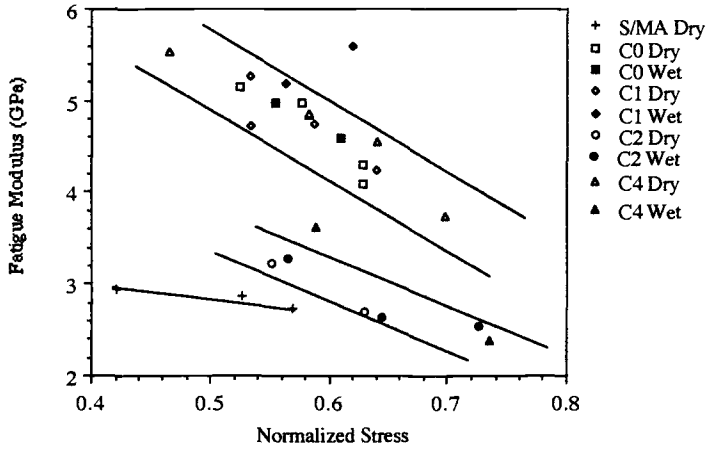

FIG. 6*b*—*The fatigue moduli at failure for the materials versus the normalized stress amplitude (maximum stress/static tensile strength). The lines outlining the data were added by the authors.*

Hysteresis Energy

The areas of the hysteresis curves were measured periodically during the fatigue tests on the experimental material. Figures 7*a* through 7*f* show how the measured hysteresis energy changed during the lives of each of the specimens. The curves display a trend toward increasing energy per cycle for increasing applied stress amplitude. Also, specimens tested in wet conditions produced a larger amount of energy per cycle than those tested in a dry environment. The unreinforced S/MA specimens had the lowest amount of hysteresis energy per cycle, and these specimens showed the most scatter in the plots of energy versus accumulated cycles.

In the composite materials, the hysteresis energy per cycle increased throughout the fatigue test. In general, this increase in energy followed the same trend as the decrease in moduli: the energy per cycle increased rapidly during the beginning of the fatigue life, then increased at a lower, steady-state rate, and then increased at a high rate again prior to failure.

Figure 8*a* shows the amount of energy on the last cycle recorded prior to failure versus the number of cycles to failure for each test. Notice that, for each material, specimens that had longer fatigue lives tended to have a lower amount of energy per cycle. The integrated hysteresis energy over the fatigue life is shown in Fig. 8*b*. This graph shows that the amount of hysteresis energy absorbed prior to failure increases almost linearly with the number of cycles to failure, even though the shorter fatigue tests absorbed a larger amount of energy per cycle (Fig. 8*a*).

Acoustic Emission

Acoustic emission was used as a form of NDE to complement the two methods of monitoring the material properties. During testing, the AE test parameters (the amount of amplification and the types of transducers and filters) were varied to optimize the amount of AE being recorded (the maximum amount of information without overloading the AE recording system). AE data were collected with several different systems; however, only data collected with the test parameters described in the experimental section are shown in this study. Because of this, the amount of AE data is limited compared to the results presented in the other sections of this study.

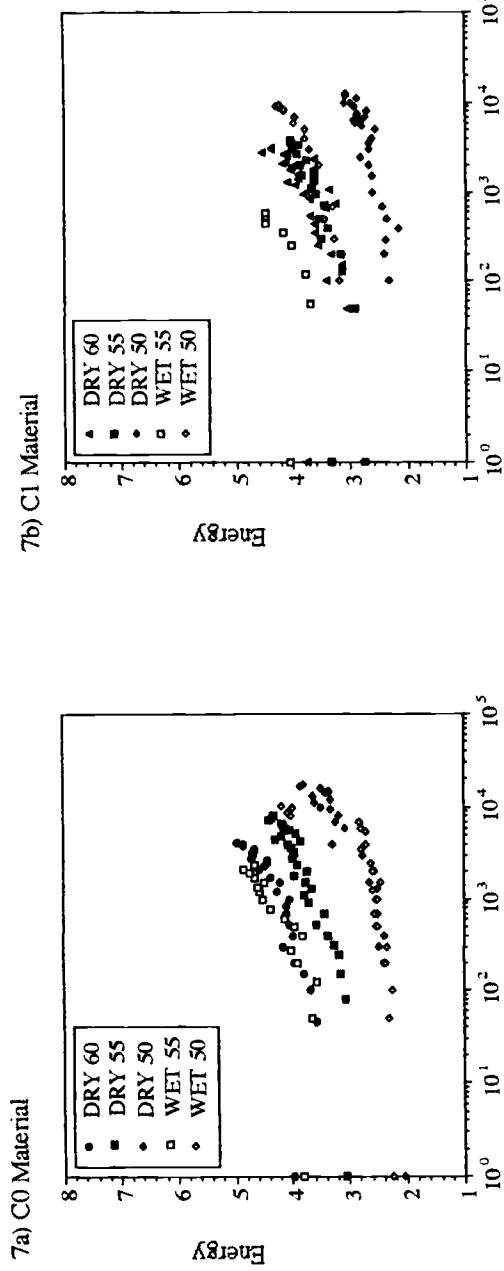

FIG. 7—*Hysteresis energy per cycle versus number of cycles for the six experimental materials.*

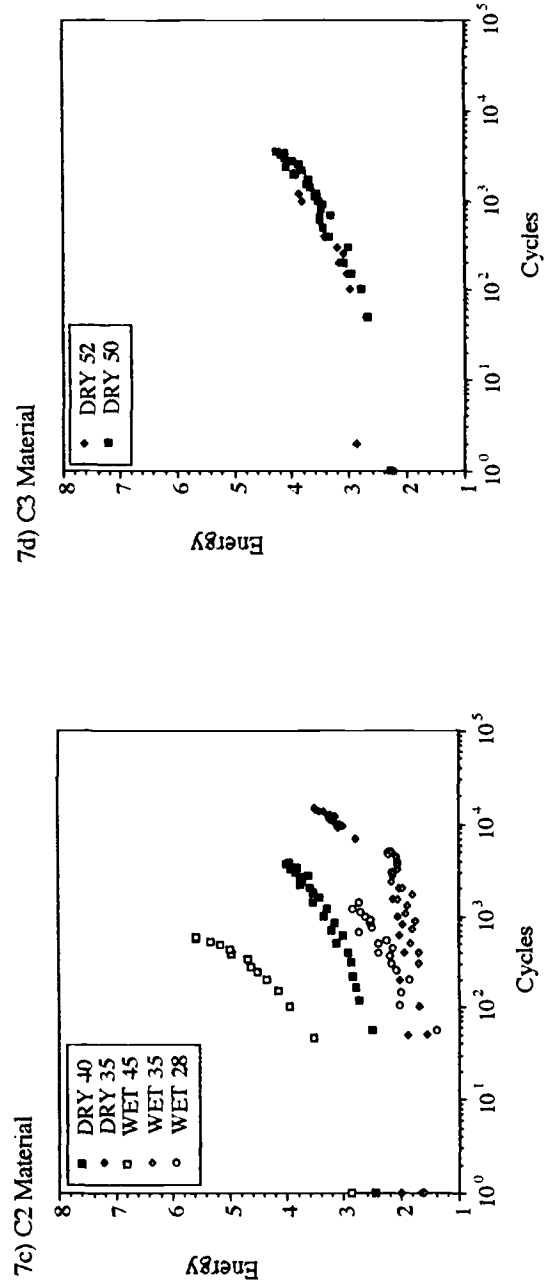

FIG. 7—*Continued.*

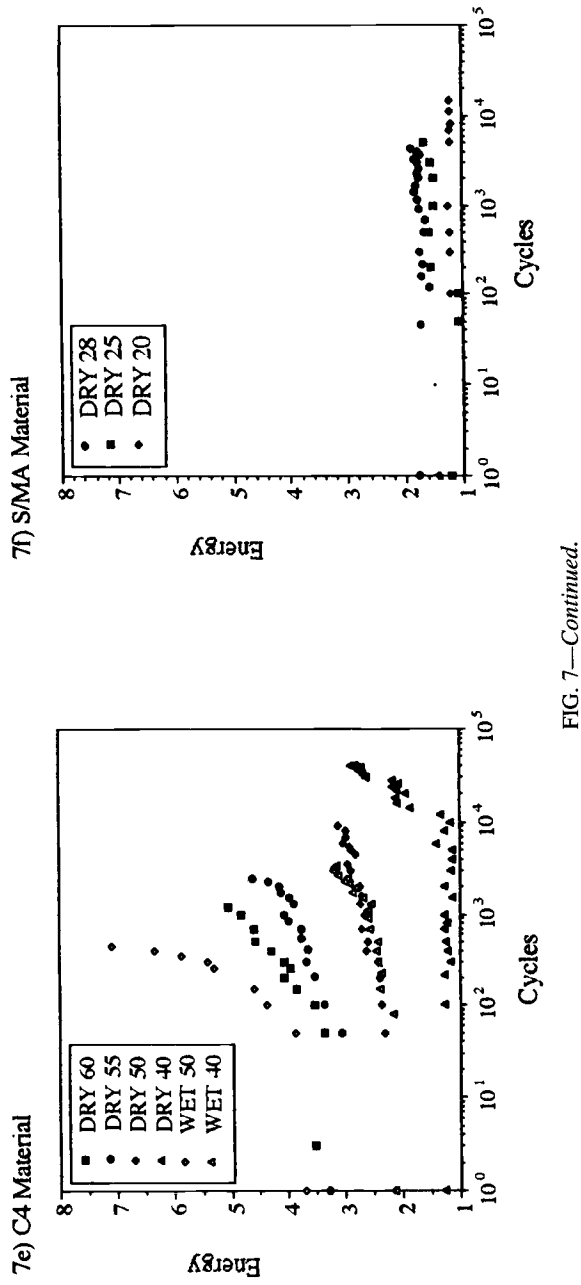

FIG. 7—*Continued.*

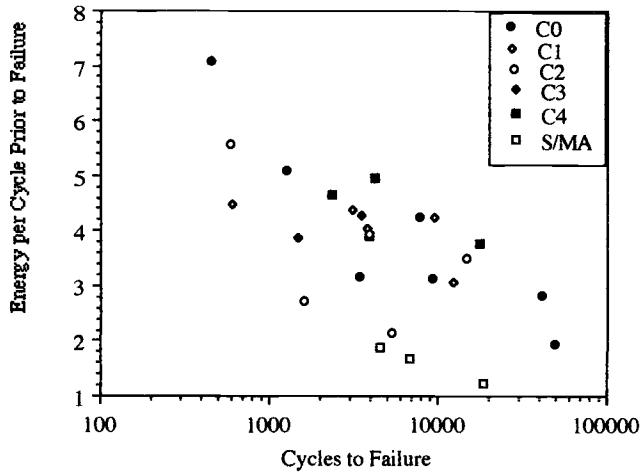

FIG. 8*a*—*Hysteresis energy at last cycle versus cycles to failure.*

Figure 9*a* shows a typical plot of the cumulative number of acoustic hits versus time during fatigue tests of two unreinforced S/MA specimens. Very few acoustic emissions were received during the tests. Since the materials underwent a large amount of plastic strain prior to failure, it is probable that the record of acoustic emissions is not representative of all of the damage in the material. The two main deformation mechanisms in this type of material (crazing and shear yielding [*25*]) may have produced acoustic emissions outside of the range that could be monitored with the experimental system.

Figure 9*b* shows the cumulative number of hits versus the normalized fatigue life for several samples of the composite material. Figure 9*c* shows the cumulative energy versus normalized life for the same specimens. The graphs show that in the beginning of the fatigue life (the first 10%) the events and energy are produced at a high rate. During the second stage, the rate of acoustic emissions is a generally lower, constant rate. Prior to failure, the rate at which emis-

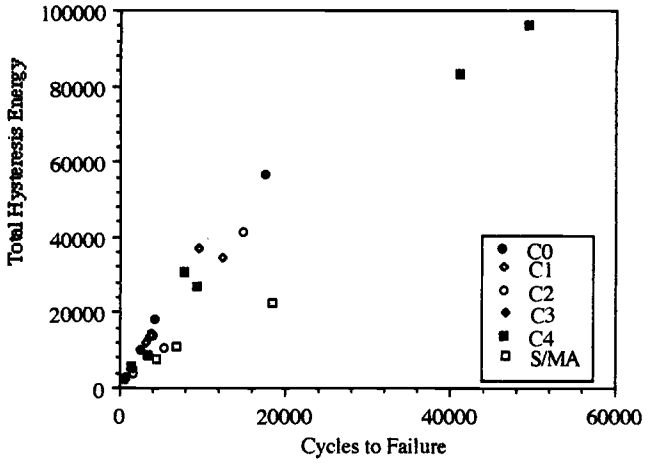

FIG. 8*b*—*Total hysteresis energy versus number of cycles to failure.*

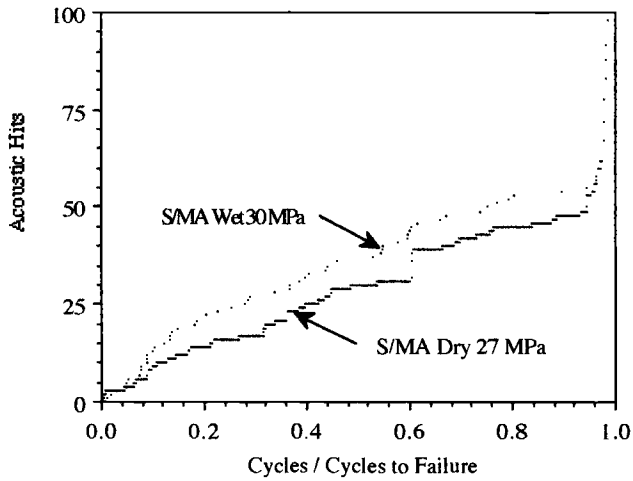

FIG. 9*a*—*Acoustic hits versus normalized cylces.*

sions are produced begins to increase markedly. During this third stage, the energy life curve tends to increase at a higher rate than the hit curve, indicating that the hits during this stage are generally higher in energy than those in the previous stages. At failure, a large number of hits and events are produced during the final fracture of the specimen.

Discussion

The fatigue behavior of the composites as manifested by the fatigue life curves showed much less scatter than the behavior of the unreinforced matrix material. The correlation coefficients for the *S-N* curves (given in Table 2) for the composites are all greater than 0.9, but, for the S/MA, the coefficients are less than 0.8 in both wet and dry conditions. The graphs of the moduli versus fatigue cycles (Fig. 5) and the hysteresis energy versus cycles (Fig. 7) also show more

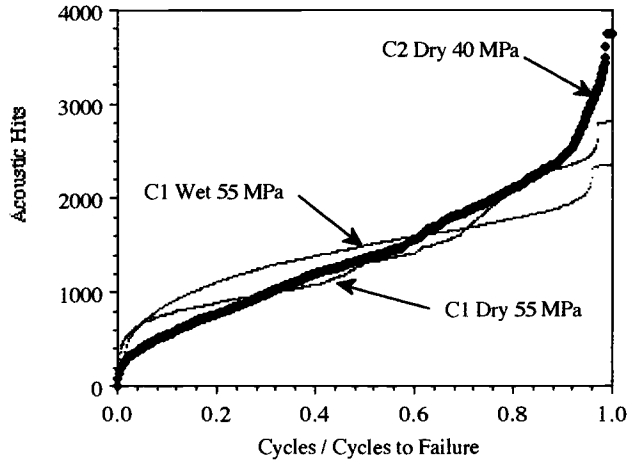

FIG. 9*b*—*Acoustic hits versus normalized cycles for composite specimens.*

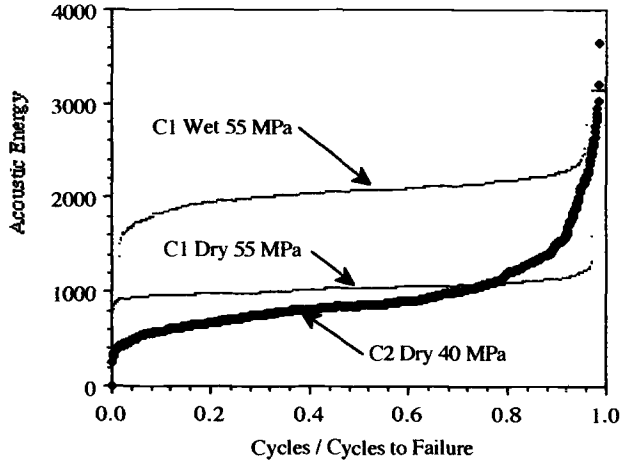

FIG. 9*c*—*Acoustic energy versus normalized cycles.*

scatter in the unreinforced material. Figures 5*f* and 7*f* demonstrate that there is very little change in the moduli or the hysteresis energy during the fatigue life. These results indicate that fatigue damage develops in a different manner in the composites than the unreinforced material. In the composites, the damage may initiate and grow from the regularly distributed fibers which serve as sites of stress concentration. This would cause the damage to grow more uniformly in the composites and cause macroscopic changes in the mechanical properties. The S/MA, which is a more homogeneous medium, does not contain the same regular array of stress concentration sources. Thus, the unreinforced material does not have the same pattern of distributed crack initiation and growth.

Comparison of Damage Evaluation Techniques

All three techniques of damage evaluation that have been used—change in moduli, hysteresis energy, and acoustic emission—show that damage develops in a three-stage process during fatigue. During the first stage, the moduli decrease at a high rate, the hysteresis energy per cycle increases rapidly, and acoustic emissions are generated throughout the fatigue cycle at a high rate. These trends indicate that a large amount of damage is occurring during this stage. All three of the evaluation techniques change at a much slower rate during the second stage when the damage appears to grow at a "steady-state" rate. In this final stage, the damage increases rapidly in the local area around the site of final failure. Since this third stage is highly localized, the three methods of evaluation do not show the rapid increase in damage to the same extent. The changes in moduli and hysteresis energy are found by measuring the stress applied to the specimen and the induced strain as measured with a 25.4-mm gage length extensometer. Thus, these methods of damage evaluation may not be sensitive enough to completely describe the local changes in the material properties. The acoustic emissions are much more sensitive to the local damage.

Figures 10*a* and 10*b* show the reduction in the secant and fatigue moduli of the materials (the values of the secant and fatigue moduli on the last recorded cycle divided by the value of the moduli on the first cycle) versus the total amount of hysteresis energy during each test. These graphs show that the materials that absorbed the lowest total amount of hysteresis energy had the highest degradation in moduli. The total hysteresis energy appears to be more a function

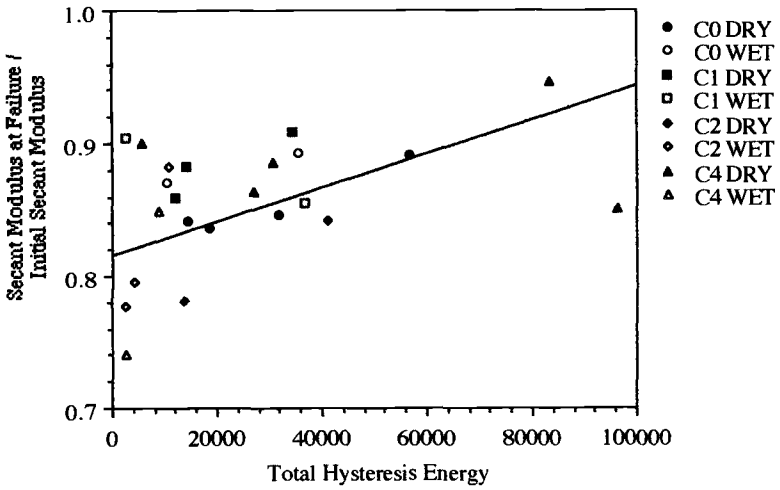

FIG. 10*a*—*Degradation of the secant modulus versus the total hysteresis energy during the fatigue tests.*

of the length of the fatigue test, while the degradation in moduli shows accumulated damage in the materials. During long tests, a large amount of hysteresis energy may be absorbed and dissipated through heat. However, during the long tests, the lower stresses do not cause as much degradation of the moduli as the high stresses during low-cycle fatigue.

In Figure 11, the total acoustic energy from each fatigue test is compared to the total hysteresis energy for each test. From this limited data, it is not possible to develop any direct correlation between these two parameters. However, there is a tendency for tests that produce larger amounts of hysteresis energy to also produce larger amounts of acoustic emission energy. More testing is needed to evaluate this trend.

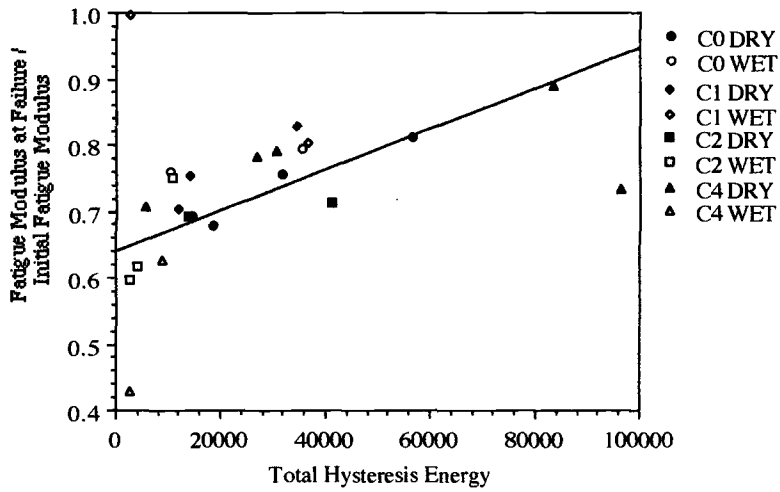

FIG. 10*b*—*Degradation of the fatigue modulus versus the total hysteresis energy during the fatigue tests.*

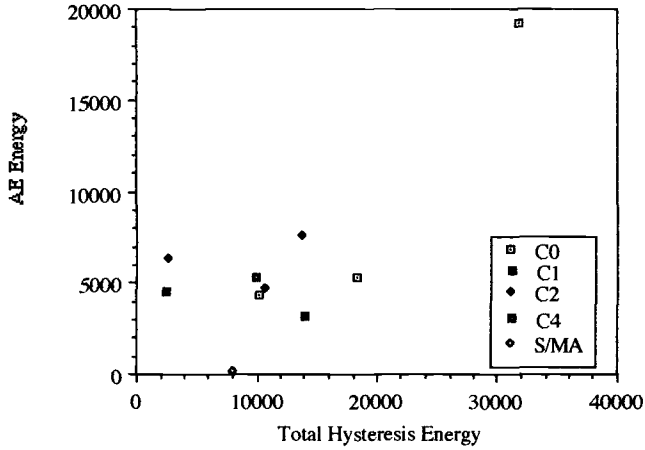

FIG. 11—*Total amount of acoustic energy versus the total amount of hysteresis energy generated during the fatigue tests.*

Conclusions

1. *S-N* curves for unreinforced S/MA indicate that moisture has very little effect on the fatigue life. However, water conditions significantly influence the fatigue life of fiber-reinforced S/MA, with the materials conditioned and tested in water displaying much shorter lifetimes than those conditioned and tested in a dry environment.

2. Coupling agents and other coatings applied to the glass fibers in the composites have a pronounced effect on the fatigue lives of the composite materials. Materials reinforced with fibers treated with a silane coating and a polyurethane sizing show the greatest strength retention in an aqueous environment. Materials for which the fibers received only a polyurethane sizing without silane or were coated with a butadiene-acrylonitrile (B/AN) latex to enhance ductility show much shorter fatigue lives when tested in water.

3. The degradation of secant and fatigue moduli, the increase in hysteresis energy, and acoustic emission have all been used to monitor damage growth in these materials. These methods reveal that the damage accumulates in a three-stage process similar to the behavior reported by Reifsnider et al. [*9,10*] for other composite materials.

4. The fatigue and secant moduli decay at higher rates and to lower values for materials tested in water; the hysteresis energies increase at higher rates and to higher values under wet conditions.

5. The secant and fatigue moduli at failure are not independent of the cyclic stress amplitude as proposed in other studies [*15,16*]. Rather, they tend to be progressively lower as the stress amplitude is increased, suggesting that more degradation in the mechanical properties is incurred at higher cyclic stresses prior to failure. The total hysteresis energy for each test increases proportionally to the number of cycles for each test.

6. At failure the total hysteresis energy absorbed by the materials is generally inversely proportional to the decrease in secant and fatigue moduli. A correlation between the AE data and the other damage parameters was not developed due to limited experimental data.

7. Further investigations should help to explain how fatigue damage develops in this material and provide more background on how these methods of nondestructive evaluation can be used to monitor cumulative damage and provide an acoustic warning of impending failure.

Acknowledgments

Funding for Christopher P. R. Hoppel's work was provided by a National Defense Science and Engineering Graduate Fellowship through DARPA. Monsanto Chemical Company, Inc. and PPG Fiberglass Industries, Inc. supplied the materials and fabricated the specimens employed in this study.

References

[1] Rotem, A., "Acoustic Emission Signature of Failure Modes," *Proceedings,* Second International Symposium on Acoustic Emission From Reinforced Composites, The Society of the Plastics Industry, Inc., Reinforced Plastics/Composites Institute, Montreal, Canada, 1986, pp. 112–116.

[2] Lang, R. W., Manson, J. A., and Hertzberg, R. W., "Mechanisms of Fatigue Fracture in Short Glass Fiber-Reinforced Polymers," *Journal of Materials Science,* Vol. 22, 1987, pp. 4015–4030.

[3] Jinen, E., "Accumulated Strain in Low Cycle Fatigue of Short Carbon-Fiber Reinforced Nylon 6," *Journal of Materials Science,* Vol. 21, No. 2, 1986, pp. 435–443.

[4] Martin, D. C., Novak, G. E., and Wyzgoski, M. G., "Fatigue Fracture of Reaction Injection Molded (RIM) Nylon Composites," *Journal of Polymer Science,* Vol. 37, 1989, pp. 3029–3056.

[5] Peterson, B. L., Pangborn, R. N., and Pantano, C. G., "Mechanical Behavior of Chopped Fiber Reinforced ABS at High Strain Rates," *ISTFA '89 Proceedings of the International Symposium for Testing and Failure Analysis,* 1989, pp. 419–427.

[6] Hofer, K. E., Skaper, G. N., Bennett, L. C., and Rao, N., "Effect of Moisture on Fatigue and Residual Strength Losses for Various Composites," *Journal of Reinforced Plastics and Composites,* Vol. 6, 1987, pp. 53–65.

[7] Lou, A. Y. and Murtha, T. P., "Environmental Effects on Glass Fiber-Reinforced PPS Stampable Composites," *Journal of Composite Materials,* Vol. 21, 1987, pp. 910–924.

[8] O'Brien, T. K., "Stiffness Change as a Nondestructive Damage Measurement," *Mechanics of Nondestructive Testing,* W. W. Stinchcomb, Ed., Plenum Press, New York, 1980, pp. 101–121.

[9] Reifsnider, K. L., Shulte, K., and Duke, J. C., "Long-Term Fatigue Behavior of Composite Materials," *Long-Term Behavior of Composites, ASTM STP 813,* T. K. O'Brien, Ed., American Society for Testing and Materials, Philadelphia, 1983, pp. 136–159.

[10] Stinchcomb, W. W. and Reifsnider, K. L.,"The Life-Limiting Process in Composite Laminate," *Basic Questions in Fatigue: Volume II, ASTM STP 924,* R. P. Wei and R. P. Gangloff, Eds., American Society for Testing and Materials, Philadelphia, 1988, pp. 294–303.

[11] Plumtree, A. and Shen, G., "Fatigue Damage Evolution and Life Prediction," *Composites—Design, Manufacture, Use, and Application, Proceedings,* Eighth International Conference on Composite Materials, Honolulu, 1991.

[12] Lee, L. J., Yang, J. N., and Sheu, D. Y., "Prediction of Fatigue Life for Matrix Dominate Composite Laminates," *Composites—Design, Manufacture, Use, and Application, Proceedings,* Eighth International Conference on Composite Materials, Honolulu, 1991.

[13] Echtermeyer, A. T., Buene, L., Engh, B., and Sund, O. E., "Significance of Damage Caused by Fatigue on Mechanical Properties of Composite Laminates," *Composites—Design, Manufacture, Use, and Application, Proceedings,* Eighth International Conference on Composite Materials, Honolulu, 1991.

[14] Hahn, H. T. and Tsai, S. W.,"On the Behavior of Composite Laminates After Initial Failures," *Journal of Composite Materials,* Vol. 8, 1974, pp. 288–305.

[15] Hahn, H. T. and Kim, R. Y., "Fatigue Behavior of Composite Laminate," *Journal of Composite Materials,* Vol. 10, 1976, pp. 156–180.

[16] Hwang, W. and Han, K. S., "Fatigue of Composites-Fatigue Modulus Concept and Life Prediction," *Journal of Composite Materials,* Vol. 20, No. 2, 1986, pp. 154–165.

[17] Xiao-Yan, T., De-Jun, W., and Hao, X., "Investigation of Cyclic Hysteresis Energy in Fatigue Failure Process," *International Journal of Fatigue,* Vol. 11, No. 5, 1989, pp. 353–359.

[18] Williams, R. S. and Reifsnider, K. L., "Investigation of Acoustic Emission During Fatigue Loading of Composite Specimen," *Journal of Composite Materials,* Vol. 8, 1974, pp. 340–355.

[19] Ishine, K., Nonaka, K., Hatsukano, K., and Shimamura, S., "A Contribution to Nondestructive Inspection of Fibrous Plastic Composites with an Emphasis on Application of AE Techniques," *Progress in Science and Engineering Composites,* Tokyo, 1982, pp. 1535–1542.

[20] Wolters, J., "Acoustic Emission Monitoring of Fracture Mechanisms in Short Fiber Reinforced

Thermoplastics: Basic Studies on Model Compounds," *Proceedings,* Second International Symposium on Acoustic Emission From Reinforced Composites, The Society of Plastics Institute, Montreal, Canada, 1986, pp. 29–36.

[*21*] Hoppel, C. P., Pangborn, R. N., and Tittmann, B. R., "The Use of Acoustic Emission to Monitor Fatigue Damage in Short Fiber Reinforced Thermoplastics," *Proceedings,* AECM-4, Fourth International Symposium on Acoustic Emission From Composite Materials, The American Society for Nondestructive Testing, Inc., 1992, pp. 79–88.

[*22*] Hall, W. J., Kruise, R. L., Mendelson, R. A., and Trementozzi, Q. A., "New Styrene-Maleic Anhydride Terpolymer Blends," *Proceedings,* 184th ACS National Meeting, American Chemical Society Division of Organic and Plastics Chemistry, 1982.

[*23*] Hwang, W. and Han, K. S., "Cumulative Damage Models and Multi-Stress Fatigue Life Prediction," *Journal of Composite Materials,* Vol. 20, No. 2, 1986, pp. 125–153.

[*24*] Chou, P. C. and Croman, R., "Residual Strength in Fatigue Based on the Strength-Life Equal Rank Assumption," *Journal of Composite Materials,* Vol. 12, 1978, pp. 177–194.

[*25*] Bucknall, C. B. and Marchetti, A., "A Novel Hysteresis Test for Studying Crazing and Shear Yielding in Rubber Toughened Polymers," *Polymer, Engineering and Science,* Vol. 24, No. 8, 1984, pp. 535–540.

R. Prasad Donti,[1] *James G. Vaughan,*[1] *and P. Raju Mantena*[1]

Effect of Pultrusion Process Variables on Cyclic Loading Damage of Graphite-Epoxy Composites

REFERENCE: Donti, R. P., Vaughan, J. G., and Mantena, P. R., **"Effect of Pultrusion Process Variables on Cyclic Loading Damage of Graphite-Epoxy Composites,"** *Cyclic Deformation, Fracture, and Nondestructive Evaluation of Advanced Materials: Second Volume, ASTM STP 1184,* M. R. Mitchell and O. Buck, Eds., American Society for Testing and Materials, Philadelphia, 1994, pp. 301–314.

ABSTRACT: Recent advances in pultruding composite materials have resulted in a high-performance, cost-effective manufacturing process. However, most research on pultruded products has centered on a specific application; a systematic study of the effects of various process variables on fatigue damage has not been conducted. The present study uses a fractional factorial statistical design to characterize the effects of pultrusion process variables and their interactions on the fatigue damage of pultruded graphite-epoxy. The composite material produced under the varying process conditions was subjected to tensile fatigue. The start and progress of damage mechanisms due to the loading and influenced by the processing conditions of the material are reflected by discernible changes in the loss factor (a measure of damping). The loss factor and modulus of the material were computed in real-time using computer methods. The changes shown by the loss factor are used to characterize the effects of the processing variables on the cyclic damage.

KEYWORDS: pultrusion, graphite-epoxy, fatigue, loss factor, modulus, regression, response volume

Pultrusion is one of the more cost-effective methods for producing composite materials such as graphite-epoxy. Pultruded composite materials have consistent mechanical properties, close dimensional tolerances, and excellent surface finish. They are used in a variety of engineering applications in which dynamic performance of the material (e.g., fatigue) is critical. Published literature on pultrusion provides information on the fatigue properties of composite material for a specified process condition. There has not been a systematic effort relating the effects of pultrusion process variables to the fatigue performance of the pultruded composite material. This paper reports the experimentally determined effects of the pultrusion process variables on fatigue damage in graphite-epoxy.

Pultrusion Process

The pultrusion of thermoset resins pulls fibers/mats from a creel system through a resin impregnation station and into a heated steel die that has been machined to the desired geometry. Heat initiates a chemical reaction in the thermoset resin and the reaction progresses under the influence of pressure within the die. Before the material exits the die, it usually achieves a high

[1] Graduate student (now at BP Chemicals Inc.), professor, and assistant professor, respectively, Department of Mechanical Engineering, The University of Mississippi, University, MS 38677.

degree of resin cure and fiber-matrix bonding. The composite material is continuously pulled by a mechanism that clamps and pulls. Though the process is simple by definition, the numerous process variables and their interactions influence the quality of the pultruded material and make it difficult to describe analytically.

Continuous reinforcements in the form of axial filaments and continuous-strand mat are used for producing pultruded materials. These fiber reinforcements have a strong influence on the mechanical properties of the material. However, due to their method of manufacture, the fiber properties are somewhat variable. The fibers are usually held in place in the composite material by resinous materials. The resin affects the chemical resistance of the composite material and provides a channel for the distribution of load between the fibers. The importance of the resin properties in an application such as fatigue loading cannot be overemphasized. Composite materials are commonly addressed as though they contain only fibers and a matrix in perfect union. It should be noted that there is an interface between them. The characteristics of the interface influence the mechanical properties of the composite material. However, the exact effect of the interface quality on fatigue properties is not completely understood [*1*].

The temperature profile of the pultrusion die and the process pull speed affects the properties of the pultruded composite materials. The resin-impregnated fiber reinforcement enters a heated die. Thermal energy is provided to the die by cartridge heaters. The pultrusion machine used for the current study has three heat zones with separate temperature control for the top and bottom part of the die. The three zone temperatures and the heat transfer conditions for the die yield a temperature die profile. A gradually increasing temperature profile is preferred to a constant die temperature in order to raise the temperature of the material to a temperature slightly less than the cure temperature and allow only a narrow temperature gradient from the surface to the interior of the material. The exotherm, due to the chemical reaction in the resin, brings the entire cross section of the material to the curing temperature after initiation of the curing on the outer surface and causes the material temperature to exceed the die temperature. The latter portion of the die receives the heat from the material to reduce the product temperature and thus minimize the thermal shock to the material as it exits the die. Under a proper set of process conditions, the resin achieves a high degree of cure. Curing of the composite with a higher degree of conversion improves the mechanical properties.

It is required that the fibers be pulled through the resin bath for impregnation of the resin and through the die for curing of the composite material in the desired geometry. The pull speed can be varied as required. However, the speed at which the material is pulled influences the location of the gelation point in the die. This directly affects the extent of cure in the composite material and thereby indirectly influences the mechanical properties of the pultruded composite material.

The above discussion on pultrusion process is presented to indicate that the pultrusion process variables affect the quality and the properties of the composite material when placed in fatigue applications. Fatigue is the cause of most failures in structural components and has attracted the attention of many researchers. These studies have resulted in a wealth of knowledge about failure by fatigue in metals; this is not the case for composite materials. Fracture mechanic failure theories can be used to explain most fatigue failures in metals by the initiation and propagation of a number of cracks into a single principal crack. However, there is no similar proven fracture mechanics failure theory to explain how early damage in composites leads to final failure.

Fatigue Damage

Damage in materials can be defined as the development of irreversible changes such as matrix cracking, fiber debonding, etc. These changes can occur due to a variety of reasons, including

thermal, chemical, radiation, and mechanical loads. The loading condition, tensile or compressive, and the loading direction with respect to the direction of fibers in the material influence the type of damage mechanisms in fatigue of composite materials. The damage mechanisms in tensile fatigue of unidirectional composites can be broadly classified [2] into: (1) fiber breakage, (2) fiber/matrix debonding, (3) matrix cracking, and (4) interfacial shear failure.

For the present study, the start and progress of damage in fatigue of pultruded composite materials was experimentally monitored using a damage index, a damping technique, and tape replication methods. The first two damage monitoring techniques require the measurement of load and strain. The load is measured using a load cell, while strain is usually monitored using strain gages for high precision. If the strain level is close to ± 3000 μ strain, dynamic strain gages are available for 10^5 test cycles. A reduced strain level allows the use of dynamic strain gages for test periods in excess of 10^5 test cycles. Fatigue testing of pultruded graphite-epoxy from 883 MPa (128 ksi) to 54.6 MPa (8 ksi) gave a maximum strain in the range of 6500 μ. This high strain level over hundreds of thousands of cycles for each test ruled out the use of strain gages for the strain measurement. Exploration of alternatives led to an extensometer recommended for dynamic applications. After a few trials, it was decided to use springs to mount the extensometer for reliable test results.

The effects of the process variables on the fatigue damage of pultruded graphite-epoxy were determined using modern statistical methods. These methods were employed in preference to the traditional one-factor-at-a-time method since the current study involves: (1) the interacting effects of numerous process variables, (2) the statistical nature of the fatigue properties, and (3) the development of complex damage state in the composite material.

Experimental Design

A basic statistical design may require the consideration of numerous variables for a detailed understanding about how a property of the material is affected [3]. However, time constraints and process economics usually limit the variables to only a significant few. Based on previous experience with pultrusion, the factors considered significant for the fatigue properties and included for this study were: (1) volume percent of graphite fibers, (2) process pull speed, (3) Zone 1 die temperature, (4) Zone 2 die temperature, and (5) Zone 3 die temperature.

The consideration of two levels for each of the five process variables over their permissible operating range allows the formulation of a linear mathematical model for a response. A level is a numerical value or set-point for a pultrusion experiment. Even at two different levels for each variable, a basic statistical design (e.g., a complete factorial design) requires 32 experiments for the five-variable study. However, a half fraction of a factorial design requires half as many experiments and can estimate principal factor effects and low-order interactions. However, fractional factorial designs confound a few factor interaction effects. Factor interactions exist when the effect of one factor on the response variable depends on the levels of the other factors.

Experimental runs for producing the material are randomized separately to limit systematic errors. The random sequence is noted in Table 1. The average values of a material property are subjected to regression analysis using SAS software routines [4]. Since the present analysis includes multiple independent variables, a multiple regression analysis technique is used to formulate a simple regression model

$$y = b_0 + b_1x_1 + \cdots + b_{12}x_1x_2 + \cdots \tag{1}$$

where b_0, b_1, b_{12} etc., in the model are estimates of unknown parameters. The least square estimates of the parameters are determined in the regression analysis.

TABLE 1—*Fractional factorial design test pattern.*

Test Plan Number	Random Plan Number	Test Variables				
		1	2	3	4	5
1	17	−1	−1	−1	−1	1
2	1	1	−1	−1	−1	−1
3	11	−1	1	−1	−1	−1
4	5	1	1	−1	−1	1
5	18	−1	−1	1	−1	−1
6	4	1	−1	1	−1	1
7	12	−1	1	1	−1	1
8	19	1	1	1	−1	−1
9	10	−1	−1	−1	1	−1
10	2	1	−1	−1	1	1
11	7	−1	1	−1	1	1
12	9	1	1	−1	1	−1
13	6	−1	−1	1	1	1
14	14	1	−1	1	1	−1
15	16	−1	1	1	1	−1
16	13	1	1	1	1	1

Key	−1	+1
*X*1 Graphite, %	60.9	63.3
*X*2 Pull speed, cm/s (in./min.)	0.42 (10)	0.59 (14)
*X*3 Zone 1 temperature, °C (°F)	165.6 (330)	176.7 (350)
*X*4 Zone 2 temperature, °C (°F)	182.2 (360)	193.3 (380)
*X*5 Zone 3 temperature, °C (°F)	182.2 (360)	193.3 (380)

In general, only selected terms are included in the model for simplicity and ease of graphical representation. However, the selection of the terms should not be arbitrary. Basic criteria followed in the selection of a parameter estimate are: (1) the "*p*" value associated with the parameter should be reasonably low, (2) addition of the parameter in the model should reduce unexplained variation without changing total variation, and (3) the addition of the parameter should increase adjusted R^2 [*5*]. A statistic such as adjusted R^2 decreases when the addition of a term doesn't improve the fit of the model; this is not the case, however, with R^2 [*4*]. It is cautioned against interpreting a large R^2 for the model as indicating that the application is very well defined [*5*]. The predictions by the model should be verified to determine if they offer sensible explanations for the application. A regression model such as Eq 1 can be graphically presented using response volume techniques. These techniques are helpful in showing regions of interest and obtaining optimum conditions.

Experimental Procedure

Graphite (Hercules' AS4-W-12K)-epoxy (Shell's EPON^R 9310/9360/537) composite material was produced under carefully monitored pultrusion process conditions as indicated in Table 1. Specimens were cut from the pultruded material and kept under a vacuum less than 1.33 Pa (10^{-2} torr). The specimens were randomly separated into three batches such that each batch consisted of one specimen from each set of process conditions. The average width and average thickness of the specimens were 0.0254 m (1 in.) and 0.0032 m (⅛ in.) and thus, differ from those recommended by ASTM Standard Test Method for Tensile Properties of Fiber-Resin

Composites (D 3039) for fatigue testing of 0° graphite fiber-reinforced composite material specimens. A specimen was removed from the vacuum chamber just before it was subjected to a fatigue test (a maximum load of 71.2 kN, a minimum load of 4.4 kN, and a test frequency of 4 Hz). Surfalloy-coated wedges, used in the present work, have allowed the fatigue test to be conducted without the use of tabs to the specimen [*6*]. A minimum of three specimens (one from each batch) were tested for each set of process conditions to determine an average response.

Outline of Testing

During each fatigue test, hysteresis loops were recorded at regular intervals. The loss factor (a measure of damping) was determined in real-time using a numerical integration routine, and the tensile modulus was computed from the loading and unloading stress-strain relationship. The maximum and minimum of the load, displacement (measured by a LVDT), the strain (measured by an extensometer), ambient temperature, and humidity were also recorded at regular intervals. The monitoring of extremes in the test variables was done to help explain any unusual developments in the damage measurements. Unless the specimen fractured, the test was continued for only 600 000 cycles due to time constraints. After one batch of specimens was subjected to fatigue, the next batch of samples was tested. The last sample for each set of process conditions was used for tape replicate observations. These observations are used to rationalize the changes noted in damage index and the measure of damping.

Damage Measurement Methods

Damping Method—Polymeric matrix composite materials are viscoelastic at temperatures even close to room temperature. This behavior causes a phase shift between load and strain and forms a hysteresis loop in a stress-strain diagram. A hysteresis loop approach, a dynamic mechanical property test method for metals and composite materials, is used to measure the loss factor [*7*]. Variations in the loss factor were used to monitor the energy dissipative mechanisms in composite materials such as short glass fiber-reinforced thermoplastics and sheet molding compounding material (SMC) [*8*].

The loss factor is determined as the ratio of dissipated energy to the energy stored at maximum displacement (shown in Fig. 1*a*) [*9*]

$$\eta = \frac{D}{2\pi U} \tag{2}$$

where η = loss factor, D = dissipated energy per cycle, and U = energy stored at maximum displacement. The loss factor was determined in real-time using the data acquired after a stabilizing period; fatigue test variables stabilized after a few hundred cycles from the start of the test. A computer method (developed in-house) determined the dissipated energy (area of the loop bounded by the loading and unloading segments) by numerically integrating the data samples of load and strain acquired for a loop [*10*]. Also, the computer method determined the maximum and minimum of the load and strain for any test cycle from which the energy stored at maximum displacement was computed. The ratio of these two energy terms provided the loss factor.

Damage Index—The microscopic damage developed in fatigue loading can lead to the decrease in modulus in fiber-reinforced composite materials. If the unloading modulus of the composite material degrades to a preset fraction of the initial modulus, the specimen is deemed

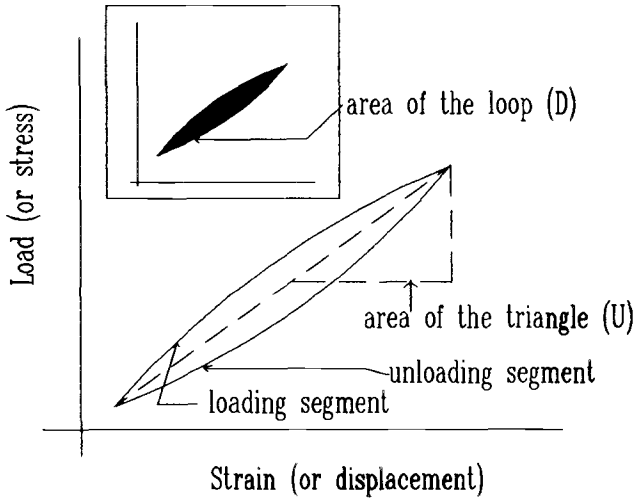

FIG. 1*a*—*Sketch of an exaggerated hysteresis loop.*

to have failed. The degradation of modulus in composite materials is usually monitored in terms of damage index (D) which is defined as

$$D = 1 - \left(\frac{\tilde{E}}{E}\right) \tag{3}$$

where E is the modulus of elasticity of the material in an undamaged state, and $\tilde{E}$ is the unloading elastic modulus of the material.

The data acquired for the loops during fatigue tests were post processed to determine the initial modulus after the stabilizing period and unloading modulus for any subsequent fatigue cycle. For mathematical simplicity, the initial modulus was determined as the slope of the center portion of the loading segment of a fatigue cycle

$$E = \frac{L_{max} - L_{min}}{A(S_{max} - S_{min})} \tag{4}$$

where E = extensional modulus, A = specimen cross-sectional area, L_{max} = maximum load, L_{min} = minimum load, S_{max} = maximum strain, and S_{min} = minimum strain. This modulus value was not significantly different from the modulus based on the slope of the first part of the loading segment of the fatigue cycle. This indicates the highly linear relationship between load and strain of the pultruded graphite-epoxy. Even the unloading segment was highly linear. The unloading modulus also was determined as the slope of the center portion of the unloading segment of a fatigue cycle. This was not significantly different from the modulus based on either end point of a hysteresis loop as the modulus measured from the first part or any part of the unloading segment was almost identical. Modulus change was computed as the difference between the initial modulus and the unloading modulus of the last cycle.

Replication Technique—Surface replication by cellulose tape is a standard technique used to follow the initiation and progression of damage [*11*]. The surface replication method was used to monitor the surface damage. The replicate tape can be observed under the scanning

electron microscope or an optical microscope [*12*]. Before the start of a test, the surface record of a test sample was obtained using replication cellulose acetate tape. Also, a surface record of the sample under load was obtained using the tape at the conclusion of its fatigue test. The two replicas were observed under a stereo microscope with an aluminum background for an increased contrast and were compared for any microstructural differences. Only qualitative observations were made, and thus, a statistical analysis was not conducted for the observed surface damage. Multiple surface replicas of unloaded test samples taken over an extended time frame showed no observable changes.

Results and Discussion

Fatigue testing of all the samples took several months of machine time. Two of the properties examined for further analysis are: (1) change in modulus due to fatigue testing, and (2) the trend and magnitude of change in loss factor during the fatigue test of the graphite-epoxy. The regression models developed for a property are graphically represented in a control volume plot. Three of the principal variables in the model are represented on three different axes. The origin of the control volume corresponds to a code value of -1 (lower limit) of a variable, and the other end of each axis corresponds to a code value $+1$ (upper limit) of the variable. Two separate plots are provided for a property to show upper and lower ends of its spectrum of values.

In the following sections of discussion, test samples are identified by sample numbers. The first two digits of the sample number indicate the random experiment number, and the last two digits of the sample number indicate the piece number of the 1.52-m (5-ft.) section in the overall length of the pultruded product for that set of process conditions. Every specimen was to have a test duration of 600 000 fatigue cycles. A few specimens fractured or developed a large grip-induced delamination that caused an early termination of their tests. The grip-induced delamination moved the extensometer attachment springs, causing extremely large spikes in the strain readings. These strain spikes were not included in the analyzed data sets.

Modulus Degradation

Modulus degradation is defined as the difference in the end modulus from the initial modulus for each specimen. The end modulus is the slope of the center portion of the unloading segment of the last cycle. The average difference in the modulus can be found in Table 2. In most cases, the change in modulus is less than 0.5% of the initial modulus. Calibration sheets on the load cell and the extensometer report that there is an error of 0.165% in the load cell and about 0.15% error in the operating range of the extensometer. The combined error could reduce the modulus by about 0.27% and increase the modulus by about 0.37%. If data transmission errors are also counted into error analysis, the change in modulus in all the cases is not significant. Since the change in modulus was not significant for most of the cases, statistical analysis was not conducted on these values.

Change in Loss Factor of Graphite-Epoxy

The pultruded graphite-epoxy specimens exhibited narrow hysteresis loops. Figure 1*b* shows a hysteresis loop with a relatively large opening for the graphite-epoxy (a loss factor of 6.4×10^{-3}). It shows the loading segment as a solid line and the unloading segment as a broken line to identify the two segments. It can be noted that it would be difficult to manually measure the loop characteristics accurately. This difficulty prompted the use of the computer-based methods to determine the loss factor in real-time during the course of a fatigue test at regular intervals.

TABLE 2—*Fatigue test results of graphite-epoxy.*

Test Plan Number	Initial Modulus, GPa (10^6 psi)		Change in Modulus, GPa (10^6 psi)		Area Units
1	136.00	(19.72)	0.34	(0.049)	1449.6
2	141.20	(20.48)	−0.46	(−0.066)	1694.9
3	135.38	(19.63)	0.41	(0.060)	675.6
4	138.97	(20.15)	−1.01	(−0.147)	1264.2
5	137.93	(20.00)	0.48	(0.069)	803.3
7	138.28	(20.05)	−0.66	(−0.095)	1286.3
8	141.24	(20.48)	−0.46	(−0.067)	1279.5
9	137.93	(20.05)	−0.80	(−0.116)	1129.8
10	143.52	(20.81)	0.57	(0.083)	1057.5
11	137.52	(19.94)	−0.17	(−0.025)	982.4
12	138.69	(20.11)	−0.77	(−0.112)	1512.4
13	137.24	(19.90)	−1.43	(−0.208)	1142.4
14	141.03	(20.45)	0.71	(0.103)	1235.6
15	139.52	(20.23)	−0.29	(−0.042)	1507.3
16	143.24	(20.77)	0.10	(0.015)	1563.7

The loss factor showed different trends for the test samples. However, the trends in loss factor were broadly divided into three different types: (1) a gradual increase in loss factor until a maximum value, then fairly unchanged to the end of the test (Fig. 2); (2) a gradual increase, then a gradual decrease to a minimum value and then without a significant trend till the end of the test (Fig. 3); and (3) a fairly unchanging loss factor trend (Fig. 4).

To rationalize the changes in loss factor, the surface features (using the tape replication

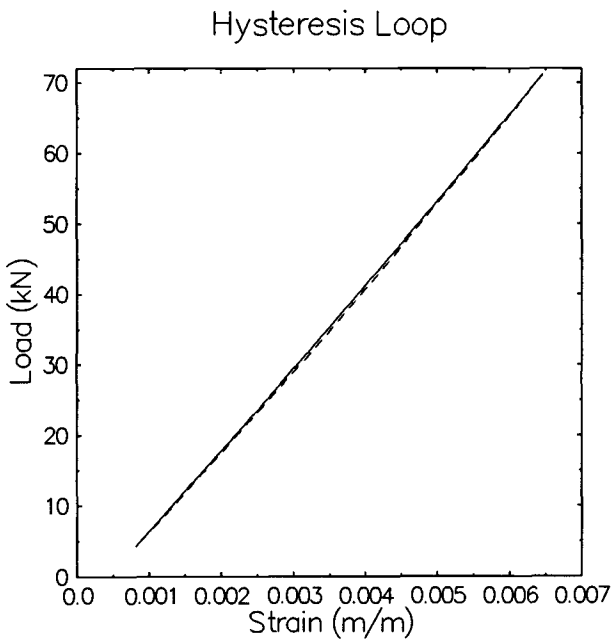

FIG. 1*b*—*A hysteresis loop of pultruded graphite-epoxy.*

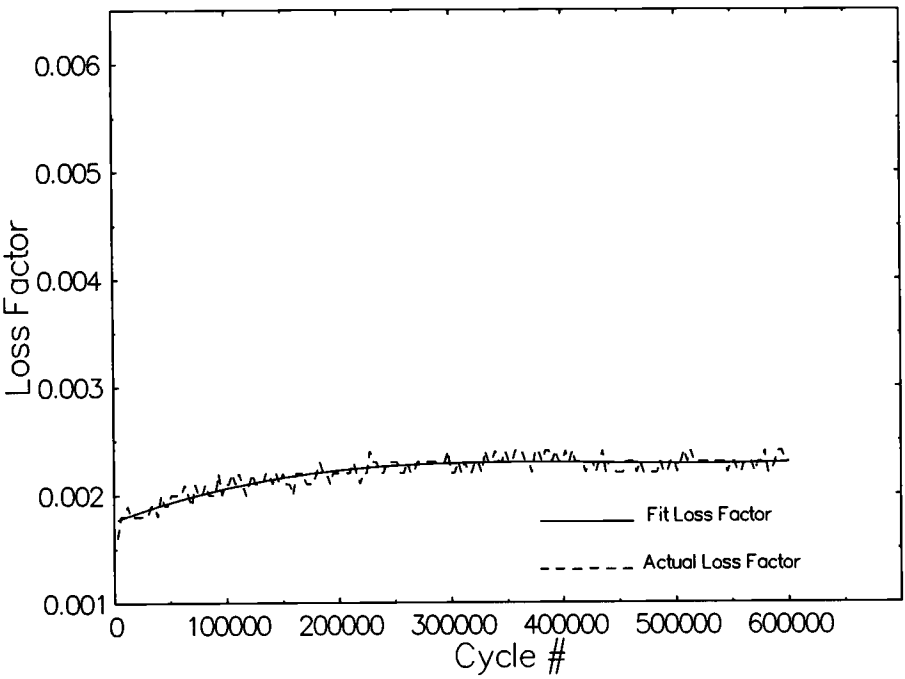

FIG. 2—*Loss factor trend for sample No. 0901.*

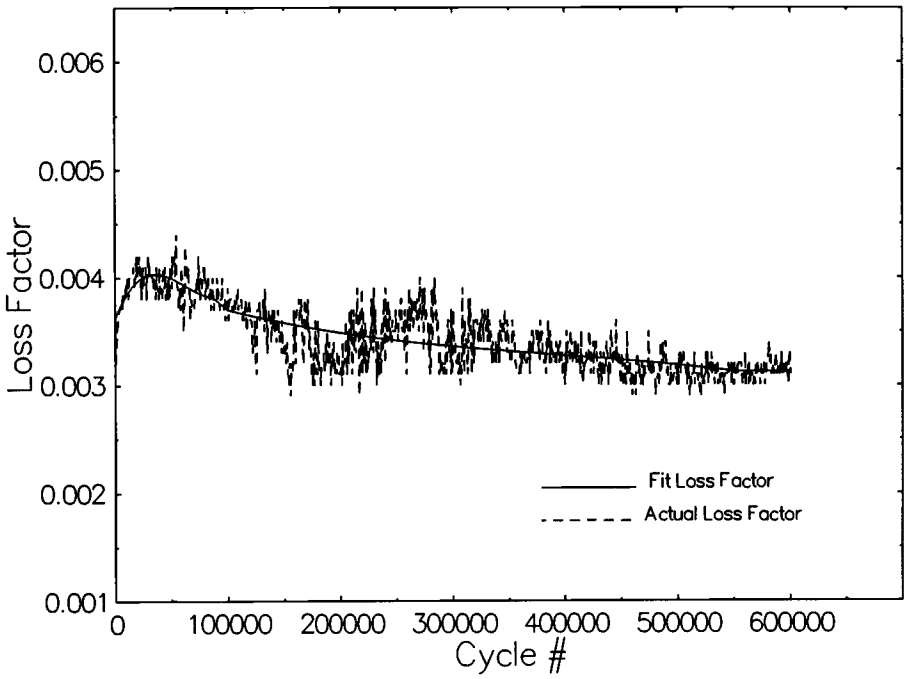

FIG. 3—*Loss factor trend for sample No. 1705.*

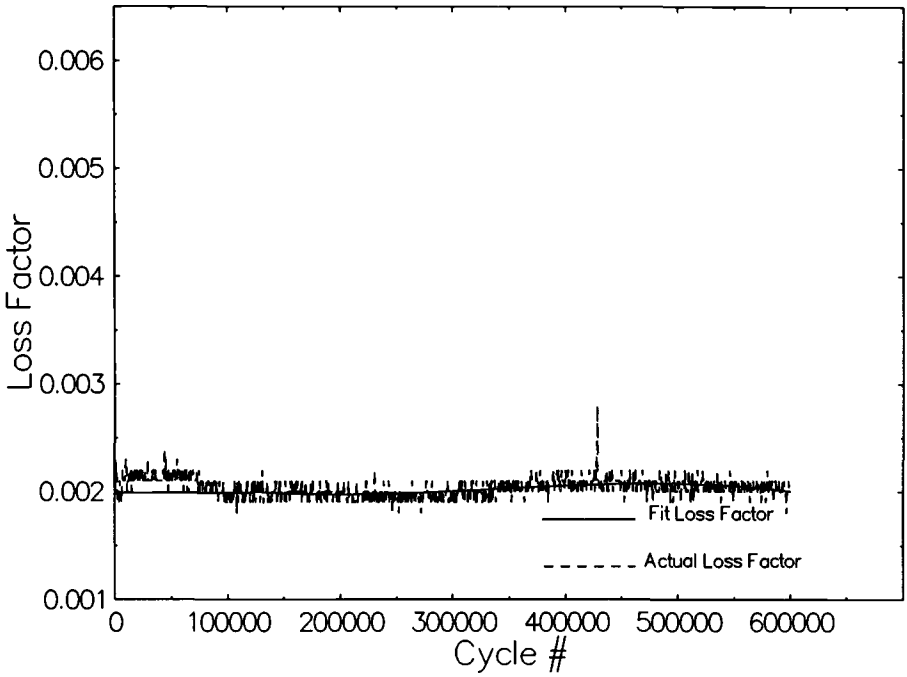

FIG. 4—*Loss factor trend for sample No. 0604.*

technique) of specimens taken before the start and at the end of the fatigue test were closely examined under a stereo microscope. Figure 5*a* is a photomicrograph of the replica taken before the start of the experiment for sample No. 0604. No unusual microstructural features can be noted in Fig. 5. The micrograph shows the continuous fibers and their distribution on the surface of the material. Almost all the samples showed identical microstructural features. However, changes were noted for different samples in the replicas taken at the end of their fatigue tests. Figure 6 is a photomicrograph of the replica (inclined for an increased contrast) taken at the end of the fatigue test for sample No. 1305. Numerous surface crazes can be noted in the direction of fibers in Fig. 6. A few surface crazes are identified by arrows in Fig. 6. The samples that displayed the loss factor trend as shown in Fig. 2 showed microstructural features as in Fig. 6 or a minor variation of Fig. 6.

Figure 5*b* is a photomicrograph of the replica taken at the end of the fatigue test for sample No. 0604. Comparison of this micrograph with Figure 5*a* reveals no significant variations in the microstructural features. This offers a possible explanation for a negligible change in loss factor as observed in Fig. 4. However, it should be mentioned that the replica showed a very small amount of surface crazing in the direction of fibers at a few other locations.

Loss factor trends as depicted in Fig. 3 can be explained based on the discussion of similar loss factor trends reported in the literature. The rising portion of the trend was attributed to the formation of new microcracks, and the falling portion of the trend was attributed to smoothing of crack surfaces and the cessation of the crack formation [*8,13,14*]. It is possible that the features of the surface crazes became smoother during the course of the fatigue test or fine cracks reached a saturation limit. Since the surface features were obtained only at the start and at the end of a test, it would be difficult to offer a more complete explanation about what happened during the course of the test.

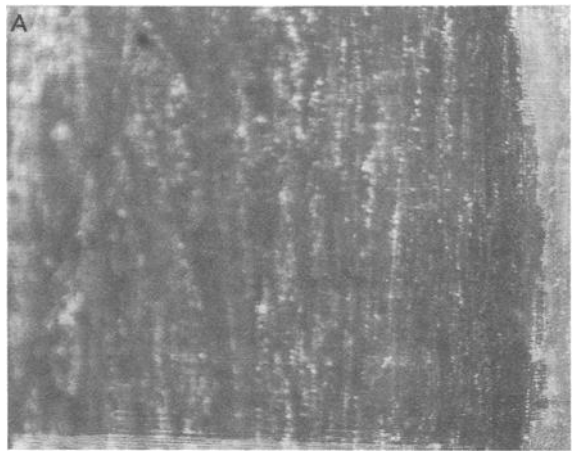

FIG. 5*a*—*Photomicrograph of replica of sample No. 0604 before its fatigue test (×34).*

Statistical Analysis—The change in loss factor is continuous in nature. Since the responses subjected to the statistical analysis are usually discrete in nature, continuous data must be reduced to a meaningful data form before the statistical analysis is conducted. After careful consideration, it was decided to determine the area between a loss factor curve and a reference base line with a Δ of 2×10^{-3} from its initial loss factor. The area determined thus would quantify only the trend and the magnitude in the change in loss factor without the influence of initial loss factor (since the initial loss factor was also affected by the pultrusion process variables [*15*]). This procedure was used to compute areas for all loss factor curves. Computation of the average of the areas for the samples pertaining to the same set of process conditions with the same test duration was straightforward. When the samples pertaining to the same set

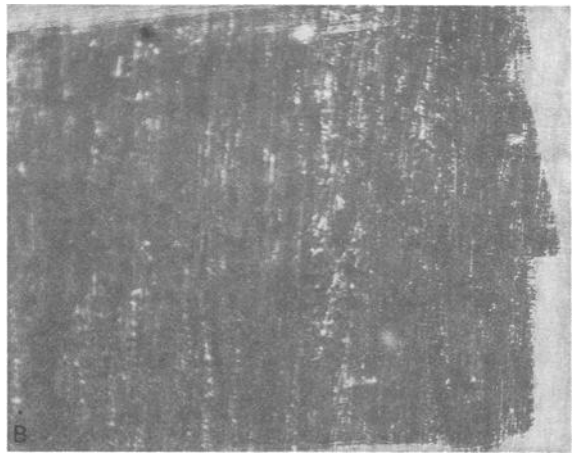

FIG. 5*b*—*Photomicrograph of replica of sample No. 0604 after its fatigue test (×34).*

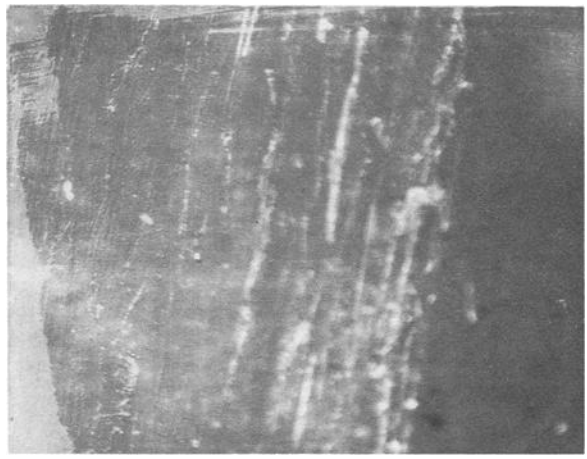

FIG. 6—*Photomicrograph of replica of sample No. 1305 after its fatigue test (×34).*

of process conditions didn't have the same test duration (due to a fracture or a large delamination), a logical procedure that noted the differences in the test duration was employed to compute the average of the areas. The following example explains the procedure used. If the test durations of the three samples (e.g., T_1, T_2, T_3) are such that $T_1 = T_3 > T_2$, then the areas under all three curves up to time T_2 were determined and averaged as $A1$. From interval T_2 to T_1 ($=T_3$), only the areas under curves of Samples 1 and 3 were determined. These two areas were averaged as $A2$. Summation of $A1$ and $A2$ provided the overall process condition average.

When the specimens corresponding to the same set of process conditions showed identical features in change in loss factor, area values were reasonably close in magnitude. When the specimens corresponding to the same set of process conditions showed a few different features in the change in loss factor, the area values in those cases were not close in magnitude. Table 2 provides the average areas.

The average areas were subjected to regression analysis. The variables that estimated best the actual values were included for the regression model. The variables included are fiber volume ($X1$), its interaction with Zone 2 die temperature ($X14$), interaction of pull speed with Zone 1 die temperature ($X23$) and with Zone 2 die temperature ($X24$), and interaction between Zone 1 and Zone 2 die temperatures ($X34$). Addition of other process variables did not improve the model. Pull speed ($X2$) affects the residence time of the fibers and resin in the die including the Zone 1 region. Zone 1 die temperature affects the viscosity of the resin before gelation of the material and indirectly influences the mobility of the fibers. The residence time and the mobility of the fibers (due to the interaction of $X2$ and $X3$) affect the fiber distribution in the material. Zone 2 die temperature and its interaction with the pull speed affect the nature of the interface between resin and the fibers. A high-fiber volume contributes to tighter packing of fibers and reduces the average fiber spacing. Under load, the uneven fiber distributions and reduced fiber spacing cause stress concentration and probably affect fiber/matrix bonding and start fine cracks in the material [*16*].

The regression model obtained using the average areas is graphically presented in Fig. 7. Figure 7*a* is a response volume plot holding fiber volume at its worst point for high damage. This region is located in two opposite corners of the control volume. Low Zone 2 die temperature and low Zone 1 temperatures, when pull speed is low, provide similar fiber distribution

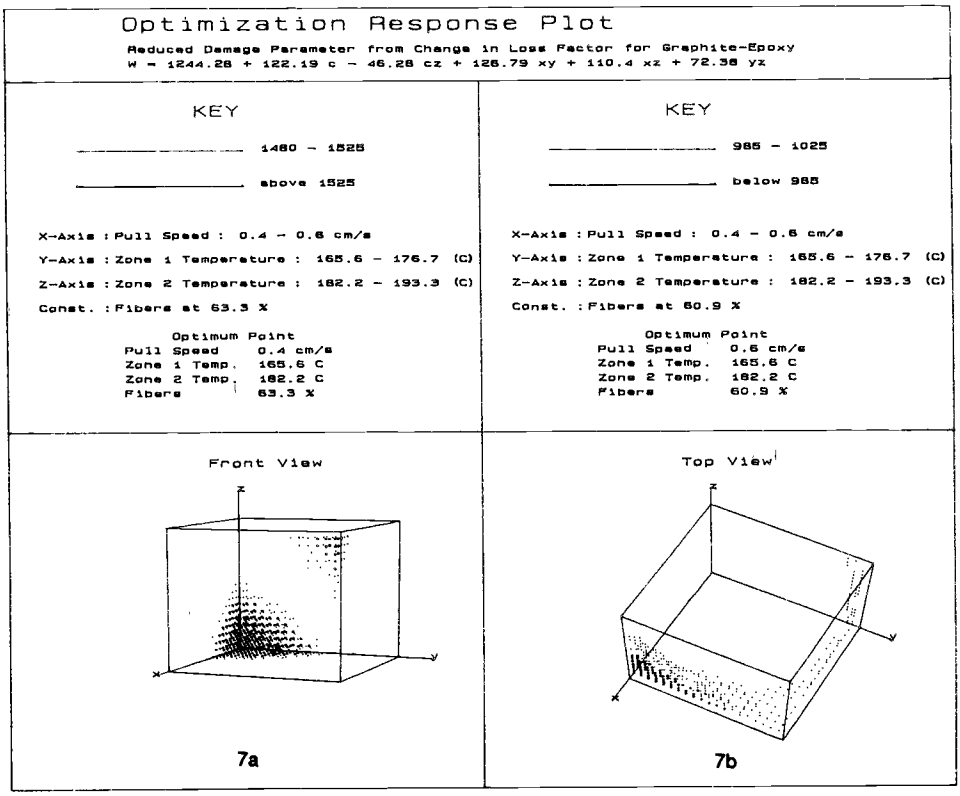

FIG. 7—(a) *Response volume plot for high damage in graphite-epoxy, and* (b) *response volume plot for low damage in graphite-epoxy.*

and resin/matrix interface as settings of high Zone 2 die temperature and high Zone 1 temperature at high pull speeds. When pull speed and die Zone 2 temperatures are low, the fiber/matrix interface would not be very strong. The increased mobility of the fibers due to high Zone 1 temperature, and the reduction in residence time of the fibers and resin by higher pull speeds compete with each other and may not allow a highly uniform fiber distribution. Intermediate interface strength, less uniform fiber distributions, and reduced fiber spacing very likely contribute to more changes in the microstructural features due to fatigue loading.

Figure 7*b* is a response volume plot holding fiber volume at its optimum point for low damage. It is noted that the optimum region for low damage is located in the region of high pull speeds and low die Zone 2 temperature over the complete range of die Zone 1 temperature. However, the optimum region changes to higher Zone 1 temperatures at lower pull speeds. The increased mobility of the fibers due to high Zone 1 temperatures and increased residence time of the fibers and resin at lower pull speeds produce more even fiber distributions in the microstructural features. Low Zone 2 temperatures at high pull speeds possibly help in forming a more flexible interface between fiber and matrix, and high die Zone 2 at low pull speed probably aids in forming a stronger interface between the fiber and matrix. Either a flexible or a stronger interface with less uneven distributions and increased fiber spacing would cause fewer changes in the microstructural features.

Conclusions

A thoughtful fatigue test methodology was employed for conducting extensive tests on pultruded graphite-epoxy. The use of computer methods offered enormous time savings in the analysis of fatigue results. Test results show that the processing conditions affect the quality and mechanical properties of the pultruded end product. Statistical methods have been used in characterizing these effects of process variables on fatigue damage in graphite-epoxy. A material damping measurement technique showed a higher sensitivity than a damage index method in monitoring the fatigue damage in unidirectional graphite-epoxy. Replication observations were used in rationalizing the damage parameters.

Acknowledgments

The authors are grateful for the support of the National Science Foundation and the Mississippi EPSCoR program; this work has been funded by the National Science Foundation under Grant EHR-91-08767. We also appreciate the help provided by Shell Development Company.

References

[1] Konur, O. and Matthews, F. L., "Effect of the Properties of the Constituents on the Fatigue Performance of Composites: A Review," *Composites,* Vol. 20, No. 4, 1989, pp. 317–328.

[2] Talreja, R., *Fatigue of Composite Materials,* Technomic Publishing Company, Inc., Warrendale, PA, 1987, pp. 27–80.

[3] Box, G. E. P., William, G. H., and Stuart, J. H., *Statistics for Experimenters,* John Wiley & Sons, Inc., New York, 1978.

[4] Freund, R. J. and Littell, R. C., *SAS*[R] *System for Regression,* 2nd ed., SAS Institute, Inc., 1991..

[5] Bowerman, B. L. and O'Connell, R. T., *Linear Statistical Models: An Applied Approach,* PWS-KENT Publishing Company, 1990.

[6] "New Wedges Adapt 647 Grips to Composites," *MTS*[R] *Testing News,* Vol. 8, No. 10, 1990.

[7] Gibson, R. F., "Vibration Test Methods for Dynamic Mechanical Property Characterization," *Experimental Mechanical Testing of Composites,* Society of Experimental Mechanics, 1989, pp. 151–164.

[8] Orth, F., Zysk, Th., Janzen, W., and Ehrenstein, G. W., "Fatigue Behavior of RP Described by Hysteresis Measurements," *Proceedings,* 45th Annual Conference, Composites Institute, The Society of Plastics Industry, Inc., 1990.

[9] Mantena, P. R., Gibson, R. F., and Place, T. A., "Damping Capacity Measurements of Degradation in Advanced Materials," *SAMPE Quarterly,* Vol. 17, No. 3, 1986.

[10] Donti, R. P. and Vaughan, J. G., "A Computer Method for Determining Damage During Fatigue Testing of Composite Materials," *Proceedings,* Tenth Annual Conference, UPCAEDM '92.

[11] "Destructive and Nondestructive Tests," *Engineered Materials Handbook,* ASM International, Metals Park, OH, Vol. 1, 1987, pp. 774–778.

[12] Mantena, P. R., Place, T. A., and Gibson, R. F., "Characterization of Matrix Cracking in Composite Laminates by the Use of Damping Capacity Measurements," *Role of Interfaces on Material Damping,* American Society of Metals, Metals Park, OH, 1985.

[13] Orth, F., Zysk, Th., Janzen, W., and Ehrenstein, G. W., "Hysteresis Measurements for Receiving Characteristic Quantities during Dynamic Fatigue," *Proceedings,* 2nd International Conference on Testing, Evaluation, and Quality Control of Composites, 1987.

[14] Renz, R., Altstadt, V., and Ehrenstein, G. W., "Hysteresis Measurements for Characterizing the Dynamic Fatigue of R-SMC," *Journal of Reinforced Plastics and Composites,* Vol. 7, 1988, pp. 413–432.

[15] Mantena, P. R., Vaughan, J. G., Donti, R. P., and Kowsika, M. V., "Influence of Process Variables on the Dynamic Characteristics of Pultruded Graphite-Epoxy Composites," *Proceedings,* International Symposium on Vibroacoustic Characterization of Materials and Structures, ASME Winter Annual Meeting 1992, American Society of Mechanical Engineers, New York.

[16] Slattery, K. T., "A Statistically Based Model of the Interacting Processes which Lead to Creep-Rupture in Filament-Wound Composite Pressure Vessels," Ph. D. dissertation, University of Mississippi, University, MS, December 1989.

David A. Stubbs,[1] *Stephan M. Russ,*[2] *and Patrick T. MacLellan*[1]

Examination of the Correlation Between NDE-Detected Manufacturing Abnormalities in MMCs and Ultimate Tensile Strength or Thermomechanical Fatigue Life

REFERENCE: Stubbs, D. A., Russ, S. M., and MacLellan, P. T., **"Examination of the Correlation Between NDE-Detected Manufacturing Abnormalities in MMCs and Ultimate Tensile Strength or Thermomechanical Fatigue Life,"** *Cyclic Deformation, Fracture, and Nondestructive Evaluation of Advanced Materials: Second Volume, ASTM STP 1184,* M. R. Mitchell and O. Buck, Eds., American Society for Testing and Materials, Philadelphia, 1994, pp. 315–334.

ABSTRACT: Titanium matrix composites containing manufacturing abnormalities were examined using ultrasonic and X-ray nondestructive evaluation techniques. The $[0/90]_s$ and $[0/90]_{2s}$ SCS-6/β21-S specimens were subjected to 650°C tension or thermomechanical fatigue tests to assess any degradation in strength or fatigue life due to the abnormalities. The usefulness of ultrasonic nondestructive evaluation to assess the integrity of the composites containing manufacturing abnormalities was shown through the correlation of the ultrasonic data with ultimate tensile strength and thermomechanical fatigue life. Additionally, the use of X-ray radiographic nondestructive evaluation appears to complement the ultrasonic data and is useful for analyzing fiber displacement, orientation, and nonparallelism. A simple damage parameter was developed to help quantify the ultrasonic NDE data from manufacturing abnormalities within the material. The test results on the specimens containing manufacturing abnormalities are presented with analysis of the degree of correlation between the NDE results and tensile strength and/or thermomechanical fatigue life.

KEYWORDS: metal matrix composites, nondestructive evaluation, ultrasonics, X-ray, thermomechanical fatigue, manufacturing defects

Nondestructive evaluation (NDE) techniques have historically been used to detect processing flaws, inherent defects, and damage such as cracks in metallic materials and more recently for manufacturing and service-induced defects in organic matrix composites. Techniques frequently used are visual, ultrasonic C-scan, X-ray, eddy current, dye penetrants, acoustic emission, and magnetic particle inspection. Applying any of these techniques to metal matrix composites (MMCs) poses several challenges. Differences in mechanical properties of the matrix and fiber constituents, such as density and modulus, complicate interpretation of ultrasonic NDE results. Second, the fiber diameters can be on the order of the ultrasonic wavelength which increases the ultrasonic scattering. Third, the damage mechanisms generally cause more subtle defects such as matrix cracking, fiber-matrix interface separation, and individual fiber cracking rather than ply delaminations or groups of broken fibers commonly found as defects in polymeric composites. To date, only visual inspection of MMC panels is performed routinely by researchers interested in the mechanical properties of these materials.

[1] University of Dayton, 300 College Park, Dayton, OH 45469-0128.
[2] Wright Laboratories/Materials Directorate, Materials Behavior Branch, Wright-Patterson AFB, OH.

Advances in the processing of metal matrix composites (MMCs) have resulted in the ability to produce flat panels from which dozens of mechanical specimens can be machined. Specimens are typically 150 to 500 mm^2, where panel dimensions can be as large as a square metre. Visual examination of a panel prior to cutting specimens out of it occasionally results in an area being avoided due to observed abnormalities such as wrinkles, exposed fibers, cracking, and "fiber swimming." Fiber swimming is a term used to refer to a location where several fibers have noticeably deviated from the desired orientation. In these instances there is generally agreement on the "good" and "bad" regions of an MMC panel; researchers can see the abnormality and are comfortable with using only specimens machined from areas passing visual inspection.

The introduction of additional nondestructive techniques having the capacity to gather information on the internal structure of the MMCs initially complicates the screening process. Areas of the panel designated as "good" through the visual inspection process may contain abnormalities detected by the additional NDE techniques. Presently, NDE techniques such as ultrasonics and X-ray yield only qualitative information on the integrity of material. There exists almost no information equating NDE results to property changes in MMCs. Without knowledge of the correlation between NDE results and material properties, the researcher often takes a conservative approach and chooses not to use material having NDE-detected abnormalities. However, often there is not the luxury of choosing between completely "good" material and material containing NDE-detected abnormalities due to the limited supply and excessive cost of advanced MMCs. The work described in this paper represents initial efforts to evaluate the correlation between NDE data and specific tensile and fatigue properties in a titanium matrix composite. The ultimate goal is to use the NDE techniques to quantitatively assess the integrity of MMCs.

Material

The titanium matrix composite used for this study consisted of silicon carbide (SCS-6) fibers in a Ti-15Mo-2.6Nb-3Al-0.2Si matrix (designated β21-S). The fiber diameter is nominally 0.142 mm. The matrix alloy was developed for its improved oxidation resistance and processing capability compared with other titanium MMCs. The composites were made by the method of foil-fiber-foil layups with subsequent hot isostatic processing. There is considerable information published about this composite and its constituents as well as the processing method; Refs *1* and *2* contain many articles for additional information. The specimens used in this study contained a cross-plied layup. Five specimens were cut from a $[0/90]_s$ panel and eight were from a $[0/90]_{2s}$ panel. The specimens were cut to be approximately 110 mm long and 12 mm wide. The typical thickness of the $[0/90]_s$ specimens was 0.82 mm, while the thickness of the $[0/90]_{2s}$ specimens was 1.86 mm. The $[0/90]_{2s}$ specimens were manufactured with a molybdenum cross-weave. The cross-weave maintains appropriate fiber spacing and alignment in the production of the fiber mats. The $[0/90]_s$ specimens were constructed with a titanium-niobium cross-weave. All specimens were fabricated using the foil-fiber-foil technique and hot isostatic processing. None of the specimens had any type of coating.

Figure 1*a* shows a photograph of the surface of the $[0/90]_{2s}$ specimens arranged in their relative position to the others before cutting. Several surface wrinkles are evident in this photograph. A photomicrograph of a specimen edge at a wrinkle location is shown in Fig. 1*b*. The depth of the wrinkles ranged from 0.05 to 0.20 mm with widths nominally 1 mm. Frequently in the photomicrographs of a specimen edge, the 0° fibers were observed to be fractured in the region of a wrinkle.

Figure 2*a* shows photographs of the surface of the $[0/90]_s$ specimens. These specimens contained very subtle wrinkles or waves running across the width of the specimens. The wrinkles were visible only if seen under proper lighting conditions. Casual visible inspection often

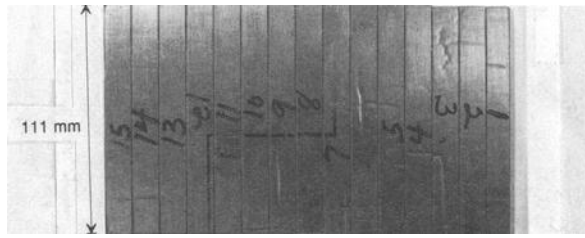

FIG. 1*a*—*This photograph is of* $[0/90]_{2s}$ *specimens cut from a portion of one plate. Manufacturing abnormalities in the form of "wrinkles" are evident.*

did not reveal any abnormalities in these specimens. A photomicrograph of the edge of a $[0/90]_s$ specimen at a wrinkle shows these wrinkles were much shallower than those found in the $[0/90]_{2s}$ specimens with depths typically less than 0.05 mm, Fig. 2*b*. In contrast to the $[0/90]_{2s}$ specimens, the photomicrographs of the edges at the wrinkle sites did not reveal broken 0° fibers.

The specimens were separated into four categories. Depending on the location and orientation of the observed wrinkles, the categories were: no abnormalities, transverse wrinkles, longitudinal wrinkles, and mixed wrinkles. The designation "transverse" refers to a wrinkle perpendicular to the loading axis of the specimen, while "longitudinal" refers to a wrinkle oriented along the length of the specimen. "Mixed" wrinkles either contained both longitudinal and transverse wrinkles or the wrinkle topography was not well defined.

The photomicrographs of the edges of the specimens shown in Figs. 1 and 2 reveal variations in the spacing of the 90° fibers. This was always found when looking at the edges of the specimens at the locations of the transverse wrinkles. This will be discussed in more detail later in this paper. Additionally, the work reported in this paper addresses only the tests conducted on specimens containing no abnormalities and transverse wrinkles.

Nondestructive Evaluation Tests

Two NDE methods, ultrasonics and X-ray radiography, were used to detect and characterize the manufacturing abnormalities in the specimens prior to tension or thermomechanical fatigue testing. Both methods can yield data on the internal conditions of the material, and ultrasonic

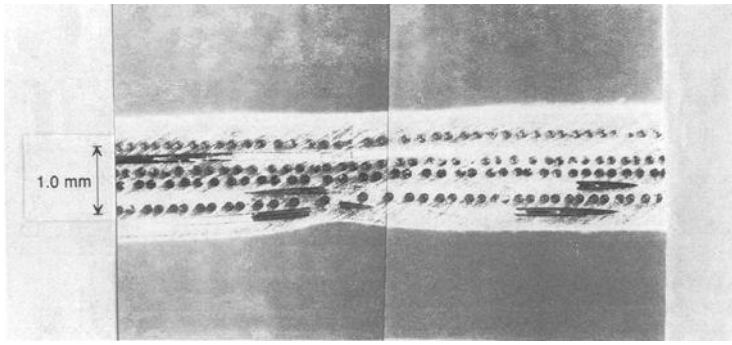

FIG. 1*b*—*This photomicrograph of an edge of a specimen before testing shows the cross-sectional shape of a wrinkle, displaced 90° fibers, and a broken 0° fiber.*

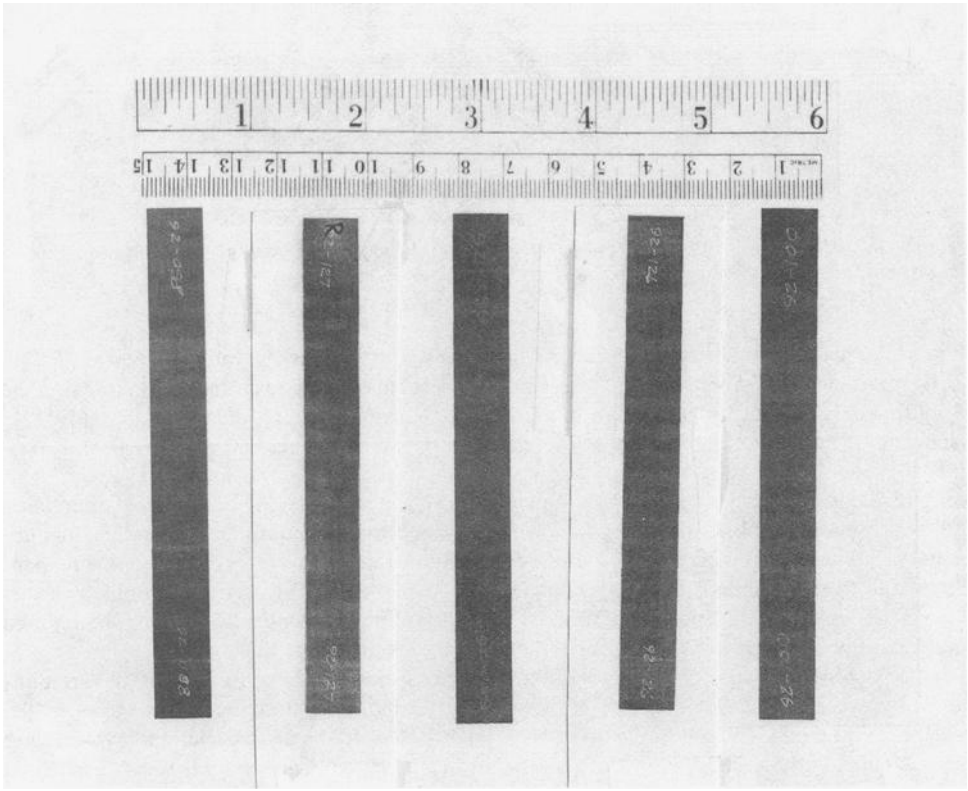

FIG. 2*a*—*Subtle wrinkles or "waves" are barely evident in this photograph of* $[0/90]_s$ *specimens.*

and X-ray NDE methods often complement each other. It was anticipated that ultrasonic evaluations would be sensitive to abnormalities in the matrix, such as lack of consolidation between foils, delamination, cracking within a ply, and other planar-type defects. The ultrasonic techniques are sensitive to modulus and/or density variations. Other research [*3*] has shown that ultrasonic methods also can be sensitive to fiber breakage. The X-ray radiography was selected

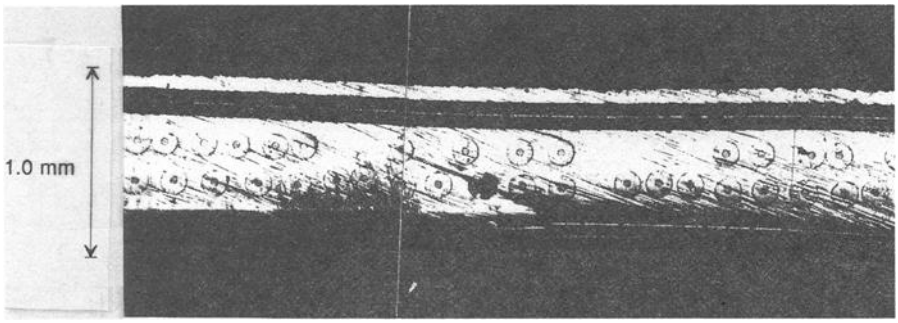

FIG. 2*b*—*Displaced 90° fibers are evident at the edge of the specimen. The wrinkle at the surface of this specimen was very subtle.*

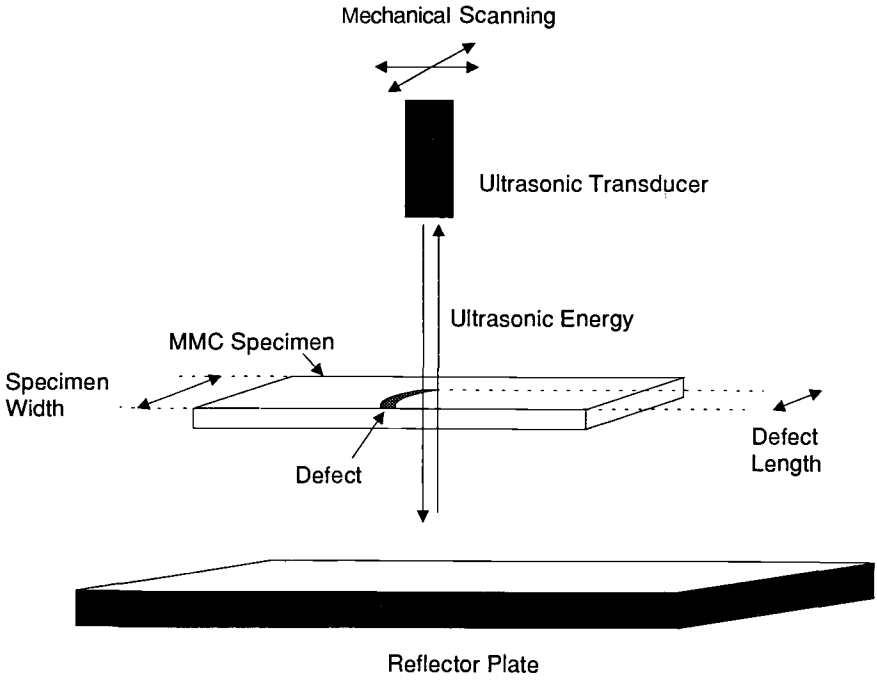

FIG. 3—*Schematic of the ultrasonic reflector plate method.*

for its capability to image fiber alignment and material abnormalities oriented perpendicular to the material surface. The X-ray technique potentially can detect cracks oriented parallel to the X-ray beam.

Ultrasonic Inspection Technique

A modified through-transmission technique, reflection plate inspection, was selected to inspect visually observed abnormalities. Figure 3 illustrates the reflection plate inspection method. One ultrasonic transducer is used to send ultrasound into and through the specimen. The ultrasound transmitted through the specimen reflects off a glass reflector plate and travels back through the MMC specimen. Ultrasonic energy reflected back through the specimen is received by the transducer and detected by the ultrasonic instrument. The transducer is scanned in a raster pattern acquiring ultrasound data at regularly spaced X, Y locations. The resulting image, of transmitted ultrasonic amplitude plotted as a function of X and Y locations, is called a C-scan. This technique is very sensitive to any change in material acoustic impedance, Z, where:

$$Z = \rho \cdot \sqrt{\frac{E}{\rho}} \cdot \sqrt{\frac{(1 - \nu)}{(1 + \nu)(1 - 2\nu)}} \tag{1}$$

where

E = Young's modulus,
ρ = material density, and
ν = Poisson's ratio.

Thus, a reflector plate C-scan produces a map of variations in material integrity. Consequently, areas of reduced transmission should have some correlation with damage in the composite.

The reflector plate technique was chosen for several reasons. Because the amplitude data that are recorded come from ultrasound that has passed through the material twice, the technique is very sensitive to changes in acoustic impedance. Of practical importance is the need for using only one transducer. Addition of a second transducer for standard through-transmission inspections requires additional fixturing and alignment and adds the second transducer's independent receiver response to the signal. Additionally, in the immersion tank the specimens can be laid flat for reflector plate scanning while vertical fixturing is usually required for through-transmission scanning using two transducers.

The ultrasonic data acquisition and imaging system consisted of a five-axis mechanical scanning system with 0.025-mm resolution, broadband ultrasonic spike pulser/receiver, and a 200-MHz, 8-bit signal digitizer. Data acquisition and imaging were controlled by a digital computer with custom software. The ultrasonic transducer was broadband with a 10-MHz center frequency, 12.7 mm diameter, and spherically focused at 75 mm. The theoretical −6 dB focal spot size was 0.9 mm. Typical step sizes (distance between adjacent X, Y data acquisition locations) were 0.25 to 0.5 mm. The reflector plate was a 6-mm-thick glass plate.

X-ray Inspection Technique

The X-ray radiographs were taken using a standard film-based X-ray system. Typical energies were 60 to 80 KeV with 5 mA current. Exposure times varied from 30 to 60 s, and high-resolution film was used. The system was set up to give a 1:1 specimen-size-to-image-size exposure. This technique was sufficient to image individual SCS-6 fibers and the molybdenum and titanium-niobium cross-weaves. Changes in material thickness at the wrinkle sites were also detectable with this technique. Differentiation of same-direction plies was not possible with this technique alone, although individual fibers in all plies were resolved.

Thermomechanical Fatigue Tests

Mechanical Fatigue Equipment

A horizontal fatigue test frame incorporating a pneumatic ram was used for applying cyclic loads to the specimens. A 20-kN load cell was used, and loads were controlled to within 0.1 kN (typically 1 MPa for these specimens). Specimens were positioned horizontally in precisely aligned, hydraulically actuated, rigid grips (see Fig. 4 and Ref *4* for further details). Gripping pressure was 60 MPa. The applied load cycle was controlled by a PC using control software developed by the University of Dayton [*5*]. Strain data were acquired using high temperature extensometers with 110-mm-long quartz rods. Typical displacement resolutions were 0.0004 mm.

Thermal Fatigue Equipment

The specimens were heated using radiant energy quartz lamp heaters. Two heating units were used, each containing four tungsten filament quartz lamps, with one heater placed above the top surface of the specimen and the other placed below (see Fig. 4). Each lamp was paired with another to form four controllable heating zones; this maintained a uniform temperature profile along a 25-mm length of the specimen. A low-velocity, low-volume stream of air was directed at the center of the specimen (from one edge) to help achieve the thermal cycle profile and to prevent a buildup of heat in the center of the specimen. The quartz lamp outputs were

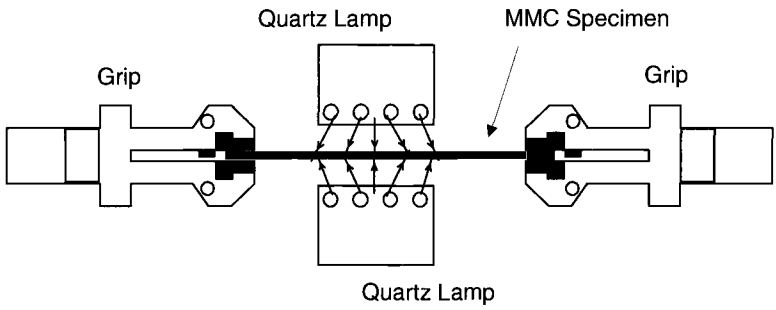

FIG. 4—*Precisely aligned gripping mechanism with quartz lamp heating.*

controlled by a commercial four-zone digital temperature controller. Temperature sensing was accomplished via four, 36-gage, type-K thermocouples welded to the top and bottom surfaces on the specimen. Additional information about the quartz lamp heating system can be found in Ref *4*. This heating system produced a temperature profile along the specimen's loading axis as shown in Fig. 5.

TMF Test Profile

A manufacturing abnormality may or may not manifest itself in a test because the type of test may not cause the abnormality to produce noticeable damage or premature specimen failure. For example, a room temperature tension test may not produce a lower ultimate tensile strength in a specimen with matrix cracks since the tensile strength is dominated by the strength of the fibers. In the specimens used for this study it was thought that many different types of defects

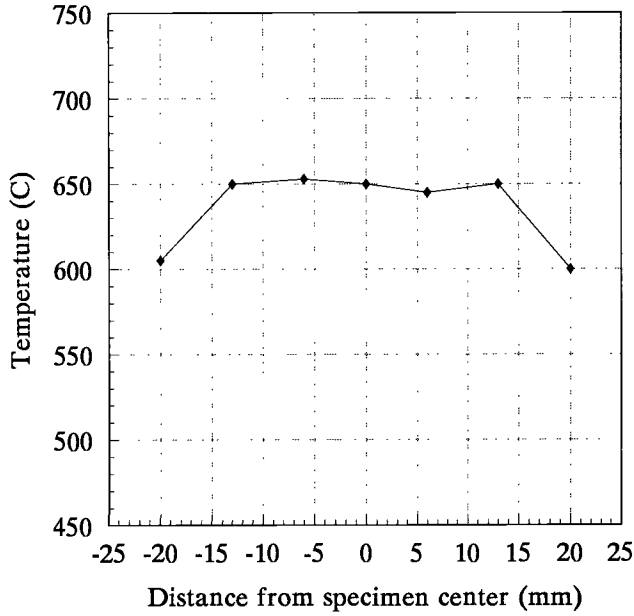

FIG. 5—*Temperature profile along the length of the specimen.*

could be present including fiber breakage, lack of matrix consolidation, matrix cracking, and degraded fiber/matrix interfaces. Recent results suggest that in-phase TMF test results are sensitive to degradation in fiber properties while out-of-phase TMF test results are affected by matrix integrity [*6*]. Due to the limited number of specimens it was desired to compare results of tests potentially affected by both fiber and matrix damage mechanisms.

A TMF test was developed that combined both in-phase and out-of-phase TMF tests into one compound cycle [*7*]. The cycle is shown in Fig. 6. The total cycle time was 360 s for the specimens tested. In actual testing the temperature was ramped from 150 to 638°C in the first 90 s of the cycle. During the second 90 s the temperature was ramped to the maximum temperature of 650°C. Ramping the temperature set points during the second 90 s resulted in the "isothermal" portion of the cycle where the actual specimen temperature was maintained between 640 and 650°C and assisted in maintaining a proper phase relationship with the load profile.

The maximum applied stress was 160 MPa with a stress ratio of 0.1. Previous TMF testing of SCS-6/β21-S $[0/90]_{2s}$ showed that the *S-N* curves for in-phase and out-of-phase TMF results experience a crossover at 340 MPa maximum stress [*8*]. However, due to the abnormalities present in these specimens, a lower maximum stress was necessary. This was determined from a series of tension tests conducted on specimens with similar abnormalities. The $[0/90]_s$ spec-

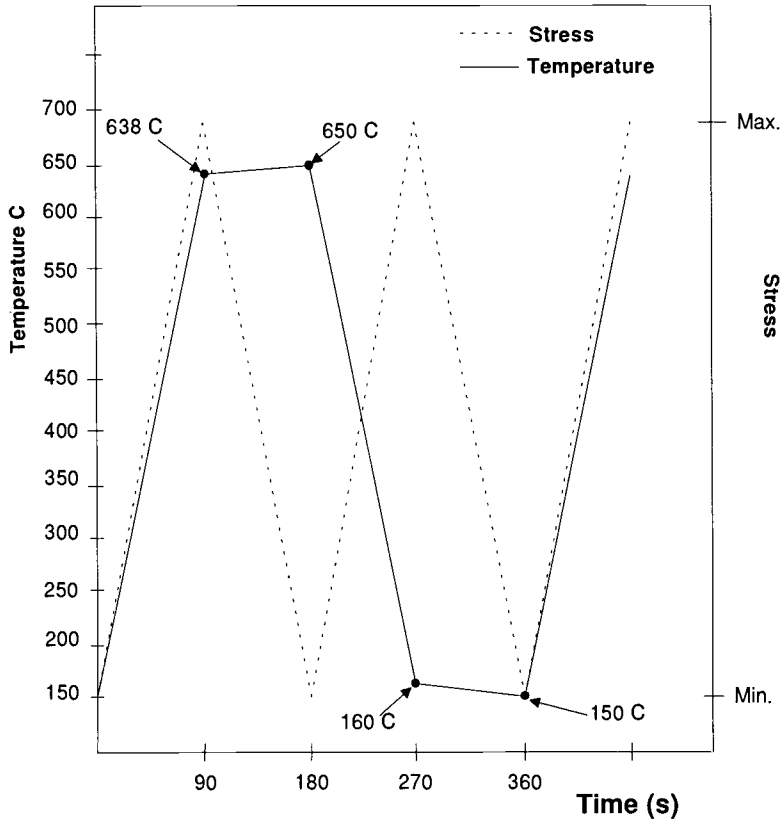

FIG. 6—*Load and temperature profiles during the thermomechanical fatigue tests.*

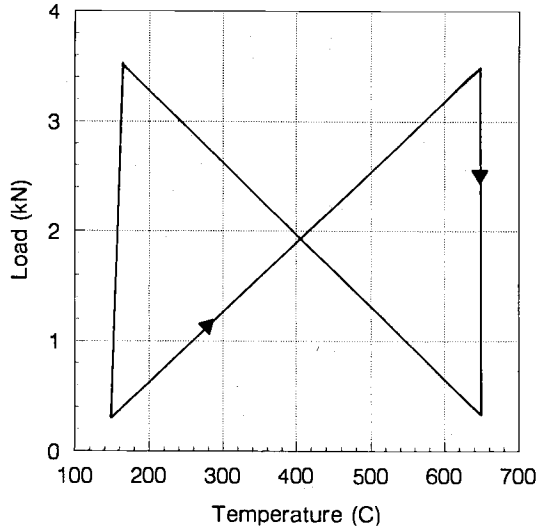

FIG. 7*a*—*Load versus temperature resulting from application of the profiles shown in Fig. 6.*

imens were tested at a maximum stress of 340 MPa as the ultrasonic data indicated the abnormalities were much less severe than in the $[0/90]_{2s}$ specimens.

For the TMF tests the maximum temperature was 650°C and the minimum temperature was 150°C. During the constant temperature portions of the cycle the temperatures were held constant to within ±10°C. This test profile produced load-temperature and stress-strain profiles as shown in Figs. 7*a* and 7*b*. The test parameters for all of the specimens are summarized in Table 1.

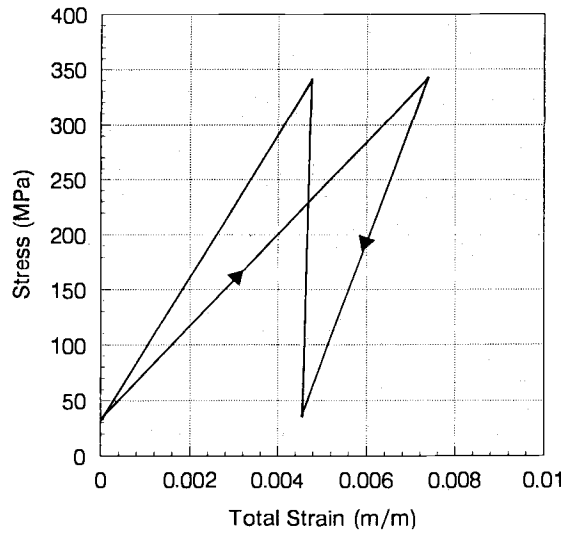

FIG. 7*b*—*Typical stress versus strain results during the TMF loading/heating profile as shown in Figs. 6 and* 7a.

TABLE 1—*Test parameters for all specimens.*

Specimen Number	Ply Configuration	Test Type	σ_{max}, MPa	R	Stress Cycle Time	T_{max}, °C	T_{min}, °C	Temperature Cycle Time, s
91-361	$[0/90]_{2S}$	Tension	N/A	N/A	5 MPa/s	650	N/A	N/A
91-366	$[0/90]_{2S}$	Tension	N/A	N/A	5 MPa/s	650	N/A	N/A
91-367	$[0/90]_{2S}$	Tension	N/A	N/A	5 MPa/s	650	N/A	N/A
91-379	$[0/90]_{2S}$	Tension	N/A	N/A	5 MPa/s	650	N/A	N/A
91-358	$[0/90]_{2S}$	TMF	160	0.1	180 s	650	150	360
91-360	$[0/90]_{2S}$	TMF	160	0.1	180 s	650	150	360
91-368	$[0/90]_{2S}$	TMF	160	0.1	180 s	650	150	360
91-380	$[0/90]_{2S}$	TMF	160	0.1	180 s	650	150	360
92-098	$[0/90]_{S}$	TMF	340	0.1	180 s	650	150	360
92-099	$[0/90]_{S}$	TMF	340	0.1	180 s	650	150	360
92-100	$[0/90]_{S}$	TMF	340	0.1	180 s	650	150	360
92-126	$[0/90]_{S}$	TMF	340	0.1	180 s	650	150	360
92-127	$[0/90]_{S}$	TMF	340	0.1	180 s	650	150	360

Results

Ultrasonic Data

Reflector plate C-scans of all of the specimens are shown in Figs. 8, 9, and 10. The color coding of the ultrasonic transmission amplitude is interpreted as follows. Full-scale amplitudes (white in these C-scans) are equivalent to the level of ultrasonic transmission in an equivalent-thickness specimen of Ti-6-4. Amplitude values within 6 dB of the maximum are within the range of amplitudes found in "good" or defect-free specimens of SCS-6/β21-S. Amplitude values less than 6 dB of the maximum may be indicative of damage within the composite and are classified as an abnormality. Areas within the composite that would produce ultrasonic amplitudes less than 10% full scale would indicate almost no transmission of the ultrasound (the transmission loss would be more than 20 dB relative to the transmission through Ti-6-4). Low ultrasonic transmission could result from voids, delaminations, or fractured fiber groups sufficient to scatter ultrasound.

Figure 8 contains the C-scans of the specimens used in the 650°C tension tests to determine the effect of the abnormalities on the tensile load-carrying ability of the specimens. To the right of each specimen C-scan is the normalized ultimate tensile strength of the specimen (an ultimate tensile strength of 635 MPa was used as the reference value for undamaged material). The specimen failure location is shown by the arrow on each specimen. The temperature distribution map that typically was present on the specimens is also shown at the bottom of Fig. 8. The ultimate tensile strength values combined with the ultrasonic data were used to determine the maximum stress value for the TMF tests.

Figure 9 contains the C-scans of the $[0/90]_{2s}$ specimens tested under TMF conditions. An arrow shows the failure location for each specimen. To the right of each C-scan is the percent cyclic life of the specimen relative to the TMF life of a specimen that was judged to have no abnormalities (a value of 3000 cycles was obtained in an identical test for a specimen from the same composite panel).

Figure 10 contains the C-scans of the $[0/90]_S$ specimens. An arrow shows the failure location for each specimen, and the percent values to the right of each C-scan shows the relative cyclic life of the specimen compared to the life of a specimen judged to be "good" (900 cycles).

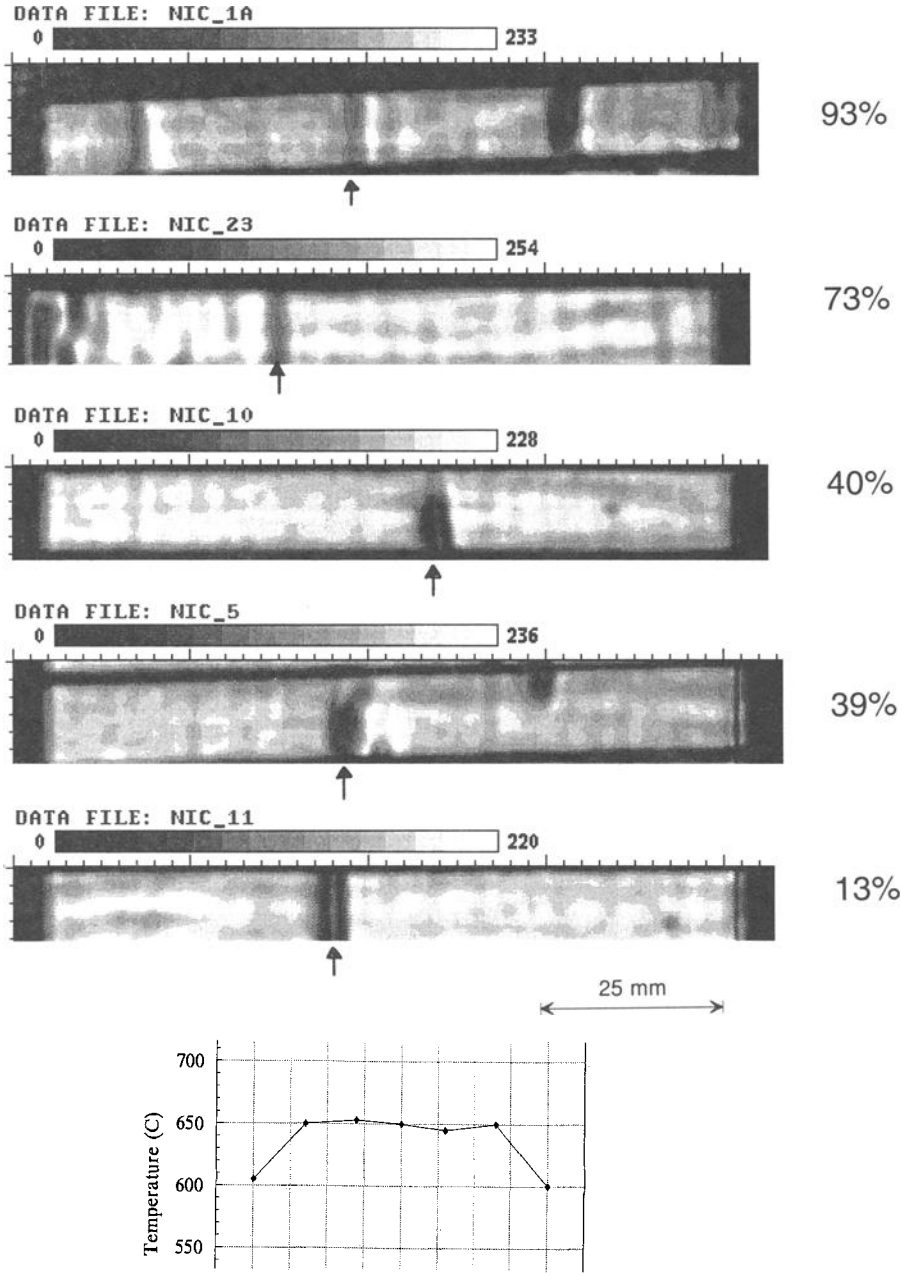

FIG. 8—*C-scans of* $[0/90]_{2s}$ *specimens before tension testing at 650°C. The darker regions represent higher attenuation of the ultrasound. The arrows indicate the location of failure. The percentages to the right indicate percent ultimate tensile strength as compared to a specimen without abnormalities. The graph at the bottom shows the temperature profile along the length of the specimens. Failure always occurred in the heated zone.*

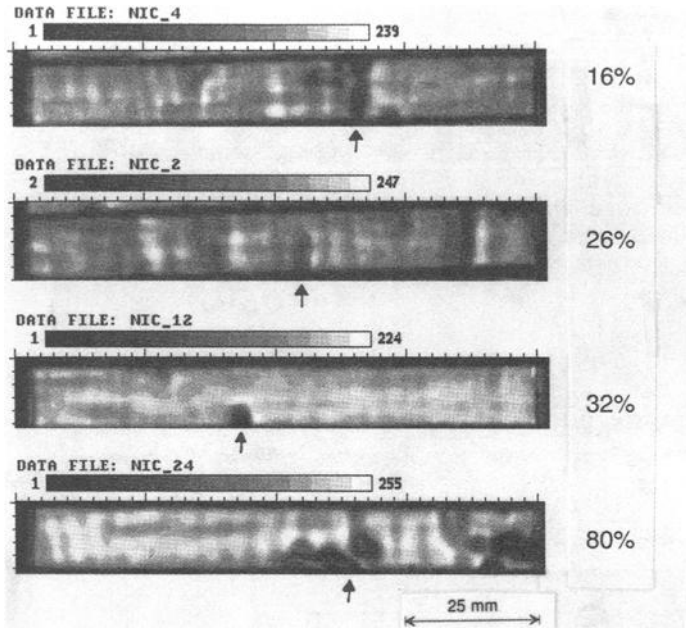

FIG. 9—*C-scans of the* $[0/90]_{2s}$ *specimens before TMF testing. The arrows indicate the location of failure. The percentages to the right indicate the resulting fatigue life as compared to a specimen without abnormalities.*

X-ray Radiography Data

Figure 11 contains radiographs of the specimens. The images of the $[0/90]_{2s}$ specimens are slightly darker than those from the $[0/90]_s$ as expected due to the additional number of plies. The location of the specimen failure is marked with an arrow. The molybdenum cross-weave is evident in the $[0/90]_{2s}$ specimens but the titanium-niobium cross-weave was not detected in the $[0/90]_s$ specimens. The molybdenum cross-weave appears as the regularly spaced dark lines running across the width of the specimens. In these radiographs, attenuation of the X-rays is seen as dark areas and relatively less attenuation is shown as lighter areas.

Individual fibers can be identified in the radiographs in Fig. 11, and 0 versus 90° fibers can be distinguished. However, it is not possible to differentiate the fibers in one 0° ply from the other 0° ply and similarly for the 90° plies. Fiber swimming and regions of low fiber density are easily detected.

Mechanical Properties Data

A summary of the mechanical test data is listed in Table 2. The room temperature modulus was obtained by loading the specimen to a low stress level (approximately 100 MPa) before performing the tension or TMF test.

Discussion of Results

The primary goal of this study was to learn if there was a correlation between the data generated by X-ray and ultrasonic NDE tests and the thermomechanical fatigue life of MMC

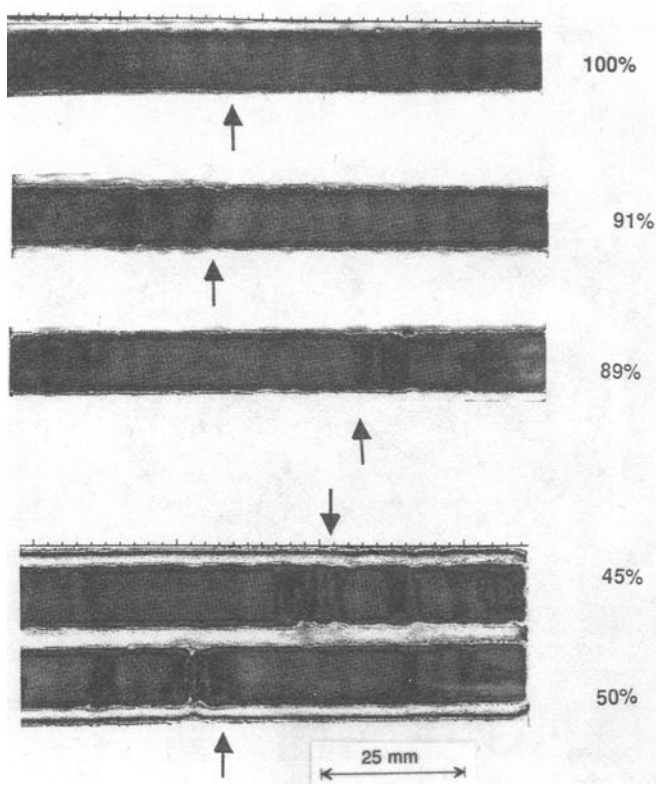

FIG. 10—*C-scans of the [0/90]$_s$ specimens before TMF testing. The arrows indicate the location of failure. The percentages to the right indicate the resulting fatigue life as compared to a specimen without abnormalities.*

specimens containing manufacturing abnormalities. To conduct an assessment of the amount of correlation it was desirable to have quantitative data from both the NDE and TMF tests. Historically, NDE data has been interpreted qualitatively; C-scans are coded by color schemes and X-ray radiographs are judged by viewing changes in contrast. The capability of the human brain to associate contrast and/or color changes with spatially distributed patterns is very good. However, determining the *degree* of correlation imposes a quantitative requirement that taxes the usual human pattern recognition capability.

With the motivation to quantify the NDE results, a simple "damage assessment" parameter was constructed to quantify the ultrasonic data. Intuition and some idea of the physics of ultrasonic propagation predict that the greater the amount of ultrasonic attenuation the greater the degree of disorder within the specimen. Additionally, it seems reasonable to assume that the larger the extent of the disorder, especially in the direction perpendicular to the axis of mechanical loading, the more degraded the strength and/or fatigue lives will be. Finally, since the cyclic stress on the fibers is highest in the region of highest temperature, where oxidation and cracking of the matrix are more likely to occur, the abnormalities within the heated portion of the specimen should dominate failure. Thus only the NDE indications from the heated region,

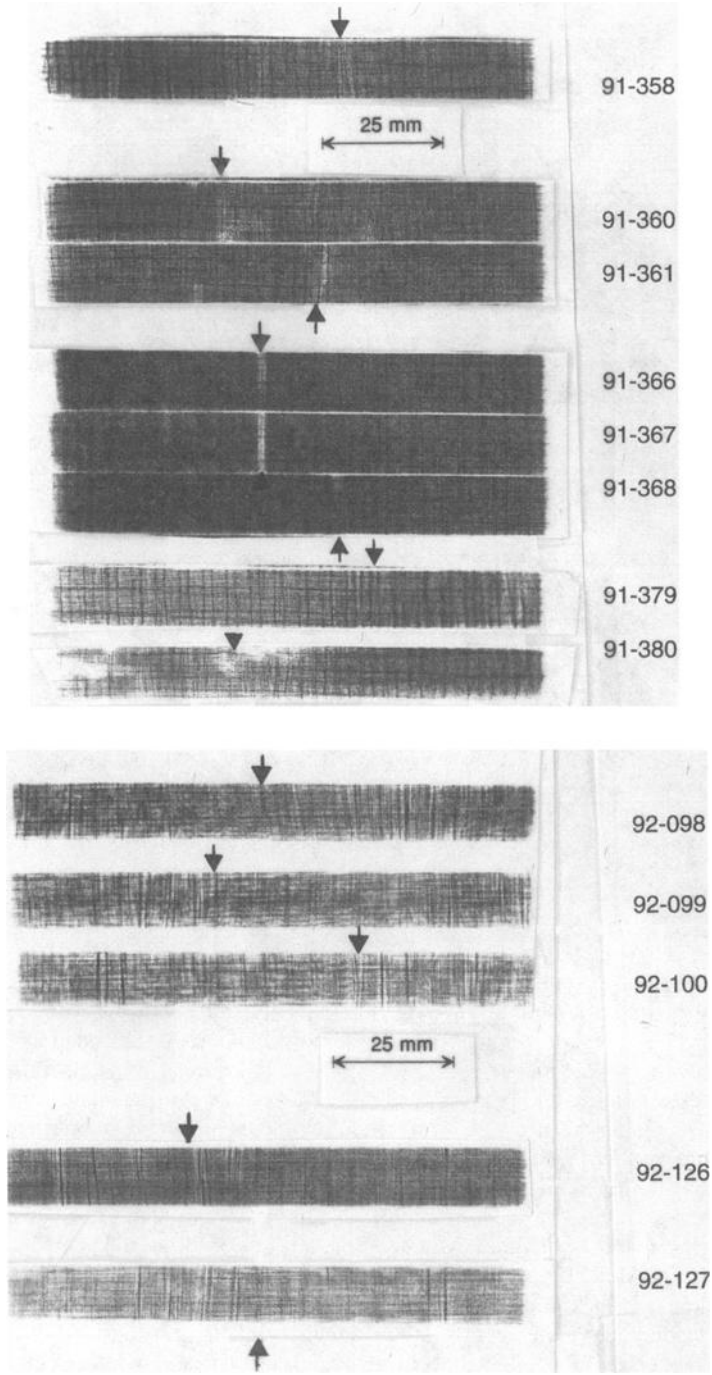

FIG. 11—*X-ray radiographs of the* $[0/90]_{2s}$ *specimens before testing. The arrows indicate the failure location. White indicates lower density; dark indicates higher density. Notice that individual fibers can be resolved, thus providing information about fiber displacement and alignment.*

TABLE 2—*Summary of the mechanical test data.*

Specimen Number	Ply Orientation	RT Modulus	UTS or Cycles-to-Failure
91-361	$[0/90]_{2S}$	130	248 MPa
91-366	$[0/90]_{2S}$	123	254 MPa
91-367	$[0/90]_{2S}$	136	85 MPa
91-379	$[0/90]_{2S}$	138	468 MPa
91-358	$[0/90]_{2S}$	...	792 cycles
91-360	$[0/90]_{2S}$	128	483 cycles
91-368	$[0/90]_{2S}$	134	969 cycles
91-380	$[0/90]_{2S}$	130	2402 cycles
92-098	$[0/90]_{S}$	151	900 cycles
92-099	$[0/90]_{S}$	137	823 cycles
91-100	$[0/90]_{S}$	151	800 cycles
92-126	$[0/90]_{S}$	...	447 cycles
92-127	$[0/90]_{S}$	...	503 cycles

± 15 mm from the center, were analyzed. A simple damage parameter was developed

$$DP = UTA * \frac{DL}{W} \tag{2}$$

where

DP = damage parameter,
UTA = ultrasonic attenuation,
DL = defect length (see Fig. 3), and
W = specimen width.

Applying this algorithm to the ultrasonically detected abnormalities in the heated portion of the specimens produced the data shown in Table 3. The percent UTS or percent life is plotted

TABLE 3—*Ultrasonically detected abnormalities.*[a]

Specimen Number	Ply Configuration	Test Type	Ultrasonic Attenuation, dB	UT-Detected Defect Length, l/width	Damage Parameter	% UTS or % Life
91-379	$[0/90]_{2S}$	Tension	8.5/7	0.1/0.9	7.2	73%
91-366	$[0/90]_{2S}$	Tension	6/12/18	0.3/0.2/0.5	13.2	40%
91-361	$[0/90]_{2S}$	Tension	8.5/14	0.25/0.65	11.1	39%
91-367	$[0/90]_{2S}$	Tension	20	1	20	13%
91-380	$[0/90]_{2S}$	TMF	18/12	0.2/0.2	6	80%
91-368	$[0/90]_{2S}$	TMF	18/12	0.17/0.17	5.1	32%
91-358	$[0/90]_{2S}$	TMF	8.5	0.55	4.6	26%
91-360	$[0/90]_{2S}$	TMF	9.5/13.6	0.5/0.5	11.6	16%
92-098	$[0/90]_{S}$	TMF	0	0	0	100%
92-099	$[0/90]_{S}$	TMF	2.5	0.25	0.6	91%
92-100	$[0/90]_{S}$	TMF	3.3	1	3.3	89%
92-126	$[0/90]_{S}$	TMF	7	1	7	45%
92-127	$[0/90]_{S}$	TMF	7/6	0.35/0.65	6.4	50%

[a] If abnormality had multiple areas of attenuation: Damage parameter = (attenuation value 1) · (defect length/specimen width 1) + (attenuation value 2) · (defect length/specimen width 2) + ...

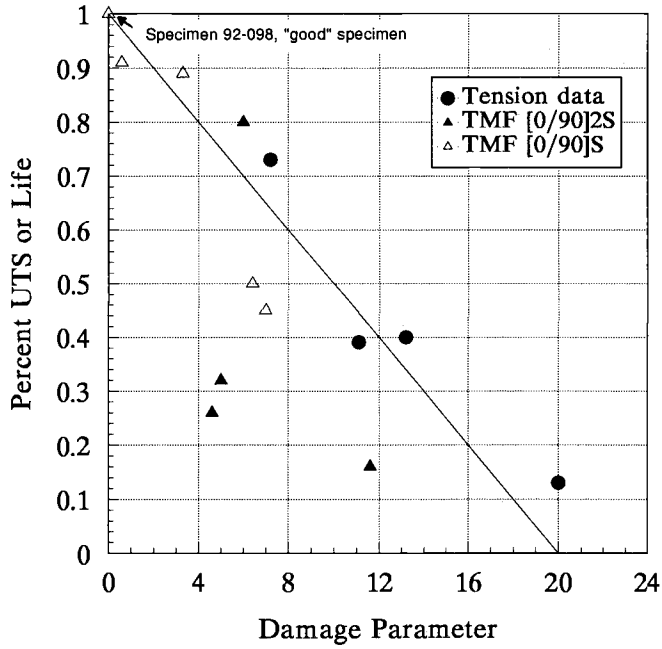

FIG. 12—*The normalized ultimate failure strengths and normalized fatigue lives are plotted as a function of a simple damage parameter derived from the ultrasonic results as described in the text. Correlation between the damage parameter and the strength or life of the specimens is observed.*

as a function of the damage parameter in Fig. 12. The line is simply the range of attenuation values (16 grey-scale levels) from the C-scan plotted linearly against the percent mechanical property. This line provides a good fit to the tension data and $[0/90]_s$ TMF data. However, three of the four $[0/90]_{2s}$ specimens tested under TMF conditions failed at considerably lower cyclic lives than predicted by the line. This could result from ultrasonic technique underestimating the actual amount of damage in the specimen. It also is possible that the higher attenuation in the C-scans indicate regions of small defects which act as preferred crack initiation sites under thermomechanical fatigue conditions.

One specimen that was sorted into the group of "good" specimens actually contained an abnormality near the end of the specimen (see the C-scan in Fig. 13). The middle section of this specimen was judged free of abnormalities. The test matrix called for this specimen to undergo an isothermal fatigue test at 150°C and a maximum stress of 500 MPa. The region

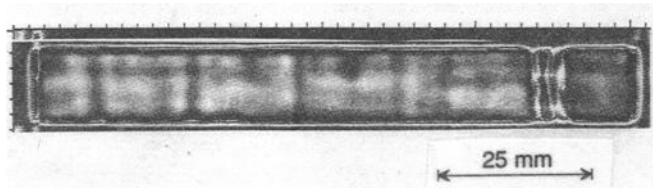

FIG. 13—*C-scan of a specimen with an abnormality near one end. This specimen failed at the location of higher ultrasonic attenuation when it was inadvertently gripped short of this location. Analysis of the ultrasonic data predicted a failure strength very close to the actual ultimate tensile strength.*

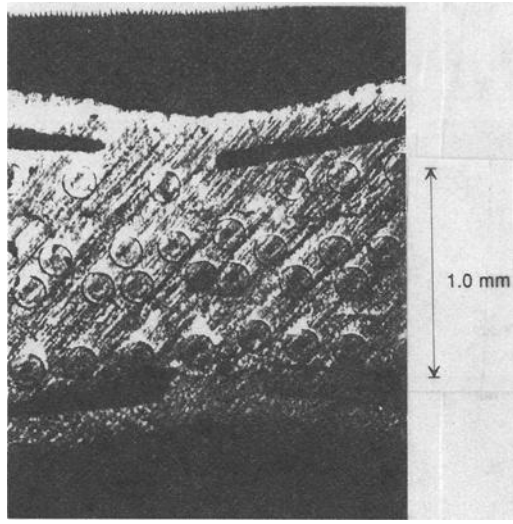

FIG. 14*a*—*Photomicrograph of the edge of a specimen containing a severe wrinkle. The 90° fibers in the row directly underneath the top 0° fiber are displaced. Both 0° fibers visible are broken.*

containing the detected abnormality was to be within the grips of the test frame; however, the wrinkle was not quite contained within the grips. Analysis of the abnormality yields a damage parameter of 12 (approximately 12 dB attenuation across the entire width of the specimen). Referring to the graph in Fig. 12 shows that a damage parameter of 12 could result in a degradation in ultimate tensile strength of approximately 40% of good material. The specimen failed on its initial loading at a stress of 476 MPa or about 48% of the ultimate tensile strength of defect-free material at 150°C.

The type of abnormality found in these specimens, when viewed at the specimen's edge, consisted of a gap or variation in spacing of the 90° fibers accompanied by bending and/or breakage of the adjacent 0° fibers. Figure 14*a* shows a photomicrograph from the edge of a $[0/90]_{2s}$ specimen containing a severe wrinkle. The outer two 0° fibers are fractured and a gap in the spacing of the 90° fibers is evident. The inner two 0° fibers are not visible. Figure 14*b* shows a photomicrograph of the edge of a $[0/90]_s$ specimen clearly showing displaced 90° fibers. In this photomicrograph, the 0° fibers are shown bending but fiber fracture is not

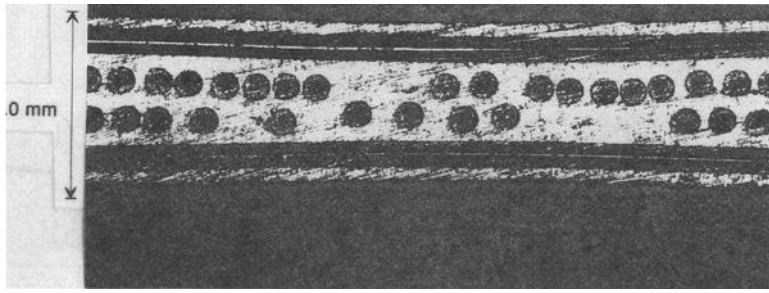

FIG. 14*b*—*Photomicrograph of the edge of a* $[0/90]_s$ *specimen showing considerable displacement of the 90° fibers.*

observed. This was generally the case for specimens with this layup. Gaps in the 90° layers, corresponding to 10 to 15 fibers, were observed at the edges of some specimens.

It is hypothesized that the combinations of surface curvature due to the wrinkle and broken fibers contribute to the attenuation of the ultrasound that occurs in these regions. Additionally, regions in the specimen where the fibers have moved closer together may also increase the ultrasonic attenuation. Figure 15 shows a C-scan of Specimen 92-127 and a photomicrograph of the edge of the specimen in the region marked on the C-scan. The correspondence of higher ultrasonic attenuation with gaps in the spacing of the 90° fibers was consistent throughout the specimens tested; however, it is not yet clear as to the exact nature of the interaction of the ultrasound with the composite constituents that causes the ultrasonic attenuation.

Examination of the X-ray radiographs consistently shows evidence of displaced 90° fibers (lighter shades) in the regions of specimen failure. In the $[0/90]_{2s}$ specimens the four 90° fiber layers make it difficult to distinguish individual displaced fibers but groups of displaced fibers are observed. Additionally, under magnification, breakage and displacement of the cross-weave for the 90° fibers at the location of failure is apparent. In contrast, the displacement of the 90° fibers in the $[0/90]_s$ specimens is easily seen in the radiographs at the eventual failure location. Displacement or swimming of the 90° fibers creates gaps of up to 1 mm across the specimen width. These gaps show some degree of spatial correlation with the regions of higher attenuation in the ultrasonic C-scans (see Fig. 16). This suggests that X-ray radiography can be used to complement the ultrasonic data, although no quantitative predictor has been developed for the X-ray data.

Conclusion

The usefulness of ultrasonic nondestructive evaluation to assess the integrity of $[0/90]_s$ and $[0/90]_{2s}$ SCS-6/β21-S composites containing manufacturing abnormalities has been shown

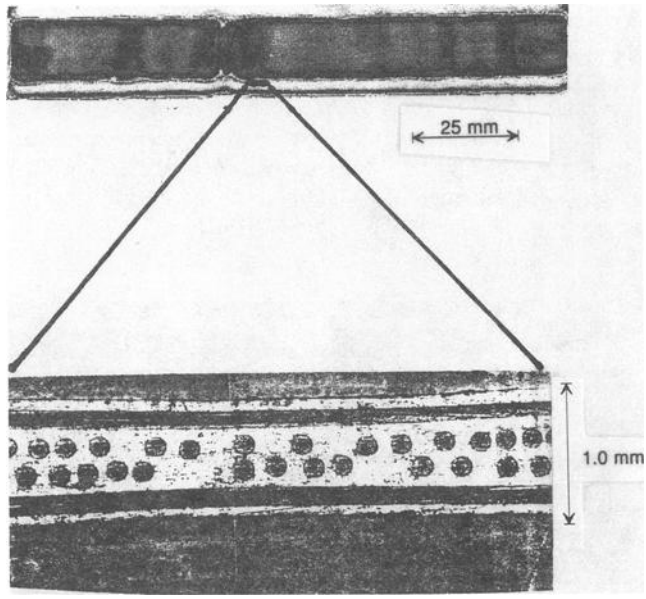

FIG. 15—*The photomicrograph at the bottom shows displaced 90° fibers in the region of higher attenuation (dark regions) indicated in the C-scan at the top of the figure. This correlation was present in all of the specimens.*

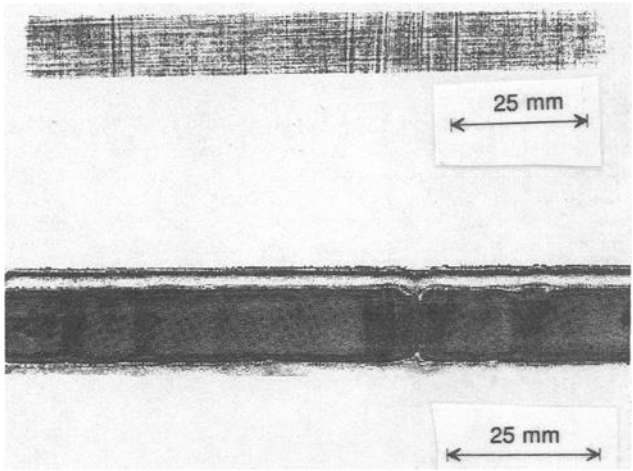

FIG. 16—*The X-ray radiograph at the top of the figure shows several regions of displacement, or bunching, of the 90° fibers (running perpendicular to the length of the specimen). These regions correspond to the regions of higher attenuation (dark grey or black) in the C-scan of the same specimen at the bottom of the figure.*

through the correlation of the ultrasonic data with ultimate tensile strength and thermomechanical fatigue life. Additionally, the use of X-ray radiographic nondestructive evaluation appears to complement the ultrasonic data and is useful for analyzing fiber displacement, orientation, and fiber swimming. A simple damage parameter was developed to help quantify the ultrasonic NDE data from manufacturing abnormalities within the material. These techniques, properly calibrated, seem to provide a useful tool for screening advanced metal matrix composites, thus preventing the use of defective material in mechanical property evaluations. Additionally, material that has been judged to be unfit for testing (through visual inspections) can be evaluated with these NDE techniques and used if the degree of damage is determined to be low.

Acknowledgments

This work was funded under Air Force contract F33615-91-C-5606. Appreciation is expressed to Ed Porter of Universal Technologies Corporation, Dayton, OH, for acquiring the X-ray radiography data. Appreciation is also expressed to the NDE Branch (WL/MLLP) of the Materials Directorate, Wright Laboratories, Wright-Patterson Air Force Base, OH, for use of their ultrasonic scanning systems.

References

[*1*] Smith, P. R., Balsone, S. J., and Nicholas, T., Eds., "Titanium Aluminide Composites," *Proceedings,* Titanium Aluminide Composite Workshop held at the Harry Gray Conference Center, Orlando, FL, 16–18 May 1990, U.S. Air Force Technical Report WL-TR-91-4020.

[*2*] Smith, P. R. and Revelos, W. C.,"Titanium Matrix Components," *Proceedings,* Titanium Matrix Composite Workshop, 6–8 Nov. 1991, Harry Gray Conference Center, Orlando, FL, U.S. Air Force Technical Report WL-TR-92-4035.

[*3*] Karpur, P., Matikas, T., Krishnamurthy, S., and Ashbaugh, N. A., "Ultrasound for Fiber Fragmentation Size Determination to Characterize Load Transfer Behavior of Matrix-Fiber Interface in Metal Matrix Composites," *Proceedings, Review of Progress in Quantitative NDE,* D. O. Thompson and D. E. Chimenti, Eds., La Jolla, CA, 19–24 July 1992, Plenum Press, New York.

[4] Hartman, G. A. and Russ, S. M., "Techniques for Mechanical and Thermal Testing of Ti_3Al/SCS-6 Metal Matrix Composites," *Metal Matrix Composites: Testing, Analysis and Failure Modes, ASTM STP 1032,* W. S. Johnson, Ed., American Society for Testing and Materials, Philadelphia, 1989, pp. 43–53.

[5] Hartman, G. A. and Ashbaugh, N. E., "A Fracture Mechanics Test Automation System for a Basic Research Laboratory," *Applications of Automation Technology to Fatigue and Fracture Testing, ASTM STP 1092,* Braun/Ashbaugh/Smith, Eds., American Society for Testing and Materials, Philadelphia, 1990, pp. 95–112.

[6] Russ, S. M., Nicholas, T., Bates, M., and Mall, S., "Thermomechanical Fatigue of SCS-6/Ti-24Al-11Nb Metal Matrix Composites," *Proceedings,* Symposium on Failure Mechanisms in High Temperature Composites," 1991 ASME Winter Annual Meeting, Atlanta, GA, 1–6 Dec. 1991, American Society of Mechanical Engineers, New York.

[7] Personal communication with Dr. Ted Nicholas, Wright Laboratories, Materials Directorate, Materials Behavior Branch, December 1991.

[8] Hanson, D. G., "Thermomechanical Fatigue of SCS-6/β21-S $[0/90]_{2s}$ Composite," master's thesis, AFIT/GAE/ENY/91D-9, Air Force Institute of Technology Air University, Wright-Patterson, OH, December 1991.

Hamid Nayeb-Hashemi[1] *and John N. Rossettos*[1]

Characterization of Adhesively Bonded Joints by Acousto-Ultrasonic Techniques and Acoustic Emission

REFERENCE: Nayeb-Hashemi, H. and Rossettos, J. N., **"Characterization of Adhesively Bonded Joints by Acousto-Ultrasonic Techniques and Acoustic Emission,"** *Cyclic Deformation, Fracture, and Nondestructive Evaluation of Advanced Materials: Second Volume, ASTM STP 1184*, M. R. Mitchell and O. Buck, Eds., American Society for Testing and Materials, Philadelphia, 1994, pp. 335–362.

ABSTRACT: Reliable applications of adhesively bonded joints require an effective nondestructive evaluation technique for their bond strength prediction. To properly evaluate factors affecting bond strength, effects of defects such as voids and disbonds on stress distribution in the overlap region must be understood. At the same time, in order to use the acousto-ultrasonic technique to evaluate bond quality, the effect of these defects on the dynamic response of single lap joints must be clear.

The stress distribution in a single lap joint with and without defects (void or disbond) is analyzed. A $\bar{\theta}$ parameter that contains adherend and adhesive thickness and properties is introduced. It is shown for bonded joints with $\bar{\theta} \geq 10$ that a symmetric void or disbond in the middle of overlap up to 70% of overlap length has a negligible effect on bond strength. In contrast, frequency response analyses by a finite element technique showed that dynamic response is affected significantly by the presence of voids or disbonds. These results have direct implication in the interpretation of acousto-ultrasonic results.

Through-transmission attenuation and a number of acousto-ultrasonic parameters for various specimens with and without defects are evaluated. It is found that, although void and disbond have similar effects on bond strength (stress distribution), they have completely different effects on wave propagation characteristics. For steel-adhesive-steel specimens with voids, attenuation changes are related to the bond strength. However, the attenuation changes for specimens with disbond are fairly constant over a disbond range. In order to incorporate the location of defects in acousto-ultrasonic parameters, a weighting function is introduced. Using an immersion system with focused transducers, a number of acousto-ultrasonic parameters are evaluated. It is found that, by incorporating weighting functions in these parameters, better sensitivities (acousto-ultrasonic parameters versus bond strength) are achieved.

Acoustic emission activities of steel-adhesive-steel specimens with $\bar{\theta} = 3.4$ are monitored. Two different formats of energy versus time have resulted, each corresponding to the perfect specimens or the specimens with void or disbond. The relative acoustic energy and number of events at failure are found to be a means of predicting bond strength.

KEYWORDS: nondestructive evaluation, adhesively bonded joints, stress distribution, attenuation, stress wave factor, composite dynamic response

Nomenclature

AUP	Acousto-ultrasonic parameter
C	Damping matrix
E, υ	Elastic modulus and Poisson's ratio

[1] Professor, Department of Mechanical Engineering, Northeastern University, Boston, MA 02115.

$F_1(\omega)$, $F_2(\omega)$	Impedence mismatch between transducers and specimen
G	Shear modulus
h_0, h_1h_2	Adhesive, adherend thickness, respectively
M	Mass matrix
$p_1(x)$, $p_2(x)$	Resultant forces per unit width in the x direction
SWF	Stress wave factor
α_1	Adherend's thermal expansion coefficient
α_2	Adhesive's thermal expansion coefficient
$\Delta\alpha(\omega)$	Longitudinal attenuation change
$\bar{\theta}$, R, $\bar{\psi}$	Nondimensional parameters
σ	Normal stress in the adherend
τ	Shear stress at the adhesive/adherend interface
u	Displacement
ϵ	Normal strain

Introduction

Over the past decade, much research has been expended and numerous test instruments developed in seeking a solution to the problem of nondestructively inspecting adhesively bonded joints [*1–8*]. Several NDT methods are recommended for the inspection of adhesively bonded joints in addition to the well-established methods for detecting localized flaws, voids, or delaminations. However, neither of these approaches nor more sophisticated ultrasonic methods (using frequency and time domain information) has been shown capable of absolutely assessing joint strength. This is due, in part, to the fact that no single ultrasonic measurement is a unique function of a single bond property; each ultrasonic measurement is sensitive to changes in several bond properties. However, the strength of the bond may or may not depend on these properties. A multi-disciplinary approach is required that combines NDE, adhesive technology, and solid mechanics analyses to form a basis for a comprehensive quality assurance solution.

Many attempts have been made to advance the state of the art in flaw classification analysis by using techniques and concepts from pattern recognition. The underlying premise is built upon linear system analysis, which assumes that the ultrasonic input energy, as it varies with time, is modified by the bond structure. The theory then asserts that if one has the system input and output (echo), then the modifying mechanism can be found and characterized. Rose et al. [*6*], using this concept, evaluated adhesively bonded aluminum-to-aluminum specimens by defining an "α" parameter as the ratio of received signal to the transmitted signal in immersion scanning experiments. The feature "α" was defined and was of known value for bond quality discrimination [*9–10*]. A low value of "α" indicates good transmission of the stress wave energy, while the high value of "α" indicates most of the energy is reflected at the interface. The values of "α" at several locations of the bond area were evaluated, and the feature "β" based on the surface integration of the "α" parameter was defined as

$$\beta = \frac{1}{4h^2} \int \int \alpha(x, y)dxdy = \sum_{i=1}^{n} w_i\alpha_i(x, y) + R \tag{1}$$

where h is the distance between scan points (square bond area), and w_i are the weighting factors. The surface integral values and log weighting function [*6*] from the center of each coupon were used to construct the feature data. These were related to the bond strength. The above equation and features can be modified by considering which area of adhesive is more responsible for the bond strength and by proposing a weighting function which brings this factor into consideration.

The initial signature techniques were based on the analysis of ultrasonic signals in the time domain and by making use of the arrival time and amplitudes. Gericke in 1963 [*11*] suggested that a source of additional discriminating characteristics might be found in the frequency spectrum of the returned echo. He indicated that if a short pulse, rich in spectral content, were used, the size, nature, and shape of flaws could be more readily determined from the frequency domain. He also proposed a method involving the use of two widely separated frequencies for inspection. The change of the returned pulse shape from one frequency range to the other could possibly yield information concerning the defect size, shape, and orientation characteristics. Henneke et al. [*12–17*] introduced several moments of the frequency spectrum as a means of damage evaluation in composite materials. A variety of additional signature techniques for ultrasonic examination both in time and frequency domains are introduced [*18–23*]. However, these parameters may not be effective when used in interrogation of the bond quality without understanding the effects of defects on both the received ultrasonic signature and bond strength.

The higher order crossing (HOC) method for signal analysis, often called the zero-crossing or level-crossing method, has been recently developed and applied in bond quality assessments [*4–5*]. Ultrasonic echo signals were obtained from several specimens representing various adhesive or cohesive bond properties. HOC features were calculated from these signals and used to characterize the various conditions of the sample joints. However, no correlation between HOC parameters and bond strength was presented.

Acoustic emission is another nondestructive evaluation technique which has been projected to have the potential of predicting structural integrity. Acoustic emission (AE) is a term describing a class of phenomena whereby transient elastic waves are generated by the rapid release of energy from localized sources within a material [*24*]. AE has developed rapidly over the last two decades as a nondestructive evaluation technique and as a tool for materials research.

Acoustic emission signals can take many forms depending upon the material and the failure mechanism in the material. AE signals from defects in composites and geological materials generally contain information at low frequencies of 0.5 to 100 kHz since attenuation is relatively high due to the complexity of these materials. Signals of significance in metals and brittle materials contain information between 100 kHz and 2 MHz. In this range, a good compromise is found for most testing applications because ambient noise is low. A number of techniques are employed to isolate valid signals from noise in the time domain. Times of arrival can be used to permit geometric elimination of obvious noise through gating and acceptance of only those signals which arrive from a particular region of the structure. At the present time, one can find many presentations of acoustic emission data in the literature. In time domain, these include: ringdown counts, rms voltage, number of events, energy rate, rise time, event duration, amplitude distribution, and numerous others.

It is also possible to analyze the frequency content of both burst and continuous types of acoustic emission. Relating such measurements to the source mechanism is an extremely complex problem not only because of the specimen and transducer resonances and frequency-dependent absorption effects, but also because of effects caused by the methods of analysis employed. Indeed, some investigators would argue that the information required to distinguish between different acoustic emission sources, or to describe the nature of operation of particular sources, is simply not available in the frequency content of the acoustic emission signals, particularly using piezoelectric transducers. Other investigators believe that spectral analysis can be of great value and that, with the proper methods of averaging and smoothing data, spectral analysis can be used to identify and discriminate acoustic emission sources [*25–26*].

As pointed out above, the nondestructive evaluation of adhesively bonded joints requires comprehensive studies of the effects of defects, sizes, and their locations on the stress distribution and dynamic response of bonded joints. These analyses provide bases for more effective interpretation of various acousto-ultrasonic data. The purpose of this paper is to present our efforts toward understanding factors affecting (1) the bond strength and dynamic response of

adhesively bonded joints, and (2) bond strength prediction by conducting various acousto-ultrasonic experiments. Acoustic-emission activities of steel-adhesive-steel and graphite epoxy composite-adhesive-graphite epoxy composite specimens with various defects were also monitored during destructive tension tests. The results of these investigations are presented in the following sections.

Theoretical Investigation of Stress Distribution in the Bonded Joints

There are various bonded joint configurations. Most of the joint configurations are designed to transfer load in shear. Of all the various joints, the single lap joint is most commonly used in design. Also, theoretical and experimental investigations of the bond strength are less complicated with the single lap joint. For this reason, in this paper the effects of processing variables (voids, disbond region, poor cohesive strength, and poor adhesive strength) on the strength of the single lap joints are studied both experimentally and theoretically.

The strength of a given type of joint depends on the shear and peel stress distributions in the bonded area. These stresses depend on adhesive and adherend properties and geometries. Assuming the adhesive layer to be homogenous and free of defects, Volkersen [*27*] derived the shear stress distribution in single lap joints using shear lag model assumptions. Goland and Reissner [*28*] modified Volkersen's analysis by considering the bending moment and peel stresses in the theoretical analysis. Other researchers have also obtained the shear and peel stresses in the bond joints by finite element analyses [*29–34*]. There have been very limited theoretical investigations on the effects of defects on the stress distribution and bond strength in single lap joints. Since the bond strength may or may not depend on the defects, the stress distribution in a single lap joint with a void is derived in this section using shear lag model assumptions. The details of the analyses can be found in Refs *35* and *36*. Here, some aspects of these analyses are briefly described and important conclusions elaborated.

The two-dimensional model consists of a simple lap joint as shown in Fig. 1 made of two plates bonded by a layer of adhesive. The problem is formulated under the following assumptions:

1. The thicknesses h_0, h_1, h_2, H are small compared to the other dimensions of the structure so that individual layers may be under generalized plane stress (i.e., $\sigma_{1y} = \sigma_{2y} = 0$).
2. The thickness variation of the stresses in the plates will be neglected under the usual assumption that the surface shear stress transmitted through the adhesive layer acts as a body force.
3. In the z direction (i.e., transverse direction), plane strain conditions will prevail such that $\epsilon_z = \epsilon_{1z} = \epsilon_{2z} = 0$.

Referring to Fig. 1, let $p_1(x)$ and $p_2(x)$ be the resultant forces per unit width in the x-direction in Plates 1 and 2, respectively, and $u_1(x)$ and $u_2(x)$ be the displacements in the x direction. The elastic properties of isotropic Material 1 are donated by E_1, ν_1, and α_1, and those for isotropic Material 2 are E_2, ν_2, and α_2. The shear modulus of the adhesive is given by G. The joint is divided into three regions.

The following variables are defined as:

x_i = beginning of each region ($x_1 = 0$, $x_2 = a_1$, $x_3 = a_2$ in Region 1, 2, 3, respectively).

Region 1: $0 \leq x \leq a_1$
Region 2: $a_1 \leq x \leq a_2$ (void)
Region 3: $a_2 \leq x \leq L$

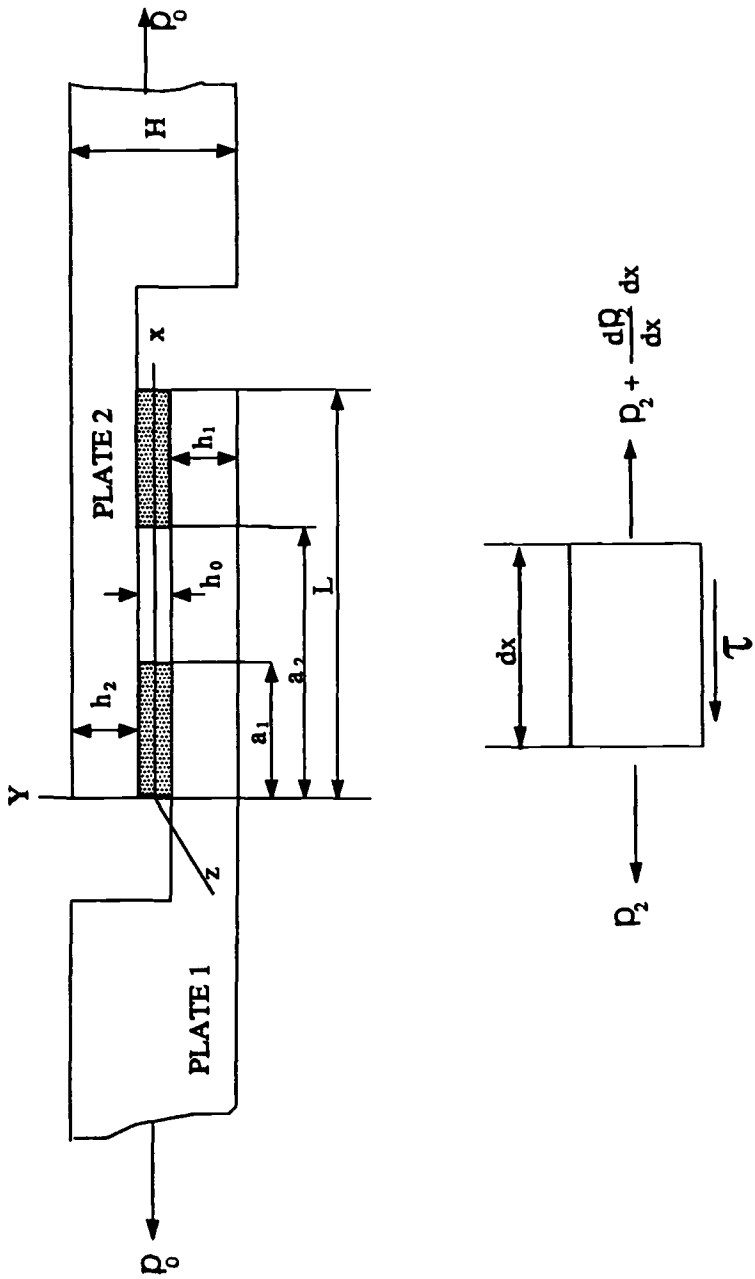

FIG. 1—*Schematic diagrams of a step lap joint with a void and a differential element.*

The shear stress distribution in the lap joint can be obtained by writing the equilibrium equation of an incremental element in Plate 2 (see Fig. 1) as

$$\frac{dp_2}{dx} - \tau(x) = 0 \tag{2}$$

where $\tau(x)$ is the shear stress. Assuming that the displacements of the top and bottom of the adhesive layer are $u_2(x)$ and $u_1(x)$ and using strain-displacement relations of

$$\epsilon_{1x} = \frac{du_1}{dx} \qquad \text{and} \qquad \epsilon_{2x} = \frac{du_2}{dx}$$

Eq 2 can be written in the form of

$$\frac{d^2p_2}{dx^2} - \frac{G}{h_0}(\epsilon_{2x} - \epsilon_{1x}) = 0 \tag{3}$$

Because of the assumptions ($\sigma_{1y} = \sigma_{2y} = 0$), the stress-strain relations in the adherends are

$$\epsilon_{1x} = \frac{1 - \nu_1^2}{E_1 h_1}[p_0 - p_2(x)] + \alpha_1 \Delta T \tag{4}$$

$$\epsilon_{2x} = \frac{1 - \nu_2^2}{E_2 h_2} p_2(x) + \alpha_2 \Delta T \tag{5}$$

Substituting Eqs 4 and 5 into Eq 3, and presenting it in a nondimensionalized form, results in

$$\frac{d^2P_2}{d\xi^2} - \bar{\theta}^2 P_2 = \frac{-\bar{\theta}^2}{1 + R} + \bar{\psi} \tag{6}$$

$$\text{where } \xi = \frac{x}{L} \tag{7}$$

$$(P_2, P_1) = \frac{1}{p_0}(p_2, p_1) \tag{8}$$

$$R = \frac{1 - \nu_2^2}{1 - \nu_1^2} \frac{E_1 h_1}{E_2 h_2} \tag{9}$$

$$\bar{\theta}^2 = \frac{L^2}{h_0 h_1} \frac{G}{E_1}(1 - \nu_1^2)(1 + R) \tag{10}$$

$$\bar{\psi} = \frac{L^2 G}{p_0 h_0}(\alpha_2 - \alpha_1)\Delta T \tag{11}$$

Equation 6 holds for Region 1 and 3; in the void region $\tau = 0$, so

$$\frac{d^2P_2}{d\xi^2} = 0 \tag{12}$$

The solution of Eqs 6 and 12 along with proper boundary conditions and continuity conditions between regions yields the normal and interfacial shear stress distribution in the adherends [*35,36*].

Theoretical Results on the Effects of Voids on Shear Stress Distribution in a Single Lap Joint

The geometric configuration of the step lap joint is given in Fig. 1, and the three parameters, R, $\bar{\theta}$, and $\bar{\psi}$, which appear in the governing Eq 6 and which influence the stress distribution, are given by Eqs 9, 10, and 11. The close observation of the aforementioned equations reveals that a change in $\bar{\theta}$ involves a change in geometry and material properties of both the adherends and the adhesive. An increase in $\bar{\theta}$ may be due to any number of possibilities, such as an increase in the length of the joint and/or an increase in the shear modulus of the adhesive, a decrease in the thicknesses of Adherend 1 and/or thickness of the adhesive layer, a decrease of Young's modulus of Plate 1, and finally an increase in R.

The parameter, R, itself represents only the geometric and material properties of the adherends. The decrease of R involves the decrease of Young's modulus and thickness of Plate 1 or the increase of the properties mentioned but applied to Plate 2. For similar adherends, it is equal to unity.

The parameter, $\bar{\psi}$, can be seen as a thermal parameter. It involves the temperature difference between the two plates and their respective thermal coefficients of expansion. The parameter, $\bar{\psi}$, increases if the thermal mismatch increases where the two plates have a large difference in coefficient of thermal expansion. It also increases when the joint length and shear modulus of the adhesive increases. Finally, $\bar{\psi}$ is inversely proportional to the thickness of the adhesive layer and the axial load.

The effect of $\bar{\theta}$ on shear stress $S(\xi) = (L/p_0)\,\tau$ distribution is shown in Fig. 2. For an adhesively bonded joint with the same adherend materials ($R = 1$), the results show that the higher $\bar{\theta}$ value causes very uniform (almost zero) stress over the bonded area with the peak shear stresses confined to the small region near the edge. Figure 3 shows the effect of a sym-

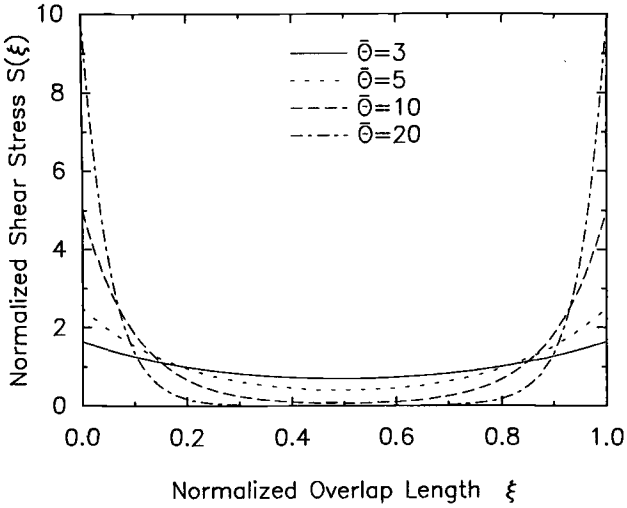

FIG. 2—*Normalized shear stress* S(ξ) *versus normalized overlap length* ξ *for adhesive joints with identical adherends* (R = *1) for several values of* $\bar{\theta}$.

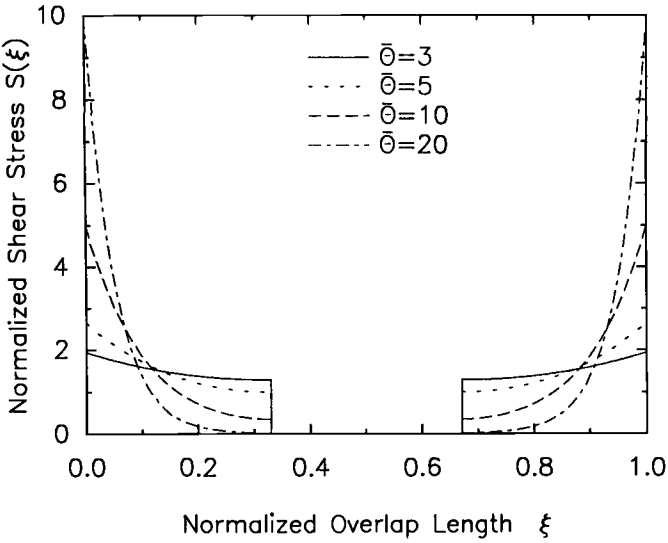

FIG. 3—*Normalized shear stress* $S(\xi)$ *versus normalized overlap length* ξ *for adhesive joints with identical adherends* (R = *1) and a center void for several values of* $\bar{\theta}$.

metric void on the shear stress distribution for different values of $\bar{\theta}$. Here, again, the peak stress distribution is confined to the edge of the bonded joint.

To evaluate the degree of stress variation as it is affected by a void and $\bar{\theta}$, a shear stress factor, SSF, has been defined as the ratio of peak stress over the average stress. The SSF has been computed for a set of increasing symmetric void sizes. Figure 4 shows that the SSF is constant over most of the void size range (up to 70% of the overlap length) for the higher values of $\bar{\theta}$. So it is expected that the failure load would be independent of a void for this range of void size. Effects of thermal mismatch between adherends are reported in detail in Ref *37*. The stress distribution is significantly changed for adherends with a large difference in the thermal expansion coefficient. The effect of a disbond on the shear stress distribution is also investigated. Here, again, disbonds up to 70% of the overlap length were found to have a negligible effect on the peak shear stress for $\bar{\theta} \geq 10$.

Theoretical Study of the Effects of Voids on Dynamic Response of Single Lap Joints

In order to understand the effects of voids on the dynamic response of lap joints, a study has been carried out on the linear frequency response of an adhesive joint with a void with particular attention given to the overlap region. This will be useful in effectively interpreting ultrasonic data for the bond quality evaluation.

In the analysis, a finite element model is used to represent a simple adhesive lap joint. A harmonic force excitation is applied at one end of the joint near the overlap region, and a displacement response at several output points is calculated over a frequency range. The modal analysis and frequency response calculation is performed for a joint with and without a void in the adhesive to determine changes in frequency response patterns caused by the void. The results indicate clear differences in the response patterns over a frequency range which covers all natural frequencies of the finite element model. The results presented here focus on the higher frequencies.

Beam elements are used for the adherends, and lateral stiffness elements are used for the adhesive. Voids are created by removal of lateral stiffness elements. The model is simple and

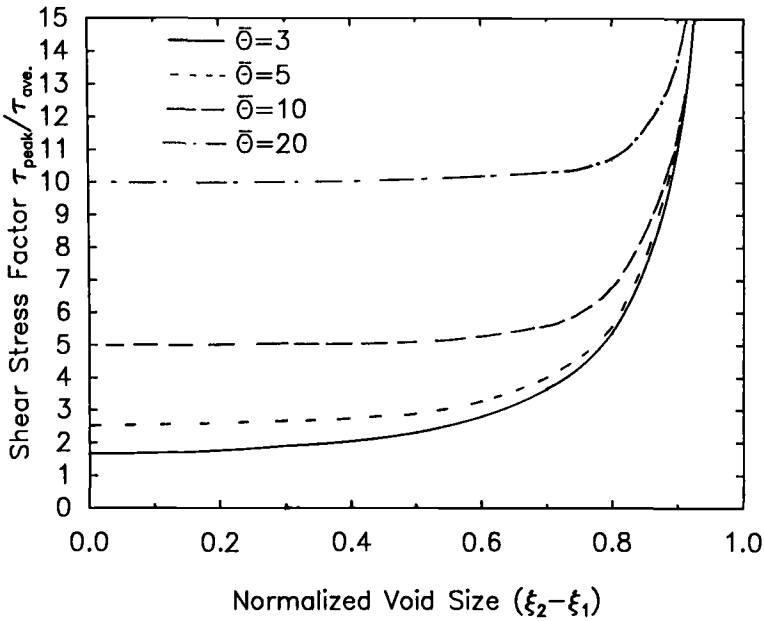

FIG. 4—*Shear stress factor τ_{peak}/τ_{av} versus normalized void size $(\xi_2 - \xi_1)$ in adhesive joints with identical adherends and a center void for several values of $\bar{\theta}$.*

will indicate the important features to be expected. The NASTRAN code has been used. Material properties are for similar aluminum alloy adherends (E = 69 GPa with adherend thickness of 3.17 mm) and Hysol EA9689 adhesive with E = 2.2 GPa and thickness of 0.13 mm. The overlap was 25.4 by 25.4 mm, and symmetric and unsymmetric voids were introduced in the overlap and dynamic responses for identical input harmonic force were evaluated.

The system equations formed for frequency response analysis include mass, damping, and stiffness matrices and the system load vector. The equations may be written in matrix notations as follows

$$M\ddot{U}(f) + C\dot{U}(f) + KU(f) = F(f) \tag{13}$$

where f is the discrete frequency value.

The harmonic excitation is frequency dependent and the solution is obtained for the desired discrete frequencies. Since all nodal motion is assumed to be steady state, the velocities and accelerations are related to the displacements by

$$\ddot{U} = -(2\pi f)^2 U, \; \dot{U} = i(2\pi f)U \tag{14}$$

The frequency response equation then becomes

$$[-(2\pi f)^2 M + i(2\pi f)C + K]U(f) = F(f) \tag{15}$$

Equation 15 represents a system of equations, and the solution for $U(f)$ can be found for every frequency point. Proportional damping is used so that

$$C = c_1 K + c_2 M \tag{16}$$

In the present study $c_2 = 0$, and c_1 is given very small values (of the order of 0.001). The frequency response is calculated for the two configurations indicated in Figs. 5 and 6. Typical frequency response curves are given in Figs. 5 and 6. For a given frequency, the ratio of the displacement with a void to the displacement without a void is plotted against void size in Figs. 7 and 8. It should be borne in mind that for different void sizes, the structural configuration changes and the natural or resonant frequencies will change so that for a fixed frequency these curves need not be monotonic.

The results of this analysis indicate that although there was little change in the peak shear stress in adhesively bonded joints with voids up to 70% of the overlap length ($\bar{\theta} \geq 10$), the dynamic response may be significantly affected by the presence of voids. These results have direct implication in nondestructive evaluation of the adhesively bonded joints.

Experimental Investigations

Adhesively bonded joint specimens were prepared by using 1018 cold-rolled steel, unidirectional graphite epoxy composite material, and aluminum 6061-T6 as adherends. Identical adherends were joined together in a single lap joint configuration using Hysol EA9689 epoxy film of 0.13 mm thickness. For joints with steel as adherends, the adherend surfaces were prepared according to ASTM Guide for Preparation of Metal Surfaces for Adhesive Bonding (D 2651-90). For joints with aluminum as adherends, the adherend surfaces were either sanded and cleaned with acetone or were just cleaned with acetone prior to bonding. The composite adherends were slightly sanded in their overlap areas in order to remove the residual mold release prior to their bonding. For metal adherends, the overlap area was 25.4 by 25.4 mm and the adherend thickness was 3.17 mm. Joints with graphite epoxy composite as adherend had overlap dimensions of 50.8 by 25.4 mm, and the thickness of the composite adherend was 1.07 mm. Various defects such as voids and disbonds were introduced in the overlap area in order to change the bond strength. Voids of different sizes were introduced by cutting the adhesive

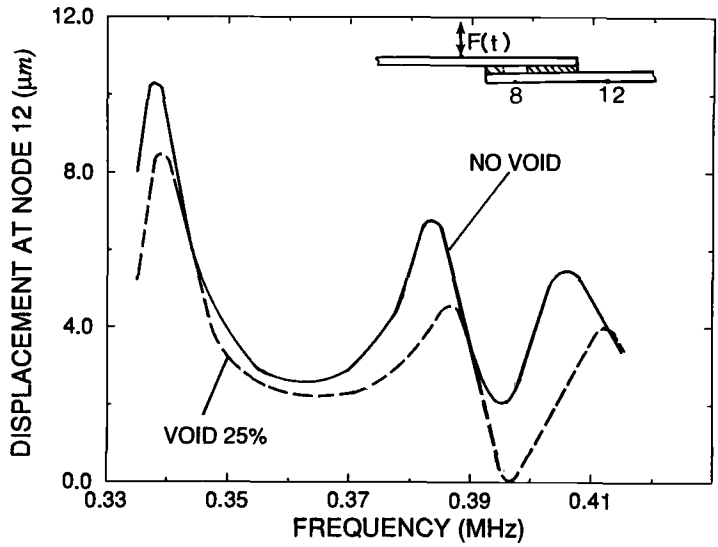

FIG. 5—*Finite element model and frequency responses at Node 12 for aluminum-adhesive-aluminum specimens with no void and a 6.35-mm void. Void starts at 3.18 mm from left end of 25.4-mm overlap.*

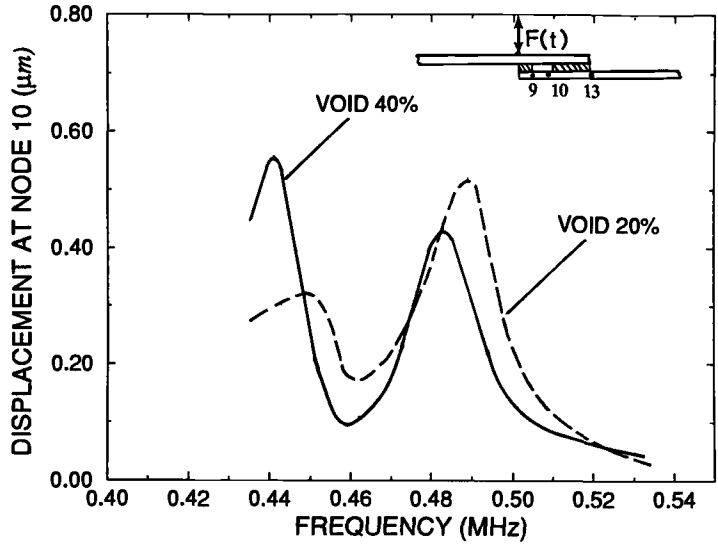

FIG. 6—*Finite element model and frequency responses at Node 10 for aluminum-adhesive-aluminum specimens with a 5.08-mm and 10.16-mm void. Void starts at 2.54 mm from left end of overlap.*

film from the desired region of the overlap and removing it from the overlap region prior to manufacturing specimens. Disbonds were created by spraying mold release agent on the sections of the overlap region. However, adhesive film was left on these regions. Thus, one may assume disbond is a zero volume void.

Various ultrasonic setups and methodologies were used to measure longitudinal pulse-echo attenuation, through transmission longitudinal and shear waves attenuation, using both direct

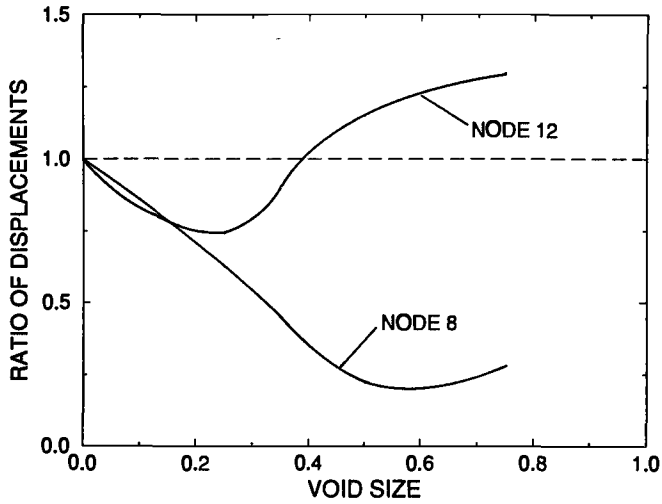

FIG. 7—*Ratio of displacements at Nodes 8 and 12 for specimens with and without void (Δ/Δ_0) versus void size at frequency of 0.39 MHz. Void starts at 3.17 mm from left end of overlap, and void size is given as percent of overlap length of 25.4 mm.*

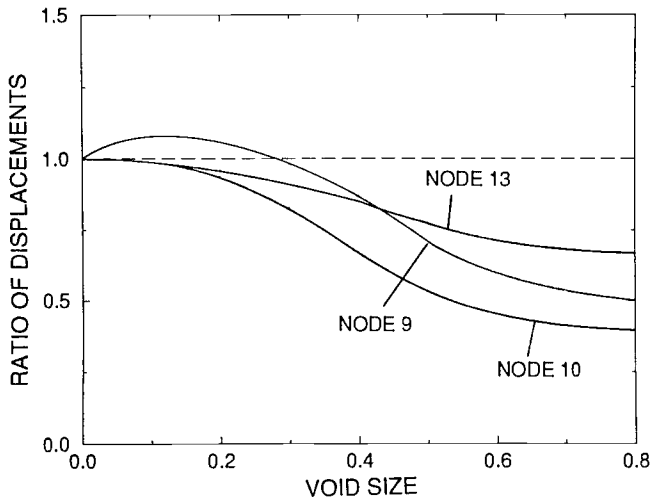

FIG. 8—*Ratio of displacements at several locations for specimens with and without void (Δ/Δ_0) versus void size at frequency of 0.49 MHz. Void starts at 2.5 mm from left end of the overlap, and size is given as percent of overlap length of 25.4 mm.*

contact and immersion techniques and acousto-ultrasonic parameters. In the attenuation experiments, narrow band Panametric transducers with center frequencies of 1 and 2 MHz were used both as transmitting and receiving transducers. Both narrow band signal (pulse oscillator) and broad band pulse were used in these experiments. In the acousto-ultrasonic experiments, a narrow band Panametric transducer with a center frequency of 1 MHz and a FC-500 AET transducer with a flat sensitivity in the frequency range of 100 kHz to 2 MHz were used as transmitting and receiving transducers, respectively. The experiments were conducted by using a broad band pulse with a center frequency of 1 MHz. The received signals were digitized in an Niclolet digital oscilloscope and stored in a PC computer and later analyzed in a SUN work station (Fig. 9). The signals were analyzed in both time and frequency domains.

In the time domain, attenuation, stress wave factor, SWF, and acousto-ultrasonic parameter AUP were measured for each specimen. Assuming that the impedance between transmitting and receiving transducers and adherends is $F_1(\omega)$ and $F_2(\omega)$, the amplitude or peak amplitude of the received signal from a perfect and a defective specimens for an input pulse oscillator or pulse can be expressed as

$$(Ar)_p = F_1(\omega)F_2(\omega)A_t\bar{e}^{\alpha_p t} \tag{17}$$

$$(Ar)_d = F_1(\omega)F_2(\omega)A_t\bar{e}^{\alpha_d t} \tag{18}$$

where A_t is the transmitted signal amplitude, α_p and α_d are the attenuation in perfect and defective specimens, t is the bond thickness, and $(Ar)_p$ and $(Ar)_d$ are the amplitude of the received signals from perfect and defective specimens at frequency ω. The change in attenuation can be obtained from Eqs 17 and 18 as

$$\alpha_d - \alpha_p = \Delta\alpha = \ln\left[\frac{(Ar)_p}{(Ar)_d}\right]\Big/ t \tag{19}$$

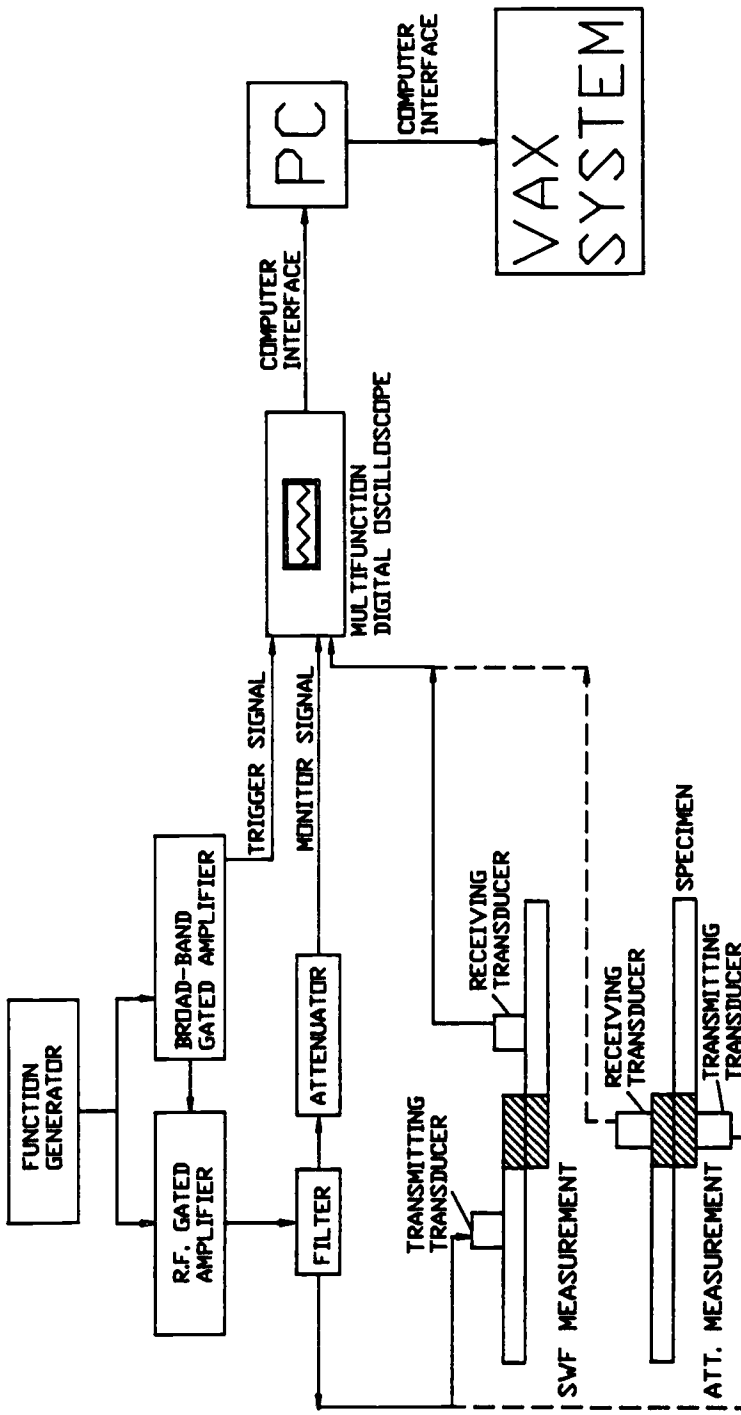

FIG. 9—*System for attenuation and acousto-ultrasonic parameters measurements.*

Stress wave propagation efficiency was evaluated by evaluating stress wave factor values [*19,21*] at several threshold levels. The stress wave factor is defined as the number of times a signal passes a threshold level. Acousto-ultrasonic parameters were also measured for all specimens. This is defined as

$$AUP = \sum_{i=1}^{n} (A_i - Th) \tag{20}$$

where A_i is the amplitude of the signal passing threshold level of Th, and n is equal to the SWF.

Upon completion of acousto-ultrasonic experiments, specimens were broken in an Instron Machine by applying tensile load at the rate of 22 N/s. Acoustic emission activities of steel-adhesive-steel and graphite epoxy composite-adhesive-graphite epoxy composite were monitored. Here the results of acoustic emission activities of the steel-adhesive-steel specimens will be discussed. Since the failure load in these specimens was much less than the load required for yielding adherends, all received activities were related to the bond failure. However, for graphite epoxy composite-adhesive-graphite epoxy composite specimens, bond failures were sometimes accompanied by fiber fracture and delamination. For this reason the correlation of these data with the bond strength was not clear.

For steel-adhesive-steel specimens, two AE transducers—each with a center frequency of 175 kHz (AC 175L)—were utilized to detect the events emitted from the specimen at a distance of 7.6 cm (3 in.) apart. Each sensor was coupled with the work piece through a B-type Panametrics couplant and held in position with the aid of four stiff springs as shown in Fig. 10. The data were gathered and analyzed using an AET 5500 system. The data collection was focused on the lap joint portion only, and all of the other AE activities were thus discarded. For the lap joint, AE event locations were established using the difference in the arrival times of the signals received by the two sensors. Some of the parameters measured during the tension tests were as follows: peak amplitude in decibels, event duration and rise time in μ seconds, ring down counts, slope, and acoustic energy. Here, slope has been defined as peak amplitude/rise time, while acoustic energy was defined as 10*log (event duration) + peak amplitude. It is notable that RMS amplitudes of events has also been used as an indicator of the relative amount of acoustic energy by some researchers. Pencil lead fracture method was used in order to calibrate the system prior to the actual run. Calibration eliminated the need to obtain the velocity of emitted waves. The detected signals were initially preamplified 60 dB to a total system gain of 80 dB. A floating threshold of 0.5 V was chosen to eliminate the background noise.

Experimental Results and Discussion

For the steel-bonded joint specimens, the value of $\bar{\theta}$ from Eq 9 is found to be 3.4. For this value of $\bar{\theta}$ the peak shear stress is affected by introduction of void and disbond in the overlap. It was suspected that the through transmission attenuation would be also affected in a similar way by the presence of void or disbond. Using both Panametric longitudinal and shear transducers with a nominal element size of 19 mm, the attenuation changes for the entire overlap length (25.4 by 25.4 mm) were evaluated at frequencies of 2 and 1 MHz. Transducers were coupled to the specimens by using either low- or high-viscosity Panametric couplants (low-viscosity couplant when using the longitudinal transducers and high-viscosity couplant when using the shear transducers). A load of 90 N was applied to each transducer by using a spring fixture device. Figures 11 and 12 show the changes in longitudinal and shear wave attenuations versus bond strength. At first glance the data suggest no correlation between bond strength and

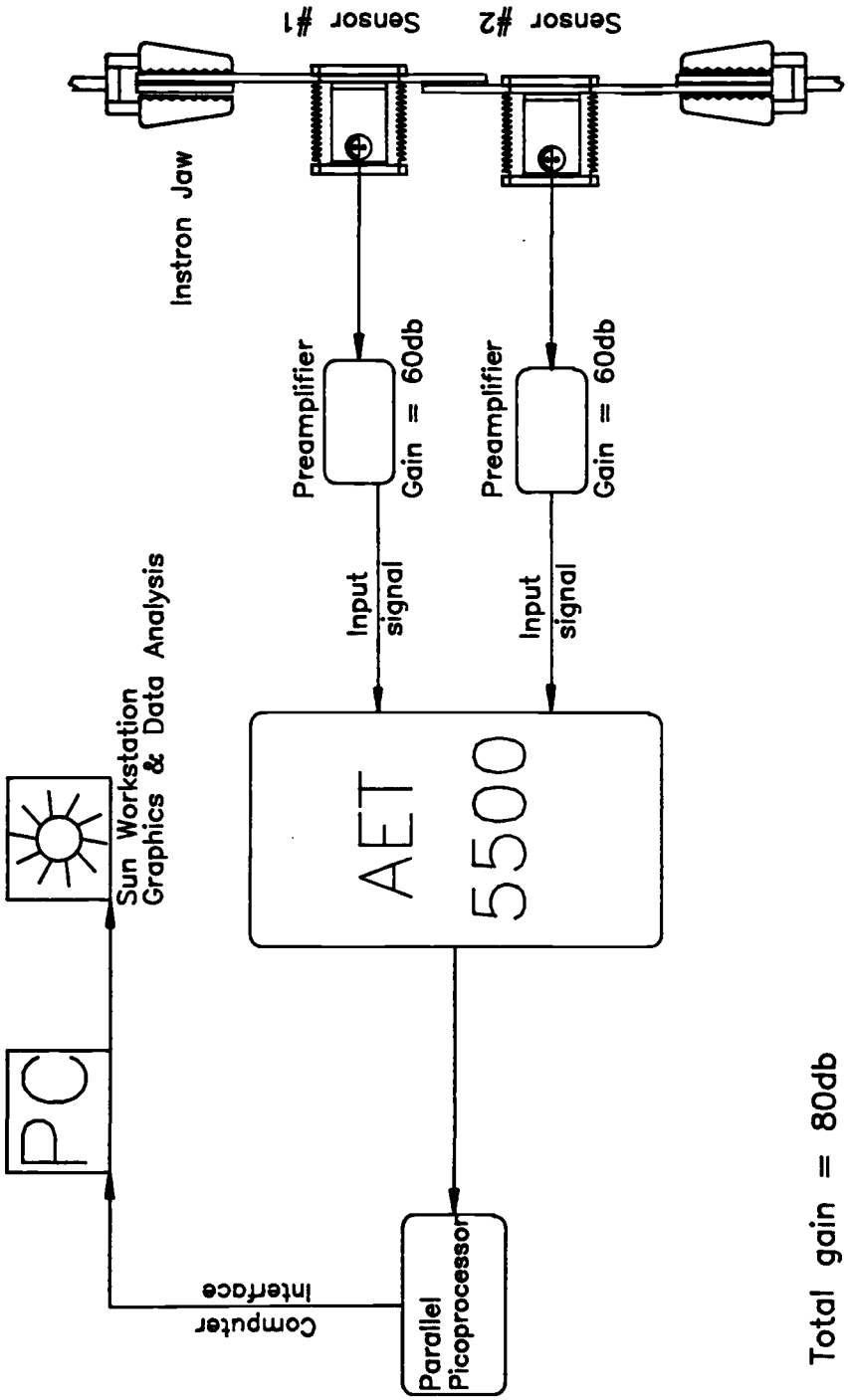

FIG. 10—*Schematic diagram of the acoustic-emission data acquisition system.*

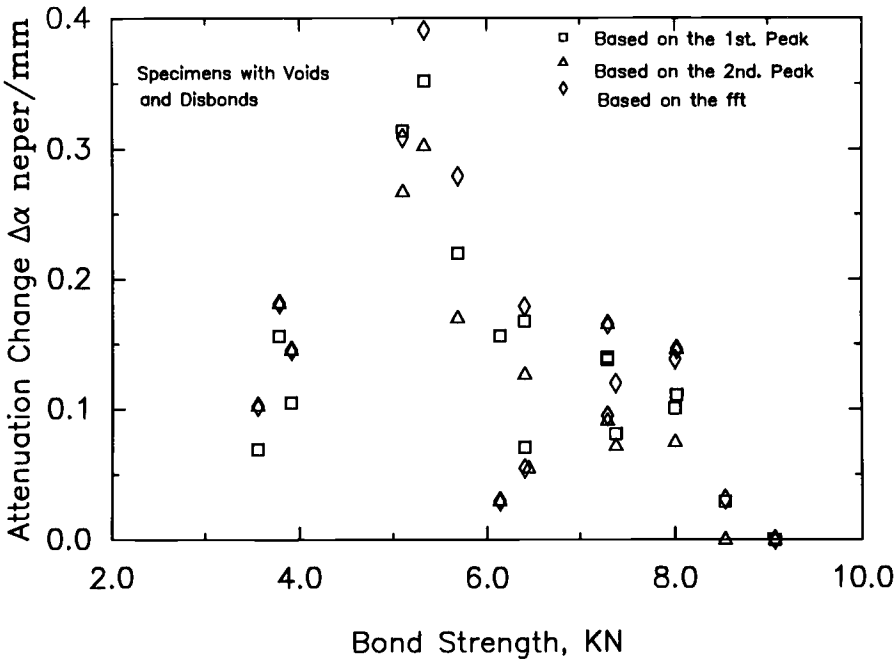

FIG. 11—*Changes of longitudinal wave attenuation versus bond strength for a pulse oscillator with the center frequency of 2 MHz propagating through the lap thickness in steel-adhesive-steel specimens with symmetric void and disbond in the middle of overlap.*

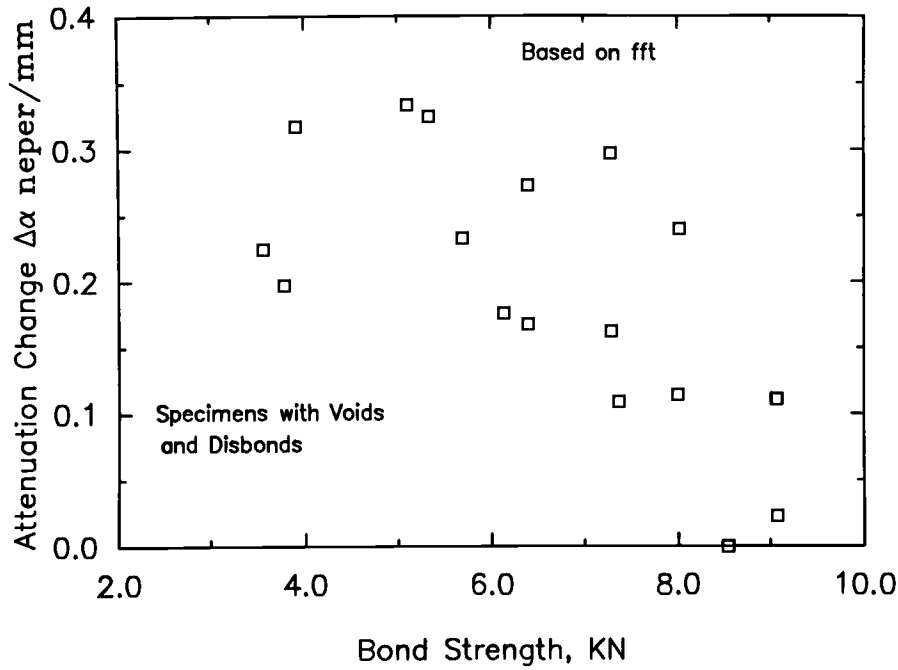

FIG. 12—*Changes of shear wave attenuation versus bond strength for a pulse oscillator with the center frequency of 1 MHz propagating through the lap thickness in steel-adhesive-steel specimens with symmetric void and disbond in the middle of overlap.*

attenuation change. However, closer examination of the data shows that although disbonds and voids have a similar effect on the bond strength, they have completely different effects on wave propagation characteristics. For specimens with a void, the transmitted wave is reflected significantly at the adherend void interface. A larger void results in more reflection and thus higher attenuation. However, the disbond is a weak bond between adherend and adhesive. The transmitted wave is not significantly affected by the presence of this region in the overlap. Furthermore, the attenuation change may not be very sensitive to the disbond length. Separating the data for specimens with voids and specimens with disbonds and plotting attenuation change versus bond strength results in an excellent correlation between attenuation change and bond strength for specimens with voids (Figs. 13 and 14). Figure 15 shows that there is no correlation between attenuation change and bond strength for specimens with disbond, and the attenuation change is fairly constant over the disbond of (3 to 19 mm) range. The correlations between the stress wave factor, SWF, and the acousto-ultrasonic parameter, AUP, and the bond strength for these specimens were not clear. This may be explained by considering the dynamic response of the systems for an input wave at one edge and received wave at the other edge (Figs. 7 and 8). Here, again, the peak amplitude of the signal is not an increasing function of disbond and void size. In contrast, bond strength is an increasing function of the void and disbond sizes.

In the acoustic emission experiments, we expected to find a good correlation between acoustic emission parameters and bond strength for all types of specimens with different defects (steel-adhesive-steel specimens, with $\bar{\theta} = 3.4$). This is due to the nature of failure location and mechanism and energy released during failure. Since for symmetric voids and disbonds in the center of the overlap, stress distribution is almost identical, the bond strength and energy released can be assumed to be the same for a specimen with identical void or disbond size.

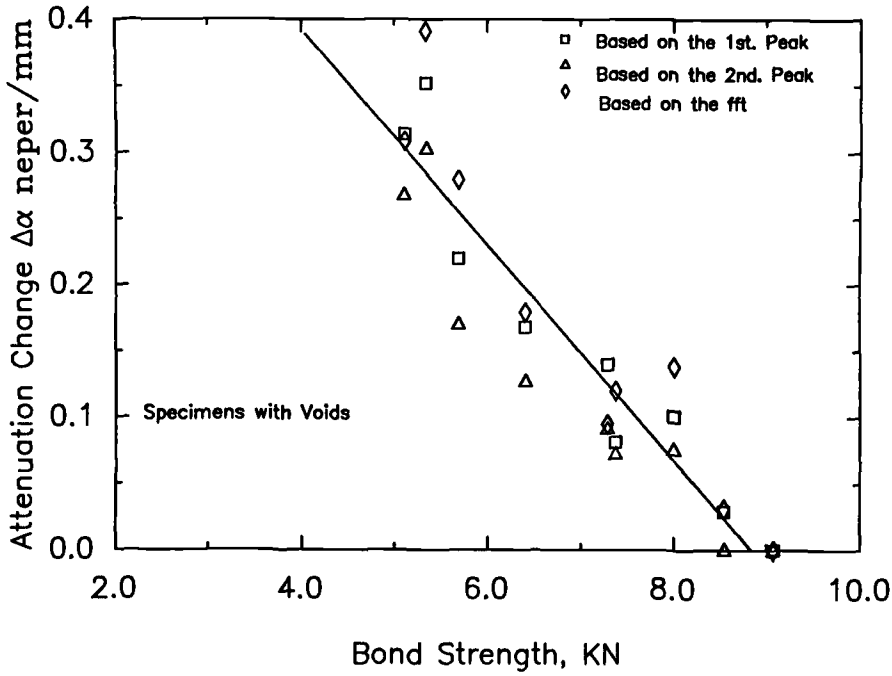

FIG. 13—*Changes of longitudinal wave attenuation versus bond strength for a pulse oscillator with a center frequency of 2 MHz propagating through the lap thickness in steel-adhesive-steel specimens with a symmetric void in the middle of the overlap.*

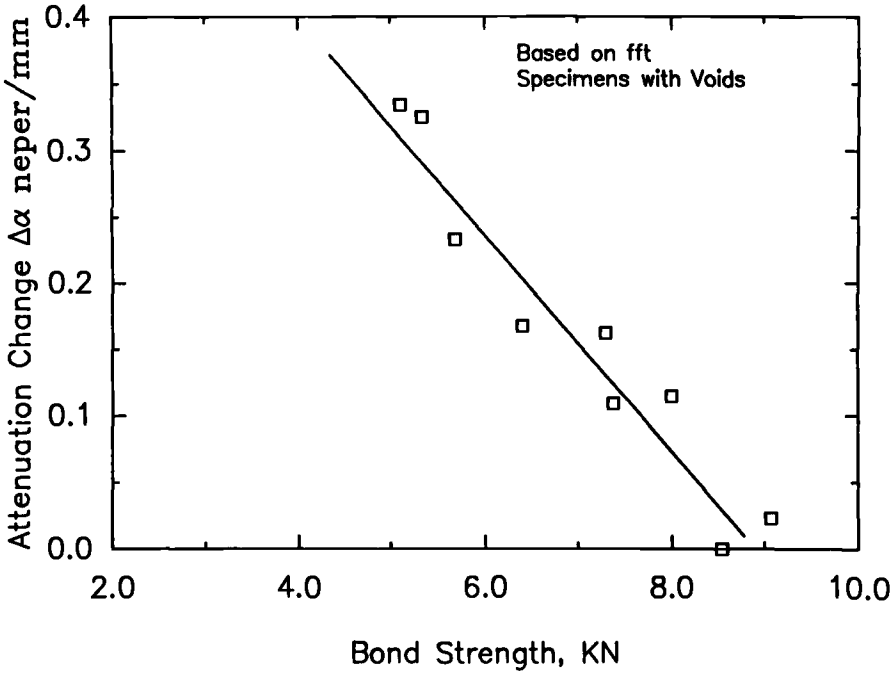

FIG. 14—*Changes of shear wave attenuation versus bond strength for a pulse oscillator with a center frequency of 1 MHz propagating through the lap thickness in steel-adhesive-steel specimens with a symmetric void in the middle of the overlap.*

Furthermore, all detected released energy is associated with the high-stress areas, which are the two edges of the overlap, which also control the bond strength. Figure 16 is a plot of a typical load-time curve of an adhesively bonded joint specimen along with its corresponding mean ring down counts (number of threshold crossing) versus time. There are three prominent peaks, the last of which corresponds to the time of failure. Having a lower amplitude, the first two peaks can be associated with crack initiation and preliminary crack growth. The source of these prominent peaks, recorded in real-time, was found to be near the end of the lap joint where the failure originated. Furthermore, most of the acoustic emission activities were confined to the edges of the overlap (Fig. 17).

Plots of energy versus time compiled every 4 s during the period in which the specimens reached their ultimate strength exhibit two principal formats as shown in Fig. 18. The specimens with a distinguished peak at failure normally depict specimens with artificial voids or disbonds, Fig. 18*a*. These specimens can be categorized as having failed in a brittle manner due to their short energy released durations. For these specimens, the energy released was relatively high at the peak compared to the perfect ones. Pollock [*38*], in his study of solids, showed that brittle materials exhibited higher peak energy and short emission duration after the maximum load than ductile materials. This may be due to the fast fracture behavior in brittle materials and crack tip blunting (crack arrest) in ductile materials. For perfect specimens, fast fracture may have been prevented by having effective adhesive in the entire overlap. This is not true for specimens with void or disbond. Figure 18*b* depicts energy released for perfect specimens. Energy emission and the number of threshold crossings were sustained at a low level for some period after the time of the maximum peak of energy. This can be due to the crack or damage

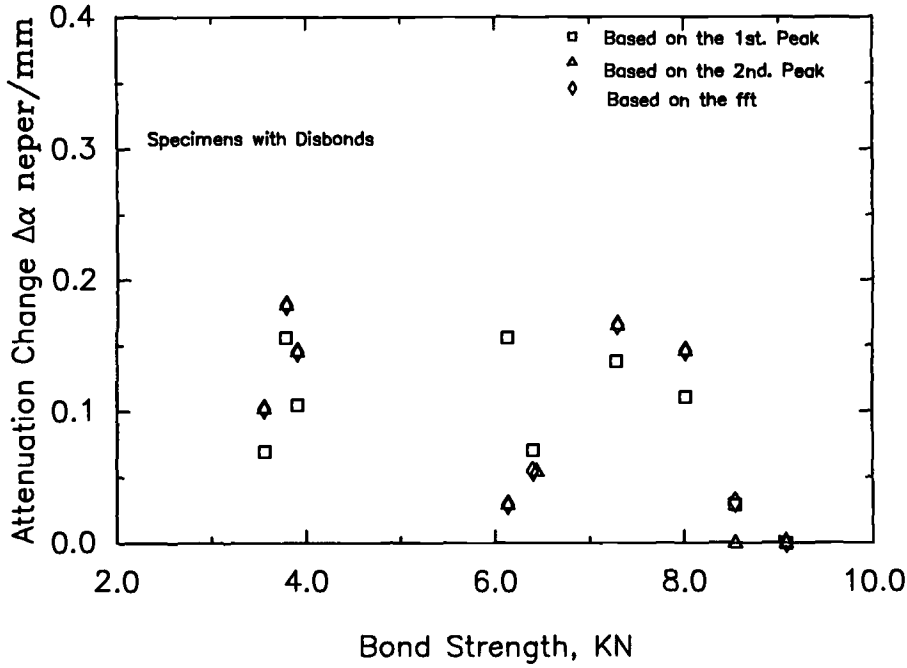

FIG. 15—*Changes of longitudinal wave attenuation versus bond strength for a pulse oscillator with a center frequency of 2 MHz propagating through the lap thickness in steel-adhesive-steel specimens with symmetric disbond in the middle of the overlap.*

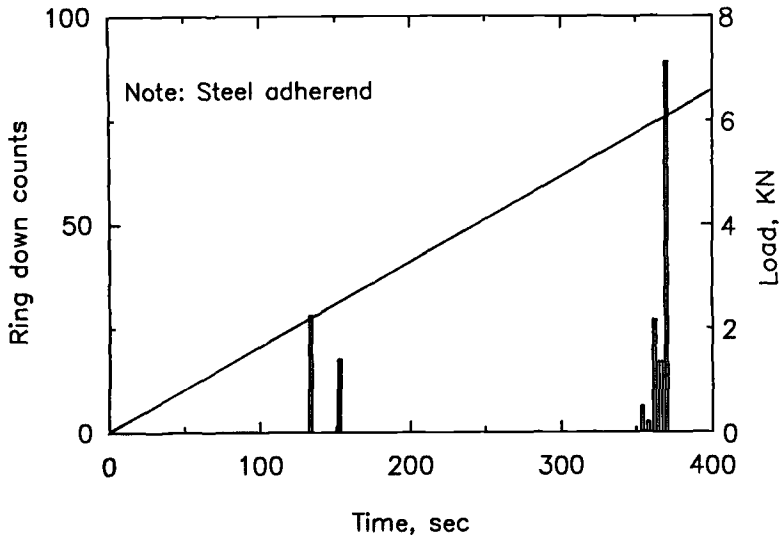

FIG. 16—*Typical load and ringdown counts versus time (interval size = 2 s)*

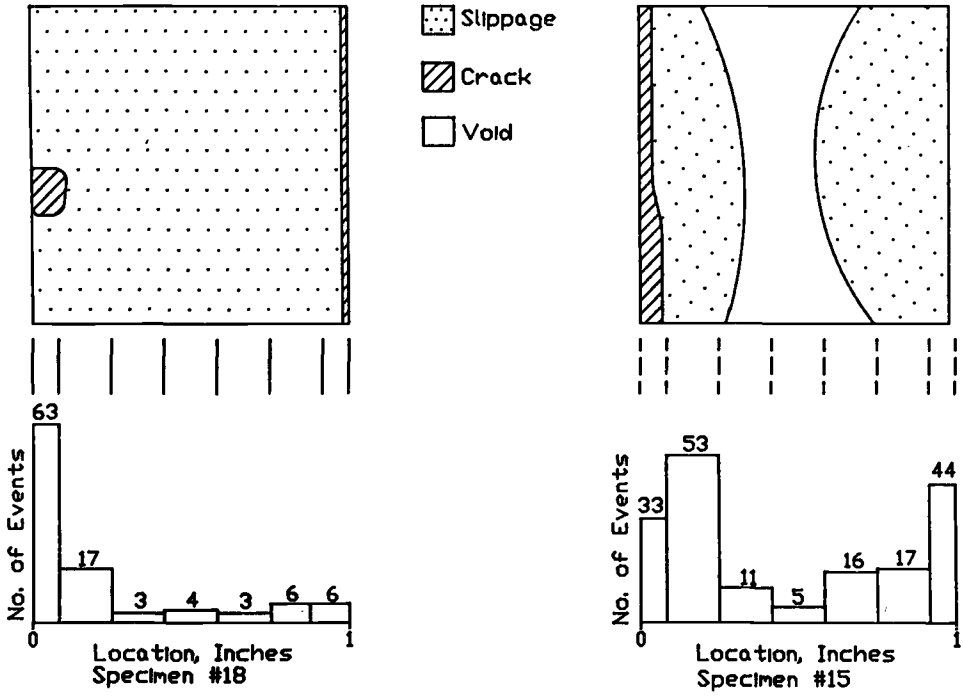

FIG. 17—*Plots of the number of events along the lap joint for two typical specimens.*

growth period in perfect specimens, which is generally greater for the perfect specimens than specimens with a defect. Figures 19 and 20 show that total energy released and number of events at and after maximum peak energy can be related to the bond strength for all types of specimens. Analysis of the acoustic emission data further showed that the events with lower rise time were associated with the crack initiation, while the one with higher rise time was associated with the crack (damage) propagation.

For the graphite epoxy composite-adhesive-graphite epoxy composite, $\bar{\theta}$ was found to be = 10. For this value of θ it was expected that symmetric void or disbond up to 70% of the overlap length would have a negligible effect on bond strength. Figure 21 shows that indeed there is little change in the bond strength for specimens with void up to 70% of the overlap length in the central region of the bonded joint. The peak amplitude of the received signal in a stress wave factor set-up experiment (Fig. 22) was found not to be very sensitive to the bond strength, and showed a trend similar to the one exhibited by dynamic analyses (Fig. 8). Other acousto-ultrasonic factors also failed to show any sensitivity to the bond strength.

To address more effectively the effects of disbond, improper adherend surface preparation, over-cured and under-cured adhesive, and deficient pressure during manufacturing of these specimens on bond strength, we set up an immersion experiment (Fig. 23). As described above, through transmission experiments utilizing a contact transducer resulted in little change in attenuation data for specimens with disbonds. Furthermore, disbonds or voids may not result in any change in bond strength as shown for composites. A disbond right at the edge and a disbond in the middle of the bond have completely different effects on the bond strength. However, using contact transducers may not be a sensitive means of evaluating any changes

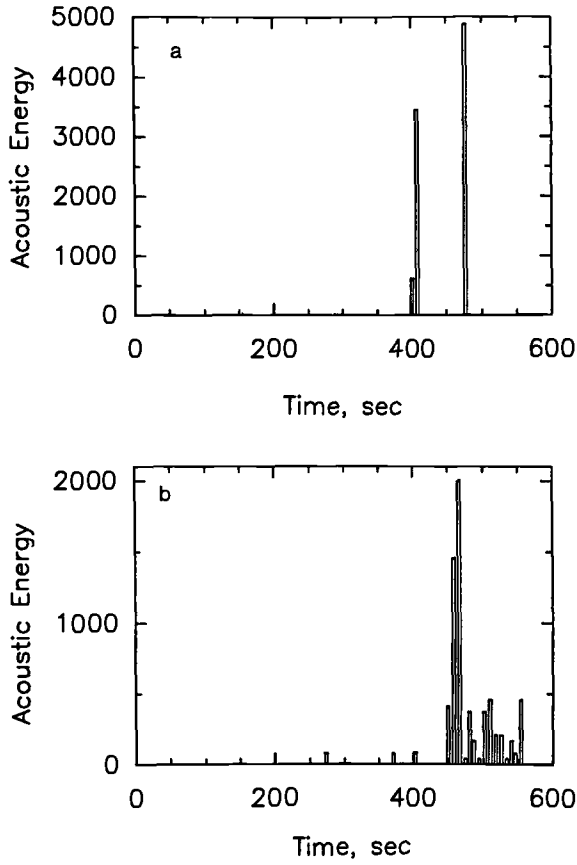

FIG. 18—*Typical plot of acoustic energy versus time for* (a) *specimens with void or disbonds, and* (b) *perfect specimens.*

in attenuation. To incorporate the location into attenuation, peak amplitude, SWF, and AUP measurements, a weighting function $w(x) = e^{\bar{\theta}x}$, which simulates the stress distribution, was introduced. Here, x is from the center of overlap. Using focus transducers with a center frequency of 2 MHz and adjusting transducer specimen distance such that the focal point lies on the adhesive adherend interface, the peak amplitude, SWF, and AUP at several locations of the over lap were measured using a pulse with a center frequency of 2 MHz. New ultrasonic parameters were introduced as

$$\text{Peak}^* = \sum_{i=1}^{j} e^{\bar{\theta}x_i} \text{Peak}(x_i) \tag{21}$$

$$SWF^* = \sum_{i}^{j} e^{\bar{\theta}x_i} SWF(x_i) \tag{22}$$

$$AUP^* = \sum_{i}^{j} e^{\bar{\theta}x_i} AUP(x_i) \tag{23}$$

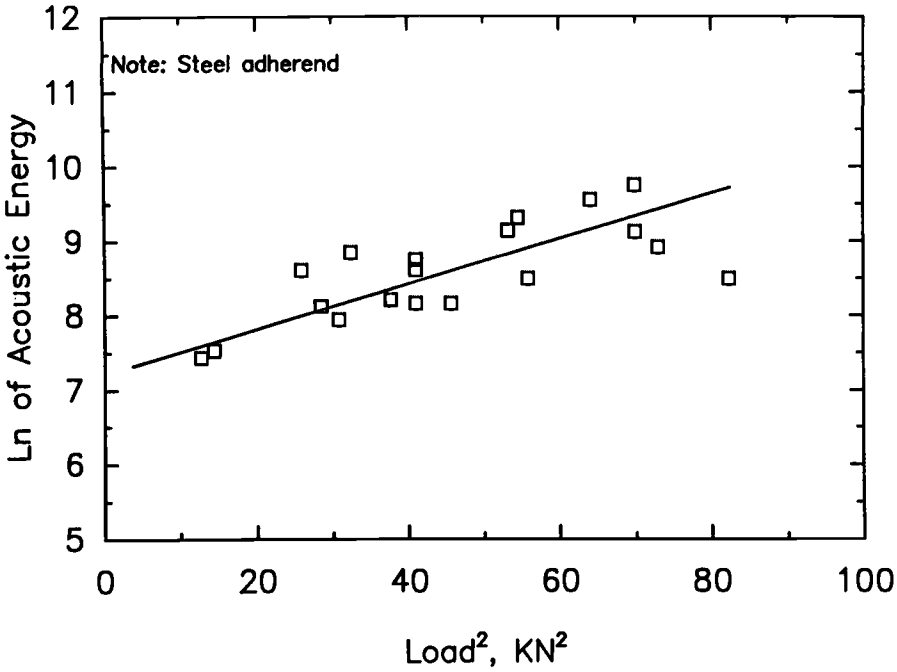

FIG. 19—*Natural log of acoustic energy released at and immediately after the peak-released energy versus the square of maximum load (bond strength)² endured.*

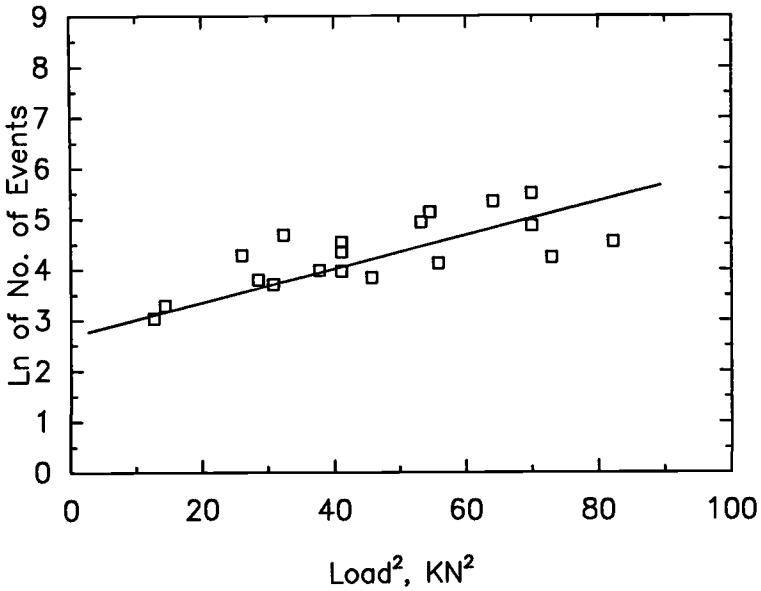

FIG. 20—*Natural log of the number of events at and after peak event (failure point) versus the square of the maximum load (bond strength)² endured.*

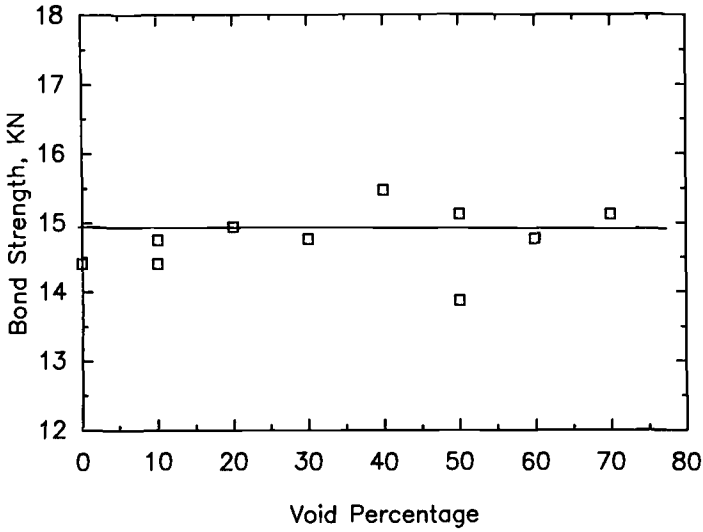

FIG. 21—*Bond strength versus void size in graphite epoxy-adhesive-graphite epoxy composite single lap joints with θ = 10. Symmetric void starts from the middle of the overlap, and void size is given as percent of overlap length of 50.8 mm.*

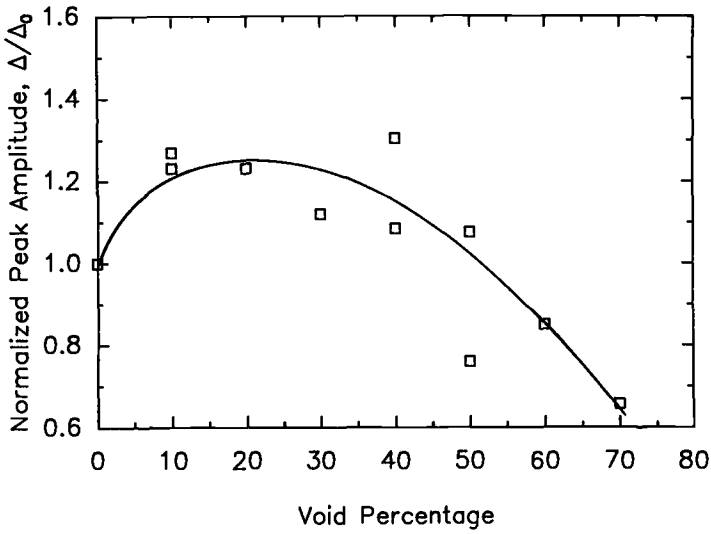

FIG. 22—*Normalized received peak amplitude in acousto-ultrasonic experiments versus void size in graphite epoxy-adhesive-graphite epoxy composite single lap joints with θ = 10. Symmetric void starts from the middle of overlap, and void size is given as percent of overlap length of 50.8 mm.*

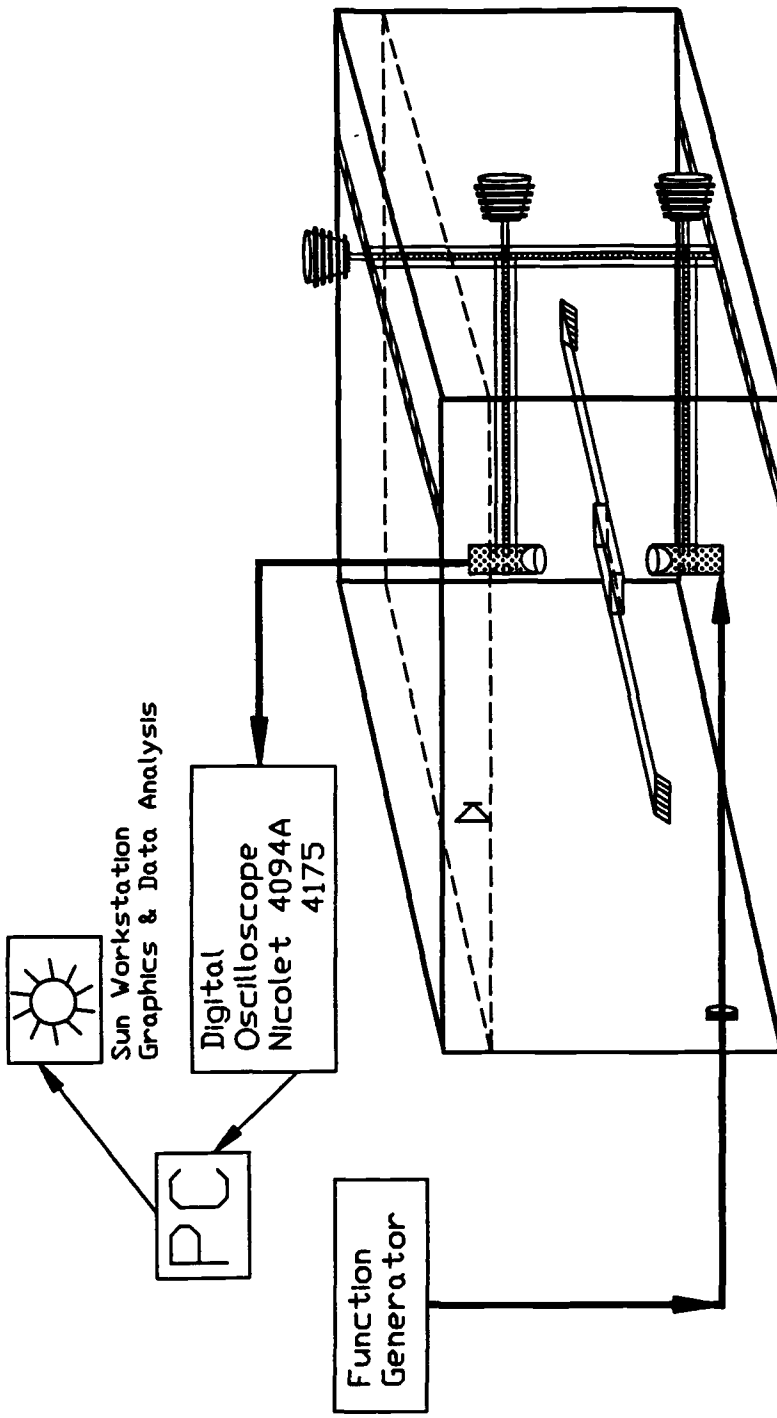

FIG. 23—*Schematic diagram of the immersion system with focused transducers.*

These parameters were also evaluated by considering the weighting function to be equal to unity. These parameters were either evaluated for the entire overlap, or the overlap was divided in half and these parameters were evaluated for each half. The bond strength was assumed to be controlled by the section with a lower specific parameter value. For a variety of aluminum-adhesive-aluminum specimens with many surface defects, minimum AUP* produced an excellent correlation with bond strength (Fig. 24). However, the correlation of the same data with the bond strength without incorporating weighting function (minimum of or total of Σ AUP(x_i) versus bond strength) was not good (Fig. 25). The results presented in this paper clearly show that the quest for an effective procedure for nondestructive evaluation of the adhesively bonded joint requires a multi-disciplinary approach. We believe that the immersion technique using focus transducers and incorporating the proper weighting function is the most effective method for bond quality interrogation. This procedure may be applied by using echo transducers. Further research must be performed to substantiate the new parameters.

Conclusions

Defects such as voids, disbonds, and improper adherends surface preparation and manufacturing procedures may affect the bond strength of adhesive joints. In order to develop a proper acousto-ultrasonic method for bond quality interrogation, effects of defects such as void and disbond on (1) the stress distribution over the overlap, (2) the dynamic response, and (3) ultrasonic wave propagation must be understood.

The stress distribution in a single lap joint with and without voids is analyzed. For identical adherends, the stress distribution depends on a nondimensionalized parameter $\bar{\theta}$. This parameter incorporates adherend and adhesive thicknesses and properties. The analyses show that for

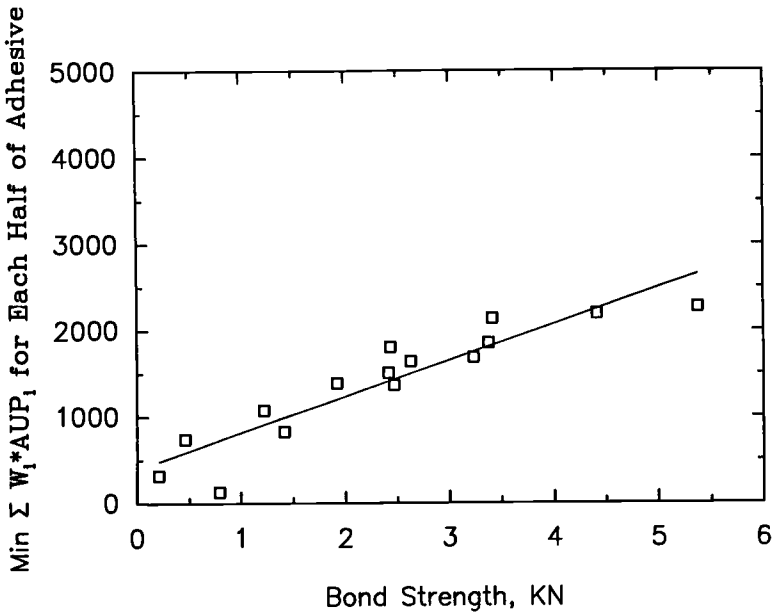

FIG. 24—*Bond strength versus minimum of* Σ *(weighted acousto-ultrasonic parameter) for aluminum-adhesive-aluminum specimens with various defects (mostly due to improper surface preparation and disbond).*

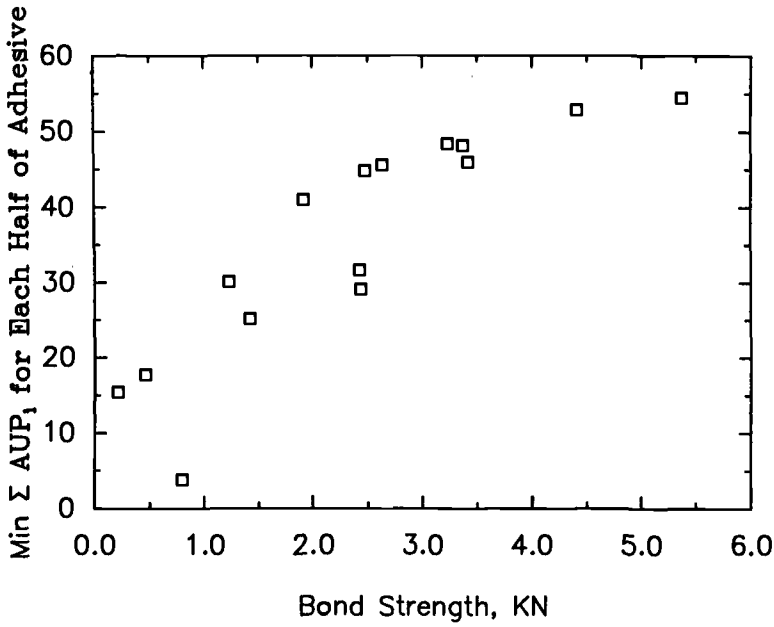

FIG. 25—*Bond strength versus minimum of* Σ *(acousto-ultrasonic parameter) for aluminum-adhesive-aluminum specimens with various defects (mostly due to improper surface preparation and disbond).*

joints with $\bar{\theta} \geq 10$ the maximum shear stress is not affected by the presence of symmetric voids or disbond in the middle of overlap (void < 70% of overlap length). In contrast, a finite element analysis shows that the dynamic response of a bonded joint is significantly affected by the presence of voids or disbonds in the overlap region. These results show that the measured ultrasonic parameters are affected by the defects. However, these measured values may or may not be related to the bond strength.

Through-transmission longitudinal and shear wave attenuation changes in steel-adhesive-steel specimens ($\bar{\theta} = 3.4$) with and without defects (symmetric voids and disbonds in the middle of overlap region) were measured using pulse oscillators with the center frequency of 1 and 2 MHz. The experimental results showed that the specimens with a larger void exhibited higher attenuation. These specimens also had lower bond strength. In contrast, specimens with disbonds in the same range size as voids exhibited little variation in the measured attenuation change. However, their strength was affected in a similar way as those with voids. Various other acousto-ultrasonic parameters also failed to show good sensitivities to the bond strength.

Since the location of defects has an important effect on the shear stress distribution and subsequent bond strength, a weighting factor $w(x_i) = \text{Exp}(\bar{\theta}x_i)$ was suggested. Using an immersion system with focused transducers, many acousto-ultrasonic parameters were evaluated. New ultrasonic parameters based on measured values and weighting function were proposed. It was shown that some of the new parameters produced a good sensitivity for bond quality prediction. However, the sensitivity of the same parameters without weighting function was somewhat poor.

Acoustic emission activities during the tensile tests were monitored, and several time-domain variables were gathered for steel-adhesive-steel specimens. Two different formats of energy versus time were observed. The specimens with a perfect bond showed an abrupt energy release

at failure followed by a short period of continuous acoustic emission activities. However, specimens with voids or disbonds also showed abrupt energy release, but followed with no additional activities. This behavior was related to the crack initiation and propagation. Acousto emission parameters were found to be a means for bond quality prediction.

Acknowledgment

This research was supported under NASA Grant NAG3-1129 with Dr. Alex Vary as monitor and is gratefully acknowledged.

References

[1] Williams, R. S. and Zwicke, P. E., "Assessment of Adhesive Properties Using Pattern Recognition Analysis of Ultrasonic NDE Data," *Material Evaluation,* Vol. 40, March 1982, pp. 312–317.

[2] Dickstein, P. A., Spelt, J. K., Sinclair, A. N., and Bushlin, Y., "Investigation of Nondestructive Monitoring of the Environmental Degradation of Structural Adhesive Joints," *Material Evaluation,* December 1991, pp. 1498–1505.

[3] Rose, J. L., "Elements of a Feature-based Ultrasonic Inspection System," *Material Evaluation,* Vol. 42, February 1984, pp. 210–218.

[4] Dickstein, P., Segal, Y., Segal, E., and Sinclair, A. N., "Statistical Pattern Recognition Techniques: A Sample Problem of Ultrasonic Determination of Interfacial Weakness in Adhesive Joints," *Journal of Nondestructive Evaluation,* Vol. 8, No. 1, 1989, pp. 27–35.

[5] Dickstein, P. A., Spelt, J. K., and Sinclair, A. N., "Application of a Higher Order Crossing Feature of Nondestructive Evaluation: A Sample Demonstration of Sensitivity to the Condition of Adhesive Joints," *Ultrasonics,* Vol. 29, September 1992, pp. 355–365.

[6] Rose, J. L., Avioli, Jr., M. J., and Bilgram, R., "A Feasibility Study on the Nondestructive Evaluation of an Adhesively Bonded Metal to Metal Bond: An Ultrasonic Pulse Echo Approach," *British Journal of NCT,* March 1983, pp. 67–71.

[7] Subramanian, C. V., Thavasimuthu, M., Palanichamy, P., Bhattacharya, D. K., and Raj, B., "Evaluation of Bond Integrity in Sandwiched Structures by Dry Couplant Ultrasonic Technique," *NDT International,* Vol. 24, No. 1, February 1991, pp. 29–31.

[8] Williams, Jr., J. H., Yuce, H., and Lee, S. S., "Ultrasonic Attenuation of a Void Containing Medium for Very Long Wavelengths," *Materials Evaluation,* Vol. 42, February 1984, pp. 219–224.

[9] Meyer, P. A. and Rose, J. L., "Ultrasonic Determination of Bond Strength Due to Surface Preparation Variations in an Aluminum-to-Aluminum Adhesive Bond System," *Journal of Adhesion,* Vol. 8, 1974, pp. 145–153.

[10] Rose, J. L. and Meyer, P. A., "Ultrasonic Procedures for Predicting Adhesive Bond Strength," *Material Evaluation,* Vol. 31, 1973, pp. 109–114.

[11] Gericke, O. R., "Determination of the Geometry of Hidden Defects by Ultrasonic Pulse Analysis Testing," *Journal of the Acoustical Society of America,* Vol. 35, No. 3, March 1963.

[12] Henneke, E. G. et al., "A Study of the Stress Wave Factor Technique for the Characterization of Composite Materials," NASA Contractor Report 3670, February 1983.

[13] Duke, Jr., J. C., et al., "Ultrasonic Stress Wave Characterization of Composite Materials," NASA Contractor Report 3670, May 1986.

[14] Sarrafzadeh-Khoee, A., Kiernan, M. T., Duke, Jr., J. C., and Henneke, E. G., "A Study of the Stress Wave Factor Technique for the Nondestructive Evaluation of Composite Materials," NASA Contractor Report 4002, July 1986.

[15] Talreja, T., Govada, A., and Henneke, II, E. G., "Quantitative Assessment of Damage Growth in Graphite Epoxy Laminates by Acousto-Ultrasonic Measurements," *Review of Progress in Quantitative Nondestructive Evaluation,* Vol. 3B, D. O. Thompson and D. E. Chimenli, Eds. 1984, pp. 1099–1106.

[16] Duke, Jr., J. C., Henneke, II, E. G., Stinchcomb, W. W., and Reifsnider, K. L., "Characterization of Composite Materials by Means of the Ultrasonic Stress Wave Factor," *Composite Structure,* Vol. 2, I. H. Marshall, Ed., Applied Science Publishers, London, England, 1984, pp. 53–60.

[17] Govada, A. K., Duke, Jr., J. C., Henneke, E. G., and Stinchcomb, W. W., "A Study of the Stress Wave Factor Technique for the Characterization of Composite Materials," NASA Contractor Report 174870, February 1985.

[18] Dickstein, P. A., Giroshovich, S., Sternberg, Y., Sinclair, A. N., and Leibovitch, H., "Ultrasonic Feature-Based Classification of the Interfacial Condition in Composite Adhesive Joints," *Research in Nondestructive Evaluation*, Vol. 2, No. 4, 1990, pp. 207–224.

[19] Vary, A., "Acousto-Ultrasonics," in *Non-Destructive Testing of Fiber-Reinforced Plastic Components*, Vol. 2, J. Summerscales, Ed., 1987, Elsevier Applied Science, London, U.K., pp. 25–54.

[20] Williams, Jr., J. H. and Lee, S. S., "Pattern Recognition Characterization of Micromechanical and Morphological Material State Via Analytical Quantitative Ultrasonics," in *Materials Analysis by Ultrasonics*, A. Vary, Ed., Noyes Data Corp., 1987, pp. 187–199.

[21] Vary, A. and Bowles, K. J., "Use of an Ultrasonic-Acoustic Technique for Nondestructive Evaluation of Fiber Composite Strength," NASA TM73813, February 1979.

[22] Vary, A. and Lark, R. F., "Correlation of Fiber Composite Tensile Strength with Ultrasonic Stress Wave Propagation Factors," NASA TM78846, April 1978 (see also *Journal of Testing and Evaluation*, Vol. 7, No. 4, ASTM, April 1979, pp. 185–191).

[23] Nayeb-Hashemi, H., Cohen, M. D., and Erturk, T., "Evaluation of Fatigue Damage on the Mechanical Properties of Fiber Reinforced Cement Pastes," *Journal of Cement and Concrete Research*, Vol. 15, September 1985, pp. 879–888.

[24] Matthews, J. R., "Acoustic Emission Evaluation," *Acoustic Emission*, J. R. Matthews, Ed., Gordon and Beach Science Publishers, 1983, pp. 1–14.

[25] Heiple, C. R. and Carpenter, S. H., "Acoustic Emission from Dislocation Motion," *Acoustic Emission*, J. R. Matthews, Ed., Gordon and Beach Science Publishers, 1983, pp. 15–103.

[26] Egle, D. M., Tatro, C. A., and Brown, A. E., "Frequency Spectra of Acoustic Emission from Nodular Cast Iron," *Material Evaluation*, Vol. 39, October 1981, pp. 1037–1044.

[27] Volkersen, O., "Die Nietkraftverteilung in Zugbeanspruchten Nietverbindungen mit Konstanten Laschenquerschnitten," *Luftfahrtforschung*, Vol. 15, 1938, pp. 41–147.

[28] Goland, M. and Reissner, E., "The Stresses in Cemented Joints," *Journal of Applied Mechanics*, Vol. 11, No. 1, March 1944, pp. A-14–A-27.

[29] Ishai, O., Peretz, D., and Gali, S., "Direct Determination of Interlaminar Stresses in Polymeric Adhesive Layer," *Experimental Mechanics*, Vol. 17, No. 7, July 1977, pp. 265–270.

[30] Adams, R. D. and Peppiatt, N. A., "Stress Analysis of Adhesive-Bonded Lap Joints," *Journal of Strain Analysis*, Vol. 9, No. 3, July 1974, pp. 185–196.

[31] Hart-Smith, L. J., "Design of Adhesively Bonded Joints," Joining Fibre-Reinforced Plastics," F. L. Matthews, Ed., Elsevier Applied Science, New York, 1987, pp. 271–311.

[32] Hart-Smith, L. J., "Designing to Minimize Peel Stresses in Adhesive-Bonded Joint," *Delamination and Debonding of Materials, ASTM STP 876*, W. S. Johnson, Ed., 1985, pp. 238–266.

[33] Cooper, P. A. and Sawyer, J. W., "A Critical Examination of Stress in an Elastic Single Lap Joint," NASA Technical Paper 1507, September 1979.

[34] Allman, D. J., "A Theory for Elastic Stresses in Adhesive Bonded Lap Joints," *Quarterly Journal of Mechanics and Applied Mathematics*, Vol. 30, Part. 4, November 1977, pp. 415–436.

[35] Rossettos, J. N. and Zang, E., "On the Peak Shear Stresses in Adhesive Joints with Voids" *ASME Journal of Applied Mechanics*, Vol. 60, No. 2, 1993.

[36] Hashemi, H. N. and Rossettos, J. N., "Nondestructive Evaluation of Adhesively Bonded Joints," Progress Report to National Aeronautics and Space Administration, Lewis Research Center, Cleveland, OH, September 1990.

[37] Rossettos, J. N., Peng, Y., and Nayeb-Hashemi, H., "Analysis of Adhesively Bonded Composites Joints with Void and Thermal Mismatch," *Plastics and Plastic Composites: Material Properties, Part Performance, and Process Simulation*, V. J. Stokes, Ed., ASME Winter Annual Meeting, MD, Vol. 29, American Society for Metals, New York, December 1991, pp. 259–268.

[38] Pollock, A. A. and Lane, G., "Prediction of the Strength of Adhesive Bonds and Diagnosis of Poor Adhesion by Means of Acoustic Emission," Information Sheet, Nondestructive Testing Center, Atomic Energy Research Establishment, Harwell, Oxfordshire, England, 1968.

Anil Tiwari[1] *and Edmund G. Henneke II*[2]

Real-Time Acousto-Ultrasonic NDE Technique to Monitor Damage in SiC/CAS Ceramic Composites Subjected to Dynamic Loads

REFERENCE: Tiwari, A. and Henneke II, E. G., **"Real-time Acousto-Ultrasonic NDE Technique to Monitor Damage in SiC/CAS Ceramic Composites Subjected to Dynamic Loads,"** *Cyclic Deformation, Fracture, and Nondestructive Evaluation of Advanced Materials: Second Volume, ASTM STP 1184*, M. R. Mitchell and O. Buck, Eds., American Society for Testing and Materials, Philadelphia, 1994, pp. 363–375.

ABSTRACT: A real-time acousto-ultrasonic (AU) nondestructive evaluation (NDE) technique was developed to study the damage mechanisms of unidirectional and cross-ply SiC/CAS ceramic composites. Real-time AU was found to be very sensitive in detecting the stress levels at which the onset of matrix cracking occurs and the stress level for saturation of matrix cracking. Real-time AU as developed and presented in this paper can continuously monitor damage under cyclic loads and hence enhance our understanding of damage mechanisms in ceramic composites.

KEYWORDS: ultrasonics, acousto-ultrasonics, AU, acoustic, real-time NDE, NDE, nondestructive test, ceramic composite, fatigue damage, damage modes, matrix cracking

Future materials used in fuel-efficient engines and certain space power applications must be able to withstand higher operating temperatures. Furthermore, such materials should offer the distinct advantages of higher strength-to-weight ratio and higher stiffness-to-weight ratio and be more damage tolerant. Ceramic composites possess all of these properties.

Presently, the processing of reliable ceramic composites is a cause for major concern in composite manufacturing industries. Processing and manufacturing of ceramic composite components can introduce defects that will affect the overall integrity of the resultant composite structure. Interest in NDE (nondestructive evaluation) as a tool or means of determining defective components during the processing stage and for in-service quality monitoring has grown. Present NDE techniques cannot detect all types of defects with reliability. To ascertain the quality of composite materials, a NDE technique is necessary to detect certain critical and subcritical flaws.

There is a need to develop NDE techniques that can assess and quantify the damage present in ceramic composites and relate a quantifiable parameter directly to strength or long-time serviceability of the component. Damage accumulation and residual strength needs to be evaluated at different stages of life. The present challenge in the field of NDE is to assess initial integrity and also damage accumulation and residual strength during service.

[1] Graduate assistant (currently research associate) and [2]professor and department head, Engineering Science and Mechanics Department, Virginia Polytechnic Institute and State University. Blacksburg, VA.

Real-Time Acousto-Ultrasonic

The acousto-ultrasonic (AU) NDE technique is a hybrid of the acoustic emission (AE) and ultrasonic methods. The AU technique excites a repeated series of ultrasonic pulses in the specimen by a broad band transducer through a couplant medium. Each pulse simulates acoustic emission in the specimen. The propagating stress wave interacts with the material micro-structure and the damage present between the sender and a receiver transducer.

A conceptual configuration of an AU setup is shown in Fig. 1. An alternative approach for analyzing the received AU signal has been developed in our laboratory [*1–8*]. This approach converts the digitized time-voltage signal from the data acquisition system into an amplitude-frequency spectrum by means of a Hartley's transform algorithm [*9–10*]. Various statistical moments of the frequency spectrum are then calculated and defined as various stress wave factors (SWF). The zeroth moment of the frequency spectrum of the received AU signal is the area under the spectral density distribution and is indicative of the total energy content of the received signal. The SWF(M_0) value is a measure of stress wave energy transmission. The SWF(M_0) values provide a way to "rate" the efficiency with which dynamic strain energy transfer takes place in the material between the two AU transducers. Studies have shown that these moments are affected by damage/flaws present in the structure in a particular manner such that they can be located and characterized. Stiffler et al. [*11*] have shown that a decrease in SWF values calculated by the moments method correlates well with the reduction of stiffness of graphite-epoxy composite specimens subjected to fatigue tests. Tiwari et al. [*8*] have used the moments method for assuring adhesive bond quality.

Researchers [*1–19*] have shown acousto-ultrasonic (AU) parameters to be more sensitive than stiffness measurements as a means of tracking damage. Although the physical interpretation of the effect of damage on wave propagation and on the AU signal is not yet understood completely, researchers have suggested that the local stress state or displacement field is modified by the damage present. By recording information on stress wave propagation characteristics, one can hope to obtain information about the value of stress concentration or impending failure modes. Research conducted by Kiernan [*5*] shows that damage has a tendency to grow in the direction of higher AU values. The moments analysis of the received signal in the frequency domain produces a stress wave factor (SWF) that can be correlated to residual strength/stiffness of the specimen with additional experimental measurements.

Real-time monitoring of damage progression in ceramic composites by an NDE technique can provide better insight into failure mechanisms under loading. Monitoring damage accumulation in real-time under dynamic loads could indicate the sequence of the occurrence of

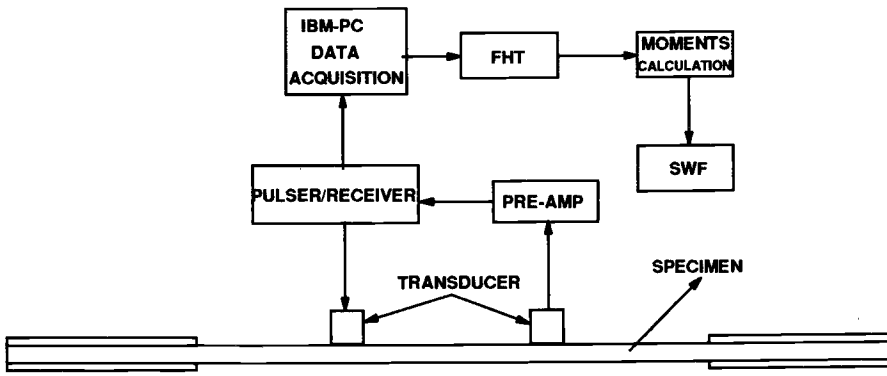

FIG. 1—*Conceptual configuration of acousto-ultrasonic setup.*

each damage mode and help us understand and model the failure mechanisms of the material. Researchers [*19*] have shown that SWF values from AU analysis are a measure of damage present. Continuous monitoring of damage accumulation by the real-time AU technique could also play an important role in assessing residual strength. Hemann et al. [*16*] studied the effect of increasing stress level on AU signals on unidirectional graphite/epoxy composite material. This is considered to be a first step towards developing real-time AU as a tool for monitoring damage under dynamic loads. The real-time acousto-ultrasonic (AU) NDE monitoring during material testing described in this paper is the first step towards understanding of the failure mechanisms of SiC/CAS (silicon carbide fiber and calcium aluminum silicate matrix) ceramic composites. This is also the first major attempt in the development and application of real-time AU for continuously monitoring damage accumulation during fatigue. Real-time AU developed by the authors monitored damage accumulation continuously under cyclic loading. The received AU signals are averaged over a load cycle and are representative of the damage state of the specimen at that point of its fatigue life.

Experimental Setup

Unidirectional and cross-ply (SiC/CAS) ceramic composites were made by Corning, Inc., with approximately 40% fiber content and less than 1% porosity. Dimensions of a typical specimen were 152.4 by 12.7 by 2.92 mm. End tabs of glass-epoxy (12.7 by 2.92 mm) were glued to the specimen using FM-300 adhesive cured at 300°F (149°C). End tabs were attached to prevent crushing when held in the grips of the testing machine. Samples U2 and U5 are unidirectional $[0_8]_s$, and Samples C3, C4, and C5 are cross-ply $[0/90]_{4s}$. Samples U2, U5, and C5 were quasi-statically ramp loaded in tension to failure in load control mode at the rate of 90.72 kg (200 lb)/min. Damage accumulation was monitored continuously by the real-time AU NDE technique. The strain was monitored by a 25.4-mm (1-in.) extensometer. In-situ observations on the edge for U2 were video recorded through an optical microscope to complement and verify AU results. Samples C3 and C4 were fatigued at 66.66 and 75% of ultimate strength, respectively, and residual stiffness measurements were taken at different stages in their fatigue life. Edge replicas of the damaged specimen were also taken to corroborate and complement AU results.

Ultrasonic pulses were introduced into the mechanically loaded specimen through a broadband transducer, Panametrics model V133RM (2.25 MHz/6.35 mm). The couplant used was Sonotrace-30. A Panametrics Model 5052-AU pulser/receiver was used to generate and receive the ultrasonic signal. The receiving transducer was the same type as the transmitter.

A transducer holder was designed and fabricated to keep the AU transducers 38.1 mm (1.5 in.) apart on the opposite side of the specimen from the extensometer. A constant pressure was maintained at the center of the transducer holder throughout the experiments. The received signal was pre-amplified and sent to the amplifier with gains being set for each individual sample. After a group of signals was saved, they were input to a Fortran program developed at Virginia Tech [*7*] to calculate the frequency spectrum and its various moments. The AU data were normalized with respect to the initial value and plotted against stress level. The zeroth moment was found to be the most sensitive parameter of the ones studied for detection of matrix cracks and is referred to as AU stress wave factor (SWF).

Results and Discussion

Sample U2

Sample U2 was unidirectional SiC/CAS with 16 plies. Sample U2 was quasi-statically ramp loaded in tension until failure at a constant loading rate of 90.72 kg (200 lb)/min. Figure 2

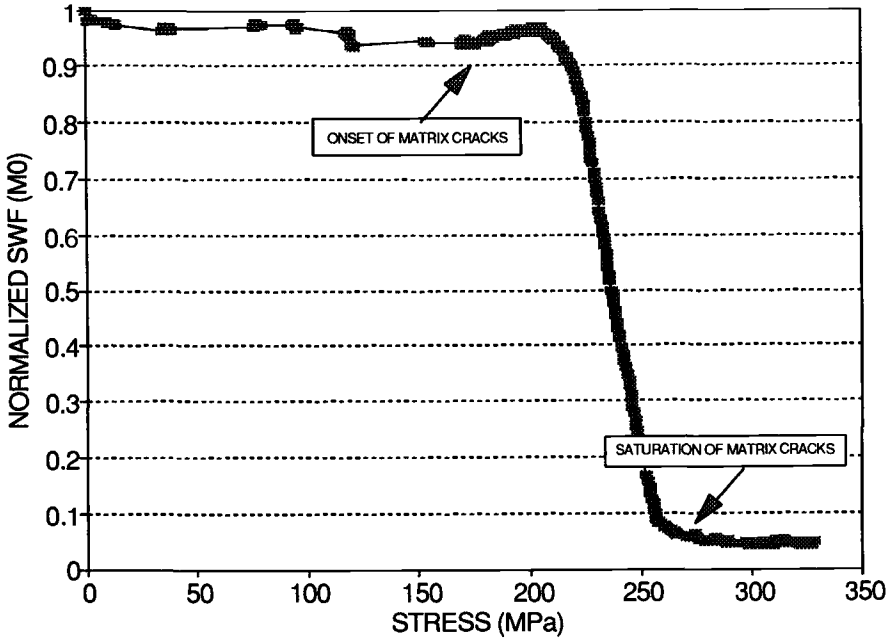

FIG. 2—*Graph of normalized SWF values versus stress of Sample U2.*

shows the normalized real-time SWF values versus stress levels. The AU data are recorded every second, thus providing near real-time NDE monitoring. Onset of large-scale matrix cracks takes place at 180 MPa, as indicated by the start of the local increase in SWF values. The AU transducer also acts as an AE transducer, receiving additional stress waves caused by the matrix cracking. The start of the nonlinear zone at 180 MPa and video recordings of first matrix cracks through the in-situ optical microscope were used to verify and complement AU results. Saturation of matrix cracks (all the cracks are fully developed) takes place at 260 MPa as indicated by the flat curve of SWF following the monotonic decrease and is verified by the start of the second linear zone in the stress strain curve.

Sample U5

Sample U5 was quasi-statically ramp loaded in tension to 340 MPa at a constant loading rate of 90.72 kg (200 lb)/min. Almost all matrix cracking has taken place at this stress level. The specimen was unloaded and reloaded to failure in displacement control mode at a constant displacement rate of 0.254 mm/min. The specimen was loaded in displacement control mode instead of load control so as to closely monitor the damage taking place near failure over an extended period of time.

Figure 3 shows the normalized SWF values of Sample U5 plotted with increasing stress levels in load control mode of Sample U5. The local increase of SWF values occurs at 180 MPa, indicating the onset of large scale matrix cracks. Saturation of matrix cracks occurs at 270 MPa, indicated by the start of the flat portion of the SWF curve. Sharp peaks of SWF values occurred at 240 and 265 MPa, respectively. These peaks may be caused by a damage mode other than matrix cracking. These "jumps" in real-time SWF values are caused by damaged-induced acoustic emission stress waves that are detected and analyzed by the AU

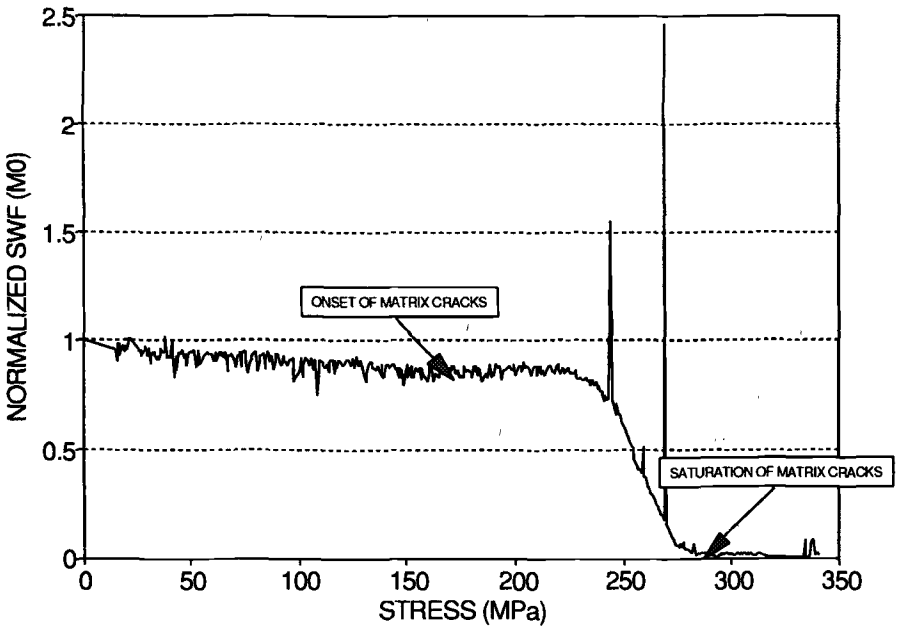

FIG. 3—*Graph of normalized SWF values versus stress of Sample U5.*

system. The sharp increase with a very high peak indicates stress waves generated by this damage mode have short duration and high energy content. We have some reason to believe that this second damage mode might be fiber breakage. Real-time radiography could give further proof of this. Figure 4 shows the stress-strain curve of Sample U5 loaded in load control mode to complement the results of the AU test.

Real-time SWF values are plotted with crosshead displacements of Sample U5 loaded in displacement control mode at 0.254 mm/min in Fig. 5. Extensive acoustic emission (AE) generated by the occurrence of damage between 0.508 mm (0.02 in.) and 0.762 mm (0.03 in.) displacement of the crosshead is being received by the AU transducer. Corresponding stress levels for these displacements are 350 and 425 MPa, as shown in Fig. 6. Several of the peaks in this region are high and sharp, indicating again the possible occurrence of fiber breaks. The smaller peaks, which are twice the order of magnitude of the input signal in terms of energy content, may indicate the occurrence of damage modes other than matrix cracking and fiber breaks. However, this possibility must be studied further. The sharp peaks close to 0.762 mm (425 MPa) indicate large-scale fiber breaks during the catastrophic failure of the specimen.

Sample C5

Sample C5 was cross-ply SiC/CAS with 16 plies. Figure 7 shows normalized real-time SWF values versus stress levels. A sharp drop of SWF values with increasing stress level is observed at 70 MPa, indicating the onset of matrix cracking in the 90° plies. The stress strain graph shown in Fig. 8 of Sample C5 indicates the start of nonlinearity at 70 MPa. The recorded SWF values remain fairly constant at about 95 MPa (as seen under enlarged scale), followed by the another sharp decrease in their values. This decrease is attributed to the matrix cracking in 0° plies followed by the saturation of matrix cracks at 150 MPa, as indicated by the fairly constant

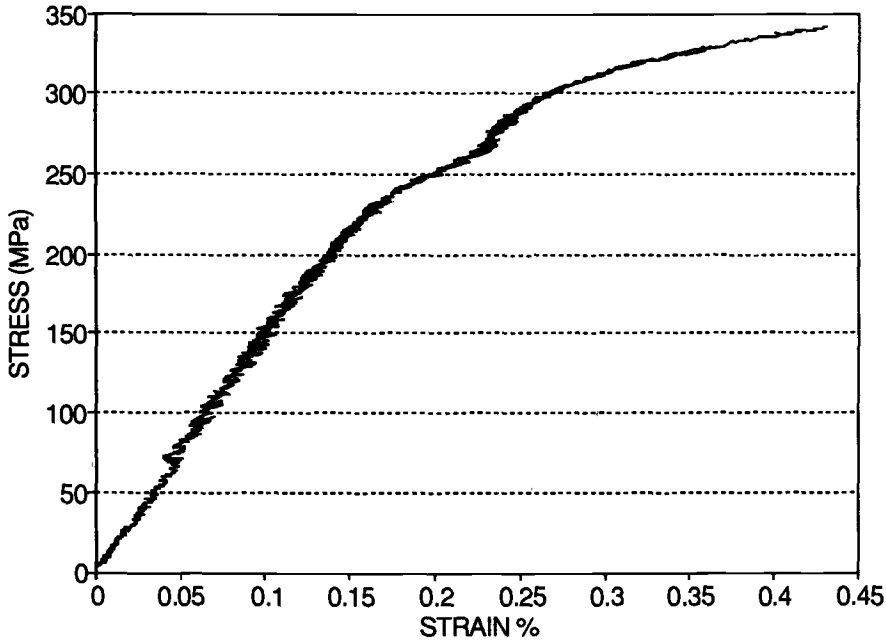

FIG. 4—*Graph of stress versus strain of Sample U5.*

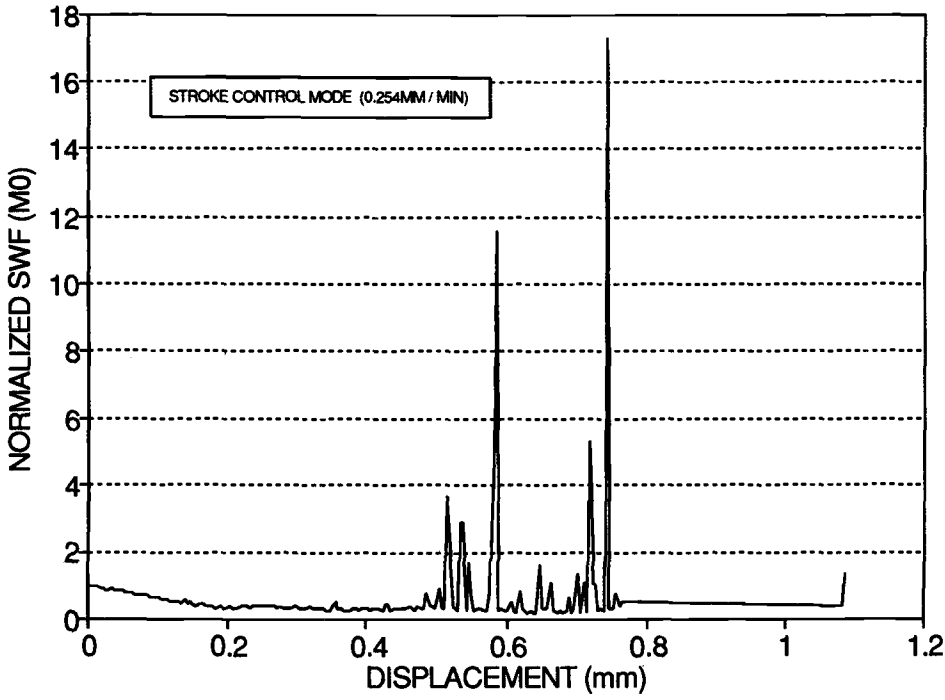

FIG. 5—*Graph of normalized SWF values versus displacement of Sample U5.*

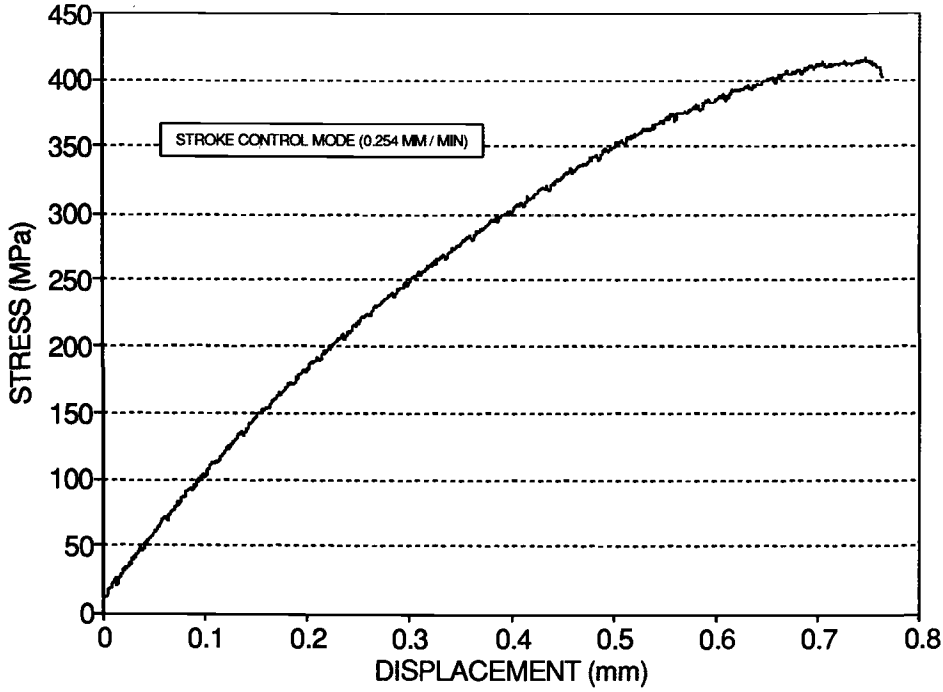

FIG. 6—*Graph of stress versus displacement of Sample U5.*

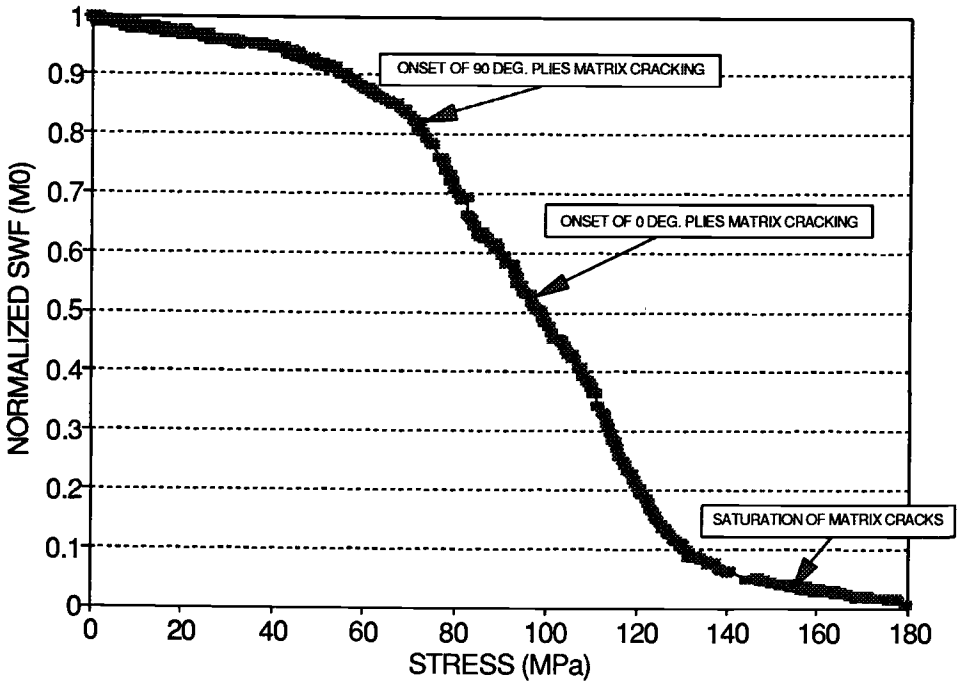

FIG. 7—*Graph of normalized SWF values versus stress of Sample C5.*

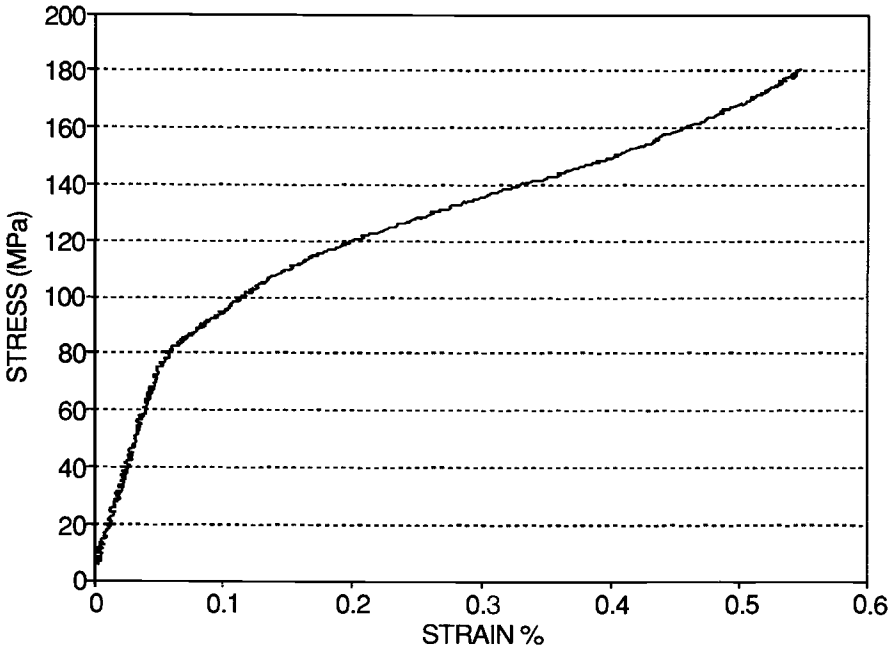

FIG. 8—*Graph of stress versus strain of Sample C5.*

SWF values following the sharp decline. The major share of the load is being carried by the 0° plies after large-scale matrix cracking of 90° plies has taken place prior to the onset (95 MPa) of 0° plies matrix cracking. The actual stress level for 8 plies of 0° is 190 MPa and is close to the stress level for the onset of large-scale matrix cracking in Sample U5. The stress strain graph after 150 MPa is linear, indicating saturation of matrix cracks in all plies and that the load is being carried by the fibers in the 0° plies.

Samples C3 and C4

Samples C3 and C4 were cross-ply SiC/CAS with 16 plies and were cyclically loaded (R = 0.1) at 66.66 and 75% of ultimate tensile strength, respectively. The ultimate nominal tensile strength obtained from static tests was 185 MPa. Stiffness measurements were taken at different points of fatigue life by loading the specimen in tension to 181.44 kg (400 lb). Edge replicas of the damaged edge were taken to qualitatively compare the damage progression at different points of the fatigue life. The AU parameter selected to monitor fatigue damage progression was M_0. Figure 9 shows the normalized real-time SWF and normalized stiffness values plotted with corresponding number of cycles of Sample C3. Similar trends in terms of damage accumulation with increasing number of cycles is followed by similar reductions in stiffness and SWF values. Specimen C3 failed near the gage section at 41 966 cycles. The failure surface indicated extensive fiber pullout. Maximum damage in Sample C3 took place between 0 to 50 cycles. After 150 cycles, the SWF values remain fairly constant, indicating no additional major damage occurring until catastrophic failure. Figure 10 shows the edge replica taken at the gage length of Sample C3, indicating progressive damage at different points of the fatigue life.

Figure 11 shows the normalized SWF and normalized stiffness values plotted with corre-

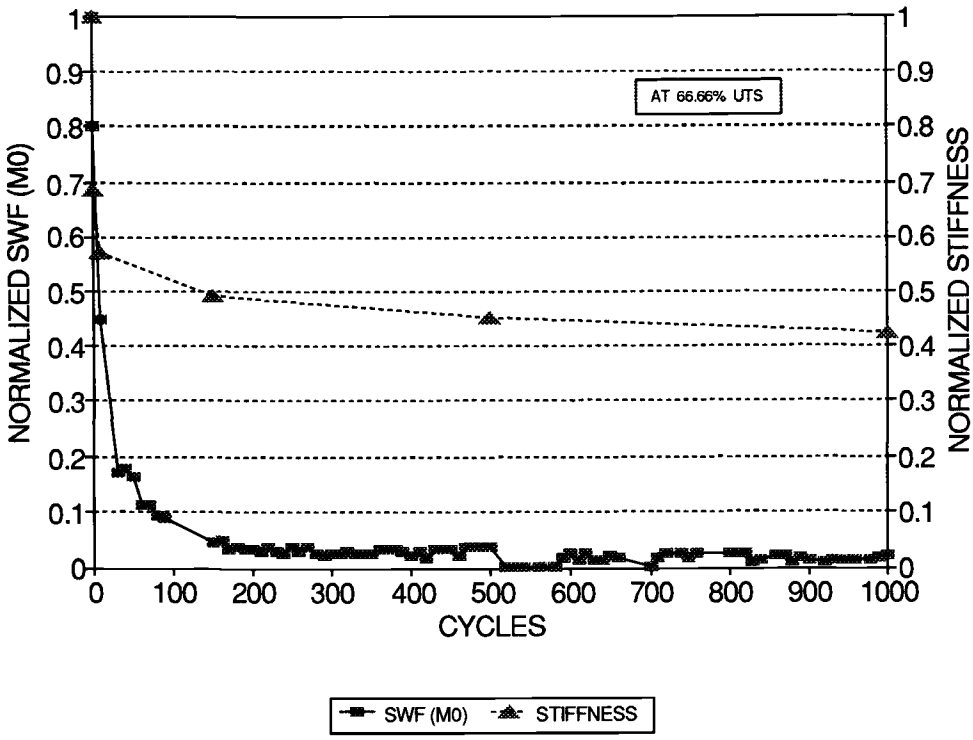

FIG. 9—*Graph of normalized SWF values and stiffness versus cycles of Sample C3.*

sponding number of cycles of Sample C4. Stiffness measurements and real-time SWF values follow the same trends, indicating damage accumulation with the increasing number of cycles. The majority of damage takes place before 25 cycles. Edge replicas shown in Fig. 12 complement the results of the AU.

Summary

A feasibility study of the real-time acousto-ultrasonic (AU) nondestructive evaluation (NDE) technique to monitor damage in SiC/CAS ceramic composites was accomplished successfully. AU data were recorded every second for real-time NDE monitoring. Results to date show that real-time AU is potentially a useful NDE tool to assess and monitor damage growth. Real-time AU was found to detect the stress levels at which the onset of matrix cracks occurred and the stress level for saturation of matrix cracks. A feasibility study for assessing damage under cyclic loads by real-time AU monitoring also has been accomplished. This is the first major attempt at real-time monitoring of fatigue damage development in composites by the AU NDE technique as far as we are aware. Data from real-time AU for fatigue tests show the same trend as reduction in stiffness at different points of the fatigue life. Normally, fatigue loading tests have to be stopped to evaluate damage by present NDE techniques. The real-time AU technique has the advantage of removing this requirement. Continuous monitoring of damage by the real-time AU NDE technique could enhance our understanding of damage mechanisms in ceramic composites.

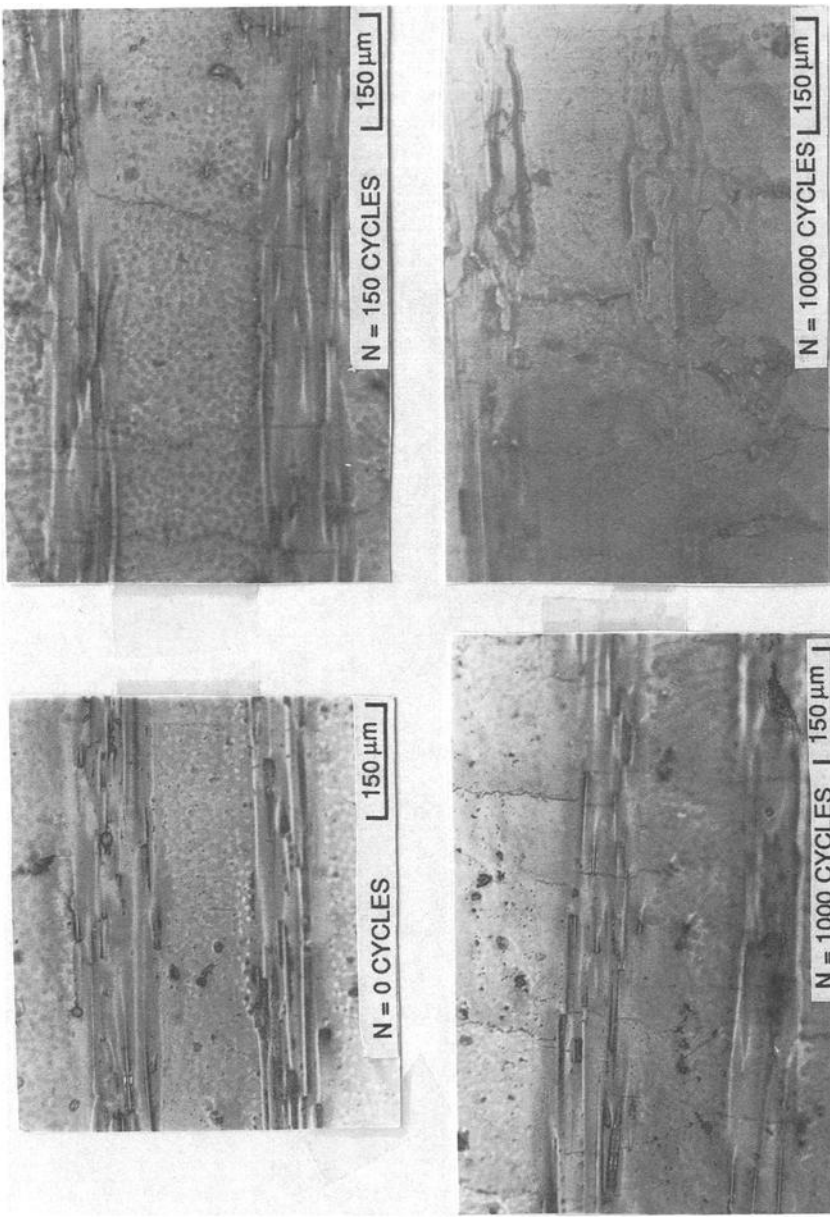

FIG. 10—*Edge replica photographs at different cycles of Sample C3.*

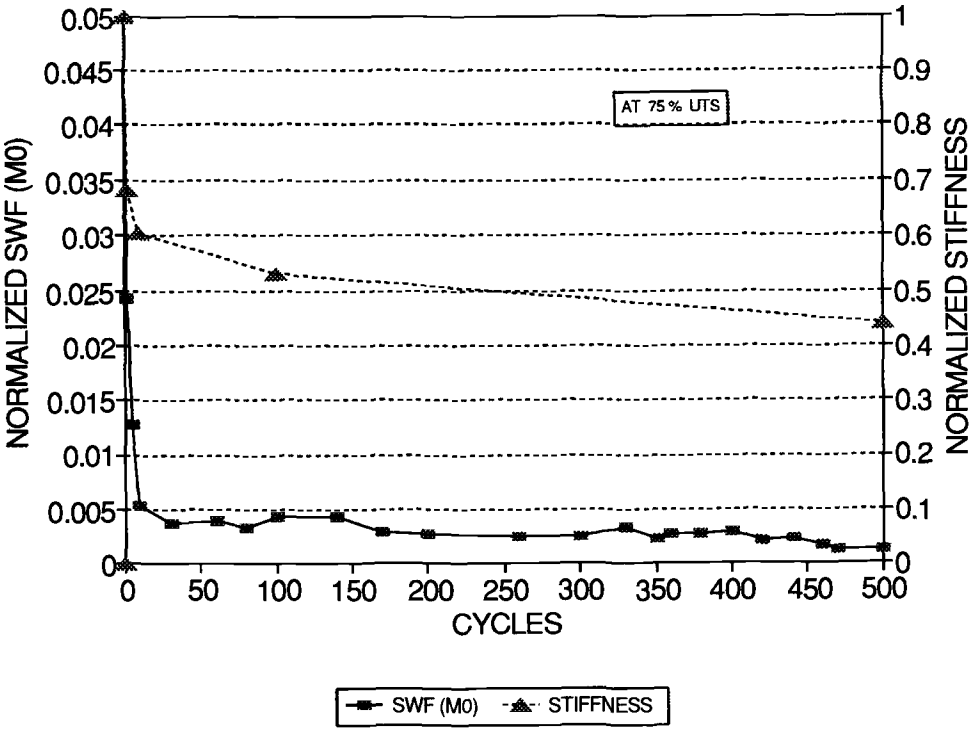

FIG. 11—*Graph of normalized SWF values and stiffness versus cycles of Sample C4.*

Conclusions

1. Real-time AU can monitor damage progression in ceramic composites subjected to quasi-static ramp loading in tension to failure.
   A. Real-time AU detects the onset of matrix cracks.
   B. Real-time AU detects the stress level at which saturation of matrix cracking takes place.
2. Real-time AU results were corroborated by in-situ optical microscope video recordings.
3. Real-time AU can monitor damage progression during fatigue.
4. Reduction in stiffness correlates with the change in AU parameter at different stages of fatigue life, and these results were complemented and verified by edge replica photographs.

Future Work

1. Develop an understanding of and model the damage process in SiC/CAS ceramic composites with the help of real-time AU NDE technique.
2. Study and design real-time AU tests at high temperature with the help of laser-based generation and detection of stress waves.

Acknowledgments

We are greatly indebted to the Structural Integrity branch at NASA Lewis Research Center for providing the facilities and Virginia Institute for Material Systems (VIMS) for providing financial support for these studies.

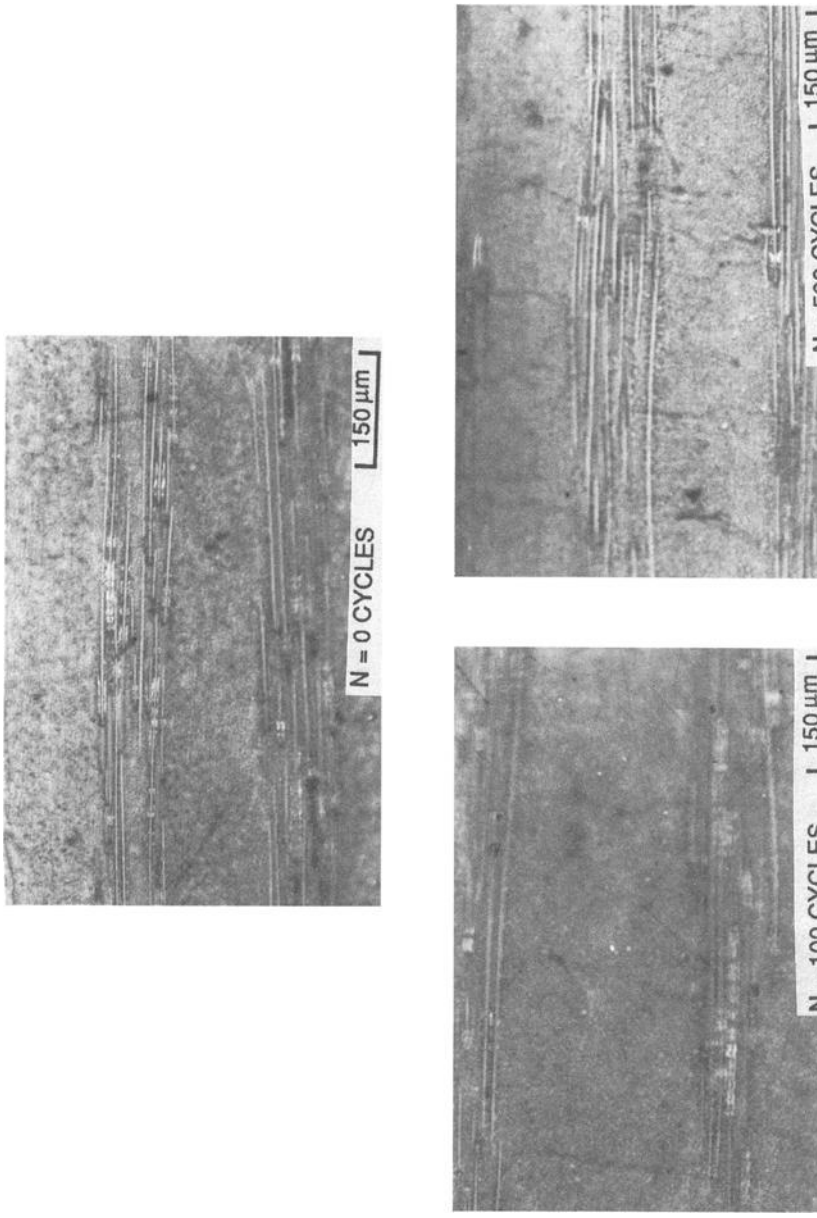

FIG. 12—*Edge replica photographs at different cycles of Sample C4.*

References

[1] Henneke II, E. G., Duke Jr., J. C., Stinchcomb, W. W., Gowda, A., and Lemascon, A., "A Study of Stress Wave Factor Technique for the Characterization of Composite Materials," NASA Contractor Report 3670, February 1983.

[2] Duke Jr., J. C., Henneke II, E. G., and Stinchcomb, W. W., "Ultrasonic Stress Characterization of Composite Materials," NASA Contractor Report 3976, May 1986.

[3] Sarrafzadeh-khoee, A., Kiernan, M. T., Duke Jr., J. C., and Henneke II, E. G., "A Study of the Stress Wave Factor Technique for the Nondestructive Evaluation of Composite Materials," NASA Contractor Report 4002, July 1986.

[4] Duke Jr., J. C., Henneke II, E. G., Kiernan, M. T., and Grosskopf, P. P., "A Study of Stress Wave Factor Technique for Evaluation of Composite Materials," NASA Contractor Report 4195, January 1989.

[5] Kiernan, M. T., "A Physical Model for the Acousto-Ultrasonic Method," Doctoral Dissertation, College of Engineering, Virginia Polytechnic Institute and State University, Blacksburg, VA, August 1989.

[6] Henneke II, E. G., Duke Jr., J. C., and Tiwari, A., "NDT Methods to Assess the Integrity and Quality of an Adhesively Bonded Sheet Metal," Interim Project Report, Ford Motor Company, 1989.

[7] Tiwari, A., "A Feasibility Study of the Acousto-Ultrasonic Technique to Assure the Quality of Adhesively Bonded Sheet Metal," Master's Thesis, College of Engineering, Virginia Polytechnic Institute and State University, Blacksburg, VA, February 1990.

[8] Tiwari, A., Henneke II, E. G., and Duke Jr., J. C., "Acousto-Ultrasonic (AU) Technique for Assuring Adhesive Bond Quality," *Journal of Adhesion,* Vol. 34, 1991, pp. 1–15.

[9] Bracewell, R. N., *The Fourier Transform and its Applications,* 2nd ed., McGraw-Hill, New York, 1986.

[10] Bendat, J. S. and Piersol, A. G., *Random Data Analysis Measurement Procedures,* 2nd ed., Wiley Interscience, New York, 1986.

[11] Stiffler, R. C., "Wave Propagation in Composite Plates," Doctoral Dissertation, College of Engineering, Virginia Polytechnic Institute and State University, Blacksburg, VA, November 1986.

[12] Vary, A., "Acousto-Ultrasonic Characterization of Fiber Reinforced Composites," *Materials Evaluation,* Vol. 40, 1982, pp. 650–662.

[13] Vary, A. and Bowles, K. J., "An Ultrasonic-Acoustic Technique for Nondestructive Evaluation of Fiber Composite Quality," *Polymer Engineering and Science,* Vol. 19, 1979, pp. 373–376.

[14] Vary, A. and Lark, R. F., "Correlation of Fiber Composite Tensile Strength with the Ultrasonic Stress Wave Factor," *Journal of Testing and Evaluation,* Vol. 7, 1979, pp. 185–191.

[15] Fahr, A., Lee, S., Tanary, S., and Haddad, Y., "Estimation of Strength in Adhesively Bonded Steel Specimens by Acousto-Ultrasonic Technique," *Materials Evaluation,* Vol. 47, 1989, pp. 233–240.

[16] Hemann, J. H. and Baaklini, G. Y., "The Effect of Stress on Ultrasonic Pulses in Fiber Reinforced Composites," NASA Contractor Report 3724, August 1983.

[17] Talreja, R., "On Fatigue Life under Stationary Gaussian Random Loads," *Engineering Fracture Mechanics,* Vol. 5, 1973, pp. 993–1007.

[18] *Acousto-Ultrasonics—Theory and Applications,* J. C. Duke Jr., Ed., Plenum Press, New York, 1988.

[19] Tiwari, A., Henneke II, E. G., Vary, A., and Chulya, A., "In-Situ Acousto-ultrasonic Technique to Monitor Damage in Ceramic Composites," *Proceedings,* Fifth Annual HITEMP conference, Cleveland, OH, 27–28 Oct. 1992.

P. K. Raju[1] *and U. K. Vaidya*[2]

Nondestructive Evaluation (NDE) of Composites Using the Acoustic Impact Technique (AIT)

REFERENCE: Raju, P. K. and Vaidya, U. K., **"Nondestructive Evaluation (NDE) of Composites Using the Acoustic Impact Technique (AIT),"** *Cyclic Deformation, Fracture, and Nondestructive Evaluation of Advanced Materials: Second Volume, ASTM STP 1184,* M. R. Mitchell and O. Buck, Eds., American Society for Testing and Materials, Philadelphia, 1994, pp. 376–391.

ABSTRACT: Due to increasing use of composites as structural materials, defect characterization in composites has attracted wide attention in recent years. Several undesirable effects in composites include: fiber breakage, inclusions, voids, improper resin distribution, delaminations, and misalignment of fibers. Acoustic methods of nondestructive evaluation (NDE) are proven candidates in identifying these defects to varying levels of success. Prominence has been given to acoustic emission (AE) and ultrasonic inspection techniques in the evaluation of composites; however, the acoustic impact technique (AIT), derived from the coin-tap test, has not been explored in depth. The coin-tap test involves tapping a specific location on a structure with a "coin" or "penny" and judging the quality of the material based on the sound emanated from the localized region. In principle, a "good" region results in an intense sound as compared to a "defective" one. Although coin tapping has been used in this fashion for several years, the most significant drawback has been its operator dependency. AIT attempts to overcome this shortcoming. In AIT, the use of sophisticated electronic instrumentation provides a reliable estimate of the quality of the material. The foundation of AIT lies in sensing and analyzing localized vibrations and disturbances generated by a low-magnitude mechanical pulse input to the structure under test. In this paper, the current status of AIT is reviewed, and new developments are discussed. Results are presented relating to the application of this technique for NDE of graphite/epoxy and graphite/phenolic composites.

KEYWORDS: acoustic impact technique, NDE, graphite fiber composite, acoustic emission, defect characterization

Defect characterization in composites has attracted much attention in the recent past due to increasing use of composites as structural materials [*1–17*]. The reliable utilization of components and structures made of composites is possible only through successful NDE methods. The search for new NDE methods and the modification of existing ones is inevitable due to varying needs in practical situations. In composites, for instance, the focus has shifted during the last decade from conventional laminated materials towards more complex architectures in the form of woven, braided, and stitched reinforcements. NDE methods such as X-ray radiography, resonant frequency technique, and ultrasonics, though well established, are time consuming and expensive, restraining their usage in the field on a routine basis.

Acoustic emission, acousto-ultrasonics, acoustic imaging, acoustic holography, and acoustic impact fall into the category of viable acoustic methods for materials testing. Due to their high

[1] Professor, Dept. of Mechanical Engineering, Auburn University, Auburn, AL 36849-5341.
[2] Assistant professor, Materials Research Laboratory, Tuskegee University, Tuskegee, AL 36088.

sensitivity to different defects, the development of these techniques is a matter of continued interest. This article is on acoustic impact technique (AIT). Previous research, drawbacks of existing methodology, and current modifications/developments are discussed. The motivation for choosing AIT as a focus of our study is its excellent potential as a technique for production testing and field maintenance of structures through quick scanning procedures.

Sonic NDE Techniques

A separate class of sonic NDE techniques comprise the following: coin tapping [*5–8*], wheel tapping [*6*], impedance method [*9,10*], membrane resonance [*11*], and acoustic impact [*11–14*]. Coin tapping is probably the oldest NDE method used intuitively by laymen for inspection of defects. This is done by tapping the structure at various locations and listening to the sound emanated from the structure. The coin-tap test involves tapping a specific location on a structure using a "coin" or a "penny" and, based on the sound emanated from the localized region, one makes a judgment on the quality of the material. This is because a defective region sounds "dull" as compared to a "good" region. In the aerospace industry, skilled and trained operators utilize coin tapping on a regular basis to identify defects in wing components and aerofoil sections. The coin-tap test should not be confused with the wheel-tap test commonly used in the railroad industry to identify cracks in wheels. The major difference is that the coin-tap test is highly localized, and individual points on the component/structure are tested. In contrast, the wheel-tap test is a global one wherein a tap at a single location is sufficient to investigate the complete component/structure. A tap in a good region "sounds different" from a tap in a defective one. The difference essentially lies in the frequency content of the sound produced by the tap. A major drawback of the coin-tap test is its operator dependency and largely subjective nature of evaluation.

AIT attempts to overcome this shortcoming. Coin tapping may be considered as a rudimentary version of AIT and involves the use of electronic instrumentation for obtaining a reliable estimate of the quality of the material under test. AIT is based on sensing and analyzing localized vibrations and pressure disturbances in the material, which are generated by providing a low-amplitude mechanical pulse input to the structure under test [*11,12*]. The underlying principles of this technique are that a defect or flaw changes the local stiffness of the structure or part under test, thereby influencing the vibrational and acoustic response of that area.

Literature Review

A number of revisions of the coin-tap method have been developed in past years. In all these studies, to a certain extent, the basic feature of instrumentation associated with AIT has been the same. The use of a device to provide vibrations (spikes, blows, or sharp impacts) of low magnitude is a prime feature of any AIT setup. The difference essentially lies in the nature of sensing, analysis, and data interpretation.

Schroeer [*1*] and his colleagues used AIT for detection of concealed cracks in jet engine components and in honeycomb and laminated structures. A mechanical pulse was applied to the specimen, and the resulting vibrations were sensed with an accelerometer. The signals were interpreted by measuring the "time-to-damp" of these vibrations. This gave an indication of the presence of anomalies. Their method was based on the concept that an anomaly changes the mechanical impedance of the structure or part and influences the vibrational response of that area. Reynolds [*2*] in an extensive review on NDE of fiber-reinforced composite materials indicated the importance of the tapping analysis and automated inspection of a large number of nominally identical items. Hagamaier and Fassbender [*3*] found that the coin-tap test could

detect more types of defects in honeycomb constructions than any other techniques except neutron radiography.

A significant amount of work on low-frequency acoustic methods of NDE originated from the Soviet Union in the late 1970s by Lange [*4*] and his colleagues. They developed the impedance method, amplitude method, acoustic topographic method, velocimetric method, and acoustic spectral method. While each of these methods utilized pulse and/or continuous-wave excitation, the difference was in the application for various geometries of the component/structure, nature of sensing, analysis, frequency ranges, and interpretation of the acquired signals. The acoustic spectral method described by these authors bears resemblance to AIT. The instrumentation in the acoustic spectral method consisted of an electrodynamic vibrator for excitation and an electrodynamic detector in the form of an accelerometer or a microphone connected to headphone. This setup was utilized to detect faults related to uncemented areas of airplane wings. The decaying elastic vibrations were detected and converted to electric signals, which were analyzed on a spectrum analyzer. The authors concluded that crack-like flaws produced high-frequency components as compared to good regions of the specimens.

Significant experimental work and some theoretical predictions related to instrumented coin-tap testing have been performed by Cawley and Adams [*5–9*]. Their working hypothesis was that difference in the sounds produced when good and defective areas are tapped must be due to a change in the force input to the test structure. Hence, if the input force was measured at various points on the specimen, it would yield a qualitative indication of the material quality. Their test configuration involved the use of a spherical-tipped striker comprising a solenoid core with a force gage attached to its lower end. The motion of the striker was monitored by an accelerometer attached to the top of the solenoid core, and the whole impact unit was placed on the specimen and moved from one testing location to another. Testing was performed on laminated beams with slots and honeycomb panels with carbon fiber-reinforced plastic skins containing embedded defects. Their data analysis included comparison of the pulse width, pulse duration, and the corresponding spectrum of the force-time history of the input force at specific locations. In general they concluded that a defective region resulted in lower values of amplitude and larger pulse widths due to the long contact time between the striker and the specimen. An important conclusion of their work was that the coin-tap technique was more sensitive to the "contact stiffness" between the striker and the specimen and hence effective primarily for detecting subsurface flaws such as disbonds between the skin and the core in honeycomb composites or gross defects in laminated composites. The technique, they concluded, had severe limitations with regard to detecting minor defects and through-the-thickness flaws.

Murthy and Vaidya [*11,12*] provided a new approach to AIT for NDE of laminated composites. In their studies on defect-induced glass fiber-reinforced composites (GFRC), they utilized AIT in conjunction with acoustic emission (AE) to increase the defect detectability of AIT. The defects included fiber breakage, delaminations, resin-rich and resin-starved areas, and inclusions. The device they utilized consisted of an impacting unit resting on the specimen. The impacting unit comprised an electronically actuated solenoid coil with a shaft acting as the striker. This provided a low-magnitude mechanical pulse input to the specimen. Data acquisition was performed using a 30-kHz AE sensor placed at a fixed distance from the striker. The experimental setup is shown in Fig. 1. Both time and frequency domain analyses were performed. The authors identified a peak frequency range from 4.0 to 4.75 kHz for the good regions in the specimen, and a peak frequency range from 1.3 to 2.5 kHz for the defective regions for the given specimen geometry and thickness. Sample results are shown in Figs. 2 and 3. They compared their results with X-ray radiography and resonant frequency methods. The important significance of this work was that sensitivity of AIT was enhanced with the use

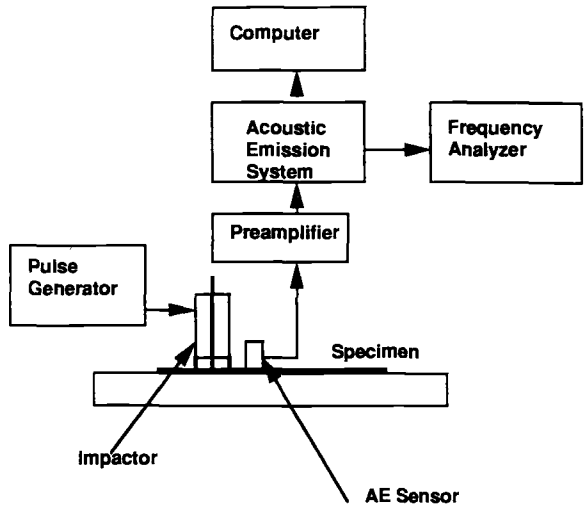

FIG. 1—*Experimental setup for acoustic impact testing* [11,12].

of an AE sensor. In addition to gross defects such as delaminations, embedded flaws such as fiber breakage and inclusions were also identified.

Murthy and co-workers [*13*] further developed an 8086 microprocessor-based instrumentation with the 8087 NDP used for fast fourier transform (FFT) analysis for AIT. They incorporated a data acquisition, memory organization, data processing, and a display unit in a single portable unit. Their emphasis was on portability and involved sensing the localized vibrational response by the AE sensor after the tap, conversion of time domain AE signals to frequency domain, identification of the maximum amplitude and the corresponding frequency in the amplitude spectrum, and storing information. With subsequent taps, comparison of the results with the previously stored values were performed and a go-nogo condition was established for detecting the presence of defects.

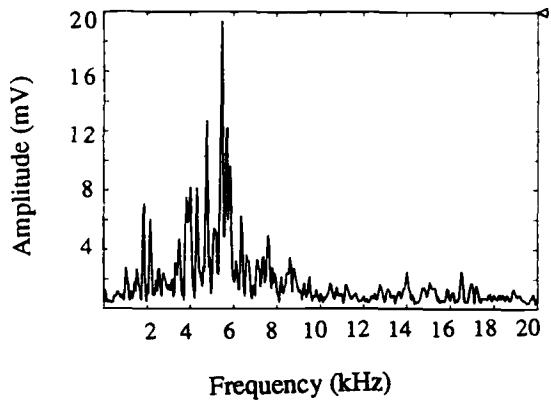

FIG. 2—*Frequency distribution of region without defect* [11].

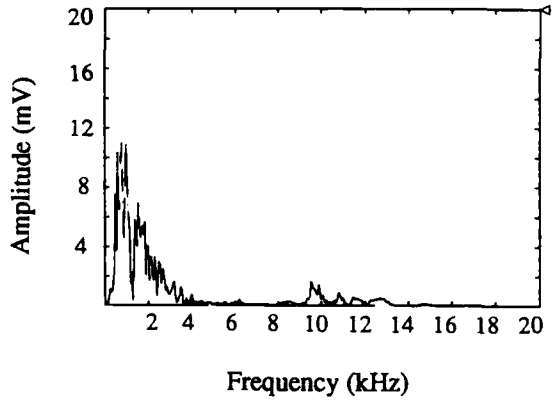

FIG. 3—*Frequency distribution of region with delamination* [11].

Drawbacks of Existing Testing Configurations

Cawley and Adams [*5*] pointed out that the sensitivity of the instrumented coin-tap testing was based on the "contact stiffness" between the striker and the specimen. Hence, comparison of force-time histories was found to be useful primarily for detecting surface defects in honeycomb composites or gross defects in laminated materials. When the defect is embedded in the material, as is often the case, the sensitivity of the test is limited. In studies utilizing accelerometers as sensing devices [*1,3,5–9*], the interpretation of the test data is limited to shifts in frequencies and amplitudes and to changes in the values of the material damping. Moreover, due to their construction, accelerometers are more sensitive to the direction of motion in which mounted, and the defect will not be detected until it grows sufficiently to cause significant variations. For minor defects, the shifts in frequencies will not always be clearly discernible, and the defect detectability is reduced when accelerometers are used.

Complexities associated with instrumentation, test configurations, and material geometries (holes, cutouts, intricate shapes, etc.) has led to setbacks in further developments of AIT. In previous studies, the impacting unit that provides the low-magnitude pulse input has been placed on the surface of the structure under test. Under such configuration, it is oftentimes difficult to investigate the quality of the material at the edges of the specimen due to problems associated with maneuvering and placing the impacting unit around the edges. Mass loading of the structure, especially for composites due to their low weights, is another problem that is often not accounted for. Depending upon the location of the impacting unit on the structure, there may be shifts in frequencies that could be mistakenly attributed to the presence of defects. In the present study, we have taken these drawbacks into account and initiated a program to investigate in-depth, various possible test conditions and their respective advantages and drawbacks.

Current Modifications

In the present study the experimental configurations shown in Fig. 4 provide a means of overcoming the limitations imposed in previous versions of AIT testing [*14–16*]. Application of conventional AIT (force-time history measurements) in conjunction with AE is an important feature of the current experimental configuration. The technique thus enables testing in two modes: (1) measurement of force-time history at the location of the tap using the impacting

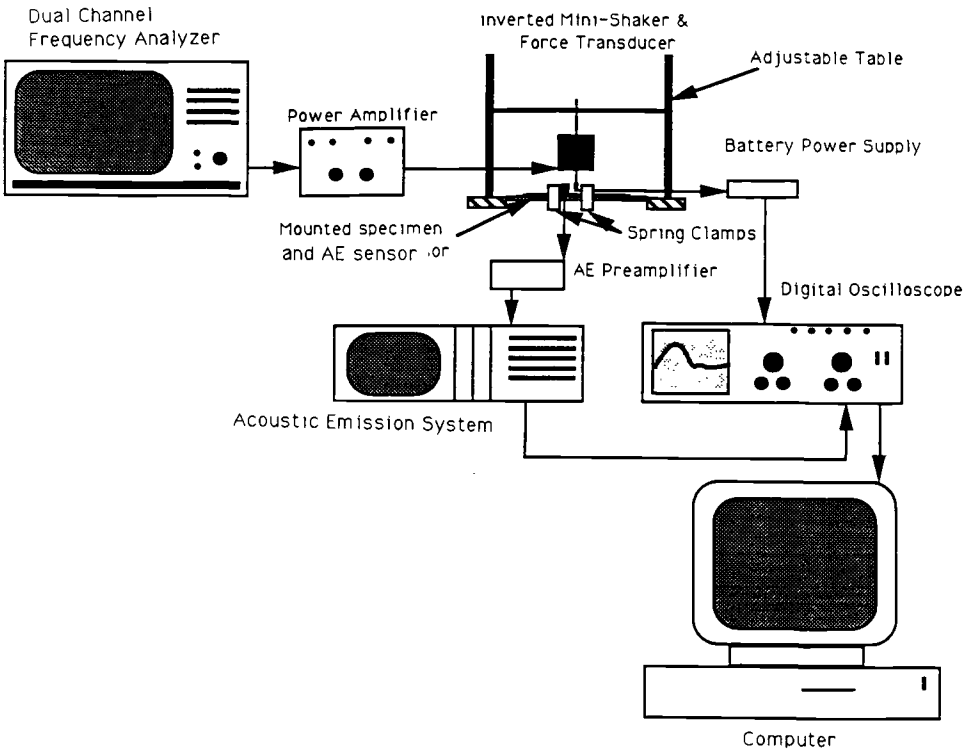

FIG. 4—*Schematic of AIT/AE test setup.*

unit alone (striker with force transducer), and (2) use of AIT in conjunction with AE wherein the AE sensor is placed in the vicinity of the striker.

This helps in two ways: (1) if there exists a gross defect such as a delamination, it will be detected by the changes in pulse width and amplitude of the force-time history; and (2) provided the defects are embedded, such as due to misaligned fibers, fiber breakage, variations in interlaminar strengths, etc., the detectability of these will be greater due to stress wave interaction with the material's microstructure in the vicinity of the tap. The material modulates and filters the stress wave. The information that reaches the sensor is a complex mixture of vibrational modes, surface waves, lamb waves, and through-the-thickness transverse resonances of the specimen. Moreover, this response is highly localized due to the low magnitude of the impact and provides an ideal means to assess material quality in a regionwise manner.

Experimental Setup

Figure 4 illustrates the schematic of the experimental setup used for AIT in this study. A variable sinusoidal excitation was fed to a mini-shaker through a power amplifier from a dual channel analyzer. The force gage was attached to the head of the mini-shaker to measure the force input. The configuration adopted for mounting the shaker guaranteed consistent reproduction of the input force and easy control of the frequency of tapping. Several specimens (both metal and composites) were tested at several locations for their force-time histories after subjecting them to the low-magnitude impact. For a given region, the force-time histories were

well repeatable regardless of the time of operation, switching the instruments on/off, and for testing between several time schedules. In the present study, the frequency of tapping adopted was 3 taps/s, which was controlled by a setting on the analyzer. The placing of the mini-shaker in an inverted manner avoided the effect of mass loading, generating a sharp strike of short duration on the specimen. An electrically actuated solenoid may be used for the identical purpose [*11–13*]. Two configurations were adopted in testing: (1) measurements of input force (designated as Configuration 1), and (2) use of a broadband AE sensor for sensing of the stress waves generated due to the impact (designated as Configuration 2). The AE sensor was of 0.7 in. in diameter, 0.65 in. high, 8 g in weight, and had a sensitivity of 55 V per m/s. The sensor was coupled to the specimen using a thin layer of water-based lubricant. The lubricant left no trace on the specimen after it was cleaned. The AE sensor was mounted in the immediate vicinity of the striker. The center-to-center distance between the sensor and the force gage was maintained at 2.5 cm (0.025 m). The height between the force transducer and specimen was kept at 2.5 mm (0.0025 m). From this configuration, we obtained a velocity of 0.22 m/s for the striker.

The output from the AE sensor was sent to a preamplifier with a filter bandwidth of 100 to 1000 kHz. The gain on the preamplifier was set at 40 dB. The output from the preamplifier was fed to a four-channel AE system. In this case only one channel was used. Data acquisition yielded AE parameters such as peak amplitude, count, rise, energy, and time. The signals obtained from the force gage and the acoustic emission sensor were in the time domain and stored through a digital storage oscilloscope. The waveforms were then digitized using an interface with a computer system to yield ASCII data files of the observed time domain signals. A program was developed to obtain the FFT of the force-time history and the AE signal. This data reduction yielded frequency domain information.

Experimental Procedure

The specimens were demarcated into specific regions prior to testing. The details of this are shown in Figs. 5 and 6. The striker impacted the specimen at the center of each of these regions with a frequency of 3 taps/s. As indicated earlier, two configurations were adopted, referred to as Configuration 1 and Configuration 2, respectively. Configuration 1 was adopted to avoid the effects of applying a couplant to the specimen which would affect the damping at the region of tap. In Configuration 2, the distance between the AE sensor and striker was maintained at 2.5 cm. Two constant-force spring clamps 5 cm apart held the specimen to a plexiglass base. The unit (striker/sensor and clamps) was moved as a whole from region to region. The two configurations chosen yielded information in two ways: Configuration 1 furnished the response of the specimen to the input force pulse at a "specific point" while Configuration 2 enabled interaction of the stress wave generated by the tap with the material in the vicinity of the point under test.

Specimens and Defect Types

Graphite/Epoxy Specimens

The specimen contained twelve plies of unidirectional graphite/epoxy (Gr/Ep) prepregs. The plies were oriented $[0/90]_{3s}$ and cured by a bag molding process in an autoclave for 60 min at 150°C and 450 Pa pressure. The specimen used was delaminated between the fifth and sixth plies, i.e., at a 0/90 interface for half its length. The delamination was introduced by wedging the specimen with a surgical knife. The delaminated end was glued by a commercially available resin/hardener system. The resulting specimen had two regions, one half being a "good" region

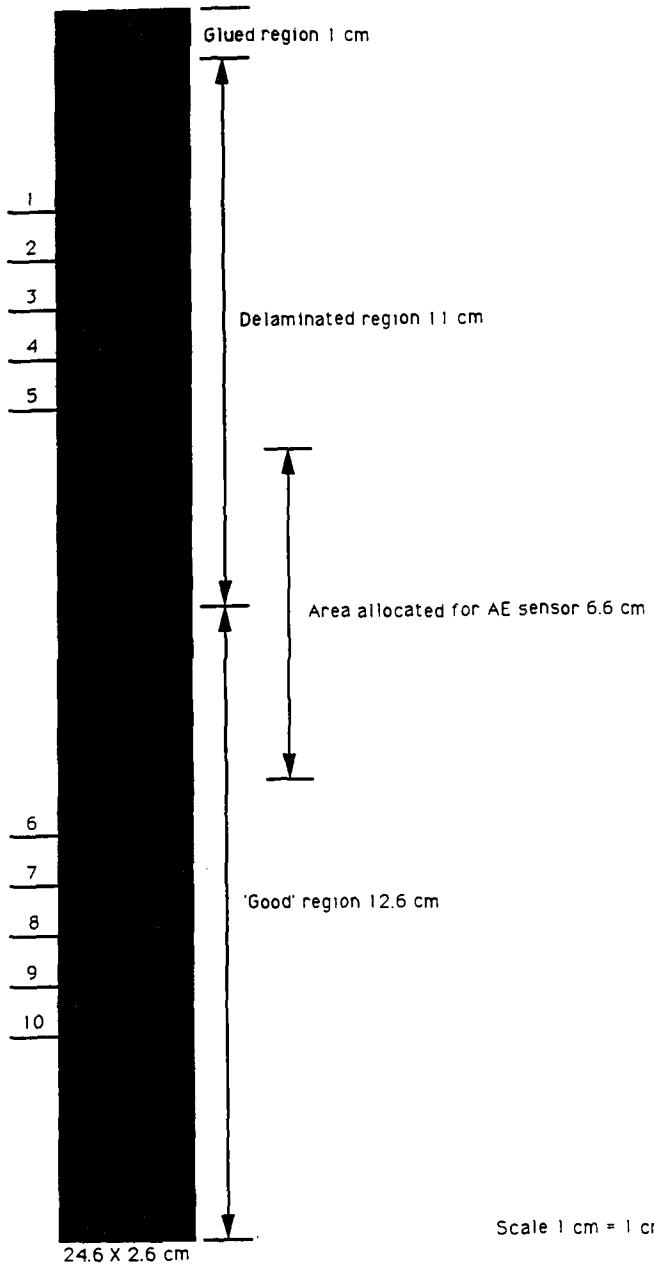

FIG. 5—*Demarcated regions for the graphite/epoxy specimen.*

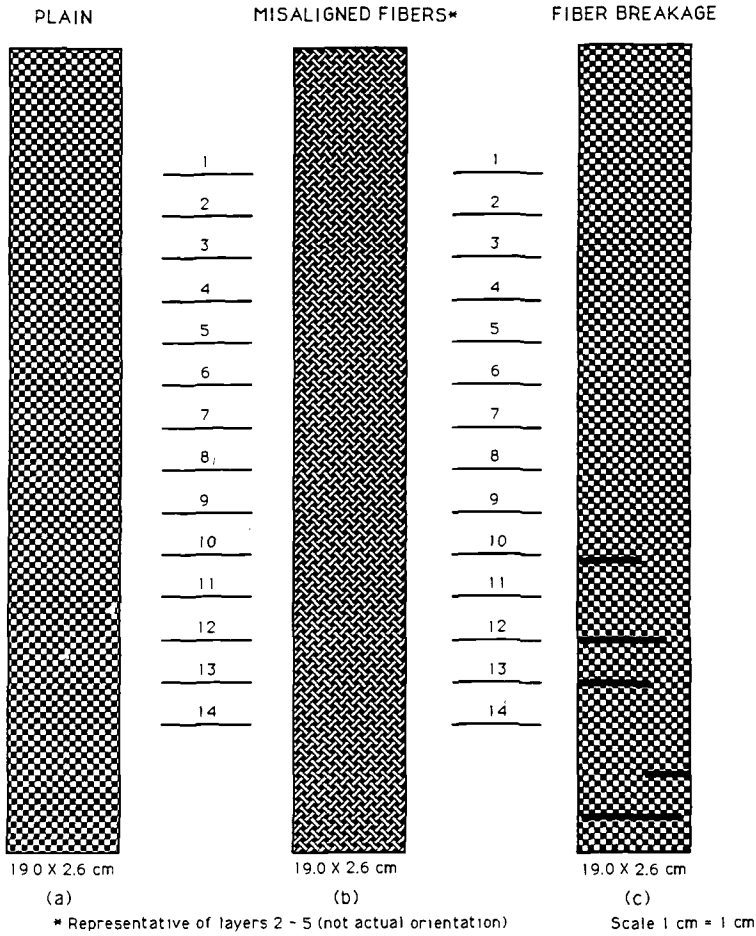

FIG. 6—*Demarcated regions for the graphite/phenolic composites:* (a) *good,* (b) *misaligned fibers,* (c) *fiber breakage.*

and the other half a delaminated region. Visual inspection after this process gave no indication of the delamination.

Graphite/Phenolic Specimens

Six layers of graphite fabric were impregnated with phenolic resin using the hand layup technique. The wet layup was cured by compression molding at 150°C and 450 Pa pressure for 70 min. Three different specimen types were studied using the same fabric/matrix system. These included nondefective and defective specimens. Defects included fiber breakage and misaligned fibers, which were introduced at the wet layup stage. In the specimen with misaligned fibers, the orientation of the fabric in Layers 2 through 5 was altered, with the first and sixth layers being "good."

Results and Discussions

Graphite/Epoxy Composite

For a typical Gr/Ep composite with a delamination, the values obtained from the force time histories via tapping the specimen at specific regions are summarized in Table 1. The force-time plots in the time domain for Regions 2 (delaminated) and 10 ("good") are shown in Fig. 7. These two regions were selected for representation purposes. Regions 6 through 10, which were the nondefective ("good") regions in the specimen, indicated an amplitude in the range of 6.6 to 8.6 V, while the delaminated Regions 1 through 5 exhibited amplitudes in the range of 6.4 to 7.2 V. More significant was the change in the duration of the pulse; the pulse width of the signal from the "good" regions was 0.56 to 0.688 ms, while in the delaminated zone a width in the range from 0.813 to 0.875 ms was observed.

These results indicate that the width of the input force pulse increases considerably in the presence of a gross area defect such as a delamination as expected and also as indicated by Cawley and Adams [*5*]. Amplitude of the force-time history is a parameter to be observed; however, this may not yield absolute information about the presence of a defect, especially if the delaminated zone is not well defined. For all regions tested in the specimen, the duration of the pulse obtained on the "good" regions was shorter as compared to regions with delamination. The duration of the pulse was smaller as the impact on a "good" region was more intense for a shorter duration, resulting in faster recovery of the striker. The duration of the input pulse at the delaminated region was consistently longer than that in a "good" region by an average of 2 ms regardless of the position of the tap.

Graphite/Phenolic Composites

Configuration 1—In this category three types of specimens were tested, including: (1) a "good" specimen, (2) a specimen with misaligned fibers (MIS), and (3) a specimen with fiber breakage (FB). Figure 8 illustrates representative force-time plots obtained for "good," MIS, and FB specimens. The test was conducted using Configuration 1, described earlier. The force-time histories were repeatable regardless of the region under test for the "good" specimen. Only slight variations in amplitudes were observed, while the duration of the pulse was almost identical, approximately 0.87 ms in all regions tested.

TABLE 1—*Values of force and time in the force-time histories for the graphite/epoxy composite (also refer to Fig. 5).*

Region	Force, V	Time, ms
	Delaminated	
1	6.6	0.875
2	7.2	0.844
3	6.6	0.875
4	6.8	0.875
5	6.4	0.813
	Good	
6	6.6	0.688
7	7.4	0.625
8	7.0	0.625
9	8.4	0.600
10	8.6	0.563

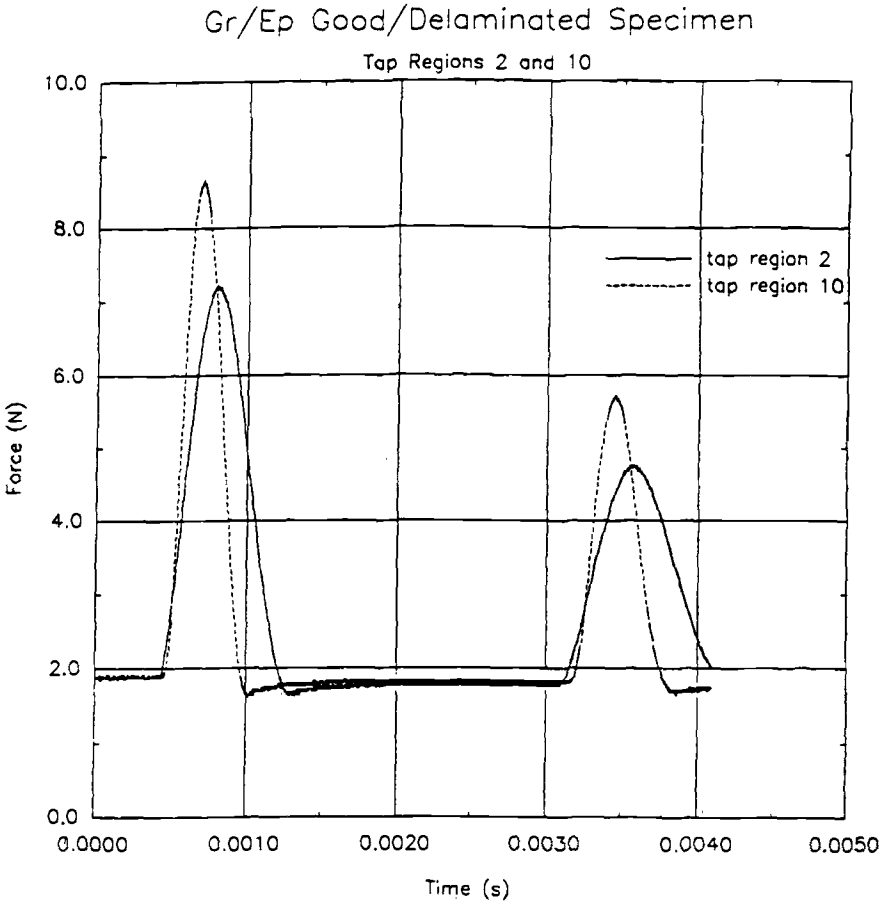

FIG. 7—*Force-time histories for the graphite/epoxy composite at Regions 2 and 10. (Note: Region 10 is the "good" region and Region 2 is the delaminated region.)*

The representative plot for Region 14 of a MIS specimen (see Fig. 6 for region number) indicates that the last three peaks are of smaller amplitude and longer time duration as compared to the "good" specimens shown in the figure. Also, the duration of the pulse for the peaks was longer (~0.87 ms) for the MIS specimen as compared to the "good" specimen. There was no noticeable change in both the pulse width and amplitude in the case of the first two peaks in the force-time plots for the "good" specimen as compared to the MIS and the FB specimens. Table 2 gives the values of force and time obtained when tested at different regions for the Gr/Ph specimens.

For the FB specimen, Regions 1 to 9 do not have defects, whereas Regions 10 to 14 had fiber breaks. Regions 1 through 9, which were away from the area of fiber breakage in the specimen, show longer duration of the input pulse ≈0.85 ms, and Regions 10, 11, and 14 show the width of the pulse to be in the range of 0.688 to 1.0 ms. Regions 10, 11, and 14 encompasss the fiber breakage and hence exhibit reduced stiffness in the vicinity of the fiber break and a longer pulse width.

In comparing the force-time histories between the "good" and the MIS specimen, the

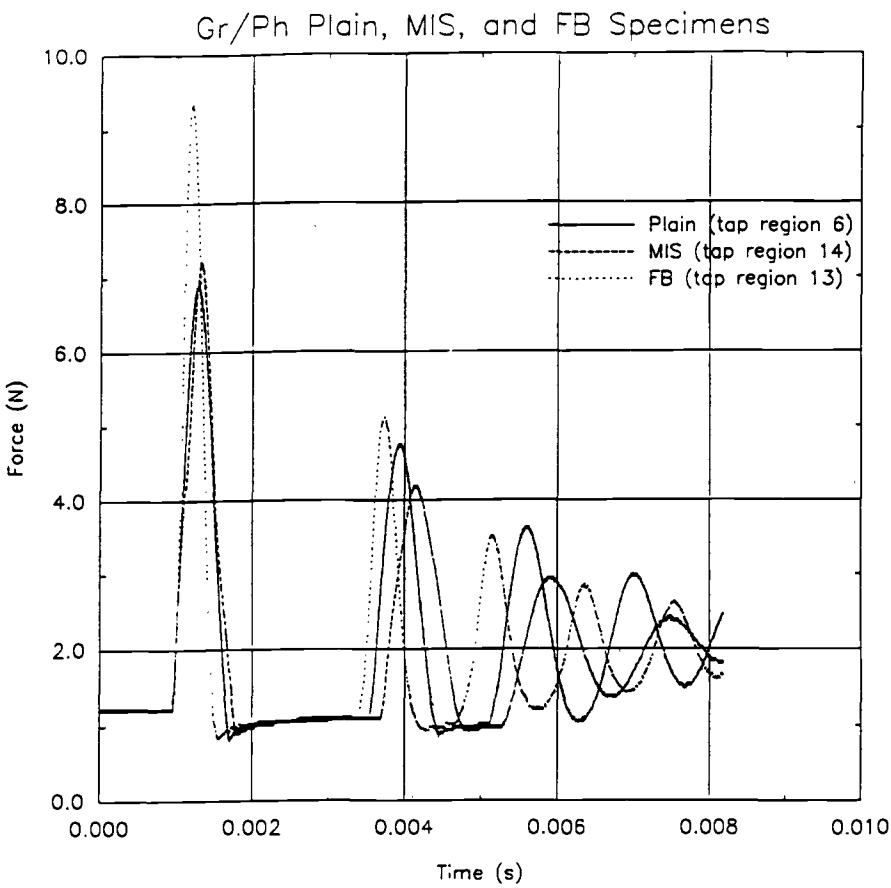

FIG. 8—*Force-time histories for the graphite/phenolic composites; "good," misaligned, and fiber breakage.*

TABLE 2—*Values of force and time in the force-time histories for the graphite/phenolic composites (also refer to Fig. 6).*

Good Specimen			Specimen with Misaligned Fibers			Specimen with Fiber Breakage		
Region	Force, V	Time, ms	Region	Force, V	Time, ms	Region	Force, V	Time, ms
1	6.800	0.857	1	6.600	0.813	1	4.500	1.250
2	6.500	0.750	2	6.500	0.813	2	6.600	0.813
3	7.000	0.750	3	6.600	0.875	3	7.400	0.688
4	7.000	0.750	4	7.500	0.750	4	7.200	0.750
5	7.200	0.750	5	6.500	0.750	5	6.900	0.688
6	6.800	0.750	6	6.700	0.750	6	6.500	0.875
7	7.200	0.750	7	7.200	0.813	7	7.100	0.813
8	7.200	0.750	8	6.300	0.813	8	7.400	0.750
9	5.800	1.000	9	6.000	0.875	9	5.800	1.000
10	6.700	0.875	10	5.900	0.875	10	6.900	0.750
11	7.200	0.750	11	5.500	1.000	11	6.600	0.688
12	6.500	0.750	12	6.500	0.875	12	8.600	0.625
13	8.400	0.625	13	7.100	0.875	13	9.400	0.563
14	6.600	0.750	14	7.200	0.875	14	5.800	1.000

changes in force-time histories are not significantly different. This is believed to be due to the low sensitivity to changes in contact stiffness at the point of impact of the striker even though the fibers are misaligned. In such a case, the use of Configuration 2 is immediately justified where the AE sensor is used in the vicinity of the striker.

Configuration 2—Figure 9 represents the time versus amplitude plot of signals arriving at the AE sensor obtained through measurement on a "good" specimen. Region 6 of the "good" specimen was used as a representative region to show the plot. The time signal contained a dominant amplitude in the wavefront, followed by a trailing decay. A similar pattern was observed in the other regions of the specimen.

Figure 10 represents the waveform for a FB specimen. A delayed rise time in the case of the AE signal from the region of the fiber break (Region 13) was observed. This could possibly be due to the interruption of the path of wave propagation due to the fiber break. The amplitude of the signal reduced slightly due to this process. A similar trend was observed in other regions of the specimen with fiber break (Regions 10 and 12).

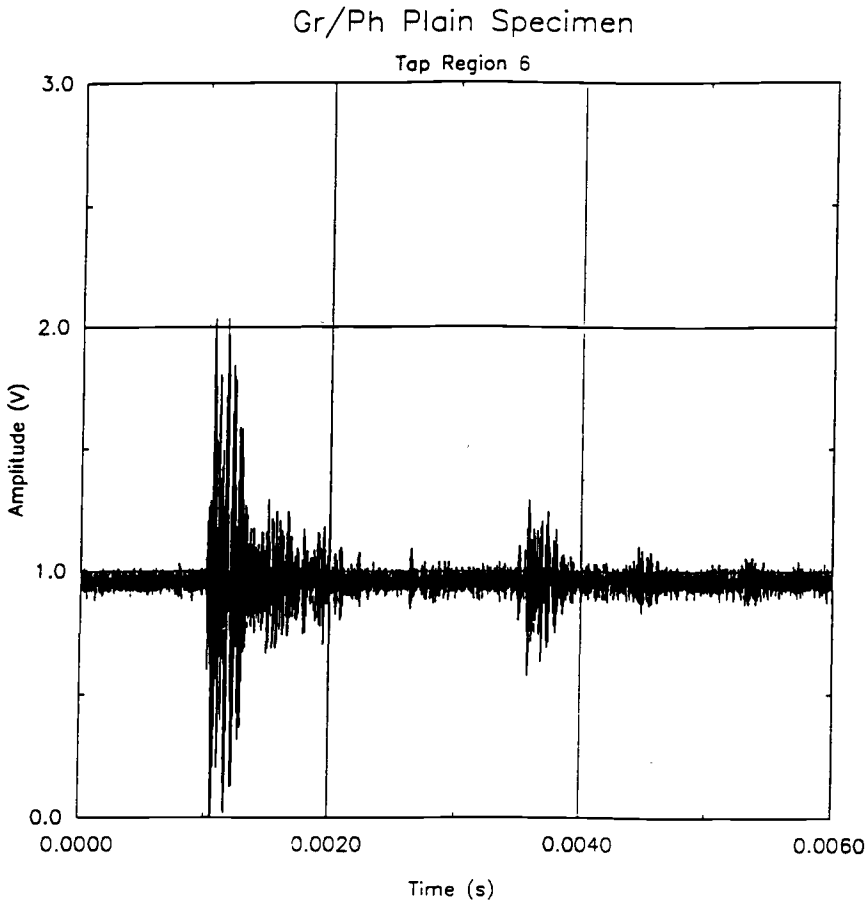

FIG. 9—*Acoustic emission waveform for Region 6 of the graphite/phenolic composite without defects.*

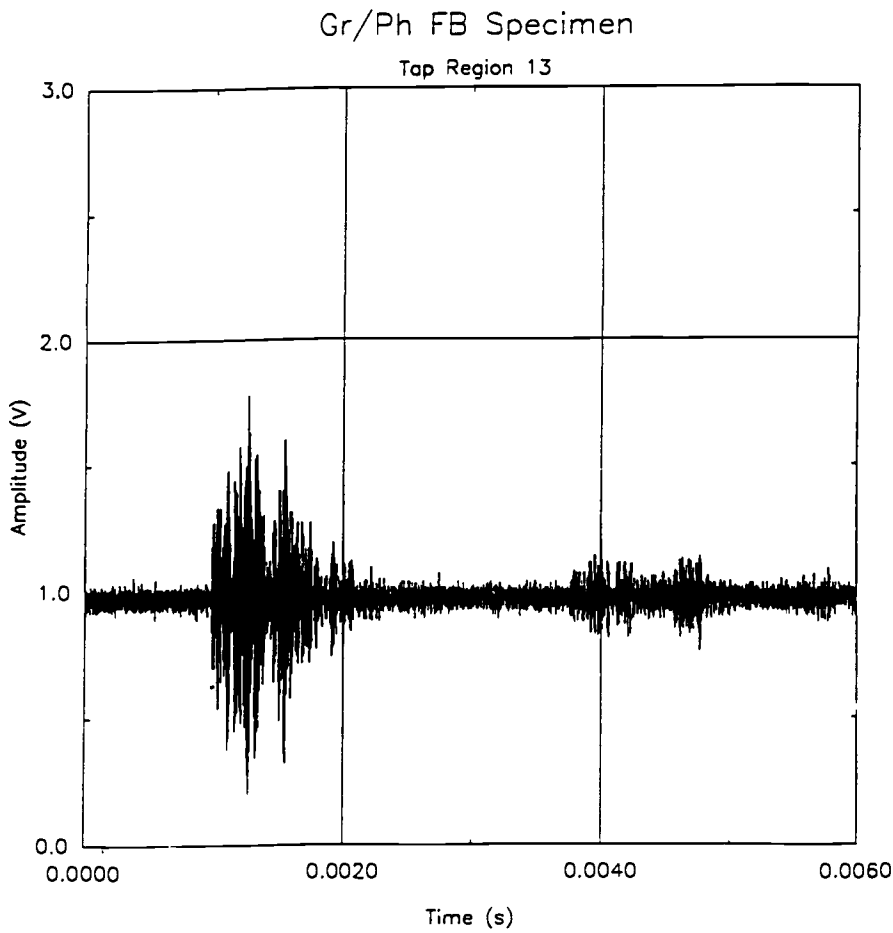

FIG. 10—*Acoustic emission waveform for Region 13 of the graphite/phenolic composite with fiber breakage. (Note: Region 13 contained the fiber breakage.)*

The MIS specimen exhibited distinctly different time versus amplitude plot as compared to the "good" and FB specimens (see Fig. 11). Many distinct wavepackets were observed in the signal as opposed to a dominant high-amplitude wavefront followed by a trailing decay as seen in a "good" specimen. These wavepackets were well separated in the time domain and were of smaller amplitude as compared to either the "good" or the FB specimens. This was observed in all the regions of the MIS specimen. As discussed earlier, the MIS specimen had misaligned fibers in Layers 2, 3, 4, and 5 out of the six layers of the Gr/Ep composite specimen. This difference in the time signal in the case of the MIS specimen suggests that the wave propagation modes are altered considerably due to the misalignment of fibers. Comparing the propagation modes in "good," FB, and MIS specimens, it can be observed that the wave packets in the MIS specimen are subjected to multiple reflections, increased scattering, and attenuation. The additional modes produced by a combination of these effects reach the receiver at different arrival times.

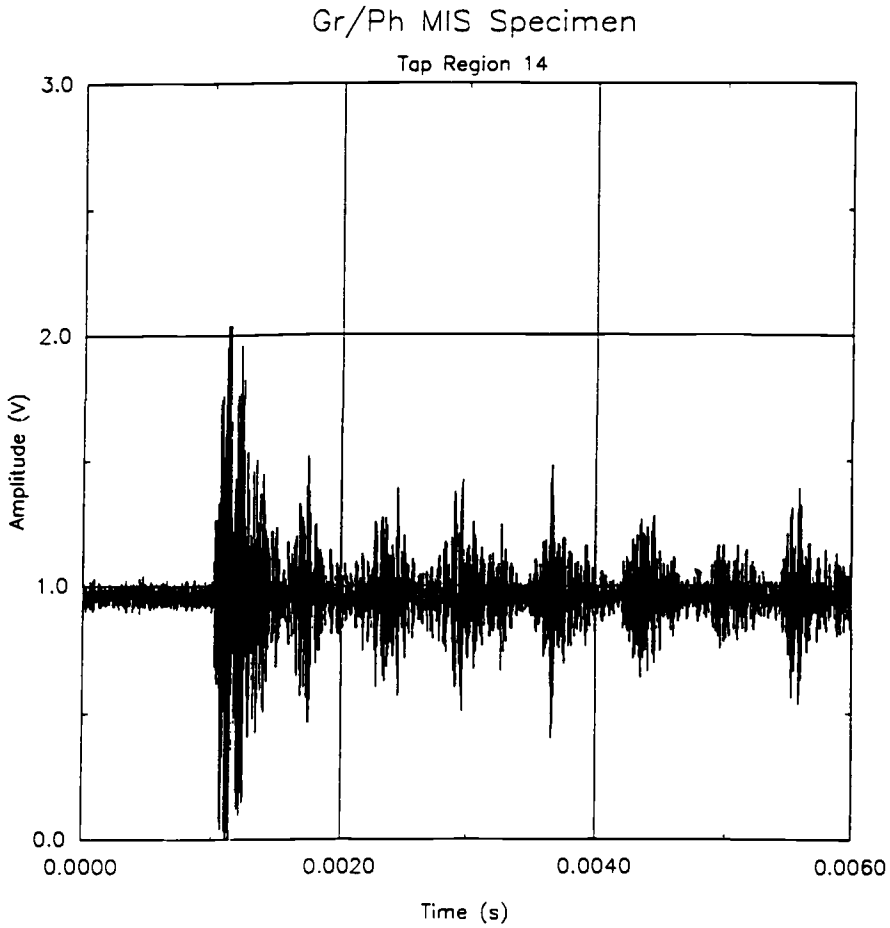

FIG. 11—*Acoustic emission waveform for Region 13 of the graphite/phenolic composite with misaligned fibers.*

Conclusion

An extensive literature search revealed five existing versions of coin-tap, instrumented coin-tap, and acoustic impact testing. Modification of existing versions of AIT into a single integrated test system incorporating conventional force-time history measurements and an AE sensor system enhanced the sensitivity of the test in graphite fiber-based composite materials. While gross delaminations in these composites were identified using conventional force-time history measurements, embedded flaws such as misaligned fibers and fiber breakage have been successfully identified by using AIT in conjunction with AE. Mass loading effects of placing the impact unit on the test structure have been eliminated. Efforts are underway to make the current modified version into a simple, portable, and automated unit.

References

[1] Schroeer, R., Roward, R., and Kamm, H., "The Acoustic Impact Technique–A Versatile Tool for Nondestructive Evaluation of Aerospace Structures and Components," *Materials Evaluation,* 1979, pp. 237–243.

[2] Reynolds, W. N., "Nondestructive Testing (NDT) of Fiber Reinforced Composite Materials," *SAMPE Quarterly,* Vol. 16, No. 4, July 1985, pp. 1–16.

[3] Hagemaier, D. and Fassbender, R., "Nondestructive Testing of Adhesively Bonded Structure," *SAMPE Quarterly,* Vol. 9, July 1978, pp. 36–58.

[4] Lange, Y. U. and Moskovenko, I. B., "Low-Frequency Acoustic Nondestructive Test Methods," *Soviet Journal of NDT,* Vol. 14, 1978, pp. 788–797.

[5] Cawley, P. and Adams, R. D., "The Mechanics of the Coin-Tap Method for Nondestructive Testing," *Journal of Sound and Vibration,* 1988, Vol. 122, No. 2, pp. 299–316.

[6] Adams, R. D. and Cawley, P., "Vibration Techniques in Nondestructive Testing," *Research Techniques in Nondestructive Testing,* R. S. Sharpe, Ed., Vol. VIII, Academic Press Inc. Ltd., London, 1985, pp. 303–360.

[7] Cawley, P. and Adams, R. D., "An Automated Coin-Tap Technique for the Nondestructive Testing of Composite Structures," *Proceedings,* 2nd International Conference on Testing, Evaluation, and Quality Control of Composites, TEQC-87, University of Surrey, Guildford, 22–24 Sept. 1987, pp. 11–15.

[8] Cawley, P. and Adams, R. D., "Sensitivity of the Coin-Tap Method of Nondestructive Testing," *Materials Evaluation,* Vol. 47, May 1989, pp. 558–563.

[9] Cawley, P., "The Sensitivity of the Mechanical Impedance Method of Nondestructive Testing," *NDT International,* Vol. 20, No. 4, August 1987.

[10] Jang, B. Z., Hsieh, H. B., and Shelby, M. D., "Real Time Cure Monitoring of Composite Structures using the Techniques of Mechanical Impedance Analysis," *Polymer Composites,* February 1991, Vol. 12, No. 1, pp. 66–74.

[11] Vaidya, U. K. and Murthy, C. R. L., "Defect Characterization in Glass Fiber Reinforced Composites (GFRC) Using the Acoustic Impact Technique (AIT)," *Journal of Non-destructive Evaluation,* ISNT, Vol. 10, No. 2, April–June 1990, pp. 30–40.

[12] Vaidya, U. K., "Nondestructive Evaluation of Defects in Glass Fibre Reinforced Composites by Acoustic Impact Technique," Master's thesis, Department of Aerospace Engineering, Indian Institute of Science, Bangalore, India, 1988.

[13] Murthy, C. R. L., Hegde, L. M., Ravindra, K. M., Sandhya, M., and Srinivasan, H. P., "Microprocessor Based Instrumentation for Acoustic Impact Testing," *Proceedings,* 89-WA/NDE-6, ASME Winter Annual Meeting, San Francisco, CA, P. K. Raju, Ed., 10–15 Dec. American Society of Mechanical Engineers, New York, 1989.

[14] Raju, P. K., Vaidya, U. K., Crocker, M. J., and Valaire, B. T., "Nondestructive Evaluation of Graphite Epoxy Composites Using Acoustic Techniques," *Proceedings,* NDE-ASME Winter Annual Meeting, San Francisco, California, P. K. Raju, Ed., Vol. 6, American Society of Mechanical Engineers, New York, December 1989.

[15] Raju, P. K., Patel, J., and Vaidya, U. K., "Characterization of Defects in Graphite Fiber Based Composite Structures using the Acoustic Impact Technique (AIT)," *ASTM Journal of Testing and Evaluation,* Vol. 21, No. 5, September 1993, pp. 377–395.

[16] Patel, J., Vaidya, U. K., and Raju, P. K., "Defects Identification of Composites using the Acoustic Impact Technique," paper presented at the annual meeting of the Alabama Academy of Sciences, University of Alabama, Tuscaloosa, AL, April 1992.

[17] *Acousto-Ultrasonics–Theory and Application,* J. C. Duke, Ed., Plenum Press, New York, 1988.

Author Index

Subject Index

ISBN: 0-8031-1989-5